# Fabrication of Hard-to-Process Ni-Based Superalloy Thin-Wall Parts Made by Laser Powder Bed Fusion

by

Apratim Chakraborty

A thesis

presented to the University of Waterloo

in fulfillment of the

thesis requirement for the degree of

Doctor of Philosophy

in

Mechanical and Mechatronics Engineering

Waterloo, Ontario, Canada, 2022

# Examining Committee Membership

The following served on the Examining Committee for this thesis. The decision of the Examination Committee is by majority vote.

| | |
|---|---|
| **External Examiner** | ALIREZA SADEGHI, Ph.D.<br>Assistant Professor<br>Department of Mechanical Engineering<br>University of Tehran |
| **Supervisor** | ÉTIENNE MARTIN, Ph.D.<br>Associate Professor<br>Department of Mechanical Engineering<br>Polytechnique Montréal<br><br>Adjunct Assistant Professor<br>Department of Mechanical and Mechatronics Engineering<br>University of Waterloo |
| **Supervisor** | MUSTAFA YAVUZ, Ph.D.<br>Professor<br>Department of Mechanical and Mechatronics Engineering<br>University of Waterloo |
| **Internal Member** | KAAN INAL, Ph.D.<br>Professor<br>Department of Mechanical and Mechatronics Engineering<br>University of Waterloo |
| **Internal Member** | KEVIN MUSSELMAN, Ph.D.<br>Assistant Professor<br>Department of Mechanical and Mechatronics Engineering<br>University of Waterloo |
| **Internal-External Member** | EIHAB ABDEL-RAHMAN, Ph.D.<br>Professor<br>Department of Systems Design Engineering<br>University of Waterloo |

# Author's Declaration

This thesis consists of material all of which I authored or co-authored: see Statement of Contributions included in this thesis. This is a true copy of the thesis, including any required final revisions, as accepted by my examiners.

I understand that my thesis may be made electronically available to the public.

# Statement of Contributions

The following co-authors have contributed to the current work as outlined below:

- Professor Étienne Martin (Polytechnique Montréal and Adjunct at University of Waterloo) supervised, conceptualized, and reviewed this PhD thesis, provided mentorship and guidance, and arranged for funding and resources to perform the experimental and simulation work.
- Professor Andrew Wessman (University of Arizona) provided some of the raw materials needed to conduct the experimental work and reviewed parts of the work.
- Professor Lang Yuan (University of South Carolina) provided some of the raw materials for the experiments, guidance for the experimental and simulation analyses, and reviewed parts of the work.
- Dr. Waqas Muhammad (Former Postdoctoral Fellow, University of Waterloo) performed EBSD analyses, provided mentorship and guidance, and helped conceptualize and review parts of the work.
- Dr. Rasim Batmaz (Former Postdoctoral Fellow, University of Waterloo) performed material preparation and microstructure characterization, provided mentorship and guidance, and reviewed parts of the work.
- Dr. Trevor Sabiston (Former Postdoctoral Fellow, University of Waterloo) helped write the discussions and analyses of the modelling sections, provided mentorship and guidance, and reviewed parts of the work.
- Reza Tangestani (PhD Candidate, University of Waterloo) conducted and analyzed the numerical simulations, helped write the discussions and analyses, and reviewed the presented modelling sections.
- Khadijeh Esmati (PhD Student, Polytechnique Montréal) performed material preparation and microstructure characterization for parts of this work.
- Philippe Plamondon (Research Associate, Polytechnique Montréal) performed SEM imaging and characterization for parts of the work.
- Jean-Philippe Masse (Research Associate – Microscopist, Polytechnique Montréal) performed TEM imaging, characterization, and analysis for parts of the work.
- Dr. Morteza Ghasri Khouzani (Postdoctoral Fellow, University of Waterloo) provided valuable advice and reviewed parts of the work.
- Nicholas Krutz helped with discussions of the modelling sections and reviewed parts of the work.
- The balance of work is my own.

The following first-author publications related to my PhD thesis have been published, submitted, or under peer review, and constitute the body of my PhD thesis:

Chapter 5 – **Chakraborty, A.**, Tangestani, R., Batmaz, R., Muhammad, W., Plamondon, P., Wessman, A., Yuan, L., & Martin, É. (2022). In-process failure analysis of thin-wall structures made by laser powder bed fusion additive manufacturing. Journal of Materials Science and Technology, 98. https://doi.org/10.1016/j.jmst.2021.05.017

Chapter 6 – **Chakraborty, A.**, Tangestani, R., Muhammad, W., Sabiston, T., Masse, J.-P., Batmaz, R., Wessman, A., & Martin, É. (2022). Micro-cracking mechanism of RENÉ 108 thin-wall components built by laser powder bed fusion additive manufacturing. Materials Today Communications, 30. https://doi.org/10.1016/j.mtcomm.2022.103139

Chapter 7 – **Chakraborty, A.**, Tangestani, R., Sabiston, T., Krutz, N., Yuan, L., & Martin, E. (2022). Effect of build height on micro-cracking of additively manufactured superalloy RENÉ 108 thin-wall components. TMS 2022 Annual Meeting and Exhibition. https://doi.org/10.1007/978-3-030-92381-5_94

Chapter 8 – **Chakraborty, A.**, Muhammad W., Masse J.-P., Tangestani, R., Khouzani, M.G., Batmaz, R., Wessman, A., & Martin, E. (2022). Micro-cracking in additively manufactured high-gamma-prime Ni-based superalloy thin-wall components. Under peer review

Chapter 9 – **Chakraborty, A.**, Tangestani, R., Sabiston, T., Esmati, K., Yuan, L., & Martin, E. (2022). Mitigating inherent micro-cracking in laser additively manufactured RENÉ 108 thin-wall components. Additive Manufacturing. Under Review. June 2022.

The research work carried out during the course of my PhD has also contributed to the following publications. These published articles do not directly influence the achievement of the research objectives. However, some of the publications provide further insight on the modelling methodologies covered in this thesis.

**Journal articles:**

Article 1 – Tangestani, R., Sabiston, T., **Chakraborty, A.**, Muhammad, W., Yuan, L., & Martin, É. (2021). An efficient track-scale model for laser powder bed fusion additive manufacturing: Part 1-thermal model. Frontiers in Materials, 477. https://doi.org/10.3389/fmats.2021.753040.

Article 2 – Tangestani, R., Sabiston, T., **Chakraborty, A.**, Yuan, L., Krutz, N., & Martin, É. (2021). An Efficient Track-Scale Model for Laser Powder Bed Fusion Additive Manufacturing: Part 2—Mechanical Model. Frontiers in Materials, 8. https://doi.org/10.3389/fmats.2021.759669.

Article 3 – Batmaz, R., Zardoshtian A., Sabiston T., Tangestani, R., **Chakraborty, A.**, Krutz, N., Pendurti, S., Natarajan A., Martin, E. (2022). An Investigation into Sinterability Improvements of 316L Binder Jet Printed Parts. Metallurgical and Materials Transactions A. https://doi.org/10.1007/s11661-021-06564-3.

Article 4 – Khouzani, M. G., Karimialavijeh, H., Pröbstle M., Batmaz, R., Muhammad, W., **Chakraborty, A.**, Sabiston, T., Harvey, J.-P., Martin, É. (2022). Microstructure and mechanical properties of A20X aluminum alloy fabricated by laser powder bed fusion with various process parameters. Journal of Materials Processing Technology. Submitted. June 1, 2022.

Article 5 – Im, S., Khouzani, M.G., Muhammad, W., Batmaz, R., **Chakraborty, A.**, Natarajan, A., Martin, É. (2022). Evaluation of different sintering agents for binder jet additive manufacturing of aluminum alloy. Metallurgical and Materials Transactions A. Submitted. July 3, 2022.

Article 6 – Tangestani, R., **Chakraborty, A.**, Sabiston, T., Yuan, L., Khouzani, M.G., Martin, É. (2022). Modular Numerical Modelling Framework to Study Part Failure in Laser Additive Manufacturing. Under Peer Review.

**Conference Proceedings:**

Article 1 – Tangestani, R., **Chakraborty, A.**, Sabiston, T., & Martin, É. (2021). Inter-dependent influences of the laser powder and printing pattern on residual stresses in laser powder bed fusion additive manufacturing. 9th International Conference on Mechanics and Materials in Design. Funchal/Portugal. 26-30 June 2022. https://paginas.fe.up.pt/~m2d/proceedings_m2d2022/.

Article 2 – **Chakraborty, A.**, Tangestani, R., Sabiston, T., Martin, É. (2022). Mitigating build defects in additively manufactured thin-wall components using laser scan strategy. TMS 2023 Annual Meeting and Exhibition. Accepted. August 8, 2022.

**Technical Presentations:**

Talk 1 – **Chakraborty, A.** (2020). Investigation of in-process cracking in LPBF thin-wall structures. GE technical presentation. April 23, 2020.

Talk 2 – **Chakraborty, A.**, Tangestani, R. (2022). High-γ' Ni-based superalloys thin-wall part fabrication by laser powder bed fusion. GE technical presentation. April 28, 2022.

# Abstract

Thin-wall part fabrication is significant for aerospace, automotive, and thermal applications, which require complex metallic features hard to manufacture using conventional manufacturing processes. Laser powder bed fusion (LPBF) additive manufacturing (AM) technique enables the construction of such components with added design flexibility. However, build challenges, such as micro-cracking and in-process failure, inherent in LPBF, limit processability and affect final part quality. Micro-cracking is especially important for high γ' Ni-based superalloys, which are used in serpentine-shaped components such as fuel nozzles and turbine vanes in gas turbine jet engines. To better understand the underlying mechanisms for thin-wall failure and determine if micro-cracking affects in-process failure, metallurgical and mechanistic factors affecting part processing must be considered. In this thesis, micro-cracking statistics, in-process stresses, part displacements, and stress triaxiality states are evaluated for thin-wall parts made with different build conditions, including different wall thicknesses, scan strategies, and alloy compositions. Experimentally-obtained and numerically-simulated results are used to explain in-process failure and determine optimal thin-wall build conditions to reduce in-process micro-cracking.

Firstly, a design of experiment (DOE1) including two different alloy compositions, RENÉ 65 (R65) and RENÉ 108 (R108), and three different part thicknesses, 5.00 mm, 1.00 mm, and 0.25 mm, is developed to evaluate the in-process failure and micro-cracking trends for thin-wall parts built with LPBF. The materials chosen in this study represent high γ' Ni-based superalloys with different γ' contents and solidification ranges, beneficial to observe different types of micro-cracking behavior. As-processed thin-wall parts demonstrate different limiting build heights (LBHs) with respect to wall thickness. Builds with thinner walls fail to achieve the designed part height, exhibiting lower LBHs compared to thicker parts for both R65 and R108. Microstructure characterization shows that micro-cracking is independent of the LBH effect as R108 thin-wall components exhibit larger crack densities than R65. The stress distributions along the build height of a thin-wall part also do not contribute to LBH as the stresses increase with wall thickness. Ultimately, the reduced LBH in thinner structures is correlated to increased part distortion, resulting from increased compressive stresses along the length and height directions. The slenderness ratio is proposed as a valuable tool to consider during design to achieve the desired height and avoid premature failure during LPBF thin-wall part fabrication.

The following study explores the effect of wall thickness on the micro-cracking tendencies and elucidates the micro-cracking mechanism in LPBF-processed thin-wall parts using the highly crack-susceptible R108. Experiment-based statistical analysis confirms increased micro-cracking with larger wall thickness, agreeing well with the previous work. Electron microscopy shows that all micro-cracks exhibit inter-dendritic morphologies indicating the solidification cracking mechanism. Contrary to other studies, micro-cracking is not caused by

carbides or borides, as the Hf-,Ta-,Ti-rich carbide phases are fine and homogeneously distributed within the microstructure. All wall thicknesses have higher tendency to form straight micro-cracks along the build direction (BD). Numerical simulations performed at the layer scale show that thicker parts generate higher in-process tensile stresses and exhibit positive stress triaxialities during build progression, supporting the higher micro-cracking propensities observed in thicker parts. Beam-scale simulations show that the stress triaxiality state becomes positive at a higher (super-solidus) temperature within the melt pool, which along with high in-process tensile stresses supports larger number of straight micro-cracks.

The effect of in-process stresses on the micro-cracking densities is supported by a short study on the influence of build position on LPBF thin-wall component micro-cracking. Experimental results show that micro-cracking is lower at the base of the build. Numerical simulations predict compressive stresses at lower build positions, supporting the experimental finding and indicating that in-process stresses contribute to micro-cracking in thin-wall parts.

Subsequently, the effect of laser scan strategy on thermally-influenced stresses and cracking behavior is studied by generating a large DOE consisting of 32 R108 thin-wall parts including four different wall thicknesses (1.00 mm, 0.75 mm, 0.50 mm, and 0.25 mm) and ten different scan strategies. The effects of vector length and scan rotation are examined separately for different wall thicknesses. Thicker parts always demonstrate higher crack densities due to earlier transition to positive stress triaxialities and larger stress magnitudes. As the vector length increases, the micro-cracking propensity increases for all wall thicknesses. This observation is explained using two separate finite element model for parts processed with short and long vector lengths, respectively. Longer vector lengths produce larger in-process stresses perpendicular to BD and transition earlier to positive stress triaxialities, supporting the larger number of micro-cracks determined experimentally. The study of inter-layer scan rotations during processing indicates that the alternating short scan strategy is preferred over the continuous 67° scan rotation strategy for thicker parts. These results open up simple viable alternatives to mitigating micro-cracking in LPBF thin-wall parts by changing the wall thickness or laser scan strategy.

Finally, the effect of alloy composition on micro-cracking is investigated to better understand the internal micro-cracking mechanisms in high-γ' Ni-based superalloys. Two LPBF-printed thin-wall components made of R65 and R108 with identical thicknesses of 1.00 mm are studied. The micro-cracking propensity of R108 is higher than R65 and the cracking behavior is interdendritic, which suggests the solidification cracking mechanism. Higher cracking in R108 is supported by finite element simulations which show that the stress triaxiality is positive at higher temperatures in R108 compared to R65. Thermodynamic simulations show that R108 has higher liquid fractions in the terminal stages of solidification which makes the material weaker at high temperatures under positive stress triaxiality conditions.

# Acknowledgements

First and foremost, I thank both my supervisors Professor Étienne Martin and Professor Mustafa Yavuz for their invaluable support and motivation during the course of my PhD journey. Professor Martin put his faith in me, provided me financial and moral support, and pushed me to achieve things I could have never imagined at the start. Professor Martin was always available for questions and helped me immensely during challenging times. Outside of work, he was like my elder brother who I could call upon at any time for life advice. Professor Yavuz has been an influential mentor and father-like figure throughout my graduate studies and he continued believing in me during difficult times. Without their continued guidance and patience, I would not be in a position to defend my PhD thesis today, so "Thank you Étienne and Professor Yavuz from the bottom of my heart. Forever grateful to you both."

My sincere thanks to my PhD examination committee members Professors Alireza Sadeghi, Eihab Abdel-Rahman, Kaan Inal, and Kevin Musselman for taking the time to review my thesis and providing their invaluable feedbacks. I am forever grateful to Professors Andrew Wessman at University of Arizona and Professor Lang Yuan at University of South Carolina for helping with part fabrication to perform my experimental tasks and providing me sage advice along the way. I am grateful and privileged to have had the opportunity to have worked with both professors.

I thank my dear colleague and friend Dr. Waqas Muhammad for his continued guidance, motivation, and strong beliefs in my abilities, which encouraged me to tackle various challenges during my PhD. "Waqas, thank you for being my inspiration as I took on the quest to conquer my PhD looking up to you as a leader and an elder brother". I also thank Professor Daniel Wei who spent countless hours teaching me about material sciences, provided me valuable advice on achieving "success" in my life and career, and inspired me to think outside the box. Both were instrumental towards preparing for my comprehensive exam and writing my first journal papers.

My heartfelt gratitude goes towards my dear colleague and friend Reza Tangestani without whose superior numerical modelling prowess I would not be able to complete my papers and this thesis. I thank him for being up with me late nights to discuss about work, life, and being there for me as a brother during difficult times. A big thanks to Dr. Rasim Batmaz who was there with me since the start of this PhD project, helping me immensely with my experimental work and providing me valuable advice as a colleague and a brother. Thanks to Dr. Trevor Sabiston for his patience, guidance, and motivation to help me with my papers, and being readily available for questions about work and life. Also, thanks to Solgang Im for being a wonderful colleague, friend, and a sister-like figure I could rely on for support and motivation during the course of my PhD.

Thanks to my all my research colleagues and friends, but special thanks goes out to Khadijeh Esmati and Heidar Karimialivijeh who helped me acclimate to life at Polytechnique after the departure of Rasim. I am sincerely grateful to Khadijeh for her experimental work leading to the submission of my 3rd first-author journal paper. Thanks to the entire research team, with special mentions to Morteza Ghasri-Khouzani, Anindya Das, Hong-Yan, Maxime Paques, Alexander Abanobi, and Abouthaina Sadallah for helping me in the quest.

The experimental work was possible due to excellent research facilities at University of Waterloo (UW) and Polytechnique Montréal (PolyMTL). I thank the MSAM, (CM)2 and LAPOM management and staff for allowing me to conduct my PhD research and complete my experimental tasks. Special thanks to Professor Ehsan Toyserkani and Henry Ma at MSAM-UW, Professor Giles L'Ésperance, Philippe Plamondon, Jean-Philippe Masse, Éric Duchesne, Olivier Girard, Étienne Boussard, and Paul Lambert at (CM)2-PolyMTL, and Professor Myriam Brochu, Josée Laviolette, Paul Provencher, Nicolas Jacquot, and Laura Pressie at LAPOM-PolyMTL.

I am deeply thankful to Natural Sciences and Engineering Research Council of Canada (NSERC) under grant no. CRDPJ 533406-18, and Amber Andreaco, working in the material supply division at GE additive, for supporting this work.

My heartfelt thanks to all my friends at UW and PolyMTL for helping me push through the PhD barrier. Special thanks to my former PhD colleagues Khaled Ibrahim, Kissan Mistry, and Inna Novodchuk for being like my siblings. Also, thanks to my former research colleagues Jaspreet Nagra, Ali Zardoshtian, Niloofar Eftekhari, and Murali Kumar to help me get through some difficult phases during the journey. Big thanks to the UW administrative staff for being approachable and available for questions. Special thanks to Jian, Adrian, Allison, Tanya, Jen, Karen, and Robyn for their support. My sincere thanks to Professors Kankar Bhattacharya and Patricia Nieva for being my mentors outside research. A big thanks to Karine Gervais for her warmth and support along the journey. To achieve my milestone, I was fortunate to have the moral support of my two dad-like figures Alain and Amador in my place in Montréal. Thank you to my close friend and brother-like Dr. Pranav Agarwal for believing in me, cheering me up during tough times, and being a big inspiration. Very special thanks to my dear friend Nivas Ramachandran, and my cousins Atul Chakraborty, Sagorika Chakraborty and Anupa Mukherjee, and sister-like Soumi Mitra for their unwavering support and belief in me during the PhD journey. A big thanks to my entire family, extended family, and anybody I missed thanking for maintaining faith in me and my abilities.

Finally, and most importantly, I would like to thank my mother, father, and brother for being there with me every step of the way during times of happiness, sadness, and my rainbow of emotional swings. "You all are my sources of strength and inspiration for my life and career. You are my everything. Love you all."

My life and this work is indebted to the ALMIGHTY, my inspirational grandparents, and my family.

## Dedication

*In Loving Memory of my Late Grandparents and my Maternal Grandma who Longs to See Me. Mitua, Amma, Dada, and Didaan, This One is for You.*

# Table of Contents

# List of Figures

# List of Tables

# List of Equations

# Chapter 1
# Introduction

## 1.1 Motivation

Additive manufacturing (AM), also known as three-dimensional (3D) printing is a revolutionary technology to fabricate complex geometries (for example, thin-wall shapes shown in **Figure 1-1**) with specialized functionalities. Compared to conventional manufacturing techniques, such as casting and welding, AM technologies such as selective laser melting (SLM) or laser powder bed fusion (LPBF) produce near net-shape parts reducing time between design and final production [1]. Applications of AM include fuel nozzles in aeroengines, skull implants, turbines in automobiles, medical dentures, heat exchangers in power plants, and drill tips for machining. Many industries are trying to adopt the AM technologies to develop a competitive edge in the global market.

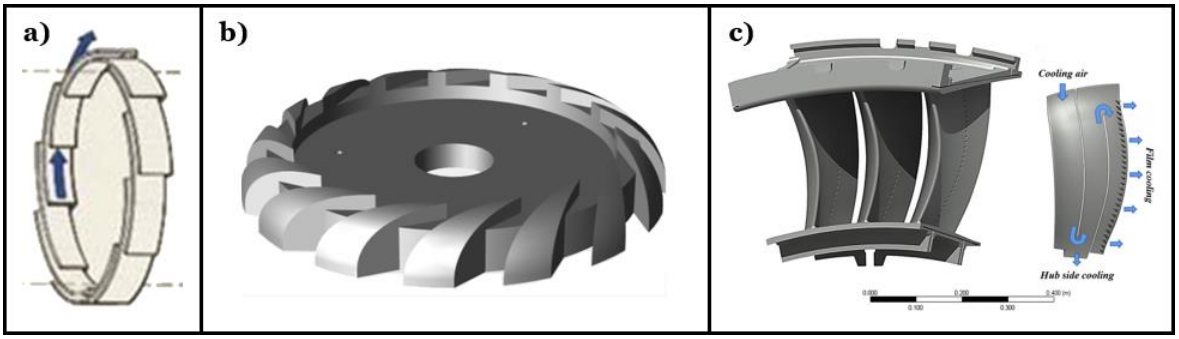


**Figure 1-1:** Static Components in a Gas Turbine Engine Exhibiting Complex Thin Wall Geometries: **(a)** Diffuser in High-Pressure Compressors [2], **(b)** Diffuser Vanes, and **(c)** Turbine Vane with Serpentine-Type Internal Passages and Film Cooling Holes on the Pressure-Side Surfaces [3].

The aerospace industry is attempting to bring AM products to the market for fabrication of complex parts with functionally-graded materials for high temperature applications. However, to achieve the desired material properties, strategies need to be implemented to develop AM capability for thin wall parts made of materials with complex microstructures. Gas turbine engines, for instance, consist of parts with very thin geometries and tight tolerances, and require materials which can maintain strength at high operating temperatures. A gas turbine engine is essential because it generates the power for jet propulsion and operation of the aircraft. Failure of these components could have catastrophic consequences such as loss of human life due to fire or engine shut down [4].

Most gas turbine engines are composed of “hot” and “cold sections as shown in **Figure 1-2**. In the hot section and the latter stages of compression in the cold section, materials are required to: (1) maintain mechanical

properties under operating temperatures close to melting point ($T_{operating}/T_{melting} > 0.6$), (2) resist mechanical degradation due to loading (creep resistance), and (3) tolerate severe environments (corrosion/oxidation resistance) [4]. Ni-based superalloys are suitable for these components (such as diffusers, combustors, fuel nozzles and turbine vanes) due to their superior strength and resistance to unfavorably harsh environmental conditions at high operating temperatures.

To meet the criteria for high temperature application in gas turbine engines, high-strength Ni-based superalloys with high volume fraction of γ' precipitates need to be manufactured. The advent of metal laser AM has boosted the capability to manufacture high-resolution complex near-net shape parts with Ni-based superalloys. Application of the process is currently limited to static parts such as diffuser, turbine and nozzle guide vanes because dynamic parts are not mature enough for AM yet. However, laser AM fabrication poses many in-process challenges such as pores, lack-of-fusion voids, micro-cracking, microstructure heterogeneity, distortion, and part failure. In order to fabricate functional defect-free parts with complex shapes, these challenges must be overcome.

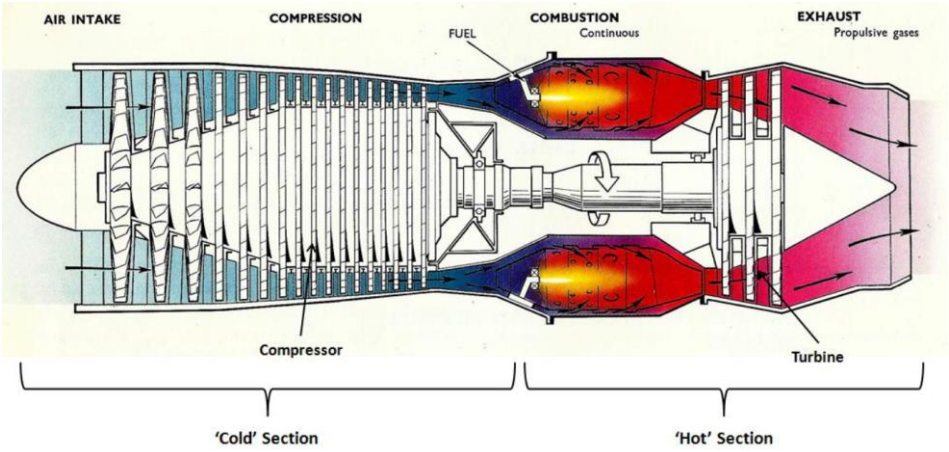


**Figure 1-2:** Key Stages and Components of a Simple Single Spool Gas-Turbine Jet Engine [5].

Successful fabrication of thin-wall parts is fundamental to the production of larger parts with complex structures using LPBF. To improve buildability, the micro-cracking mechanism and in-process failure observed in LPBF thin-wall parts must be better understood. Micro-cracking is especially important for high-γ' Ni-based superalloys possibly due to heavy elements vulnerable to wider solidification range, severe microsegregation, and overlapping solvus and solidus causing large thermal bending strains during processing. The thermally-induced stresses generated due to the rapid solidification process and tight-threshold geometry likely also contribute to in-process failure and increased micro-cracking. To enhance thin-wall part processability and facilitate adaptation

of high-γ' Ni-based superalloys to the LPBF process, the complex geometry-process-chemistry relationship must be thoroughly investigated and custom build strategies must be developed.

## 1.2 Thesis Scope and Outline

The goal of this research is to understand and propose ways to improve thin-wall part buildability using LPBF. Fabrication challenges such as in-process failure and micro-cracking, specific to hard-to-weld high-γ' Ni-based superalloys, are examined in detail. The micro- and macro-scale characteristics of the processed thin-wall parts are studied using both experimental and simulation analyses to shed light on the underlying reasons responsible for the build impediments. The PhD thesis consists of 10 chapters, where the first chapter covered here is the introduction. Brief summaries of the subsequent chapters are provided below:

- **Chapter 2** provides background of the additive manufacturing process, Ni-based superalloys, the LPBF microstructure, and the methodologies relevant to this study.
- **Chapter 3** presents critical literature elucidating the limiting factors for high-γ' Ni-based superalloy thin-wall part fabrication.
- **Chapter 4** discusses the research strategy and map tying the research work to the thesis goal. Content overview for each chapter is provided in detail.
- **Chapter 5** investigates the causes for in-process failure observed in LPBF thin-wall parts. A simple mechanistic explanation for the in-process failure is presented.
- **Chapter 6** assesses the micro-cracking phenomenon in thin-wall parts made of a high-γ' Ni-based superalloy. The effect of varying wall thicknesses on the micro-cracking behavior is studied. From this chapter onwards, the focus shifts to micro-cracking only.
- **Chapter 7** elucidates the effect of build position on the micro-cracking phenomenon in LPBF thin-wall parts. The effect of in-process stresses on micro-cracking during processing is discussed.
- **Chapter 8** studies the effect of alloy composition on LPBF micro-cracking for a fixed wall thickness and fixed processing conditions. The micro-cracking tendencies for two different Ni-based superalloys with high γ' content are investigated in detail.
- **Chapter 9** explores the effect of wall thickness and scan strategy on inherent micro-cracking during LPBF processing. Several samples covering a large range of scanning conditions and wall thicknesses are investigated for micro-cracking behavior. Approaches to mitigate micro-cracking in thin-wall parts made by LPBF are proposed.
- **Chapter 10** provides the major conclusions obtained from the PhD research work and gives recommendations for improving thin-wall part processability and minimizing LPBF micro-cracking.

# Chapter 2
# Background

## 2.1 Superalloys

The prefix "super" in superalloy implies supreme strength perhaps depicting the strength of a popular fictitious DC Comics hero named Superman. The origin of this name is still a mystery to many, but the "Man of Steel" was an inspiration to the development of arguably the strongest family of metal alloys known to mankind [6,7]. The following sections provide a brief overview of the history and types of superalloys, with special emphasis on Ni-based superalloys due to their relevance to the thesis topic.

### 2.1.1 Brief History

An integral part of the industrial revolution, led by the invention of the first steam engine by Thomas Newcomen in 1712 [8], resulted in the development of gas turbine and jet engines. The invention of the first airplane at the beginning of the 20$^{th}$ century by the famous Wright Brothers accelerated the need for engines which could sustain operation at high temperatures. Materials were needed to help build the turbosupercharger for internal combustion of the air/fuel mixtures at high altitudes [9]. Scientists concluded that turbulent drag, lift and supersonic forces necessitated the development of the jet-powered engines. Around the same time period, austenitic stainless steel was discovered in search of improved corrosion-resistance. The austenitic (corrosion-resistant Ni and Cr-rich) gamma ($\gamma$) phase of the stainless steel inspired the birth of the first superalloys in the 1920s [9]. Due to the resurgence of strengthened nickel-chromium alloys, Bradley and Taylor were encouraged to further enhance the properties of superalloys by identifying the tiny coherent gamma prime ($\gamma$') phase within the $\gamma$ matrix in 1940. The prefix "super" became a household term around this time due to the budding fame of the name 'Superman' which was first coined in 1938 [10]. From then on, France, England, United States, and Germany were the frontrunners in the rapid advancement of the "super" alloys [6,9,11].

Superalloys represent a class of metal alloys that show improved strength relative to other metals or metal alloys at elevated temperatures (between 1000 °F (540 °C) and 2000 °F (1100 °C) [11]. Typically, metals become more ductile as the temperature increases, but superalloys are stronger at high temperatures due to the unique strengthening effect of coherent ordered $\gamma$' phase within the disordered face-centered-cubic (FCC) $\gamma$ phase (see **Section 2.1.2** for more details). This property makes superalloys very suitable for high-temperature applications such as turbine blades and compressor vanes in aircraft gas turbine engines [11]. In addition to high-temperature tensile, stress rupture, and creep strength, superalloys also have good impact resistance to go along

with good ductility, resistance to high and low-cycle mechanical fatigue, and thermal fatigue. Applications are not just limited to aircraft, as superalloys are used in marine and land-based turbines, space vehicles, rocket engines, nuclear reactors, submarines, steam power plants and petrochemical equipment [11]. Common categories of superalloys include nickel-based (Ni-based), iron-based (Fe-based) and cobalt-based (Co-based) superalloys. The Ni-based superalloys have shown the highest phase stability (maintains FCC structure) at medium to high temperatures and are widely used in the hot zone of the aircraft gas turbine engines [12,13]. The following section reveals key traits of Ni-based superalloys.

## 2.1.2 Ni-based Superalloys

Most Ni-based superalloys used in commercial applications are strengthened either by solid solution strengthening or precipitation strengthening mechanisms [14,15]. The primary focus of this section is to examine the precipitation-strengthened superalloys, as high γ'-strengthened superalloys have shown significantly larger tensile strengths compared to other categories of Ni-based superalloys [15]. Also, for readers unfamiliar with the Ni-based microstructures and phases, a brief overview is provided below.

### 2.1.2.1 Microstructure and Phases

The microstructure of Ni-based superalloys is complex and is based on the distribution of nickel and ten or more alloying elements, as shown in **Table 2-1**. These alloys are primarily made up of an average composition of 60 wt/% nickel (Ni), 10 wt.% chromium (Cr), 6.5 wt.% aluminium (Al) and titanium (Ti), 7.5 wt.% molybdenum (Mo) and W, 2.5 wt.% niobium (Nb) and tantalum (Ta), 0.6 wt.% iron (Fe), 8.8 wt.% cobalt (Co), 0.1 wt.% carbon (C), 0.08 wt.% boron (B) and zirconium (Zr), and 0.3 wt.% hafnium (Hf) [16]. However, as observed in **Table 2-1**, the composition differs based on the desired material properties. During manufacturing, the melting and consequent cooling of the elements determine the final solidification microstructure. Some fundamental phases which affect the strength of the microstructure are discussed briefly in this section.

The parent austenitic phase is known as the γ phase which is a solid solution matrix of Ni and randomly distributed solute elements such as Cr, Co, Mo, and W. Depending on the manufacturing and subsequent thermo-mechanical processing, the constituent elements could segregate to grain boundaries or interdendritic regions (further details will be provided in **Sections 2.1.2.5** and **2.3.2** respectively).

Conventional superalloy manufacturing typically starts with a liquid melt consisting of all the required alloying elements. In directional solidification, for instance, an ingot is formed from a hot liquid melt by rotating a seed crystal with a desired crystal orientation, and simultaneously pulling it at a constant slow rate to control grain morphology and maintain anisotropic growth in the direction of the thermal gradient [17]. The ingot

gradually forms as the liquid melt cools at a steady rate, and the rate of solidification determines the material's final microstructure (further details provided in **Section 2.3.1.1**). As solidification progresses, secondary phases such as γ' ($Ni_3(Al,Ta)$) and carbides start to form alongside the parent matrix [4]. As the weight % of Cr decreases, the strength of the microstructure becomes greatly dependent on the distribution of coherent γ' precipitates within the parent phase [18].

**Table 2-1:** Ni-based Single-Crystal Superalloys Used in Gas Turbine Engines (Adapted from [4]).

| Generation | Superalloy | Element Weight % | | | | | | | | | | | | |
|---|---|---|---|---|---|---|---|---|---|---|---|---|---|---|
| | | **Cr** | **Co** | **Mo** | **W** | **Ta** | **Re** | **Nb** | **Al** | **Ti** | **Hf** | **C** | **B** | **Y** |
| First | PWA 1480 | 10.0 | 5.0 | | 4.0 | 12.0 | | | 5.0 | 1.5 | | | | |
| | René N4 | 9.8 | 7.5 | 1.5 | 6.0 | 4.8 | | 0.5 | 4.2 | 3.5 | 0.15 | 0.05 | 0.00 | |
| | CMSX-3 | 8.0 | 5.0 | 0.6 | 8.0 | 6.0 | | | 5.6 | 1.0 | 0.10 | | | |
| Second | PWA 1484 | 5.0 | 10.0 | 2.0 | 6.0 | 9.0 | 3.0 | | 5.6 | | 0.10 | | | |
| | René N5 | 7.0 | 7.5 | 1.5 | 5.0 | 6.5 | 3.0 | | 6.2 | | 0.15 | 0.05 | 0.00 | 0.01 |
| | CMSX-4 | 6.5 | 9.0 | 0.6 | 6.0 | 6.5 | 3.0 | | 5.6 | 1.0 | 0.10 | | | |
| Third | René N6 | 4.2 | 12.5 | 1.4 | 6.0 | 7.2 | 5.4 | | 5.8 | | 0.15 | 0.05 | 0.00 | 0.01 |
| | CMSX-10 | 2.0 | 3.0 | 0.4 | 5.0 | 8.0 | 6.0 | 0.1 | 5.7 | 0.2 | 0.03 | | | |

Gamma prime precipitate morphology changes from coarser to finer microstructures (spherical to cuboidal to dendritic) with increasing cooling time (see **Section 2.3.1** for details). The finer the γ' particle, the stronger the microstructure in precipitation-strengthened Ni-based superalloys (see details in **Section 2.1.2.4**). **Figure 2-1** shows different morphologies of γ' and carbides such as MC and $M_{23}C_6$ as the Cr content changes – Cr-rich regions contain small spherical γ' particles, while Cr-depleted regions indicate larger shapes labelled as nodules. The larger shape of γ' in Cr-depleted regions is attributed to the higher relative content of aluminium (Al) within the low-Cr region compared to that of the Cr-rich region. Notably, the microstructures representing high Cr content are characteristic of wrought Ni-based superalloys (such as Nimonic 80A, U-500, and N-115 in order of decreasing Cr content), and those representing low Cr content are characteristic of cast superalloys (such as IN-100 and MAR-m246 in order of decreasing Cr content) respectively [11].

#### 2.1.2.2 Phase Diagrams and Transformation-Time-Temperature (TTT) Diagrams

Ni-based superalloys are manufactured using numerous alloying elements to enhance mechanical properties for high-temperature applications. However, Al is an essential element in the formation of primary

strengthening phase, γ'. To understand the composition-temperature effect of Al on the solidification behavior of the superalloy, it is necessary to review the binary Ni-Al phase diagram and Ni-Al-X ternary systems.

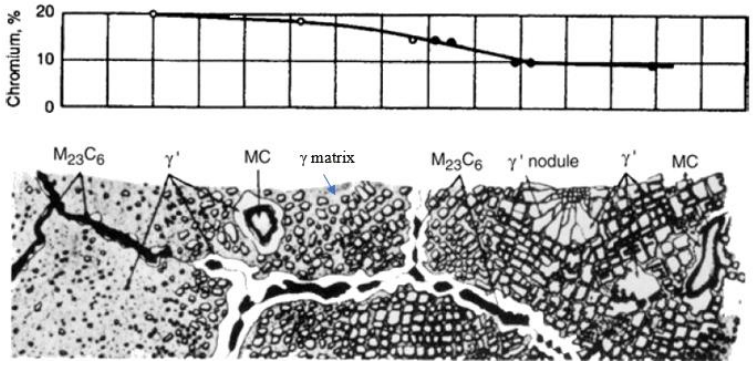


**Figure 2-1:** Microstructure Evolution of Ni-Based Superalloys (Adapted from [11]).

Binary phase diagrams are used to identify the equilibrium *liquidus* and *solidus* curves, which are critical measures in analyzing the solidification microstructures. Referring to **Figure 2-2**, the liquidus curve is the temperature-composition curve above which the alloy is in liquid phase. On the other hand, the solidus curve is the curve below which only primary solid phases (such as γ) exist in a solid solution matrix. Another critical measure to determine the solidification of secondary phases such as γ' is the *solvus*, which can be retrieved from performing differential scanning calorimetry (DSC) experiments [19]. When a Ni-based superalloy is cooled below the solvus temperature of γ', the solid solubility of γ is exceeded, which results in the formation of γ' particles. The size of the γ' particle depends on the cooling rate and reheating during LPBF processing (see **Figure 2-16**). *Supersolvus* and *subsolvus* refer to the temperature-composition combinations above and below the solvus curve respectively. In precipitation-strengthened Ni-based superalloys, the liquidus, solidus, and solvus curves in the Ni-Al binary phase diagram are useful in identifying ways to promote the precipitation of γ' during processing. However, binary phase diagrams do not account for non-equilibrium conditions, and therefore other graphs such as ternary phase diagrams (not shown here) need to be utilized. Ternary phase diagrams of Ni-Al-X for instance show the effect of different alloying elements on the formation of secondary phases in the superalloy.

For ternary alloys with complex phase changes, and high sensitivity to changes in composition, a transformation-time-temperature (TTT) diagram is used. **Figure 2-3** shows a TTT diagram (originally retrieved from the American Welding Society, 1986) for γ"-strengthened IN 718. The main takeaway from the diagram is the effect of cooling rate (see **Section 2.3.1**) on the phase formation at different temperatures. In LPBF processes, the solidification time is small due to high cooling rates, and primary gamma phase is likely to be observed at lower temperatures. However, as the solidification time increases and more time is given for elements to diffuse

back into the solid phase, secondary phases are observed. The continuous cooling transformation (CCT) curves (not shown here) provide better understanding of this phenomenon.

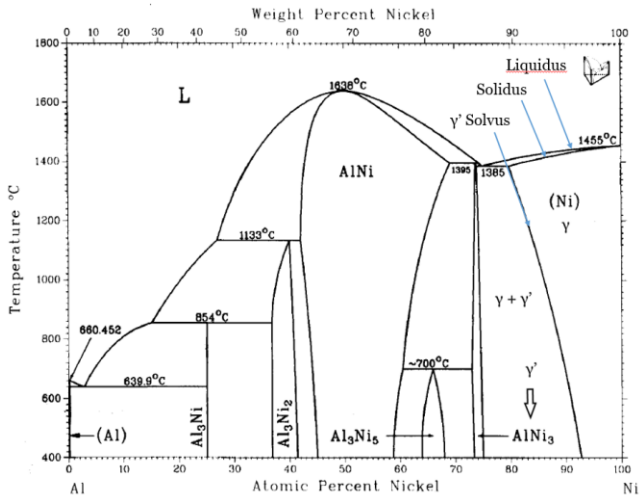


**Figure 2-2:** Binary Ni-Al Phase Diagram Showing Important Curved Lines (Adapted from [20]).

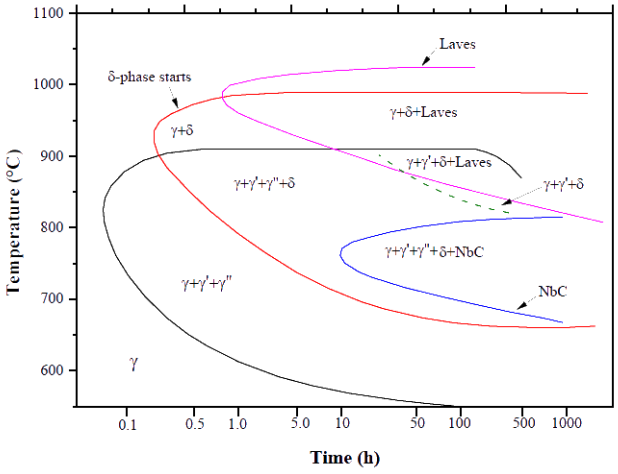


**Figure 2-3:** TTT Diagram for IN 718 (Taken from [21]).

### 2.1.2.3 Strengthening Mechanisms

To achieve good mechanical properties such as tensile strength, creep strength and ductility, the superalloy's microstructure must be strengthened. There are three major types of strengthening mechanisms in Ni-based superalloys, namely grain boundary, solid solution and precipitation strengthening [22]. Grain boundary strengthening is improved by precipitates segregating to the grain boundaries impeding dislocation motion. Solid

solution strengthening results from the addition of alloying elements which introduce lattice strains within the γ phase. Finally, precipitation strengthening refers to strengthening with precipitates such as γ' and carbides. The materials used in this study are high-γ' superalloys incorporated with a significant level of γ' (>40% volume fraction) for enhanced high-temperature strength and creep resistance [23].

#### 2.1.2.4 Significance of Gamma Prime and Precipitation Strengthening

So far, the importance of γ' has been reiterated several times in this document, however, the underlying reason for the significance has not yet been established. The goal of this section is to briefly discuss the reasons behind the emphasis on γ' and precipitation strengthening mechanisms in Ni-based superalloys. Firstly, a high volume fraction of gamma prime contributes to increased flow stress (stress value in between the yield strength and ultimate tensile strength of the material) as shown in **Figure 2-4 (a)**. The effect of γ' is more pronounced at high temperatures as a result of the thermally-activated cross-slipping mechanism triggered at the onset of yielding [4]. As stress is applied beyond the yield point, γ' cross-slips from the $\{111\}$ plane to the $\{001\}$ cross-slip plane due to the anisotropy of the antiphase boundary energy and elastic anisotropy [4]. Cross-slipped segments resist deformation by forming microstructural locks known as Kear-Wilsdorf (KW) locks [4], thus improving the strength of the superalloy as temperature is increased (this phenomenon is known as *anomalous yielding*). Beyond the peak stress temperature, further increase in temperature promotes slipping in the $a/2\,\langle 1\bar{1}0\rangle\{001\}$ slip system (known as the cube-slipping mechanism), which results in material softening.

Unique to the gamma prime phase is the primitive $L1_2$ ordered FCC structure shown in **Figure 2-4 (b)** and **c)**, which necessitates the creation of an antiphase boundary (APB) for dislocation motion at the γ/γ' interface. The APB is the boundary created between two γ' structures as unit dislocations try to penetrate the γ' phase from the γ phase [24]. To remove the APB created by a unit dislocation, dislocations must travel in pairs through the γ/γ' structure, and these paired dislocations are termed superdislocations [4,15,25]. Contrary to the γ' structure shown in **Figure 2-4 (b)**, where the Al atoms are arranged at the corners of the FCC unit cell, in the γ crystal structure, the edge atoms are replaced by Ni or Al atoms in no specific order – hence γ is described as a disordered FCC phase. The energy required to form the APB is 0.1 J/m$^2$ and depending on various factors such as particle size and lattice spacing, the strength to overcome the APB can vary from approximately 140 to 400 MPa [4].

Precipitation-strengthened Ni-based superalloys heavily depend on the size, morphology and volume fraction of γ' particles and solid-solution strengthening of both γ and γ' [12]. Planar defects known as stacking faults arise from missing (intrinsic) or extra (extrinsic) planes of atoms which inhibit dislocation motion. The major stacking faults which contribute to the strengthening of γ' particles are the APB, superlattice intrinsic stacking fault (SISF), superlattice extrinsic stacking fault (SESF) and complex stacking fault (CSF). However,

APB faults are believed to have a profound impact on the strength of precipitation-strengthened Ni-based superalloys due to the powerful dependence of fault energy on crystal orientation [12]. Consequently, the stacking fault energy (SFE) deeply affects the critical resolved shear stress (CRSS) of a precipitation-hardened material. Beyond the CRSS, a material yields and plastic deformation begins. Therefore, γ'-strengthening is necessary to strengthen the microstructure of a precipitation-strengthened Ni-based superalloy.

The principal models used to describe γ' strengthening are the particle cutting and Orowan bowing models. Previous studies have shown that the deformation mechanism changes from cutting by weakly paired dislocations to strongly paired dislocations as particle size increases up to a critical size beyond which dislocations bypass particles through Orowan bowing or looping [4,26]. Strengthening models associated with lattice misfit and coherency strains have shown insignificant impact on strengthening of ordered γ' particles [26].

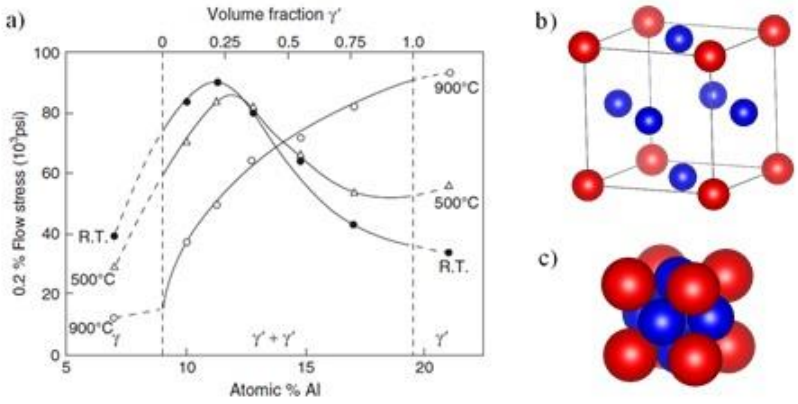


**Figure 2-4: (a)** Effect of Volume Fraction of γ' on 0.2% Flow Stress of Ni-Based Superalloy at Different Temperatures [27], **(b)** $L1_2$ Ordered FCC Structure $Ni_3Al$ (Blue Spheres Represent Ni Atoms and Red Spheres Represent Al Atoms) (Made Using Vesta©), **(c)** Close-Packed Structure Depicting Atom Packing in Gamma Prime (Made Using Vesta©)

Particle cutting occurs when the associated APB energy, $\gamma_{APB}$ [J/m$^2$], is overcome through the formation of paired $a/2\langle 1\bar{1}0\rangle\{111\}$ dislocations as shown in **Figure 2-5**. The net shearing stress required for particle cutting to occur is given by **Equation (2-1)**.

$$\tau_c \cong \frac{\gamma_{APB}}{2b}\left(\frac{2r_1}{\lambda_1} - \frac{2r_2}{\lambda_2}\right), \quad \textbf{(2-1)}$$

where $b$ is the Burgers vector (vector indicating displacement of atoms in a crystal lattice), $r_1$ and $r_2$ are the radii of sphere-shaped γ' particles as shown in **Figure 2-5**, and $\lambda_1$ and $\lambda_2$ represent the spacing (also called Friedel spacing) between particles on dislocation lines 1 and 2 respectively.

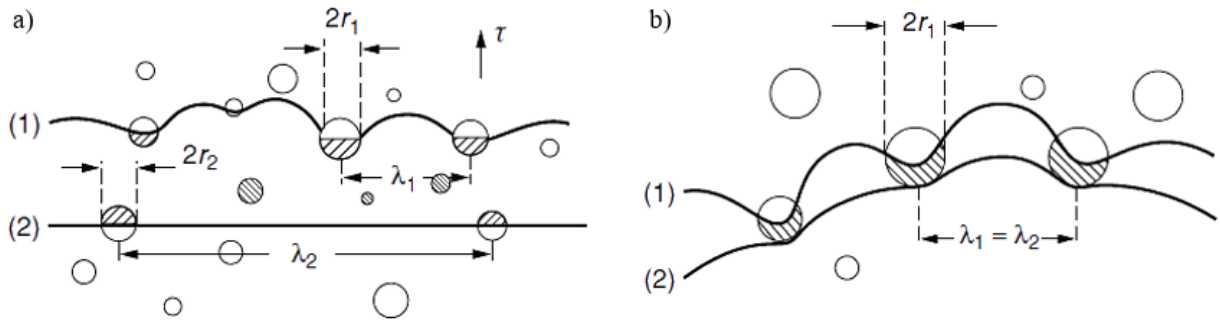


**Figure 2-5:** Particle Shearing of Ordered γ' for **(a)** Weakly Coupled Dislocations and **(b)** Strongly Coupled Dislocations (Adapted from [4]).

As particle sizes get larger, the leading dislocation line starts to bow to accommodate the pinning forces exerted by the particle on the dislocation pair. The difference between the weak and strong pair-coupling is that the Friedel spacing of the two dislocation lines are identical for the strongly coupled dislocation. Elastic repulsive force becomes a critical component in determining the shear stress for particle cutting [4].

#### 2.1.2.5 Effect of Alloying Elements on Mechanical Properties

Tighter control of the alloy composition provides a route to improve the strength of the microstructure and the final mechanical properties. Each alloying element has important implications on the strength of the microstructure, as shown in **Figure 2-6**. For instance, elements such as Cr, W, Ta, and Re are beneficial for solid-solution strengthening. On the other hand, elements such as Al, Ti, Ta, and Hf are included during the manufacturing process to assist in γ'-strengthening (see **Section 2.3.2**). Some elements promote the formation of grain-boundary strengthening phases such as borides and carbides. Elements such as Cr, Mo, and W assist the formation of borides $M_3B_2$, $M_5B_3$ and $M_2B$, while elements such as Ta, W, Hf, Ti, and Cr favor the formation of carbides MC, $M_6C$ and $M_{23}C_6$, where the letter "M" represents the metallic element associated with the phase. The rate of solidification during manufacturing plays an integral part in the segregation of alloying elements to preferential regions within the microstructure.

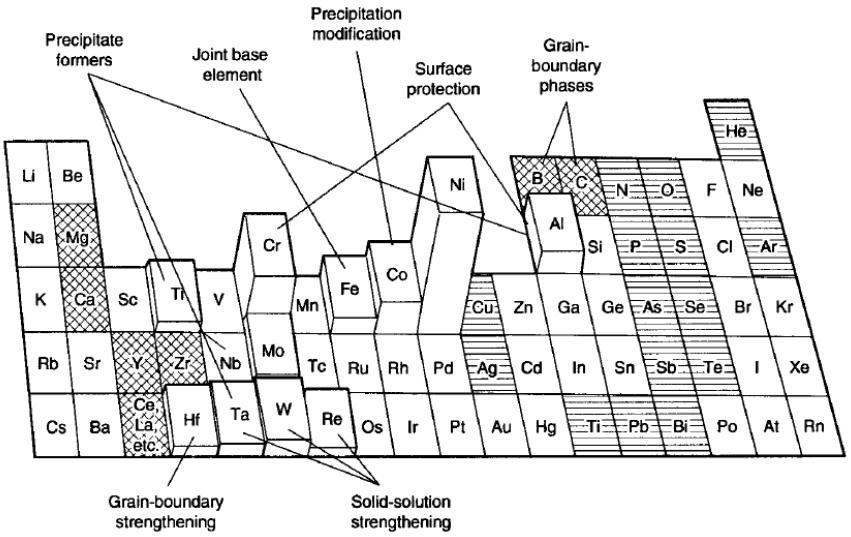


**Figure 2-6:** Roles of Alloying Elements in Ni-Based Superalloys [28].

## 2.2 Additive Manufacturing

The drive to automate manufacturing and reduce environmental waste facilitated the development of *additive manufacturing (AM)*, commonly recognized as '3D printing'. The AM process allows rapid automated three-dimensional (3D) parts manufacturing using a bottom-up (additive) layer-by-layer approach achieved through computer aided design (CAD) and 3D printing machines. Conventional manufacturing techniques used to fabricate commercially valuable parts require subtractive approaches, such as computer numerical control (CNC), lathes, milling and other machining methods which generate large quantities of material waste. Furthermore, depending on the application, many post-processing steps such as hot working and thermal processing may be needed to achieve the final product. Using AM, complex 3D parts close to the final desired shape (*near net shape*) can be produced with a minimal number of manufacturing steps. The number of iterations required to design a component are reduced depending on the type of AM technology used – one such method is laser AM. While laser AM is a costly process (LPBF facility costs over 700,000 CAD [1]), the ability to manufacture complex parts, reduce material waste, and design customized parts based on functionality outweigh the cost factor for niche applications such as gas turbine engines in aircraft. This section provides a concise overview of AM and highlights current challenges associated with laser AM of metals and metallic alloys.

### 2.2.1 Introduction

In the last three decades, AM has come a long way with the progress of information technology and is now destined to foster the rapid development of 'Industry 4.0' – dubbed to be the future of industrial manufacturing [29]. The very first additively manufactured parts were printed in the late 1980s with the invention of smart CAD-based ceramic/polymer manufacturing techniques [30–32]. One of the setups used to make these 3D parts was patented as the stereolithography apparatus (SLA) by Charles W. Hull in 1986 [33]. Also, known by some as stereolithography (STL) [31], this production technique creates 3D objects by using a focused laser beam to solidify thin layers of ultraviolet (UV) light-sensitive photopolymer (resin) [31,34]. Around the same time, a master's student at Texas University, named Carl R. Deckard, was pursuing a similar idea of creating 3D objects in coordination with CAD. Deckard explored printing parts with polymeric powder instead of liquid polymer. Like Hull, he patented and copyrighted his method in 1986, but named the AM system selective laser sintering (SLS) [30,32] which got modified, refiled and reissued in 1997 [35]. The expiration of the latter SLS patent on January 28, 2014 sparked renewed interest in 3D printing.

Since 2014, the polymer 3D printing technology has stimulated the rapid growth of metal AM technologies such as laser powder bed fusion (LPBF), electron beam melting (EBM), direct energy deposition (DED) and binder jetting (BJ) [32]. The most popular of the lot is arguably LPBF, which can be further categorized into selective laser melting (SLM), or direct metal laser melting (DMLM), and direct metal laser sintering (DMLS). These setups allow manufacturers to fabricate customized metal parts for niche applications in the rapid prototyping, aerospace, and land-based gas turbine industries [30,32].

### 2.2.2 Rapid Solidification Processing

The term rapid solidification processing (RSP) has been used since the 1960s [36] to describe the rapid extraction of thermal energy to include both latent heat and superheat during the liquid to solid phase transition of a metal or alloy. The rate at which the heat is extracted (cooling rate) can result in *undercoolings* as high as 100 °C. Cooling rates for RSP methods are typically higher than $10^4$ K $s^{-1}$. When a material is undercooled, the liquid has reached a temperature well below its equilibrium freezing point [37]. Undercoolings are critical as they play a significant role in determining the final solidification microstructure of the material. Large undercoolings and high solidification front velocity contribute to non-equilibrium solidification which results in smaller grains and fine scale microsegregation (see **Section 2.3.2**) [37].

Types of RSP include powder metallurgy (PM), strip casting, melt spinning, laser spin atomization, droplet quenching, and gas atomization [36]. Laser melting also falls in the category of rapid solidification as the cooling rate associated with the process is between $10^6$-$10^7$ $Ks^{-1}$ [38]. Grain size, segregation, solubility, and post-

solidification phase transformations are some of the microstructural characteristics affected by rapid solidification [37]. These traits could be used to improve material properties such as tensile, fatigue and creep strength, along with oxidation and corrosion resistance. This is especially critical at elevated temperatures in gas turbine engines, which undergo enormous amounts of thermomechanical stress during operation.

## 2.2.3 Laser Additive Manufacturing

Hard-to-weld high-γ' Ni-based superalloys need to be manufactured using laser AM technologies to create functional complex objects. There are two varieties of laser AM, namely powder-based and wire-based systems, which use powder and wire material as the starting materials for laser processing. Powder-based systems can be subdivided into machines which are powder-spread, such as laser melting (LM) or laser sintering (LS), or powder-fed, such as laser metal deposition (LMD) or direct metal deposition (DMD) [39]. The LM (or selective laser melting – LPBF) and LS (or selective laser sintering – SLS) mechanisms are grouped into LPBF as laser processing takes place on a powder-bed-based system utilizing a layer-by-layer approach. In the remainder of this thesis, LPBF setups are alternatively called 'laser AM'.

### 2.2.3.1 Current Challenges of Laser AM for Thin-Wall Part Fabrication

Thin-wall components are important for aerospace applications, such as fuel nozzles and turbine vanes, which consist of serpentine features difficult to fabricate using conventional manufacturing methods. Laser AM is a convenient technique to create such parts, however build defects such as porosity, residual stress and micro-cracking could cause in-process failure and diminish final part quality. This section defines these defects and explains how they occur in LPBF.

#### 2.2.3.1.1 Porosity

Incomplete melting is a common side effect of rapid heating and cooling cycles in laser AM. Fusion of powder particles can be affected by surface defects such as pre-alloyed particles, powder packaging and micro-segregation. This results in non-melted regions or holes which are called pores in laser AM. Typically, the term porosity is used instead of pores to describe the ratio of pore volume to the whole volume of the porous material. LPBF parts exhibit surface and sub-surface porosity in the transition zones between the hatching zone and contour path in the laser processed region. The presence of porosity in a LPBF material leads to increased local stress concentration which could lead to in-process cracks as shown in **Figure 2-7**.

In addition to surface defects, laser processing conditions significantly affect the formation of porosity in a LPBF material. For instance, two specific modes of laser energy distribution, known as keyhole and conduction modes, are responsible for the formation of different kinds of porosity. Keyhole mode is a product of

high laser energy density which creates a vapor capillary or keyhole due to the induced recoil pressure [40,41]. Conduction mode, on the other hand, is the preferred mode for laser AM due to smaller energy density (lower laser power and faster scanning speeds) which reduces the probability of element vaporization, and hence minimizes porosity [42,43]. Melt pool stability is also negatively affected due to the keyhole effect, and this is detrimental for the AM material's microstructure (see **Figure 2-8**).

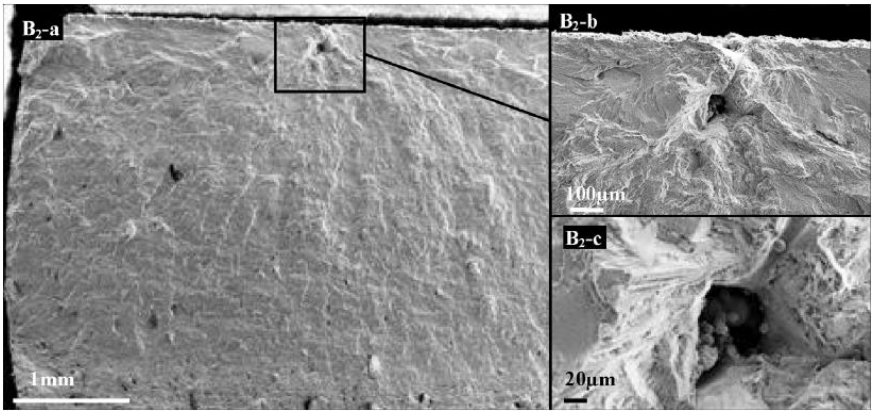


**Figure 2-7:** SEM Images of Crack Initiation Location for LPBF IN 625 [44].

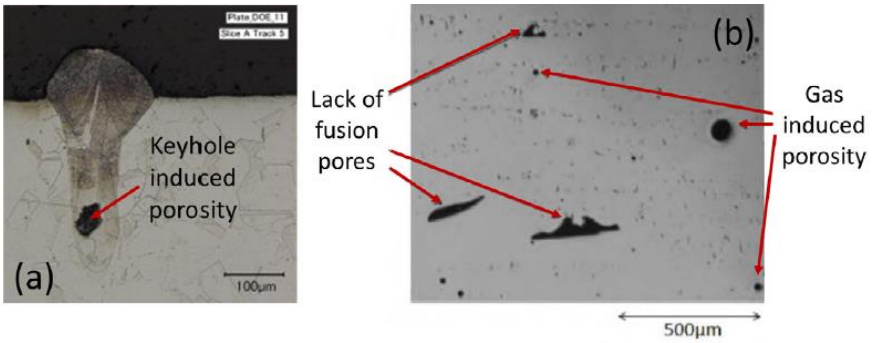


**Figure 2-8: (a)** Keyhole Porosity, **(b)** Lack of Fusion Pores and Gas Induced Porosity [42].

Laser power and scanning speed alone do not contribute to the overall material porosity. Shielding gas and inadequate penetration of the molten pool of an upper layer into the substrate or previously deposited layer also present opportunities for porosity formation (see **Figure 2-8**). Rapid heating and cooling representative of the laser AM process could lead to the formation of open or closed pores [45]. Open pores are connected with a surface and can be filled with fluids whereas closed pores are surrounded by fully dense material. Low energy densities and high dynamic viscosity lead to open-pore formation [45]. Another type of porosity called shrinkage porosity results due to part volume shrinkage during material solidification.

#### 2.2.3.1.2 Residual Stress

Thermal expansion and contraction due to the rapid heating and cooling cycles could result in *residual stress* between successive layers. The residual stress in a material is defined as "the stresses inside a body that is stationary and at equilibrium with its surroundings" [46]. Accumulation of stress concentrations occur between solidified layers, at the corners or stress concentrations near the base plate. This may lead to stresses higher than the strength of the material and lead to the formation of macro cracks [47] as shown in **Figure 2-9**.

Stress formation mechanisms such as the temperature gradient mechanism (TGM) and cool-down phase are responsible for the residual stresses imposed on a LPBF part. The TGM method explains how the material reacts through elastic compression due to the thermal expansion of a layer on laser interaction [48]. Further heating up to the yield stress temperature ($T_0$) results in plastic compression. During the cool-down phase, the opposite phenomena describes the material exerting tensile stress to counteract the contraction due to cooling. Plastic tension takes place as the temperature decreases below $T_0$ [42]. The larger the localized heat fluctuations, the larger the thermal gradient, and this leads to increased residual stresses.

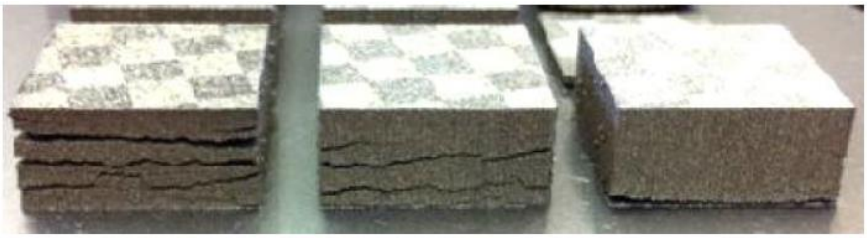

**Figure 2-9:** Crack Formation in M2 High Speed Steel Due to Residual Stress Generated by LPBF [47].

#### 2.2.3.1.3 In-Process Cracking

Porosity and residual stress are two process-induced defects which could initiate cracking in additively manufactured metal specimen, resulting in fracture (mechanism of crack propagation) and possibly material failure. In-process cracking results from the rapid cooling of samples governed by laser processing conditions such as laser power, scan speed, hatch spacing and scan strategy (see **Figure 2-10**) [49,50]. Laser AM cracking can be subdivided into liquid-state cracking and solid-state cracking. Liquid-state cracking occurs while the material is still undergoing liquid to solid phase transition and can be further classified as liquation cracking and solidification cracking (see **Figure 2-10**). Solid-state cracking, which occurs in the solid state when the solidified material contracts during cooling, can be subcategorized as ductility dip cracking (DDC) and strain-age cracking (SAC). Brief descriptions of these cracking mechanisms are provided below, but further details are available in **Chapter 3**.

Weld solidification cracking is a type of liquid-state crack which occurs when liquid films are distributed along solidification grain boundaries [15]. When the shrinkage strains produced from thermal contractions are too large, and the terminal liquid is distributed along the grain boundaries as a continuous film, solidification cracks begin to appear. Segregation (discussed in more detail in **Section 2.3.2**) of minor alloying elements such as phosphorus (P), sulfur (S), boron (B), carbon (C) and zirconium (Zr) to the grain boundaries can strongly affect the formation of solidification cracks in the fusion zone (FZ) of high-γ' Ni-base superalloys [15]. Lowering the weight percentage of elements such as B and Zr have shown to significantly improve resistance to solidification cracks in these alloys as these elements have strong segregation tendencies during solidification and form deleterious phases [51].

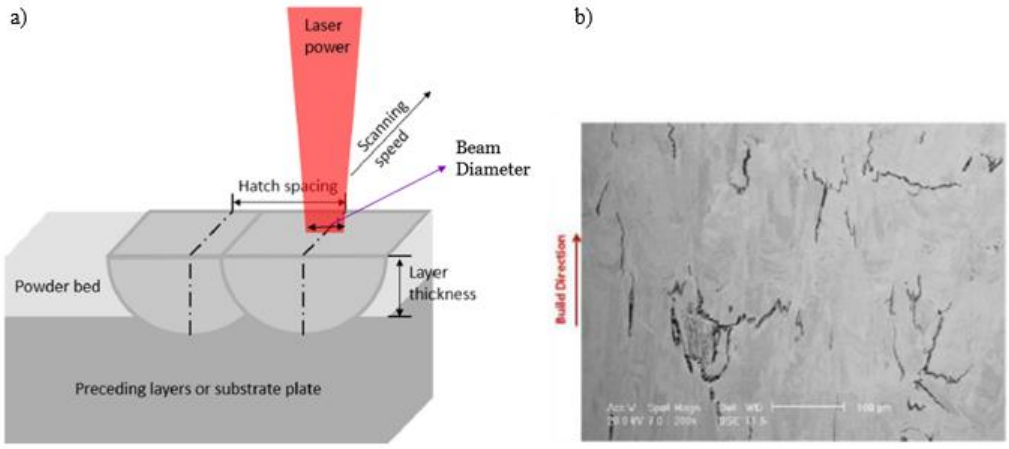


**Figure 2-10: (a)** Laser Processing Parameters Affecting Material Microstructure [50], **(b)** SEM Image Showing Solidification Cracks in a High-Energy LPBF Build [49].

Liquation cracking or heat affected zone (HAZ) liquation cracking in precipitation-strengthened Ni-base superalloys occurs due to liquid film formation along grain boundaries in the partially melted zone (PMZ) [15]. This type of cracking has been attributed to constitutional liquation of niobium carbides and laves phase as intergranular films in Nb-rich wrought materials such as IN 718, which has been extensively studied in literature due to its favorable weldability [52]. Alternatively, in cast IN 718, re-melting of the Laves phase in the inter-dendritic regions of the casting results in HAZ liquation cracking during laser welding.

The DDC mechanism is a solid-state cracking mechanism mainly observed in solid-solution-strengthened superalloys. The presence of DDC is determined through the loss of ductility in the material over the temperature range between the solidus ($T_S$) and approximately $0.5T_S$. To explain the effect of DDC, Hemsworth et al. [53] separated cracking into intergranular-liquid-film-based "segregation" (or hot) cracking and

DDC as shown in **Figure 2-11**. The acronym DTR stands for ductility temperature range and BTR stands for brittleness temperature range. In precipitation-strengthened alloys, DDC has not been studied extensively as this type of cracking does not require the formation of strengthening precipitates or grain boundary impurity segregation [15].

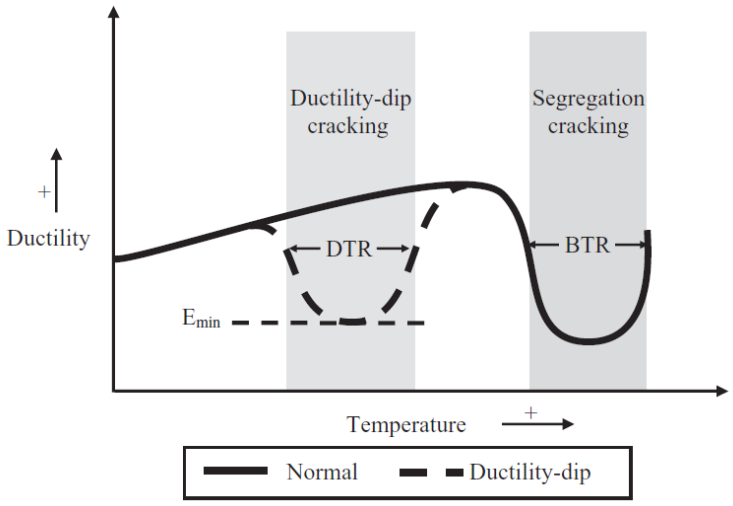


**Figure 2-11:** Ductility as a Function of Temperature. The Dotted Line Shows Solid-State Ductility Dip [54].

The strain-age cracking (SAC) phenomenon is a form of solid-state cracking revealed due to local accumulation of strain in the precipitation-strengthened microstructure. This occurs due to the relaxation of weld residual stresses and precipitation-induced stresses in the solidified state. The "age" term in strain-age cracking is derived from the process of precipitation and hardening during precipitate aging, and is not to be confused with aging during heat treatment [15]. Ni-based superalloys with high γ' content are typically considered "hard-to-weld" due to their susceptibility to SAC owing to the high levels of Ti and Al (Al+Ti wt.% > 6%). Reducing the heat input and grain size of the base material has shown to improve resistance to SAC [55,56]. Alloys strengthened by γ'', such as IN 718, are used in welding-based applications due to their resistance to SAC.

## 2.3 LPBF Microstructures

Before delving into the microstructural features of LPBF-processed materials, the key attributes of the LPBF process must be compared to those of different AM processes. The LPBF process is a laser AM technique which is capable of fully melting powder material to create a fully dense near net-shape component without post-processing treatments. Also, compared to binder-based laser sintering AM processes, higher product quality, processing time and manufacturing reliability can be achieved [50].

The setup of an LPBF machine normally consists of a base plate to build the part, a powder bed from which powder is spread onto the build plate, and a laser source to melt the powder according to the CAD model. After the first layer of powder is spread onto the build plate, the laser is scanned across the powder surface (X direction in **Figure 2-12**) at scanning speeds between 15 to 400 mm/s [50]. During the laser scan, part of the powder layer already scanned with the laser beam experiences thermal contraction due to cooling, and the part which momentarily interacts with the beam undergoes thermal expansion as illustrated in **Figure 2-12**. The hot regions neighboring the molten pool are identified as the HAZ regions. Solidification microstructures are affected significantly due to the localized heat fluctuations in each layer as laser processing proceeds in the Z direction (build direction). Therefore, the LPBF microstructures need to be studied to understand how laser processing affects the material properties.

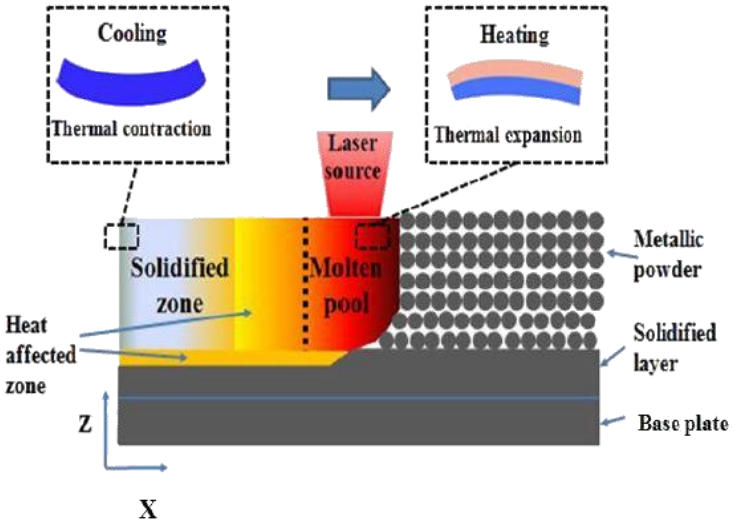


**Figure 2-12:** LPBF Process Showing Different Regions Affected by the Laser Source [57].

### 2.3.1 Grain Structures and Texture

Many of the LPBF microstructures are similar to those observed in cast, wrought or directionally solidified (DS) microstructures. These structures include planar, cellular, columnar, equiaxed, eutectic or peritectic grains as shown in **Figure 2-13**. Two key solidification parameters affecting the grain structures are the thermal gradient (G) and the solidification (or growth) rate (R). The ratio G/R is used to determine the grain morphology while G*R (often called the *cooling rate*) is used to determine the size of the solidified microstructure, as shown in **Figure 2-14**.

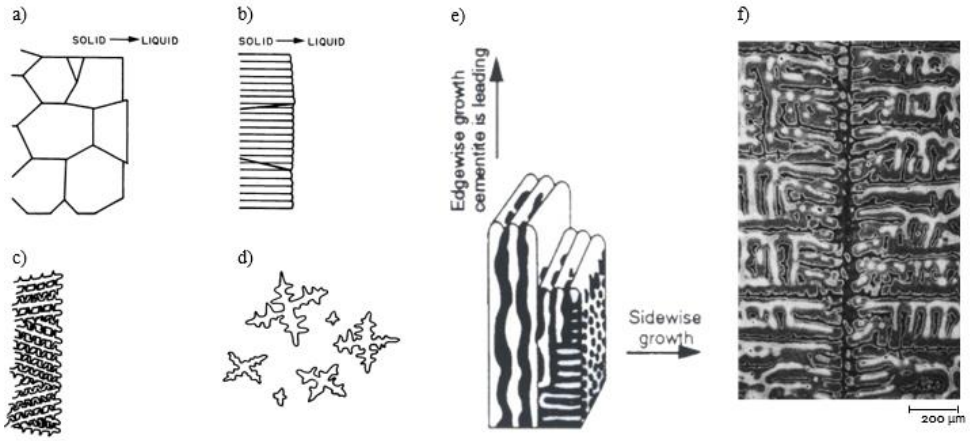


**Figure 2-13:** Grain Structures in Metal Manufacturing: **(a)** Planar, **(b)** Cellular, **(c)** Columnar, **(d)** Equiaxed, **(e)** Eutectic, **(f)** Peritectic [58–60].

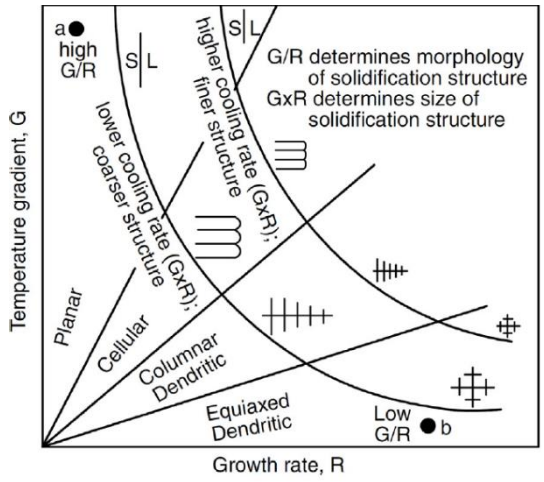


**Figure 2-14:** Effect of Solidification Parameters on Grain Structures of a DS Material [61].

### 2.3.1.1 Cast/Directionally Solidified (DS) Microstructures

Cast/DS microstructures exhibit coarser grains due to slower cooling rates ($10^{-2}$-$10^{0}$ $Ks^{-1}$) relative to laser AM (see **Section 2.3.2** for reasoning). As the cooling rate decreases, the dendrite arm spacing (DAS) increases (see **Figure 2-15**) and segregation of alloying elements also increases due to more time for diffusion.

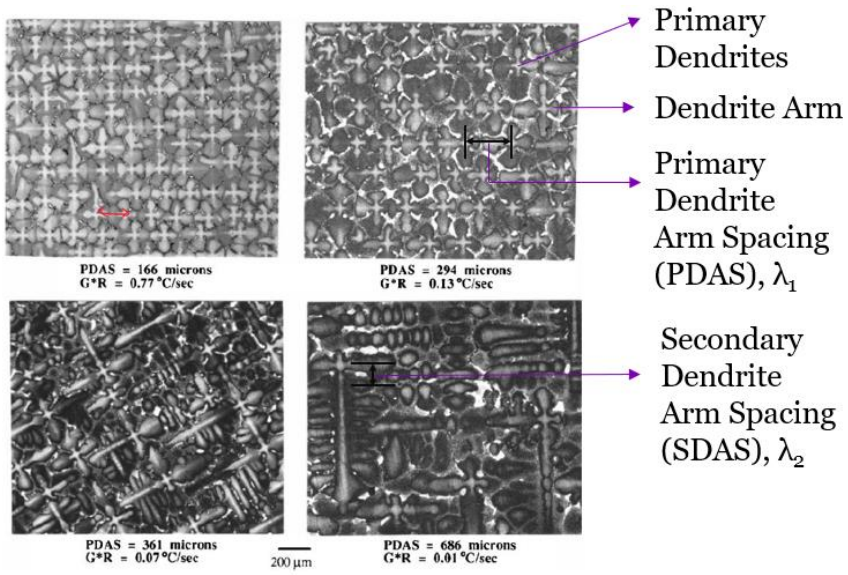


**Figure 2-15:** Effect of Cooling Rate on Dendrite Arm Spacing in Cast Material (Adapted from [62]).

### 2.3.1.2 Effect of LPBF Solidification Parameters on Gamma Prime Grain Morphology

The grain morphology of γ' changes from fine spherical structures to coarse dendritic structures as the cooling rate decreases (see **Figure 2-16**). Adoption of the spherical shape is due to larger surface (interfacial) energy relative to strain energy which is volumetric in nature. Decreasing cooling rates lead to the formation of cuboidal structures as more time is provided for the atoms to diffuse deeper into the melt pool, leading to increased lattice strain energy. Arrays of cubes and dendrites start to form at slower cooling rates when more thermal energy is available to promote crystal growth.

### 2.3.1.3 Effect of LPBF Solidification Parameters on Grain Texture

Laser-processed superalloys exhibit columnar grains in the build direction and finer equiaxed grains in the normal direction. Popovic et al. [63] studied the effect of functional temperature gradients on the grain texture of LPBF IN 718 by EBSD-based (see **Section 2.6.2.5**) inverse pole figure (IPF) colored maps. They determined that regions of the material processed with higher laser power demonstrated columnar grain texture, while regions processed with lower laser power showed finer equiaxed grains (see **Figure 2-17**). Zone 2 in the IPF map shown in the figure illustrate highly directional (anisotropic) grains with (100) crystal orientation. The strong anisotropy of the columnar grains is caused by remelting of previous layers, epitaxial growth, competitive growth mechanism and heat flow via conduction through previous layers [63,64]. The formation of large columnar grains for 950 W laser power is attributed to larger and deeper melt pool due to higher applied energy [63]. Zones 1 and 3 show

finer equiaxed grains with random orientations as a result of lower thermal gradient. This results in a lower G/R ratio which results in equiaxed dendritic grains as shown in **Figure 2-14** and verified by Liu et al. [65].

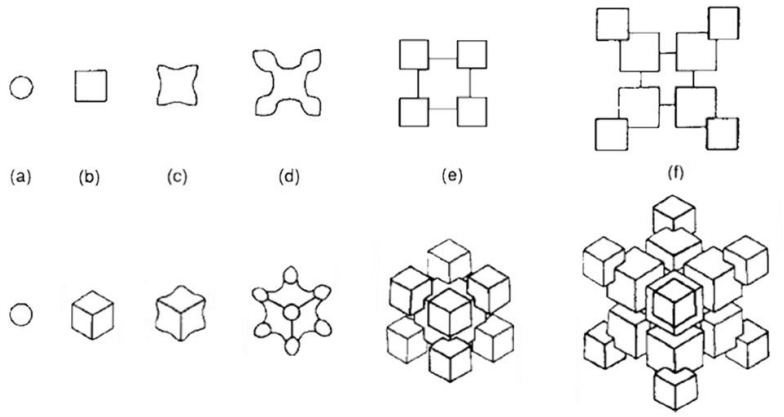


**Figure 2-16:** Gamma Prime Grain Morphology as Cooling Rate is Decreased from Left to Right: **(a)** spherical, **(b)** cuboidal, **(c)-(d)** Morphed Cuboidal, **(e)** Array of Cubes, **(f)** Dendritic Structure (Adapted from [4]).

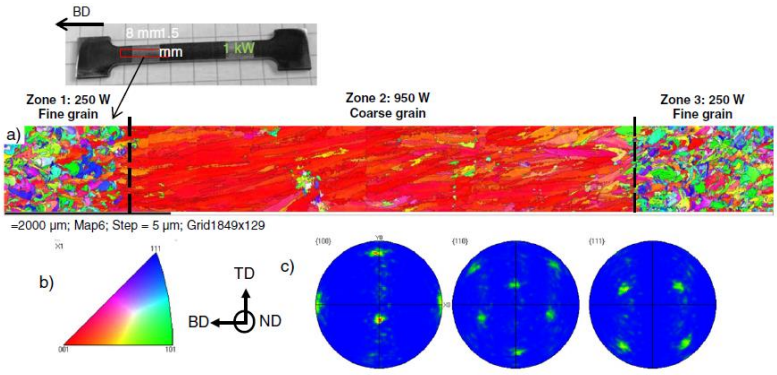


**Figure 2-17: (a)** LPBF IN 718 EBSD Image – IPF Colored Map, **(b)** Index Map of IPF and Reference Coordinate, and **(c)** Pole Figures for Zone 2 [63].

## 2.3.2 Micro-Segregation of Alloying Elements

The term "segregation" has been alluded to often in the text, however the meaning and significance of the term has not yet been clarified. The purpose of this section is to shed some light on the micro-segregation of elements during LPBF processing, and how that affects the superalloy's microstructure. Segregation effectively refers to differences in chemical composition [66] which could occur in the macro or micro scale. Microsegregation is the concentration gradient created due to local compositional differences as a result of solute

partitioning at the solid/liquid interface [67]. The length scale for microsegregation is comparable to the size of cellular and dendritic structures [68].

For slower solidification rates, such as those used in directional solidification or single crystal casting, since there is sufficient time for solute redistribution into the solid phase from the liquid phase, dendritic-level segregation is insignificant. In LPBF, there is less time for diffusional changes at the solid/liquid interface, which results in segregation of solute elements to the interdendritic regions where the last liquid solidifies [66]. New non-equilibrium secondary phases form and affect the homogeneity of the microstructure.

To better understand the effect on microstructure, the key factors affecting microsegregation of alloying elements must be identified. The most important driving force is the partitioning coefficient, k, which is given by **Equation (2-2)**, where $C_s$ and $C_0$ represent the composition of the solid at equilibrium and the initial alloy composition, respectively. The lower the k value, the higher the amount of interdendritic microsegregation.

$$k = C_s/C_0, \tag{2-2}$$

The second major solidification parameter affecting microsegregation is the diffusivity coefficient ($D_s$) of the element embedded in the solid phase of the alloy. These two parameters are used to determine the concentration of solute in the solid phase. Many scientists have previously worked on improving the famous solute segregation relationship proposed by Scheil ($C_s = kC_0(1 - f_s)^{(k-1)}$) [30], but for the purpose of general understanding, Brody and Fleming's optimized solute partitioning equation, **Equation (2-3)**, is shown. Unlike Scheil's equation, Brody and Fleming's mathematical finding assumes *back-diffusion*, which suggests that there might be a small amount of solute redistribution into the solid phase.

$$C_s = k^* C_0^* \left(1 - F_s(1 + \alpha^* k)\right)^{(k-1)}, \tag{2-3}$$

where $\alpha = 4D_s t_f/d^2$, $t_f$ is the local solidification time, $d$ is half of the SDAS, and $F_s$ is the solid fraction. Even though the rapid solidification of AM processes doesn't allow time for solute redistribution, Brody and Fleming's relationship is still more realistic compared to Scheil's due to the flexibility of solid-state diffusion. Both alloy solidification models, however, are formulated on the basis of straight liquidus and solidus lines which utilize a constant partitioning ratio [69].

In precipitation-strengthened Ni-base superalloys, such as IN718, microsegregation of alloying elements such as Nb and Mo lead to the formation of laves phase in the γ/γ' interdendritic regions [70], as shown in **Figure 2-18**. This occurs due to the rejection of Nb and Mo solute particles (low k values) at high solidification rates, typical of LPBF processes [71].

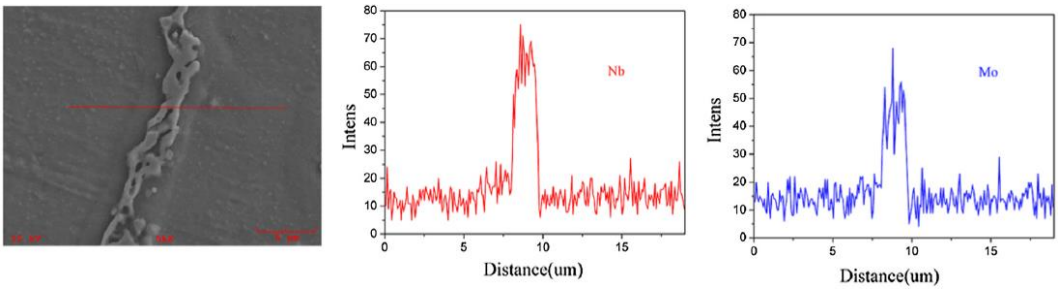


**Figure 2-18:** EDX Analysis Showing Micro-Segregation of Mo and Nb in Interdendritic Regions (Adapted From [70]).

## 2.4 Part Printing

In this work, thin-wall part models were designed using SolidWorks© and post-processed using Autodesk Netfabb to generate step files (*cli format) as input for part processing in the LPBF machine. The components were constructed using the Aconity$^{TM}$ MIDI LPBF printer using pre-defined laser conditions (laser power 200 W, scan speed 1000 mm/s, hatch spacing 90 µm, spot size 120 µm, powder layer thickness 40 µm, and bidirectional scan strategies). The operating laser processing conditions were optimized for thin-wall part processing based on previous studies performed at the discretion of the LPBF operator. An example Netfabb *.cli format file for a thin-wall sample printed on a LPBF base plate is attached in **Appendix A**.

## 2.5 Image Analysis and Statistical Methodologies

Image analysis is a widely used approach to quantify microstructure features of a specimen from micrographs, typically acquired using optical or electron microscopy. Micrographs with known scale bars are used to obtain statistics of select features within the material microstructure. In this work, image analysis software, ImageJ [72], coupled with visual basics for applications (VBA) scripts were employed to distinguish micro-cracks from surface contaminations and other defects such as lack-of-fusion voids and pores in the LPBF microstructure. **Figure 2-19** illustrates the procedure used to obtain micro-crack statistics for each sample grind level. Between 3 to 5 grind-level planar XY surfaces were analyzed per sample. An excess of 100 images per sample were analyzed to generate an adequate dataset for statistical analysis. Image analysis data for micro-cracks were filtered

using the following conditions: area $<$ 1500 µm$^2$, minor axis value $<$ 5 µm, aspect ratio < 2.5, circularity < 0.5, and roundness < 0.4.

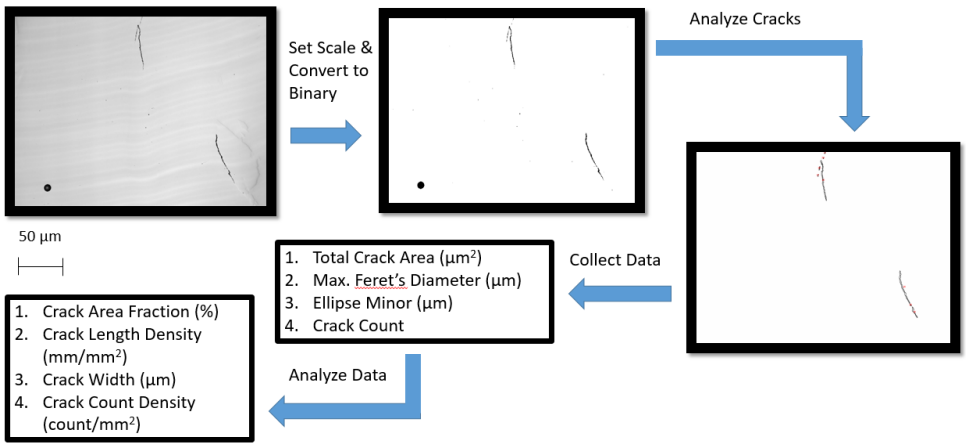


**Figure 2-19:** Micro-Crack Analysis Process for LPBF Thin-Wall Parts.

Micro-crack statistics such as crack area fraction (CAF), crack length density (CLD), crack count density (CCD), crack length (CLen), and crack width (CWid) for a given polished surface were calculated. The crack area fraction (%) is defined as the sum of micro-crack areas per image normalized by the image area ($A_{image}$), as shown in **Equation (2-4)**. The crack length density (mm/mm$^2$) is defined as the sum of micro-crack lengths (maximum ferret diameters, $L_{crack,x}$, where $x$ represents a single crack) per image normalized by the image area, as shown in **Equation (2-5)**. The crack count density (mm$^{-2}$) is defined as the number (count, $n$) of cracks per image normalized by the image area, as shown in **Equation (2-6)**. The crack length (µm) and crack width (µm) parameters are defined as the average micro-crack length ($L_{crack,x}$) and width ($W_{crack,x}$) per sample, as shown in equations **(2-7)** and **(2-8)**.

$$CAF\ (\%) = \frac{\sum_{x=1}^{n} A_{crack,x}}{A_{image}} \times 100\% \quad \textbf{(2-4)}$$

$$CLD\ (mm/mm^2) = \frac{\sum_{x=1}^{n} L_{crack,x}}{A_{image}} \quad \textbf{(2-5)}$$

$$CCD\ (mm^{-2}) = \frac{n}{A_{image}} \quad \textbf{(2-6)}$$

$$CLen\ (\mu m) = \frac{\sum_{x=1}^{n} L_{crack,x}}{n} \quad \textbf{(2-7)}$$

$$CWid\ (\mu m) = \frac{\sum_{x=1}^{n} W_{crack,x}}{n} \quad \textbf{(2-8)}$$

All statistical data include 95% confidence levels (CLs) that provide meaningful representation of the range within which the mean values are expected to belie 95% of the time, upon repetition of the analysis with an identical sample. The built-in equation used to derive the confidence level using the Microsoft Excel "Descriptive Statistics" add-in is shown in **Equation (2-9)**.

$$95\%\ CL = t_{95\%} \times \frac{\sum(x - \bar{x})^2}{\sqrt{n(n-1)}}, \quad \textbf{(2-9)}$$

where $x$ represents the observed value, $\bar{x}$ is the sample mean, $n$ is the number of values in the sample population, and $t_{95\%}$ is the 95% t value determined by Excel. Contrary to conventional methods using $t_{95\%} = 1.96$, reliable for $n > 26$, Excel automatically manipulates the value depending on the sample size. For instance, the repeatability of the mean value is less reliable for smaller sample sizes due to larger 95% CL values. The confidence interval is determined by adding up the 2.5% cut-off values at either end of the t-distribution, which is slightly different from the normal curve in that it is flatter in its center and thicker in its tails. In this study, the sample population consists of sample micrographs, and the sample size is computed using the total number of clean images per sample. Both the mean and 95% CL are computed over 3-5 different grind levels on the XZ plane for each sample. Average means and 95% confidence intervals are obtained and plotted for all samples.

## 2.6 Experimental Methodologies

The experiments performed in this work included part design, sample preparation and microstructure characterization. Brief descriptions of the processes are provided in this section.

### 2.6.1 Materials Studied

Two crack-susceptible high-γ' Ni-based superalloys, RENÉ 65 (R65) and RENÉ 108 (R108), are chosen for this research. The materials represent two extreme cases for hard-to-weld γ'-strengthened Ni-based superalloys, one just above the weldability line, with lower γ' volume fraction (42% [73]), and one with a significantly larger γ' volume fraction (63% [74]), theoretically more susceptible to SAC-type cracks, as demonstrated in **Figure 3-11**. The constitutional alloying elements include Ni, Cr, Co, Al, Ti, Ta, W, Mo, Nb, Hf, Fe, B, Zr, and C, all of which are known to improve the material properties in some capacity. **Table 2-2** shows the elemental contents (in wt.%) of R65 and R108 powder, obtained using the inductive coupled plasma optical emission spectroscopy (ICP-OES) technique at Activation Laboratories (ACTLABS © Canada).

**Table 2-2:** Powder Composition of RENÉ 65 and RENÉ 108 in Weight Percent (wt.%).

| Alloy | Ni | Cr | Co | Al | Ti | Ta | W | Mo | Nb | Hf | Fe | B | Zr | C |
|---|---|---|---|---|---|---|---|---|---|---|---|---|---|---|
| R65 | Bal. | 15.86 | 13.22 | 2.15 | 3.65 | 0.04 | 4.25 | 4.03 | 0.75 | | 1 | 0.01 | 0.05 | 0.01 |
| R108 | Bal. | 8.64 | 10 | 5.36 | 0.75 | 3.02 | 10.03 | 0.53 | | 0.87 | 0.27 | 0.01 | 0.01 | 0.01 |

R108 has a higher Al + Ti wt.% content (6.11%) than R65 (5.80%), higher γ' volume fraction for increased strength at elevated temperatures, demonstrates higher susceptibility to SAC, and is designed to reduce solidification cracking. The key alloying additions in R108 include Hf and Ta, where Ta is a strong gamma prime former and Hf is added to reduce solidification cracking through grain refinement. On the other hand, R65 contains more Zr, which increases the solidification range. The two alloys have similar level of B, but different amount of boride formers (Mo, W and Cr). Boride formers modify the solvus temperature of the borides which affects solidification cracking mechanism(s). Moreover, difference in major elements like Cr, W, Mo, Al, Hf, Ta, Zr and B also impact the solidification range due to different partitioning ratios.

The large window of alloy compositions represented using R65 and R108 allows observation of different micro-cracking mechanisms as alloy composition changes. In addition, since crack-susceptible materials are hard to process with LPBF, thin-wall part failure mechanisms can be examined in detail. Comprehensive understanding of the micro-cracking and in-process failure mechanisms will enable development of methodologies to reduce build failures and optimize final part quality in thin-wall components processed using LPBF.

## 2.6.2 Microstructure Characterization

### 2.6.2.1 Optical Microscopy

Optical microscopy is a technique used to examine the meso- and micro-structural features of a reflective surface. This method of microstructure characterization is a widely used means of determining the grain size of metals as detailed by the American Standards of Testing and Materials (ASTM). In addition to grain size measurement, optical microscopy can also be used to identify and count other interesting features (such as cracks) within the parent microstructure. These features (>0.2 μm) are visible to the naked eye due to the elastic scattering of visible light (400 – 700 nm wavelength) off the metal specimen [75].

### 2.6.2.2 Scanning Electron Microscopy (SEM)

Contrary to optical microscopy, scanning electron microscopy (SEM), as the name suggests, makes use of electrons instead of light (optics) to view a material at the micro-scale level. The resolution of an SEM image

is in the order of 0.1 nm – 0.3 μm [75] due to the small wavelength of the electron (in the range of picometers). This allows the user to obtain close-up images of the material's microstructure and detect fine features not visible using optical microscopy. Depending on the emission of backscattered electrons (BSE) or secondary electrons (SE), various microstructural attributes such as surface morphology and phases can be observed.

The SEM is composed of the microscope column, signal detector systems, and computer hardware and software to collect and process data [75]. Some disadvantages of the SEM compared to the optical microscope include: (a) longer time taken to acquire a high-resolution image due to the vacuuming and image scanning process, and (b) higher usage cost due to the complexity of the setup.

#### 2.6.2.3 Transmission Electron Microscopy (TEM)

Transmission electron microscopy (TEM) is an effective tool for advanced analysis of the material's nano- and micro-scale features. However, TEM requires thin specimen (less than 100 nm) for electrons to pass through the sample without energy loss. Scattered electrons transmitted through the TEM specimen are collected and processed to view high resolution (in the order of angstroms) images of the material's morphological features. TEM imaging requires high electron energies between 100 to 400 keV to generate sufficient transmitted electrons. The fundamental aspect which distinguishes TEM from other microstructural characterization methods is the ability to image both in the real and reciprocal spaces at high resolutions. Images obtained in the real space provide morphological information of select features such as precipitates and dislocations, which affect the strength of the material. The crystallographic orientations of these features can be determined using selective area electron diffraction (SAED) patterns obtained from the reciprocal space. The two approaches can be used in tandem to develop a sound understanding of the material's microstructure attributes [75].

Scanning TEM (STEM) is a highly versatile microstructure characterization method that enables imaging, diffraction, and spectroscopy of a TEM specimen at atomic resolution. The process involves raster scanning of a select area on the material surface to collect various types of scattering as a function of position [76]. Two types of detectors, the energy dispersive X-ray spectroscopy (EDX) and electron energy loss spectroscopy (EELS), are used with the STEM to obtain information on the compositional differences at the atomic scale. Further information on EDX, employed in parts of this work, is provided in **Section 2.6.1.4**.

#### 2.6.2.4 Energy Dispersive X-Ray Spectroscopy (EDX)

For further analysis of the material's microstructure, energy-dispersive spectroscopy (EDS) or energy-dispersive X-ray spectroscopy (EDX) is required. This technique is used in conjunction with SEM or STEM to identify local compositional differences within the microstructure. The operation principle of EDX is based on the inelastic interaction between the incident beam and the material. When the primary electrons interact with the

atoms of a given alloying element, characteristic X-rays are emitted, which enable detection of the element on the EDX detector. The current EDX systems use the silicon drift detector (SDD) that converts the analog X-ray energy into digital information, shown as a peak in the EDX spectrum on the computer screen. The spectrum consists of peaks representing characteristic X-ray energies for a range of elements depending on the local phases, precipitates, or particles scanned by the incident beam. In this work for instance, the EDX was used to identify key alloying elements and phases potentially responsible for micro-cracking. The EELS approach, not used here, can be used to provide more accurate detection of elements with lower atomic numbers, such as carbon and boron.

#### 2.6.2.5 Electron Backscatter Diffraction (EBSD)

Electron backscatter diffraction (EBSD) is a means of performing advanced microstructure characterization in unison with SEM. The EBSD method employs a computer software which allows the user to select a region within the captured SEM image to determine the local crystallographic orientation of the specimen. In LPBF Ni-based superalloys for instance, the crystal orientations obtained in the build direction (BD), normal direction (ND) and transverse direction (TD) help in evaluating the type of grains (columnar or equiaxed). This helps shed further light on the material's behavior at the microscopic scale.

## 2.7 Modelling Methodology

Numerical simulations are conducted using finite element modelling (FEM) with commercial software ABAQUS. The FEM technique solves a 3D model of an actual part by dividing the geometry into smaller segments called elements. Model elements are typically cuboidal and consist of 8 nodes and 6 faces [77]. Finite element analysis (FEA) solves nodal displacements ($X$) using the material stiffness ($K$) and applied nodal forces ($R$) as shown in equation **(2-10)**. Gaussian integration points are used to solve the FEM equations by the numerical integration approach.

$$K\{X\} = R \tag{2-10}$$

To simulate the AM process, the fully or sequentially coupled modelling method can be employed. The fully coupled method allows simultaneous simulations of the thermal and mechanical equations, as shown in **Equation (2-11)**. In this case, it is assumed that the mechanical behavior affects the thermal behavior of the material and vice versa. Conversely, in the sequentially coupled modelling approach, the thermal behavior affects the mechanical behavior but not vice versa. **Equations (2-12)** and **(2-13)** define the sequentially coupled method.

$$\begin{bmatrix} K_{XX} & K_{X\theta} \\ K_{\theta X} & K_{\theta\theta} \end{bmatrix} \begin{Bmatrix} X \\ \theta \end{Bmatrix} = \begin{Bmatrix} R_X \\ R_\theta \end{Bmatrix} \tag{2-11}$$

$$[K_{XX}]\{X\} = \{R_X\} \quad \textbf{(2-12)}$$

$$[K_{\theta\theta}]\{\theta\} = \{R_\theta\} \quad \textbf{(2-13)}$$

The matrices $K_{\theta\theta}$ and $K_{XX}$ define the thermal and mechanical properties, respectively; the external load and boundary conditions are represented by $R_\theta$ and $R_X$; and the temperature and nodal displacements are given by $\theta$ and $X$, respectively. The sequentially coupled approach is less computationally expensive than the coupled approach and allows the thermal and mechanical equations to be solved separately. This enables greater flexibility during modelling as various schemes can be chosen to reduce the solver time [78].

The governing equations for simulating the thermal history and mechanical response to LPBF are provided below:

1. Thermal model:

    a. Temperature field $T\ (x, y, z, t)$ obtained through the domain:

    $$\rho C \frac{\partial T}{\partial t} = \frac{\partial}{\partial x}\left(k \frac{\partial T}{\partial x}\right) + \frac{\partial}{\partial y}\left(k \frac{\partial T}{\partial y}\right) + \frac{\partial}{\partial z}\left(k \frac{\partial T}{\partial z}\right) + Q\ , \quad \textbf{(2-14)}$$

    where $T$ represents the temperature, $\rho$ is the density, $C$ is the specific heat, $k$ is the heat conductivity, and $Q$ is the latent heat.

    b. Boundary conditions:

        i. Heat radiation:

        $$q_{rad} = \varepsilon \sigma_b (T_s^4 - T_\infty^4)\ , \quad \textbf{(2-15)}$$

        where $\varepsilon$ is the surface emissivity, $\sigma_b$ is the Stefan-Boltzmann constant, $T_s$ is the surface temperature of the workpiece, and $T_\infty$ is the ambient temperature.

        ii. Heat convection:

        $$q = h(T_s - T_\infty)\ , \quad \textbf{(2-16)}$$

        where $h$ is the convective heat transfer coefficient.

2. Mechanical model:

    a. General form:

    $$\nabla \sigma = 0\ , \quad \textbf{(2-17)}$$

    where $\sigma$ is the stress.

b. Mechanical constitutive law:

$$\sigma = C\varepsilon_e \,, \tag{2-18}$$

where $C$ is the fourth order material stiffness tensor and $\varepsilon_e$ is elastic strain.

c. Strain for small deformation:

$$\varepsilon = \varepsilon_e + \varepsilon_P + \varepsilon_T \,, \tag{2-19}$$

where $\varepsilon$, $\varepsilon_P$, and $\varepsilon_T$ are the total strain, plastic strain, and thermal strain, respectively.

i. Thermal strain:

$$\varepsilon_T = \alpha(T - T^{ref}) \,, \tag{2-20}$$

where $\alpha$ is the thermal expansion coefficient and $T^{ref}$ is the reference temperature.

ii. Plastic strain

$$f = \sigma_m + \sigma_y\left(\varepsilon_p, T\right) \leq 0 \,, \tag{2-21}$$

$$\dot{\varepsilon_p} = \dot{\varepsilon_q} a \,, \tag{2-22}$$

$$a = \left(\frac{\partial f}{\partial \sigma}\right) \,, \tag{2-23}$$

where $f$ is the yield function, $\sigma_m$ is Mises stress, $\sigma_Y$ is yield stress, $\varepsilon_q$ is the equivalent plastic strain, and $a$ is the flow vector [79].

The purpose of the numerical simulations conducted in this study is to predict the stresses and strains developed in the LPBF process. The stress-strain results from the model can be used to better understand the mechanisms of failure in LPBF thin-wall parts made of high-γ' Ni-based superalloys.

# Chapter 3
# Literature Review – Fabrication of Thin-Wall Components Using LPBF γ'-Strengthened Ni-based Superalloys

Failure in materials can result from damage through external influence, by deterioration of material properties over time or through internal defects incurred during manufacturing or post-processing. The formation of micro-cracks within regions susceptible to crack initiation can be linked to mechanical failure following fracture. Controlling the microstructure during manufacturing is necessary to avoid macro-scale fracture and maintain the integrity of the desired commercial part.

Several factors can cause thin-wall part failure during rapid solidification processing, including: i) macroscopic stresses, and ii) material compositions. High-γ' nickel superalloys are known to be especially susceptible to weld cracking[1] [1]. This increases the chances of build failure during processing and reduces the final part quality. To better understand the underlying mechanisms for part failure and find means to optimize part processability, the effects of part geometry, alloy composition, and laser parameters need to be studied. The goal of this chapter is to provide the reader **a fundamental understanding of the conventional failure mechanisms in rapid solidification processing** and a review of literature on inherent failure in LPBF thin-wall parts and high-γ' Ni-based superalloys.

## 3.1 Introduction

Localized heating and cooling of metals or metal alloys brings about phase changes from solid to liquid and liquid to solid, respectively. Phase changes create stresses within the material during processing which could promote micro-cracking and in-process failure. The elastic and plastic stresses generated by the heating-cooling effect within the material are demonstrated in **Figure 3-1 (a)**. When the laser beam irradiates the material surface, the material state changes from powder to liquid phase as the temperature exceeds the melting point of the material. In the liquid state, the atoms move freely and no stress is generated. As the laser beam moves away from the irradiated surface and the material begins to cool down, the material state changes from liquid to solid phase. During the liquid-solid phase transition, while the material is still hot, the locally solidified region exerts tensile stresses to the surrounding solidified regions. To counterbalance the tensile stresses and achieve near equilibrium,

[1] Laser processing is considered analogous to welding due to the localized heating/melting of the material.

the neighboring regions exert compressive stresses on the locally solidified region. The heating-induced stress creation mechanism is defined as the temperature gradient mechanism (TGM), as previously discussed in **Section 2.2.3.1.2**. As the material cools down further, the locally solidified region exerts compressive stresses to the surrounding regions, which in turn exerts tensile stresses on the material. The cooling-induced stress creation mechanism is defined as the cool-down phase. Accumulation of tensile stresses perpendicular to the crack growth direction favors micro-cracking in locally susceptible regions within the material.

During laser AM, the heat distribution surrounding the melt pool determines the consequent localized temperature gradient, cooling rate, and stresses, which affect the final material microstructure and part properties. The heat distribution within the material is affected by the part build conditions. Local variations in heating and cooling introduce local changes in composition and stresses during processing. High cooling rates inherent in LPBF ($10^6$-$10^7$ K/s [80]) result in dendritic microstructures as the material solidifies. Such extreme conditions could generate extensive micro-segregation and localized regions of tensile stresses, which could promote in-process micro-cracking. Excessive build-up of in-process stresses could also ultimately lead to macro-scale build failure. To better understand the underlying failure mechanisms inherent in LPBF, the regions surrounding the melt pool must be identified, as demonstrated in **Figure 3-1 (b)**. Upon interaction with the laser beam, the powder material is completely melted and rapidly liquifies resulting in the formation of a melt pool (or fusion zone (FZ)). The heat generated from the laser creates two distinct zones, namely the partially melted zone (PMZ) and the heat affected zone (HAZ), surrounding the melt pool. The PMZ is defined as the transition region between 100% liquid to 100% solid state across the fusion boundary [81]. The true-HAZ (T-HAZ) describes the region around the melt pool where all metallurgical reactions occur in solid-state and no melting occurs [81].

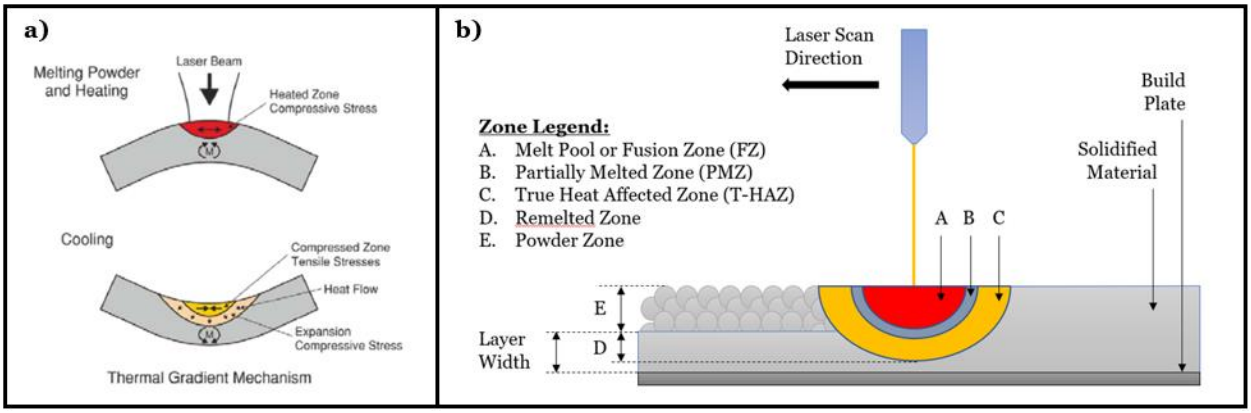


**Figure 3-1: (a)** Demonstration of the Temperature Gradient Mechanism in LPBF [82]. **(b)** Simplified Illustration Showing Different Cross-Sectional Regions Developed During LPBF.

Dendrite growth occurs as the melt pool solidifies and the growth direction is dependent on the preferential direction for heat flow. In LPBF, the dendrites typically exhibit columnar morphologies along the build direction (BD) and small PDAS values due to the high cooling rates [80,83,84]. As the laser beam scans the part, the solidification process continues and the primary dendrites coalesce to form grains, creating a solid part. However, during solidification, several defects such as porosities, voids and micro-cracks can affect part processability and the final part quality. Micro-cracking, which is especially important for hard-to-weld high-γ' Ni-based superalloys, can be further exacerbated due to localized regions of in-process tensile stresses.

To better understand the micro-cracking phenomenon, it is important to consider both the in-process stresses and the stress state surrounding the micro-crack opening. The stress state can be fully derived from the Lode angle parameter and the stress triaxiality [85]. The Lode angle parameter is derived from the deviatoric stress components acting on the material. However, in LPBF, stress triaxiality is more representative of the stress state and more likely to contribute to micro-cracking due to the influence of thermal gradient on hydrostatic stress. Stress triaxiality is defined as a unit-less parameter given by the ratio of the hydrostatic stress ($\sigma_m$) and the equivalent stress ($\sigma_e$) which is equated to the Von Mises yield criterion (see **Equation (3-1)**) [86]. The terms $\sigma_1$, $\sigma_2$ and $\sigma_3$ are known as the principal stress terms. High triaxiality results in lower fracture toughness and increased cracking propensity [86,87].

$$T = \frac{\sigma_m}{\sigma_e} = \frac{[(1/3)(\sigma_1 + \sigma_2 + \sigma_3)]}{\{(1/2)[(\sigma_1 - \sigma_2)^2 + (\sigma_2 - \sigma_3)^2 + (\sigma_3 - \sigma_1)^2]\}} \quad \textbf{(3-1)}$$

Significant work has been performed on part-scale modelling techniques depicting the residual stress and associated plastic deformation in complex parts fabricated by laser AM [88,89], however there is a *lack of knowledge on the mechanisms affecting cracking at the microstructural level in LPBF*. The following sections explain two different categories of micro-cracking mechanisms relevant to γ'-strengthened Ni-based superalloys and identify methods used to distinguish the different types of micro-cracks.

## 3.2 Liquid-State Micro-Cracking

Liquid-state micro-cracking occurs when the surrounding tensile stresses created by thermal shrinkage around the liquid exceeds the interfacial energy. The two types of liquid-state micro-cracking have traditionally been defined as liquation and solidification cracking, as identified in **Chapter 2**. However, in the rest of this section, the terminology used to describe the different phases of liquid-state cracking will be **hot cracking** and **hot tearing**, which form as a result of the material solidification process during cooling. This section aims to impart further knowledge to the reader on the mechanisms and means of identifying liquid-state micro-cracks. Examples of hot cracks and hot tears in Ni-based superalloys are provided below for reference.

### 3.2.1 Solidification Cracking Mechanism

Welding literature describes solidification cracking as the type of liquid-film-based micro-cracking phenomena which occurs in the terminal stages of melt pool solidification [81]. The presence of liquid film along the solidification grain boundary (SGB) and thermal shrinkage of the surrounding material result in the formation of solidification cracks.

Various theories describing the mechanism of solidification cracking have been proposed by materials scientists from the late 1940s to early 1960s [81]. Among these theories, the modified generalized theory developed by Matsuda et al. [90,91] has been widely accepted as the root mechanism for the formation of solidification cracks. However, in this thesis, a modified version of Matsuda's theory suggested by Santillana et al. [92] will be presented to describe the different stages of solidification which lead to solidification cracking (**Figure 3-2**). The solidification stages are grouped into two zones – the **hot tear zone ($\sim 0.8 \leq f_s \leq 0.9$)** exhibiting **interdendritic** fracture morphologies, and the **hot crack zone ($f_s > 0.9$)** exhibiting **intergranular** fracture morphologies respectively [92].

According to Santillana, the hot tear zone begins at a temperature where the solute fraction ($f_s$) is around 0.8 (denoted the zero strength temperature (ZST) limit in **Figure 3-2 (a)**) and ends as the material cools to a temperature where the solute fraction $f_s = 0.9$. The increase in solute fraction occurs due to the segregation of solute particles to the interdendritic regions as the liquid cools. This region is identified by dendritic features (**Figure 3-2 (b)**) and a high volume fraction of liquid as the material temperature drops below the liquidus following localized heating. The hot crack zone approximately begins at the liquid isolation temperature (LIT) which shows granular morphology up to a temperature close to the solidus (known as the zero-ductility temperature (ZDT)) near the end of solidification. This zone reflects the transition from dendritic to granular morphology as the dendrites coalesce to form grains. The region between the ZST and ZDT, called the brittle temperature range (BTR), helps qualify hot crack sensitivity [93,94]. Solid-state cracking occurs when the material is cooled below the solidus as explained in **Section 3.3**.

Crack initiation occurs when the undercooled liquid is trapped between the interlocking dendrites as the solute fraction increases above $f_s = 0.8$ during solidification. This is attributed to the formation of isolated droplets and the resultant low-strength non-continuous liquid film between the primary dendrites [92]. Dantzig et al. [95] described this process as **percolation** and Lippold et al. [81] confirmed that solidification cracks formed by this method are affected by material composition, presence of grain boundary (GB) liquid films and intrinsic or extrinsic restrains imposed on the material by thermal or mechanical means. Distinguishing solidification

cracks through microstructural characterization is required to understand the extent of damage inflicted by the above factors.

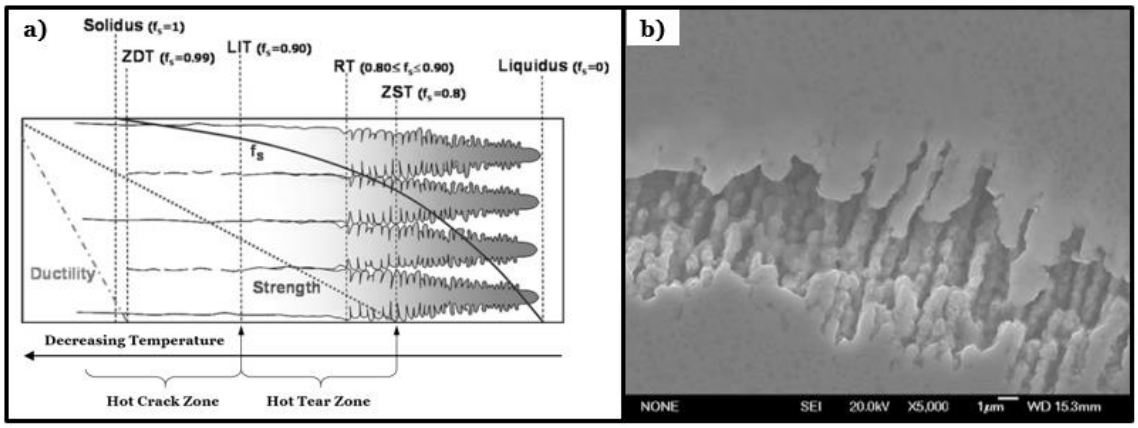


**Figure 3-2: (a)** Schematic Showing the Hot Crack and Hot Tear Zones Representing Solidification Cracks (Adapted from [92]). **(b)** High Magnification Scanning Electron Microscope (SEM) Image Showing Dendritic Features Representative of Hot Tears in high-γ' LPBF CM247LC Alloy [96].

Hot tears are correlated with the formation of dendritic arms in the grain microstructure as shown in **Figure 3-3 (a)**. The fracture morphology of the hot tear zone clearly indicates the formation of dendritic features as liquid solidifies at the ZST. A close-up of the dendrite in **Figure 3-3 (a)** reveals the presence of liquid in the **interdendritic** regions as illustrated by the observation of white-colored features in **Figure 3-3 (b)**.

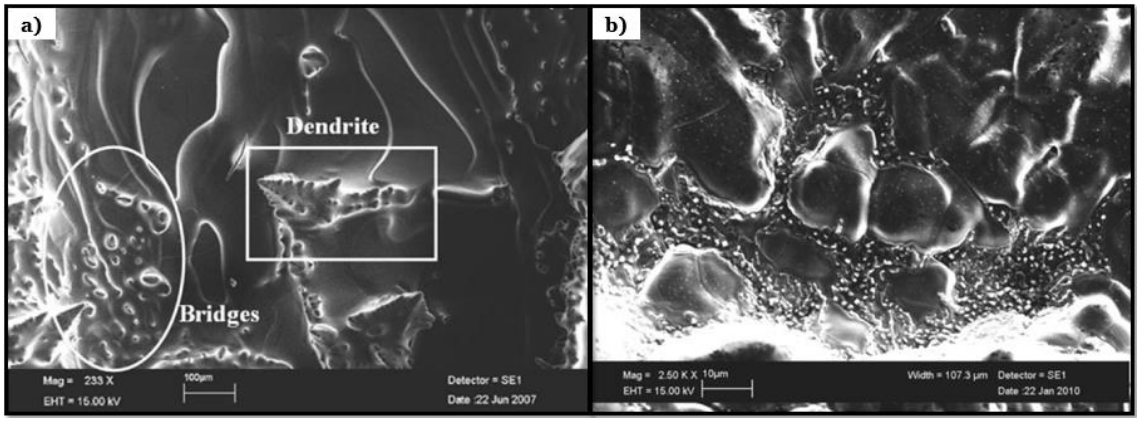


**Figure 3-3:** SEM Image Showing Fracture Surface Indicating Dendritic Features Representative of Hot Tears in **(a)** Low Magnification and **(b)** High Magnification (Adapted from [92]).

Hot cracks are characterized by faceted microstructures and liquid films along clearly identifiable GBs as shown in **Figure 3-4**. The formation of hot cracks takes place in the PMZ which is consistent with the attributes of liquation cracks in reheated weld metals. Closer inspection of **Figure 3-4 (b)** shows the presence of lighter and darker regions in the PMZ, reflective of eutectic morphology.

The fracture morphology provides further insight into eutectic structures in the hot cracked zone as shown in **Figure 3-5**. As temperature lowers below the LIT (see **Figure 3-5 (a)**), the liquid films transform to isolated droplets, and the resultant features are eutectic in nature. Recall from **Section 2.3.1**, eutectic or lamellar morphologies are commonly seen in rapidly solidified metallic material. Lamellar growth occurs due to competition between solute particles leading to solute rejection at the interface between two distinct solid phases formed as a result of rapid cooling. During reheating, elements and compounds with low melting points segregate to the highly energetic GBs between the lamellae. Since eutectics melt at lower temperatures, microsegregation at the eutectic grain boundaries is prominent in LPBF during repeated heating.

Cooling a material up to the ZDT (or the minimum ductility temperature (MDT) as described by Santillana) promotes grain growth portrayed by the faceted planes observed in **Figure 3-5 (b)**. Liquid film and voids are trapped at the GBs due to the percolation behavior and wetting at the GB. Segregation of elements to the **intergranular** liquid film lowers the melting point of the liquid. Similar to the case of eutectics, reheating promotes microsegregation at the GB due to the low melting point of this region. The severity of hot cracking in LPBF is significantly affected by the type, size and distribution of particles segregating to these grain boundaries [97–99].

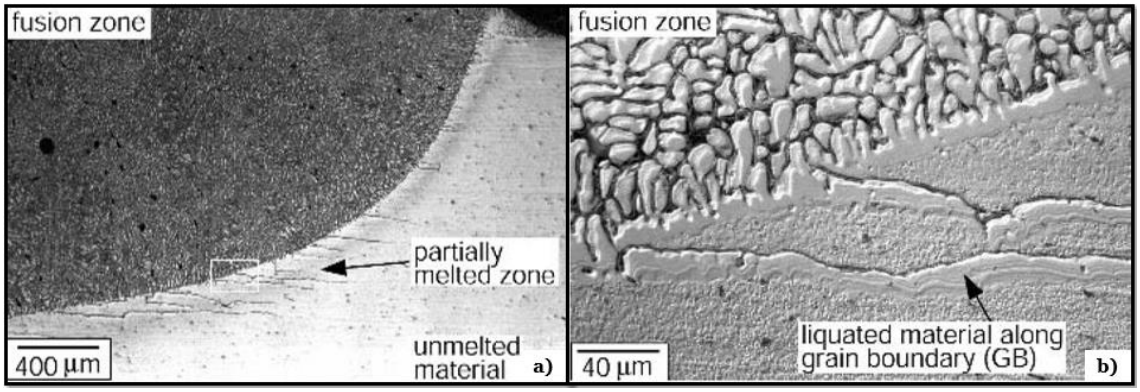


**Figure 3-4:** Appearance of Hot Cracks in the PMZ of Gas-Metal Arc Welded (GMAW) 6061 Aluminum shown in **(a)** Low Magnification and **(b)** High Magnification (Adapted from [61]).

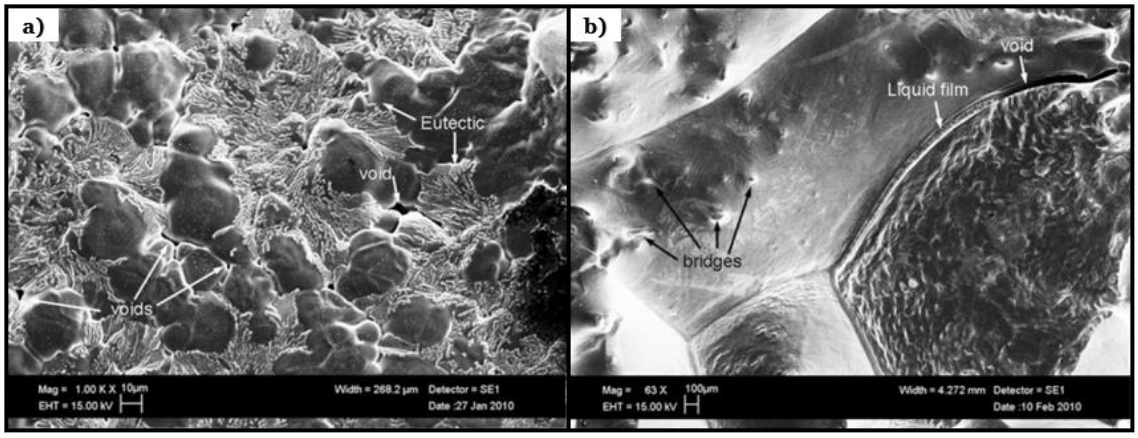


**Figure 3-5:** SEM Images Showing Fracture Surfaces of the **(a)** LIT and **(b)** ZDT Regions (Adapted from [92]).

The micro-crack mechanism described in this section offers a reasonable understanding of the different stages of solidification cracking. However, a detailed illustration showing the effect of the solidification process on material microstructure is necessary to clearly distinguish the potential regions susceptible to solidification cracking. The subsequent subsection attempts to explain a unified solidification crack theory proposed by Lee Alan Aucott [100] based on synchrotron X-ray imaging studies.

### 3.2.2 Unification Theory of Solidification Cracks

In addition to the hot tearing and hot cracking zones, intermediate solidification stages are required to develop a sound understanding of **crack initiation, growth and propagation at the microstructural level**. The **metallurgical science behind microscale cracking** can be used as a building block to improve modelling and process optimization in the part scale. Note that the following paragraphs offer two different metallurgical explanations for the solidification process of metals based on Aucott's in-situ monitoring of weld cracking [100]. **No plausible explanation has been presented for solidification cracking in LPBF or laser AM processes**.

Considering the schematic shown in **Figure 3-6**, welding of a local region within a metal alloy with poor wettability leads to melting and weld pool formation (synonymous to the melt pool shown in **Figure 3-1 (b)**) near the interface between the welding electrode and the material surface. The ensuing solidification stages are named: **stage A1** – sub-surface intergranular hot crack initiation; **stage A2** – hot crack coalescence; **stage A3** – hot tearing. Solidification of the molten liquid begins as the temperature drops following the localized melting inflicted by the moving electrode. Based on Santillana's schematic in **Figure 3-2 (a)**, the solute fraction at the beginning of solidification is low and as the temperature decreases below the liquidus, the material microstructure transforms from dendrites to grains. This transition occurs in the HAZ region below the weld pool, where the volume fraction

of the liquid ($\boldsymbol{Vf_L}$) is low and solute elements segregate to the grain boundaries lowering the melting point of the liquid film. Hot cracks initiate within this region and form around the circumference of the weld pool upon the application of a bending load generated by cooling of the surrounding material **(stage A1)**. As the bending load increases, hot cracks coalesce and propagate into the dendritic region in the solidifying weld pool through the fracture of network separating bridges **(stage A2)**. To accommodate for the increased bending load and the hot cracks in the y direction, the transverse tensile strain in the x direction increases and results in the separation of the primary dendrites. This behavior corresponds to the interdendritic hot tears observed close to the surface where the weld electrode initially interacted with the solid metal alloy and $\boldsymbol{Vf_L}$ is high **(stage A3)**. The direction of crack propagation depends on the growth direction of dendrites dictated by the G/R ratio corresponding to welding in this case.

An alternative justification for the cracking behavior pertaining to the transformation from intergranular hot cracks to interdendritic hot tears in alloyed material is illustrated in **Figure 3-7**. Solidification stages are labelled: **stage B1** – precursors to cracking composed of **stage B1a** (base metal microstructure) and **stage B1b** (grain growth in HAZ); **stage B2** – solidification and precipitation of precipitate particles highlighted as black circles; **stage B3** – microvoid nucleation around precipitate particles (Ti (C,N) in this case); **stage B4** – microvoid coalescence and propagation; **stage B5** – hot tearing. The base material has fine grained features with precipitate particles made up of the alloyed elements Ti (C,N) occupying intergranular sites (**stage B1a**). As the weld arc comes in contact with the material surface, melting occurs and the precipitate particles dissolve in the molten weld pool. Precipitate growth allows grain growth due to reduced Zener pinning efficiency (s**tage B1b**). When the weld electrode moves away, the weld pool solidifies and epitaxial growth occurs above the solid in the underlying HAZ. Anisotropic columnar solidification ensues due to favorable (<100>) orientation promoted by G, R and competitive grain growth. The coalescence of primary dendrites is triggered by the precipitate particles in the interdendritic regions (s**tage B2**). The application of tensile strain leads to ductile fracture around the precipitate creating microvoids (**stage B3**). Coalescence of these microvoids in the intergranular region (s**tage B4**) leads to hot crack propagation and consequent hot tearing in favorable sites along the interdendritic regions (**stage B5**).

The mechanisms described above provide deeper insight into the crack nucleation and growth during weld solidification, however, the actual source of cracking depends on the material's chemical composition and various other factors affected by process parameters and material characteristics. Particularly high G/R ratios in LPBF mean that melt pool solidification occurs rapidly, and some phases may not have the chance to grow completely. This would imply a higher degree of segregation of low melting point elements (such as carbides like

NbC and TiC [81]) in interdendritic regions, which could worsen during reheating. To shed further light on the potential crack initiation regions during rapid solidification, solid-state cracking is discussed below.

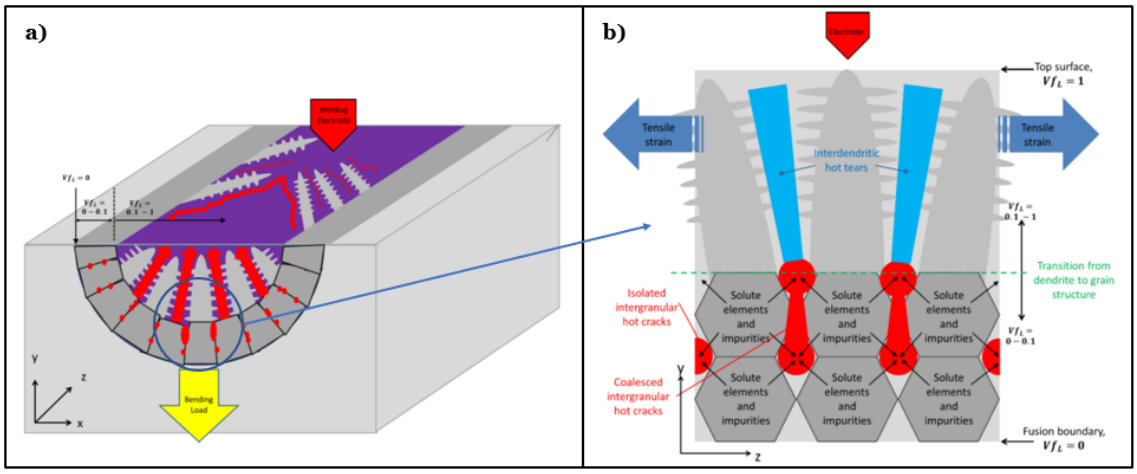


**Figure 3-6:** Schematics Showing the Microstructural Evolution (Stage A3) of a Metal Alloy With Poor Weldability During Solidification in (a) 3D, and (b) 2D (Adapted from [100]).

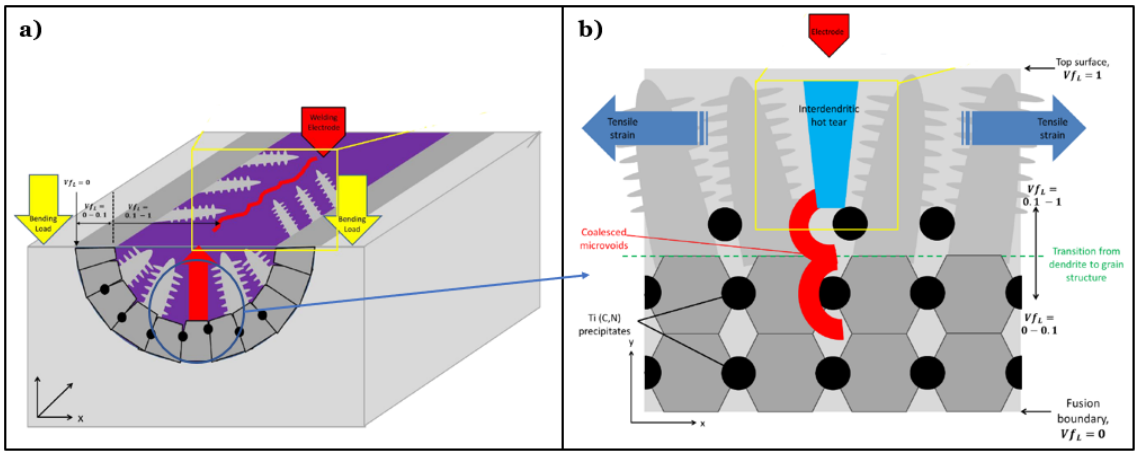


**Figure 3-7:** Schematics Showing the Microstructural Evolution (Stage B5) of a Metal Alloy during Solidification in **(a)** 3D, and **(b)** 2D (Adapted from [100]).

## 3.3 Solid-State Micro-Cracking

Solid-state micro-cracking occurs in the T-HAZ where no melting occurs, and only solid-state phase transitions take place. This type of cracking is common in steels, Ni-base alloys, Cu-base alloys, and aluminium alloys [81]. In Ni-base superalloys processed by LPBF, high solidification rates result in rapid cooling of the microstructure increasing the tensile hydrostatic strains imposed by the surrounding material during cool down. These strains can surpass the material's limited fracture strain at high temperature and induce solid-state cracks along high-angle grain boundaries (HAGBs).

Contrary to liquid-state micro-cracking, where hot tears and hot cracks exhibit interdendritic and intergranular microstructure morphologies respectively, solid-state micro-cracks (both DDC and SAC) show *intergranular cracking* along straight grain boundaries (see **Figure 3-8**). Solid-state micro-cracking is observed below solidus and is suspected to range between the γ' solvus temperature and some temperature below the maximum ductility temperature (MaxDT). Due to the intergranular features in hot tears and solid-state cracks, it is **hard to distinguish between the two**, and further studies need to be performed to achieve a more comprehensive understanding of cracking during the transition from liquid-state to solid-state cracking. Also, note that the ductility starts decreasing below MaxDT as the atoms become more closely packed (representative of solid structures) and get harder to stretch at lower temperatures.

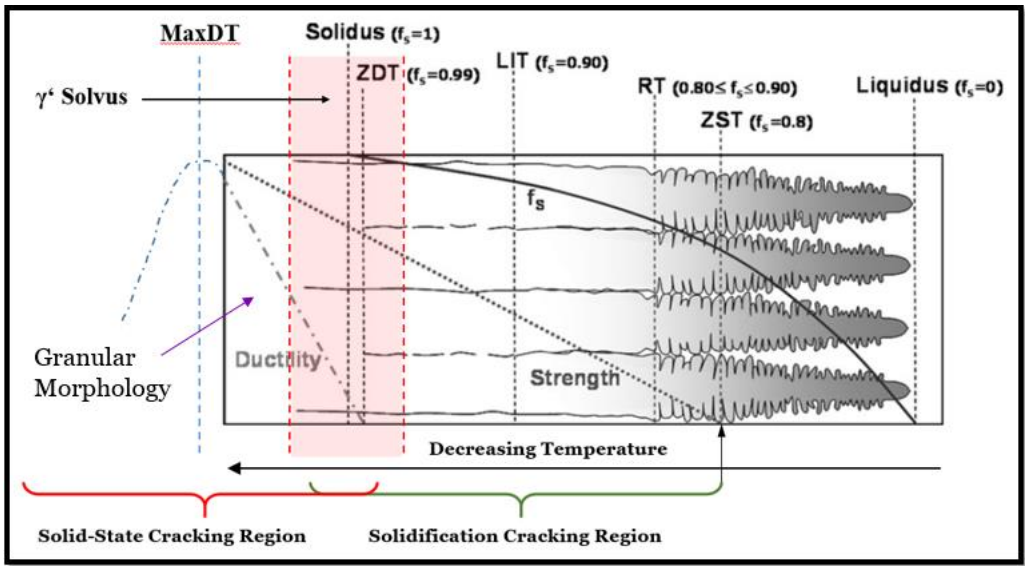


**Figure 3-8:** Extension of the Solidification Schematic Showing Approximate Regions for Solid-State Cracking and Solidification Cracking in Metal Alloys. The Red Zone Indicates the Approximate Zone for γ' Solvus Temperatures as Variability May Exist due to Microsegregation. (Adapted from [92]).

The aim of this section is to provide the background to differentiate between DDC and SAC and recognize the main mechanisms responsible for solid-state cracking. Note that a majority of the mechanisms covered in this section are based on welding literature and are not specifically directed to LPBF studies. Most welding papers deal with instances of DDC in filler or base metals, and in LPBF, the effect of layered deposition on powder bed must be taken into consideration. Therefore, the following mechanisms should only be used as a reference to obtain general knowledge on the fundamentals of solid-state cracking in rapid solidification processing.

## 3.3.1 Ductility Dip Cracking

### 3.3.1.1 Conditions and Criteria

Austenitic (FCC) alloys are known to exhibit DDC along grain boundaries in both the weld metal and HAZ. Literature survey shows that DDC in weld metals are more common than those in HAZ [14,27]. The presence of DDC in the weld metal is justified by a sharp dip in ductility in a temperature range between the solidus ($T_s$) and half of the solidus as shown in **Figure 3-9 (a)** [81]. Materials susceptible to DDC normally show a significant reduction in ductility between approximately $0.9T_s$ and $0.6T_s$ which corresponds to a temperature range between 800 °C and 1150 °C in stainless steels and Ni-base alloys respectively. The formation of DDC is dependent on many factors such as grain boundary character, temperature, composition and restraint. The effect of restraint on the ductility or minimum strain in the ductile temperature region (DTR) is shown in **Figure 3-9 (b)**. As the restraint applied to the material increases with increasing temperature, the possibility of DDC crack formation increases. This is especially important for high-temperature application of materials, for instance, high temperature gradients in LPBF lead to high thermal stresses during solidification.

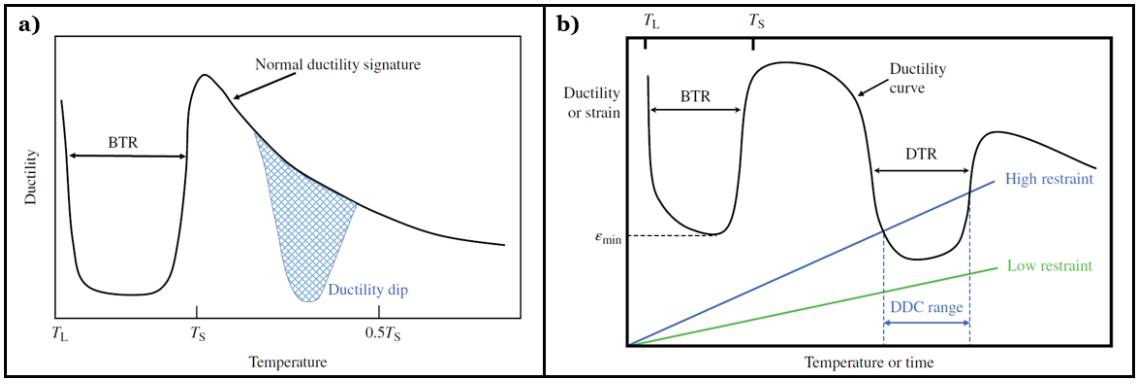


**Figure 3-9: (a)** Ductility Dip Signature in DDC, and **(b)** Effect of Restraint on DDC (Adapted from [81]).

### 3.3.1.2 Mechanism

Elevated temperature DDC is common in solid-solution strengthened Ni-base alloys, but not significant in precipitation-strengthened alloys according to Lippold [81]. This is because the DDC appears along the migration grain boundary (MGB) which has a different composition component from its parent solidification grain boundary (SGB). These boundaries often represent high crystallographic misorientation (greater than 30°) which are typical of HAGBs. Lippold claims that for precipitation-strengthened alloys, the SGB cannot migrate due to grain boundary pinning of precipitate particles. Grain boundary sliding (GBS) results in the formation of voids at triple points of straight grain boundaries where the stress concentration is the highest. The inclusion of precipitates at the grain boundaries make these regions "tortuous" and more resistant to GBS due to the mechanical locking effect of the tortuous boundary [81]. Since the stresses are now concentrated at both the triple point and the precipitate-grain boundary interface, the possibility of DDC formation in the material is lowered due to stress distribution.

Many other scientists before Lippold have proposed that grain boundary shearing [101], sulfur segregation and embrittlement [102], a combination of effects up to recrystallization temperature [103], GBS and microvoid formation [104], and carbide distribution and morphology at the grain boundary [105] could be responsible for DDC formation [15]. A rather contradictory theory to Ramirez [104] and Lippold [81], involving precipitation-induced cracking, was suggested by Young et al. in 2008 [106]. Carbide precipitation at the grain boundaries and stresses induced during heating and solidification result in the creation of microscopic voids (see **Figure 3-10 (a)**). These voids act as crack initiation points under large stresses produced by thermal or mechanical restraint imposed on the material during processing. Recently, Boswell et al. [107], further highlighted the difficulty in pinpointing the mechanism of DDC formation. Cracks showing ductility dip appeared at grain boundary irregularities such as carbides and triple points, which is consistent with Watanabe's theory proposed in 1983 [108].

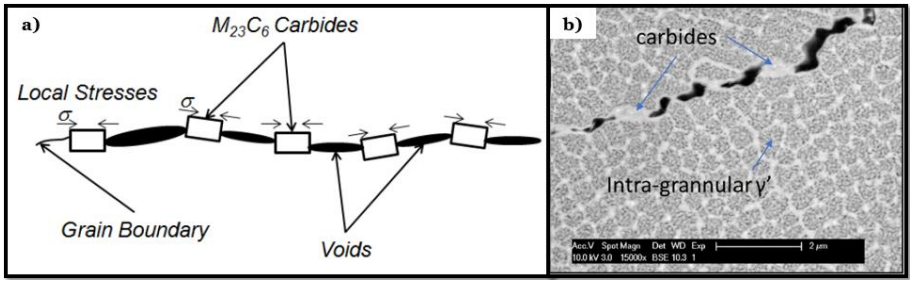


**Figure 3-10:** Illustration of the DDC Mechanism Using a **(a)** Schematic [1,106], and **(b)** SEM Image [107].

Since the cracking mechanism linked to DDC is still highly unclear, and widely debated amongst materials scientists, this is an avenue which needs further investigation. Special attention to the formation of HAGB cracking typical of DDC in LPBF Ni-base superalloys is needed, as the phenomena is not well studied in laser AM. Qian et al. recently reported that edge-type dislocations are responsible for introducing high stress concentrations at HAGBs in a 3D printed Ni-base superalloy [109]. This was attributed to high thermal gradients and the accompanying tensile thermal stresses activating geometrically necessary dislocations (GNDs). Ultimately, it was suggested that discontinuities at these HAGBs result in local strain which surpass the material ductility leading to void formation, coalescence and eventual crack formation [109]. Note, that this conclusion was made solely from a μXRD-based statistical study, and further studies are required to better predict the DDC mechanism.

## 3.3.2 Strain Age Cracking

### 3.3.2.1 Conditions and Criteria

Unlike DDC, strain age cracking (SAC) has been identified as a common cracking mechanism in precipitation-strengthened materials, specifically high-γ' Ni-base superalloys. In most Ni-base superalloys alloys with Al+Ti ratios greater than 6-7% [110], the SAC susceptibility is high due to large content of γ' in the matrix (see **Figure 3-11**). The line (referred to as the "weldability line") representing the susceptibility threshold is highlighted in red and shaded on either side to emphasize the effect of restraint on SAC. Metal alloys exhibiting SAC behavior are considered unweldable due to the high residual stresses imposed during welding.

Most authors have linked the occurrence of SAC to the stresses generated as a result of precipitation and thermal stresses introduced during heating and cooling [15,81,104]. If the rate of precipitation is faster than the rate at which the surrounding material relaxes by creep deformation, the chances of SAC are higher. Consequently, as precipitation increases, the likelihood of SAC occurring during reheating or post-weld heat treatment (PWHT) increases. A good representation of such behavior is observed when the C-curve is overlapped with the heating curves for the alloy as shown in **Figure 3-12 (a)**. The C-curve indicates the effect of temperature and time on precipitation. Both heating curves intersecting the C-curve show tendencies of cracking, while the other heating curves show resistance to cracking. The importance of thermal history to the development of residual stresses, stress relaxation and precipitate aging during welding (or laser AM) is further emphasized in **Figure 3-12 (b)**, and the associated mechanism is presented in the following section.

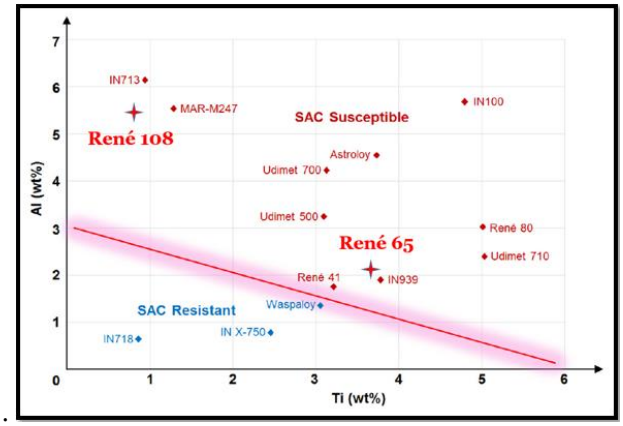


**Figure 3-11:** Effect of Al and Ti content on susceptibility to SAC (Adapted from [111]).

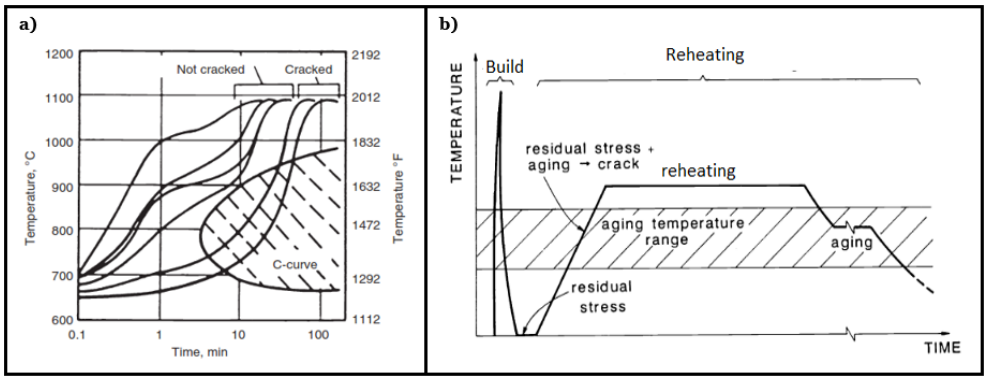


**Figure 3-12: (a)** Effect of Heating Rate and Precipitation Behavior on SAC Susceptibility [112], and **(b)** Thermal History During Welding and PWHT of Ni-Base Superalloys [113].

### 3.3.2.2 Mechanism

Similar to DDC, the strain-age-cracking mechanism in Ni-base alloys is not clearly defined, but previous studies show that SAC is dependent on compositional and restraint factors affected by the thermal profile [81]. According to Lippold [81], rapid heating to subsolidus followed by rapid cooling initiates grain growth depending on the thermal cycle and base material microstructure. This could also be accompanied by HAZ liquation (synonymous to hot cracking as per the terminology introduced in **Section 2.3.1**) at the fusion boundary. In stage B, the liquid films solidify, and residual stress begins to accumulate in the system. Reheating to a solution-annealing temperature slightly above $0.5T_s$ results in some stress relaxation, but upon heating into the

precipitation temperature range, contraction stresses accumulate due to precipitation. A culmination of precipitation and relaxation stresses promotes *intergranular cracking* in stage D.

A simpler take on the SAC mechanism involves considering a stress-strain plot showing two different curves (**Figure 3-13 (a)**) – one showing ductile fracture (marked in red), and the other showing brittle fracture (marked in blue). Initially, the precipitation rate is slower than the relaxation of stresses by creep deformation, therefore the material exhibits ductile behavior, and the strain to fracture is high. As the precipitation rate becomes faster than the rate of relaxation, the material strength increases, ductility decreases and the strain to fracture decreases. Depending on the cooling rate, the morphology of γ' changes (as discussed in **Section 2.3.1.3**) and the ductility due to precipitation is affected. The latter case suggests that the material is more susceptible to SAC when precipitation stresses exceed the relaxation stresses. **Figure 3-13 (b)** indicates that Ni-based superalloys with higher Al + Ti content are more susceptible to SAC due to higher amount of precipitation and faster precipitation rate [81]. The material with high Al + Ti content requires finer control of the heating rate to suppress precipitation and reduce cracking propensity.

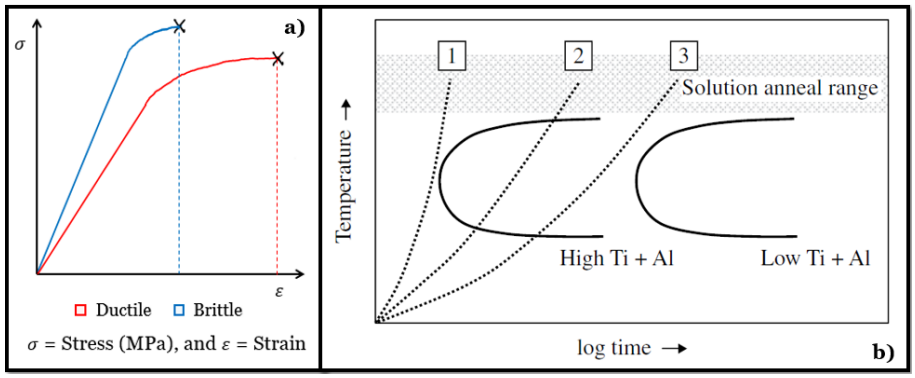


**Figure 3-13: (a)** Stress vs. Strain Plot Showing the Effect of Precipitation Rate on SAC Formation. **(b)** Graph Showing the Susceptibility Difference of Alloys with High and Low Al + Ti Content Respectively [81].

In summary, superalloys that are intentionally designed to exhibit high-strength characteristics at elevated temperatures are susceptible to SAC due to the rapid precipitation by the high volume fraction of γ' precipitates. In laser AM, the high temperature gradients and cooling rates result in ductility reduction, solute trapping, and increased precipitation rates which promote micro-cracking.

## 3.4 Micro-Cracking in LPBF-Processed High-γ' Ni-Based Superalloys

Weld cracking of Ni-based superalloys has been well documented in literature [4,15,28,81], however interest in LPBF micro-cracking of high-γ' Ni-based superalloys has only blossomed recently [1,111,114–116] to meet rising demands to produce parts with complex geometries. Recent research has underlined the importance of optimizing process parameters on the temperature distribution and the residual stresses during laser AM processing [48,117,118]. However, the alloy composition must be adapted to the LPBF process to produce high quality complex parts. This can be achieved by distinguishing the micro-cracking mechanisms, identifying the root causes of micro-cracking, and proposing an appropriate solution to mitigate cracking during LPBF. For instance, if the dominant micro-cracking mechanism is liquid-state micro-cracking and the root cause is solidification or micro-segregation, then the solidification range must be reduced. Conversely, if DDC is observed and the root cause is GB and void precipitation at GBs, then the composition must be modified to reduce the GB precipitates. If the method of micro-cracking is SAC and the root cause is the competing stresses due to precipitation and stress relaxation by creep deformation, then the volume fraction of γ' must be modified. Therefore, further investigation is required to realize a sound thermomechanical model including metallurgical considerations predicting the micro-cracking behavior in laser AM. The following section explains the significance of different factors affecting micro-cracking in LPBF-processed high-γ' Ni-based superalloys.

### 3.4.1 Factors Affecting LPBF Micro-Cracking

The difficulty with laser processing lies in the challenge of controlling many different factors to mitigate micro-cracking in the sample. Specifically, for layer-by-layer printing using LPBF, rapid cooling rates result in strains and anisotropic microstructures which could promote micro-cracking. Similarly, porosities and lack of fusion defects due to gas bubbles and incomplete melting of the powder particles lead to increased crack propensity. Among many factors affecting micro-cracking, material composition, scanning strategies, laser process parameters, powder thickness and part geometry have shown profound effect on the product quality [42]. Fine control of these parameters is essential to maintain mechanical integrity due to micro-cracking.

As highlighted in **Chapter 1**, high-temperature control is necessary to avoid material failure during thermal cycling representative of the on and off cycles experienced by the gas turbine engine during take-off and landing in airplanes. Hence, factors affecting micro-cracking need to be elucidated to **learn the actual behavior of the material from a microstructural point of view during LPBF processing**. Specifically, three factors are chosen to emphasize the **combined effect** of part geometry, laser scanning, and material on micro-cracking, and these are: (1) build part thickness, (2) laser scan (vector) length, and (3) alloy composition. Build part thickness is a critical factor due to the challenges arising from the fabrication of parts with complex geometries and serpent-

like shapes such as nozzle guide vanes and turbine vanes. Vector length is considered because it affects the melt pool size and allows the melt pool to remain in the conduction zone without decreasing the build speed, hence reducing costs. Alloy composition is chosen to facilitate transition and enable adaptation of high-γ' superalloys from slower ($10^1$ °C/s) conventional manufacturing processes to the faster ($10^6$-$10^7$ °C/s [80]) LPBF process.

#### 3.4.1.1 Part Thickness

Few authors have explained the influence of build part thickness on the processability of thin-wall parts using LPBF. For instance, Ahmed et al. [119] reported significantly reduced distortion above a wall thickness of 0.5 mm (**Figure 3-14 (a)**). The authors attributed this behavior to reduced thermal strains, shrinkage and bending as the wall thickness increases. The thinner samples between 0.5 to 1.5 mm show statistically larger variations in distortion (**Figure 3-14 (b)**) compared to the thicker samples due to increased susceptibility to residual stresses developed from laser heat thermal cycling [119]. Wu et al. [120] performed a detailed study on the fabrication limits of thin-wall parts produced using LPBF and demonstrated high surface roughness in parts thinner than 0.3 mm. The authors suggested using different scan strategies for different ranges of wall thicknesses to optimize part fabrication and recommended adding support structures with spacings smaller than 60 mm to avoid part failure due to distortion. Support structures are useful in minimizing the effect of material shrinkage and the inherent stresses in LPBF, but they are expensive and generate material waste [121].

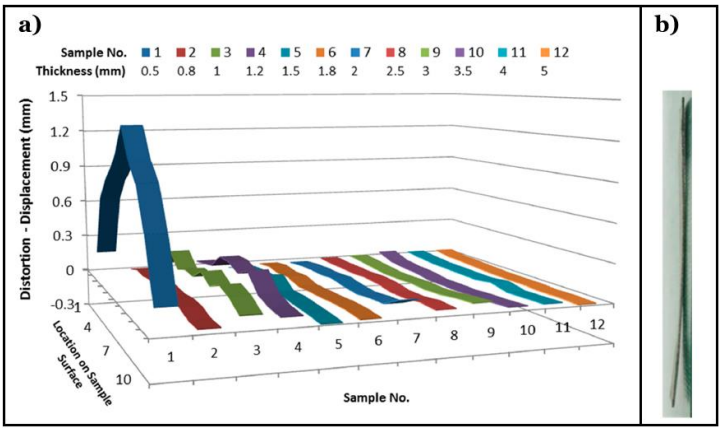


**Figure 3-14: (a)** Distortion Profile of AlSi10Mg, and **(b)** Distorted Thin-Wall Sample (Taken from [119]).

Both studies highlighted the significance of high thermal stresses due to rapid cooling ($10^5$-$10^6$ °C/s) on thin-wall processability. Increased in-process tensile stresses promote micro-cracking during part construction. Therefore, it is important to correlate the thickness effect on in-process stresses with the micro-cracking behavior at the microstructure level. So far, *no scientific studies have directly examined the effect of thin-wall thickness on*

*micro-cracking and there exists no clear correlation between micro-cracking and in-process failure for LPBF-processed parts.*

### 3.4.1.2 Alloy Composition

Cracking literature presents the importance of material composition on the crack susceptibility of LPBF-processed Ni-based superalloys [13,49,107,122]. For instance, Chauvet et al. highlight hot cracking as the root cracking mechanism in a high-γ' Ni-based superalloy composed of Ti + Al wt% = 8.6 [13]. Borides (of the MB, $M_2B$ and $M_5B_3$ type) rich in Cr and Mo are shown to reside along grain boundaries close to cracked regions (see **Figure 3-15 (a) and (b)**). The intergranular HAGB cracks in a sample cross-sectioned in the XZ plane parallel to BD (**Figure 3-16 (a)**) coincide with the presence of continuous liquid films, and dendritic morphology (see **Figure 3-16 (b)**), which according to the terminology adopted in **Section 3.2**, reflect hot tearing and the onset of hot cracking respectively. These low-melting point phases are formed due to the increased tendency of borides to segregate to the grain boundaries [123], which lowers the solidus temperature and increases the solidification range. As the solidification range increases, the susceptibility of the material to solidification cracking (or liquid-state cracking) increases. This is especially important in laser melting because remelting of previous layers promotes dissolution and cooling of the intergranular boride precipitates, which, in combination with low eutectic wetting of the GB enhances the severity of microsegregation and aggravates cracking at the grain boundaries. The uncracked region is claimed to have dimples and isolated liquid drops (**Figure 3-16 c)**) linked to the coalescence of secondary dendrite arms [13].

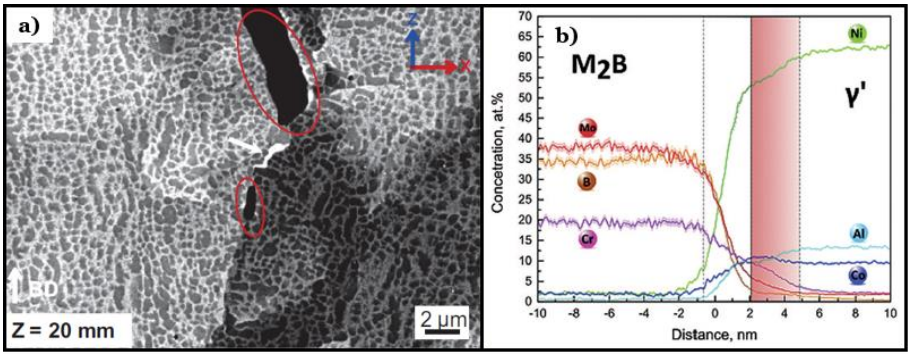


**Figure 3-15: (a)** Borides (indicated by white arrows) at the Grain Boundaries of a High-γ' Ni-Based Superalloy with Ti + Al wt% = 8.6 Observed at the Tip of a Crack, **(b)** Concentration Profile Analysis at γ'/$M_2B$ Interface Showing Concentration of Ni, Al, Co, Mo, B and Cr Based on Atom Probe Tomography (APT) Near Crack Tips. The Red Shaded Region Indicates Suspected Liquid Film (Taken from [13]).

Another hard-to-weld Ni-based superalloy, CM247LC (variant of R108), composed of Al + Ti wt% = 6.2, was manufactured by LPBF and subjected to post-process heat treatments to determine the main causes for cracking [107]. Evidence of DDC and SAC was shown through SEM images, and attributed to the presence of carbides (see **Figure 3-10 b)**), observation of triple point cracks (see **Figure 3-17 (a)**) and void coalescence at higher temperatures indicative of creep fracture (see **Figure 3-17 (b)**) [107]. This shows that solid-state cracks are also possible in high-γ' Ni-based superalloys produced by LPBF depending on the thermal history. On the contrary, Lee et al. [122] show that segregation of minor elements such as Ta and W contribute to liquid-film-based cracking in the final stages of solidification of LPBF Mar-M247 (Al + Ti wt% = 6.2%). The difference between the cracked and crack-free region is clearly discernible as the crack-free region does not exhibit any elemental segregation.

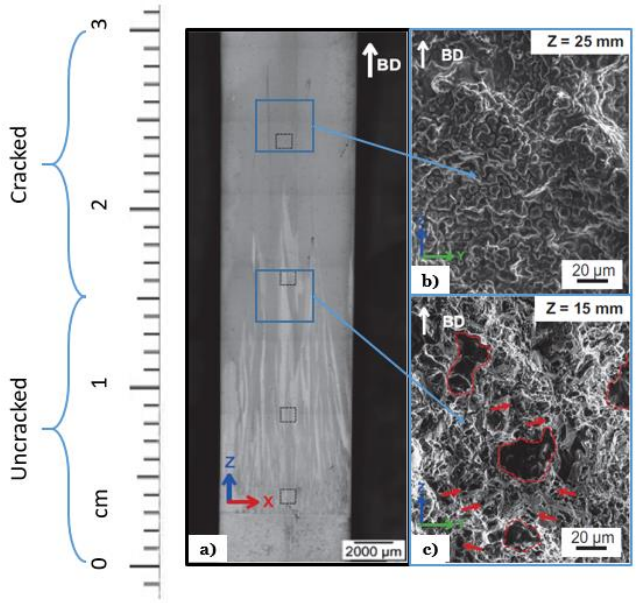


**Figure 3-16: (a)** Optical Micrograph Showing Macrostructure of Sample Cross-Sectioned in the XZ Plane Parallel to the Build Direction along the Z Axis. The Top Half of the Sample has Cracks and the Bottom Half does not have Cracks. **(b)** Fracture Morphology of the Cracked Region Showing Dendritic Morphology. **(c)** Fracture Morphology of the Uncracked Region Showing Dimples (Marked by Red Arrows) and Suspected Isolated Liquid Drops (Highlighted using Red Circles) (Taken from [13]).

Zhang et al. [49] demonstrate the appearance of DDC cracks at GB triple points (**Figure 3-18 (a)**, **(b)** and **(c)**) and at the bottom of liquation cracks (**Figure 3-18 (d)**). Cracking is attributed to high accumulated stress at the GBs which occurs due to the precipitation of γ' and carbide formation (**Figure 3-18 (d)**) leading to cavity

nucleation. Oxides rich in Al are also observed near the triple points as shown in **Figure 3-18 (c)**. Such behavior is claimed to be a product of dynamic embrittlement (DE) and stress assisted grain boundary oxidation (SAGBO) which is attributed to short and long range diffusion of oxygen in front of the crack-tip [49]. The authors make this claim based on the deduction that the necessary conditions for in-process LMD cracking are similar to that of fatigue crack mechanisms.

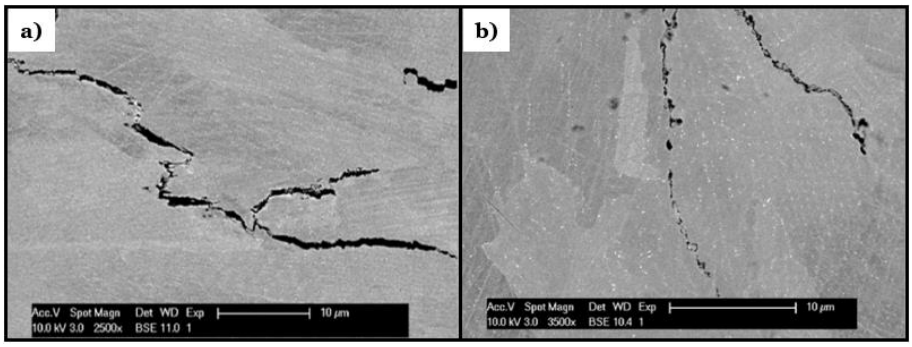


**Figure 3-17:** Effect of Post-Processing on LPBF CM247LC Cracking: **(a)** DDC **(b)** SAC (Taken from [107]).

All the examples described above signal the significance of alloy composition on cracking observed in LPBF-processed Ni-based superalloys. Both Chauvet et al. [13] and Lee et al. [122] propose liquid-state cracking as the dominant cracking mechanism during e-beam and laser processing respectively. Conversely, Boswell et al. [107] suggest that solid-state cracking is prevalent in post-processed LPBF parts. Others such as Zhang et al. [49] argue that DDC is observed with liquation or "hot" cracks. However, *none of these authors provide a complete picture of the cracking behavior associated with high-γ' Ni-based superalloys fabricated by LPBF*. Moreover, the explanations for the claimed cracking mechanisms are not conclusive due to a lack of advanced microstructural characterization (such as APT or Transmission Electron Microscopy – TEM), thermomechanical modelling and FEM-based modelling to further validate the claims.

For instance, the SEM images showing carbides (**Figure 3-10 (b)**) and borides (**Figure 3-15 (a)**) appear the same, and Boswell et al. [107] do not perform high magnification microstructure characterization to show the formation of fine $M_{23}C_6$ at elevated temperatures. They claim that the appearance of a Cr peak observed through energy dispersive X-ray spectroscopy (EDS) analysis of the cracked region is associated with the transformation of MC to $M_{23}C_6$ plus γ' [107]. On the other hand, Chauvet et al. [13] are not able to clarify the exact reason for the crack. They also suggest that unknown black regions (refer to **Figure 3-16 (c)**) are entrapped liquid drops, and the uncracked region shows signs of ductile failure. The latter proposition is not clear from the SEM image, and further evidence is required to differentiate the cracked and uncracked regions. In both cases, the crack

mechanism is not well defined, and any thermodynamic analysis performed is not representative of the type of crack formed (for example, the solute fraction determined by Chauvet et al. [13] indicates hot cracking, not hot tearing as claimed by the authors). This might also have to do with a lack of consistency in the terminologies used to define cracking in materials processed by LPBF.

Finally, recall that the reasoning for crack category diversifications stems from old terminologies such as “solidification crack” or “liquation cracks”, not clearly distinguishable by solute fractions. Moreover, papers considering solute fraction use the Scheil-Gulliver equation [124,125], which assumes complete mixing in liquid and no diffusion in solid state. Most authors who present thermodynamic analyses use the Scheil-Gulliver equation to predict the lower bound for solidus and obtain a larger solidification temperature range. For non-equilibrium solidification, common in LPBF, Brody and Flemings [126] provide a better estimate of the actual solidus temperature due to the inclusion of a back-diffusion coefficient during thermodynamic calculations. Furthermore, there are many variants of high-γ’ Ni-based superalloys with very different alloy compositions which could contribute to different cracking behaviors. Therefore, there is a significant need to distinguish cracking regimes for LPBF-processed Ni-based superalloys by implementing appropriate crack resolution strategies through the means of advanced microstructural characterization and modelling methods.

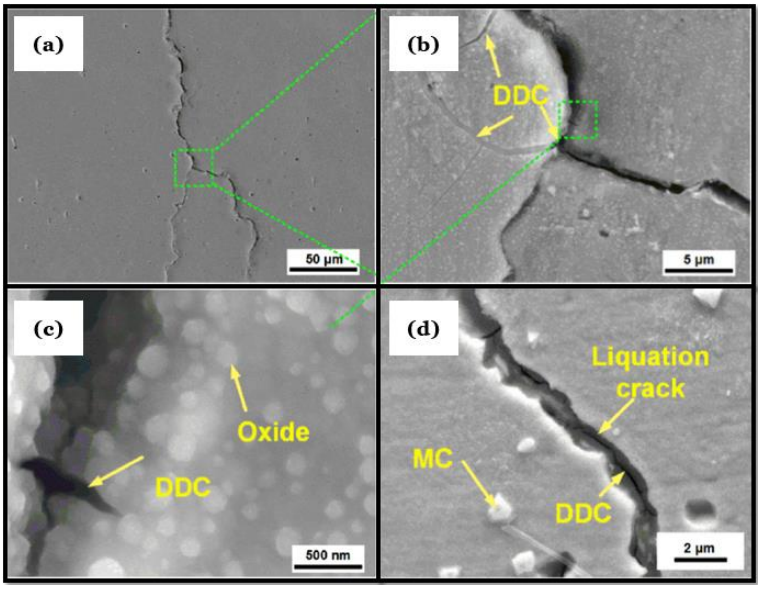


**Figure 3-18: (a)** DDC observed at GB Triple Point. **(b)** Close-up Image of Triple Point Crack. **(c)** Presence of Nanometer-Scale Oxide Particles Near the DDC. **(d)** DDC Embedded in the Base of Liquation Crack Showing Coarse MC Carbides Near the Cracked Region (Taken from [49]).

#### 3.4.1.3 Vector Length

The effect of scan strategies on LPBF micro-cracking has been studied extensively by the likes of Carter et al. [96], Cheng et al. [127], Catchpole-Smith et al. [128] and Li et al. [117]. Island scan strategies (**Figure 3-19 (a)**) have been recommended to distribute the heating more evenly [96], while 45° line scanning and 67° rotate scanning method have been implemented to reduce the effect of reheating on the previously printed layer [127]. All three methods attempt to reduce the accumulation of thermal strains minimizing the possibility of crack formation. However, there is limited literature directly demonstrating the effect of laser scan length on LPBF micro-cracking and thin-wall part in-process failure.

Fractal scan strategies with reduced vector lengths in the order of 100 µm (**Figure 3-19 (b)** and **(c)**) have been suggested by Catchpole-Smith et al. [128] as means to increase bulk density (**Figure 3-19 (d)**) and reduce crack length density (**Figure 3-19 (e)**). Uniform thermal strains are generated due to the mathematical area filling strategy which reduces thermal anisotropy representative of contour and raster scans.

Li et al. [117] show that the thermal stresses in thin-walled parts built on a Ti6Al4V powder bed (see **Figure 3-20 (a)**) are influenced by the scan length. The neighboring scan vector produces the highest temperature, and the second peak temperature is above the melting point, implying formation of a molten pool in the neighboring region (see **Figure 3-20 (b)**). As scan length increases, the maximum temperature remains unchanged, but the second peak temperature decreases as shown in **Figure 3-20 (c)**. This is attributed to wider heat spread for longer vector lengths and more homogeneous temperature field distribution for shorter vector lengths. Asymmetry in heat flow increases the generation of non-uniform thermal strains resulting in increased crack susceptibility during LPBF material processing.

Deficiencies in describing the micro-cracking mechanisms linked to the observed trend for scan length versus temperature and thermal stresses prevents the reader from forming a clear connection between the residual stress and crack formation. It is not apparent if the thermo-mechanically-induced strains are accumulated during solid-state or liquid-state, and further information is necessary to determine the location of void formation, coalescence, and ensuing development into micro-cracks. In addition, there appears to be no clear identification for scan length cut-off in LPBF cracking.

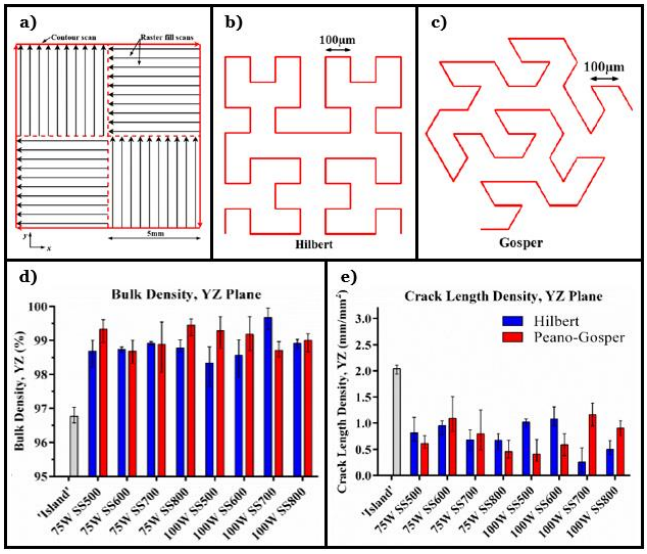


**Figure 3-19: (a)** Optimum Island Scan Strategy Determined by Carter et al. [96] – 5 mm x 5 mm Islands with Contour and Raster Fills. Fractal Scan Strategies Employing Mathematical Area-Filling Curves with Scan Vector Lengths in the Order of 100 μm: **(b)** Hilbert and **(c)** Gosper. Effect of Scan Strategy on **(d)** Bulk Density and **(e)** Crack Length Density in the YZ Plane Parallel to the Build Direction (Taken from [128]).

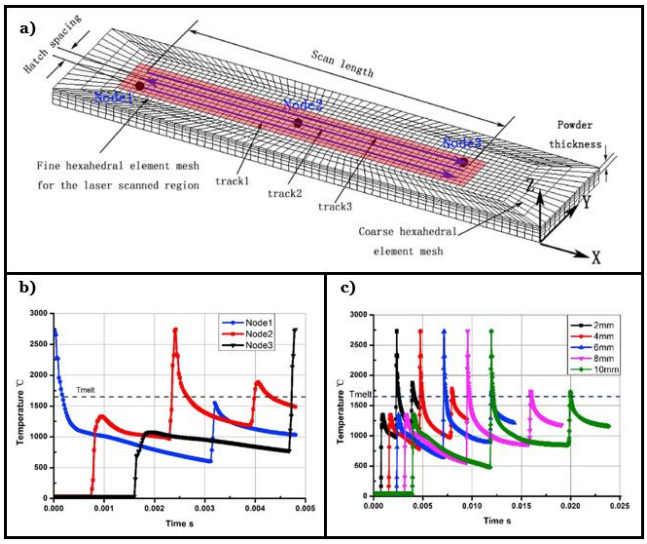


**Figure 3-20:** (a) 3D FEM Model Showing a Single Layer Thin-Walled Part Built on Ti6Al4V Powder Bed. (b) Variations of Temperature at Node 1, Node 2 and 3. (c) Temperature Variations at Node 2 for Different Scan Lengths (Taken from [117]).

### 3.4.2 Knowledge Gaps

Through thorough literature survey of failure in AM thin-wall structures (key works detailed in the preceding sections within this chapter), the following knowledge gaps were identified:

1. There are *no studies on the mechanism for macro-scale failure of thin-wall components*. Most literary works on LPBF thin-wall structures elucidate the influence of wall thickness on build defects such as distortion, surface roughness, and residual stresses. The presented studies clearly explain the significance of wall thickness on final part quality and printability but fail to provide the underlying reason for part failure. Industrially, it is widely understood that thin-wall structures fail due to in-process cracking, but this hypothesis has not been proven in literature. Further studies on the matter can help better understand and mitigate thin-wall macro-scale failure.

2. *No clear consensus on the micro-cracking phenomena of high-γ' Ni-based superalloys has been reached yet*. Authors are primarily split between the solidification cracking (liquid-state) and SAC (solid-state) mechanisms. To reduce micro-cracking, improve printability, and facilitate the development of the next generation of superalloys for application in LPBF processes, the following untouched subjects must be investigated in detail:
    a. The effect of part geometry on the micro-cracking mechanism remains unexplored. The effect of *wall thickness* and *build position* along the part height on micro-cracking phenomenon is especially pertinent to thin-wall part design.
    *b.* The *influence of alloy composition on the micro-cracking mechanism has not been discussed in depth for a wide range of high-γ' Ni-based superalloys*. For instance, alloys richer in hafnium can promote the formation of Hf-rich carbides, which could promote solidification (liquid-state) cracking. Conversely, alloys richer in Al and Ti are reported to exhibit the strain age (solid-state) cracking mechanism. Advanced microstructural characterization and numerical simulations must be conducted to isolate the root causes and understand how to mitigate internal micro-cracking mechanisms in superalloys.

3. Processing parameters can greatly affect the stresses and minimize LPBF build defects. However, *there is no known notable work on the effect of laser vector length on the micro-cracking tendencies to-date*. The continuous 67° scan rotation strategy is widely considered the optimal processing strategy for LPBF parts. However, the effect of the optimal scan strategy has not been investigated for different part geometries. More particularly, there are no studies performed on the correlation between scan strategies and the micro-cracking mechanism. Vector length modification is an easier and cheaper process alteration approach to study the *mitigation of micro-cracking tailored for LPBF thin-wall parts*.

# Chapter 4
# Research Overview

## 4.1 Research Strategy

To address the knowledge gaps highlighted in **Section 3.4.2**, the research is broken down into five key areas to explain LPBF thin-wall build failure at the macro- and micro-scales, with *special emphasis on micro-cracking in high-γ' Ni-based superalloys*. The studies employ *extensive experimental and simulation analyses, providing both metallurgical and mechanistic information to obtain optimal thin-wall part processability*.

### 4.1.1 Analysis of the Macro-Scale Failure Mechanisms in LPBF High-γ' Ni-based Superalloy Thin-Wall Parts – Knowledge Gaps 1&2, Paper 1, Chapter 5

This study combines experimental and numerical modelling techniques to examine the causes of macro-scale failure in LPBF thin-wall parts. In-process failure is quantified using the limiting build height (LBH) parameter that defines the height at which the thin-wall part aborts during LPBF fabrication. Microstructure characterization and statistical analyses are performed for two different types of high-γ' Ni-based superalloys covering the lower and upper extremes of micro-cracking. Evaluation of micro-cracking is especially significant as industries have previously correlated macro-scale failure to high micro-cracking in thin-wall parts. Micro-crack densities are analyzed for different wall thicknesses to determine if micro-cracking is a dominant cause of the LBH. Numerical modelling techniques are employed to evaluate the effect of in-process stresses, strains, and part distortion on LBH. Experimental and simulation results are compared and a theory for macro-scale failure in LPBF-based thin-wall parts is proposed.

### 4.1.2 Explaining the Micro-Cracking Phenomenon in High-γ' Ni-Based Superalloy Thin-Wall Parts Produced by LPBF – Knowledge Gap 2b, Paper 2, Chapter 6

The micro-cracking mechanism in thin-wall parts produced by LPBF is investigated as micro-cracking affects processability and diminishes final part quality. The main focus of this work is to study the effect of part thickness on micro-cracking. Experimental characterization, image and statistical analysis, and numerical modelling techniques are used to understand the micro-cracking mechanism. The importance of stress triaxiality on the micro-cracking mechanism is demonstrated using numerical simulations. The simulated results are correlated to experimental findings explaining the metallurgical factors responsible for micro-cracking. A theory for micro-cracking in LPBF-processed thin-wall parts is proposed based on the results.

### 4.1.3 Investigating the Effect of Build Position on Micro-Cracking in LPBF-Based Thin-Wall Components – Knowledge Gap 2a, Paper 3, Chapter 7

To further understand the significance of stress triaxiality on micro-cracking, the effect of build position on micro-cracking densities is investigated using experimental and numerical simulation methodologies. The LPBF process is known to exhibit variation in microstructure and generate in-process stresses along the part height due to the rapid heating and cooling effects. The degree of change in micro-cracking along the part height is examined using statistical methods and compared using stress triaxiality plots created using numerical simulation methods. The results agree well with the view that stress triaxiality causes micro-cracking in LPBF thin-wall parts.

### 4.1.4 Examining the Effect of Composition on Micro-Cracking in High-γ' Ni-Based Superalloy Thin-Wall Structures Produced by LPBF – Knowledge Gap 2b, Paper 5, Chapter 8

This work elucidates the effect of composition on micro-cracking observed in high-γ' Ni-based superalloys processed with LPBF. Fabrication of crack-free parts are especially challenging for these alloys and is further complicated by the rapid solidification process and fine-scale geometries representative of thin-wall components. Two different alloys with varying levels of γ' contents are studied to explain the metallurgical factors responsible for micro-cracking. Experimental approaches are used to determine the micro-crack statistics for the two alloys under fixed processing conditions and wall thickness. Advanced microstructure characterization tools are employed to investigate the differences in compositions and their effects on the micro-cracking behaviors.

### 4.1.5 LPBF Thin-Wall Part Micro-Cracking Mitigation Using Laser Scanning Strategies – Knowledge Gap 3, Paper 4, Chapter 9

Due to the heightened significance of in-process stresses and stress triaxialities (as discussed in previous sections), the effects of wall thickness and scan strategies on the in-process stresses, stress triaxialities, and micro-cracking propensities in LPBF high-γ' Ni-based superalloy thin-wall parts are investigated. A large-scale design of experiment (DOE) encompassing four different wall thicknesses between 0.25 mm and 1 mm and ten different laser scan strategies are developed to minimize micro-cracking. Experimental and statistical analyses are used to explain the micro-cracking tendencies for different build conditions. The experimental findings are linked to in-process stresses and stress triaxialities, predicted using numerical modelling methods, to gain comprehensive

understanding of LPBF thin-wall micro-cracking. Based on the presented findings, scan strategies to minimize in-process stresses and mitigate micro-cracking are proposed.

## 4.2 Research Map

To provide a holistic view of the correlations between the research strategies (**Section 4.1**), goal (**Section 1.2**), and objectives (**Section 1.2**), a research map is presented in **Figure 4-1**. The in-process failure study presented in **Chapter 5** (Paper 1) covers *knowledge gaps 1 and 2*, whereas the micro-cracking works presented in **Chapter 6-Chapter 8** (Papers 2, 3 and 5) cover *knowledge gap 2*. The effect of changing vector length on micro-crack mitigation (*knowledge gap 3*) is presented in **Chapter 9** (Paper 4).

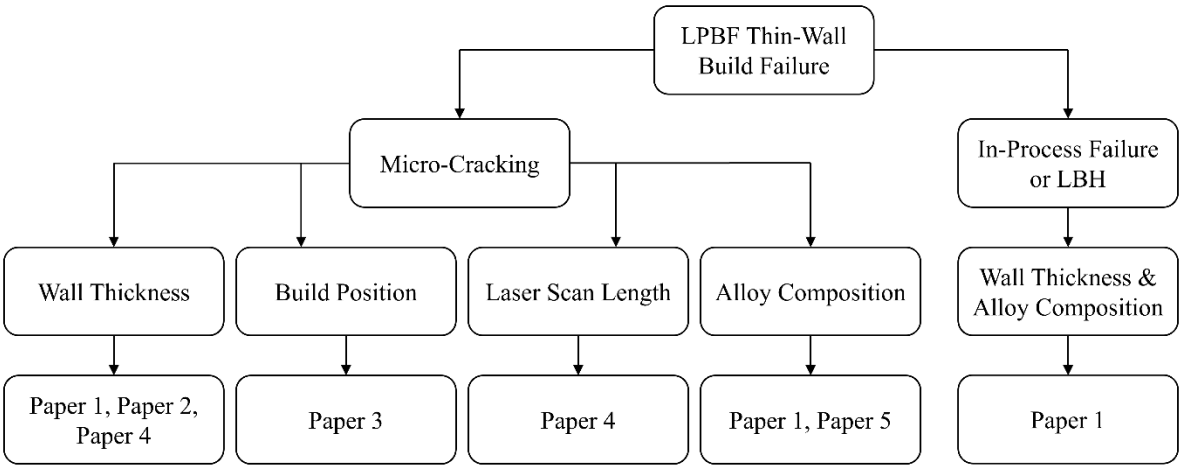


**Figure 4-1:** Research Map Demonstrating Correlations Between Research Strategies Presented as Papers.

# Chapter 5

# Analysis of the Macro-Scale Failure Mechanisms in LPBF High-γ' Ni-Based Superalloy Thin-Wall Parts

In this chapter, *a mechanism for macro-scale thin-wall part failure during LPBF processing is proposed*. Experimental and numerical simulation techniques are employed to evaluate the effect of micro- and macro-scale factors on part failure. Statistical tools are used to evaluate the micro-cracking propensities of two different crack-susceptible materials. High-γ' Ni-based superalloys are used as they are known to be susceptible to micro-cracking under rapid solidification processing conditions. Numerical simulation approaches are used to depict the effect of macro-scale factors such as stresses, strains, and part distortion on part failure. The experimental observations are successfully verified using simulated results.

The chapter presents an accepted manuscript of an article published in the Journal of Materials Science & Technology.

***Journal of Materials Science & Technology 98 (2022): 233-243. https://doi.org/10.1016/j.jmst.2021.05.017***

## 5.1 Introduction

Laser powder bed fusion (LPBF) is a type of laser additive manufacturing (AM) technique that enables cost-effective production of parts with complex shapes [42,129]. Aerospace applications such as serpentine-shaped turbine vanes and curved thin-wall fuel nozzles have greatly benefited from the growth of LPBF technologies worldwide [30,130]. Conventional fabrication of these critical aircraft components by casting and welding technologies have employed high gamma prime (γ') Ni-based superalloys, which provide high-temperature creep and fatigue strength coupled with excellent oxidation and corrosion resistance [131–135]. Processing of these high-strength alloys through LPBF provides a promising route to construction of near-net shape, tight-tolerance components capable of withstanding extreme environmental and loading conditions [96].

The LPBF manufacturing process is complex and requires optimization of process parameters to fabricate defect-free, high-quality parts. Thin-wall part fabrication using LPBF is especially challenging and the thinnest parts successfully produced to-date measure 100 µm [136]. Rapid solidification of small powder particles [115] could generate undesirable properties and consequently reduce final part integrity [119,137,138]. Internal micro-cracking has been identified as a source of failure in LPBF-based thin-wall parts [15,28]. Alloy composition significantly affects in-process micro-crack formation in precipitation-strengthened Ni-based superalloys [13,124,139]. The formation of solidification and solid-state micro-cracks are attributed to insufficient liquid feeding and brittle grain boundary (GB) phases such as carbides and borides. Changes in macro properties (such as stresses and distortion) between 0.25 and 1 mm [119,140] wall thickness also contribute to part failure. Thermal stresses develop from large thermal strain fluctuations induced by rapid heating and cooling of material, which could upset the overall stress balance and affect the final build [117,141]. Part distortion has been attributed to phenomena such as temperature gradient mechanism (TGM) [48] and constraining force-induced distortion (CFID) [137,142]. According to Yang et al. [137], longer and taller thin-wall structures are more vulnerable to distortion due to inconsistencies in microstructures and melt pool boundaries. Despite concerted efforts in identifying specific causes for part failure in complex LPBF-based structures, systematic studies on the failure mechanism(s) in thin-wall sections are yet to be conducted.

The aim of this study is to explore the effect of internal micro-cracking, thermal stresses, and distortion on the limiting build height (LBH) of LPBF-based thin-wall parts. Statistical image analysis and microstructure characterization techniques are used to determine if internal micro-cracking leads to part failure. Subsequently, finite element modelling (FEM) is employed to determine stress distributions with respect to part thickness. Finally, displacements from experiments and simulations are compared to demonstrate the effect of distortion on LBH.

## 5.2 Experimental Procedures

### 5.2.1 Materials

Two different high γ' Ni-based superalloys, RENÉ 65 (R65) and RENÉ 108 (R108), were used for LPBF. Both alloys contain high Al + Ti content and high γ' volume fraction: (1) R65 has a Al + Ti wt.% content of 5.6 and γ' volume fraction of 42% [73], and; (2) R108 has a Al + Ti wt.% content of 6.15 and γ' volume fraction of 63% [74]. These alloys are categorized as crack-susceptible materials according to welding literature [110]. The initial R65 and R108 powders were gas-atomized by ATI Powder Metals and Powder Alloy Corporation (PAC), respectively. Both R65 and R108 constitute of mostly spherical powder particles with a size range ($D_{10}$-$D_{90}$) of 12-40 µm. The median particle sizes ($D_{50}$) for both R65 and R108 are ~19 µm. Both powders contain small fraction of satellite particles attached to larger particles. Sample images of the powder morphology and particle size distribution (PSD) of R108 are shown in **Figure 5-1 (a)** and **(b)**, respectively. Chemical compositions of both alloys are given in **Table 5-1**. The elemental contents (in wt.%) were determined by inductively coupled plasma - optical emission spectroscopy (ICP-OES) at Activation Laboratories (ACTLABS © Canada).

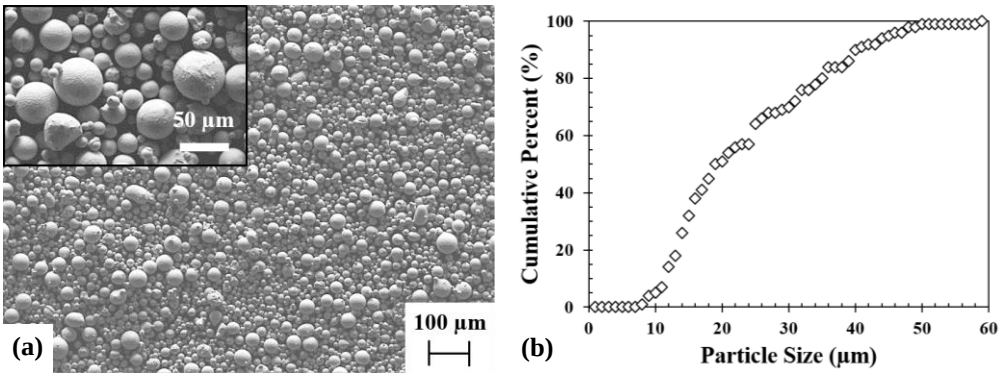


**Figure 5-1:** (a) SEM Image Showing R108 Powder Morphology. (b) Cumulative Particle Size Distribution of R108 Powder. Both R65 and R108 had Similar Powder Morphologies and Particle Size Distributions.

**Table 5-1:** Powder Compositions of R65 and R108 in wt.%.

| Alloy | Ni | Co | Fe | Cr | Al | Ti | Ta | Nb | W | Mo | Hf | B | Zr |
|---|---|---|---|---|---|---|---|---|---|---|---|---|---|
| R65 | Bal. | 13.22 | 1 | 15.86 | 2.15 | 3.65 | 0.04 | 0.75 | 4.25 | 4.03 | 0 | 0.01 | 0.05 |
| R108 | Bal. | 10 | 0.9 | 8.64 | 5.36 | 0.75 | 3.02 | 0 | 10.03 | 0.53 | 0.87 | 0.01 | 0.01 |

### 5.2.2 LPBF Printing

Parts were constructed using the AconityTM MIDI under the build conditions listed in **Table 5-2**. A design of experiment (DOE) including two different alloy compositions – R65 and R108 – and three different part thicknesses – 0.25 mm, 1.00 (1) mm and 5.00 (5) mm – was constructed. A three-dimensional (3D) view of the setup, including the three parts and the build substrate, is shown for one sample plate in **Figure 5-2 (a)**. The three thin-wall parts (5 mm, 1 mm and 0.25 mm) were printed at the center of the build plate and had the same scan orientations. Two repeats for both alloys were printed to demonstrate the repeatability of the experimental results. Overall, four build plates, one for each alloy and its repeats for the three part thicknesses, were used to avoid build variation due to neighboring parts during printing.

Bidirectional scan strategy with a hatch angle of 15 degrees (**Figure 5-2 (b)**) with respect to the part thickness was employed to print the first layer and scans were not rotated for subsequent layers. All scans were performed at an angle of 45 degrees relative to the recoating direction to avoid sample printing perpendicular to the recoater's movement. No further parameter optimizations were performed for the purpose of this study. Finished parts with smaller wall thicknesses exhibited reduced LBHs (**Figure 5-3**), corresponding to the final part heights after printing.

**Table 5-2:** Build Parameters for LPBF-Based R65 and R108 Thin-Wall Parts.

| Build Parameter | Value |
|---|---|
| Laser Power, P (W) | 200 |
| Scan Speed, v (mm/s) | 1000 |
| Spot Size, $d_{spot}$ (µm) | 120 |
| Hatch Spacing, h (µm) | 90 |
| Hatch Angle, θ (°) | 15 |
| Powder Layer Thickness, t (µm) | 40 |
| Designated Part Height (mm) | 50 |
| Part Thickness, $t_{part}$ (mm) | 0.25, 1, 5 |

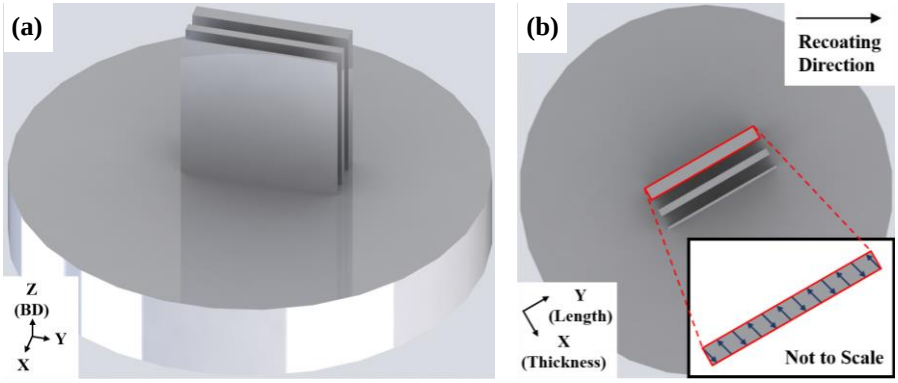


**Figure 5-2:** CAD Model of a Printed Plate with the Three Thin-Wall Parts. In **(a)** 3D View and **(b)** Top View Showing Thin-Wall Parts with Thicknesses of 5 mm, 1 mm, and 0.25 mm, Respectively. The Red Box in **(b)** Highlights the 5 Mm Thick Part with a Corresponding Close-Up Image Shown as an Inset. Blue Arrows Indicate Bidirectional Scan Strategy at a Hatch Angle of 15 Degrees with respect to the Part Thickness, Employed for all the Thin-Wall Samples. The Laser was Scanned at a 45-Degree Angle with Respect to the Recoating Direction (Top Right).

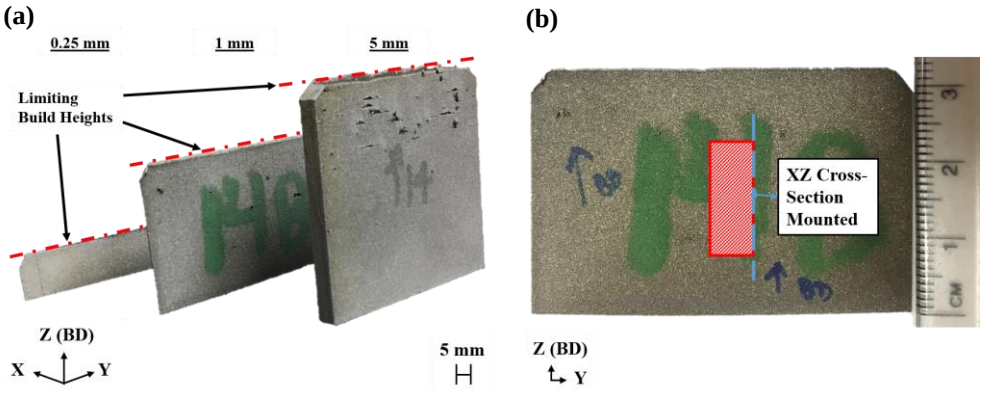


**Figure 5-3: (a)** As-Built LPBF R108 Thin-Wall Parts Arranged in Order of Increasing Thicknesses (0.25 mm - 1 mm – 5 mm) from Left to Right. The Red Dashed Line Shows the Variation in LBH for Each Part. **(b)** Example of a Specimen Taken from the Center Region of a 1 mm Sample for Metallurgical Studies.

### 5.2.3 Microscopic Characterization

Optical micrographs were analyzed to calculate the crack densities for the different conditions considered in the DOE. As-printed samples were extracted from the build plate (**Figure 5-3 (a)**) and the YZ-plane midsection (**Figure 5-3 (b)**) was selected for metallurgical studies to avoid heterogeneities in microstructure at

the part edges. Sectioned specimens were mounted, ground, and polished for microstructure observation. Final polishing was performed using 0.04 µm colloidal silica finish and the polished samples were viewed under the Keyence VK-X200 confocal optical microscope.

Failure analysis of the as-built parts was performed under the JEOL JSM-7600F FEG-SEM equipped with an Oxford Instruments X-Max 80 mm energy dispersive spectroscopy (EDS) detector. Key metallurgical attributes such as pores, particles and lack of fusion zones were identified to help explain possible sources of failure associated with the LBHs observed in **Figure 5-3 (a)**.

### 5.2.4 Image Analysis and Internal Micro-Crack Quantification

To determine internal micro-crack propensity of the as-built parts, crack area fractions were quantified using the procedure outlined and shown in **Figure 5-4**. The crack area fraction (CAF) is defined as a percentage of the total area of cracks in an image normalized by the image area. All samples were ground and polished five (5) times to provide an adequate number of planes (approximately 1 mm inter-planar distance) for CAF analyses. The XZ plane was chosen to observe cracks along BD over a larger area across the part thickness. Total sample image area was between 2.5 $mm^2$ and 32 $mm^2$ depending on part thickness. More than 30 optical images per plane were collected from the midsection of each polished thin-wall specimen. The image analysis program ImageJ was employed to segregate the cracks from the parent matrix and compute the average CAF values with 95% confidence levels for each sample.

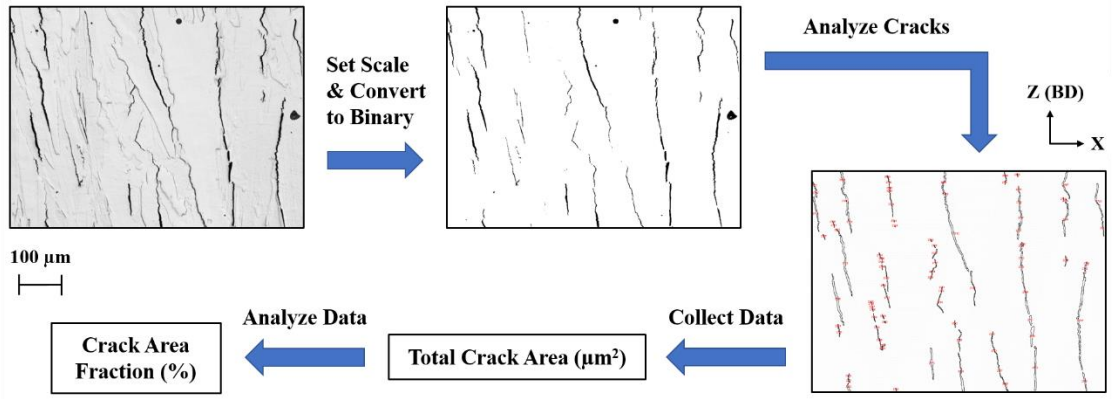


**Figure 5-4:** Image Analysis Process for Crack Quantification of R65 Thin-Wall Samples. The Red Dots in The Processed Image Indicate Cracks Identified by ImageJ.

## 5.3 Modeling Methodology

Rapidly changing stresses cannot be extracted experimentally, therefore, the in-process thermal stresses were predicted through finite element modelling (FEM) of thin-wall parts with different wall thicknesses. The ABAQUS-based FEM methodology proposed by Yang et al. [141] was used to simulate these stresses. Both substrate and thin-wall part were modelled with identical experimental setups. An example of a 5 mm thick sample is shown in **Figure 5-5**. A simplified layer-heating approach was used to reduce the computational time of the simulations [143]. Each element layer was composed of 5 build layers (40 µm powder layer thickness) in the build direction. A sequentially coupled thermo-mechanical procedure was used to obtain thermal strains and stresses [144]. This method allows accurate prediction of mechanical results such as strain, stress and distortion [145] according to Yang et al. [143]. RENÉ 65 was chosen to simulate the effect of thermal stresses on the LBH phenomenon. Temperature-dependent material properties of R65, including density, specific heat, latent heat, thermal conductivity, Young's modulus, plasticity, and thermal expansion, were applied.

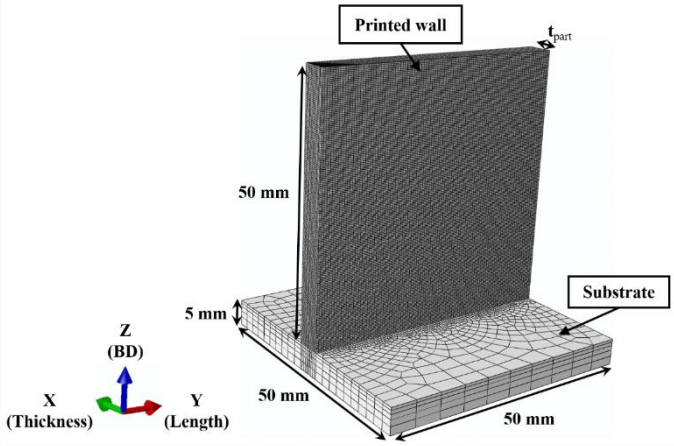


**Figure 5-5:** The FE Model Geometry and Mesh of Thin-Wall Structure Printed on Substrate. Mesh Size is Refined for the Printed Wall and Coarse for The Substrate.

Thermal analysis was performed with three steps for each element layer – deposition, heating, and cool-down. The heating time was determined by the laser interaction time with the powder (t), and the cooling time consists of both the time required to cool the powder (9 seconds) and the powder recoating time (1 seconds). The simulation began with the build plate and sequentially activated each mesh layer using an activation time resembling the real printing process. Each layer included 196 scanning lines lumped into one concentrated heat source, which along with reduced number of model elements increases the time efficiency [143]. Laser scanning pattern was implemented using event series replicating the movement of the laser scanning strategy

[141,146,147]. Based on the mesh sensitivity study, four elements in the X direction and one hundred elements in the Y direction were found adequate. The element type used for the thermal study was DC3D8. Build parameters identical to the actual LPBF printing conditions (**Table 5-2**) were used to create the thermo-mechanical models. Standard equations for heat loss due to convection and radiation accounted for the surfaces exposed to the environment [143].

After completion of the thermal model, the thermal history was imported as a predefined field in the mechanical analysis to drive the prediction of thermal stresses and distortion in the thin-wall parts. The mechanical model mesh setup was identical to the thermal model. For the mechanical boundary conditions, all the nodes on the substrates' surfaces were fixed in every direction to ensure no displacement [23]. The element type used for the mechanical model was C3D8.

## 5.4 Results

### 5.4.1 Limiting Build Height and Internal Micro-Cracking

The effects of part thickness (PT) on LBH for R65 and R108 are shown in **Figure 5-6 (a)**. Full build height is achieved at 5 mm thickness for both alloys: the average LBH values are (1) R65 – 47.45 mm, and (2) R108 – 47.92 mm. The small variation in LBH for the 5 mm thick part is associated with inexact sample removal from the build plate. As PT decreases below 5 mm, LBH average value also decreases: (a) at PT = 1 mm, LBH values were 31.62 mm and 31.17 mm for R65 and R108, respectively, and (b) at PT = 0.25 mm, LBHs were 8.70 mm and 9.95 mm for R65 and R108, respectively.

CAFs of R65 and R108 for part thicknesses of 5 mm, 1 mm and 0.25 mm are quantified in **Figure 5-6 (b)**. For both alloys, CAF is relatively stable at 5 mm and 1 mm and decreases rapidly at 0.25 mm. As PT decreases from 1 mm to 0.25 mm, CAF decreases by approximately 99% from 0.462% to 0.006% for R65 and by approximately 77% from 1.980% to 0.454% for R108. Alloy composition also significantly affects internal micro-cracking, as observed by higher CAF values for R108 compared to R65. As the material changes from R108 to R65, (1) at PT = 5 mm, CAF decreases by 80% from 1.781% to 0.352% , (2) at PT = 1 mm, CAF decreases by 77% from 1.98% to 0.462%, and (3) at PT = 0.25 mm, CAF decrease by approximately 99% from 0.454% to 0.006%. The large error bars for PT = 1 mm in **Figure 5-6** indicate inconsistencies in internal micro-cracking due to inter-planar crack-density variation.

Cracks for both alloys are aligned with BD as demonstrated by optical micrographs of parts with wall thicknesses of 5 mm (**Figure 5-7**). However, the number of cracks in R108 are visibly higher than R65. Furthermore, the crack morphologies are straighter in R65 (**Figure 5-7 (a)**) and more serrated in R108 (**Figure**

**5-7 (b)**). Micro-cracking in high gamma prime superalloys takes place by solidification and ductility dip cracking [148].

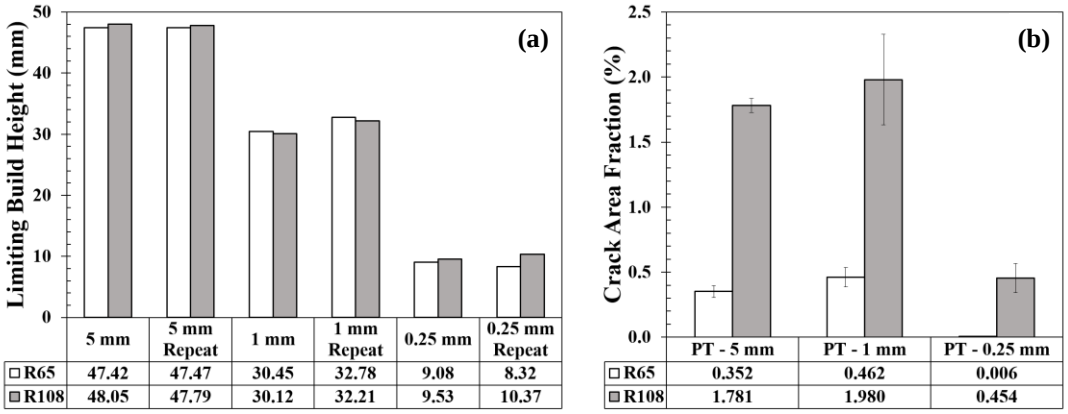


**Figure 5-6: (a)** Effect of Part Thickness on the LBH of 3D-Printed Thin-Wall Parts. The Intended Build Height for the Printed Features was 50 mm. Two Parts were Built for Each Alloy. **(b)** Effect of Part Thickness on the Crack Area Fraction.

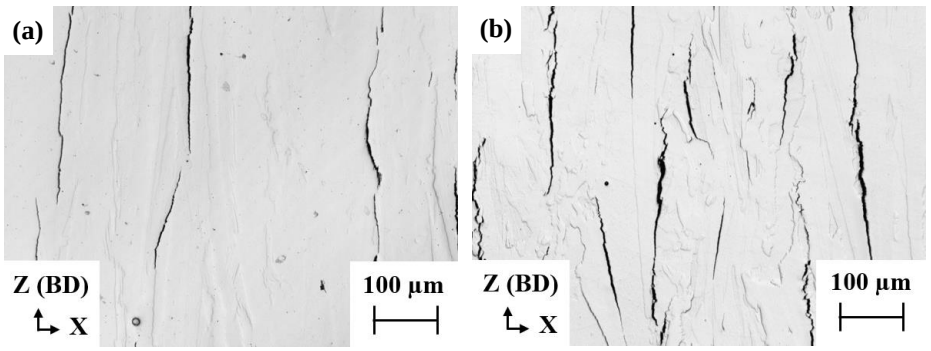


**Figure 5-7:** Internal Micro-Cracks Along BD in 5 mm Thick **(a)** R65 and **(b)** R108 Thin-Wall Parts.

## 5.4.2 Numerical Simulation of 3D Parts

Since **Figure 5-6 (a)** demonstrates negligible effect of alloy composition on LBH, only R65 was chosen for the FEM simulations. Three thin-wall parts were simulated to demonstrate the effect of part thickness on LBH and equivalent stress distribution (**Figure 5-8**). The simulations for parts with wall thicknesses of 0.25 mm (**Figure 5-8 (a)**) and 1 mm (**Figure 5-8 (b)**) terminated prematurely due to negative Jacobian matrices caused by excessive mesh distortion, while the 5 mm thick part (**Figure 5-8 (c)**) simulated to the full designated build height

(50 mm) similar to the actual test runs. The 0.25 mm part simulation of distortion began experiencing convergency issues at a height of 6.20 mm and consequently aborted at 8.50 mm. The corresponding as-built 0.25 mm parts failed at average heights of 8.70 mm and 9.95 mm for R65 and R108, respectively (see **Figure 5-6 (a)**). Similarly, the 1 mm part simulation first demonstrated convergency problems at a height of 24.0 mm and consequently aborted at 25.8 mm. The corresponding as-built 1 mm parts failed at average heights of 31.62 mm and 31.17 mm for R65 and R108, respectively (see **Figure 5-6 (a)**).

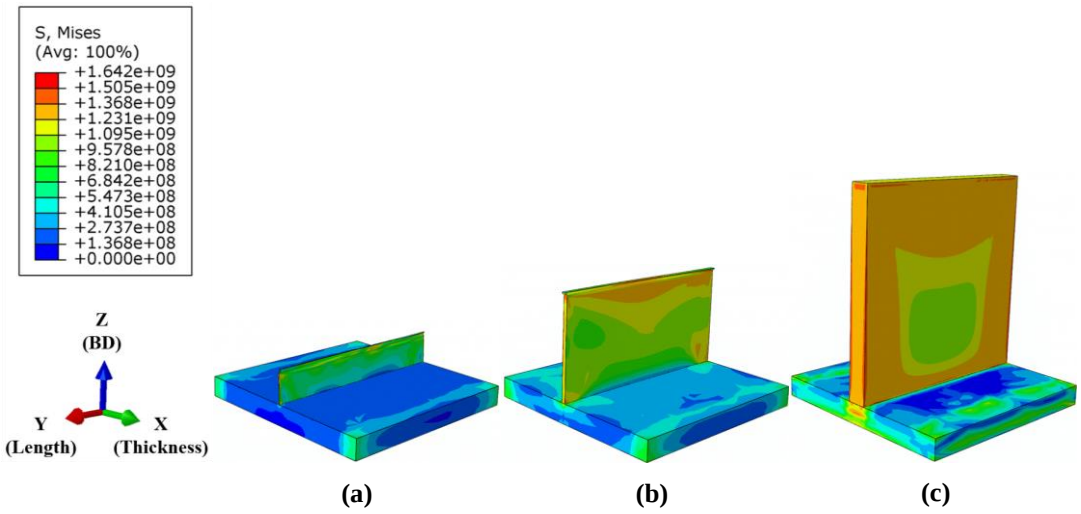


**Figure 5-8:** Simulated Von Mises Stress Distribution in Fully Printed LPBF Thin-Walled Structures with Varying Thicknesses **(a)** 0.25 mm, **(b)** 1 mm, and **(c)** 5 mm. Thicknesses Lower than 5 mm Show LBH.

### 5.4.3 Predicted Stress Distributions in 3D Parts

In-process stress distributions in the 0.25 mm, 1 mm and 5 mm parts were predicted using FEM simulations. The stresses along the X (thickness), Y (length) and Z (BD) directions were investigated carefully. The stress distribution along BD is found to be more relevant since it helps capture the evolution of the stress with respect to the LBH. The regions chosen to examine stress distributions in the thin-wall parts are shown in **Figure 5-9**. Stresses are computed at the edge and center within the midsection (YZ mid-plane) of each part as shown in **Figure 5-9 (a)**. The mid-plane was chosen because the temperature distribution is more homogeneous in the middle. The lines were placed parallel to BD along the edge and center of the XZ plane as shown in **Figure 5-9 (b)**. Since the model applies the heat uniformly on each subsequent build layer, the stress distribution through the X and Y directions are symmetric. Therefore, only one of the edges was chosen to extract stresses near either part edge. The stresses were extracted one second after the deposition of the final layer.

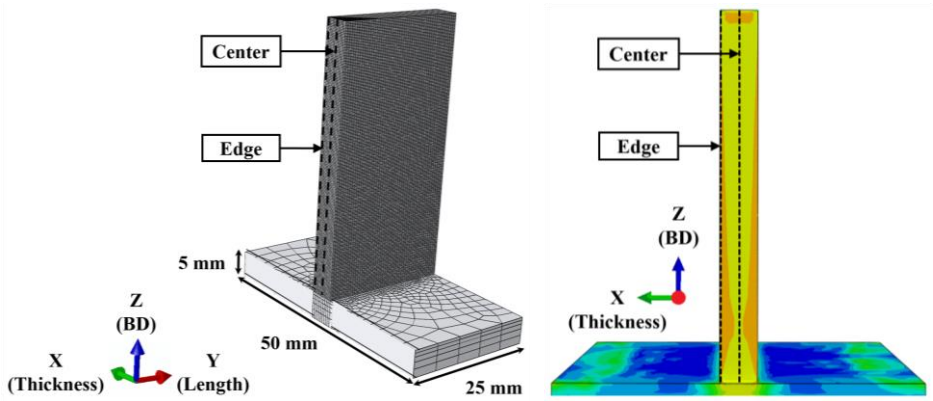


**Figure 5-9: (a)** 3D Cross-Section of a 5 mm Thin-Wall Part Taken from the Middle of the Y Axis Showing Center and Edge Dashed Lines Used for Extraction of Stress Data. **(b)** Cross-Section of the XZ Plane Showing the Locations of the Extracted Stresses and Demonstrating Symmetrical Stress Distribution in the Part.

Stresses were computed at a common restricted part height of 6 mm (corresponding to the height observed in the 0.25 mm part) to develop a fair comparison between parts with different wall thicknesses. **Figure 5-10 (a)** and **(b)** show Mises stress distributions computed at different positions after all parts grow 6 mm tall. Stress plots along the part edge (**Figure 5-10 (a)**) show that the stresses are highest in the 5 mm part and remain relatively constant at different positions along the restricted part height. The stress behavior in the central section (**Figure 5-10 (b)**) indicates higher stresses in thinner parts at some locations near the final part height. For instance, the stress taken at 5 mm along the restricted part height is around 900 MPa for the 1 mm part but is 850 MPa for the thicker 5 mm part. Generally, though, the stress component magnitudes are higher in thicker parts. This is also observed in the X and Y directions (not shown here).

To determine the effect of in-process stress variations on LBH of thin-wall structures, it is necessary to evaluate the stress direction (tensile or compressive) for each part. The stresses along BD are compared in **Figure 5-10 (c)** and **(d)** for the three thicknesses. The stress is compressive at the edge (**Figure 5-10 (c)**) and becomes tensile closer to the center (**Figure 5-10 (d)**) for all simulated parts. Thicker parts have higher stresses near the substrate and lower stresses near the top surface. Stresses along the length (Y) direction are also shown for the three thicknesses in **Figure 5-10 (e)** and **(f)**. These stresses are compressive and of comparable magnitude through the part thickness. In some regions, thinner parts (1 mm and 0.25 mm) have even higher stress magnitudes than the thicker part. For example, the stresses extracted at 5 mm along the restricted part height are approximately 860 MPa for the 1 mm part and 600 MPa for the 0.25 mm part, compared to 540 MPa for the thicker 5 mm part.

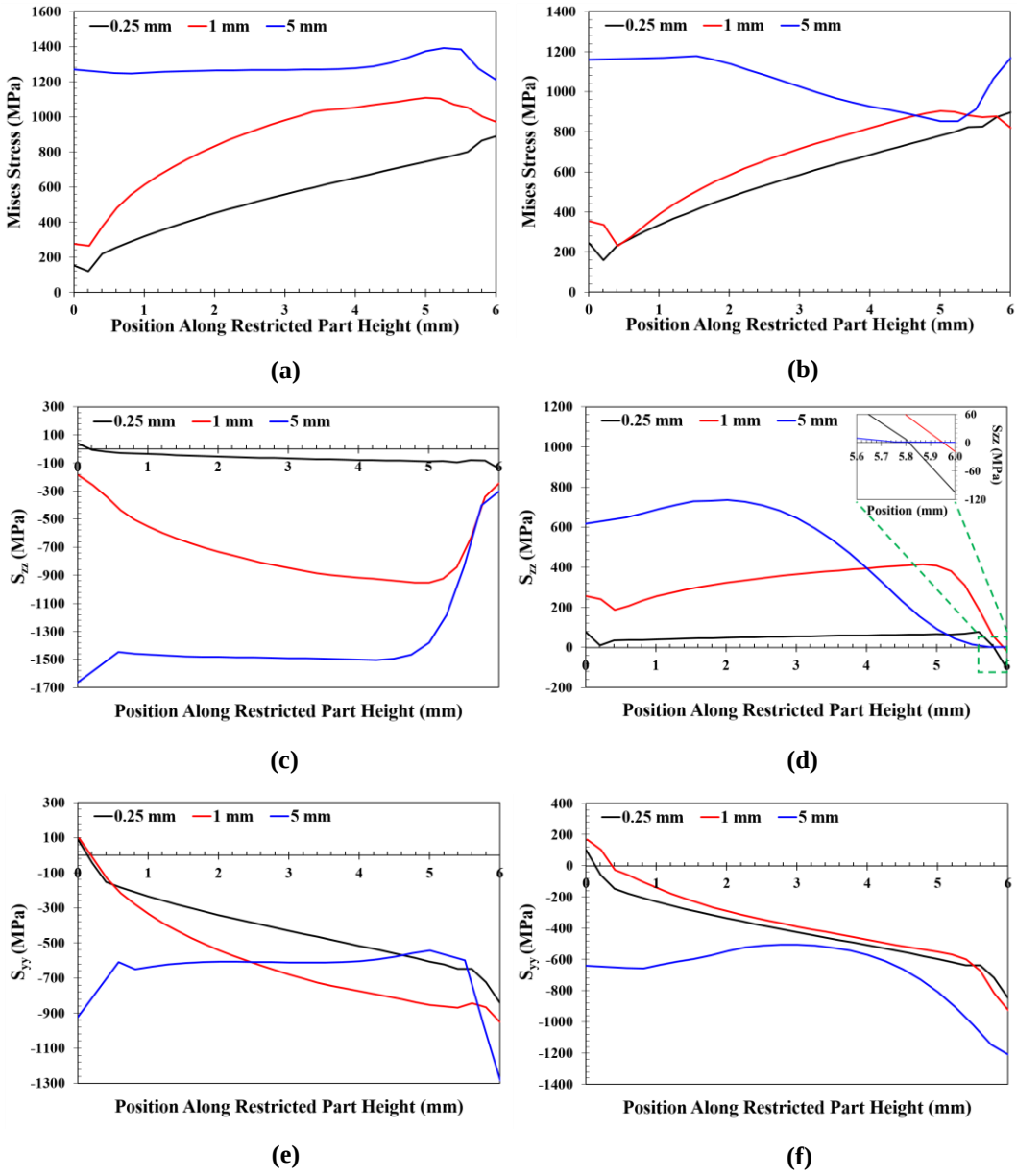


**Figure 5-10:** Simulated Stresses of Thin-Wall Parts with Different Thicknesses Extracted at **(a),(c),(e)** the Edge and **(b),(d),(f)** the Center. Stress Distributions are Organized as Follows: **(a),(b)** Von Mises Stresses; **(c),(d)** Stresses in Z Direction; **(e),(f)** Stresses in Y Direction. The Inset in **(d)** Shows Close-Up of the Compressive Stresses Observed in the Final Layers for the Thinner 0.25 mm and 1 mm Parts. The Stress Distributions were Taken at Different Positions Along the Build Direction, as Shown in **Figure 5-9**.

## 5.5 Discussion

Analysis of the experimental results indicates no correlation between the internal micro-cracks and LBHs. Internal micro-cracks are parallel to BD (**Figure 5-7**) while LBHs result from failure perpendicular to BD (**Figure 5-3 (a)**). Parts with thinner walls have fewer internal micro-cracks and lower LBHs, while parts with thicker walls have higher number of cracks and larger LBHs. Furthermore, when the alloy composition changes from R65 to R108, there is a significant increase in crack quantity but negligible change in LBH. These findings suggest that LBH primarily depends on thickness and is minimally affected by the build material and internal micro-cracks.

In general, **Figure 5-8** and **Figure** 5-10 show that stresses are higher in parts with thicker walls. Considering the successful build completion of the 5 mm part, it is evident that the stress magnitude is not the most important parameter contributing to part failure. Accordingly, the top surfaces of the failed parts (0.25 mm and 1 mm) do not exhibit features associated with fractures observed in metals. An example of a SEM image showing the top surface of a R65 part with a wall thickness of 0.25 mm is shown in **Figure 5-11**. The surface exhibits features associated with the powder melting process [98,149,150]. Lack of fusion zones (red box in **Figure 5-11 (a)**) and track irregularities (black arrow in **Figure 5-11 (b)**) represent typical solidification defects in the LPBF process. In addition, **Figure 5-11 (b)** shows dendritic morphologies depicting solidified regions. These observations show that the LBH phenomena is not associated with a conventional fracture mode [151].

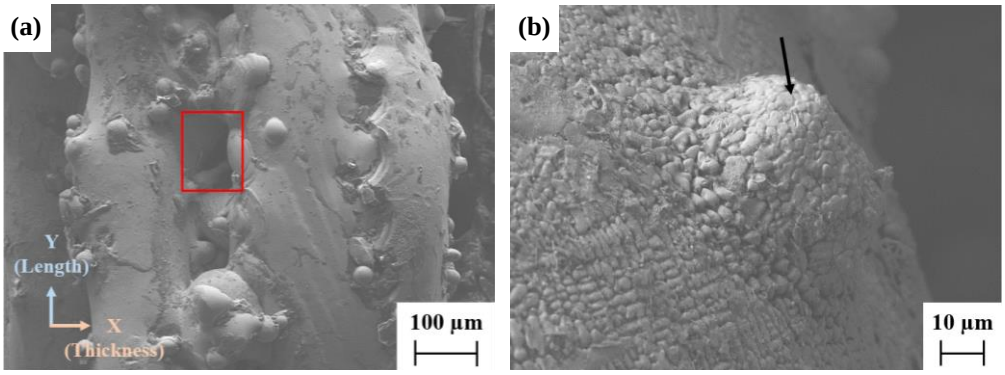


**Figure 5-11:** Top Surface SEM micrographs of 0.25 mm Thick R65 As-Built Thin-Wall Part Indicating a **(a)** Lack of Fusion Zone and **(b)** Track Irregularity Surrounded by Dendritic Features Showing Material Solidification.

In thin-wall structures, the stress direction (tension versus compression) plays an important role in the stability of the structure. Long and slender members are susceptible to lateral deflection when subjected to

compressive loading. To explain the LBH observed in thinner parts during LPBF processing, two factors will be considered in the following sections. Firstly, the effect of part thickness on stress state will be discussed. The cross-section area affects the cooling rate and in-process stress distribution in the part. Secondly, the effect of in-process local distortion on the final built part integrity will be discussed. Thinner walls can support less stress and are more susceptible to warpage during LBPF.

### 5.5.1 Effect of Part Thickness on Stress Rate

Closer evaluation of the stresses at different positions along BD in **Figure 5-10 (c)** and **(d)** shows fully compressive stresses aligned with BD in the last deposited layers (from the edges (**Figure 5-10 (c)**) to the center (**Figure 5-10 (d)**) in the thinner walls, as observed at a height of 5.8 mm for the 1 mm and 0.25 mm parts. The inset in **Figure 5-10 (d)** shows compressive stresses of 105 MPa and 20 MPa in 0.25 mm and 1 mm parts, respectively. Conversely, the stress along the center reaches approximately zero at the same height for the 5 mm part. A top view (X-Y plane) of the last layer deposited at 6 mm part height is shown in **Figure 5-12**. In the 5 mm part, most of the cross-section is under tensile stress along the BD and a small area along the edges is in compression. On the other hand, the entire surface of the 0.25 mm and 1 mm parts remain in compression one second after the completion of the build.

The simulation results shown in **Figure 5-10 (e)** and **(f)** also indicate that the parts are under compressive stresses of similar magnitude along the Y direction for all part thicknesses. Compression from the Y and Z directions in the last deposited layer constrains the thinner parts, favoring warping along the X direction.

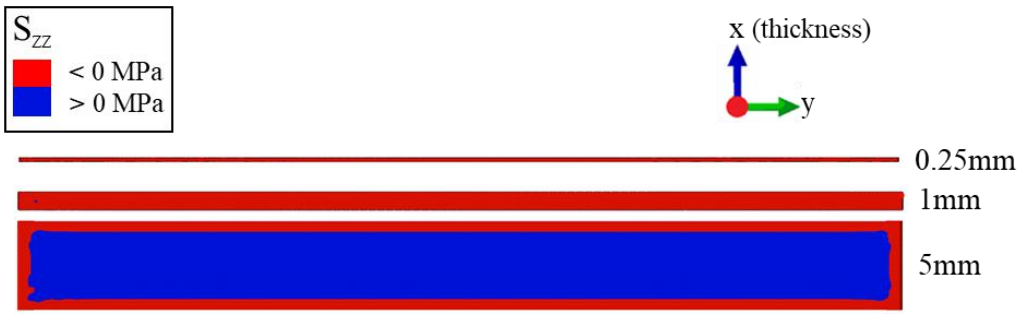


**Figure 5-12:** Stress Distribution in the X-Y Plane of the Last Layers Taken at 6 mm Build Height. It Corresponds to the Inset Region in **Figure 5-10 (d)**. The Red and Blue Colors Highlight Regions Undergoing Compressive and Tensile Stresses, Respectively.

### 5.5.2 Effect of Part Thickness on Local Distortion

To evaluate the effect of lateral deflection of the parts on LBH, **Figure 5-13** shows the maximum part displacement in the X direction as a function of position along the unrestricted part height for the three thicknesses investigated in this study. These displacements are measured after the deposition of each layer up to the part surface. Each data point represents the maximum displacement extracted from the entire part up to a position along the unrestricted part height. For instance, in the 5 mm part, the maximum displacement for the entire part at 10 mm of the build height is around 0.04 mm.

The maximum displacement in the 5 mm part increases rapidly up to a part height of approximately 4 mm and remains relatively constant afterward. For the first built layer, the heating mass increases due to the specific heat capacity. When a new layer is added to the structure, it conducts heat to the previous layers increasing the total mass contributing to the distortion of the part. As the build progresses, the heat affected zone reaches a constant mass leading to the steady state displacement regime observed in **Figure 5-13**. The steady state displacement is smaller in thinner parts as the mass of material that is undergoing contraction during cooling is smaller.

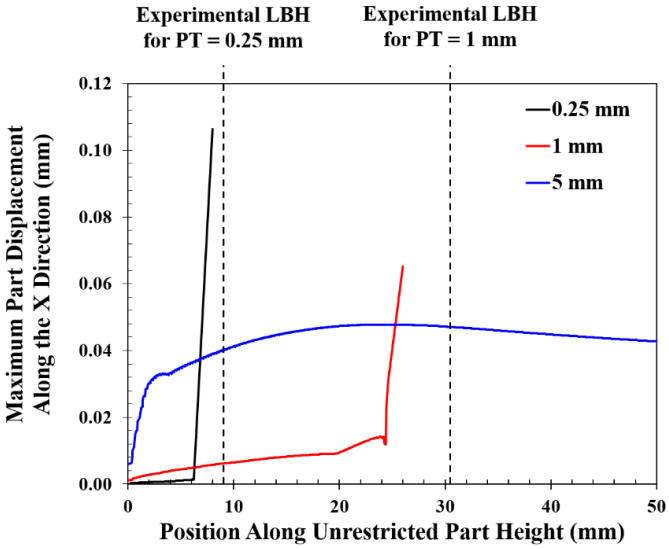


**Figure 5-13:** Maximum Part Displacement Along the X (Part Thickness) Direction as a Function of the Position Along the Unrestricted Part Height (See **Figure 5-12** for Reference Axes). Three Different Part Thicknesses (0.25 mm, 1 mm, and 5 mm) are Compared Here. The Experimental LBH Values are also Marked Using Dashed Lines.

The displacements rise sharply in the thinner parts near the final part height due to high distortion in the top build layers. Close-up images of distortion observed in the as-printed and simulated cases for the 0.25 mm R65 thin-wall part are shown in **Figure 5-14 (a)** and **(b)**. In both cases, major distortion is observed close to the prematurely terminated built height. In **Figure 5-14 (a)**, the distortion along X direction near the part surface is exemplified by the red-dashed line indicating displacement of the center (blue-dashed) line. This coincides with the compressive stresses constraining the thinner parts in the Y-Z directions as explained in **Section 5.5.1**. The simulated 3D model in **Figure 5-14 (b)** also displays warp-like distortion along the X-direction and significant distortion near the terminated part height.

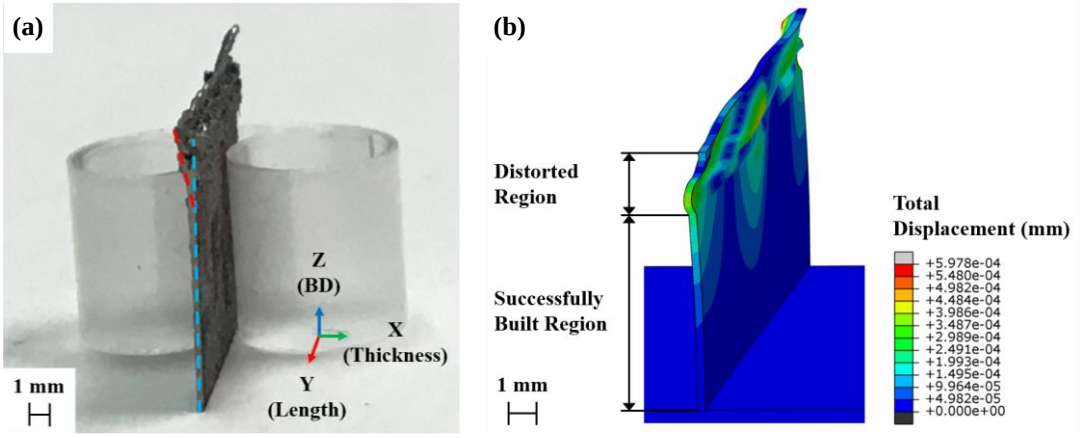


**Figure 5-14:** Part Distortion Observed in the R65-0.25 mm Thin-Wall Part in (a) As-Printed and (b) Simulated Conditions.

The propensity of a thin-wall part for distortion can be analyzed with the slenderness ratio ($S$). The slenderness ratio is the critical geometrical factor for calculation of the Euler buckling defined as

$$S = \frac{L_e}{r_g}, \tag{5-1}$$

where the effective height of a fixed free support ($L_e$) is twice the LBH of the part. The average LBH shown in **Figure 5-6 (a)** is used for buckling calculations. The radius of gyration ($r_g$) is calculated from the second moment of area (I) as

$$r_g = \sqrt{\frac{I}{A}}. \tag{5-2}$$

The lowest $I_{xx}$ and $I_{yy}$ values are used to determine the slenderness ratio. Finally, the area (A) represents the cross-sectional area of the X-Y plane.

The slenderness ratios for R65 and R108 are shown in **Table 5-3**. The reduced LBHs observed in the 0.25 mm (~9 mm LBH) and 1 mm (~31 mm LBH) parts are associated with similarly high slenderness ratios of ~215 and ~275, respectively. The 5 mm parts have a much lower ratio (~66) even though the effective height used for the calculation is much higher (~47 mm). This clearly demonstrates that the thinner parts are more susceptible to buckling during LPBF and that the LBH correlates well with the slenderness ratio of the part build.

**Table 5-3:** Slenderness Ratios for R65 and R108 Thin-Wall Parts.

| Part thickness (mm) | Slenderness ratio (R65) | Slenderness ratio (R108) |
|---|---|---|
| 0.25 | 241.1 | 275.7 |
| 1 | 219.0 | 215.9 |
| 5 | 65.7 | 66.4 |

### 5.5.3 Effect of Thin-wall Distortion During LPBF

The simple FE models presented in **Figure 5-8** are valuable means to estimate the LBH phenomena. The built heights derived from the three model predictions of distortion for part failure match well with measured LBH values for actual as-built thin-wall parts (~95%, ~86% and 100% accuracy for the 0.25 mm, 1 mm, and 5 mm R65 parts, respectively). When lateral bending begins in the parts due to buckling, the new layer becomes shifted from the previous plane. This causes the compressive stresses to be applied off the centerline of the part leading to more distortion. The model cannot capture the excessive distortion generated in the thinner walls. Hence, the simulation underestimates the maximum build height associated with the part thickness as discussed in **Section 5.4.2**.

In real life, this mechanism would likely cause part failure due to excessive stress applied on the side of the parts. However, the LBH observed in thin-wall parts is not caused by a fracture mechanism, as discussed previously. Hence, the LBH cannot be caused solely by the buckling observed during the simulation. During LPBF manufacturing, the subsequent layers become harder to build when lateral displacement of the solid section happens. **Figure 5-15 (a)** shows that a new layer cannot be placed on the previous layer of the build when the thin-wall displaces by $\delta$ in the X direction. Thus, there would be an overhang region between the new and

previously printed layers. Accordingly, the build becomes staggered in **Figure 5-14 (a)** when the part begins bending along the X-axis, ultimately leading to part failure. This effect becomes less detrimental when part thickness increases. If the wall thickness shown in **Figure 5-15 (a)** becomes four (4) times larger (**Figure 5-15 (b)**), the new layer would be printed and overlapped on top of the previous layer and the printing process would continue.

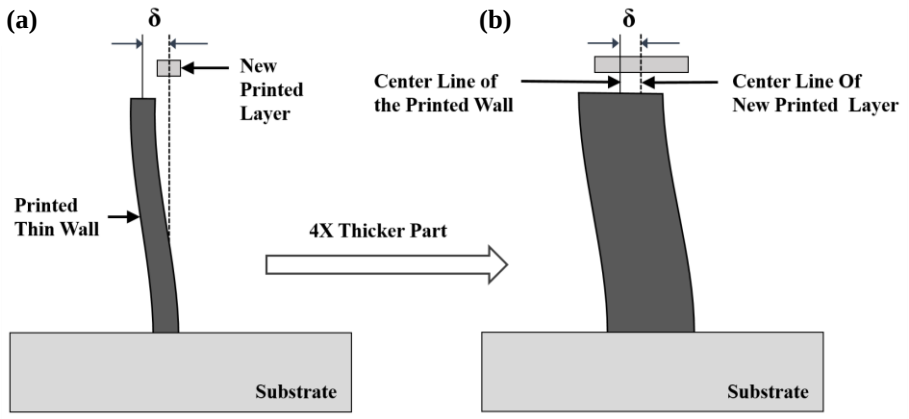


**Figure 5-15:** Schematic Demonstrating the Mechanism Associated with Limiting Build Height in Thin-Wall Parts. Thinner Parts like **(a)** are More Sensitive to Displacement in X Compared to Thicker Parts like **(b)** – 4X Thicker than **(a)**.

## 5.6 Conclusions

The effect of part thickness on the LBH in LPBF-based thin-wall structures was investigated. The materials studied were chosen for two hard-to-weld high γ' Ni-based superalloys with different levels of γ' volume fraction to initially identify differences in internal micro-crack mechanisms and later determine LBH in as-processed thin-wall parts. As-printed samples were examined at the microscopic and macroscopic levels for both alloys to discover the causes behind reduced LBH observed in thinner walls. Three main potential sources of failure were studied – internal micro-cracks, in-process stresses, and part distortion.

The internal micro-cracks were significantly affected by alloy composition and part thickness, and were all aligned parallel to BD. The R108 samples had higher internal micro-cracks than R65 and the thicker walls exhibited higher crack densities. These results indicated no correlation between reduced LBH and internal micro-cracking. FEM simulations of the stress distributions along the build heights of R65 thin-wall parts showed that the stress component magnitudes also do not contribute to LBHs as the stresses generally increase with part

thickness. Analysis of surface morphology showed identical surfaces for both fully-built and failed thin-wall parts. These results showed reduced LBH is not related to fracture mechanisms.

Experimental observations coupled with FEM simulations showed reduced LBH is a distortion-related build problem in as-built thin-wall parts. Higher in-process distortion results in subsequent layer misalignment with the part centerline as the build progresses along the part height, causing LBH. Walls thinner than 5 mm were found to be more susceptible to in-process distortion in the current study. A combination of compressive stresses in the length (Y) and height (Z) directions is observed in the last layers of the thinner walls. The unbalanced stresses constrain the thinner parts leading to warpage, hence reducing LBH. It is suggested that thinner wall sections in complex AM components are designed carefully with respect to part geometry and build parameters. Thereupon, the slenderness ratio appears to be a valuable tool to evaluate the propensity for lateral deflection and LBH in thin-wall parts. To reduce the distortion and increase the build to design height ratio, it is also important to reduce the variation of thermal stresses and strains during processing. This can be achieved by reducing the thermal gradients and cooling rates, which affect the thin-wall parts more severely than the thicker parts. For example, the scanning strategy, substrate temperature or part width are among engineering solutions that can reduce the thermal constraints and increase the LBH.

# Chapter 6

# Explaining the Micro-Cracking Phenomenon in High-γ' Ni-Based Superalloy Thin-Wall Parts Produced by LPBF

In this chapter, *a mechanism for inherent micro-cracking in thin-wall parts during LPBF processing is proposed based on both experimental and numerical simulation methods*. Micro-cracking is a significant challenge as it adversely affects the part processability and quality. This is especially true for hard-to-weld Ni-based superalloys and thin-wall structures used in aerospace applications such as turbine vanes and fuel nozzles. Microstructure characterization and statistical analysis tools are used to quantify micro-cracking for a high-γ' Ni-based superalloy, RENÉ 108, for different wall thicknesses. Advanced microstructure characterization techniques are used to identify metallurgical factors (such as phases) responsible for micro-cracking. Numerical simulation approaches are used to predict the stresses and stress triaxialities at the layer and beam scales. The experimental observations are successfully verified using simulated results.

The chapter presents an accepted manuscript of an article published in the journal Materials Today Communications.

***Materials Today Communications 30 (2022) https://doi.org/10.1016/j.mtcomm.2022.103139***

## 6.1 Introduction

Laser powder bed fusion (LPBF) additive manufacturing (AM) is of great interest to automotive, aerospace and medical industries for near net-shape metal part fabrication [50,152,153]. The LPBF technology is especially useful for fabricating complex serpentine-shaped cooling paths in combustors, diffusors, and nozzles, prevalent in the aero-engine and gas turbine power industries. Such components are conventionally produced using stamped sheet metals, composed of cast or welded nickel-based (Ni-based) superalloys, at low yields and high costs. Befittingly, LPBF offers a viable alternative due to added design flexibility and higher part tolerances (≥100 μm) at increased production speeds and reduced costs for greater part complexities [154,155]. However, studies highlight significant manufacturing challenges, which must be overcome to successfully produce thin metallic parts [120,156,157].

Wu et al. [120] reported difficulties in producing parts with wall thicknesses smaller than 300 μm. Material shrinkage and scan strategies affect the final wall thickness and as-printed part quality. Part distortion has also been identified as a major challenge in the fabrication of thin-wall components. Yang et al. [137] found that longer and taller structures are more susceptible to distortion due to larger variation in microstructure, while Ahmed et al. [119] demonstrated larger distortion for thinner parts. Conversely, Brown et al. [140] suggested that parts thinner than 0.25 mm are not feasible for fabrication due to high surface roughness and imperfections. Furthermore, Chakraborty et al. [158] recently showed that the limiting build height (LBH) effect must be considered for varying part thicknesses. Smaller LBHs for thinner walls are attributed to part distortion and larger slenderness ratios. Hence, the wall thickness must be controlled carefully to maintain part integrity during processing.

Furthermore, common LPBF material defects, such as pores, lack-of-fusion voids, spatter particles and micro-cracks, can negatively influence mechanical properties, bulk density, and final part integrity. Pores can be generated due to high power densities, gas entrapments or insufficient melt pool penetration into the previous layers during building [42,159]. Inadequate melt pool penetration can also produce elongated lack-of-fusion voids, which are much larger than the gas-induced porosities [160]. In addition, spatter particles can be produced in high power densities due to high recoil pressure resulting in ejection of molten droplets from the melt pool [161]. Micro-cracking also occurs due to stresses which accumulate along the grain boundaries due to the rapid heating and cooling of the surrounding material during processing. Defects can be minimized by selective manufacturing of powder with optimized rheology, morphology and particle size distribution (PSD) to improve powder flowability, packing density and thermal conductivity [162]. For thin-wall part fabrication, fine spherical powders with median sizes (D50) between 16 μm and 24 μm are beneficial to achieve fine features with small

layer thicknesses [115]. Provided optimal powder characteristics for the construction of thin-wall parts, micro-cracking is difficult to eliminate for hard-to-weld materials processed using LPBF.

Several micro-cracking mechanisms have been reported in literature for high gamma prime (γ') Ni-based superalloys [13,96,139,146]. Laser processing parameters strongly influence micro-crack formation during part fabrication. Carter et al. [96] observed different micro-cracking mechanisms by varying laser scanning conditions. The authors proposed that lower energy densities are linked to straight micro-cracks aligned with the build direction, while higher energy densities promote melt-pool micro-cracking. The melt-pool micro-cracks were shown to be more sensitive to energy density variation. Li et al. [117] modified part lengths to examine the influence of scanning length on stresses. The authors demonstrated larger stress variation with increasing scanning length. Cheng et al. [127] performed a detailed study on the effect of scan strategies on stresses and deformation. The authors found that the scan vector angle and interlayer scan rotation affect the residual stresses and the heat distribution. These studies show the importance of laser parameters on heat distribution, residual stresses, and micro-cracking, but they do not consider the effect of part thickness, which can alter the scanning length and the thermal gradients during processing. The effect of part thickness on micro-cracking largely remains unexplored and requires thorough investigation.

In this study, the effect of part thickness on the micro-cracking mechanism in a LPBF-processed high γ' Ni-based superalloy is investigated using microstructure characterization and numerical modelling techniques. Statistical crack analysis is performed to quantify and categorize micro-cracks observed in the microstructure. Scanning electron microscopy (SEM), transmission electron microscopy (TEM) and electron backscatter diffraction (EBSD) are employed to assess micro-crack morphologies, evaluate cooling rates and identify phases assisting micro-crack formation and growth. Finally, finite element modelling (FEM) methodologies replicating the experimental conditions are developed to simulate the in-process stresses and stress triaxialities.

## 6.2 Experimental Procedures

### 6.2.1 Materials

The crack-susceptible Ni-based superalloy RENÉ (R108), comprised of 6.15 wt.% Al+Ti content and 63% γ' volume fraction [74], was used to fabricate LPBF-based thin-wall structures. Gas-atomized R108 powder provided by Powder Alloy Corporation, consisting of mostly spherical powder particles with a size range ($D_{10}$-$D_{90}$) of 12-40 µm and median particle size ($D_{50}$) of ~19 µm, was used for this study. The as-received powder contains a small fraction of satellite particles attached to larger particles. Images of the powder morphology and PSD are shown in **Figure 6-1 (a)** and **(b)**, respectively. Chemical composition, including contents (in wt.%) of

the alloying elements determined by inductively coupled plasma - optical emission spectroscopy (ICP-OES) at Activation Laboratories (ACTLABS © Canada), is provided in **Table 6-1**.

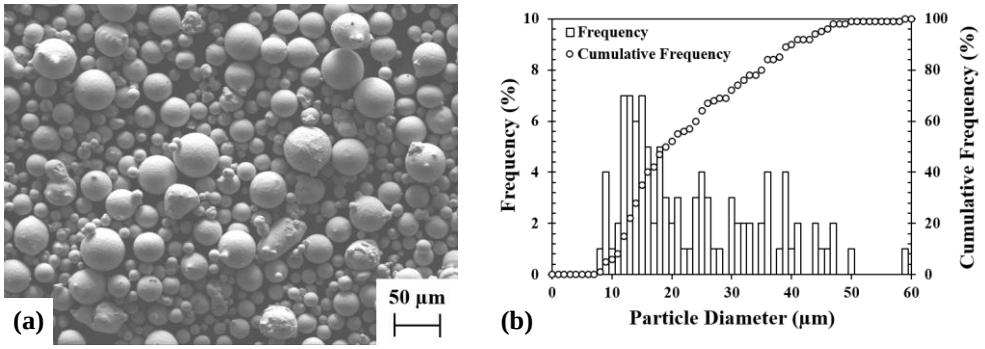


**Figure 6-1: (a)** SEM Image Showing R108 Powder Morphology. **(b)** Particle Size Distribution of R108 Powder.

**Table 6-1:** Powder Composition of R108 in wt.%.

| Ni | Cr | Co | Al | Ti | Ta | W | Mo | Hf | B | Zr | C |
|---|---|---|---|---|---|---|---|---|---|---|---|
| Bal. | 8.64 | 10 | 5.36 | 0.75 | 3.02 | 10.03 | 0.53 | 0.87 | 0.01 | 0.01 | 0.01 |

## 6.2.2 LPBF Printing

In this study, thin-wall parts were directly built on a stainless steel substrate in an Aconity$^{TM}$ MIDI LPBF printer using the build parameters given in **Table 6-2**. The parameters were selectively chosen to achieve optimal final part quality with minimal defects such as pores, voids, and micro-cracks. A three-dimensional (3D) view of the full setup including the parts and the substrate is shown in **Figure 6-2 (a)**. Bidirectional scan strategy with a hatch angle of 75 degrees (**Figure 6-2 (b)**) to the thickness axis (X) was utilized to print all build layers and no scan rotation was employed between layers. The laser was scanned at an angle of 45 degrees relative to the recoating direction to avoid processing the parts perpendicular to the recoater's movement. Three thin-wall parts with wall thicknesses of 5.00 (5) mm, 1.00 (1) mm and 0.25 mm were used, and a single sample was printed for each condition, as shown in **Figure 6-2 (b)**. The design part height and width for each specimen was maintained at 50 mm. The thickest part reached the design height, but the 1 mm and 0.25 mm parts failed at LBHs of 30.12 mm and 9.53 mm, respectively. The cause for reduced LBH in thinner parts is explained in detail by Chakraborty et al. [158]. According to the authors, the LBH effect is repeatable for different wall thicknesses under fixed processing conditions.

**Table 6-2:** Build Parameters for LPBF-Based R108 Thin-Wall Parts.

| Build parameter | Value |
|---|---|
| Laser power, P (W) | 200 |
| Scan speed, v (mm/s) | 1000 |
| Spot size, $d_{spot}$ (μm) | 120 |
| Hatch spacing, h (μm) | 90 |
| Hatch angle, θ (°) | 75 |
| Powder layer thickness, t (μm) | 40 |
| Designated part height (mm) | 50 |
| Part thickness, $t_{part}$ (mm) | 0.25, 1, 5 |

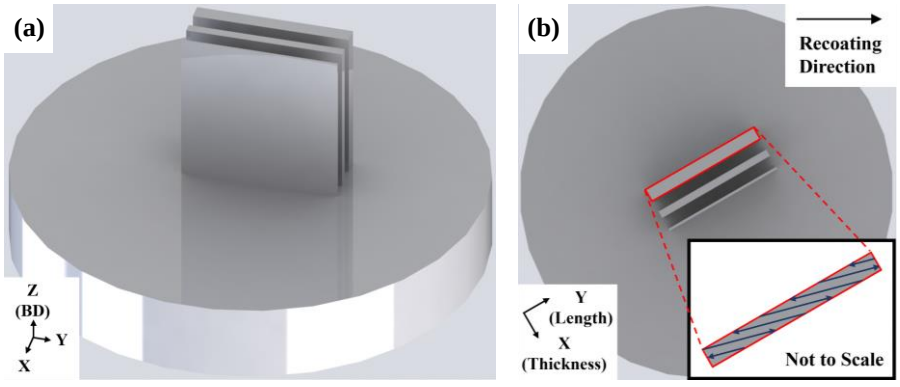


**Figure 6-2:** Print Model of LPBF Thin-Wall Parts in **(a)** 3D View and **(b)** Top View Showing Thin-Wall Parts with Thicknesses of 5 mm, 1 mm, and 0.25 mm, Respectively. The Red Box in **(b)** Highlights the 5 mm Thick Part with a Corresponding Close-Up Image Shown as an Inset. Blue Arrows Indicate Bidirectional Scan Strategy at a Hatch Angle of 75 Degrees with respect to the Part Thickness, Employed for All the Thin-Wall Samples. Laser Scanning is Performed at a 45-Degree Angle Compared to the Recoating Direction (Top Right).

### 6.2.3 Microstructure Characterization

#### 6.2.3.1 Optical Microscopy

The as-printed parts were removed from the build plate and thin-wall sections, 5 mm x 15 mm (length-Y x height-Z) in dimension, were extracted for metallurgical sample preparation. Due to the varying LBH values and to evaluate the effect of part thickness, centrally-located regions along the XZ plane were taken at different heights (24 mm for 5 mm, 15 mm for 1 mm and, 4.75 mm for 0.25 mm) with respect to the base plate. The center location was chosen for microstructure analysis to avoid microstructure heterogeneities generally observed near the edges and in the vicinity of the base plate. All specimens were mounted, ground, and polished using standard metallography methods. Final polishing was performed using 0.04 µm colloidal silica finish and the polished samples were viewed under the Keyence VHX7000 digital microscope. Optical micrographs were analyzed to calculate statistical micro-crack attributes such as crack densities, lengths, widths, and eccentricities.

#### 6.2.3.2 Scanning Electron Microscopy

As-polished samples were etched with glyceregia (15 mL HCl, 10 mL Glycerol, 5 mL $HNO_3$) for 10 s to reveal melt pools, dendrites, and micro-cracking tendencies. Microstructure characterization was performed using a JEOL JSM-7600F field emission gun SEM (FEG-SEM) equipped with an Oxford Instruments X-Max 80 mm EDX detector. Low, medium, and high magnification SEM micrographs were obtained to examine micro-crack morphologies for different part thicknesses. Elemental analyses were performed using EDX at an accelerating voltage of 10 kV, beam current of 1.9 nA, and aperture of 110 µm to qualitatively identify detrimental phases in the as-processed microstructures. Advanced microstructure characterization was conducted using a Thermo Scientific Quattro Environmental FEG-SEM equipped with Thermo Scientific Lumis EBSD detector. Five different regions from the 5 mm, 1 mm and 0.25 mm parts were analyzed at an accelerating voltage of 20 kV using a step size of 200 nm to generate EBSD plots with respect to the build direction (BD). The EBSD data was further processed using TSL OIM$^{TM}$ coupled with a MATLAB script to obtain maps showing grain misorientations (GMOs) and kernel average misorientations (KAMs). KAM maps illustrate the average intragranular misorientations and serve as good indicators of strain in crystalline materials. The acquired data was used to identify differences in local and intergranular misorientations, and qualitatively analyze strain distributions at high angle boundaries (HABs) for different micro-crack morphologies.

#### 6.2.3.3 Transmission Electron Microscopy

A 1x3 mm XY section near the center position along the part height of an as-printed 1 mm thick part was extracted, mounted, ground and polished using standard metallography methods. The XY plane was selected to allow the use of the lift-out method in focused ion beam (FIB). A final sample thickness (along the Z-direction)

of around 1 mm was achieved using a Gatan disc grinder. The FEG-SEM was operated in secondary electron (SE) and backscatter electron (BSE) modes to select a region containing a HAB close to a micro-crack. The specimen was fixed to a copper lift-out TEM grid, and a thin lamella (5 µm x 10 µm x 100 nm – X x Z x Y) was selectively extracted using a HITACHI FB-2000A Ga-FIB. Microstructure on the lamella, perpendicular to the XY plane, was examined using a JEOL 2100 FEG-TEM, equipped with an Oxford Xplore TEM EDX detector. Imaging and phase analysis at the HAB was performed at 190 kV in both conventional TEM and scanning TEM (STEM) modes.

### 6.2.4 Image Analysis and Internal Micro-Crack Quantification

Image analysis software, ImageJ [72], and custom VB scripts were used to distinguish micro-cracks from other characteristics such as pores, voids, and contaminations through comprehensive examination of around 500 optical micrographs taken from the as-polished specimen (see **Section 6.2.3.1**). Feature parameters such as area, ellipse minor axis length, aspect ratio, circularity and roundness [163] were used to filter out the unwanted defects and extract only micro-crack statistics. Feature areas less than 1500 µm$^2$, minor axis lengths less than 5 µm, aspect ratios less than 2.5, circularities less than 0.5 and roundness values less than 0.4 were chosen based on the selected images. Micro-crack lengths and widths were calculated by averaging maximum feret and minor axis lengths of the filtered features over each optical micrograph.

Internal micro-crack propensity for different thicknesses were obtained by computing crack area fractions and crack count densities using the procedure outlined previously in [158]. Crack area fraction (CAF) is defined as a percentage of the total area of micro-cracks per image normalized by the image area. Crack count density (CCD) is defined as the total number of micro-cracks per image normalized by the image area. Furthermore, crack eccentricities were calculated to distinguish micro-crack morphologies for different thicknesses, as done in [164]. Eccentricity (ECC) is defined as a function of the minor ($b$) and major axis ($a$) lengths of a micro-crack, and is given by:

$$ECC = \sqrt{1 - \frac{b^2}{a^2}}\ , for\ b < a, \tag{6-1}$$

where the low ECC values (minimum near zero) indicate circular micro-cracks while high ECC values (maximum 1) represent elongated needle-shaped micro-cracks.

All samples were ground and polished five times to generate an adequate number of planes (approximately 1 mm inter-planar distance) for micro-crack geometry and density analyses. Micro-crack quantification along BD across the part thickness was fully captured by performing image analysis on the XZ

plane. Cumulative sample areas of 18.75 $mm^2$, 75 $mm^2$ and 375 $mm^2$ were used for the 0.25 mm, 1 mm, and 5 mm parts, respectively. Over 150 centrally-situated optical images (30 per plane) were analyzed to compute micro-crack quantities including 95% confidence levels for each sample.

### 6.2.5 Primary Dendrite Arm Spacing

Four 5000X magnification BSE-SEM images, from different crack-free regions near straight columnar dendrites, were taken at the center of the LBH where the crack analysis was performed for each thin-wall part (see **Section 6.2.3.1**). These regions were located centrally within the melt pool to allow easier quantification of dendrites. The images were analyzed using the linear intercept method [165,166] to determine the average primary dendrite arm spacing (PDAS) values for the parts.

## 6.3 Modeling Methodology

The effect of varying wall thickness on in-process stresses is evaluated using the FEM technique. However, the simulation of the entire part at the laser beam scale is not feasible because of the computation time. The LPBF process covers a large length scale, from the laser spot size (50 µm to 250 µm) to the final part scale (centimeter range). Accurate modeling of the in-process micro- and macroscopic thermo-mechanical behavior using the finite element (FE) method requires a minimum of $10^6$ elements and increment time [167]. In order to overcome these limitations, two FE models are used to simulate the material behavior at the micro- and macroscopic scales in this study.

For both models, some common conditions are employed. Convective and radiative heat losses are incorporated for all surfaces exposed to the external environment, having a temperature of 25 °C. The convection coefficients are adjusted to the part geometry following the procedures described by Chao et al. [168] to account for the conduction between the solid build material and the surrounding powder bed.

Temperature-dependent material properties of R108 including density, specific heat, latent heat, thermal conductivity, Young's modulus, plasticity, and thermal expansion are applied. The temperature-dependent thermal properties between room temperature and 1400 °C were kindly provided by and proprietary to General Electric, while the mechanical properties below 1150 °C were taken from Martin et al. [169]. For the mechanical properties above 1150 °C, constant yield strength and ultimate tensile strength values were taken from Kissinger et al. [170]. The implicit solver in ABAQUS is used for both thermal and mechanical models. The output from the thermal model is fed into the mechanical model to obtain stress-strain properties. This method allows accurate prediction of mechanical results such as strain, stress and distortion [141].

### 6.3.1 Beam Heat Source Model

For the microscopic evaluation of in-process stresses, a beam-scale model is developed. The laser beam heat source is simulated using the exponentially decaying model [171]. The heat input model and phase transition were implemented using DFLUX and USDFLD subroutines. The framework and details of implementation are explained in [172,173]. Results are computed using a sequentially coupled thermo-mechanical modelling procedure similar to [144]. The geometry of the model includes both powder and solidified layers sized 2×1×0.25 mm as shown in **Figure 6-3 (a)**. Based on a mesh sensitivity study, the region interacting with the laser requires element sizes of 30×10×10 μm, as recommended in [173]. In addition, coarser element sizes are used for regions further away from the laser track. The element types for the thermal and mechanical models are DC3D8 and C3D8, respectively. These are fully integrated brick elements formulated using linear shape functions implemented in ABAQUS. Since the track is surrounded by solidified layers, planar symmetric boundary conditions are considered for all surfaces. To obtain accurate prediction of the cooling rate and temperature distribution, the conduction coefficient of the powder is reduced to 1.5% of solid state as recommended by Sih et al. [174] for the packing density of 65%. The initial nodal temperatures from the last layer are incorporated to mimic the printing process. The residual stresses from the previous layer are not considered here due to problems in transferring stress tensors over different simulation scales. The initial stress state is thus set to zero. The printing process continues for 2 ms until the laser reaches the end of the track. The in-process results are captured at the center of the track inside the melt pool (40 μm in depth) and at the melt pool boundary (60 μm in depth), as shown in **Figure 6-3 (a)**.

### 6.3.2 Layer Heat Source Model

For the macroscopic evaluation of in-process stresses, the ABAQUS-based FEM methodology proposed by Yang et al. [141] is employed. Like beam-scale, the coupled FE model is utilized to predict thermal and mechanical results for R108 at the layer scale. This model works by lumping all the tracks into a single heat source. Five physical layers are combined into a single layer in the model (200 μm thickness) to improve computational efficiency.

All part geometries and boundary conditions are developed based on the experimental setup to replicate the effect of wall thickness on thermal stresses during LPBF processing. The total printing time varies between 3.5 hrs and 4.5 hrs depending on the wall thickness and is replicated in the simulation. The input energy was implemented using the toolpath-mesh intersection module that applies uniform heat into pretrained elements to calculate the nodal temperature [141,158]. The element preparation and deposition follow machine settings using the event series as explained in [141]. All the model preparation settings including heat input definitions and

material deposition were conducted using the ABAQUS additive manufacturing plugin [141,146,147]. Element sizes of 250 and 200 were used for Y (length) and Z (height), and at least 4 elements were used for the wall thickness (as done in [158]) in both thermal and mechanical models. The predicted results have shown to be independent of the mesh size. The element types and formulations are the same as those used for the beam scale model (see **Section 6.3.1**). The remaining details of the model are explained in a previous study on LBH, conducted by Chakraborty et al. [158].

The methodology is described in detail by Chakraborty *et al.* [158]. Part heights for 5 mm, 1 mm and 0.25 mm thick samples are normalized using their LBHs to provide comparable evaluation of the predicted results. The nomenclature used to describe the normalized heights along the Z direction is labelled build progress (BP). A point central to the part thickness (along the X direction) and length (along the Y direction) is used in this study for stress analysis as shown in **Figure 6-3 (b)**. The stress is always analyzed at the build height of LBH/2 as this was where micro-cracks were characterized. The in-process stress is recorded at this point (BP = 50%) as subsequent layers are added up to LBH (BP = 100%).

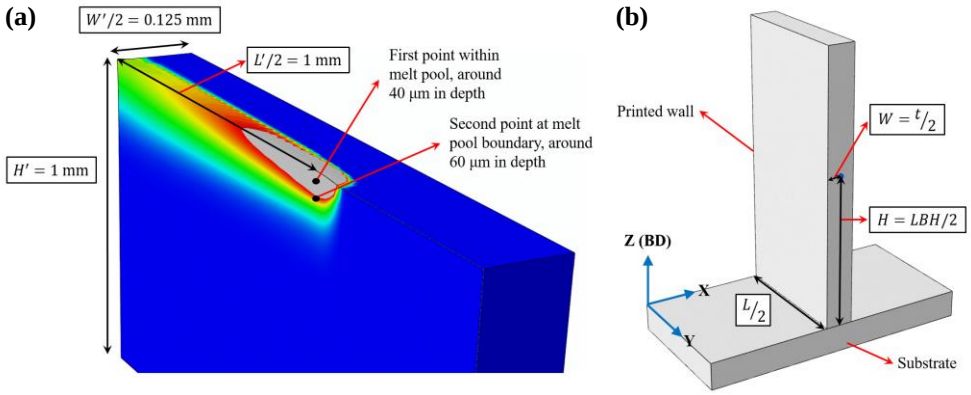


**Figure 6-3:** Cross-Section Images Illustrating **(a)** the Beam and **(b)** the Layer Heat Source Models Used to Simulate the Stresses Experienced by a Thin-Wall Part During LPBF. Results are Extracted at (a) the Black Points in the Beam-Scale Model, and **(b)** the Blue Point in the Layer-Scale Model. $\boldsymbol{L'}$, $\boldsymbol{W'}$ and $\boldsymbol{H'}$ Represent the Length, Width, and Height of the Beam-Scale Model, Whereas $\boldsymbol{L}$, $\boldsymbol{W}$ and $\boldsymbol{H}$ Represent the Length, Width, and Height of the Layer-Scale model. The Part Thickness ($\boldsymbol{t}$) Used for this Demonstration is 0.25 mm and LBH Represents the Limiting Build Height.

## 6.4 Results and Discussion

### 6.4.1 Micro-Crack Quantification

**Figure 6-4 (a)** shows the effect of part thickness on the average lengths and widths of micro-cracks. As the part thickness increases, the micro-cracks grow longer and wider. For instance, the 5 mm part contains micro-cracks that are 24.55 μm long and 3.62 μm wide on average, while the 0.25 mm part contains micro-cracks with average lengths and widths of 9.62 μm and 1.27 μm, respectively. Likewise, **Figure 6-4 (b)** shows that the 5 mm part has higher CAF (0.91%) compared to the 0.25 mm (0.29%) part. However, the 1 mm part breaks the trend as the micro-crack propensity is higher (1.46%) and demonstrates larger variation ($\pm$0.30%) compared to the thicker part. The large variation of CAF in 1 mm reflects significant differences in micro-cracking densities between micrographs observed on the XZ plane through 5 mm of the part length (along the Y-direction). This means that some planes along the part length demonstrate higher micro-cracking propensity compared to others. Similar anomalous micro-cracking behavior, including large inter-planar variations, at the 1 mm part thickness has previously been reported in literature for other materials and build conditions [158]. Therefore, the higher micro-crack propensity at the 1 mm part thickness found in this study is not uncharacteristic and will be further investigated (see **Section 6.4.4**).

Typical micro-cracks observed in R108 are shown in **Figure 6-5**. The micro-cracks are either straight (red arrows) or jagged (black arrows) for all the thin-wall parts. Extensive SEM work was completed to ensure that the micro-cracks are not caused by lack-of-fusion defects, gas-entrapped porosities, voids, or spatter contamination (see **Section 6.1**). Micro-cracks resulting from these defects exhibit different morphologies, dissimilar to those shown in **Figure 6-5**. In addition, customized ImageJ micro-crack selection criteria (see **Section 6.2.4**) were used to isolate micro-cracks characteristic of the material. Ghoussoub et al. [164] distinguished inherent micro-cracking modes in a similar material, CM247LC, using the crack eccentricity criterion (see **Section 6.2.4**). High ECC micro-cracks, such as the straight micro-cracks in **Figure 6-5**, were attributed to the solid-state cracking mechanism, whereas the jagged-shaped low ECC micro-cracks were correlated to the solidification cracking mechanism.

**Figure 6-6** demonstrates the distribution of CAFs for different ECCs at part thicknesses of 5 mm, 1 mm, and 0.25 mm. The CAF values for the 1 mm part are highest for most ECCs followed by the 5 mm and 0.25 mm parts, consistent with the overall CAF results reported in **Figure 6-4 (b)**. Furthermore, the 1 mm part displays larger variation (see error bars in **Figure 6-4** and **Figure** 6-6) in CAF compared to the other parts. The crack density increases with higher ECC for all parts, indicating the tendency to form straighter micro-cracks. Subsequently, since the CAF values in **Figure 6-4 (b)** and **Figure** 6-6 result from crack nucleation and growth,

both phenomena are considered in the following sections to elucidate the micro-cracking mechanism and discuss the effect of wall thickness on CAF.

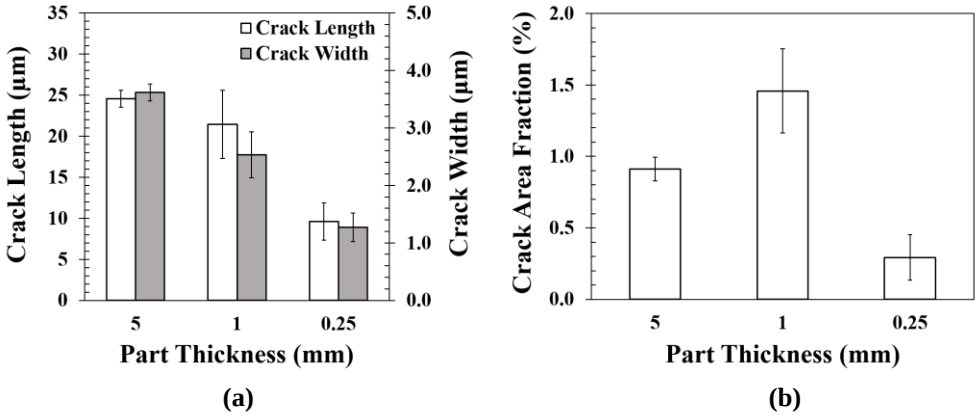


**Figure 6-4:** Plots Showing **(a)** the Average Crack Lengths and Widths, and **(b)** Average Crack Area fractions for Thin-Wall Part Thicknesses of 5 mm, 1 mm, and 0.25 mm.

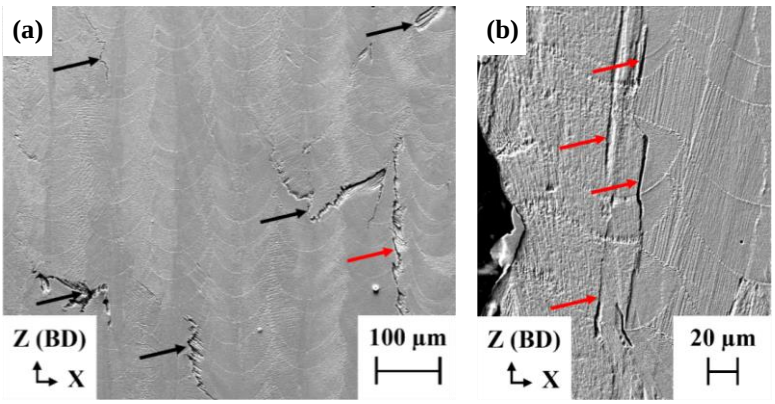


**Figure 6-5:** Example Secondary Electron SEM (SE-SEM) Images of **(a)** 1 mm and **(b)** 0.25 mm Parts Demonstrating Cracks with High ECC (>0.99) in Red and Low ECC (≤0.99) in Black Arrows, Respectively.

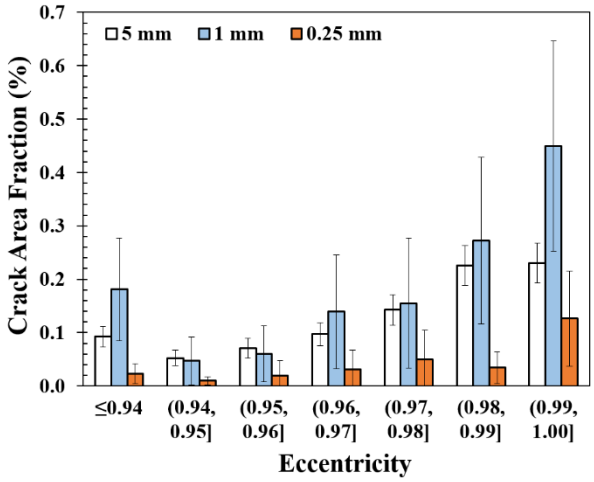


**Figure 6-6:** Plot Showing the Crack Area Fractions for Different Crack Eccentricities Encompassing Thin-Wall Part Thicknesses of 5 mm, 1 mm, and 0.25 mm.

## 6.4.2 Micro-Cracking Mechanism

### 6.4.2.1 Micro-Cracks with High ECC Values (>0.99)

Straight micro-cracks are aligned with BD for all three parts 5 mm, 1 mm, and 0.25 mm. **Figure 6-7 (a)** shows an example of a straight micro-crack with high ECC (~0.99). Carter et al. [1] also observed straight micro-cracks in a similar alloy (CM247LC), but could not isolate the crack formation mechanism, suggesting either solidification (interdendritic) or solid-state cracking (intergranular). In this case, the dendritic nature of micro-cracks can be observed clearly in the close-up SEM image in **Figure 6-7 (b)**. The cracked boundary is sandwiched by dendrites of two distinct non-complementary orientations preferentially propagating along BD. EBSD maps taken near the three high ECC micro-cracks highlighting the GMO and KAM are shown in **Figure 6-8**. The GMO map in **Figure 6-8 (a)** shows three micro-cracks propagating towards BD along dendrite boundaries with high misorientation angle (>15°). Hariharan et al. [175] observed similar micro-cracks in IN738LC also propagating along boundaries with high misorientation angles and classified them as solidification cracks. According to Rappaz et al. [176], the liquid film remains more stable and continuous at lower temperatures, hence facilitating the formation of micro-cracks.

**Figure 6-7 (b)** shows a large amount of fine (~20-50 nm diameter) spherical white particles, homogeneously distributed in the matrix. Ramirez and Lippold [177] suggested a solid-state cracking mechanism based on high stress concentrations due to the combined effect of grain boundary sliding and locking carbides.

Accordingly, the KAM map in **Figure 6-8 (b)** shows high ECC micro-cracks forming preferentially in highly strained regions.

Detailed microstructure characterization near a HAB region close to a micro-crack is performed using bright field TEM (BF-TEM) and dark field STEM (DF-STEM), accompanied with EDX analysis, as shown in **Figure 6-9**. The small white particles observed in **Figure 6-9** effectively consist of carbides rich in Hf, Ti and Ta, neighboring lower concentrations of fine oxide particles rich in Hf. However, the carbides appear to be fine and discrete particles unlikely to assist solid-state cracking.

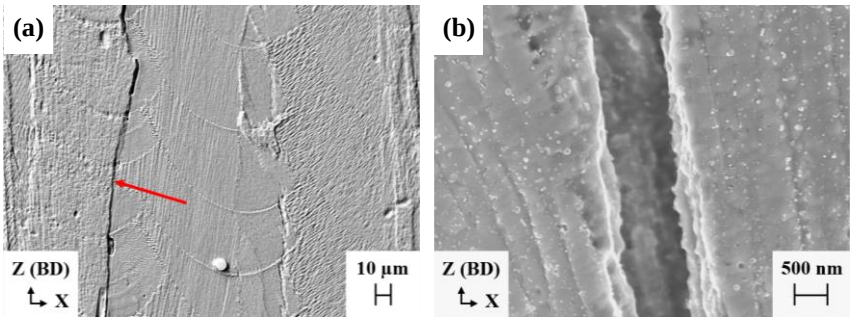


**Figure 6-7:** SE-SEM Micrographs Showing Examples of High-Eccentricity (Straight) Micro-Cracks with Eccentricity Values Between 0.99 and 1. A Representative Medium Magnification Image Taken at **(a)** 2000X Showing a Straight Micro-Crack, Propagating Along BD, Indicated by a Red Arrow. High Magnification Images Taken at **(b)** 10000X Showing Dendritic Morphologies for One Such Micro-Crack.

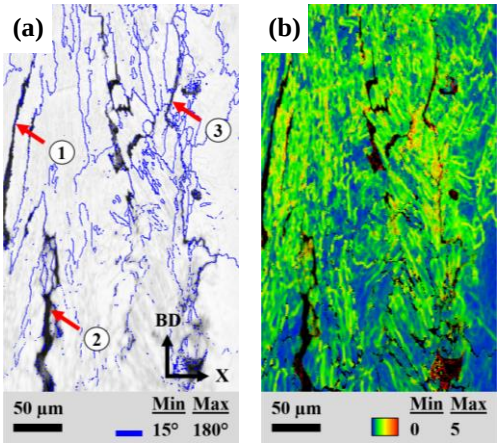


**Figure 6-8:** EBSD **(a)** GMO and **(b)** KAM Maps Demonstrating High-Eccentricity Micro-Cracks. Red Arrows Show Three Such Micro-Cracks Propagating Along Columnar Boundaries Parallel to BD.

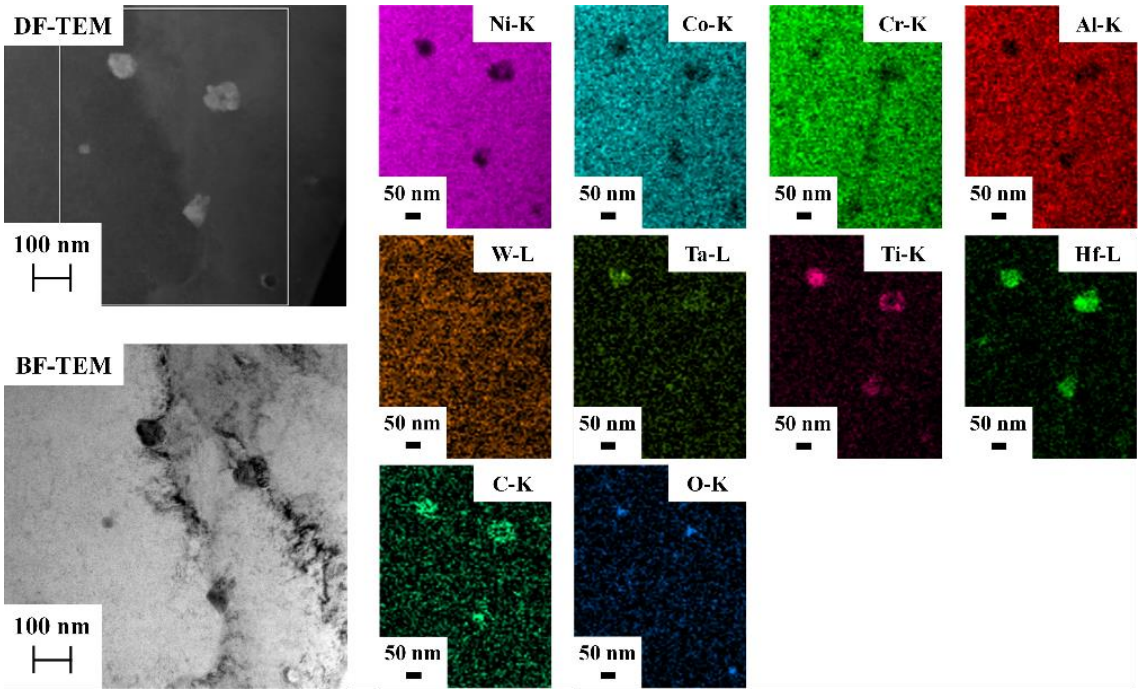


**Figure 6-9:** Bright Field (BF) TEM and Dark Field (DF) STEM Images with Corresponding EDS Maps at a HAB near a Micro-crack. The HAB is Homogeneously Distributed with Precipitate Particles Consisting of Hf- and Ti-Rich Carbides and Apparent Hf-Rich Oxides. These Particles Also Contain Trace Quantities of Ta and are Depleted in Matrix Elements such as Ni, Co, Cr and Al.

### 6.4.2.2 Micro-Cracks with Low ECC Values (≤0.99)

Two examples of low ECC micro-cracks are shown in **Figure 6-10 (a)-(d)**. The jagged micro-crack (~0.98 ECC) in **Figure 6-10 (a)** is irregular in shape while the second instance (~ 0.95 ECC) in **Figure 6-10 (c)** clearly forms along the melt pool boundary. In both cases, the micro-crack surfaces portray dendritic morphologies as shown in **Figure 6-10 (b)** and **(d)**. The GMO and KAM maps are taken in regions where melt-pool micro-cracks form as shown in **Figure 6-11**. These micro-cracks also form along HABs in regions portraying high local deformation. Both characteristics suggest solidification cracking during the terminal stage of solidification [178], consistent with Carter [1] who observed solidification cracking in a similar alloy, CM247LC, under high energy density conditions.

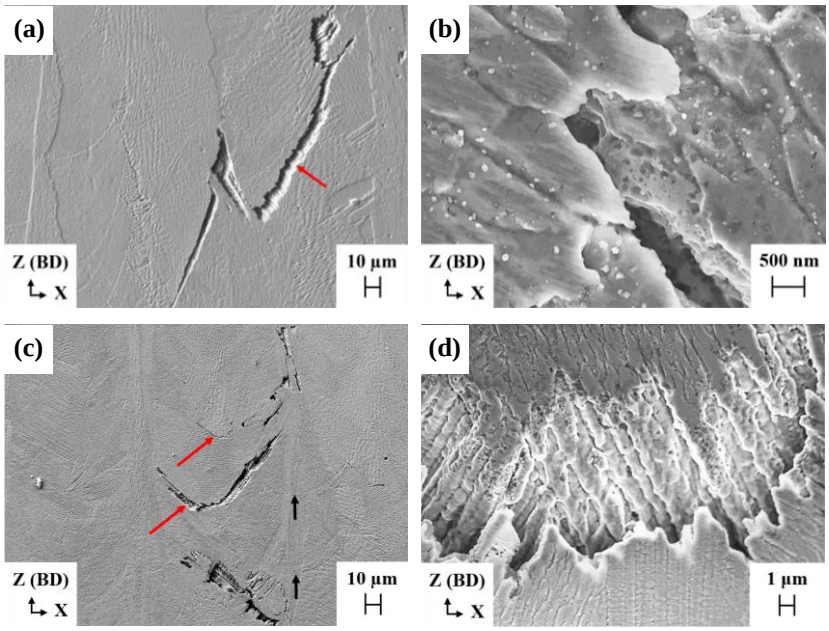


**Figure 6-10:** SE-SEM Micrographs Showing Examples of Low-Eccentricity Micro-cracks with Eccentricity Values Between **(a)**-**(b)** 0.96 and 0.99, and **(c)**-**(d)** Less than or Equal to 0.96. Medium Magnification Images Taken at 2000X Showing Different Micro-Crack Morphologies, Indicated by Red Arrows, are Shown in **(a)** and **(c)**. High magnification Images Taken at **(b)** 10000X and **(d)** 5000X Showing Dendritic Morphologies for All Low-Eccentricity Micro-Cracks. Black Arrows in **(c)** Point Towards Melt Pool Boundaries Stacked Along BD.

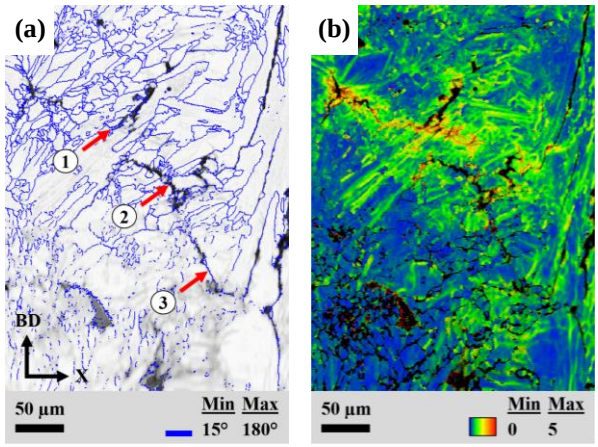


**Figure 6-11:** EBSD **(a)** GMO and **(b)** KAM Maps Demonstrating Micro-Cracks with Low Eccentricities. Red Arrows Show Three Such Micro-Cracks Propagating Along Melt Pool Boundaries Perpendicular to BD.

### 6.4.2.3 Evaluation of Micro-Cracking Mechanism Using the Beam-Scale Model

Irrespective of the micro-crack eccentricity, the formation and propagation of micro-cracks are influenced by strains and stresses developed during processing (see **Figure 6-8** and **Figure** 6-11). Moattari et al. [179] showed that evaluation of the stress triaxiality is more important than the individual stress components for micro-crack initiation and growth along a weld line. Stress triaxiality (T), commonly used in fracture mechanics to predict crack initiation and growth [86,179], is defined as a unitless parameter given by the ratio of the hydrostatic stress ($\sigma_m$) and the equivalent stress ($\sigma_e$):

$$T = \frac{\sigma_m}{\sigma_e} \quad \textbf{(6-2)}$$

The beam-scale model described in **Section 6.3.1** is used to evaluate the stress triaxiality state and temperature at the melt-pool scale to differentiate between the solid-state and solidification cracking mechanisms. **Figure 6-12 (a)-(b)** show the stress triaxialities and temperature profiles simulated at the center of the melt pool (where the >0.99 ECC cracks are observed) and close to the melt pool boundary (where low ECC cracks are observed). In both cases, the stress triaxiality is negative under the heat source (~1 ms) and increases rapidly as the material cools (>1 ms). The stress triaxiality must be positive for crack nucleation under the absence of external loading [180]. Accordingly, the simulation in **Figure 6-12 (a)** shows that the stress triaxiality becomes positive inside the melt pool at a temperature (~1400 °C) situated above the solidus of R108 (1310°C [169]). This combination of positive stress triaxiality and super-solidus temperature supports the view of high ECC cracks resulting from the solidification cracking mechanism.

The stress triaxiality becomes positive at a lower temperature (~1200 °C) close to the melt pool boundary, as shown in **Figure 6-12 (b)**. This means that the formation of micro-cracks is less favorable along the melt pool boundaries compared to the columnar dendrite boundaries. Accordingly, the fraction of low ECC cracks is significantly lower than the high ECC micro-cracks in **Figure 6-6** for all the parts, which also suggests that significant undercooling occurs during LPBF.

Higher cooling rates result in reduced solidus temperatures, which contribute towards larger solidification range [181] and undercooling [182]. The coupled effect of large undercooling and solidification range promotes solidification cracking along the melt pool boundaries. Increasing the temperature inside the melt pool increases the temperature along the melt pool boundary, potentially achieved by increasing the line energy density [183,184]. This could explain why melt-pool micro-cracking increases as the laser power increases and scan speed decreases [1].

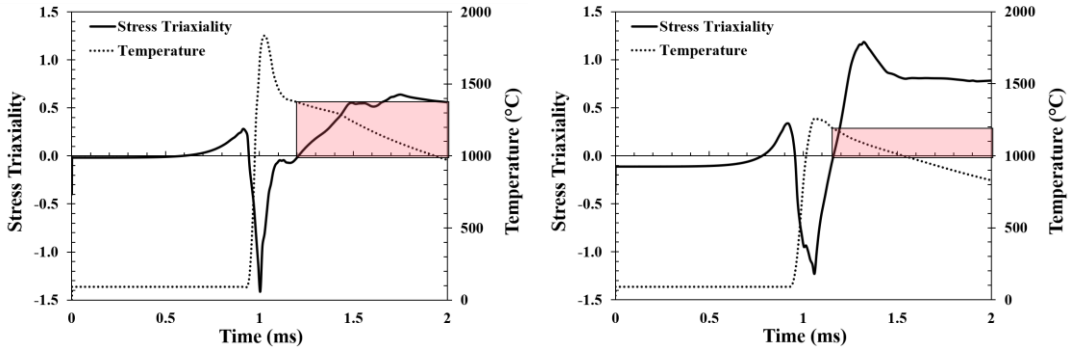


**Figure 6-12:** Beam Heat Source Simulation of the Stress Triaxiality and Temperature Variation During Processing **(a)** within the Melt Pool and **(b)** close to the Melt Pool Boundary. The Red Boxes Highlight the Temperatures for the Onset of Positive Stress Triaxialities.

### 6.4.3 Effect of Wall Thickness on Micro-Cracking

Micro-cracking in high γ' Ni-based superalloys depends on several criteria, including alloy composition [175], HAB misorientation and stresses (see **Figure 6-8** and **Figure** 6-11). In this study, the micro-crack variation between the different wall thicknesses observed in **Figure 6-4** cannot be attributed to composition as the same material is used for all the parts. The HAB also plays an important role in micro-crack formation. **Figure 6-13** compares HAB area fractions for different wall thicknesses. The HAB area fraction is highest in the 0.25 mm part, however, the CAF value is clearly lowest in the thinnest part as shown in **Figure 6-4 (b)**. This indicates that there is no correlation between HAB area fraction and the micro-cracking phenomena observed in the thin-wall parts. Part geometry has a significant effect on the in-process stress during LPBF [168]. Consequently, changing the wall thickness is likely to affect in-process stresses and micro-cracking.

#### 6.4.3.1 Analysis of Thermal Stresses Using the Layer Heat Source Model

To evaluate the effect of wall thickness on stresses, the FE layer-scale model described in **Section 6.3.2** is employed. The time increment used for the layer heat source model produces a uniform heat distribution through the layer and is unable to predict the stress state during the early stages of melt pool solidification accurately. The model can thus provide limited information on the crack nucleation tendency. However, it is fairly accurate in predicting the residual stresses that develop during the cool down of the part as shown by Yang et al. [141]. Consequently, the layer-scale model can provide a good indication of the effect of wall thickness on the propagation of the micro-cracks.

**Figure 6-14** shows the stress distributions at the center of the part as a function of the build progress (BP) for the three wall thicknesses. Since the final height (LBH) is dependent on part thickness, BP is used to provide a comparison of the computed stress distributions for different wall thicknesses during laser processing (see **Section 6.3.2**). When BP = 50%, the layer temperature rises causing thermal expansion of the material. This leads to compressive stresses in the material along the X and Y directions as shown in **Figure 6-14 (a)** and **(b)**. When BP increases, the material cools causing thermal contraction and development of tensile stresses at the centers of all parts as shown in **Figure 6-14 (a)** and **(b)**. When BP = 100%, the last layer is heated indicating the completion of the part. This expansion-contraction of the material during LPBF is consistent with previous observations [185].

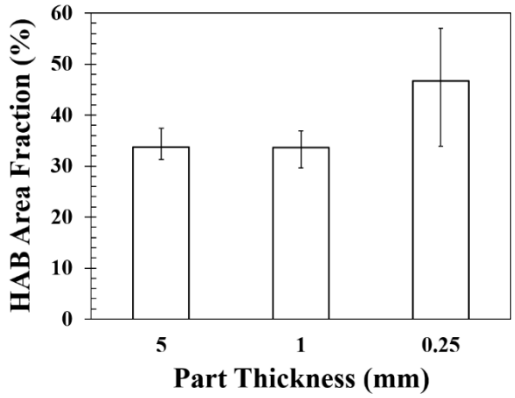


**Figure 6-13:** Plot Showing the Effect of Part Thickness on High Angle Boundary (HAB) Area Fraction. Values Computed Using 4 EBSD Scans Taken from Different Regions for Each Part Thickness.

The effect of part thickness on stress distributions can be explained with respect to the plate theory [186,187]. Thin-wall parts can only support loads along the in-plane direction (Y-Z) and the stresses in the through-thickness direction (X) are negligible. The plane stress condition is clearly seen in the 0.25 mm part in **Figure 6-14** where the stress in the X-direction (**Figure 6-14 (a)**) vanishes rapidly once BP exceeds 56%. Increasing wall thickness allows more stress to be supported in the through-thickness direction as seen by the increased stress magnitudes for the 1 mm and 5 mm parts in **Figure 6-14 (a)**. The stresses in the Y direction in **Figure 6-14 (b)** are mostly compressive but transition to tensile as BP progresses for the 1 mm and 5 mm parts. Interestingly, the Y-stress in the 0.25 mm part remains in compression, increasing continuously with BP until it reaches a negative steady state value (~ -300 MPa).

In the unconstrained Z direction (BD), all parts develop very low compressive stresses at the beginning (see **Figure 6-14 (c)**). As the build progresses, cooling of the compressed upper layer causes material shrinkage

towards the laser path introducing tensile stress in BD, as demonstrated in **Figure 6-14 (c)**. The stress magnitudes in the Z direction increase with part thickness due to the higher cooling rates and thermal gradients towards BD caused by the added wall thickness (see **Section 6.4.4.2**). This tensile stress is likely to favor the formation and propagation of micro-cracks along the melt pool boundaries (note that the stress axis is mostly perpendicular to the melt pool plane). Considering the CAF values for 5 mm, 1 mm and 0.25 mm part thicknesses at different micro-crack eccentricities (see **Figure 6-6**), thicker wall structures have higher proportion of melt-pool (ECC ≤0.99) to straight (ECC >0.99) micro-cracks than thinner walls (3.1, 1.6 and 1.3 in the 5 mm, 1 mm, and 0.25 mm, respectively).

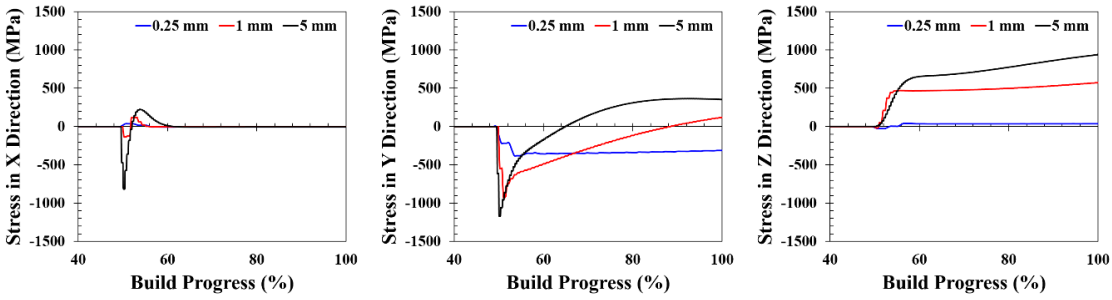


**Figure 6-14:** Layer Heat Source Simulation of the Stresses in (a) X Direction, (b) Y Direction and (c) Z Direction (See **Figure 6-2 (a)** for Axis Reference) Extracted at BP = 50% During the Process up to the End of Simulation (BP = 100%). Results Include Stresses for the 5 mm (Black), 1 mm (Red) and 0.25 mm (Blue) Thin-Wall Parts.

### 6.4.3.2 Analysis of Stress Triaxiality Using the Layer Heat Source Model

The evolution of stress triaxiality calculated at the center of the parts with respect to BP is shown in **Figure 6-15**. The negative stress triaxiality observed when the first layer is activated is due to the large step increment and the uniform heat distribution through the layer as mentioned earlier. As the build progresses, the wall thickness is shown to impact the residual stress significantly. The stress triaxiality value increases with increasing part thickness, suggesting favored micro-crack growth for larger wall thicknesses. This is consistent with **Figure 6-4 (a)** where the micro-crack size increases with the part thickness. The 0.25 mm part rapidly reaches steady state at T~ -0.33, corresponding to uniaxial compression in **Figure 6-15**. Micro-crack growth is thus suppressed as the build progresses, which partially explains the significantly lower CAF value in the thinnest part (**Figure 6-4 (b)**).

Furthermore, residual stresses from previous layers affect micro-crack growth. Higher residual stresses in the part are likely to affect the local stress triaxiality surrounding the melt pool region and delay the transition between negative and positive stress triaxialities shown in **Figure 6-12**. Consequently, increasing the part thickness should result in higher propensity to micro-cracking. Accordingly, micro-crack quantification in Fig. 4b indicates more micro-cracks in the thickest part (5 mm) compared to the thinnest part (0.25 mm), suggesting direct proportionality between part thickness and micro-crack propensity.

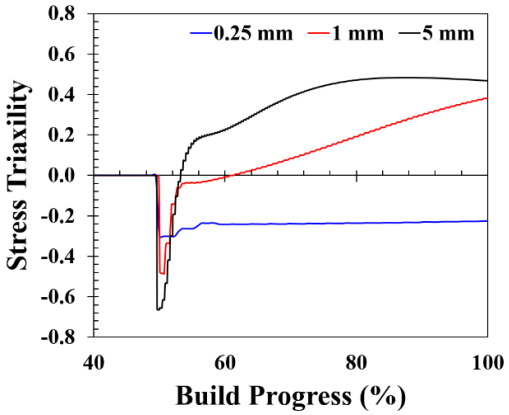


**Figure 6-15:** Layer Heat Source Simulation of the Stress Triaxialities for the 5 mm, 1 mm, and 0.25 mm Parts.

However, the higher CAF in the 1 mm part compared to the 5 mm part represents a discontinuity in this trend. A similar micro-crack analysis performed using different build conditions (15° scan angle relative to the X-direction) and materials (RENÉ 65 and RENÉ 108) reached similar conclusions [158]. In all cases, the 1 mm part always showed higher crack density and higher local variation compared to its counterparts. Therefore, the trend of higher crack density for larger wall thickness (**Figure 6-4 (b)**) clearly exhibits an anomalous behavior between 0.25 mm and 5 mm wall thickness. Simple FE models detailed in **Section 6.3** are not sufficient for explaining the anomalous behavior associated with heterogeneous distribution of micro-cracks in the 1 mm part. The macro- and micro-scale models are unable to capture the thermal interaction between adjacent laser tracks, thus, the local thermal gradient cannot be captured. To capture the long- and short-range thermal gradients responsible for micro-cracking, a more efficient multi-scale LPBF model is required.

### 6.4.4 Anomalous Micro-Cracking Behavior in Thin-Wall Structures

Microstructures are the strategic link between materials processing and behavior. The dendritic structure is the most frequently observed pattern in solidified alloys. The microstructural scales of dendrites control the segregation profiles, the formation of secondary phases within interdendritic regions, and the micro-cracking

behavior. The following sub-sections evaluate the effect of wall thickness on the dendritic structure in an attempt to explain the anomalous micro-cracking behavior observed in the 1 mm thick parts.

### 6.4.4.1 Effect of Wall Thickness on PDAS

**Figure 6-16 (a)-(c)** show sample BSE-SEM images illustrating dendrite morphologies for 5 mm, 1 mm, and 0.25 mm parts, respectively. All dendrites exhibit columnar morphologies and small PDASs typical of high cooling rates observed in laser AM [80,83,84]. Columnar dendrites near the melt pool centerline are aligned with BD. Intersecting dendrites away from the melt pool centerline exhibit a wide range of growth angles with respect to BD. These angles vary between 9° and 77° for 5 mm, 5° and 63° for 1 mm, and 7° and 21° for 0.25 mm. Deviations in dendrite angles occur due to heterogeneous nucleation sites and varying heat flow directions developed along the melt pool boundaries [188,189]. Decreasing the wall thickness leads to more directional heat flow and preferential dendrite growth along BD.

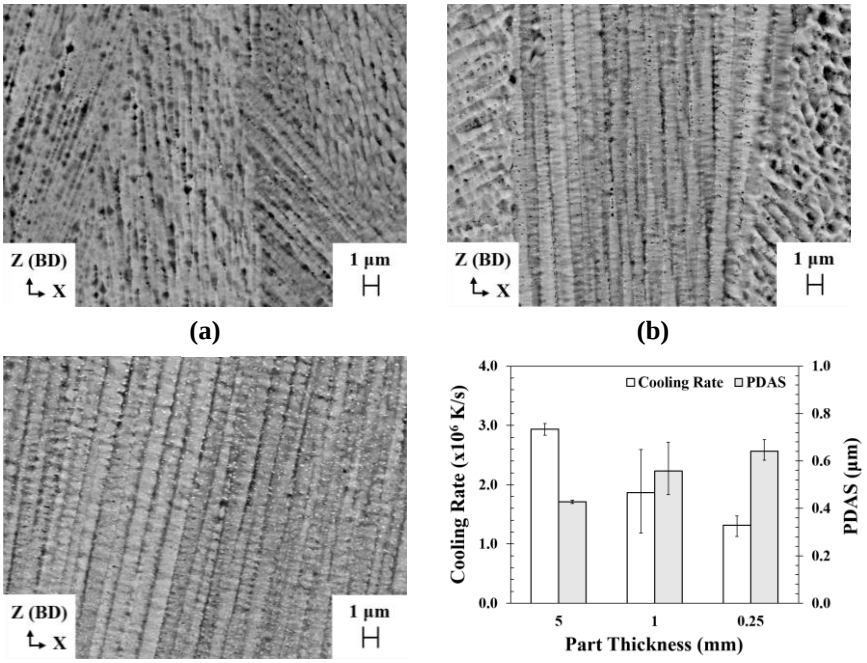


**Figure 6-16:** BSE-SEM Images Showing Fine Columnar Dendrites for Parts with Wall Thicknesses of **(a)** 5 mm, **(b)** 1 mm and **(c)** 0.25 mm. **(d)** Plot Showing Effect of Part Thickness on PDAS and Cooling Rate. PDAS Values were Measured at the Center of the Melt Pool, and a Solidification Rate of 0.6 m/s was Chosen to Calculate the Cooling Rates.

**Figure 6-16 (d)** shows the effect of part thickness on average PDAS calculated from four BSE-SEM images for the 5 mm, 1 mm and 0.25 mm parts (see **Section 6.2.5**). The average PDAS value for columnar dendrites is lower for the 5 mm (0.43 μm) part compared to the 1 mm (0.60 μm) and 0.25 mm (0.64 μm) parts.

### 6.4.4.2 Effect of Wall Thickness on Cooling Rates

The measured PDAS values were used to calculate cooling rates for the three parts. A power-law-based model for superalloys defined by Hunt and Kurtz-Fisher was adopted to evaluate the average thermal gradientsm($G$) and solidification velocities ($V$) [190,191]. Cooling rates were calculated using the product of $G$ and $V$. The general form of the equation is:

$$\lambda_1 = A_o G^{-m} V^{-n}, \quad \textbf{(6-3)}$$

where $A_o$ is a proportional constant, and $m$ and $n$ are power law constants of $G$ and $V$, respectively. The values for $A_o$, $m$ and $n$ were set to 832, 0.5 and 0.25, respectively, based on a computational-fluid-dynamics-based (CFD-based) solidification model by Sabau et al. [166]. The value of $V$ was set to 0.6 m/s to provide a rough estimate of $G$ and $\dot{T}$ ($G * V$) at the center of the melt pool. The solidification velocity range likely lies between a fraction of the scanning speed (minimum at the bottom of the melt pool) and the full scanning speed (maximum at the trailing edge of the melt pool – 1 m/s in **Table 6-2**).

**Figure 6-16 (d)** shows that the average cooling rate decreases as part thickness decreases. The 5 mm part exhibits higher cooling rate (2.94 x $10^6$) compared to the 1 mm (1.87 x $10^6$) and 0.25 mm (1.32 x $10^6$) parts. Cooling rates for all parts are similar to LPBF cooling rates reported in literature [80]. This observation appears to be counterintuitive as thinner parts possess greater surface to volume ratios, implying faster cooling than thicker parts. Nevertheless, this can be interpreted using heat transfer/flow operation in the powder bed: 1) surrounding powder particles act as insulators, and 2) heat conduction is limited to the solidified part of the build [79]. Builds with thicker walls encompass significantly larger masses of solid material within the powder than their thinner counterparts. The bulky solid material underneath the melt pool acts as a heat sink conducting heat away rapidly, resulting in higher cooling rates in the thicker parts. This is consistent with the stress plots in **Figure 6-14** showing larger thermal stresses for larger wall thicknesses. The macroscopic thermal gradient increases with part thickness leading to higher micro-crack growth rate and a higher number of melt-pool micro-cracks in the thicker parts (5 mm compared with 0.25 mm), as discussed in **Section 6.4.3.1**.

#### 6.4.4.3 Core-to-Edge Effect on Micro-Cracking in Thin-Wall Parts

The evaluation of the cooling rates using the PDAS measurements (**Section 6.4.4.2**) agrees with the stress analysis (**Section 6.4.3.1**). Increasing the wall thickness increases the cooling rate and the associated thermal stresses. Interestingly, the 1 mm part shows larger variation in PDAS and cooling rate, implying higher fluctuation of the local thermal gradient in the 1 mm part compared to the 0.25 mm and 5 mm parts. This can explain the higher amount and variation in CAF for the 1 mm part observed in **Figure 6-4 (b)** and **Figure** 6-6. The local thermal gradient likely promotes the formation of high ECC micro-cracks aligned with BD.

The elevated thermal gradient experienced by parts with wall thicknesses between 0.25 mm and 5 mm can be attributed to the core-to-edge effect stemming from the heat transfer mechanism during processing. Lower heat transfer at the edges due to powder insulation coupled with higher heat transfer in the center through the solidified core can lead to high thermal gradient in the part. However, studies of cooling rates based on location-dependent PDASs were inconclusive. Alternatively, the laser path vector length, proportional to the wall thickness, can affect the thermal gradient. In the future, it is of interest to study thin-wall parts with a wider range of laser scanning strategies and wall thicknesses to better capture the effect of thermal gradient on the micro-cracking behavior.

## 6.5 Conclusions

The micro-cracking mechanism in thin-wall LPBF high γ' Ni-based superalloy, RENÉ 108, was investigated. The micro-cracks were statistically analyzed for parts with three different wall thicknesses. Electron microscopy characterization was performed to evaluate the micro-cracking mechanism. Finite element analysis was conducted to calculate the in-process stresses. Two different FE models, considered at beam and layer scales, were used to predict the stress states at the micro- and macroscopic levels. The beam-scale model used an ED heat source to mimic the laser beam, while the layer-scale model used a 'lumped' heating approach.

Two types of micro-cracks were observed in the thin-wall parts. Most micro-cracks were straight and aligned along the build direction, while others formed along melt pool boundaries. All micro-cracks demonstrated dendritic morphologies and formed along high angle boundaries, characteristic of solidification cracking. The beam-scale simulation results support the apparent solidification cracking mechanism. The comparison between the simulated stress triaxialities and temperatures showed that solidification cracking is favored within the melt pool, consistent with the higher fraction of straight micro-cracks observed along the dendrite boundaries. The simulation also showed that micro-crack formation is more difficult along the melt pool boundaries. In these areas, the stress triaxiality becomes positive when the temperature is significantly lower compared to the center

of the melt pool. Laser power, speed and part thickness all influence the temperature within the melt pool, consequently affecting the formation of melt-pool micro-cracks.

With the laser conditions and part thicknesses considered, the cooling rates for all parts were in the order of $10^6$ °C/s, typical of laser-based AM. The thicker parts exhibited higher cooling rates compared to the thinner parts due to heat transfer mechanisms associated with the part surface area to volume ratio. Accordingly, numerical simulations showed higher stresses in thicker walls and more micro-cracks were observed in the 5 mm compared to the 0.25 mm part. Micro-crack propagation is favored for builds with thicker walls because the stress triaxiality increases with wall thickness. At 0.25 mm wall thickness, the simulation displays compressive residual stress state, which transitions to tensile stress state as the build thickness increases.

The micro-cracking behavior is discontinuous between 0.25 mm and 5 mm, determined by the significantly higher micro-crack propensity in the 1 mm part. In addition, microstructure analysis showed evidence of higher fluctuation of thermal gradients within the 1 mm part, compared to the other parts. Therefore, a small variation in part thickness alone can drastically change the micro-crack volume fraction. Crack density increases by 5X when the wall thickness increases from 0.25 mm to 1 mm and decreases by 1.6X when the wall thickness further increases to 5 mm. These results reflect the significance and sensitivity of internal micro-cracking to changing wall thicknesses, which must be weighed carefully during part design. To obtain improved empirical evidence for the maximum threshold wall thickness value for micro-cracking, more samples and part thicknesses need to be considered.

# Chapter 7
# Investigating the Effect of Build Position on Micro-Cracking in LPBF-Based Thin-Wall Components

In this chapter, *the effect of build height on micro-cracking density in a LPBF-printed thin-wall part is investigated and a theory for the observed micro-cracking trends is proposed*. It is well documented that high cooling rates and thermal gradients (inherent in LPBF) influence the formation of heterogeneous microstructures during processing. The microstructure variation coupled with the created in-process stresses could affect the micro-cracking behavior along the part height. This study combines both experimental and numerical simulation techniques to determine the micro-cracking tendencies at three different positions along the LBH. A RENÉ 108 1 mm thin-wall sample is chosen as it demonstrates high micro-cracking propensities. The effect of PDAS, cooling rates and in-process stresses on micro-cracking are discussed for the three cases.

The chapter presents a published article in the TMS 2022 151st Annual Meetings & Exhibitions Proceedings

***TMS 2022 151st Annual Meeting & Exhibition Supplemental Proceedings (2022), Chapter 94***

## 7.1 Introduction

Additive manufacturing of metallic components is of particular interest to fabricate complex features with thin-wall sections for aerospace and land turbine engine applications [30]. Sustainable high-temperature materials such as Ni-based superalloys, which provide good creep and fatigue strength in conjunction with excellent oxidation and corrosion resistance [131–135,169], are required to produce parts such as serpentine-shaped fuel nozzles and turbine vanes. However, many challenges arise during the production of thin-wall structures using hard-to-weld high gamma prime (γ') Ni-based superalloys due to the complex process-geometry-chemistry relationship. Micro-crack formation during laser powder bed fusion (LPBF) processing is one such problem not understood in depth [13,96,175].

In this study, the effect of build height on micro-cracking of LPBF-printed RENÉ 108 thin-wall components is investigated. A "layer heat source model" is used to evaluate the effect of residual stress state on micro-crack propagation along the part height, while primary dendrite arm spacing (PDAS) analysis is used to determine the effect of build height on crack nucleation.

## 7.2 Experimental Procedures

### 7.2.1 Materials

The high-γ' "hard-to-weld" Ni-based superalloy RENÉ (R108), with 6.15 wt.% Al+Ti content and 63% γ' volume fraction, was used to manufacture LPBF-based thin-wall structures. The powder was provided by Powder Alloy Corporation, consisting of mostly spherical powder particles with a size range ($D_{10}$-$D_{90}$) of 12-40 µm and median particle size ($D_{50}$) of ~19 µm. The chemical composition (in wt. %) of the powder was determined by inductively coupled plasma - optical emission spectroscopy (ICP-OES) at Activation Laboratories (ACTLABS © Canada) (**Table 7-1**).

**Table 7-1:** Chemical Composition of As-Received RÉNÉ 108 Powder in wt.%.

| Ni | Cr | Co | Al | Ti | Ta | W | Mo | Hf | B | Zr | C |
|---|---|---|---|---|---|---|---|---|---|---|---|
| Bal. | 8.64 | 10 | 5.36 | 0.75 | 3.02 | 10.03 | 0.53 | 0.87 | 0.01 | 0.01 | 0.01 |

### 7.2.2 LPBF Printing

Three thin-wall parts with thicknesses 5.00 (5) mm, 1.00 (1) mm and 0.25 mm were built using an Aconity$^{TM}$ MIDI LPBF printer with machine conditions similar to [158]. The laser scan pattern was bidirectional

with a hatch angle of 75 degrees to the thickness (along the X direction) and no scan rotation was incorporated between layers. The design part length (along the Y direction) and height (along the Z direction) for each specimen was 50 mm. Parts with thicker walls had higher limiting build heights (LBHs) compared to thinner walls as explained in [158]. In this study, only the 1 mm part was chosen to investigate the effect of build height on micro-cracking behavior in LPBF thin-wall parts. The LBH of the 1 mm part was 44.50 mm, rounded to 45 mm for simplicity.

### 7.2.3 Microstructure Characterization

The as-printed parts were removed from the build plate and thin-wall sections, approximately 5 mm x 15 mm (length x height) in dimension, were extracted for metallurgical sample preparation. Different regions, top (T), middle (M) and bottom (B), central to the part width (see **Figure 7-1**) were sectioned with respect to the base plate. All samples were mounted, ground, and polished, with final polishing conducted using 0.04 μm colloidal silica finish. The polished samples were viewed under the Keyence VHX7000 digital microscope for micro-crack observation and quantification.

Furthermore, samples were etched with glyceregia (15 mL HCl, 10 mL Glycerol, 5 mL $HNO_3$) for 10 s to reveal melt pools, dendrites, and micro-cracking behavior. Microstructure characterization was performed using a JEOL JSM-7600F field emission gun SEM (FEG-SEM).

### 7.2.4 Image Analysis, Micro-Crack Quantification, and Primary Dendrite Arm Spacing

Micrographs of as-polished specimens were analyzed using image analysis software, ImageJ [72], coupled with a custom visual basic script. The micro-crack analysis procedure outlined previously in [158] was utilized to extract the crack area fractions and crack length densities for T, M and B sections (see **Figure 7-1**) of the 1 mm part. Crack area fraction (CAF) is defined as a percentage of the total area of micro-cracks per image normalized by the image area. Crack length density (CLD) is defined as the sum of lengths of micro-cracks per image normalized by the image area.

All samples were ground and polished five times to generate an adequate number of planes (approximately 1 mm inter-planar distance) for crack density analyses. Micro-crack quantification along build direction (BD) across the part thickness was fully captured by performing image analysis on the XZ plane. Over 30 micrographs per plane were analyzed, and micro-crack quantities including 95% confidence levels were computed for each sample. Average primary dendrite arm spacing (PDAS) values were computed using four 5000X magnification backscatter electron SEM (BSE-SEM) images from different crack-free regions near

straighter dendrites for each specimen. Micrograph PDAS measurements were taken using the linear intercept method [166].

## 7.3 Modeling Methodology

The effect of spatial variation along BD on in-process stresses is evaluated using the "layer heat source" finite element modelling (FEM) technique described in [158]. Convective and radiative heat losses are incorporated for all surfaces exposed to the external environment (25 °C) [168]. Temperature-dependent properties are proprietary and provided by General Electric, whereas mechanical properties are obtained from Kissinger et al. [170]. The layer-scale ABAQUS-based FEM methodology proposed by Yang et al [141] is employed to obtain accurate prediction of in-process stress results. Results are computed using a sequentially coupled thermo-mechanical modelling procedure similar to [144]. The model utilizes a lumped-track approach to simulate a single heat source. Five physical layers are combined into a single layer in the model (200 µm thickness) to improve computational efficiency.

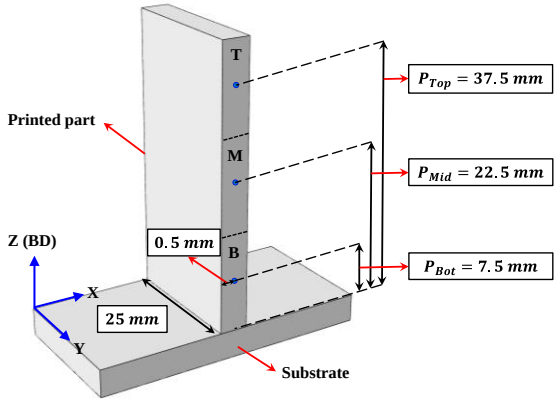


**Figure 7-1:** 3D Finite Element Model Illustrating the Positions (Blue Points) along the Build Direction Used to Capture the Stress Triaxialities in the 1 mm Thick Part for the Bottom (B), Middle (M) and Top (T) Regions (Separated by Dashed Lines) During Processing. The Cracks were Analyzed in the Vicinity of the Points Used for Simulation. The LBH Considered in the Model was Rounded to 45 mm for Simplicity.

**Figure 7-1** shows the three-dimensional (3D) finite element model illustrating the positions (blue points) taken for stress analysis in the top, middle and bottom of the 1 mm part during LPBF processing. To compare stress results for T, M and B, the terminology build progress (BP), representing the normalized height of the part along BD is used. Each point considered for stress analysis is taken central to the part thickness (along the X direction) and length (along the Y direction), as shown in **Figure 7-1**. The stress is analyzed at the center of the

section to correlate with the location of micro-crack characterization. For the middle region, M, for instance, the in-process stress is always recorded at BP = 50% as subsequent layers are added up to LBH (BP = 100%).

## 7.4 Results and Discussion

### 7.4.1 Micro-Cracking Morphology

**Figure 7-2** shows micro-graphs of typical micro-cracks observed in the R108 1 mm thick sample on the XZ plane. Most micro-cracks appear to propagate towards BD, and some appear in the vicinity of the melt pool boundary, as shown in **Figure 7-2 (a)**. A close-up of a micro-crack, highlighted using a red box in **Figure 7-2 (a)**, is shown in **Figure 7-2 (b)**. The dendritic morphology on either side of the cracked boundary likely indicates solidification cracking according to some [13,175], however others such as Carter et al. [96] suggest that solid-state cracking cannot be ruled out. Detailed investigation of the micro-cracking mechanism requires advanced microstructure characterization and beam-scale FEM analysis, not in the scope for this publication.

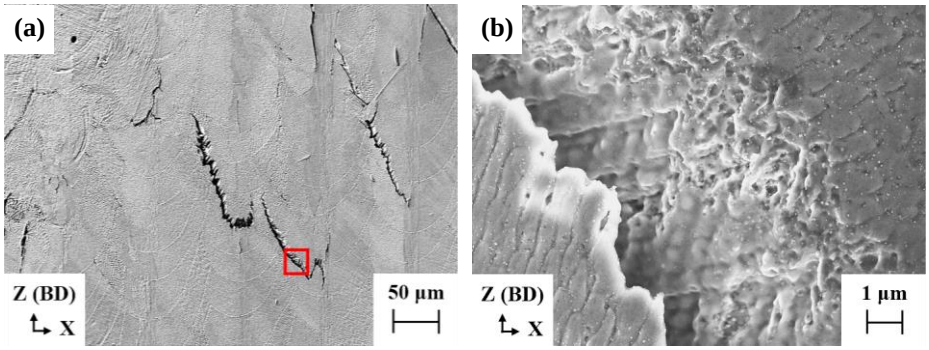


**Figure 7-2:** SE-SEM Micrographs Showing Examples of **(a)** Micro-cracks at Low Magnification 250X and **(b)** a Close-Up of Micro-Crack in **(a)** (Highlighted Using the Red Box) at High Magnification 10000X. The Micro-Crack is Observed in the Vicinity of the Melt Pool Boundary as Shown in **(a)** and Clearly Exhibits Dendritic Morphologies. Both Images were Taken from the Midsection of the Printed Part.

### 7.4.2 Effect of Build Height on Micro-Cracking

To assess the effect of spatial variation on micro-crack propagation, the effect of build height on micro-crack propensity and stress triaxiality is demonstrated in **Figure 7-3**. The crack area fractions (CAFs) and crack length densities (CLDs) are higher near the top of the build and lower near the base plate, as shown in **Figure 7-3 (a)**. Also, all selected regions in the 1 mm part exhibit high CAF and CLD variation, consistent with a previous study on similar high-γ' Ni-based superalloys for 1 mm wall thickness [158].

The "layer heat source model" described in **Section 7.3** was used to evaluate the stress along the build height. This model is fairly accurate for predicting the residual stresses generated during the cool down of the part as shown by Yang et al. [141]. **Figure 7-3 (b)** shows the stress triaxialities for the top (T), middle (M) and bottom (B) sections of the 1 mm part. In each case, the newly added layer experiences compression (negative stress triaxiality) and transitions to tension (positive stress triaxiality) as the build progresses. The transition from compression to tension occurs faster for M and T compared to B. For instance, M changes from compression to tension rapidly from BP = 52% to BP ≥ 60%, while B changes from compression to tension relatively slowly from BP = 20% to BP ≥ 48%.

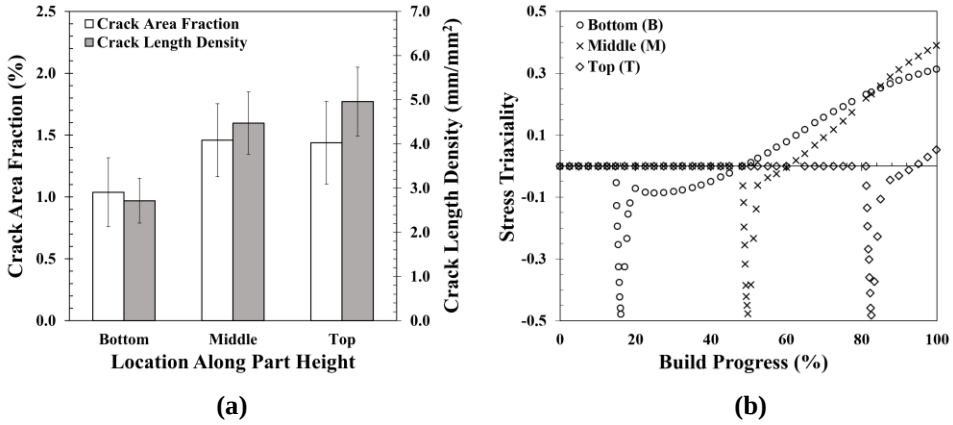


**Figure 7-3:** Plots Showing **(a)** the Average Crack Area Fractions and Crack Length Densities, and **(b)** Simulated Stress Triaxialities as the Build Progresses at the Bottom, Middle and Top of the 1 mm Part.

The steeper transition for M and T is attributed to less constrain, due to fewer layers near the top surface compared to the substrate. Also, note that the stress triaxiality for T reaches a lower value compared to B and M because it is close to the top surface, which consists of the fewest printed layers. The simulations correspond well with the experimental CAF and CLD values in **Figure 7-3 (a)**. While the model cannot capture the crack nucleation tendency, it shows a lower propensity for crack growth close to the base plate. This is because the time increment used for the "layer heat source model" creates uniform heat distribution through the layer and is unable to predict the stress state during the early stages of melt pool solidification accurately. Overall, the simulation and experimental results highlight the significance of stress triaxiality on micro-crack volume fraction after LPBF processing.

### 7.4.3 Effect of Build Height on Cooling Rate

To evaluate the effect of crack nucleation on the CAF and CLD, the PDAS and the associated cooling rates were computed at different positions along the part height. Increasing cooling rate is reported to negatively affect solidification crack nucleation in Ni-rich alloys [192]. Cooling rates were calculated based on the Hunt and Kurtz-Fisher model for superalloys,

$$\lambda_1 = A_o G^{-m} V^{-n}, \quad \textbf{(7-1)}$$

where $\lambda_1$ is the PDAS, $A_o$ is a proportional constant, $G$ is the temperature gradient, $V$ is the solidification rate, and $m$ and $n$ are power law constants of $G$ and $V$, respectively. The constants $A_o$, $m$ and $n$ were set to 832, 0.5 and 0.25 based on the work by Sabau et al. [166]. The measured PDAS was used for $\lambda_1$. Finally, the cooling rate was computed using the product of $G$ and $V$, assuming $V = 0.6\ m/s$, representative of solidification rates near the center of the melt pool.

Dendrites passing through the center of the melt pool are fine (approximately 0.6 µm width), columnar and propagate along BD, as shown in **Figure 7-4 (a)**. The columnar dendritic morphology has been observed for laser-processed materials elsewhere [83]. The interdendritic regions also demonstrate etch pits (red arrows) due to strong wet etching conditions, necessary to observe the melt pool and the dendrites. **Figure 7-4 (b)** shows that the average measured PDAS values of the columnar dendrites for all regions are similar and lie between 0.5 and 0.8 µm, with cooling rates lying between 1 and 3 x $10^6$, typical of laser AM [80].

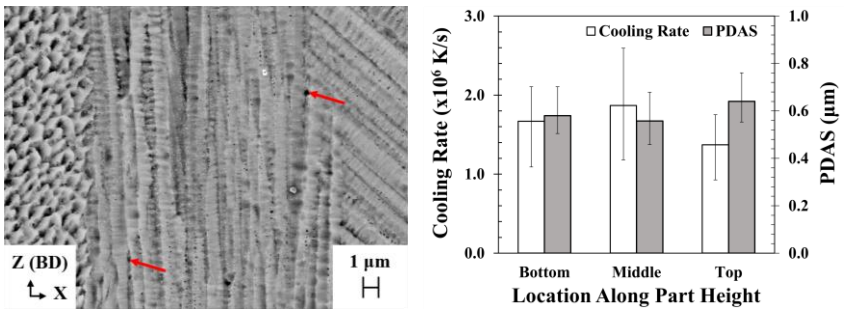


**(a)** **(b)**

**Figure 7-4: (a)** BSE-SEM Image Showing Fine Columnar Dendrites in the Middle of the 1 mm Part, where the Red Arrows Indicate Etch Pits. **(b)** Plot Showing the Effect of Part Thickness on PDAS and Cooling Rate. All PDAS Values were Measured at the Center of the Melt Pool and 0.6 m/s Solidification Rate was Used to Compute the Cooling Rates.

There is no significant difference in the PDAS and cooling rate values between the three different sections of the 1 mm thick part. This is attributed to similar processing conditions resulting in similar solidification patterns and high cooling rates along the part height. Hence, cooling rate does not cause the variation in stress triaxiality along BD.

## 7.5 Conclusions

The effect of build height on the micro-cracking behavior in thin-wall parts made of high gamma prime Ni-based superalloys was investigated. Micro-cracks demonstrated dendritic morphologies, representative of cracking in the final stages of solidification. Micro-crack densities were found to be lower close to the base plate and higher for the middle and top sections. The analysis of the cooling rates observed along the build height suggests a similar tendency for crack nucleation. The reduced crack density close to the base plate is attributed to the more compressive state stress suppressing crack propagation.

# Chapter 8

# Examining the Effect of Composition on Micro-Cracking in High-γ' Ni-Based Superalloy Thin-Wall Structures Produced by LPBF

In this chapter, *the effects of material composition on the micro-cracking tendencies in high-γ' Ni-based superalloys are elucidated*. Two different Ni-based superalloys, RENÉ 65 (γ' ~42%) and RENÉ 108 (γ' ~63%), covering a wide range of alloy compositions within the crack-susceptibility window are selected for this study. Various microstructure characterization tools such as SEM, TEM, EDX and EBSD, coupled with thermodynamic and numerical simulations, are used to compare and explain the micro-cracking behaviors of the two materials.

---

The chapter presents a manuscript of an article being prepared for journal submission.

***Under Peer Review***

## 8.1 Introduction

Laser powder bed fusion (LPBF) enables the production of complex thin-wall metal components such as vanes and fuel nozzles in gas turbine jet engines [50,193]. Near-net shape three-dimensional (3D) parts are built layer-by-layer through selective processing of the powder layers using computer aided design (CAD) at rapid solidification rates [42,166]. This adds a layer of complexity during fabrication, which could adversely affect the part quality and ultimately result in build failure [119,158]. To develop defect-free LPBF thin-wall structures, factors such as wall thickness [120], laser scanning strategy [127], laser energy density [96], and alloy composition [194], must be considered carefully during part design.

Components  Alloy composition has a significant effect on the processability of a metal part. High-gamma-prime (high-γ') nickel-based (Ni-based) superalloys are of particular interest as they boast excellent creep and fatigue strengths, coupled with oxidation and corrosion resistance at elevated temperatures [131,133,134]. These alloys are difficult to process due to their enhanced susceptibility to micro-cracking during rapid solidification processing [13,158,195]. Several authors [175,194,196] recently showed that the alloy compositions can be modified to produce LPBF parts with few micro-cracks. However, the studies overlooked advanced metallurgical investigations in describing the micro-cracking mechanisms. Improved understanding of the cracking mechanism furthers development of the next generation of high-γ' superalloys compatible with LPBF processing conditions.

There exists an ongoing debate on the types of micro-cracking mechanisms observed during LPBF. The two types of micro-cracking mechanisms discussed widely include solidification cracking and solid-state cracking. Solidification cracking typically occurs in the final stages of solidification when the undercooled liquid is the last to solidify due to solute enrichment at the grain boundaries (GBs) [176]. Solid-state cracking occurs when there is no remaining liquid and there is a reduction in ductility at the GBs formed during rapid solidification [15]. These cracks are typically distinguished using morphological observations – solidification cracks exhibit interdendritic morphologies, whereas solid-state cracks display intergranular morphologies [15].

Few authors have studied micro-cracking mechanisms for LPBF-processed high-γ' Ni-based superalloys with Al+Ti contents exceeding 6 wt%, preferential for micro-cracking [15]. For instance, Chauvet et al. [13] considered an additively manufactured Ni-based superalloy with Al+Ti wt% = 8.6, proposing that micro-cracks preferentially aligned with the build direction (BD) exhibit interdendritic morphologies depicting the solidification cracking mechanism. The authors explained that Mo- and Cr-rich borides promote solidification cracking at high angle grain boundaries (HAGBs), owing to the presence of a stable liquid film and large tensile thermal stresses favoring micro-crack propagation. On the other hand, Ghoussoub et al. [194] suggested that

LPBF-processed high-γ' Ni-based superalloys exhibit both solid-state and solidification cracking, but the dominating micro-cracking mechanism is influenced by the γ' content and the solidification range of the alloy. The authors proposed that straight cracks aligned with BD exhibit intergranular solid-state cracking, whereas jagged cracks exhibit interdendritic solidification cracking, consistent with observations by Carter et al. [96] for the alloy CM247LC, with Al+Ti wt% = 6.5. According to Ghoussoub et al. [194], straight cracks are attributed to reduced ductility and higher γ' contents, whereas jagged cracks are correlated to wider solidification intervals and the increased presence of Hf/Ta-rich carbides at the crack tips. Interestingly, Hariharan et al. [175] who studied IN738LC, a variant of CM247LC with Al+Ti wt% = 6.2, demonstrated dendritic morphologies, suggesting the solidification cracking mechanism, for all LPBF micro-cracks aligned with BD. The authors attributed solidification crack formation to the enrichment of minor alloying elements such as Zr and Si at the HAGBs, highlighting the importance of solute diffusion rates on micro-segregation and solute enrichment at the HAGBs. Recently, Chakraborty et al. [197] studied LPBF micro-cracking in a similar alloy, RENÉ 108, with Al+Ti wt% = 6.2. The authors observed interdendritic crack morphologies and proposed the solidification cracking mechanism. Solidification cracking is preferred along columnar boundaries parallel to BD as positive stress triaxiality state is maintained at higher temperatures within the melt pool core compared to the melt pool boundary [197]. To gain further insight on the inherent nature of micro-cracking in LPBF high-γ' Ni-based superalloys, the effect of alloy composition on the micro-crack formation mechanism must be elucidated.

In this study, the underlying mechanisms for varying micro-cracking behaviors in LPBF-processed alloys with different compositions are thoroughly investigated through statistical analysis, finite element analysis (FEA), and advanced microstructure characterization. Two different high-γ' Ni-based superalloys, RENÉ 65 (R65) and RENÉ 108 (R108), are chosen to assess the differences in micro-cracking tendencies for varying γ' contents and alloy compositions. Optical microscopy combined with image and statistical analyses is used to determine the micro-cracking densities. Electron microscopy and electron backscatter diffraction (EBSD) techniques are employed to observe the parent microstructure, crack morphologies, and to further identify the phases and misorientation angles preferential for micro-cracking. The solidification behaviors are compared using thermodynamic simulations and the factors affecting LPBF micro-cracking are presented.

## 8.2 Experimental Procedures

### 8.2.1 Powder Characteristics

Two hard-to-weld high-γ' Ni-based superalloys, R65 and R108, with γ' volume fractions of 42% [73] and 63% [74], were used in the study. The alloys were chosen to encompass a wide range of alloy compositions susceptible to micro-cracking during rapid solidification processing [110]. Gas-atomized powders for R65 and

R108 were supplied by ATI Powder Metals and Powder Alloy Corporation (PAC), respectively. The size ranges (D10- D90) and median sizes (D50) of the powder particles for both materials were 12-40 µm and ~19 µm, respectively. The particles were mostly spherical and consisted of few satellite particles attached to larger particles [158]. The chemical compositions of the as-received powders, obtained through inductively coupled plasma – optical emission spectroscopy (ICP-OES) at Activation Laboratories (ACTLABS© Canada), are provided in **Table 8-1**.

**Table 8-1:** Powder Compositions of R65 and R108 in wt.%.

| Alloy | Ni | Cr | Co | Al | Ti | Ta | W | Mo | Nb | Hf | Fe | B | Zr | C |
|---|---|---|---|---|---|---|---|---|---|---|---|---|---|---|
| R65 | Bal. | 15.86 | 13.22 | 2.15 | 3.65 | 0.04 | 4.25 | 4.03 | 0.75 | | 1 | 0.01 | 0.05 | 0.01 |
| R108 | Bal. | 8.64 | 10 | 5.36 | 0.75 | 3.02 | 10.03 | 0.53 | | 0.87 | 0.27 | 0.01 | 0.01 | 0.01 |

Two thin-wall parts were manufactured on separate build plates by the Aconity$^{TM}$ MIDI printer using the build conditions provided in **Figure 8-1 (a)**. Details of the printing parameters are available in [158]. Bidirectional scan strategy at a 15° scan angle with respect to the wall thickness (X-direction) was used. The parts were oriented at a 45° angle relative to the recoating direction to avoid printing the parts perpendicular to the recoater motion. An image of the as-built thin-wall parts is presented in **Figure 8-1 (b)**. A wall thickness of 1.00 mm was considered because it showed the highest cracking density for both materials [158]. The part widths (Y-direction) and heights (Z-direction or build direction (BD)) for the parts were set to 50 mm. The as-printed part heights (or limiting build heights – LBHs) for R65 and R108 were 30.45 mm and 30.12 mm, respectively.

| Build parameter | Value |
|---|---|
| Laser power, P (W) | 200 |
| Scan speed, v (mm/s) | 1000 |
| Spot size, $d_{spot}$ (µm) | 120 |
| Hatch spacing, h (µm) | 90 |
| Hatch angle, θ (°) | 15 |
| Powder layer thickness, t (µm) | 40 |
| Designated part height (mm) | 50 |
| Part thickness, $t_{part}$ (mm) | 1 |

**(a)**

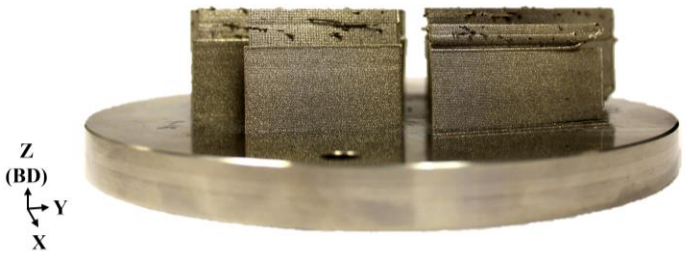


**(b)**

**Figure 8-1: (a)** LPBF Process Parameters Used to Fabricate R65 and R108 Thin-Wall components. **(b)** A Side-View Image of the As-Printed Components.

### 8.2.2 Microscopic Characterization

#### 8.2.2.1 Optical Microscopy

As-built components were removed from the base plate and sectioned along the XZ plane central to the part length. The XZ plane was chosen to cover the entire wall thickness along BD for microstructure characterization, as done in [158,196]. Thin-wall 1.00 mm × 10.00 mm (X × Z) sections were extracted from central locations to avoid microstructure heterogeneities at the sample edges and the base plate. Standard metallurgical sample preparation procedure including mounting, grinding, and polishing was utilized. The finishing steps included polishing with 0.04 μm colloidal silica, cleaning in an ultrasonic deionized (DI) water bath, rinsing with DI water, and drying with compressed air. The specimens were inspected under the Keyence VHX7000 digital microscope and over 100 optical micrographs (taken at 1000X) were obtained for part-scale qualitative and micro-crack statistical analysis.

#### 8.2.2.2 Electron Microscopy

The scanning electron microscopy (SEM) technique was used to observe and compare micro-crack morphologies as well as the phase distributions in the vicinity of micro-crack boundaries. As-polished samples were etched for 5s with glyceregia to reveal melt pools and dendrites within the material microstructure. A JEOL JSM-7600F field emission gun SEM (FEG-SEM) was used to acquire low (250X) and high (5000X-10000X) magnification images of micro-cracks with different morphologies.

To better examine the microstructure near micro-cracks, electron back scatter diffraction (EBSD) was used to obtain crystallographic information. The EBSD measurements were performed using a Thermo Scientific Quattro Environmental FEG-SEM equipped with Thermo Scientific Lumis EBSD detector. Plots from 5 different regions per sample were acquired at an accelerating voltage of 20 kV using a step size of 200 nm and the data was further processed using TSL OIM$^{TM}$ and a MATLAB script. For each region, two maps showing grain misorientations (GMOs) and kernel average misorientations (KAMs) were generated. The KAM maps are beneficial to provide qualitative representation of strain in crystalline materials. In this work, the maps are used to compare local and intergranular misorientations and qualitatively examine strain distributions in the vicinity of high angle boundaries (HABs) for different micro-crack morphologies.

Transmission electron microscopy (TEM) was employed to further investigate phase distributions at select HABs near micro-cracks on the XZ plane. Specimens were prepared to explore potential metallurgical factors responsible for contrasting micro-cracking propensities between the two alloys. Central sections with dimensions of 1.00 × 3.00 × 1.50 mm (X × Y × Z) were extracted from the as-printed thin-wall parts. The samples were mounted on a Gatan disc grinder on the XY surface and thinned to heights (Z) of 1.00 mm using standard

metallographic grinding and polishing steps. The FEG-SEM was used to select regions (one per sample) containing HABs near micro-cracks for TEM sample preparations using the focussed ion beam (FIB) method, as shown in **Figure 8-2 (a)**. A HITACHI FB-2000A Ga-FIB was used to produce thin specimens with dimensions of 15 × 0.1 × 10 µm (X × Y × Z), as illustrated in **Figure 8-2 (b)**. The samples were made to reveal the microstructure on the XZ plane (containing BD) using a JEOL JEM 2100F FEG-TEM equipped with an Oxford Xplore TEM energy dispersive X-ray spectroscopy (EDX) detector. Analyses were carried out in both conventional and scanning TEM (STEM) modes at 200 kV operating voltage. Controlled tilting techniques and selected area electron diffraction (SAED) patterns were used to distinguish HABs and identify γ' precipitates within the microstructure.

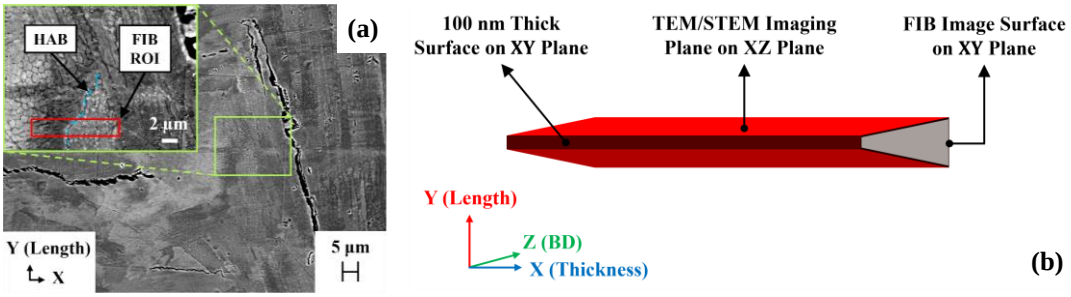


**Figure 8-2: (a)** Sample SEM image of R108 with inset (green box) showing a region of interest (ROI – red box) near a micro-crack for focused ion beam (FIB) lift-out. **(b)** Schematic showing the TEM/STEM imaging region on the XZ surface of the thinned lamella after FIB lift-out. Z is aligned with the build direction (BD).

### 8.2.3 Image and Statistical Analysis Procedures

Micro-crack statistics were generated through image analysis (using ImageJ [72]) and statistical data computation methods (through Visual Basic for Applications (VBA) scripts). Over 100 optical micrographs were used to produce sufficient micro-cracking data for statistical analysis. All images were inspected thoroughly to identify appropriate filtering parameters for inherent micro-cracks. Criteria such as minor axis lengths less than 5 µm, areas less than 1500 $\mu m^2$, circularities less than 0.6, roundness values less than 0.4, and aspect ratios less than 2.5 were utilized to distinguish inherent LPBF micro-cracks from other defects such as voids, porosities, or large defect-induced micro-cracks.

The micro-crack quantification procedure is outlined in [158]. The micro-crack area and count data were used to compute crack area fractions (CAFs) and crack count densities (CCDs), respectively. The CAF is defined as the area fraction of micro-cracks over the image area, while the CCD is defined as the total number of micro-cracks over the image area. Maximum Feret diameters and minor axis lengths were used to calculate the average

crack lengths and widths per sample, respectively. The micro-crack eccentricity (ECC) criterion was used to distinguish the different micro-cracking tendencies in both alloys, as done in [195,198]. The ECC is defined as a function of the minor (b) and major (a) axes lengths of a micro-crack, as shown in **Equation (8-1)**. High ECC values (around 1.0) reflect straighter micro-cracks than low ECC values (near 0.0), which represent rounder micro-cracks. All intermediate ECC values represent micro-cracks with varying shapes.

$$ECC = \sqrt{1 - \frac{b^2}{a^2}}\ , for\ b < a, \tag{8-1}$$

To generate an acceptable number of repetitions for representative statistical analysis on the XZ plane along the part length, samples were ground and polished five times along the Y-direction at inter-planar spacings of 1 mm. Cumulative sample areas of 50 $mm^2$, central to the polished specimen, were considered for both samples. Over 150 optical micrographs (50 per plane) were randomly selected from central regions and micro-crack statistics including 95% confidence levels were computed for both samples.

### 8.2.4 Differential Scanning Calorimetry

Alloy solidification characteristics were captured experimentally using the differential scanning calorimetry (DSC) methodology. A NETSZCH STA 449 Jupiter DSC machine was operated at a heating rate of 10 °C/s and temperature range between 25 °C (room temperature) and 1500 °C. The first derivative method was used to convert the generated DSC data into separate differential heating and cooling curves for easy identification of the phase transition temperatures of both alloys.

## 8.3 Simulation Methodologies

### 8.3.1 Thermodynamic Simulation Procedure

The effects of alloy composition and solute partitioning on the solidification behavior were evaluated through thermodynamic calculations using the ThermoCalc software, based on the available database for Ni-based superalloys (TCNI6). The equilibrium and Scheil-Gulliver models were compared to predict the actual solidification behavior in the LPBF process. The equilibrium model assumes infinite diffusion in solid and liquid states, depicting processes with low cooling rates similar to the DSC conditions [198]. On the contrary, the Scheil-Gulliver (S-G) model assumes infinite diffusion in liquid state and no diffusion in solid state, depicting processes with extremely high cooling rates similar to the LPBF conditions [199].

### 8.3.2 Numerical Simulation Procedure

The effect of alloy composition on in-process stresses and temperature at the microscopic (50-250 µm) scale is evaluated using the finite element modelling (FEM) technique. The beam-scale FEM framework presented in [172,173] is used as a basis to generate two separate models for R65 and R108 in this study. **Figure 8-3 (a)** shows a representative beam-scale model describing the common model geometry and mesh distribution. Both model geometries are set to 1.00 × 2.00 × 0.20 mm (X × Y × Z) to simulate the single track. The surface shaded in blue indicates the symmetry plane, where the symmetry plane boundary conditions are applied. The conditions include no displacement along X and no rotations in Y- and Z-directions. The bottom surface is constrained in all directions.

A sequentially coupled thermomechanical simulation based on [144] is implemented with the exponential decaying heat input model [171]. The thermo-physical properties include latent heat of fusion, thermal conductivity, laser absorption coefficient, specific heat capacity, and density for temperature ranging between 25 °C and 1600 °C. The R65 properties were taken from [172]. Thermo-physical properties of R108 were extracted from works on superalloys (such as CM247 LC [200] and MAR-M247 [205,206]) with similar chemical compositions. The liquidus, solidus and solvus temperatures for both superalloys were obtained by DSC, as shown in **Table 8-2**. The DSC on-cooling and on-heating temperatures are denoted by O-C and O-H, respectively.

**Table 8-2:** Phase Transition Temperatures and Solidification Ranges for R65 and R108 Obtained from DSC Plot Measurements.

| Alloy | Method | Liquidus (°C) | Solidus (°C) | γ' Solvus (°C) | Solidification Range (°C) |
|---|---|---|---|---|---|
| **R65** | DSC O-C | 1370 | 1260 | - | 110 |
| | DSC O-H | 1380 | 1270 | 1130 | 110 |
| **R108** | DSC O-C | 1405 | 1310 | - | 95 |
| | DSC O-H | 1425 | 1310 | 1250 | 115 |

The mechanical properties such as Young's modulus, Poisson's ratio, and plasticity are extracted from [169,207] assuming similar expected strengths for R65 and R108 due to the absence of γ' at supersolvus temperatures. The value of the stress is fixed at 120 MPa according to experimental values given in [169]. Two

separate layer-scale models based on [172,173] are constructed to acquire the nodal temperatures from the final layers. These values are incorporated as initial conditions for the beam-scale models. In-process stresses are evaluated at the center of the part (X: 0.50 mm, Y: 15 mm, Z: LBH/2 ≈ 15 mm) within the melt pool core (depth 40 µm) in both cases, as indicated using a black point in **Figure 8-3 (b)**.

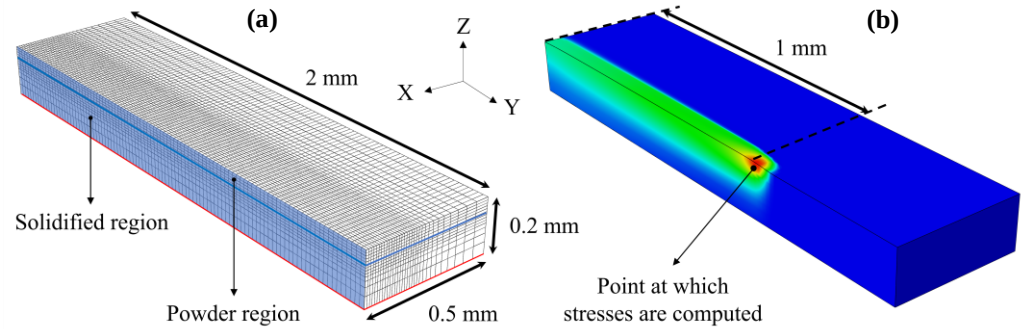


**Figure 8-3: (a)** Representative Beam-Scale FE Model Geometry Including the Powder and Solidified Regions. **(b)** Illustration Showing the Point at which Stresses are Computed for Both R65 and R108.

## 8.4 Results

### 8.4.1 Micro-Cracking Quantification

**Figure 8-4 (a)** shows the CAFs and CCDs for the 1.00 mm thick R65 and R108 parts. Both CAFs and CCDs increase as the alloy composition changes from R65 to R108. The CAF and CCD values for R65 are 0.462 ± 0.074 % and 458.1 ± 46.20 counts/mm2, 77% and 32% lower than the CAF and CCD for R108, which are 1.980 ± 0.349 % and 678.0 ± 58.30 counts/mm2, respectively. Conversely, the micro-crack lengths and widths for R65 are similar to R108 (approximately 3 µm shorter and 0.3 µm thinner), as demonstrated in **Figure 8-4 (b)**. The large variation in R108 CAF (**Figure 8-4 (a)**) is attributed to inter-planar variation in micro-cracking propensities, as explained in [158].

**Figure 8-4 (c)** shows the distribution of CAFs with respect to the micro-crack eccentricities in R65 and R108. For both alloys, the CAF distributions are similar and the micro-cracking propensity increases with ECC. Approximately 45% of the micro-cracks have ECCs ≤0.99 (low ECC), and >55% of the micro-cracks have ECCs >0.99 (high ECC). However, the CAF magnitudes for R108 are higher and more varying for all ECCs compared to R65. This is consistent with results presented in **Figure 8-4 (a)** which show higher CAFs in R108.

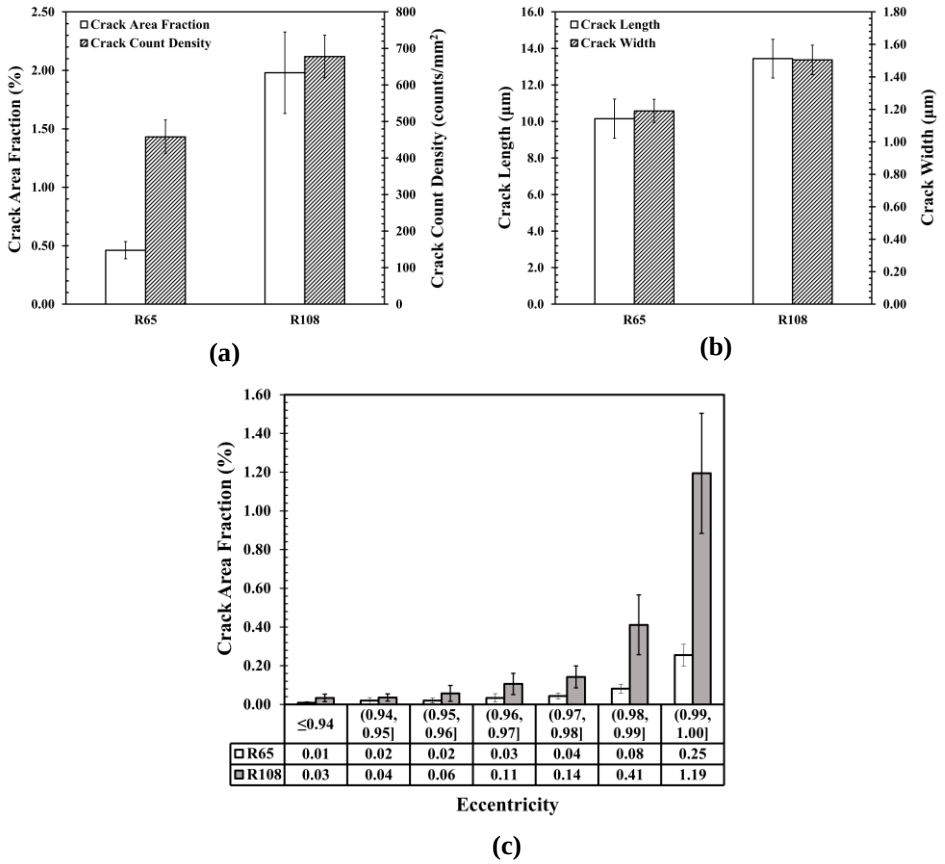


**Figure 8-4:** Plots Showing **(a)** the Total Crack Area Fractions and Crack Count Densities, **(b)** Average Crack Lengths and Widths, and **(c)** Crack Area Fraction Distribution by the Level of Eccentricity for As-Built R65 and R108 Thin-Wall parts. Cracks with Eccentricity Values Closer to 0 are Rounder, While Those with Values Near 1 are Straighter.

## 8.4.2 Micro-Cracking Qualification

**Figure 8-5** shows low magnification (250X) secondary electron SEM (SE-SEM) micro-graphs for R65 (**Figure 8-5 (a)**) and R108 (**Figure 8-5 (b)**). Both materials have a mixture of high ECC (red arrows) and low ECC (black arrows) micro-cracks. The high ECC micro-cracks are more frequent, straighter, and aligned with BD, whereas the low ECC micro-cracks are less frequent, more jagged (zipper-like) and aligned with melt pool boundaries. The following sections provide morphological and crystallographic information on both types of micro-cracks.

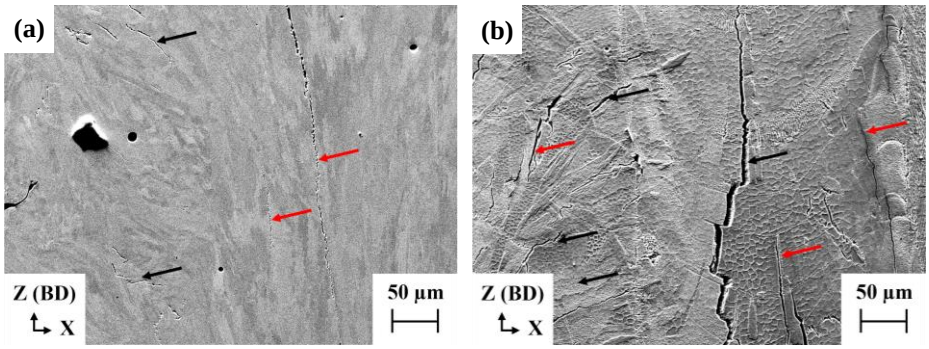


**Figure 8-5:** Secondary Electron SEM (SE-SEM) Images Taken at 250X Showing the Microstructures of As-Processed **(a)** R65 and **(b)** R108. Micro-Cracks are Labelled as Low ECC (Black) and High ECC (Red).

### 8.4.2.1 High ECC Micro-Cracks

**Figure 8-6** shows high magnification (5000X) backscatter electron SEM (BSE-SEM) micro-graphs of high ECC micro-cracks. Both R65 (**Figure 8-6 (a)**) and R108 (**Figure 8-6 (b)**) show micro-cracks aligned with BD, exhibiting dendritic morphologies on the crack surface. The R108 sample has a larger amount of fine spherical particles (see **Section 8.4.3** for composition) in the interdendritic regions compared to R65. For both alloys, there appears to be no accumulation of particles along the crack boundary. **Figure 8-7** shows the EBSD GMO and KAM maps in regions containing two straight (or high ECC) micro-cracks for both alloys. The GMO maps in **Figure 8-7 (a)** and **(b)** show that the straight micro-cracks propagate along high angle boundaries (HABs) with misorientation angles above 15°, consistent with results presented by Chakraborty et al. [197]. The KAM maps in **Figure 8-7 (c)** and **(d)** show that the micro-cracks are surrounded by highly strained regions, preferential for micro-crack propagation [104].

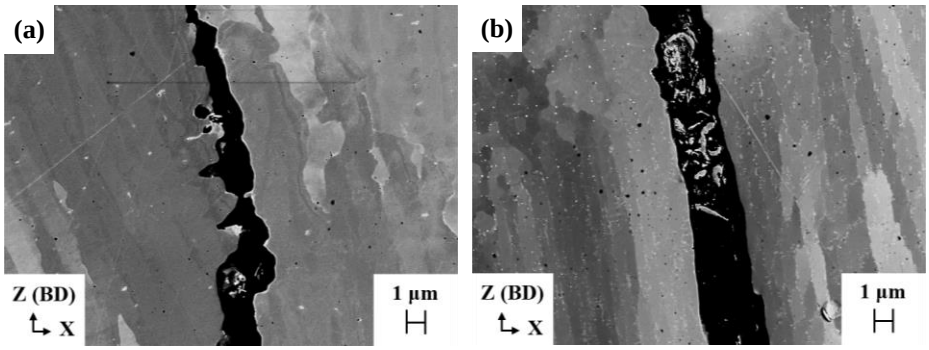


**Figure 8-6:** Backscatter Electron SEM (BSE-SEM) Micrographs Taken at 5000X Showing Examples of High ECC Micro-Cracks in (a) R65 and (b) R108 with Eccentricity Values Between 0.99 and 1.

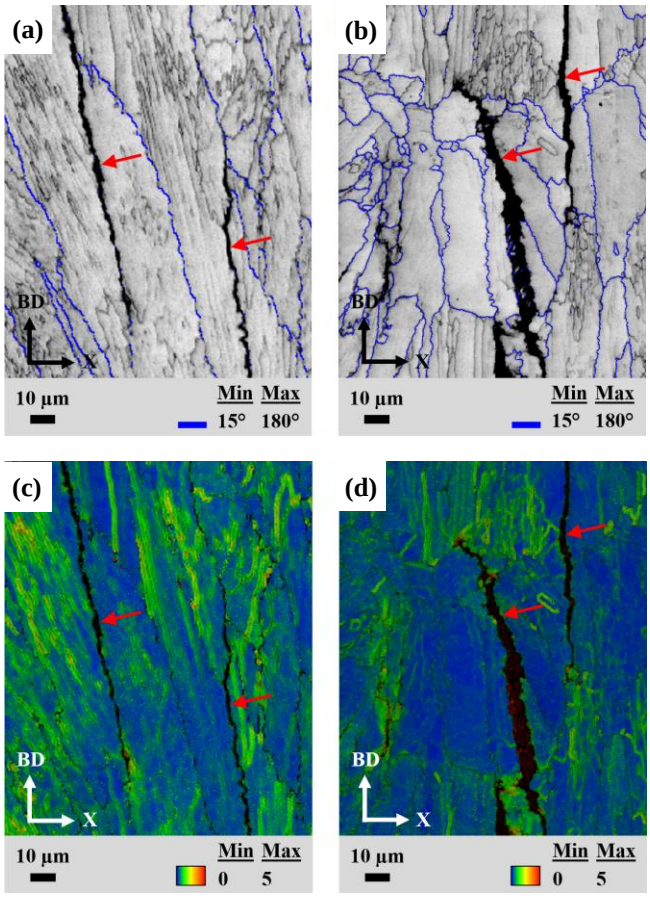


**Figure 8-7:** EBSD Maps Showing the **(a)-(b)** Grain Misorientations and **(c)-(d)** Kernel Average Misorientations for High ECC Micro-Cracks in **(a)**,**(c)** R65 and **(b)**,**(d)** R108, respectively.

### 8.4.2.2 Low ECC Micro-Cracks

**Figure 8-8** shows high magnification (5000X) BSE-SEM micrographs of low ECC micro-cracks. Both R65 (**Figure 8-8 (a)**) and R108 (**Figure 8-8 (b)**) show micro-cracks aligned with the melt pool boundary, exhibiting dendritic morphologies on the crack surface. Fine intercellular particles are more prominent in R108 than R65, and in both cases, there appears to be no particle accumulation at the crack boundary, matching the observations in **Figure 8-6**. **Figure 8-9** shows the EBSD GMO and KAM maps in regions containing two zipper (or low ECC) micro-cracks for both alloys. These micro-cracks propagate along HABs with high misorientation angles (**Figure 8-9 (a)**, **(b)**) and are surrounded by highly strained regions (**Figure 8-9 (c)**, **(d)**) like the straight micro-cracks.

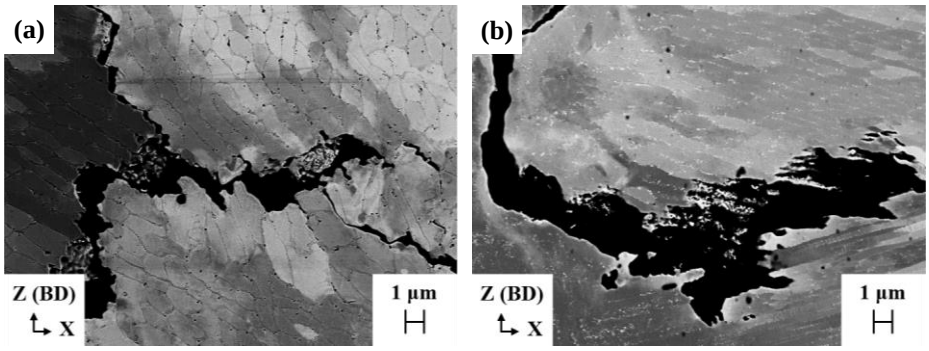


**Figure 8-8:** BSE-SEM Micrographs Taken at 5000X Showing Examples of Low ECC Micro-Cracks in **(a)** R65 and **(b)** R108 with Eccentricity Values Less Than 0.99.

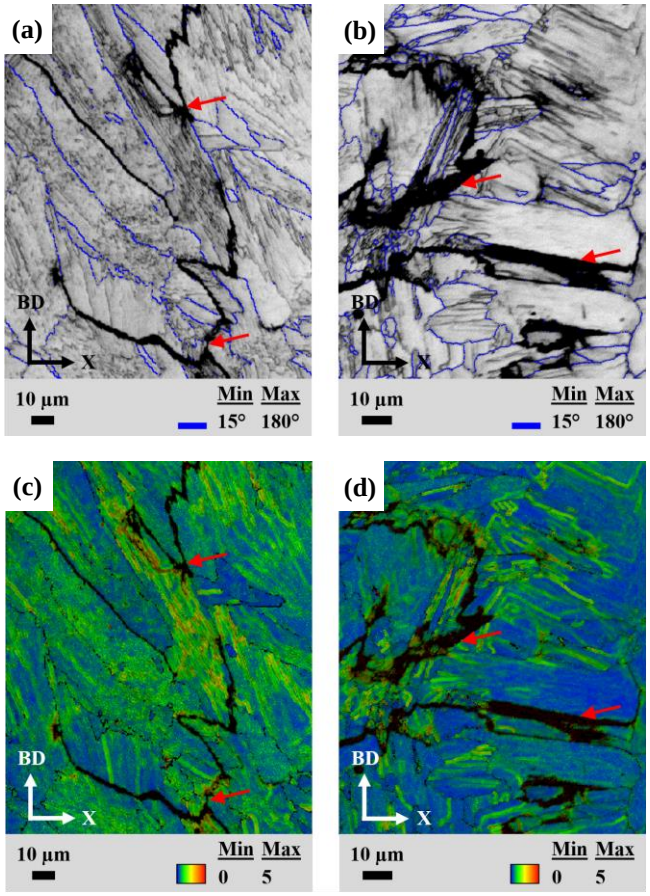


**Figure 8-9:** EBSD Maps Showing the **(a)-(b)** Grain Misorientations and **(c)-(d)** Kernel Average Misorientations for Melt-Pool Micro-Cracks in **(a)**,**(c)** R65 and **(b)**,**(d)** R108, Respectively.

### 8.4.3 Matrix and Intercellular Phase Analysis

To elucidate the effect of alloy composition on micro-cracking, firstly the microstructure and phase distributions in the matrix and intercellular regions for R65 and R108 are compared. **Figure 8-10 (a)** and **(b)** show high magnification BSE-SEM images illustrating cellular features inherent in the R65 and R108 microstructure, respectively. The R108 microstructure includes fine spherical particles at the CBs, whereas R65 has very few intercellular particles. The intercellular particles in R108 are discrete and relatively evenly distributed at the CBs. To gain further insight on the composition and distribution of phases at the CBs, an extensive TEM characterization was performed on both superalloys. The main observations are summarized below.

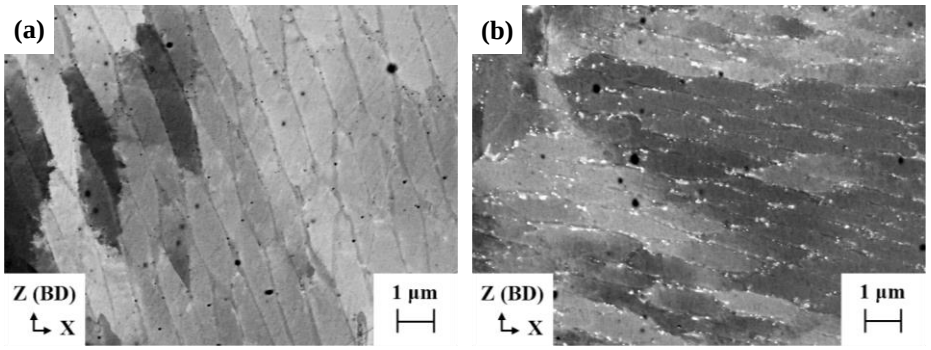


**Figure 8-10:** BSE-SEM Micrographs Taken at 10000X Showing Cellular Microstructure Within the Matrix of **(a)** R65 and **(b)** R108.

#### 8.4.3.1 Phase Analysis of R65 Cell Boundaries

**Figure 8-11 (a)** shows a representative TEM image of R65 containing ~1 µm wide columnar dendrites (or cells) parallel to BD. The cell boundary is distinguished from the HAB using SAED patterns (see **Figure 8-12**). Generally, there is a scarce quantity of intercellular particles, which agrees well with **Figure 8-6 (a)**, **Figure** 8-8 **(a)**, and **Figure** 8-10 **(a)**. Closer inspection reveals the presence of some very fine globular particles in the vicinity of the CB, as highlighted using a red-dashed rectangle in **Figure 8-11 (b)**. Chemical composition analysis shows that the particles are rich in Al, Ti, Zr, Nb, C and O, and depleted in matrix strengthening elements such as Ni, Cr, W, Co, and Fe, as demonstrated in **Figure 8-11 (c)**. The spectrum also consists of Cu picked up from the TEM specimen holder.

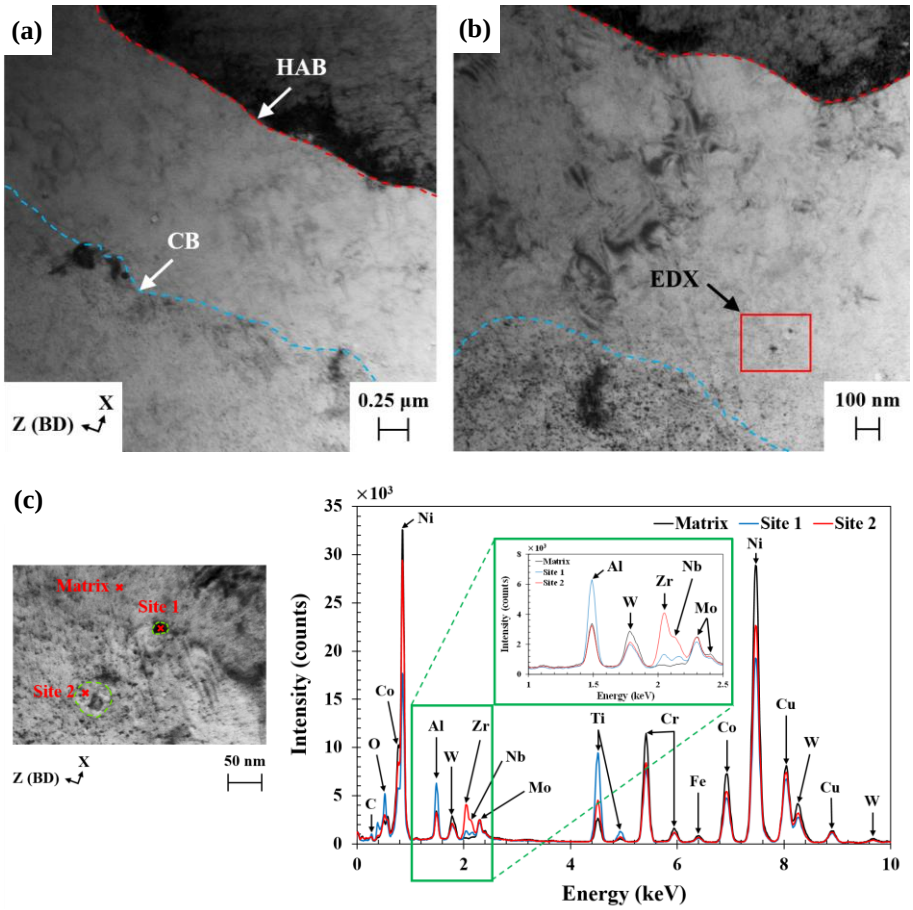


**Figure 8-11:** TEM Images Showing Cellular Microstructure of R65 Along BD at **(a)** 5000X and **(b)** 10000X. **(c)** STEM EDX Analysis of Red Square in **(b)** Showing Compositions of Some Precipitates Near the CB**.**

A closeup view of the EDX spectrum (see inset in **Figure 8-11 (c)**) shows that the small black particles (~20 nm diameter – Site 1) are richer in elements such as Ti, Al, O, and C. Titanium is widely recognized as a carbide former [28], and Ti-rich MC-type carbides have previously been observed in a similar material, RENÉ 88DT [204]. Surface oxides rich in aluminum and titanium have also been reported for Ni-based superalloys [205]. In contrast, the large white particles (~40 nm diameter – Site 2 in **Figure 8-11 (c)**) are richer in elements such as Zr and Nb. Niobium is known as a carbide former [81], whereas zirconium promotes boride formation [206]. Carbon and boron contents are not picked up in the STEM-EDX composition analysis because they are absorbed by the other constitutional elements due to their low atomic numbers and scarce concentrations. Nonetheless, the increased concentrations of Nb and Zr suggest solute enrichment in the remaining liquid at the CBs during the final stages of rapid solidification. According to Paccou et al. [207], $Al_2O_3$ oxide particles act as

preferential sites for formation of MC-type carbides rich in Ti and Nb. However, the high cooling rates inherent in LPBF [173,197] inhibit sustained coarsening and agglomeration of the secondary phases, hence no continuous film can be observed in the intercellular regions.

### 8.4.3.2 Characterization at R65 HABs

The fine discrete Ti-Nb rich carbo-oxides found along the R65 CBs in **Figure 8-11** were not observed along the HABs. **Figure 8-12** shows an example of a secondary-phase-free HAB separating two regions (R1 and R2) with different crystallographic orientations. The SAED patterns for both regions are shown, and the SAED pattern for R1 is taken near the [013] zone axis (ZA). The bottom region (R1) displays a g200 crystallographic orientation with respect to the ZA, whereas the top region (R2) has no specific crystallographic orientation compared to R1. Since the regions on either side of the boundary have distinctly unique diffraction patterns, the boundary is identified as a HAB.

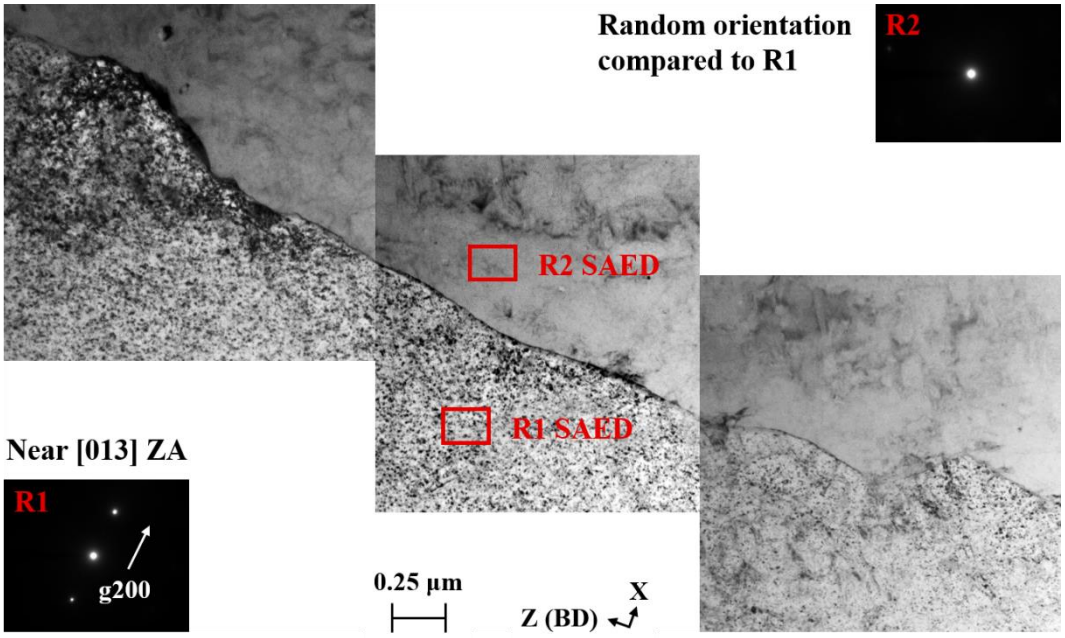


**Figure 8-12:** Stitched TEM Image showing a HAB parallel to BD near a micro-crack for R65. SAED patterns of region 1 (R1) and region 2 (R2) are shown. The SAED for R1 is taken at [013] zone axis (ZA) showing the g200 vector. The SAED for G2 is taken at a random orientation with respect to R1.

On one particular occasion, small HAB areas rich in Nb and Ti were discovered . An example of such a region with the corresponding STEM-EDX elemental distribution is shown in **Figure 8-13**. The top portion of

the HAB demonstrates enrichment of Ti and Nb and depletion of matrix-strengthening elements such as Ni, Cr, Co, and W. However, this does not appear to be a secondary phase.

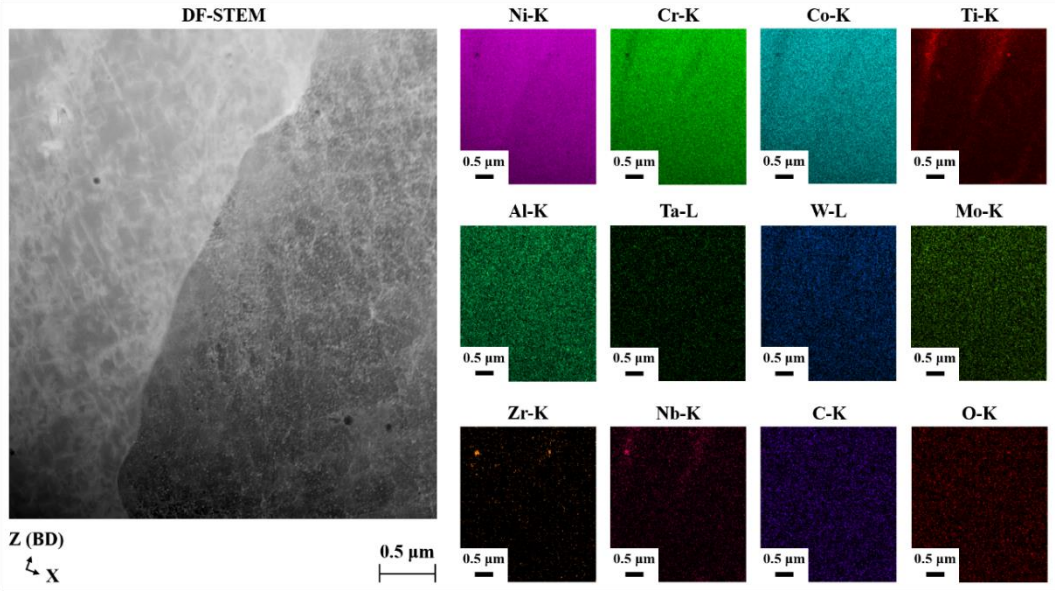


**Figure 8-13:** DF-STEM image and corresponding EDX map showing phase distribution at a HAB of R65.

### 8.4.3.3 Phase Analysis of R108 Cell Boundaries

**Figure 8-14 (a)** shows a representative TEM image of R108 containing several cells (~0.5-1 µm diameter) oriented perpendicular to the BD. Unlike R65, the CBs (blue dashed outlines) in R108 are decorated with several fine (~50 nm) homogeneously distributed discrete particles, as shown in **Figure 8-14 (b)**. Chemical composition analysis (**Figure 8-14 (c)**) reveals that the particles are rich in Hf, Ta, Ti, C, and O and depleted in Ni, Cr, and Co with respect to the matrix. Wang et al. [116] reported similar intercellular micro-segregations in an analogous material, CM247LC, produced by LPBF. The authors demonstrated increased presence of Hf/W/Ti/Ta-rich carbides and/or oxides at the CBs. According to Courtright et al. [208], the oxidation of Hf/Ta-rich MC-type carbides produces thin $HfO_2$ oxide layers at high temperatures (>1800 °C).

In this case, a close-up view of the EDS spectra (see inset in **Figure 8-14 (c)**) shows that the intercellular carbides and/or oxides are notably richer in Hf and/or Ta, which supports the high-temperature oxidation behaviour. The precipitate morphology varies from spherical to blocky with varied levels of solute partitioning, likely dictated by the diffusion kinetics and local thermal history in the vicinity of the CB [209]. Titanium is also richer at the CBs, which agrees well with the STEM-EDX results presented by Chakraborty et al. [197] for LPBF R108.

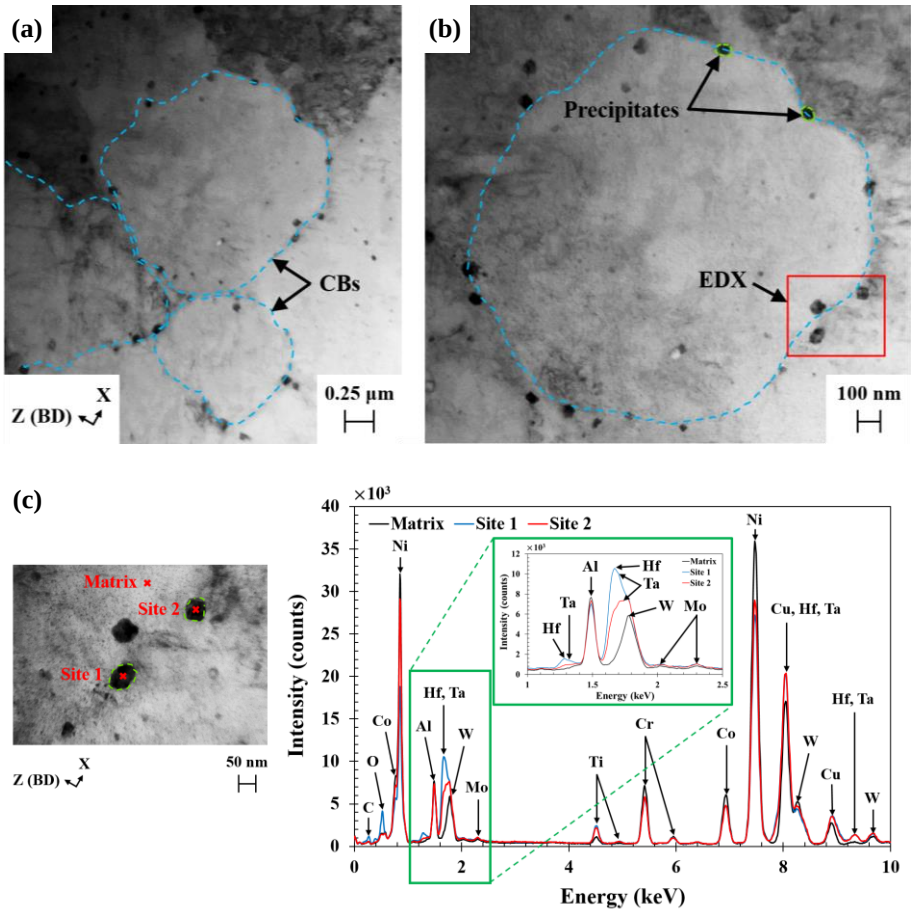


**Figure 8-14:** TEM Images Showing Cellular Microstructure of R108 Perpendicular to BD at **(a)** 5000X and **(b)** 10000X. **(c)** STEM EDX Analysis of Red Square in **(b)** Showing Compositions of Intercellular Precipitates.

### 8.4.3.4 Characterization at R108 HABs

A representative TEM area (~6.6 µm$^2$) including a HAB separating two regions (R1 and R2) is shown in **Figure 8-15**. The top region (R1) has a SAED pattern reflecting a g200 crystallographic orientation taken near the [001] ZA. The bottom region (R2) has a random diffraction pattern compared to R1, which indicates that the boundary considered is a HAB. The stitched image shows a small concentration of fine white discrete particles.

**Figure 8-16** shows phase distributions near the selected R108 HAB, collected through STEM-EDX mapping. The HAB exhibits Ti, Hf, and C enrichment, identical to phase distributions at the CBs (**Figure 8-14**). Depletion of elements such as Ni, Co, Cr, and W is not evident at the HAB due to high solute concentrations

picked up from the surrounding matrix. The quantity of oxides and carbides at the HABs is much lower than along the CBs.

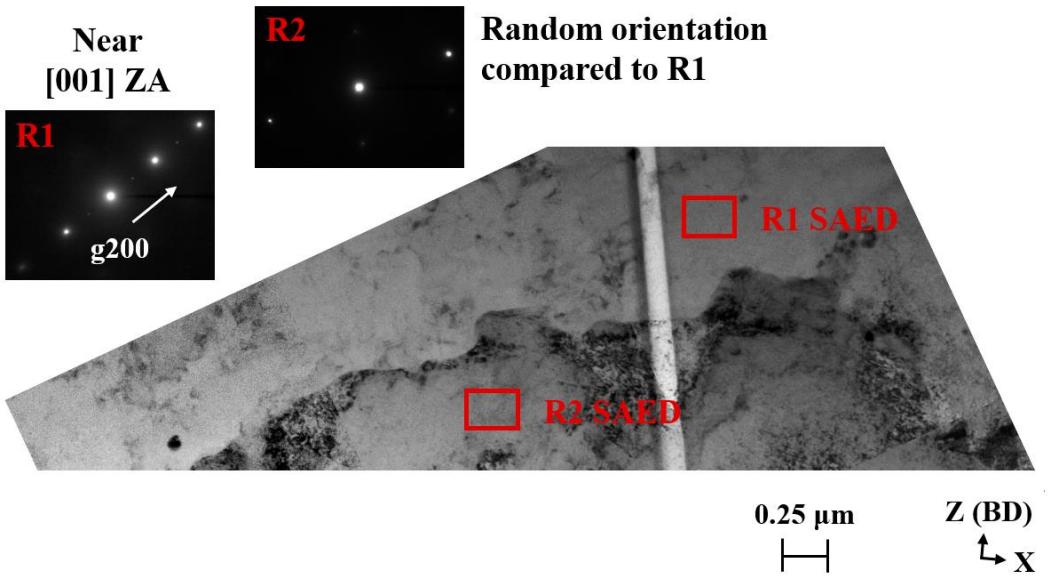


**Figure 8-15:** Stitched TEM Image Showing a HAB Perpendicular to BD Near a Micro-Crack. SAED Patterns of Region 1 (R1) and Region 2 (R2) are Shown. The SAED for R1 is Taken at [001] Zone Axis (ZA) Showing the g200 Vector. The SAED for R2 is Taken at a Random Orientation with Respect to R1.

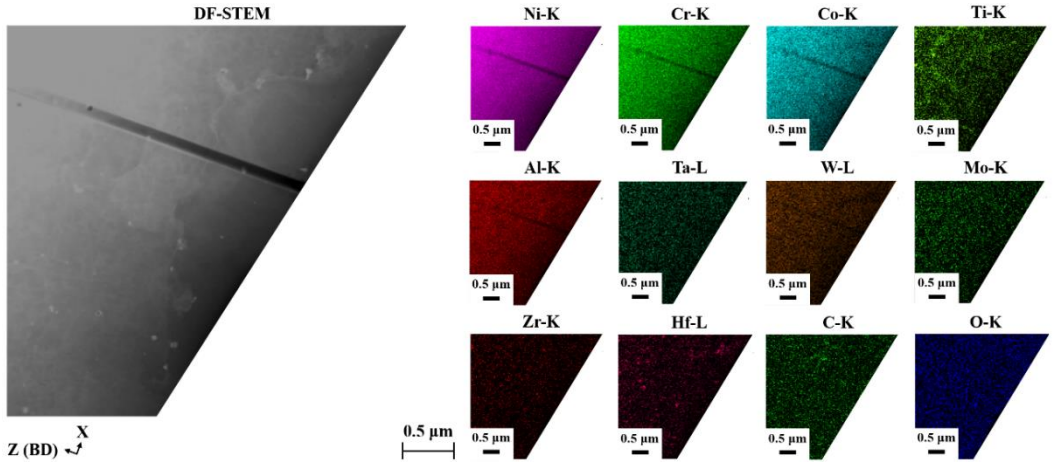


**Figure 8-16:** DF-STEM Image and Corresponding EDX Map Showing Phase Distribution at a HAB of R108. The Thick Black Line Parallel to BD is Not to be Mistaken as a Micro-Crack.

### 8.4.3.5 Stress Triaxiality

The stress triaxiality state (T) is beneficial to detect the material's susceptibility to micro-cracking and is given by **Equation (8-2)**. Stress triaxiality is defined as the ratio of the hydrostatic stress ($\sigma_m$) to the von Mises equivalent stress ($\sigma_e$):

$$T = \frac{\sigma_m}{\sigma_e}, \tag{8-2}$$

where $\sigma_m$ is the hydrostatic stress and $\sigma_e$ the equivalent stress. **Figure 8-17** depicts the simulated stress triaxiality and temperature distributions of R65 (**Figure 8-17 (a)**) and R108 (**Figure 8-17 (b)**) along the center of the laser beam path, when the laser traverses 2 mm in approximately 2 ms. For both superalloys, the stress triaxiality is negative as the metal powder is exposed to the laser beam (temperature rise during the first millisecond). Subsequently, the stress triaxiality increases sharply to positive state as the laser moves away (temperature drop during the second millisecond). It is evident that the stress triaxiality profiles of R65 and R108 are different. This difference cannot be attributed to dissimilar mechanical properties as both materials exhibit similar strengths above the solvus temperature. Moreover, latent heat of fusion and thermal conductivity can be ruled out as they are similar (due to similar chemical compositions) for both superalloys. However, the contrasting solidification and γ' phase transition behaviors create a difference in magnitude of the specific heat capacity between the two materials over the related temperature range (from solvus to liquidus temperature). Therefore, the thermo-mechanical behavior of materials (an important factor in stress triaxiality) at higher temperatures is altered.

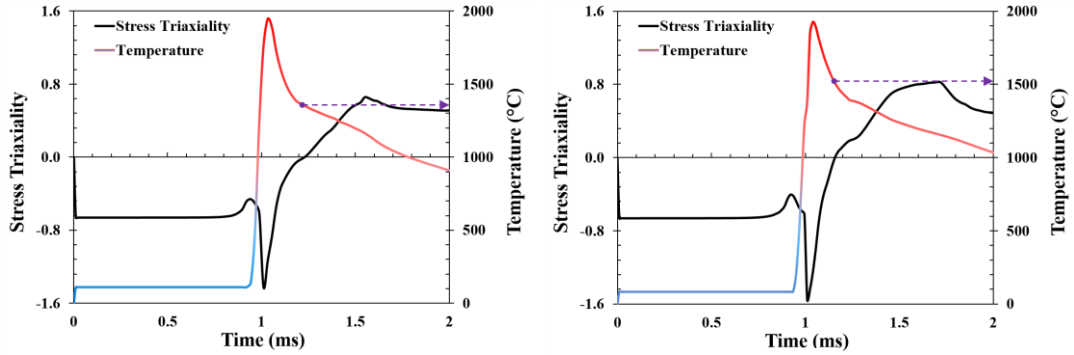


**Figure 8-17:** Beam-Scale Simulations of the Stress Triaxiality and Temperature Variation During Processing within the Melt Pool of **(a)** R65 and **(b)** R108. The Red Boxes Highlight the Temperatures Corresponding to the Onset of Positive Stress Triaxialities.

## 8.5 Discussion

### 8.5.1 Micro-Cracking Mechanism

Recall from **Figure 8-4 (a)** that R108 has 329% higher micro-cracking density than R65. However, it is difficult to explain the micro-cracking mechanism by solely evaluating the bulk crack densities. Ghoussoub et al. [194] used the crack eccentricity criterion to characterize the micro-cracking types. According to the authors, the high ECC micro-cracks are attributed to solid-state cracking, whereas the low ECC micro-cracks correspond to solidification cracking. In this study, the micro-crack distributions for both alloys are identical, as explained in **Section 8.4.1**. In other words, the high to low ECC ratio for R65 (1.23) is similar to the ratio for R108 (1.51). This is supported by similar micro-crack morphologies for both alloys, as demonstrated in **Figure 8-6** and **Figure** 8-8, respectively.

Both low (**Figure 8-6**) and high (**Figure 8-8**) ECC micro-cracks demonstrate interdendritic behavior, suggesting the solidification cracking mechanism. Recently, Chakraborty et al. [197] used FEM simulations to show that solidification cracking is more likely to occur within the melt pool core because it is hotter than the melt pool boundary. Interestingly, the high ECC micro-cracks were observed in the melt pool core. This suggests that the ECC characterization method is inappropriate to evaluate the in-process cracking mechanism for RENÉ 65 and RENÉ 108.

At temperatures higher than solidus, a positive stress triaxiality is necessary for solidification cracking to occur [180]. As denoted by purple arrows in **Figure 8-17**, the stress triaxiality becomes positive for R65 and R108 when the temperature exceeds 1360 °C and 1510 °C, respectively. These temperatures are above the solidus temperature ($T_s$) for both the superalloys (1270 °C and 1310 °C, respectively, as listed in **Table 8-2**). Since both alloys experience positive $T$ within the melt pool core, they are susceptible to cracking along BD. Moreover, the materials are weakened by the presence of liquid at super-solidus temperatures, which favors micro-cracking during the final stages of solidification.

R108 (**Figure 8-17 (b)**) exhibits positive T at higher temperatures compared to R65 (**Figure 8-17 (a)**), which is attributed to the difference in solidification and γ' phase transition behavior between the two superalloys, as shown in **Table 8-2**. Phase transition temperatures such as solvus and solidus temperatures are expected to be different for R65 and R108 because of their varying alloy compositions and γ' contents. The combination of positive stress triaxiality and remaining liquid fraction at the HABs causes solidification cracking [214,215]. Interestingly, the solidification range ($\Delta T = T_l - T_s$) is similar for both alloys – 110 °C for R65 and 95 °C for R108. However, the solidification ranges in LPBF are expected to differ from the DSC experiments because of

their contrasting cooling rates (>$10^5$ °C/s order difference). In order to better evaluate the solidification window during LPBF, thermodynamic simulations are conducted.

### 8.5.2 Thermodynamic Simulation of Solidification Range During LPBF

**Table 8-3** displays the phase transition temperatures, including the liquidus, solidus and γ' solvus temperatures obtained through DSC analysis and thermodynamic simulations for R65 and R108. The DSC data (10° C/s cooling rate) is closer to equilibrium conditions (low cooling rates), whereas the Scheil-Gulliver (S-G) data depicts temperatures closer to the actual LPBF process ($10^6$-$10^7$ °C/s cooling rates [166]). The equilibrium theory assumes infinite diffusion in both liquid and solid states, typical of processes with low cooling rates allowing sufficient time for solute diffusion. Accordingly, the ΔT values predicted using the thermodynamic equilibrium condition are similar to DSC results for R65 (55 °C) and R108 (50 °C). This is further examined in **Figure 8-18 (a)** where the material temperature is plotted against the equilibrium calculation of the solute fraction. The solidus temperature is over-estimated due to infinite diffusion everywhere in the equilibrium condition. This results in small ΔT and conceals the effect of solute partitioning at highly energetic HABs.

**Table 8-3:** Phase transition temperatures and solidification ranges for R65 and R108 obtained from DSC plot measurements and thermodynamically simulated data calculated by ThermoCalc with the TiN6 database.

| Alloy | Method | Liquidus (°C) | Solidus (°C) | γ' Solvus (°C) | Solidification range (°C) |
|---|---|---|---|---|---|
| **R65** | DSC O-C | 1370 | 1260 | - | 110 |
| | DSC O-H | 1380 | 1270 | 1130 | 110 |
| | Equilibrium | 1375 | 1320 | - | 55 |
| | Scheil-Gulliver | 1356 | 1155 | 1090 | 201 |
| **R108** | DSC O-C | 1405 | 1310 | - | 95 |
| | DSC O-H | 1425 | 1310 | 1250 | 115 |
| | Equilibrium | 1385 | 1335 | - | 50 |
| | Scheil-Gulliver | 1378 | 1105 | 1245 | 273 |

Alternatively, a large difference (72 °C) in solidification range between R108 ($\Delta T_{R108}$ = 273 °C) and R65 ($\Delta T_{R65}$ = 201 °C) is predicted under the thermodynamic S-G condition, as shown in Figure 8-18 **(b)**. Both

$\Delta T$ values are significantly larger (2X – 4X larger) compared to the DSC and equilibrium cases as increased solute partitioning at the HABs lowers the solidus temperatures of the alloys. Since no back-diffusion is allowed in the S-G model, the solidus temperatures are lowered. Since LPBF occurs under non-equilibrium conditions and possesses inherently high cooling rates that limit solute diffusion during processing, the $T_s$ values are likely closer to those predicted using the S-G model. Therefore, it is reasonable to deduce that the $\Delta T$ value for R108 is significantly larger compared to R65, assuming the $T_l$ values do not vary significantly from the S-G case in the actual LPBF process.

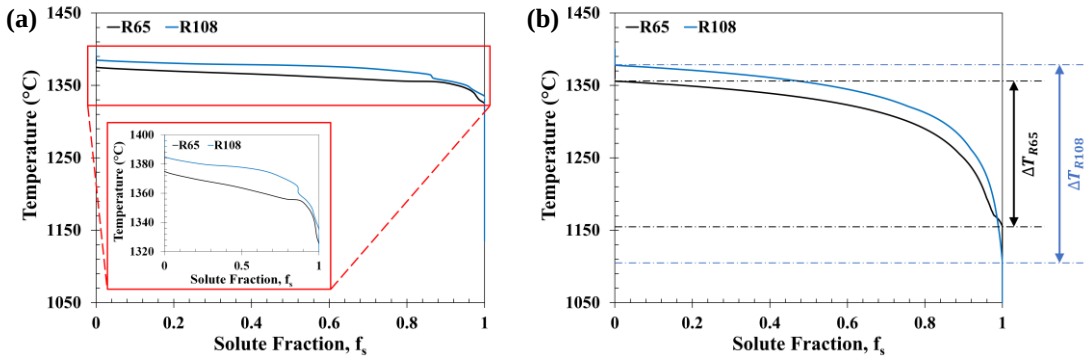


**Figure 8-18:** Thermodynamic simulations, predicted using **(a)** equilibrium and **(b)** Scheil-Gulliver (S-G) models, demonstrating the solidification behaviors of R65 and R108.

A large solidification window is favorable for solidification cracking because it lowers the material ductility over a wide temperature range [194]. When the solidification range is larger, the last liquid solidifies at lower temperatures along the HABs. The ductility along the HAB is inversely proportional to the volume of liquid fraction. High liquid fractions reduce the material's ductility along the HAB, promoting solidification cracking under positive stress triaxiality conditions. **Figure 8-19** shows the liquid fractions (plotted in log scale) with respect to the temperature for R108 and R65 predicted using the S-G model. During the final stages of solidification, between 95% and 99% solid fraction, R65 begins to solidify faster (steeper slope) than R108. As the solidification progresses, R65 becomes >99% solid at a higher temperature (around 1150 °C) than R108 (1106 °C). Hence, the terminal stages of solidification take place at significantly lower temperatures in R108. This effect is further exacerbated by the presence of a positive stress triaxiality state, which along with increased liquid phase favors higher micro-cracking propensities. The micro-cracks would appear linear and tend to follow the CBs where the last liquid phase would reside. This agrees well with the notably larger CAF (329% larger), CCD (48% larger), crack length (32% longer), and crack width (26% wider) in R108 than R65 (**Figure 8-4**).

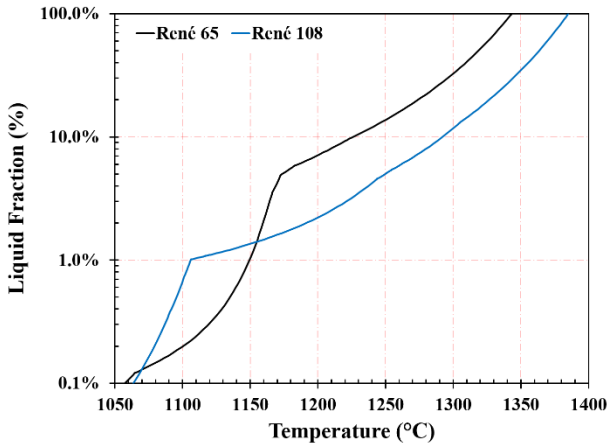


**Figure 8-19:** Thermodynamic Scheil-Gulliver Plot Showing Predicted Liquid Fractions for R65 and R108 as Temperature Changes.

### 8.5.3 Effect of Gamma Prime on Micro-Cracking

Superalloys with higher γ' contents are known to exhibit increased micro-cracking [194]. The hardening phase nucleates first along the HAB reducing their ductility. This phenomenon has also been observed in welded high γ' superalloys [15]. TEM images shown earlier failed to reveal any evidence of γ'. This is surprising provided that R65 and R108 are expected to have 42% [73] and 63% [74] of γ' phase. To shed further light on the effect of γ', SAED pattern analyses were performed in the as-printed state for both alloys. **Figure 8-20** and **Figure** 8-21 compare the γ' contents of R65 and R108, through SAED patterns taken at HABs near micro-cracks, respectively. For R65, the selected area in R1 (see **Figure 8-20 (a)**) is used to acquire a SAED pattern (**Figure 8-20 (b)**) showing the g100 (γ') and g200 (γ+γ') vectors. The 2beam-1g condition displays very weak intensities of γ', as demonstrated in **Figure 8-20 (c)**. For R108, the selected area in R2 (**Figure 8-21 (a)**) provides a SAED pattern (**Figure 8-21 (b)**) showing the g100 (γ') and g200 (γ+γ') vectors. The 2beam-1g condition of R108 (Fig. 21c) demonstrates higher γ' intensity than R65 (**Figure 8-20 (c)**), suggesting higher γ' content in R108. This means that γ' forms during rapid solidification and has a stronger effect on the ductility of R108 due to higher volume fraction.

The S-G R65 solvus (1090 °C) lies outside the R65 solidus temperature window (1155-1320 °C), whereas the S-G R108 solvus (1245 °C) lies within the R108 solidus temperature window (1105-1335 °C). Despite the overlap, it is suspected that the actual solidus temperature in the LPBF-printed part is higher than the solvus temperature. A smaller gap between solvus and solidus is expected to cause a drop in ductility and increased micro-cracking due to the coupling effect of liquid and γ' along the HAB of R108. Conversely, the

combination of lower liquid fraction and absence (or lower volume fraction) of γ' reduces the tendency for solidification cracking in R65.

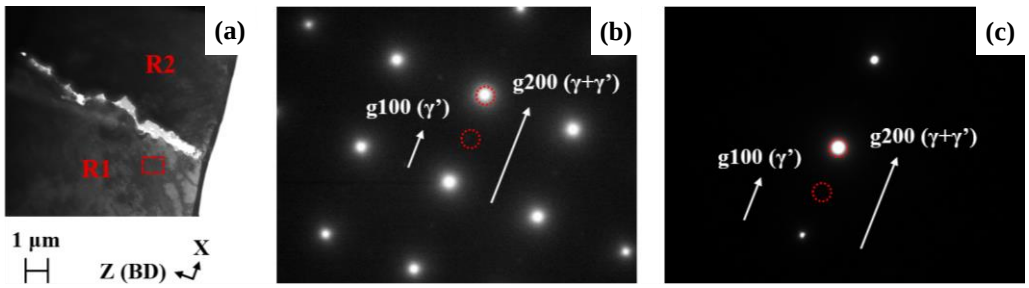


**Figure 8-20: (a)** TEM Micro-Graph Showing the Microstructure Including Two Grains, R1 and R2, in the Vicinity of a Micro-Crack in R65. **(b)** SAED Pattern of R1 for the Red-Dashed Box Region Shown in **(a)**. **(c)** 2beam-1g Condition Showing the g Vectors for the Coherent γ' and γ+γ' phases. Red-Dashed Circles Indicate the Positions for the g Vectors in **(b)** and **(c)**.

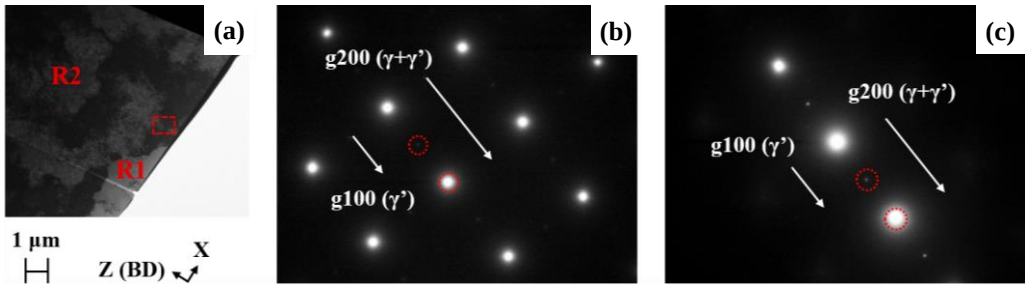


**Figure 8-21: (a)** TEM Micro-Graph Showing the Microstructure Including Two Grains, R1 and R2, in the Vicinity of a Micro-crack in R108. **(b)** SAED Pattern of R1 for the Red-Dashed Box Region Shown in **(a)**. **(c)** 2beam-1g Condition Showing the g Vectors for the Coherent γ' and γ+γ' Phases. Red-Dashed Circles Indicate the Positions for the g Vectors in **(b)** and **(c)**.

### 8.5.4 Contribution of Secondary Phase Particles to Micro-Cracking

The presented experimental and simulation results point towards the solidification cracking mechanism for both R65 and R108. This agrees well with previous works reporting interdendritic micro-cracks in similar alloys processed under high VEDs [1,198,216]. Solidification cracking is known to take place in the final stages of solidification when there exists a small amount of liquid (>1% liquid fraction) at the GB [13]. This remaining liquid is typically enriched in solute elements and is the last to solidify. Deleterious phases could form at the GBs, but the role of such phases on micro-cracking is not clear. Phases such as metal carbides, borides, and oxides,

have long been understood as ideal sites for crack nucleation at the GBs during rapid solidification. Lippold et al. [81] suggested that MC-type carbides rich in Nb and Ti promote constitutional liquation cracking in Nb-containing superalloys such as IN718, owing to the presence of a continuous liquid film. Wojcik et al. [213] demonstrated that Cr- and Mo-rich $M_3B_2$- and $M_5B_3$-type borides preferentially form at GBs, decreasing the resistance of R65 to micro-cracking due to phase brittleness. Hariharan et al. [175] proposed that the preferential segregation of Zr to HAGBs promotes solidification cracking in a high-γ' Ni-based superalloy, IN738LC, processed by LPBF. According to Cloots et al. [214], Zr and B enrichment at the GB reduces the solidus and increases the solidification range. Similarly, oxides promote HAGB embrittlement, enhancing the material's susceptibility to micro-cracking [215]. Moreover, for γ'-strengthened materials, γ+γ' eutectics could also act as preferential sites for crack growth at high temperatures [216].

Interestingly, R108 has more precipitates (carbides and oxides) than R65 in interdendritic regions, as demonstrated in **Figure 8-10 (b)** and **Figure** 8-14. These precipitates can either be a source of crack initiation or assist crack propagation. Considering crack propagation, R108 is expected to have longer cracks than R65 because of a higher quantity of precipitates. However, **Figure 8-4 (b)** shows that both alloys have similar average crack lengths (~10 μm), implying that the precipitates are unlikely to favor crack growth. Alternatively, complex phases can also serve as crack nucleation sites due to their low melting points [217]. Ghoussoub et al. [194] suggested that Hf/Ta-rich carbides at the crack tips are responsible for crack formation in similar materials. Because the precipitates are fine and not agglomerated, they are unlikely to cause higher CAF in R108 compared to R65 (**Figure 8-4 (a)**). Evidence of other detrimental low melting phases were not observed along HAB and phases such as carbides, oxides, borides, γ+γ' eutectics can be ruled out as possible reasons for high cracking tendency of R108. In general, the precipitates for both R65 and R108 are fine (<50 nm), discontinuous, and are unlikely to promote solidification cracking at the HABs.

## 8.6 Conclusions

Micro-cracking mechanisms in high-gamma prime Ni-based superalloys, RENÉ 65 (R65) and RENÉ 108 (R108), have been studied. Scanning electron microscopy shows inter-dendritic crack morphologies suggesting the solidification cracking mechanism. Electron backscatter diffraction reveals that all micro-cracks occur at high angle boundaries (HABs) surrounded by regions depicting high thermal strains. Transmission electron microscopy conducted in conventional and scanning modes shows fine discrete inter-cellular carbides and oxides rich in Hf/Ti/Ta in R108. Phase analysis within the matrix of R65 reveals few Nb-/Ti-rich carbides, oxides containing Ti/Al, and Zr enrichment in the intercellular regions. However, advanced phase analyses

conducted at the HABs of both R65 and R108 reveal no localized regions of precipitate accumulation, suggesting detrimental phases are not directly responsible for micro-cracking.

Statistical analysis reveals R65 has 77% smaller micro-cracking densities and over 20% reduction in crack size compared to R108. Beam-scale finite element modelling simulations of in-process stresses within the melt pool core of both materials demonstrates positive stress triaxialities above the solidus temperature in both materials. However, the higher phase transition temperatures in R108 promotes positive stress triaxiality at higher temperatures compared to R65. Moreover, the equilibrium thermodynamic simulations reveal a stronger effect of cooling rate on R108 solidus temperature, leading to a higher liquid volume fraction than R65 under positive stress triaxiality conditions. Moreover, the Scheil-Gulliver thermodynamic simulations reveal a smaller gap between the solvus and solidus temperatures during rapid solidification in R108, further reducing the ductility along the grain boundaries. Precipitation of more γ', coupled with the large solidification window and higher solvus temperature, leads to low ductility under positive stress triaxiality conditions, promoting higher micro-cracking propensities in R108 compared to R65.

# Chapter 9

# Understanding the Effect of Wall Thickness and Scan Strategy on LPBF Thin-Wall Micro-Cracking

In this chapter, *a novel scan strategy to mitigate micro-cracking in LPBF thin-wall parts is proposed*. To achieve this feat, a comprehensive design of experiment including four different part thicknesses and ten different scan strategies is constructed. The micro-cracking propensities and in-process stresses are evaluated using experimental and numerical simulation approaches, respectively. The highly crack-susceptible material, RENÉ 108, is employed for the construction of all components. The experimental observations are successfully verified using simulated results.

---

The chapter presents a manuscript of an article submitted to a journal and is currently under review.

***Additive Manufacturing, Under Review, June 2022***

## 9.1 Introduction

Laser powder bed fusion (LPBF) additive manufacturing (AM) enables construction of complex near-net-shape parts with very small feature sizes in the order of hundreds of microns [154]. Thin-wall part fabrication is especially valuable for industrial applications such as turbine vanes and serpentine-shaped fuel nozzles [152,222]. However, these structures are challenging to manufacture due to distortion [119], limiting build height (LBH) [158], surface roughness [219] and micro-cracking [197], which adversely affect the as-printed part quality [120].

Components made of high-γ' Ni-based superalloys have excellent creep and fatigue properties coupled with oxidation and corrosion resistance at elevated temperatures [131–135]. However, these materials introduce challenges during part manufacturing due to their susceptibility to micro-cracking. Several studies have reported high micro-cracking propensities in heritage-grade hard-to-weld superalloys such as IN738LC [115,216] and CM247LC [96,164]. Recently, Ghoussoub et al. [194] performed a comprehensive study reporting extensive micro-cracking in several high-γ' Ni-based superalloys printed using LPBF.

To mitigate inherent micro-cracking in LPBF, recent findings suggest wall thickness (WT) and scan strategy modification as promising routes for micro-crack reduction in thin-wall components. The effect of WT on micro-cracking was recently investigated by Chakraborty et al. [158], who reported reduced micro-cracking below a 1 mm WT. Wu et al. [120] studied the processability of a wide range of thin-wall parts, reporting high surface roughness in as-printed parts thinner than 0.25 mm. Overall, both studies highlight the heightened sensitivity of LPBF parts to defect formation as WTs descend below 1 mm.

Alternatively, Tangestani et al. [173] recently showed that the laser scan strategy has significant implications on the residual stresses post LPBF processing. Carter et al. [96] previously demonstrated variation in micro-cracking propensity by changing the laser power and scan speed under a fixed contour (island) scan strategy with short 5 mm scan (vector) lengths. Catchpole-Smith et al. [128] introduced mathematically-area-filled fractal scan strategies with very short vector lengths (VLs), in the order of 100 μm, to minimize the stresses and micro-cracking propensity caused by thermal anisotropy at the contour boundaries. Li et al. [117] proposed that shorter VLs produce more homogeneous temperature field distribution and smaller thermal gradients compared to longer VLs. However, these studies employ the island scan strategy, not suitable for thin-wall parts with small surface areas. Other authors such as Cheng et al. [127] demonstrated that inter-layer scan angle rotation is beneficial to reduce residual stresses and deformation in LPBF.

To improve processability and reduce micro-cracking in LPBF thin-wall parts, the effects of both WT and scan strategy are evaluated in this work. A crack-susceptible high-γ' Ni-based superalloy (RENÉ 108) is used

to study the micro-cracking tendencies. Thirty-two parts with four different WTs between 0.25 mm and 1 mm and ten different scan strategies with and without inter-layer scan rotations are considered. These scan strategies are compared with the conventional continuous 67° scan rotation strategy, widely accepted as an optimal scan strategy for LPBF part production [96,122]. Microscopic and statistical analyses are conducted to assess the micro-cracking characteristics and trends, respectively. Finite element modelling (FEM) techniques are employed to compute and analyze in-process stresses for the different build parameters. The simulation results are compared with the experimental observations and a novel method is proposed to reduce micro-cracking in LPBF-printed thin-wall structures.

## 9.2 Experimental Procedures

### 9.2.1 Powder Characteristics

The high γ' (volume fraction 63% [24]) Ni-based superalloy RENÉ 108 (R108) was employed to construct thin-wall parts. The powder provided by Powder Alloy Corporation was produced using the gas atomization process. The particle size distribution ($D_{10}$-$D_{90}$) and median particle size ($D_{50}$) were 12-40 µm and ~19 µm, respectively [158]. The powder morphology was mainly spherical, including some large particles attached to satellite particles, as shown in **Figure 9-1**. The elemental contents (in wt.%) of the as-received powder were acquired at Activation Laboratories (ACTLABS © Canada) through inductively coupled plasma - optical emission spectroscopy (ICP-OES), as listed in **Table 9-1.**

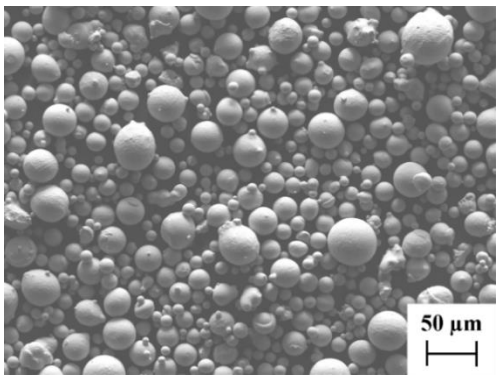


**Figure 9-1:** Powder Morphology of RENÉ 108 (R108).

**Table 9-1:** Elemental Contents of As-Received R108 Powder in wt.%.

| Ni | Cr | Co | Al | Ti | Ta | W | Mo | Hf | B | Zr | C |
|---|---|---|---|---|---|---|---|---|---|---|---|
| Bal. | 8.64 | 10 | 5.36 | 0.75 | 3.02 | 10.03 | 0.53 | 0.87 | 0.01 | 0.01 | 0.01 |

### 9.2.2 Part Fabrication

The Aconity$^{TM}$ MIDI LPBF printer was used to generate parts under the build conditions described in **Table 9-2**. The design of experiment included 32 thin-wall parts on a singular stainless steel base plate, as illustrated in **Figure 9-2 (a)**. The part lengths and heights were set to a constant value of 30 mm. The varying build parameters include 3 different WTs – $1.00\ mm$, $0.75\ mm$, and $0.50\ mm$ – and 10 different scan strategies per thickness, as shown in **Figure 9-2 (c)**, **(d)**, and **(e)**. In addition, two samples with $0.25\ mm$ WTs were included to investigate the effect of WT on micro-cracking. Scan strategies are categorized as zero-, alternating- and continuous-rotation strategies, as shown in **Figure 9-2 (c)**, **(d)**, and **(e)**, respectively.

**Table 9-2:** Constant Build Parameters for LPBF R108 Thin-Wall Parts.

| Build parameter | Value |
|---|---|
| Laser power, P (W) | 200 |
| Scan speed, v (mm/s) | 1000 |
| Spot size, $d_{spot}$ (μm) | 120 |
| Hatch spacing, h (μm) | 90 |
| Hatch angle, θ (°) | 75 |
| Powder layer thickness, t (μm) | 40 |
| Designated part height (mm) | 50 |
| Part thickness, $t_{part}$ (mm) | 0.25, 1, 5 |

The scan strategies were modified between layers to examine the significance of varying vector lengths on the micro-cracking propensities. The vector length (VL) is defined as the distance between the end (red) points of the longest scan line for a layer scan, as shown in **Figure 9-2 (c)** for two sample cases. In this work, the VL

refers to the group of vectors scanned at a specific angle ($\theta_0$) relative to the part thickness in a given build layer. The scan angle was varied to obtain different VLs for a given part thickness. Positive values for $\theta_0$ indicate scan angles measured clockwise, and negative values indicate counter-clockwise measurements with respect to the X-axis defined for **Figure 9-2 (c)-(e)**. Nine scan angles, 0°, 15°, −15°, −30°, 75°, −75°, 87°, −87°, and 90°, were considered for the zero- and alternating-rotation strategies illustrated in **Figure 9-2 (c)** and **(d)**. The shortest VL, $ES$, is achieved at $\theta_0 = 0°$, when the scanning vector is parallel to the WT. Intermediate VLs include: three short VLs, $S$, $\bar{S}$, and $\overline{S^*}$, at $\theta_0 = 15°$, $\theta_0 = -15°$, and $\theta_0 = -30°$, respectively; two long VLs, $L$ and $\bar{L}$ at $\theta_0 = 75°$ and $\theta_0 = -75°$, respectively; and two extra long VLs, $EL^*$ and $\overline{EL^*}$ at $\theta_0 = 87°$ and $\theta_0 = -87°$, respectively. The VLs $\overline{S^*}$, $EL^*$, and $\overline{EL^*}$ were added to investigate the effect of alternative short and extra long VLs on the micro-cracking behaviour. The longest VL, $EL$, is achieved at $\theta_0 = 90°$, when the scanning vector is perpendicular to the WT.

Four zero-rotation scan strategies, $ES$, $S$, $L$, and $EL$, were employed for the $0.50\,mm$, $0.75\,mm$, $1.00\,mm$ thick parts and the VL was maintained for each build layer. Only two zero-rotation scan strategies ($S$ and $L$) were investigated for the thinnest wall ($0.25\,mm$). Furthermore, six different scan rotation strategies including alternating and continuous rotations were studied. Five different VL combinations were explored for the alternating rotation category, as shown in **Figure 9-2 (d)**. Each strategy in this category includes two different VLs incorporated in alternating build layers during part processing. Layer 1 (black arrows) and Layer 2 (red arrows) indicate the contrasting scan directions for the odd and even layers, respectively. The strategies include $ES + EL$, $S + \bar{S}$, $L + \bar{L}$, $EL + \overline{S^*}$, and $EL^* + \overline{EL^*}$, as shown in **Figure 9-2 (d)**. A single continuous 67° scan rotation strategy ($Cont.$) was employed between layers, as shown in **Figure 9-2 (e)**. The starting layer (Layer 1) was processed using the $ES$ scan strategy (black arrows), and every subsequent layer was scanned at angles rotated 67° with respect to the previous layer scan. For instance, Layer 2 was scanned at $\theta_0 = 67°$ (red arrows), and Layer 3 was scanned at $\theta_0 = -46°$ (blue arrows), as shown in **Figure 9-2 (e)**. As the build progresses, a wide assortment of short VLs (~70% count fraction including 61 unique variations) and long VLs (~30% count fraction including 30 unique variations) is produced due to continual scan angle variation between the build layers. Details for the varying build parameters employed in this study are provided in **Table 9-3.**

As-printed parts exhibited varying limiting build heights (LBHs) with WTs and scan strategies. The LBH is defined as the height at which the part fails during processing, limiting the thin-wall part from reaching the design height. The thicker $1.00\,mm$ and $0.75\,mm$ parts reached the design height of 30 mm, but the thinner $0.25\,mm$ and $0.50\,mm$ parts failed prematurely. The reduction in LBH with the WT agrees with previous works on similar materials [158,197].

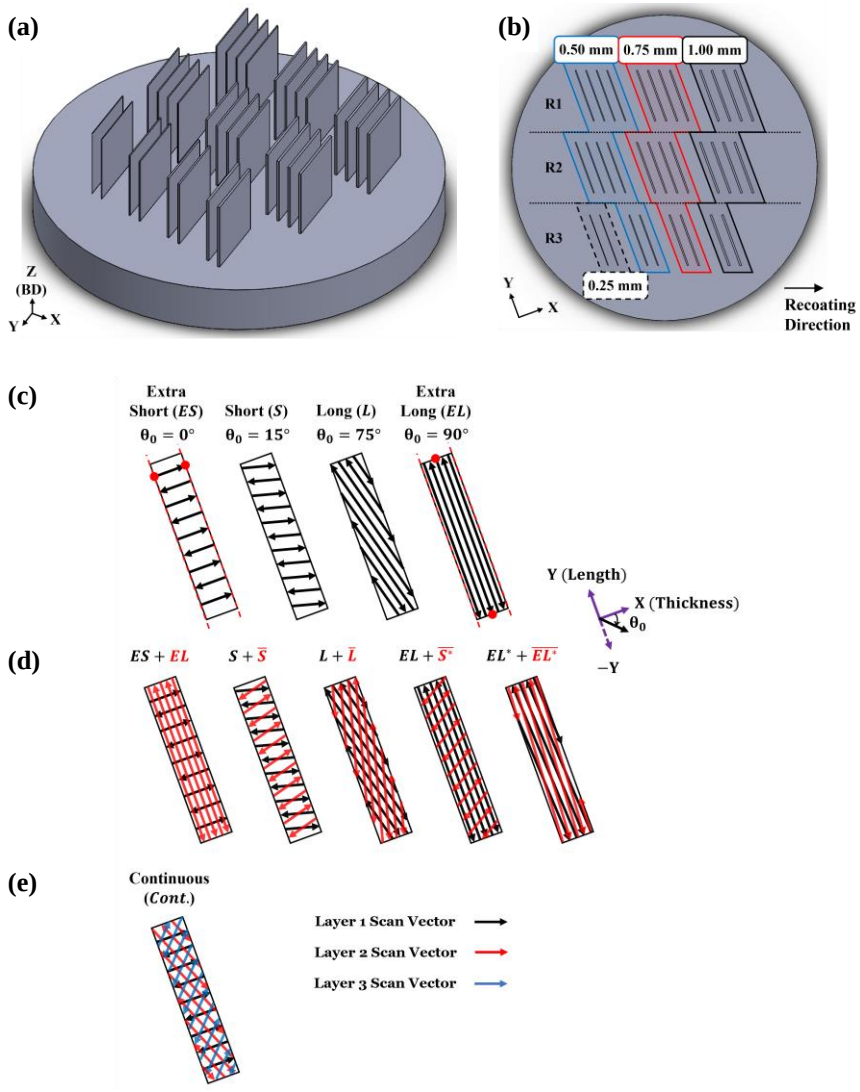


**Figure 9-2:** Design of Experiment Model in **(a)** 3D and **(b)** Top Views Showing 32 Thin-Wall Parts with Four Different Part Thicknesses and Ten Different Scan Strategies, Including **(c)** Zero (R1), **(d)** Alternating (R2, R3), and **(e)** Continuous (R3) Layer-Wise Scan Rotation. Only Two Scan Strategies (***S*** and ***L***) were Employed for the $\mathbf{0.25}\ \boldsymbol{mm}$ Parts in R3, as shown in **(b)**. Red dots in **(a)** Highlight the End Points of the Scan Line.

### 9.2.3 Microstructure Analyses

As-built parts were extracted from the build plate and sectioned central to the built part height (LBH/2) and length to exclude microstructure heterogeneities at the part edges, as done in [158]. Standard mounting,

grinding and polishing techniques, including 0.04 µm colloidal silica polishing, were conducted to prepare samples for metallurgical studies. The as-polished samples were viewed under the Keyence VHX7000 digital microscope. Optical micrographs taken at 1000X magnification were analyzed to calculate micro-crack statistics, as explained in **Section 9.2.4**.

**Table 9-3:** Varying Build Conditions Considered in this Study. A Total of Ten Different Scan Strategies and Four Different Part Thicknesses were Investigated. The Plus and Minus Sigs in Column Four Indicate Clockwise and Counter-Clockwise Scan Rotation Angles, Respectively.

| Scan Strategy | Part Thicknesses (mm) | Layer 1 Scan Angle (°) | Rotation Angle (°) |
|---|---|---|---|
| $\boldsymbol{ES}$ | 0.50, 0.75, 1.00 | 0 | 0 |
| $\boldsymbol{S}$ | 0.25, 0.50, 0.75, 1.00 | 15 | 0 |
| $\boldsymbol{L}$ | 0.25, 0.50, 0.75, 1.00 | 75 | 0 |
| $\boldsymbol{EL}$ | 0.50, 0.75, 1.00 | 90 | 0 |
| $\boldsymbol{ES + EL}$ | 0.50, 0.75, 1.00 | 0 | $\pm 90$ |
| $\boldsymbol{S + \bar{S}}$ | 0.50, 0.75, 1.00 | 15 | $\pm 150$ |
| $\boldsymbol{L + \bar{L}}$ | 0.50, 0.75, 1.00 | 75 | $\pm 30$ |
| $\boldsymbol{EL + \overline{S^*}}$ | 0.50, 0.75, 1.00 | 90 | $\pm 60$ |
| $\boldsymbol{EL^* + \overline{EL^*}}$ | 0.50, 0.75, 1.00 | 87 | $\pm 6$ |
| $\boldsymbol{Cont.}$ | 0.50, 0.75, 1.00 | 0 | $+67$ |

Micro-crack morphologies were studied in detail using scanning electron microscopy (SEM). To reveal dendrites and melt pool boundaries, as-polished specimens were etched for 5s with glyceregia (15 mL HCl, 10 mL Glycerol, 5 mL $HNO_3$). A JEOL JSM-7600F field emission gun SEM (FEG-SEM) operated at low (250X) and high (10000X) magnifications was employed to assess the micro-cracking behaviour of the as-printed samples specimens were etched for 5s with glyceregia (15 mL HCl, 10 mL Glycerol, 5 mL $HNO_3$) to reveal dendrites and melt pool boundaries. Imaging was performed using a JEOL JSM-7600F field emission gun scanning electron microscope (FEG-SEM) at low (250X) and high (10000X) magnifications to assess the micro-cracking tendencies in the as-printed samples.

Advanced characterization was performed using transmission electron microscopy (TEM) to determine the metallurgical factors contributing to micro-cracking. A $1.00\ mm$ thin-wall part was machined down to a 1.00 × 3.00 × 1.50 mm (X × Y × Z) specimen central to the part height near the region chosen for quantitative micro-crack analysis. The sample was mounted on a Gatan disc grinder with the XY surface facing up to enable the use of the lift-out method in focused ion beam (FIB) milling. Standard metallographic grinding and polishing procedures were conducted to produce a 1.00 mm tall sample required for the FIB. A region containing a high angle boundary (HAB) in the vicinity of a micro-crack was selected using the FEG-SEM. The lift-out method was performed in a HITACHI FB-2000A Ga-FIB to machine a thin specimen (5.00 × 0.10 × 10.00 µm (X × Y × Z)) for TEM characterization. A JEOL JEM 2100 FEG-TEM equipped with an Oxford Xplore TEM energy dispersive X-ray spectroscopy (EDS) was employed to identify nano-scale particles at the chosen HAB perpendicular to the XY plane. Imaging and phase analysis were conducted at 200 kV in both conventional and scanning TEM (STEM) modes.

### 9.2.4 Statistical Analysis

Micro-crack statistics were obtained through image and statistical analyses using ImageJ [72] and customized visual basic (VB) scripts. were used to isolate cracks from other microstructural features such as voids, pores and inclusions. Features such as voids, pores and inclusions were filtered out using parametric thresholds following observation of around 100 images per sample, as done in [197]. Internal micro-crack densities, crack lengths (CLs) and crack widths (CWs) were obtained by calculating crack area fractions, maximum feret diameters and ellipse minor axis lengths using the procedure demonstrated in **Figure 9-3**. The crack area fraction (CAF) for a singular image is given by the total crack area divided by the image area. Micro-crack lengths and widths for each sample are computed using average maximum feret diameters and ellipse minor axis lengths.

To produce an acceptable number of planes (with 1 mm spacing) for statistical analyses, all specimen were ground and polished three times. Micro-crack analysis was performed on the XZ plane to capture more cracks across the part thickness (X-direction) along the build direction (BD or Z-direction). Cumulative sample areas no smaller than 45.00 $mm^2$, 33.75 $mm^2$ and 22.50 $mm^2$, 11.88 $mm^2$ were used for the $1.00\ mm$, $0.75\ mm$, $0.50\ mm$, and $0.25\ mm$ parts, respectively. Over 90 optical micrographs (30 per plane) were randomly collected from the center of each specimen. All computed data included 95% confidence levels to provide a sense of experimental deviations.

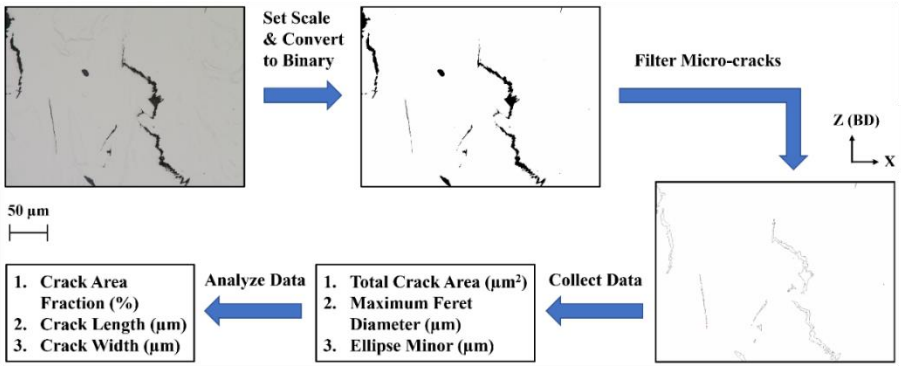


**Figure 9-3:** Micro-Crack Analysis Procedure Including Image and Statistical Analysis for a Single Optical Micrograph.

## 9.3 Modeling Methodology

FEM is used to evaluate the effect of wall thicknesses and vector length combinations on in-process stresses. The procedure described by Chakraborty et al. [197], highlighting the necessity to use two FEM approaches, is employed. In the current study, the layer-scale heat input (referred as layer-scale) model is used to determine the stresses introduced by varying WTs, while a beam-scale heat input (referred as beam-scale) model evaluates the stresses affected by changing VLs at the microscale level.

Both models use identical convective and radiative heat loss conditions, which are applied to all surfaces exposed to the external surroundings, at 25 °C. Conduction between the solid material and powder bed is accounted for using convective coefficients for different part geometries, based on work performed by Chao et al. [168]. Temperature-dependent material properties of R108 between room temperature and 1400 °C, such as specific heat, thermal conductivity, and thermal expansion, were kindly provided by and proprietary to General Electric [197]. Mechanical properties, such as constant yield strength and ultimate tensile strength, below and above 1150 °C were taken from Martin et al. [169] and Kissinger et al. [170], respectively. The results generated by the thermal model are used as input for the mechanical model to obtain accurate prediction of mechanical results such as strain, stress and distortion [141].

### 9.3.1 Layer-Scale Model

To model the effect of WT on in-process stresses at the macroscale level, the ABAQUS finite element (FE) method proposed by Yang et al. [141] is implemented. According to the authors, a sequentially coupled layer-scale modelling procedure allows accurate prediction of mechanical results such as strain, stress, and distortion for full-size parts. Thermal and mechanical results are computed using this approach, as done in [144].

The model geometries and boundary conditions are set in accordance with the experimental setup to replicate the LPBF processing procedure. The FEM methodology is described in detail in Chakraborty *et al.* [158]. Five build layers are lumped into a single layer in the model (200 µm thickness) to improve computational efficiency. To account for the varying LBHs for different WTs, part heights for the four WTs – $1.00\ mm$, $0.75\ mm$, $0.50\ mm$, and $0.25\ mm$ – are normalized with their corresponding LBH values. The terminology, build progress (BP), is used to describe the normalized heights along BD. The point selected for stress analysis is central to the part thickness (X-direction) and length (Y-direction), as shown in **Figure 9-4**. The stress results are always computed at the build height of LBH/2, coinciding with the region used for micro-crack characterization. The in-process stress is recorded at this point (BP = 50%) as subsequent layers are added along BD up to the completion of the build at LBH (BP = 100%).

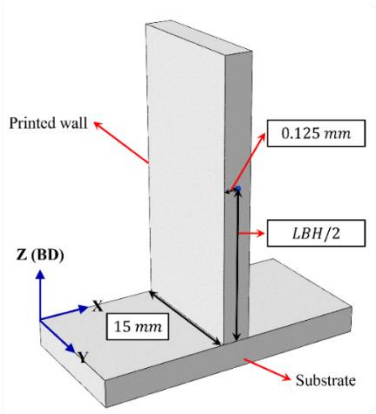


**Figure 9-4:** Cross-Sectioned 3D Image Along the **XZ** Plane Illustrating the Layer Model Used to Simulate the Macro-Scale Stresses Experienced by a Thin-Wall Part during LPBF. Results are Extracted at the Blue Point in the Layer-Scale Model.

### 9.3.2 Beam-Scale Model

To simulate the effect of VL on micro-cracking, a beam-scale modelling approach is implemented to evaluate the in-process stresses at the microscopic scale. The modelling methodology is based on the exponentially decaying model, which is used to simulate the laser beam heat source [171], as done in [197]. This approach is beneficial to predict microscopic stresses, as demonstrated in [173,202]. Results are obtained using a sequentially coupled thermo-mechanical modelling procedure similar to [144]. The base geometry and mesh sizes are illustrated in **Figure 9-5**. The model size is 0.50 × 30 × 0.40 mm (X × Y × Z), which includes both the powder and solidified layers. The part height includes 9 solidified layers and one powder layer interacting with

the laser. The length of the model is 1/10 of the actual part to reduce the computational time. Finer element sizes of 20 μm in X and Y directions and 10 μm in Z-direction are used for the region interacting with the laser, based on a mesh sensitivity study conducted in [172]. Conversely, coarser element sizes are used for regions further away from the laser track, as shown in **Figure 9-5**. The bottom surface of the component is constrained from moving in all directions and the effect of part movement in the $10^{th}$ layer is assumed to be insignificant. The conduction and Young's modulus of the powder are decreased to 1.5% and 1% of the solid state, as performed in previous studies [174,197]. The material initial temperature is taken from the part-scale model to replicate the process. The residual stresses from the previous layer are not considered and the initial stress state is set to zero to avoid the challenges associated with transferring stress tensors over varying simulation length scales.

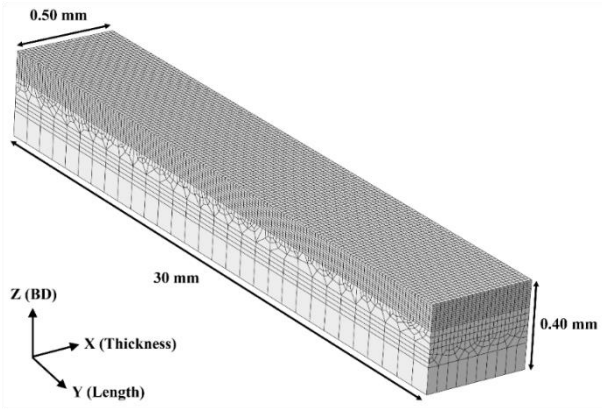


**Figure 9-5:** Image Illustrating the Base Geometry and Mesh Sizes used for the Beam-Scale Modelling Methodology used to Simulate the Micro-Scale Stresses Experienced by a Thin-Wall Part during LPBF.

**Figure 9-6 (a)** and **(b)** demonstrate two distinct beam-scale models used to predict the in-process stresses for the extra short and extra long vector scan paths, respectively. The stress results are captured at the center of the track inside the melt pool (40 μm in depth) for both the $ES$ (**Figure 9-6 (a)**) and $EL$ (**Figure 9-6 (b)**) laser tracks. These values are evaluated over a unitless parameter called normalized time, which accounts for the time between the first instance of laser irradiation (0.0) on the material and approximately 2.5 ms after the laser beam passes away from the center along the scan direction (1.0). The 2.5 ms time duration allows the nodal results (such as stress, strain, and temperature) to become stable, enabling the evaluation of the stress results.

## 9.4 Results and Discussion

### 9.4.1 Micro-Crack Characterization

All samples exhibit two distinct micro-crack growth directions, demonstrated using a representative microstructure in **Figure 9-7**. Most micro-cracks propagate along BD (black arrows) while others propagate along melt pool boundaries perpendicular to BD (red arrows). These micro-cracks are categorized as zipper and melt-pool micro-cracks, respectively. High magnification SE-SEM imaging of the zipper (**Figure 9-8 (a)**) and melt-pool (**Figure 9-8 (b)**) micro-cracks reveals inter-dendritic morphologies in the surrounding microstructures for both cases. Zipper micro-cracks have been reported in Carter et al. [96] and melt-pool micro-cracks have been demonstrated by Chakraborty et al. [197] for similar alloys under high energy density conditions. Both studies demonstrate interdendritic morphologies, suggesting micro-cracking during the final stages of solidification. Further details of the underlying reasoning for the different micro-crack growth directions are provided in [197]. The authors report identical solidification cracking mechanisms for both micro-cracks, but the interdendritic micro-cracks aligned with BD are more likely to form due to positive stress triaxiality above the solidus temperature (~1310 °C [169]). The melt-pool micro-cracks are suggested to be sensitive to the scanning conditions [96,198].

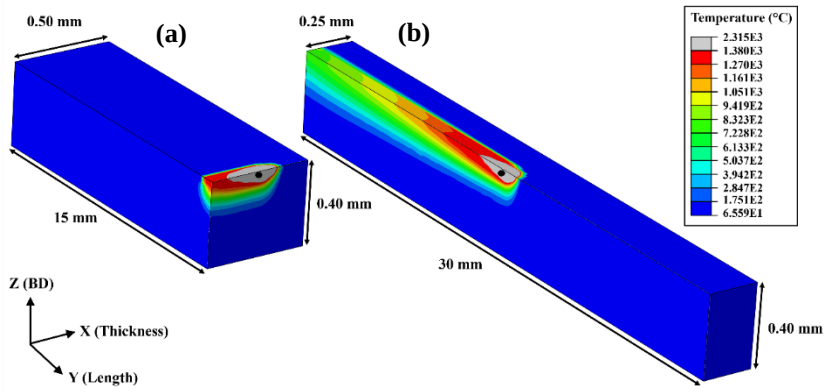


**Figure 9-6:** Beam-Scale Models for the Thin-Wall Parts with **(a)** Extra Short (***ES***) and **(b)** Extra Long (***EL***) Vector Lengths. The Black Dots for each Model Indicate the Locations of the Points at which Stress Triaxialities were Calculated within the Melt Pool. In **(a)**, a Central Cross-Section along the **XZ** Plane is Taken, and in **(b)**, a Central Cross-Section along the **XY** Plane is Taken to Illustrate the Temperature Profiles for the ***ES*** and ***EL*** Parts, respectively. The Legend Shows the Temperature Profile Values for Both Models in °C.

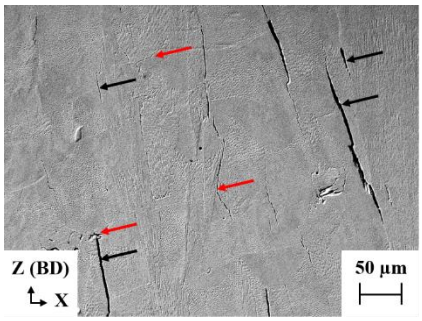


**Figure 9-7:** SE-SEM Micrograph, Taken from the $\mathbf{1.00}\ \boldsymbol{mm}$ Thick $\boldsymbol{ES + EL}$ Part, Showing Zipper Micro-Cracks (Black Arrows) Propagating along BD and Melt-Pool Micro-Cracks (Red Arrows) Propagating along Melt Pool Boundaries.

Elemental analysis of a high angle boundary (HAB) near a micro-crack is performed using the STEM-EDX analysis technique, as shown in **Figure 9-8 (c)**. The spherical white particles observed near the interdendritic micro-cracks (**Figure 9-8 (a)** and **(b)**) are fine carbides rich in Hf, Ti and Ta, as illustrated in **Figure 9-8 (c)**. These particles are discrete and homogeneously distributed in the material, and are likely not responsible for micro-cracking, agreeing with findings presented by Chakraborty et al. [197].

### 9.4.2 Effect of Wall Thickness on Micro-Cracking Propensity

**Figure 9-9** shows the crack statistics obtained from the optical image analysis of thin-wall parts with different wall thicknesses (WTs) and vector lengths (VLs). The effect of WT on CAF, crack length and crack width of the zero-rotation parts illustrated in **Figure 9-2 (c)** is discussed here. As WT decreases, the CAF values drop for all VLs, as shown in **Figure 9-9 (a)**. For instance, parts processed with shorter VLs, such as the *S* parts, demonstrate a 68% decrease in micro-cracking, from 0.914% $\pm$ 0.212% to 0.293% $\pm$ 0.159%, as WT decreases by 75%, from $1.00\ mm$ to $0.25\ mm$. Similarly, parts scanned with longer VLs, such as the *L* parts, exhibit a 65% decrease in CAF, from 1.333% $\pm$ 0.529% to 0.454% $\pm$ 0.113% as WT decreases by 75%. The direct proportionality between WT and micro-crack propensity agrees with previous studies by the author [158,197]. Moreover, micro-crack lengths (**Figure 9-9 (b)**) and widths (**Figure 9-9 (c)**) decrease with decreasing WT. For instance, considering the shortest VL ($ES$), the crack length decreases by 43% from 15.729 µm $\pm$ 3.535 µm to 8.939 µm $\pm$ 1.597 µm as WT decreases by 50%, from $1.00\ mm$ to $0.50\ mm$. Similarly, the crack width decreases by 25% from 1.227 µm $\pm$ 0.227 µm to 0.917 µm $\pm$ 0.099 µm as WT decreases by 50%. To explain this phenomenon, the effect of WT on stress triaxiality is evaluated.

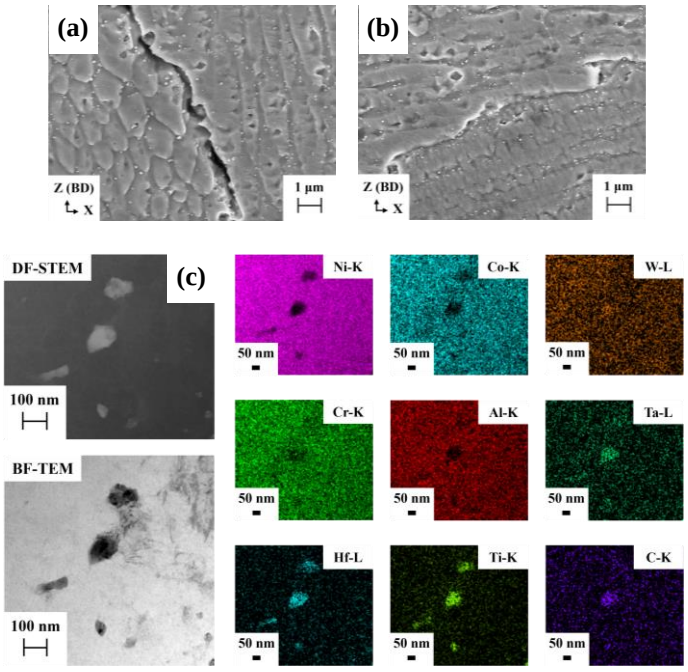


**Figure 9-8:** SE-SEM Micrographs, Taken from the $\mathbf{1.00}\ \boldsymbol{mm}$ Thick $\boldsymbol{ES + EL}$ Part, Illustrating Examples of **(a)** a Zipper Micro-Crack, and **(b)** a Melt-Pool Micro-Crack. **(c)** BF-TEM and DF-STEM Images with Corresponding STEM-EDX Maps Demonstrating Contents of Spherical White Particles in **(a)** and **(b)**.

### 9.4.3 Evaluation of Stress Triaxialities Computed Using the Layer-Scale Model

Stress triaxiality (T) is a commonly used parameter in fracture mechanics to predict crack initiation and growth [86,179]. Stress triaxiality is defined in **Equation (9-1)** as the ratio of the hydrostatic stress ($\sigma_m$) to the von Mises equivalent stress ($\sigma_e$):

$$T = \frac{\sigma_m}{\sigma_e} \tag{9-1}$$

**Figure 9-10 (a)** shows the evolution of stress triaxiality states, computed using the layer-scale methodology described in **Section 9.3.1**, at the centers of four different thin-wall parts as printing progresses along BD. All parts exhibit negative stress triaxiality when the first layer is activated. In the layer heating approach, layer activation at high temperatures results in negative stress triaxialities [197]. Lumping the layers to enhance the computational efficiency causes skipped data steps between each layer scan. As the builds progress along BD, stress triaxialities increase rapidly as the parts cool down and converge to steady state value. As the WT increases from $0.25\ mm$ to $1.00\ mm$, the stress triaxiality increases at lower build progresses.

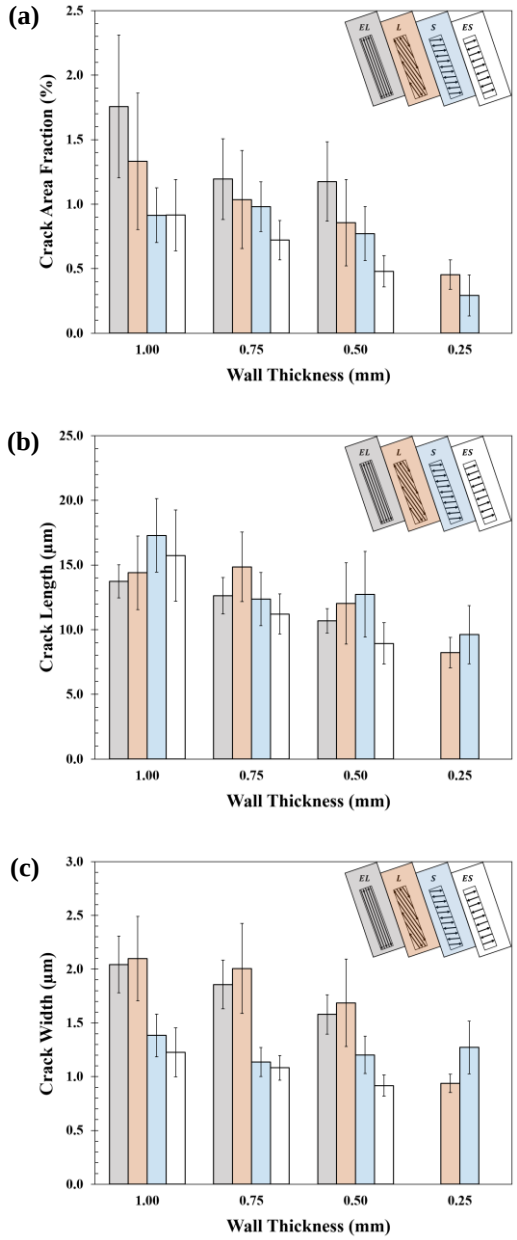


**Figure 9-9:** Plots Showing the Effect of Vector Length on the Average **(a)** Crack Area Fractions, **(b)** Crack Lengths, and **(c)** Crack Widths for Parts with Four Different Wall Thicknesses, as Described in **Table 9-3**.

Positive stress triaxiality indicates a tensile hydrostatic stress state favoring crack initiation and propagation. This supports the observed higher micro-cracking propensity coupled with increased micro-crack

length and width as WT increases, as shown in **Figure 9-9**. The increased stress triaxiality in thicker parts is caused by higher cooling rates and thermal gradients due to larger thermal stresses and heat dissipation from the bulk of the sample [197].

### 9.4.4 Effect of Vector Length on Micro-Cracking Propensity

Thermal stresses can be affected by varying the scan strategy during part processing. First, the effect of varying the VL without scan rotation is investigated. The effect of VL on micro-cracking is shown in **Figure 9-9**. Micro-cracking density (or CAF) decreases with decreasing VL for all WTs, as illustrated in **Figure 9-9 (a)**.

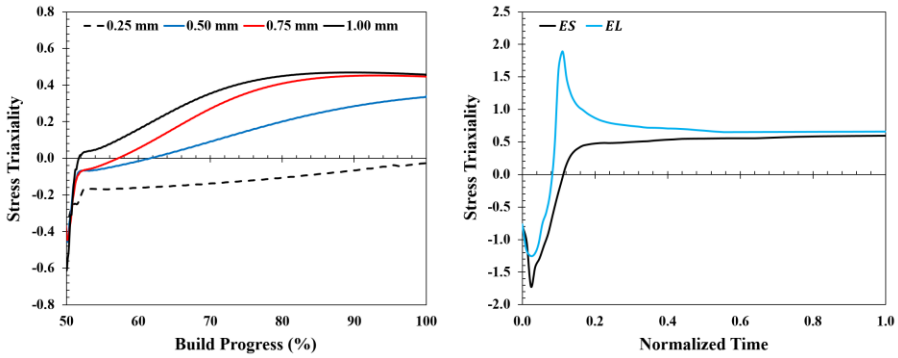


**(a)** **(b)**

**Figure 9-10: (a)** Stress Triaxiality Distribution during Build Progression from the Center along the Part Height for Four Part Thicknesses between $\mathbf{0.25}\ \boldsymbol{mm}$ and $\mathbf{1.00}\ \boldsymbol{mm}$, predicted by the layer-scale FEM approach. (b) Stress Triaxiality Distribution over Normalized Time within the Melt Pool for the $\mathbf{0.50}\ \boldsymbol{mm}$ thick $\boldsymbol{ES}$ and $\boldsymbol{EL}$ parts, predicted using the beam-scale approach.

For example, considering the 0.50 $mm$ part, as the scan angle decreases from 90° ($EL$) to 0° ($ES$), the CAF value decreases by 59%, from 1.175% $\pm$ 0.308% to 0.480% $\pm$ 0.121%. Similar behavior is also observed in thicker parts, but the CAF values are higher due to the increased thickness and stress triaxiality, as discussed in **Section 9.4.2**. The CAF value increases by a factor of 1.92, from 0.915% $\pm$ 0.277% to 1.757% $\pm$ 0.553% at a part thickness of 1.00 $mm$. Generally, the crack sizes also increase with vector length as observed in the case of 0.50 $mm$ for instance. As vector length increases from $ES$ to $EL$, the crack length increases by a factor of 1.20, from 8.939 µm $\pm$ 1.597 µm to 10.688 µm $\pm$ 0.954 µm, as shown in **Figure 9-9 (b)**, and the crack width increases by a factor of 1.92, from 0.917 µm $\pm$ 0.099 µm to 1.579 µm $\pm$ 0.182 µm, as shown in **Figure 9-9 (c)**. The increased micro-cracking propensity and sizes can be explained through the evaluation of stress triaxialities at the beam scale.

### 9.4.5 Evaluation of Stress Triaxialities and Thermal Stresses Computed Using the Beam-Scale Model

The beam-scale FEM approach described in **Section 9.3.2** is beneficial to evaluate stress triaxialities and in-process stresses at a microscopic scale, enabling prediction of the vector length effect on micro-cracking. To speed up the simulation, the initial temperature is captured from the layer-scale model after the part cools down for 10s (cooling time), as done in [197].

#### 9.4.5.1 Effect of Stress Triaxialities on Micro-Cracking

The stress triaxiality distribution over normalized time is computed for the $ES$ and $EL$ simulations at beam scale and displayed in **Figure 9-10 (b)**. For both $ES$ and $EL$ simulations, the stress triaxiality is initially negative on the first instance of laser irradiation at the center of the part. As the laser moves away from the center and proceeds along the scan line, the stress triaxiality increases rapidly and transitions to a positive stress triaxiality state, until a plateau is reached at around 0.6 normalized time. According to [180], the positive stress triaxiality condition is preferential for micro-crack nucleation under the absence of external loading. The $EL$ simulation transitions to positive stress triaxiality state earlier (0.1 normalized time) compared to the $ES$ simulation (0.15 normalized time). The early transition to positive stress triaxiality is significant during rapid solidification as it indicates that the laser is still in close proximity to the center of the track, as demonstrated in **Figure 9-6 (b)**. This means that the stress triaxiality in the $EL$ path becomes positive at a higher temperature. When the material is hot and not completely solid, it is more susceptible to solidification cracking at positive stress triaxialities. Therefore, the $EL$ part is more susceptible to solidification cracking as it reaches positive stress triaxiality earlier than the $ES$ part. The simulated results agree well with the experimental results in **Figure 9-9**, showing more micro-cracks with increased lengths and widths in the $EL$ part compared to the $ES$ part.

#### 9.4.5.2 Effect of Thermal Stresses on Micro-Cracking

To further understand the micro-cracking versus VL phenomenon, stresses in the XY plane are evaluated over a normalized time for the shortest ($ES$) and longest ($EL$) VLs in the 0.50 mm thick part. These stresses are of interest as they are perpendicular to the direction of micro-crack propagation (BD here). **Figure 9-11 (a)** and **(b)** show the longitudinal (along the scan direction) and transverse (perpendicular to the scan direction) stresses evaluated within the melt pool for the $ES$ and $EL$ simulations, respectively. Note that the scan direction is aligned with the X-direction for $ES$ and Y-direction for $EL$. For all cases, the stresses are initially compressive as the laser first irradiates the center of the part (0.0 normalized time). As the laser beam passes along the scan line away from the center of the track, the stresses increase rapidly transitioning to tensile stress state as the part cools. This

continues for 2.5 ms (1.0 normalized time), where a maximum stress threshold is observed. For both $ES$ and $EL$ simulations, the peak longitudinal stresses (**Figure 9-11 (a)**) are higher than the peak transverse stresses (**Figure 9-11 (b)**). For instance, considering the $EL$ simulation curves in **Figure 9-11 (a)** and **(b)**, the peak longitudinal stress is ~1440 MPa (**Figure 9-11 (a)**), 80% higher than the peak transverse stress of ~800 MPa (**Figure 9-11 (b)**). This shows that the longitudinal stress is more critical for micro-cracking compared to the transverse stress with respect to the laser scan direction.

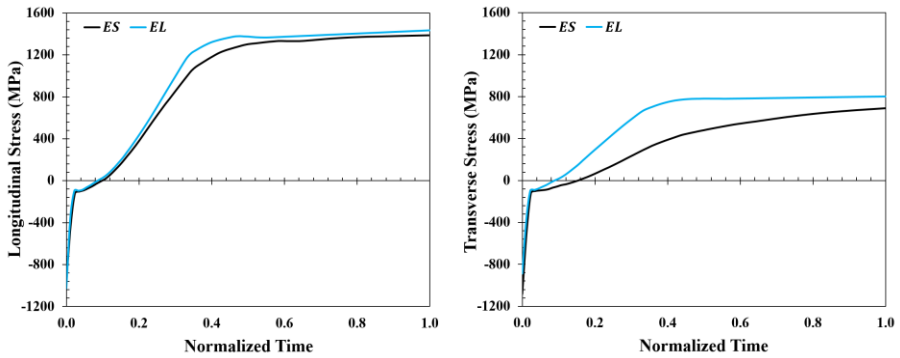


**Figure 9-11:** Stress Plots Demonstrating **(a)** Longitudinal Stresses, **(b)** Transverse Stresses, and **(c)** Stress Triaxialities over Normalized Time within the Melt Pool for the 0.50 mm thick ES and EL parts.

Considering the longitudinal stresses in **Figure 9-11 (a)**, the $EL$ longitudinal stress is always higher than the $ES$ longitudinal stress. This difference in stress is small throughout the process because only a single track is simulated, the phase transition of the material is unidirectional, and the initial stress is not considered. To develop a more accurate estimation of the in-process stresses, multi-track simulations are necessary. Multi-track simulations consider bidirectional scans to completely process the part and predict much larger stresses in the longitudinal direction for $EL$ compared to $ES$ [173]. The larger stress difference obtained using the multi-track approach is attributed to the accumulation of stresses developed over the creation of tracks and layers.

### 9.4.6 Effect of Scan Rotation and Changing Vector Lengths on Micro-Cracking Propensity

The laser scan rotation strategy has important implications on the defects produced in LPBF. Cheng et al. [127] conducted FEA simulations to show that scan rotations reduce directional stresses and deformation. The authors demonstrated that the 67° continuous scan rotation strategy ($Cont.$) generates the smallest directional stress differences amongst the scan rotation strategies studied. Dunbar et al. [220] developed an experimental

method to show that the $Cont.$ scanning approach also decreases the part distortion by 37.6% compared to a non-rotated scan. Recently, Tangestani et al. [173] illustrated using FEA simulations that scan rotations produce more isotropic stress distributions than the non-rotated scans, which could explain the minimized defects in scan-rotation parts.

Accordingly, the effect of scan rotation strategies on micro-cracking is investigated here. **Figure 9-12** illustrates the effect of six different scan rotation strategies, described in detail in **Figure 9-2 (d), (e)** and **Table 9-3**, on micro-crack density and size of the $1.00\ mm$, $0.75\ mm$, and $0.50\ mm$ parts. The CAF decreases with decreasing WT for all scan strategies as shown in **Figure 9-12 (a)**, which agrees well with the decrease in CAF observed as WT decreases in **Figure 9-9 (a)**. Considering **Figure 9-12 (a)**, micro-cracking decreases by 52%, from 1.407% $\pm$ 0.212% to 0.669% $\pm$ 0.220% as WT decreases by 50% from $0.50\ mm$ to $1.00\ mm$ for the $EL + \overline{S^*}$ case. Similarly, the crack lengths and widths decrease by 35%, from 14.810 µm $\pm$ 1.278 µm to 9.609 µm $\pm$ 1.528 µm, as shown in Fig. 12b, and 28%, from 1.549 µm $\pm$ 0.144 µm to 1.122 µm $\pm$ 0.194 µm, as shown in **Figure 9-12 (c)**, respectively. As described in **Section 9.4.2**, the larger micro-crack densities and sizes come from higher stress triaxialities for thicker parts.

In general, a large majority (~90%) of the scan-rotation strategies (**Figure 9-12 (a)**) exhibit reduced CAFs (by 12-62%, between 0.347% $\pm$ 0.101% and 1.178% $\pm$ 0.516%) compared to the CAFs for the zero-rotation strategies (between 0.480% $\pm$ 0.121% and 1.757% $\pm$ 0.553% –**Figure 9-9 (a)**). For example, considering the $1.00\ mm$ WT in **Figure 9-9 (a)**, the $S$ and $EL$ parts exhibit CAFs of 0.914% $\pm$ 0.212% and 1.757% $\pm$ 0.553%, respectively. When scan rotation is introduced (by replacing the alternate layer scans with $\bar{S}$ and $ES$), the resultant $S + \bar{S}$ and $ES + EL$ parts exhibit 54% and 42% reduction in CAFs to 0.418% $\pm$ 0.118% and 1.023% $\pm$ 0.152%, respectively, as shown in **Figure 9-12 (a)**. Scan rotations have similar effects on the crack lengths and widths. The crack lengths and widths for over 75% of the scan-rotation strategies are reduced by 4-39% and 6-43%, respectively, as shown in **Figure 9-12 (b)** and **(c)**. The average crack lengths and widths for the scan-rotation parts (CL=~11.27 µm, CW=~1.31 µm) are considerably lower than those without rotations (CL=~13.05 µm, CW=~1.52 µm). Reduced cracking in the scan-rotation parts can be linked to more homogeneous stress distributions compared to the zero-rotation parts [173].

Interestingly, layer-to-layer VL variation generates a noticeable trend in micro-cracking behavior. Micro-cracking propensities are higher when scans with longer VLs are added between layers and lower when shorter VLs are incorporated during processing, as demonstrated in **Figure 9-12 (a)**. Thin-wall parts processed solely with shorter VLs demonstrate 50-70% smaller CAFs compared to parts printed solely with longer VLs.

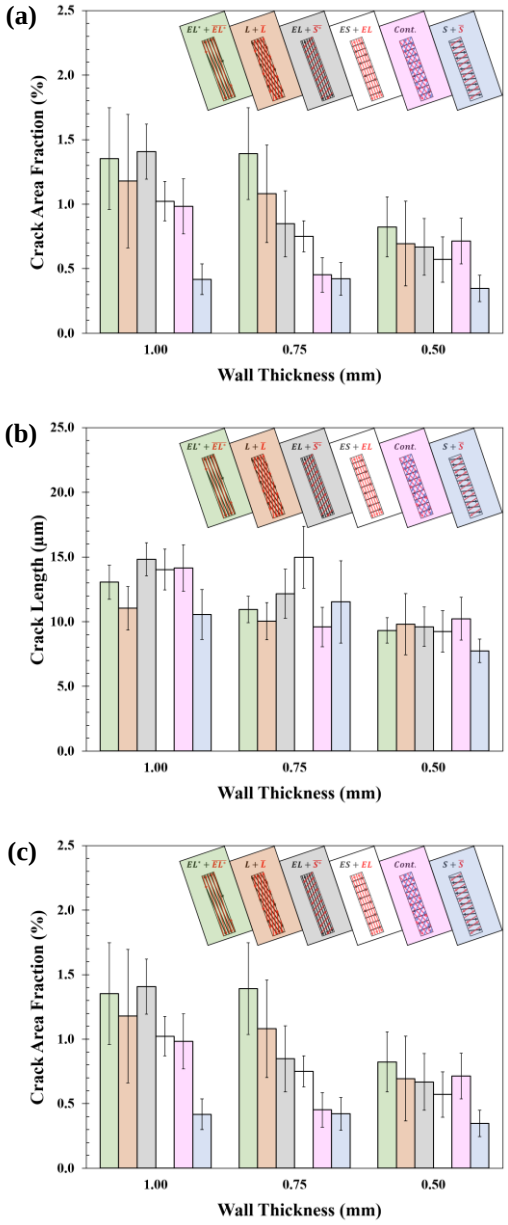


**Figure 9-12:** Plots Showing the Average **(a)** Crack Area Fractions, **(b)** Crack Lengths, and **(c)** Crack Widths for Thin-Wall Parts with Six Different Inter-Layer Scan Rotation Strategies Described in **Table 9-3**.

Higher CAFs for longer VLs are attributed to higher stresses in the scan direction, as discussed in **Section 9.4.4**. In cases with mixed VLs, shorter VLs are shown to be more beneficial to reduce micro-cracking. For all WTs, the $ES + EL$ strategy generates 11-27% lesser CAFs compared to the $EL + \overline{S^*}$ strategy. Notably, the $Cont.$

strategy also generates low CAF values between 0.452% $\pm$ 0.134% and 0.983% $\pm$ 0.213% for all WTs. The $Cont.$ strategy generates mixed short and long vector lengths along BD, as elucidated in **Section 9.2.2**. Therefore, the CAFs for $Cont.$ are closer to scan strategies, such as $ES + EL$ and $EL + \overline{S^*}$, which include equivalent mixtures of short and long vector lengths. At $0.75\ mm$ WT, the CAF for $Cont.$ is considerably lower than the mixed cases, which could be linked to experimental errors in the CAF measurement method.

The significance of scan rotations on micro-cracking is influenced by the wall thickness. Thicker parts exhibit higher crack propensities and are more sensitive to VL changes during build progression. Under such circumstances, the incorporation of shorter VLs is evidently more significant for micro-crack mitigation, as shown in **Figure 9-12 (a)**. As the wall thickness decreases, the laser travel distance decreases and the difference between short and long vector lengths is reduced. For instance, the maximum difference between the $S$ and $EL^*$ strategies at $1.00\ mm$ WT (18.07 mm) is significantly larger than at $0.50\ mm$ WT (9.04 mm). Smaller laser travel distances promote smaller stress accumulation along the scan direction, favoring lower micro-cracking densities in thinner walls. The diminished effect of vector length is apparent at $0.50\ mm$ WT, where the CAFs are similar (between 0.347% $\pm$ 0.101% and 0.824% $\pm$ 0.232%) for all vector length combinations. Similarly, the advantage of using the alternating short VL technique over the continuous scan rotation strategy for micro-crack mitigation decreases as WT decreases. For instance, considering the $0.75\ mm$ WT, the CAFs for $S + \bar{S}$ (0.421% $\pm$ 0.127%) and $Cont.$ (0.452% $\pm$ 0.134%) are similar. Nevertheless, the alternating short VL approach remains the ideal scan strategy for micro-crack reduction at all WTs.

Layer-wise variation of scan lengths is a simple strategy that can facilitate homogenization of the heat flow and stresses developed during laser processing. This is beneficial to minimize micro-cracking in LPBF thin-wall parts designed for niche applications. In this study, the authors showed that the adverse effect of small WT on micro-cracking can be countered using the alternating short VL scan strategy, which reduces the stresses and decreases the part's susceptibility to micro-cracking during LPBF processing.

## 9.5 Conclusions

The effect of wall thickness (WT) and vector length (VL) on the micro-cracking propensity in as-processed thin-wall LPBF high-γ' Ni-based superalloy, RENÉ 108, was investigated. Four different part thicknesses and ten different scan strategies were studied. Optical microscopy and image analysis techniques were employed to calculate micro-crack statistics such as crack area fraction, crack length and crack width for all print strategies. Finite element analysis was utilized to evaluate the stress triaxialities and in-process stresses. Two different FE models, namely layer-scale and beam-scale, were used to evaluate the stress states at the macro- and micro-scopic scales. The layer-scale model used a 'lumped' heating approach to simulate the effect of WT on

stress triaxialities, whereas the beam-scale model used an ED heat source to simulate the effect of VL on stress triaxialities and in-process stresses parallel and perpendicular to the scan direction.

Micro-cracking propensity increased with WT for all scanning conditions. All micro-cracks exhibited inter-dendritic morphologies and homogeneously distributed fine spherical Hf/Ti/Ta-rich carbides in the surrounding material microstructure. Statistical analysis revealed larger micro-crack quantities, lengths, and widths in the thicker parts, ruling out carbides as a cause for micro-cracking. Layer-scale models showed that the higher micro-crack densities in the thicker parts were caused by higher stress triaxialities during build progression. The results indicated that reducing the WT is a useful route to minimize inherent micro-cracking in LPBF.

To further mitigate micro-cracking, scan strategies were varied for four WTs $1.00\ mm$, $0.75\ mm$, $0.50\ mm$, and $0.25\ mm$, respectively. Firstly, identical VLs were maintained for each layer along the part height during build progression. The higher micro-cracking propensities observed in parts scanned with longer VLs is attributed to higher tensile longitudinal stresses and earlier transition to positive stress triaxiality state during processing. Shorter VLs are preferred as they generate reduced in-process tensile stresses perpendicular to BD, diminishing micro-cracking in the XZ plane for all thin-wall parts.

Subsequently, the effect of scan rotation on micro-cracking was investigated. In this work, six different scan rotation strategies (five alternating and one continuous) were employed. Scan rotation reduces micro-cracking by 12-62%, which is attributed to the development of more homogeneous stress distribution during part construction. The continuous 67° ($Cont.$) and alternating short VL ($S + \bar{S}$) scan rotation strategies are more advantageous for micro-crack mitigation for all WTs. The $Cont.$ strategy is beneficial to reduce micro-cracking due to improved stress homogenization generated by the larger array of short and long VLs (70% short VLs and 30% long VLs). Micro-cracking is reduced further, by 50-70% compared to the alternating long VL scan strategies, when the $S + \bar{S}$ strategy is employed. The lower micro-crack densities in parts processed with the $S + \bar{S}$, compared to the $Cont.$ strategy, are attributed to reduced thermal stresses along the scan direction generated by a higher number of short VLs. However, as the WT decreases, the effectiveness of the $S + \bar{S}$ strategy on micro-crack reduction is less significant compared to the other scan strategies. In fact, for the $0.50\ mm$ WT, while scan rotation generally reduces micro-cracking, the differences in micro-cracking between various scan rotation combinations become negligible. Therefore, short VL scan rotations can be tailored to the wall thickness to produce LPBF thin-wall components with the fewest micro-cracks.

.

# Chapter 10
# Conclusions and Recommendations

## 10.1 Major Conclusions

This PhD thesis focuses on improving the fabrication of high-γ' Ni-based superalloy thin-wall parts using laser powder bed fusion (LPBF). The associated mechanisms for macro-scale failure and micro-scale cracking are elucidated. The build parameters investigated include the part geometry, alloy composition, and vector length. The key points of this research are as follows:

Macro-Scale Failure

- Construction of thin-wall structures is challenging because of the limiting build height (LBH) phenomenon. The LBH represents the printed part height, significantly affected in the LPBF process.
    - The LBH phenomenon occurs due to the in-process distortion of thin-wall structures. During processing, the uppermost layers are displaced due to compressive stresses along the part length and build direction (BD). This causes warpage which prevents the part from achieving the maximum design part height, promoting the reduction in LBH.
    - Two major build factors affect the LBH including laser parameters and wall thickness. The scanning strategy is important for LBH because it affects the compressive stresses along BD. Conversely, wall thickness affects the slenderness ratio, which is critical for buckling and consequently LBH of thin-wall components.
    - To reduce the distortion and increase the printed to design part height ratio, it is also important to reduce the variation of thermal stresses and strains during processing. This can be achieved by reducing the thermal gradients and cooling rates, which affect the thin-wall parts more severely than the thicker parts. For example, the scanning strategy, substrate temperature or part width are among engineering solutions that can reduce the thermal constraints and increase the LBH.

Micro-Scale Cracking

- In-process micro-cracking poses a significant challenge for the LPBF fabrication of high-γ' Ni-based superalloy thin-wall parts.
    - For all thin-wall build conditions investigated, the associated micro-cracking mechanism is the solidification cracking mechanism.
    - The solidification cracking mechanism occurs in the final stages of solidification when the liquid remains more stable and continuous at the high angle boundaries (HABs). Due to the brittle nature of the liquid film and the high accumulated stresses at the HABs, the material becomes susceptible to in-process micro-cracking.
        - The morphologies for all internal micro-cracks are interdendritic, which suggests micro-cracking in the terminal stages of solidification prior to the complete coalescence of primary dendrites.
        - All materials exhibit positive stress triaxiality at supersolvus temperatures in the melt pool core, supporting solidification cracking along BD. Higher temperatures make the material softer and more susceptible for micro-cracking at positive stress triaxiality states.
- Part geometry is significant because it affects the stress triaxiality state, which is critical for micro-cracking. The two geometrical factors investigated here include the wall thickness and build position.
    - Micro-cracking generally increases as wall thickness increases proportionally from 0.25 mm to 5.00 mm for both materials.
        - Generally, as the wall thickness increases, the in-process stresses and stress triaxiality values also increase. Positive stress triaxiality conditions favor micro-crack propagation and explains higher micro-crack propensity in the thicker parts.
        - The thicker parts exhibited higher cooling rates compared to the thinner parts due to heat transfer mechanisms associated with the part surface area to volume ratio. Accordingly, numerical simulations demonstrated larger in-process stresses, supporting larger micro-cracking propensities in the thicker components.
    - A disruption in proportionality (anomalous behavior) between micro-cracking density and wall thickness is observed at a wall thickness of 1.00 mm, where there is significantly higher micro-cracking density than expected. This is attributed to large fluctuations in the thermal gradient and is suspected to be affected by the vector length.

- Micro-cracking densities are lower for lower regions in the thin-wall sample along the part height.
  - The stress triaxiality states are compressive near the base plate which suppresses micro-cracking in the bottom regions of the thin-wall part.

- Alloy composition is a key factor for micro-cracking in superalloys. R108 exhibits higher micro-cracking densities compared to R65.
  - Higher micro-cracking in R108 is attributed to the material experiencing positive stress triaxialities at higher temperatures compared to R65. This is due to the contrasting solidification and GP phase transition behaviors which create a difference in magnitude of the specific heat capacity between the two materials between the solvus and liquidus temperatures. Therefore, the thermo-mechanical behavior of materials (an important factor in stress triaxiality) at higher temperatures is altered.
  - The micro-cracking densities are also affected by the difference between the solidus and solvus. R108 has larger liquid fractions at the terminal stages of solidification, which makes it more susceptible to solidification cracking at high temperatures.

- Vector length has a significant effect on the micro-cracking propensity of thin-wall parts. Components scanned with shorter vector lengths have lower micro-cracking densities. Also, scan rotations help further reduce micro-cracking by 12-62%. Alternating scan rotations with shorter vector lengths demonstrate lower micro-cracking densities than the conventional 67° continuous scan rotation strategy.
  - Shorter vector lengths generate smaller in-process tensile stresses perpendicular to BD which suppresses micro-cracking during part processing.
  - Scan rotations enable homogenization of the in-process stresses causing significant reduction in micro-cracking propensities. The alternating scan rotation strategy with shorter vector lengths is better than the 67° continuous scan rotation strategy because it has more instances of short vector lengths, which reduces the magnitude of the in-process stresses.
  - The alternating scan rotation strategy with shorter vector lengths is preferred to mitigate micro-cracking in thin-wall parts.

## 10.2 Recommendations and Future Work

Research findings show that LPBF thin-wall micro-cracking can be mitigated by reducing the in-process stresses through varying wall thicknesses and scan strategies to optimize part processing. The following recommendations and future studies are suggested:

- Determine the cause for higher liquid fraction in R108 than R65 through extensive characterization at atomic-scale resolutions.
- Evaluate the effect of the contour scan patterns on the micro-cracking phenomenon. Contour strategies are beneficial to improve the surface quality, but their effects on micro-cracking in thin-wall structures is largely unexplored.
- Consider a larger design of experiment including more materials to better understand the effect of alloy compositions and solidification range on the micro-cracking densities.
- Investigate the effect of laser scan strategies, slenderness ratio, and other part geometries such as part length and curvature on the LBH.

# References


[1] L.N. Carter, Selective laser melting of nickel superalloys for high temperature applications, (2013).

[2] Thai Technics, Aircraft Gas Turbine Engines - Engine Construction, (2017). https://www.thaitechnics.com/engine/engine_construction.html (accessed March 13, 2020).

[3] H. Chung, H.-S. Sohn, J.S. Park, K.M. Kim, H.H. Cho, Thermo-structural analysis of cracks on gas turbine vane segment having multiple airfoils, Energy. 118 (2017) 1275–1285.

[4] R.C. Reed, The superalloys: fundamentals and applications, Cambridge university press, 2006.

[5] Rolls-Royce Limited, The jet engine, Second, John Wiley & Sons, Derby, England, 2015.

[6] A. Kracke, A. Allvac, Superalloys, the most successful alloy system of modern times-past, present and future, in: 7th Int. Symp. Superalloy, 2010.

[7] E. Akca, A. Gürsel, A review on superalloys and IN718 nickel-based INCONEL superalloy, Period. Eng. Nat. Sci. 3 (2015).

[8] H.W. Dickinson, A short history of the steam engine, Cambridge University Press, 2011.

[9] C.T. Sims, A history of superalloy metallurgy for superalloy metallurgists, Superalloys. 1984 (1984) 399–419.

[10] J.H. Crary, Planet Superman: An ecocritical analysis of the Man of Steel from 1938-2017, (2017).

[11] C.T. Sims, W.C. Hagel, The Superalloys-vital high temperature gas turbine materials for aerospace and industrial power, John Wiley & Sons, 1972.

[12] C.T. Sims, N.S. Stoloff, W.C. Hagel, superalloys II, Wiley New York, 1987.

[13] E. Chauvet, P. Kontis, E.A. Jägle, B. Gault, D. Raabe, C. Tassin, J.-J. Blandin, R. Dendievel, B. Vayre, S. Abed, Hot cracking mechanism affecting a non-weldable Ni-based superalloy produced by selective electron Beam Melting, Acta Mater. 142 (2018) 82–94.

[14] N. El-Bagoury, N.B. Superalloys, Casting Technology, Metallurgy, Development, Properties and Applications, Int. J. Eng. Sci. Res. Technol. 5 (2016) 108–152.

[15] J.N. DuPont, J.C. Lippold, S.D. Kiser, Welding Metallurgy and Weldability of Nickel-Base Alloys, John Wiley & Sons, 2009. https://doi.org/10.1002/9780470500262.

[16] B. Geddes, H. Leon, X. Huang, Superalloys: alloying and performance, Asm International, 2010.

[17] J. Deschamps, M. Georgelin, A. Pocheau, Crystal anisotropy and growth directions in directional solidification, EPL (Europhysics Lett. 76 (2006) 291.

[18] N.J. Harrison, Selective Laser Melting of Nickel Superalloys: solidification, microstructure and material response, University of Sheffield, 2016.

[19] S. Miura, Y.-M. Hong, T. Suzuki, Y. Mishima, Liquidus and solidus temperatures of Ni-solid solution in Ni-Al-X (X: Ti, Zr, and Hf) ternary systems, J. Phase Equilibria. 20 (1999) 193.

[20] T.B. Massalski, J.L. Murray, L.H. Bennett, H. Baker, Binary alloy phase diagrams. 1986, Am. Soc. Met. Met. Park. OH. (1986).

[21] A. Mostafa, I. Picazo Rubio, V. Brailovski, M. Jahazi, M. Medraj, Structure, texture and phases in 3D printed IN718 alloy subjected to homogenization and HIP treatments, Metals (Basel). 7 (2017) 196.

[22] J.K. Tien, J.P. Collier, G. Vignoul, The role of niobium and other refractory elements in superalloys, in: Superalloy 718, 1989.

[23] A.J. Goodfellow, Strengthening mechanisms in polycrystalline nickel-based superalloys, Mater. Sci. Technol. 34 (2018) 1793–1808.

[24] Y.M. Wang-Koh, Understanding the yield behaviour of L12-ordered alloys, Mater. Sci. Technol. 33 (2017) 934–943.

[25] J.T.M. De Hosson, Superlattice dislocations in L12 ordered alloys and in alloys containing L12 ordered precipitates, Mater. Sci. Eng. 81 (1986) 515–523. https://doi.org/10.1016/0025-5416(86)90288-0.

[26] M. Preuss, J.Q. da Fonseca, B. Grant, E. Knoche, R. Moat, M. Daymond, The effect of γ′ particle size on the deformation mechanism in an advanced polycrystalline nickel-base superalloy, Superalloys. 11 (2008) 405–414.

[27] P. Beardmore, R.G. Davies, T.L. Johnston, Temperature Dependence of the Flow Stress of Nickel-Base Alloys, TRANS MET SOC AIME. 245 (1969) 1537–1545.

[28] M.J. Donachie, S.J. Donachie, Superalloys: a technical guide, ASM international, 2002.

[29] U.M. Dilberoglu, B. Gharehpapagh, U. Yaman, M. Dolen, The role of additive manufacturing in the era of industry 4.0, Procedia Manuf. 11 (2017) 545–554.

[30] W.J. Sames, F.A. List, S. Pannala, R.R. Dehoff, S.S. Babu, The metallurgy and processing science of metal additive manufacturing, Int. Mater. Rev. 61 (2016) 315–360.

[31] M. Brandt, The role of lasers in additive manufacturing, Laser Addit. Manuf. (2017) 1–18.

[32] T.D. Ngo, A. Kashani, G. Imbalzano, K.T.Q. Nguyen, D. Hui, Additive manufacturing (3D printing): A review of materials, methods, applications and challenges, Compos. Part B Eng. 143 (2018) 172–196.

[33] C.W. Hull, Apparatus for production of three-dimensional objects by stereolithography, (1986).

[34] T. Wohlers, T. Gornet, History of additive manufacturing, Wohlers Rep. 24 (2014) 118.

[35] 3ders.org, Let the revolution begin : key 3D printing patent expires today, 3ders.Org 3D Print. News. (2014) 2–4. http://www.3ders.org/articles/20140128-let-the-revolution-begin-key-3d-printing-patent-expires-today.html.

[36] E.J. Lavernia, T.S. Srivatsan, The rapid solidification processing of materials: science, principles, technology, advances, and applications, J. Mater. Sci. 45 (2010) 287–325.

[37] B. Cantor, Fundamentals of rapid solidification, in: Sci. Technol. Undercooled Melt, Springer, 1986: pp. 3–28.

[38] S. Ghosh, L. Ma, N. Ofori-Opoku, J.E. Guyer, On the primary spacing and microsegregation of cellular dendrites in laser deposited Ni–Nb alloys, Model. Simul. Mater. Sci. Eng. 25 (2017) 65002.

[39] D.D. Gu, W. Meiners, K. Wissenbach, R. Poprawe, Laser additive manufacturing of metallic components: materials, processes and mechanisms, Int. Mater. Rev. 57 (2012) 133–164.

[40] E.-M. Stanciu, A.C. Păvălache, G.-M. Dumitru, O.G. Dontu, D.B.I.M. Vasile, Mechanism of keyhole formation in laser welding, Rom. Rev. Precis. Mech. Opt. Mechatronics. (2010).

[41] M. Courtois, M. Carin, P. Le Masson, S. Gaied, M. Balabane, A new approach to compute multi-reflections of laser beam in a keyhole for heat transfer and fluid flow modelling in laser welding, J. Phys. D. Appl. Phys. 46 (2013) 505305. https://doi.org/10.1088/0022-3727/46/50/505305.

[42] T. DebRoy, H.L. Wei, J.S. Zuback, T. Mukherjee, J.W. Elmer, J.O. Milewski, A.M. Beese, A. Wilson-Heid, A. De, W. Zhang, Additive manufacturing of metallic components – Process, structure and properties, Prog. Mater. Sci. 92 (2018) 112–224. https://doi.org/https://doi.org/10.1016/j.pmatsci.2017.10.001.

[43] W.E. King, A.T. Anderson, R.M. Ferencz, N.E. Hodge, C. Kamath, S.A. Khairallah, A.M. Rubenchik, Laser powder bed fusion additive manufacturing of metals; physics, computational, and materials challenges, Appl. Phys. Rev. 2 (2015) 041304. https://doi.org/10.1063/1.4937809.

[44] I. Koutiri, E. Pessard, P. Peyre, O. Amlou, T. De Terris, Influence of SLM process parameters on the surface finish, porosity rate and fatigue behavior of as-built Inconel 625 parts, J. Mater. Process. Technol. 255 (2018) 536–546. https://doi.org/https://doi.org/10.1016/j.jmatprotec.2017.12.043.

[45] Q. Jia, D. Gu, Selective laser melting additive manufacturing of Inconel 718 superalloy parts: Densification, microstructure and properties, J. Alloys Compd. 585 (2014) 713–721. https://doi.org/https://doi.org/10.1016/j.jallcom.2013.09.171.

[46] P.J. Withers, H.K.D.H. Bhadeshia, Residual stress. Part 1 – Measurement techniques, Mater. Sci. Technol. 17 (2001) 355–365. https://doi.org/10.1179/026708301101509980.

[47] B. Vrancken, Study of residual stresses in selective laser melting, (2016).

[48] P. Mercelis, J.-P. Kruth, Residual stresses in selective laser sintering and selective laser melting, Rapid Prototyp. J. 12 (2006) 254–265.

[49] X. Zhang, H. Chen, L. Xu, J. Xu, X. Ren, X. Chen, Cracking mechanism and susceptibility of laser melting deposited Inconel 738 superalloy, Mater. Des. 183 (2019) 108105.

[50] C.Y. Yap, C.K. Chua, Z.L. Dong, Z.H. Liu, D.Q. Zhang, L.E. Loh, S.L. Sing, Review of selective laser melting: Materials and applications, Appl. Phys. Rev. 2 (2015) 41101.

[51] E.P. George, S.S. Babu, S.A. David, B.B. Seth, IN-939 based superalloys with improved weldability, Proc. Balt. V (Helsinki, Finland). (2001).

[52] R.G. Thompson, S. Genculu, Microstructural evolution in the HAZ of Inconel 718 and correlation with the hot ductility test, Weld. J. 62 (1983) 337s-345s.

[53] B. Hemsworth, T. Boniszewski, N.F. Eaton, Classification and definition of high-temperature welding cracks in alloys, Met. Constr. 1 (1969) 5–16.

[54] N.E. Nissley, Intermediate temperature grain boundary embrittlement in nickel-base weld metals, (2006).

[55] K.C. Wu, R.E. Herfert, Microstructural studies of Rene 41 simulated weld heat-affected zones, Weld. J. 46 (1967) S32.

[56] W.P. Hughes, T.F. Berry, A study of the strain-age cracking characteristics in welded Rene 41: phase I., General Electric Co., Cincinnati, 1967.

[57] H.-S. Park, N.-H. Tran, A.M. Jonaet, Prediction of Temperature Distribution and Residual Stress in SLM Printed Parts, in: ASME 2018 13th Int. Manuf. Sci. Eng. Conf., American Society of Mechanical Engineers Digital Collection, 2018.

[58] S.A. David, J.M. Vitek, Correlation between solidification parameters and weld microstructures, Int. Mater. Rev. 34 (1989) 213–245.

[59] L. Nastac, D.M. Stefanescu, Prediction of the gray-to-white transition in cast iron through solidification modeling, AFS Trans. 103 (1995) 329–337.

[60] F.C. Campbell, Peritectic Alloy Systems, Phase Diagrams Underst. Basics, ASM Int. Mater. Park. Ohio. (2012).

[61] S. Kou, Welding metallurgy, New Jersey, USA. (2003) 431–446.

[62] T.M. Pollock, S. Tin, Nickel-based superalloys for advanced turbine engines: chemistry, microstructure and properties, J. Propuls. Power. 22 (2006) 361–374.

[63] V.A. Popovich, E. V Borisov, A.A. Popovich, V.S. Sufiiarov, D. V Masaylo, L. Alzina, Functionally graded Inconel 718 processed by additive manufacturing: Crystallographic texture, anisotropy of microstructure and mechanical properties, Mater. Des. 114 (2017) 441–449.

[64] L. Thijs, M.L.M. Sistiaga, R. Wauthle, Q. Xie, J.-P. Kruth, J. Van Humbeeck, Strong morphological and crystallographic texture and resulting yield strength anisotropy in selective laser melted tantalum,

Acta Mater. 61 (2013) 4657–4668.

[65] X. Liu, C. Zhao, X. Zhou, Z. Shen, W. Liu, Microstructure of selective laser melted AlSi10Mg alloy, Mater. Des. 168 (2019) 107677.

[66] M.D. Charre, The microstructure of superalloys, Clima Molybd. Co. Sym., Zurikh. (1997).

[67] M.C. Flemings, Solute Segregation, in: Encycl. Mater. Sci. Technol. (Second Ed., Elsevier, 2001: pp. 8753–8755. https://doi.org/https://doi.org/10.1016/B0-08-043152-6/01566-7.

[68] R.W. Cahn, P. Haasen, Physical metallurgy, North-Holland, Amsterdam, 1996.

[69] T.S.P. Kumar, Casting Simulation Methods, (2014).

[70] L. Zhu, Z.F. Xu, P. Liu, Y.F. Gu, Effect of processing parameters on microstructure of laser solid forming Inconel 718 superalloy, Opt. Laser Technol. 98 (2017) 409–415. https://doi.org/10.1016/j.optlastec.2017.08.027.

[71] M. Solecka, A. Kopia, A. Radziszewska, B. Rutkowski, Microstructure, microsegregation and nanohardness of CMT clad layers of Ni-base alloy on 16Mo3 steel, J. Alloys Compd. 751 (2018) 86–95.

[72] W. Rasband, ImageJ, US National Institutes of Health, Bethesda, Maryland, USA. (2009) http://rsb.info.nih.gov/ij/.

[73] A.E. Wessman, Physical Metallurgy of Rene 65, a Next-Generation Cast and Wrought Nickel Superalloy for use in Aero Engine Components, (2016).

[74] Ł. Rakoczy, O. Milkovič, B. Rutkowski, R. Cygan, M. Grudzień-Rakoczy, F. Kromka, A. Zielińska-Lipiec, Characterization of γ'Precipitates in Cast Ni-Based Superalloy and Their Behaviour at High-Homologous Temperatures Studied by TEM and in Situ XRD, Materials (Basel). 13 (2020) 2397.

[75] D. Brandon, W.D. Kaplan, Microstructural Characterization of Materials: 2nd Edition, John Wiley & Sons, 2008. https://doi.org/10.1002/9780470727133.

[76] M. Al-Jassim, Scannin Transmission Electron Microscopy, (n.d.). https://www.nrel.gov/materials-science/scanning-transmission.html (accessed February 17, 2022).

[77] L.E. Criales, Y.M. Arısoy, T. Özel, Sensitivity analysis of material and process parameters in finite element modeling of selective laser melting of Inconel 625, Int. J. Adv. Manuf. Technol. 86 (2016) 2653–2666.

[78] V. Abaqus, 6.14 Documentation, Dassault Syst. Simulia Corp. 651 (2014).

[79] M. Gouge, P. Michaleris, Thermo-mechanical modeling of additive manufacturing, Butterworth-Heinemann, 2017.

[80] Y. Wang, J. Shi, Y. Liu, Competitive grain growth and dendrite morphology evolution in selective laser

melting of Inconel 718 superalloy, J. Cryst. Growth. 521 (2019) 15–29.

[81] J.C. Lippold, Welding metallurgy and weldability, Wiley Online Library, 2015.

[82] J.H. Robinson, I.R.T. Ashton, E. Jones, P. Fox, C. Sutcliffe, The effect of hatch angle rotation on parts manufactured using selective laser melting, Rapid Prototyp. J. (2019).

[83] V.D. Divya, R. Muñoz-Moreno, O. Messé, J.S. Barnard, S. Baker, T. Illston, H.J. Stone, Microstructure of selective laser melted CM247LC nickel-based superalloy and its evolution through heat treatment, Mater. Charact. 114 (2016) 62–74.

[84] J. Li, H.M. Wang, H.B. Tang, Effect of heat treatment on microstructure and mechanical properties of laser melting deposited Ni-base superalloy Rene′ 41, Mater. Sci. Eng. A. 550 (2012) 97–102.

[85] A.E. Wilson-Heid, A.M. Beese, Fracture of laser powder bed fusion additively manufactured Ti–6Al–4V under multiaxial loading: Calibration and comparison of fracture models, Mater. Sci. Eng. A. 761 (2019) 137967.

[86] J. Chen, R. Cao, Micromechanism of cleavage fracture of metals: a comprehensive microphysical model for cleavage cracking in metals, Butterworth-Heinemann, 2015.

[87] X. Zhang, J. Wen, X. Zhang, X. Wang, S. Tu, Effects of the stress state on plastic deformation and ductile failure: Experiment and numerical simulation using a newly designed tension-shear specimen, Fatigue Fract. Eng. Mater. Struct. 42 (2019) 2079–2092.

[88] Q. Chen, X. Liang, D. Hayduke, J. Liu, L. Cheng, J. Oskin, R. Whitmore, A.C. To, An inherent strain based multiscale modeling framework for simulating part-scale residual deformation for direct metal laser sintering, Addit. Manuf. 28 (2019) 406–418.

[89] N.E. Hodge, R.M. Ferencz, R.M. Vignes, Experimental comparison of residual stresses for a thermomechanical model for the simulation of selective laser melting, Addit. Manuf. 12 (2016) 159–168.

[90] F. Matsuda, H. Nakagawa, K. Sorada, Dynamic observation of solidification and solidification cracking during welding with optical microscope (I): Solidification front and behavior of cracking (materials, metallurgy & weldability), Trans. JWRI. 11 (1982) 67–77.

[91] F. Matsuda, Solidification crack susceptibility of weld metal, in: Recent Trends Weld. Sci. Technol., ASM International Metals Park, OH, 1990: pp. 127–136.

[92] B. Santillana, R. Boom, D. Eskin, H. Mizukami, M. Hanao, M. Kawamoto, High-temperature mechanical behavior and fracture analysis of a low-carbon steel related to cracking, Metall. Mater. Trans. A. 43 (2012) 5048–5057.

[93] D.G. Eskin, L. Katgerman, Mechanical properties in the semi-solid state and hot tearing of aluminium alloys, Prog. Mater. Sci. 49 (2004) 629–711.

[94] K. Hansson, On the hot crack formation during solidification of iron-base alloys., (2001).

[95] J.A. Dantzig, M. Rappaz, Dendritic Growth, in: Solidification, EPFL Press, 2009: pp. 287–342.

[96] L.N. Carter, M.M. Attallah, R.C. Reed, Laser powder bed fabrication of nickel-base superalloys: influence of parameters; characterisation, quantification and mitigation of cracking, Superalloys. 2012 (2012) 577–586.

[97] Y. Chen, K. Zhang, J. Huang, S.R.E. Hosseini, Z. Li, Characterization of heat affected zone liquation cracking in laser additive manufacturing of Inconel 718, Mater. Des. 90 (2016) 586–594.

[98] L. Rickenbacher, T. Etter, S. Hövel, K. Wegener, High temperature material properties of IN738LC processed by selective laser melting (SLM) technology, Rapid Prototyp. J. (2013).

[99] O. Messé, R. Muñoz-Moreno, T. Illston, S. Baker, H.J. Stone, Metastable carbides and their impact on recrystallisation in IN738LC processed by selective laser melting, Addit. Manuf. 22 (2018) 394–404.

[100] L.A. Aucott, Mechanism of solidification cracking during welding of high strength steels for subsea linepipe, (2015).

[101] F.N. Rhines, P.J. Wray, Investigation of the intermediate temperature ductility minimum in metals, ASM TRANS Q. 54 (1961) 117–128.

[102] S. Yamaguchi, H. Kobayashi, T. Matsumiya, S. Hayami, Effect of minor elements on hot workability of nickel-base superalloys, Met. Technol. 6 (1979) 170–175.

[103] Y.-C. Zhang, H. Nakagaw, R. Matsuda, Weldability of Fe-36% Ni alloy (Report V), Trans. JWRI. 14 (1985) 119–124.

[104] A.J. Ramirez, J.C. Lippold, New insight into the mechanism of ductility-dip cracking in Ni-base weld metals, in: Hot Crack. Phenom. Welds, Springer, 2005: pp. 19–41.

[105] F.F. Noecker, J.N. DuPont, Metallurgical investigation into ductility dip cracking in Ni-based alloys: Part II, Weld. J. 88 (2009) 62s-77s.

[106] G.A. Young, T.E. Capobianco, M.A. Penik, B.W. Morris, J.J. McGee, The mechanism of ductility dip cracking in nickel-chromium alloys, Weld. JOURNAL-NEW YORK-. 87 (2008) 31.

[107] J.H. Boswell, D. Clark, W. Li, M.M. Attallah, Cracking during thermal post-processing of laser powder bed fabricated CM247LC Ni-superalloy, Mater. Des. 174 (2019) 107793.

[108] T. Watanabe, Grain boundary sliding and stress concentration during creep, Metall. Trans. A. 14 (1983) 531–545.

[109] D. Qian, J. Xue, A. Zhang, Y. Li, N. Tamura, Z. Song, K. Chen, Statistical study of ductility-dip cracking induced plastic deformation in polycrystalline laser 3D printed Ni-based superalloy, Sci. Rep. 7 (2017) 1–9.

[110] M. Prager, C.S. Shira, Welding of precipitation-hardening nickel- base alloys(Welding precipitation hardenable Ni base alloys noting heat treatment, microfissuring, strain age cracking and other

intricacies), Weld. Res. Counc. Bull. (1968).

[111] A.S. Shaikh, Development of γ'Precipitation Hardening Ni-Base Superalloy for Additive Manufacturing, (2018).

[112] T.F. Berry, W.P. Hughes, A study of the strain-age cracking characteristics in welded Rene 41. II(Postweld heating cycle for circular patch test to predict strain age cracking susceptibility in welded Rene 41), Weld. JOURNAL, Res. Suppl. 48 (1969).

[113] S. Kou, Welding Metallurgy, 1987, A Wiley-Interscience Publ. New York. (n.d.) 29–59.

[114] L.N. Carter, C. Martin, P.J. Withers, M.M. Attallah, The influence of the laser scan strategy on grain structure and cracking behaviour in SLM powder-bed fabricated nickel superalloy, J. Alloys Compd. 615 (2014) 338–347.

[115] R. Engeli, T. Etter, S. Hoevel, K. Wegener, Processability of different IN738LC powder batches by selective laser melting, J. Mater. Process. Technol. 229 (2016) 484–491.

[116] X. Wang, L.N. Carter, B. Pang, M.M. Attallah, M.H. Loretto, Microstructure and yield strength of SLM-fabricated CM247LC Ni-Superalloy, Acta Mater. 128 (2017) 87–95.

[117] Z. Li, R. Xu, Z. Zhang, I. Kucukkoc, The influence of scan length on fabricating thin-walled components in selective laser melting, Int. J. Mach. Tools Manuf. 126 (2018) 1–12.

[118] L.A. Parry, I.A. Ashcroft, R.D. Wildman, Geometrical effects on residual stress in selective laser melting, Addit. Manuf. 25 (2019) 166–175.

[119] A. Ahmed, A. Majeed, Z. Atta, G. Jia, Dimensional Quality and Distortion Analysis of Thin-Walled Alloy Parts of AlSi10Mg Manufactured by Selective Laser Melting, J. Manuf. Mater. Process. . 3 (2019). https://doi.org/10.3390/jmmp3020051.

[120] Z. Wu, S.P. Narra, A. Rollett, Exploring the fabrication limits of thin-wall structures in a laser powder bed fusion process, Int. J. Adv. Manuf. Technol. 110 (2020) 191–207.

[121] J. Jiang, X. Xu, J. Stringer, Support structures for additive manufacturing: a review, J. Manuf. Mater. Process. 2 (2018) 64.

[122] Y.S. Lee, M.M. Kirka, S. Kim, N. Sridharan, A. Okello, R.R. Dehoff, S.S. Babu, Asymmetric Cracking in Mar-M247 Alloy Builds During Electron Beam Powder Bed Fusion Additive Manufacturing, Metall. Mater. Trans. A. 49 (2018) 5065–5079. https://doi.org/10.1007/s11661-018-4788-8.

[123] D. Lemarchand, E. Cadel, S. Chambreland, D. Blavette, Investigation of grain-boundary structure-segregation relationship in an N18 nickel-based superalloy, Philos. Mag. A. 82 (2002) 1651–1669. https://doi.org/10.1080/01418610208235682.

[124] G.H. Gulliver, The quantitative effect of rapid cooling upon the constitution of binary alloys, J. Inst. Met. 9 (1913) 120–157.

[125] E. Scheil, Remarks on the crystal layer formation, Z. Met. 34 (1942) 70.

[126] M.C. MC FLEMINGS, D.R. Poirier, R.V.B. RV, Microsegregation in iron-base alloys, in: J Iron Steel Inst, 1970: pp. 371–381.

[127] B. Cheng, S. Shrestha, K. Chou, Stress and deformation evaluations of scanning strategy effect in selective laser melting, Addit. Manuf. 12 (2016). https://doi.org/10.1016/j.addma.2016.05.007.

[128] S. Catchpole-Smith, N. Aboulkhair, L. Parry, C. Tuck, I.A. Ashcroft, A. Clare, Fractal scan strategies for selective laser melting of 'unweldable' nickel superalloys, Addit. Manuf. 15 (2017). https://doi.org/10.1016/j.addma.2017.02.002.

[129] T. Pereira, J. V Kennedy, J. Potgieter, A comparison of traditional manufacturing vs additive manufacturing, the best method for the job, Procedia Manuf. 30 (2019) 11–18.

[130] J.J. Lewandowski, M. Seifi, Metal additive manufacturing: a review of mechanical properties, Annu. Rev. Mater. Res. 46 (2016) 151–186.

[131] N. Eftekhari, W. Muhammad, F. Haftlang, A. Zarei-Hanzaki, É. Martin, Microstructural evolution and corrosion behavior of Sanicro 28 during thermomechanical processing, Mater. Today Commun. (2020) 101228.

[132] J.-C. Stinville, E. Martin, M. Karadge, S. Ismonov, M. Soare, T. Hanlon, S. Sundaram, M.P. Echlin, P.G. Callahan, W.C. Lenthe, Competing modes for crack initiation from non-metallic inclusions and intrinsic microstructural features during fatigue in a polycrystalline nickel-based superalloy, Metall. Mater. Trans. A. 49 (2018) 3865–3873.

[133] J.C. Stinville, E. Martin, M. Karadge, S. Ismonov, M. Soare, T. Hanlon, S. Sundaram, M.P. Echlin, P.G. Callahan, W.C. Lenthe, Fatigue deformation in a polycrystalline nickel base superalloy at intermediate and high temperature: Competing failure modes, Acta Mater. 152 (2018) 16–33.

[134] A. Thatte, E. Martin, T. Hanlon, A Novel Experimental Method for LCF Measurement of Nickel Base Super Alloys in High Pressure High Temperature Supercritical CO2, in: Turbo Expo Power Land, Sea, Air, American Society of Mechanical Engineers, 2017: p. V009T38A030.

[135] A. Thatte, A. Loghin, E. Martin, V. Dheeradhada, Y. Shin, B. Ananthasayanam, Multi-Scale Coupled Physics Models and Experiments for Performance and Life Prediction of Supercritical CO2 Turbomachinery Components, in: 5th Int. Symp., 2016.

[136] B. Ahuja, A. Schaub, M. Karg, M. Lechner, M. Merklein, M. Schmidt, Developing LBM process parameters for Ti-6Al-4V thin wall structures and determining the corresponding mechanical characteristics, Phys. Procedia. 56 (2014) 90–98.

[137] T. Yang, D. Xie, W. Yue, S. Wang, P. Rong, L. Shen, J. Zhao, C. Wang, Distortion of Thin-Walled Structure Fabricated by Selective Laser Melting Based on Assumption of Constraining Force-Induced Distortion, Metals (Basel). 9 (2019) 1281.

[138] A. Vasinonta, J.L. Beuth, M. Griffith, Process maps for predicting residual stress and melt pool size in

the laser-based fabrication of thin-walled structures, (2007).

[139] P. Kontis, E. Chauvet, Z. Peng, J. He, A.K. da Silva, D. Raabe, C. Tassin, J.-J. Blandin, S. Abed, R. Dendievel, Atomic-scale grain boundary engineering to overcome hot-cracking in additively-manufactured superalloys, Acta Mater. 177 (2019) 209–221.

[140] B. Brown, W. Everhart, J. Dinardo, Characterization of bulk to thin wall mechanical response transition in powder bed AM, Rapid Prototyp. J. (2016).

[141] Y. Yang, M. Allen, T. London, V. Oancea, Residual strain predictions for a powder bed fusion Inconel 625 single cantilever part, Integr. Mater. Manuf. Innov. 8 (2019) 294–304.

[142] D. Xie, J. Zhao, H. Liang, Z. Tian, L. Shen, M. Xiao, M.N. Ahsan, C. Wang, Assumption of constraining force to explain distortion in laser additive manufacturing, Materials (Basel). 11 (2018) 2327.

[143] Y.P. Yang, M. Jamshidinia, P. Boulware, S.M. Kelly, Prediction of microstructure, residual stress, and deformation in laser powder bed fusion process, Comput. Mech. 61 (2018) 599–615.

[144] E.R. Denlinger, P. Michaleris, Effect of stress relaxation on distortion in additive manufacturing process modeling, Addit. Manuf. 12 (2016) 51–59.

[145] K. An, L. Yuan, L. Dial, I. Spinelli, A.D. Stoica, Y. Gao, Neutron residual stress measurement and numerical modeling in a curved thin-walled structure by laser powder bed fusion additive manufacturing, Mater. Des. 135 (2017) 122–132.

[146] Q. Zhang, J. Xie, Z. Gao, T. London, D. Griffiths, V. Oancea, A metallurgical phase transformation framework applied to SLM additive manufacturing processes, Mater. Des. 166 (2019) 107618.

[147] Q. Zhang, J. Xie, T. London, D. Griffiths, I. Bhamji, V. Oancea, Estimates of the mechanical properties of laser powder bed fusion Ti-6Al-4V parts using finite element models, Mater. Des. 169 (2019) 107678.

[148] S.P. Murray, K.M. Pusch, A.T. Polonsky, C.J. Torbet, G.G.E. Seward, N. Zhou, S.A.J. Forsik, P. Nandwana, M.M. Kirka, R.R. Dehoff, A defect-resistant Co–Ni superalloy for 3D printing, Nat. Commun. 11 (2020) 1–11.

[149] D. Wang, S. Wu, F. Fu, S. Mai, Y. Yang, Y. Liu, C. Song, Mechanisms and characteristics of spatter generation in SLM processing and its effect on the properties, Mater. Des. 117 (2017) 121–130.

[150] R. Casati, J. Lemke, M. Vedani, Microstructure and fracture behavior of 316L austenitic stainless steel produced by selective laser melting, J. Mater. Sci. Technol. 32 (2016) 738–744.

[151] A. Pineau, A.A. Benzerga, T. Pardoen, Failure of metals I: Brittle and ductile fracture, Acta Mater. 107 (2016) 424–483.

[152] L.E. Murr, Frontiers of 3D printing/additive manufacturing: from human organs to aircraft fabrication, J. Mater. Sci. Technol. 32 (2016) 987–995.

[153] I. Yadroitsev, I. Smurov, Selective laser melting technology: from the single laser melted track stability to 3D parts of complex shape, Phys. Procedia. 5 (2010) 551–560.

[154] B. Song, X. Zhao, S. Li, C. Han, Q. Wei, S. Wen, J. Liu, Y. Shi, Differences in microstructure and properties between selective laser melting and traditional manufacturing for fabrication of metal parts: A review, Front. Mech. Eng. 10 (2015) 111–125.

[155] Z. Liu, Economic comparison of selective laser melting and conventional subtractive manufacturing processes, (2017).

[156] H. Yang, J. Yang, W. Huang, Z. Wang, X. Zeng, The printability, microstructure, crystallographic features and microhardness of selective laser melted Inconel 718 thin wall, Mater. Des. 156 (2018) 407–418.

[157] C. Qiu, H. Chen, Q. Liu, S. Yue, H. Wang, On the solidification behaviour and cracking origin of a nickel-based superalloy during selective laser melting, Mater. Charact. 148 (2019) 330–344.

[158] A. Chakraborty, R. Tangestani, R. Batmaz, W. Muhammad, P. Plamondon, A. Wessman, L. Yuan, É. Martin, In-process failure analysis of thin-wall structures made by laser powder bed fusion additive manufacturing, J. Mater. Sci. Technol. 98 (2022) 233–243. https://doi.org/10.1016/j.jmst.2021.05.017.

[159] J. Robinson, M. Stanford, A. Arjunan, Stable formation of powder bed laser fused 99.9% silver, Mater. Today Commun. 24 (2020) 101195.

[160] T. Mukherjee, J.S. Zuback, A. De, T. DebRoy, Printability of alloys for additive manufacturing, Sci. Rep. 6 (2016) 1–8.

[161] K.A. Mumtaz, N. Hopkinson, Selective laser melting of thin wall parts using pulse shaping, J. Mater. Process. Technol. 210 (2010) 279–287.

[162] P. Moghimian, T. Poirié, M. Habibnejad-Korayem, J.A. Zavala, J. Kroeger, F. Marion, F. Larouche, Metal Powders in Additive Manufacturing: A Review on Reusability and Recyclability of Common Titanium, Nickel and Aluminum Alloys, Addit. Manuf. (2021) 102017.

[163] National Institutes of Health, Analyze Menu, (2017). https://imagej.nih.gov/ij/docs/menus/analyze.html (accessed March 3, 2021).

[164] J.N. Ghoussoub, Y.T. Tang, C. Panwisawas, A. Németh, R.C. Reed, On the influence of alloy chemistry and processing conditions on additive manufacturability of Ni-based superalloys, in: Superalloys 2020, Springer, 2020: pp. 153–162.

[165] J.J. Blecher, T.A. Palmer, T. DebRoy, Solidification map of a nickel-base alloy, Metall. Mater. Trans. A. 45 (2014) 2142–2151.

[166] A.S. Sabau, L. Yuan, N. Raghavan, M. Bement, S. Simunovic, J.A. Turner, V.K. Gupta, Fluid Dynamics Effects on Microstructure Prediction in Single-Laser Tracks for Additive Manufacturing of IN625, Metall. Mater. Trans. B. (2020) 1–19.

[167] J. Irwin, P. Michaleris, A line heat input model for additive manufacturing, J. Manuf. Sci. Eng. 138 (2016).

[168] C. Li, M.F. Gouge, E.R. Denlinger, J.E. Irwin, P. Michaleris, Estimation of part-to-powder heat losses as surface convection in laser powder bed fusion, Addit. Manuf. 26 (2019) 258–269.

[169] E. Martin, A. Natarajan, S. Kottilingam, R. Batmaz, Binder jetting of "Hard-to-Weld" high gamma prime nickel-based superalloy RENÉ 108, Addit. Manuf. 39 (2021) 101894.

[170] R.D. Kissinger, Cooling path dependent behavior of a supersolvus heat treated nickel base superalloy, Superalloys. 1996 (1996) 687e95.

[171] S. Liu, H. Zhu, G. Peng, J. Yin, X. Zeng, Microstructure prediction of selective laser melting AlSi10Mg using finite element analysis, Mater. Des. 142 (2018) 319–328.

[172] R. Tangestani, T. Sabiston, A. Chakraborty, W. Muhammad, L. Yuan, É. Martin, An Efficient Track-Scale Model for Laser Powder Bed Fusion Additive Manufacturing: Part 1- Thermal Model, Front. Mater. 8 (2021). https://doi.org/10.3389/fmats.2021.753040.

[173] R. Tangestani, T. Sabiston, A. Chakraborty, L. Yuan, N. Krutz, É. Martin, An Efficient Track-Scale Model for Laser Powder Bed Fusion Additive Manufacturing: Part 2—Mechanical Model, Front. Mater. 8 (2021). https://doi.org/10.3389/fmats.2021.759669.

[174] S.S. Sih, J.W. Barlow, The prediction of the emissivity and thermal conductivity of powder beds, Part. Sci. Technol. 22 (2004) 427–440.

[175] A. Hariharan, L. Lu, J. Risse, A. Kostka, B. Gault, E.A. Jägle, D. Raabe, Misorientation-dependent solute enrichment at interfaces and its contribution to defect formation mechanisms during laser additive manufacturing of superalloys, Phys. Rev. Mater. 3 (2019) 123602.

[176] M. Rappaz, A. Jacot, W.J. Boettinger, Last-stage solidification of alloys: theoretical model of dendrite-arm and grain coalescence, Metall. Mater. Trans. A. 34 (2003) 467–479.

[177] A.J. Ramirez, J.C. Lippold, High temperature behavior of Ni-base weld metal: Part II–Insight into the mechanism for ductility dip cracking, Mater. Sci. Eng. A. 380 (2004) 245–258.

[178] S. Kou, Solidification and liquation cracking issues in welding, Jom. 55 (2003) 37–42.

[179] M. Moattari, M.M. Shokrieh, H. Moshayedi, H. Kazempour-Liasi, Evaluations of residual stresses in repair welding of Ni-based IN939 superalloy, J. Therm. Stress. 43 (2020) 801–815.

[180] D. Mohr, S. Henn, Calibration of stress-triaxiality dependent crack formation criteria: a new hybrid experimental–numerical method, Exp. Mech. 47 (2007) 805–820.

[181] S. Thompson, Effect of cooling rate on solidification characteristics of aluminum alloys A356 and AA5182, (2003).

[182] J.W. Elmer, The influence of cooling rate on the microstructure of stainless steel alloys, Lawrence

Livermore National Lab., CA (USA), 1988.

[183] M. Majeed, H.M. Khan, I. Rasheed, Finite element analysis of melt pool thermal characteristics with passing laser in SLM process, Optik (Stuttg). 194 (2019) 163068.

[184] D. Dai, D. Gu, Thermal behavior and densification mechanism during selective laser melting of copper matrix composites: Simulation and experiments, Mater. Des. 55 (2014) 482–491.

[185] J.L. Bartlett, X. Li, An overview of residual stresses in metal powder bed fusion, Addit. Manuf. 27 (2019) 131–149.

[186] W. Guo, C.H. Wang, L.R.F. Rose, The influence of cross-sectional thickness on fatigue crack growth, Fatigue Fract. Eng. Mater. Struct. 22 (1999) 437–444.

[187] A. Kotousov, C.H. Wang, Fundamental solutions for the generalised plane strain theory, Int. J. Eng. Sci. 40 (2002) 1775–1790.

[188] H.L. Wei, J. Mazumder, T. DebRoy, Evolution of solidification texture during additive manufacturing, Sci. Rep. 5 (2015) 1–7.

[189] H.L. Wei, G.L. Knapp, T. Mukherjee, T. DebRoy, Three-dimensional grain growth during multi-layer printing of a nickel-based alloy Inconel 718, Addit. Manuf. 25 (2019) 448–459.

[190] J.D. Hunt, Steady state columnar and equiaxed growth of dendrites and eutectic, Mater. Sci. Eng. 65 (1984) 75–83.

[191] W. 1 Kurz, B. Giovanola, R. Trivedi, Theory of microstructural development during rapid solidification, Acta Metall. 34 (1986) 823–830.

[192] L. YD, K. Hansson, H. Fredriksson, Influence of cooling rate on the hot cracking formation of nickel rich alloys, ISIJ Int. 42 (2002) 512–519.

[193] B. Blakey-Milner, P. Gradl, G. Snedden, M. Brooks, J. Pitot, E. Lopez, M. Leary, F. Berto, A. du Plessis, Metal additive manufacturing in aerospace: A review, Mater. Des. 209 (2021) 110008.

[194] J.N. Ghoussoub, Y.T. Tang, W.J.B. Dick-Cleland, A.A.N. Németh, Y. Gong, D.G. McCartney, A.C.F. Cocks, R.C. Reed, On the influence of alloy composition on the additive manufacturability of Ni-based superalloys, ArXiv Prepr. ArXiv2109.15274. (2021).

[195] A. Chakraborty, R. Tangestani, T. Sabiston, N. Krutz, L. Yuan, E. Martin, Effect of build height on micro-cracking of additively manufactured superalloy RENÉ 108 thin-wall components, in: TMS 2022 Annu. Meet. Exhib., Anaheim, California, USA, 2022.

[196] Y.T. Tang, C. Panwisawas, J.N. Ghoussoub, Y. Gong, J.W.G. Clark, A.A.N. Németh, D.G. McCartney, R.C. Reed, Alloys-by-design: Application to new superalloys for additive manufacturing, Acta Mater. 202 (2021) 417–436.

[197] A. Chakraborty, R. Tangestani, W. Muhammad, T. Sabiston, J.P. Masse, R. Batmaz, A. Wessman, É.

Martin, Micro-cracking mechanism of RENÉ 108 thin-wall components built by laser powder bed fusion additive manufacturing, Mater. Today Commun. 30 (2022). https://doi.org/10.1016/j.mtcomm.2022.103139.

[198] G.N. Lewis, M. Randall, K.S. Pitzer, L. Brewer, Thermodynamics, Courier Dover Publications, 2020.

[199] E. Scheil, Bemerkungen zur Schichtkristallbildung, Int. J. Mater. Res. 34 (1942) 70–72. https://doi.org/10.1515/IJMR-1942-340303.

[200] M. Mostafaei, S.M. Abbasi, Solutioning and solidification process control in Ta-modified CM247 LC superalloy, J. Mater. Process. Technol. 231 (2016) 113–124.

[201] R. Przeliorz, F. Binczyk, P. Gradoń, M. Góral, T. Mikuszewski, Evaluation of Heat Capacity and Resistance to Cyclic Oxidation of Nickel Superalloys, Arch. Foundry Eng. 14 (2014).

[202] A.J. Torroba, O. Koeser, L. Calba, L. Maestro, E. Carreño-Morelli, M. Rahimian, S. Milenkovic, I. Sabirov, J. LLorca, Investment casting of nozzle guide vanes from nickel-based superalloys: part I–thermal calibration and porosity prediction, Integr. Mater. Manuf. Innov. 3 (2014) 344–368.

[203] T.P. Gabb, J. Gayda, P.T. Kantzos, T. Biles, W. Konkel, The tensile properties of advanced nickel-base disk superalloys during quenching heat treatments, in: 2001 Fall Meet., 2001.

[204] S.T. Wlodek, M. Kelly, D.A. Alden, The structure of Rene 88 DT, Superalloys. 1996 (1996) 129–136.

[205] A.P. Gordon, M.D. Trexler, R.W. Neu, T.J. Sanders Jr, D.L. McDowell, Corrosion kinetics of a directionally solidified Ni-base superalloy, Acta Mater. 55 (2007) 3375–3385.

[206] W.G. Fahrenholtz, G.E. Hilmas, I.G. Talmy, J.A. Zaykoski, Refractory diborides of zirconium and hafnium, J. Am. Ceram. Soc. 90 (2007) 1347–1364.

[207] E. Paccou, M. Mokhtari, C. Keller, J. Nguejio, W. Lefebvre, X. Sauvage, S. Boileau, P. Babillot, P. Bernard, E. Bauster, Investigations of powder reusing on microstructure and mechanical properties of Inconel 718 obtained by additive manufacturing, Mater. Sci. Eng. A. 828 (2021) 142113.

[208] E.L. Courtright, J.T. Prater, G.R. Holcomb, G.R. St Pierre, R.A. Rapp, Oxidation of hafnium carbide and hafnium carbide with additions of tantalum and praseodymium, Oxid. Met. 36 (1991) 423–437.

[209] S. Singh Handa, Precipitation of Carbides in a Ni-based Superalloy, (2014).

[210] T. Azimzadegan, S.A.A.A. Mousavi, Investigation of the occurrence of hot cracking in pulsed Nd-YAG laser welding of Hastelloy-X by numerical and microstructure studies, J. Manuf. Process. 44 (2019) 226–240.

[211] Z. Chen, Y. Xiong, H. Qiu, G. Lin, Z. Li, Stress intensity factor-based prediction of solidification crack growth during welding of high strength steel, J. Mater. Process. Technol. 252 (2018) 270–278.

[212] D. Grange, J.D. Bartout, B. Macquaire, C. Colin, Processing a non-weldable nickel-base superalloy by Selective Laser Melting: role of the shape and size of the melt pools on solidification cracking,

Materialia. 12 (2020) 100686.

[213] T. Wojcik, M. Rath, E. Kozeschnik, Characterisation of secondary phases in Ni-base superalloy Rene 65, Mater. Sci. Technol. 34 (2018) 1558–1564.

[214] M. Cloots, P.J. Uggowitzer, K. Wegener, Investigations on the microstructure and crack formation of IN738LC samples processed by selective laser melting using Gaussian and doughnut profiles, Mater. Des. 89 (2016) 770–784.

[215] A.A.N. Németh, D.J. Crudden, D.E.J. Armstrong, D.M. Collins, K. Li, A.J. Wilkinson, C.R.M. Grovenor, R.C. Reed, Environmentally-assisted grain boundary attack as a mechanism of embrittlement in a nickel-based superalloy, Acta Mater. 126 (2017) 361–371.

[216] L. Zheng, G. Zhang, T.L. Lee, M.J. Gorley, Y. Wang, C. Xiao, Z. Li, The effects of Ta on the stress rupture properties and microstructural stability of a novel Ni-base superalloy for land-based high temperature applications, Mater. Des. 61 (2014) 61–69.

[217] O.A. Ojo, N.L. Richards, M.C. Chaturvedi, Liquation of various phases in HAZ during welding of cast Inconel* 738LC, Mater. Sci. Technol. 20 (2004) 1027–1034.

[218] R. Liu, Z. Wang, T. Sparks, F. Liou, J. Newkirk, Aerospace applications of laser additive manufacturing, in: Laser Addit. Manuf., Elsevier, 2017: pp. 351–371.

[219] J. Delgado, J. Ciurana, C.A. Rodríguez, Influence of process parameters on part quality and mechanical properties for DMLS and SLM with iron-based materials, Int. J. Adv. Manuf. Technol. 60 (2012) 601–610.

[220] A.J. Dunbar, E.R. Denlinger, J. Heigel, P. Michaleris, P. Guerrier, R. Martukanitz, T.W. Simpson, Development of experimental method for in situ distortion and temperature measurements during the laser powder bed fusion additive manufacturing process, Addit. Manuf. 12 (2016) 25–30.

# Appendix

## CLI Code for Sample Thin-Wall Part

$$HEADERSTART

$$ASCII

$$UNITS/00000000.005000

$$VERSION/200

$$LABEL/1,part1

$$DATE/260820

$$LAYERS/000752

$$HEADEREND

$$GEOMETRYSTART

$$LAYER/0.0

$$HATCHES/1,6,-6435.28613,9839.15918,-4383.16455,4201.00195,-4366.23828,4207.12451,-6418.35938,9845.28125,-6401.43311,9851.40527,-4349.31104,4213.24707,-4332.38428,4219.37012,-6384.50586,9857.52734,-6367.57910,9863.64941,-4315.45752,4225.49219,-4298.53125,4231.61523,-6350.65234,9869.77148

$$LAYER/8.0

$$HATCHES/1,6,-6435.28613,9839.15918,-4383.16455,4201.00195,-4366.23828,4207.12451,-6418.35938,9845.28125,-6401.43311,9851.40527,-4349.31104,4213.24707,-4332.38428,4219.37012,-6384.50586,9857.52734,-6367.57910,9863.64941,-4315.45752,4225.49219,-4298.53125,4231.61523,-6350.65234,9869.77148

$$LAYER/16.0

$$HATCHES/1,6,-6435.28613,9839.15918,-4383.16455,4201.00195,-4366.23828,4207.12451,-6418.35938,9845.28027,-6401.43213,9851.40430,-4349.31104,4213.24707,-4332.38428,4219.37012,-

6384.50537,9857.52637,-6367.57861,9863.64844,-4315.45752,4225.49219,-4298.53125,4231.61523,-6350.65186,9869.77148

$$LAYER/24.0

$$HATCHES/1,6,-6435.28613,9839.15918,-4383.16455,4201.00195,-4366.23828,4207.12451,-6418.35938,9845.28027,-6401.43213,9851.40430,-4349.31104,4213.24707,-4332.38428,4219.37012,-6384.50537,9857.52637,-6367.57861,9863.64844,-4315.45752,4225.49219,-4298.53125,4231.61523,-6350.65186,9869.77148

$$LAYER/32.0

$$HATCHES/1,6,-6435.28613,9839.15918,-4383.16455,4201.00195,-4366.23828,4207.12451,-6418.35938,9845.28027,-6401.43213,9851.40430,-4349.31104,4213.24707,-4332.38428,4219.37012,-6384.50537,9857.52637,-6367.57861,9863.64844,-4315.45752,4225.49219,-4298.53125,4231.61523,-6350.65186,9869.77148

$$LAYER/40.0

$$HATCHES/1,6,-6435.28613,9839.15918,-4383.16455,4201.00195,-4366.23828,4207.12451,-6418.35938,9845.28027,-6401.43213,9851.40430,-4349.31104,4213.24707,-4332.38428,4219.37012,-6384.50537,9857.52637,-6367.57861,9863.64844,-4315.45752,4225.49219,-4298.53125,4231.61523,-6350.65186,9869.77148

$$LAYER/48.0

$$HATCHES/1,6,-6435.28613,9839.15918,-4383.16455,4201.00195,-4366.23828,4207.12451,-6418.35938,9845.28027,-6401.43213,9851.40430,-4349.31104,4213.24707,-4332.38428,4219.37012,-6384.50537,9857.52637,-6367.57861,9863.64844,-4315.45752,4225.49219,-4298.53125,4231.61523,-6350.65186,9869.77148

$$LAYER/56.0

$$HATCHES/1,6,-6435.28760,9839.16309,-4383.16455,4201.00195,-4366.23828,4207.12451,-6418.36084,9845.28516,-6401.43359,9851.40820,-4349.31104,4213.24707,-4332.38428,4219.37012,-6384.50684,9857.52930,-6367.57959,9863.65039,-4315.45752,4225.49219,-4298.53125,4231.61523,-6350.65234,9869.77246

$$LAYER/64.0

$$HATCHES/1,6,-6435.28613,9839.15918,-4383.16455,4201.00195,-4366.23828,4207.12451,-6418.35938,9845.28027,-6401.43213,9851.40430,-4349.31104,4213.24707,-4332.38428,4219.37012,-6384.50537,9857.52637,-6367.57861,9863.64844,-4315.45752,4225.49219,-4298.53125,4231.61523,-6350.65186,9869.77148

$$LAYER/72.0

$$HATCHES/1,6,-6435.28613,9839.15918,-4383.16455,4201.00195,-4366.23828,4207.12451,-6418.35938,9845.28027,-6401.43213,9851.40430,-4349.31104,4213.24707,-4332.38428,4219.37012,-6384.50537,9857.52637,-6367.57861,9863.64844,-4315.45752,4225.49219,-4298.53125,4231.61523,-6350.65186,9869.77148

$$LAYER/80.0

$$HATCHES/1,6,-6435.28613,9839.15918,-4383.16455,4201.00195,-4366.23828,4207.12451,-6418.35938,9845.28027,-6401.43213,9851.40430,-4349.31104,4213.24707,-4332.38428,4219.37012,-6384.50537,9857.52637,-6367.57861,9863.64844,-4315.45752,4225.49219,-4298.53125,4231.61523,-6350.65186,9869.77148

$$LAYER/88.0

$$HATCHES/1,6,-6435.28613,9839.15918,-4383.16455,4201.00195,-4366.23828,4207.12451,-6418.35938,9845.28027,-6401.43213,9851.40430,-4349.31104,4213.24707,-4332.38428,4219.37012,-6384.50537,9857.52637,-6367.57861,9863.64844,-4315.45752,4225.49219,-4298.53125,4231.61523,-6350.65186,9869.77148

$$LAYER/96.0

$$HATCHES/1,6,-6435.28613,9839.15918,-4383.16455,4201.00195,-4366.23828,4207.12451,-6418.35938,9845.28027,-6401.43213,9851.40430,-4349.31104,4213.24707,-4332.38428,4219.37012,-6384.50537,9857.52637,-6367.57861,9863.64844,-4315.45752,4225.49219,-4298.53125,4231.61523,-6350.65186,9869.77148

$$LAYER/104.0

$$HATCHES/1,6,-6435.28613,9839.15918,-4383.16455,4201.00195,-4366.23828,4207.12451,-6418.35938,9845.28027,-6401.43213,9851.40430,-4349.31104,4213.24707,-4332.38428,4219.37012,-6384.50537,9857.52637,-6367.57861,9863.64844,-4315.45752,4225.49219,-4298.53125,4231.61523,-6350.65186,9869.77148

$$LAYER/112.0

$$HATCHES/1,6,-6435.28906,9839.16895,-4383.16455,4201.00195,-4366.23828,4207.12451,-6418.36279,9845.28906,-6401.43457,9851.41016,-4349.31104,4213.24707,-4332.38428,4219.37012,-6384.50732,9857.53027,-6367.57959,9863.65039,-4315.45752,4225.49219,-4298.53125,4231.61523,-6350.65186,9869.77051

$$LAYER/120.0

$$HATCHES/1,6,-6435.28613,9839.15918,-4383.16455,4201.00195,-4366.23828,4207.12451,-6418.35938,9845.28027,-6401.43213,9851.40430,-4349.31104,4213.24707,-4332.38428,4219.37012,-6384.50537,9857.52637,-6367.57861,9863.64844,-4315.45752,4225.49219,-4298.53125,4231.61523,-6350.65186,9869.77148

$$LAYER/128.0

$$HATCHES/1,6,-6435.28613,9839.15918,-4383.16455,4201.00195,-4366.23828,4207.12451,-6418.35938,9845.28027,-6401.43213,9851.40430,-4349.31104,4213.24707,-4332.38428,4219.37012,-

6384.50537,9857.52637,-6367.57861,9863.64844,-4315.45752,4225.49219,-4298.53125,4231.61523,-6350.65186,9869.77148

$$LAYER/136.0

$$HATCHES/1,6,-6435.28613,9839.15918,-4383.16455,4201.00195,-4366.23828,4207.12451,-6418.35938,9845.28027,-6401.43213,9851.40430,-4349.31104,4213.24707,-4332.38428,4219.37012,-6384.50537,9857.52637,-6367.57861,9863.64844,-4315.45752,4225.49219,-4298.53125,4231.61523,-6350.65186,9869.77148

$$LAYER/144.0

$$HATCHES/1,6,-6435.28613,9839.15918,-4383.16455,4201.00195,-4366.23828,4207.12451,-6418.35938,9845.28027,-6401.43213,9851.40430,-4349.31104,4213.24707,-4332.38428,4219.37012,-6384.50537,9857.52637,-6367.57861,9863.64844,-4315.45752,4225.49219,-4298.53125,4231.61523,-6350.65186,9869.77148

$$LAYER/152.0

$$HATCHES/1,6,-6435.28613,9839.15918,-4383.16455,4201.00195,-4366.23828,4207.12451,-6418.35938,9845.28027,-6401.43213,9851.40430,-4349.31104,4213.24707,-4332.38428,4219.37012,-6384.50537,9857.52637,-6367.57861,9863.64844,-4315.45752,4225.49219,-4298.53125,4231.61523,-6350.65186,9869.77148

$$LAYER/160.0

$$HATCHES/1,6,-6435.28613,9839.15918,-4383.16455,4201.00195,-4366.23828,4207.12451,-6418.35938,9845.28027,-6401.43213,9851.40430,-4349.31104,4213.24707,-4332.38428,4219.37012,-6384.50537,9857.52637,-6367.57861,9863.64844,-4315.45752,4225.49219,-4298.53125,4231.61523,-6350.65186,9869.77148

$$LAYER/168.0

$$HATCHES/1,6,-6435.28613,9839.15918,-4383.16455,4201.00195,-4366.23828,4207.12451,-6418.35938,9845.28027,-6401.43213,9851.40430,-4349.31104,4213.24707,-4332.38428,4219.37012,-6384.50537,9857.52637,-6367.57861,9863.64844,-4315.45752,4225.49219,-4298.53125,4231.61523,-6350.65186,9869.77148

$$LAYER/176.0

$$HATCHES/1,6,-6435.28613,9839.15918,-4383.16455,4201.00195,-4366.23828,4207.12451,-6418.35938,9845.28027,-6401.43213,9851.40430,-4349.31104,4213.24707,-4332.38428,4219.37012,-6384.50537,9857.52637,-6367.57861,9863.64844,-4315.45752,4225.49219,-4298.53125,4231.61523,-6350.65186,9869.77148

$$LAYER/184.0

$$HATCHES/1,6,-6435.28613,9839.15918,-4383.16455,4201.00195,-4366.23828,4207.12451,-6418.35938,9845.28027,-6401.43213,9851.40430,-4349.31104,4213.24707,-4332.38428,4219.37012,-6384.50537,9857.52637,-6367.57861,9863.64844,-4315.45752,4225.49219,-4298.53125,4231.61523,-6350.65186,9869.77148

$$LAYER/192.0

$$HATCHES/1,6,-6435.28613,9839.15918,-4383.16455,4201.00195,-4366.23828,4207.12451,-6418.35938,9845.28027,-6401.43213,9851.40430,-4349.31104,4213.24707,-4332.38428,4219.37012,-6384.50537,9857.52637,-6367.57861,9863.64844,-4315.45752,4225.49219,-4298.53125,4231.61523,-6350.65186,9869.77148

$$LAYER/200.0

$$HATCHES/1,6,-6435.28613,9839.15918,-4383.16455,4201.00195,-4366.23828,4207.12451,-6418.35938,9845.28027,-6401.43213,9851.40430,-4349.31104,4213.24707,-4332.38428,4219.37012,-6384.50537,9857.52637,-6367.57861,9863.64844,-4315.45752,4225.49219,-4298.53125,4231.61523,-6350.65186,9869.77148

$$LAYER/208.0

$$HATCHES/1,6,-6435.28613,9839.15918,-4383.16455,4201.00195,-4366.23828,4207.12451,-6418.35938,9845.28027,-6401.43213,9851.40430,-4349.31104,4213.24707,-4332.38428,4219.37012,-6384.50537,9857.52637,-6367.57861,9863.64844,-4315.45752,4225.49219,-4298.53125,4231.61523,-6350.65186,9869.77148

$$LAYER/216.0

$$HATCHES/1,6,-6435.28613,9839.15918,-4383.16455,4201.00195,-4366.23828,4207.12451,-6418.35938,9845.28027,-6401.43213,9851.40430,-4349.31104,4213.24707,-4332.38428,4219.37012,-6384.50537,9857.52637,-6367.57861,9863.64844,-4315.45752,4225.49219,-4298.53125,4231.61523,-6350.65186,9869.77148

$$LAYER/224.0

$$HATCHES/1,6,-6435.28613,9839.15918,-4383.16455,4201.00195,-4366.23828,4207.12451,-6418.35938,9845.28027,-6401.43213,9851.40430,-4349.31104,4213.24707,-4332.38428,4219.37012,-6384.50537,9857.52637,-6367.57861,9863.64844,-4315.45752,4225.49219,-4298.53125,4231.61523,-6350.65186,9869.77148

$$LAYER/232.0

$$HATCHES/1,6,-6435.28613,9839.15918,-4383.16455,4201.00195,-4366.23828,4207.12451,-6418.35938,9845.28027,-6401.43213,9851.40430,-4349.31104,4213.24707,-4332.38428,4219.37012,-6384.50537,9857.52637,-6367.57861,9863.64844,-4315.45752,4225.49219,-4298.53125,4231.61523,-6350.65186,9869.77148

$$LAYER/240.0

$$HATCHES/1,6,-6435.28613,9839.15918,-4383.16455,4201.00195,-4366.23828,4207.12451,-6418.35938,9845.28027,-6401.43213,9851.40430,-4349.31104,4213.24707,-4332.38428,4219.37012,-

6384.50537,9857.52637,-6367.57861,9863.64844,-4315.45752,4225.49219,-4298.53125,4231.61523,-6350.65186,9869.77148

$$LAYER/248.0

$$HATCHES/1,6,-6435.28613,9839.15918,-4383.16455,4201.00195,-4366.23828,4207.12451,-6418.35938,9845.28027,-6401.43213,9851.40430,-4349.31104,4213.24707,-4332.38428,4219.37012,-6384.50537,9857.52637,-6367.57861,9863.64844,-4315.45752,4225.49219,-4298.53125,4231.61523,-6350.65186,9869.77148

$$LAYER/256.0

$$HATCHES/1,6,-6435.28613,9839.15918,-4383.16455,4201.00195,-4366.23828,4207.12451,-6418.35938,9845.28027,-6401.43213,9851.40430,-4349.31104,4213.24707,-4332.38428,4219.37012,-6384.50537,9857.52637,-6367.57861,9863.64844,-4315.45752,4225.49219,-4298.53125,4231.61523,-6350.65186,9869.77148

$$LAYER/264.0

$$HATCHES/1,6,-6435.28613,9839.15918,-4383.16455,4201.00195,-4366.23828,4207.12451,-6418.35938,9845.28027,-6401.43213,9851.40430,-4349.31104,4213.24707,-4332.38428,4219.37012,-6384.50537,9857.52637,-6367.57861,9863.64844,-4315.45752,4225.49219,-4298.53125,4231.61523,-6350.65186,9869.77148

$$LAYER/272.0

$$HATCHES/1,6,-6435.28613,9839.15918,-4383.16455,4201.00195,-4366.23828,4207.12451,-6418.35938,9845.28027,-6401.43213,9851.40430,-4349.31104,4213.24707,-4332.38428,4219.37012,-6384.50537,9857.52637,-6367.57861,9863.64844,-4315.45752,4225.49219,-4298.53125,4231.61523,-6350.65186,9869.77148

$$LAYER/280.0

$$HATCHES/1,6,-6435.28613,9839.15918,-4383.16455,4201.00195,-4366.23828,4207.12451,-6418.35938,9845.28027,-6401.43213,9851.40430,-4349.31104,4213.24707,-4332.38428,4219.37012,-6384.50537,9857.52637,-6367.57861,9863.64844,-4315.45752,4225.49219,-4298.53125,4231.61523,-6350.65186,9869.77148

$$LAYER/288.0

$$HATCHES/1,6,-6435.28613,9839.15918,-4383.16455,4201.00195,-4366.23828,4207.12451,-6418.35938,9845.28027,-6401.43213,9851.40430,-4349.31104,4213.24707,-4332.38428,4219.37012,-6384.50537,9857.52637,-6367.57861,9863.64844,-4315.45752,4225.49219,-4298.53125,4231.61523,-6350.65186,9869.77148

$$LAYER/296.0

$$HATCHES/1,6,-6435.28613,9839.15918,-4383.16455,4201.00195,-4366.23828,4207.12451,-6418.35938,9845.28027,-6401.43213,9851.40430,-4349.31104,4213.24707,-4332.38428,4219.37012,-6384.50537,9857.52637,-6367.57861,9863.64844,-4315.45752,4225.49219,-4298.53125,4231.61523,-6350.65186,9869.77148

$$LAYER/304.0

$$HATCHES/1,6,-6435.28613,9839.15918,-4383.16455,4201.00195,-4366.23828,4207.12451,-6418.35938,9845.28027,-6401.43213,9851.40430,-4349.31104,4213.24707,-4332.38428,4219.37012,-6384.50537,9857.52637,-6367.57861,9863.64844,-4315.45752,4225.49219,-4298.53125,4231.61523,-6350.65186,9869.77148

$$LAYER/312.0

$$HATCHES/1,6,-6435.28613,9839.15918,-4383.16455,4201.00195,-4366.23828,4207.12451,-6418.35938,9845.28027,-6401.43213,9851.40430,-4349.31104,4213.24707,-4332.38428,4219.37012,-6384.50537,9857.52637,-6367.57861,9863.64844,-4315.45752,4225.49219,-4298.53125,4231.61523,-6350.65186,9869.77148

$$LAYER/320.0

$$HATCHES/1,6,-6435.28613,9839.15918,-4383.16455,4201.00195,-4366.23828,4207.12451,-6418.35938,9845.28027,-6401.43213,9851.40430,-4349.31104,4213.24707,-4332.38428,4219.37012,-6384.50537,9857.52637,-6367.57861,9863.64844,-4315.45752,4225.49219,-4298.53125,4231.61523,-6350.65186,9869.77148

$$LAYER/328.0

$$HATCHES/1,6,-6435.28613,9839.15918,-4383.16455,4201.00195,-4366.23828,4207.12451,-6418.35938,9845.28027,-6401.43213,9851.40430,-4349.31104,4213.24707,-4332.38428,4219.37012,-6384.50537,9857.52637,-6367.57861,9863.64844,-4315.45752,4225.49219,-4298.53125,4231.61523,-6350.65186,9869.77148

$$LAYER/336.0

$$HATCHES/1,6,-6435.28613,9839.15918,-4383.16455,4201.00195,-4366.23828,4207.12451,-6418.35938,9845.28027,-6401.43213,9851.40430,-4349.31104,4213.24707,-4332.38428,4219.37012,-6384.50537,9857.52637,-6367.57861,9863.64844,-4315.45752,4225.49219,-4298.53125,4231.61523,-6350.65186,9869.77148

$$LAYER/344.0

$$HATCHES/1,6,-6435.28613,9839.15918,-4383.16455,4201.00195,-4366.23828,4207.12451,-6418.35938,9845.28027,-6401.43213,9851.40430,-4349.31104,4213.24707,-4332.38428,4219.37012,-6384.50537,9857.52637,-6367.57861,9863.64844,-4315.45752,4225.49219,-4298.53125,4231.61523,-6350.65186,9869.77148

$$LAYER/352.0

$$HATCHES/1,6,-6435.28613,9839.15918,-4383.16455,4201.00195,-4366.23828,4207.12451,-6418.35938,9845.28027,-6401.43213,9851.40430,-4349.31104,4213.24707,-4332.38428,4219.37012,-

6384.50537,9857.52637,-6367.57861,9863.64844,-4315.45752,4225.49219,-4298.53125,4231.61523,-6350.65186,9869.77148

$$LAYER/360.0

$$HATCHES/1,6,-6435.28613,9839.15918,-4383.16455,4201.00195,-4366.23828,4207.12451,-6418.35938,9845.28027,-6401.43213,9851.40430,-4349.31104,4213.24707,-4332.38428,4219.37012,-6384.50537,9857.52637,-6367.57861,9863.64844,-4315.45752,4225.49219,-4298.53125,4231.61523,-6350.65186,9869.77148

$$LAYER/368.0

$$HATCHES/1,6,-6435.28613,9839.15918,-4383.16455,4201.00195,-4366.23828,4207.12451,-6418.35938,9845.28027,-6401.43213,9851.40430,-4349.31104,4213.24707,-4332.38428,4219.37012,-6384.50537,9857.52637,-6367.57861,9863.64844,-4315.45752,4225.49219,-4298.53125,4231.61523,-6350.65186,9869.77148

$$LAYER/376.0

$$HATCHES/1,6,-6435.28613,9839.15918,-4383.16455,4201.00195,-4366.23828,4207.12451,-6418.35938,9845.28027,-6401.43213,9851.40430,-4349.31104,4213.24707,-4332.38428,4219.37012,-6384.50537,9857.52637,-6367.57861,9863.64844,-4315.45752,4225.49219,-4298.53125,4231.61523,-6350.65186,9869.77148

$$LAYER/384.0

$$HATCHES/1,6,-6435.28613,9839.15918,-4383.16455,4201.00195,-4366.23828,4207.12451,-6418.35938,9845.28027,-6401.43213,9851.40430,-4349.31104,4213.24707,-4332.38428,4219.37012,-6384.50537,9857.52637,-6367.57861,9863.64844,-4315.45752,4225.49219,-4298.53125,4231.61523,-6350.65186,9869.77148

$$LAYER/392.0

$$HATCHES/1,6,-6435.28613,9839.15918,-4383.16455,4201.00195,-4366.23828,4207.12451,-6418.35938,9845.28027,-6401.43213,9851.40430,-4349.31104,4213.24707,-4332.38428,4219.37012,-6384.50537,9857.52637,-6367.57861,9863.64844,-4315.45752,4225.49219,-4298.53125,4231.61523,-6350.65186,9869.77148

$$LAYER/400.0

$$HATCHES/1,6,-6435.28613,9839.15918,-4383.16455,4201.00195,-4366.23828,4207.12451,-6418.35938,9845.28027,-6401.43213,9851.40430,-4349.31104,4213.24707,-4332.38428,4219.37012,-6384.50537,9857.52637,-6367.57861,9863.64844,-4315.45752,4225.49219,-4298.53125,4231.61523,-6350.65186,9869.77148

$$LAYER/408.0

$$HATCHES/1,6,-6435.28613,9839.15918,-4383.16455,4201.00195,-4366.23828,4207.12451,-6418.35938,9845.28027,-6401.43213,9851.40430,-4349.31104,4213.24707,-4332.38428,4219.37012,-6384.50537,9857.52637,-6367.57861,9863.64844,-4315.45752,4225.49219,-4298.53125,4231.61523,-6350.65186,9869.77148

$$LAYER/416.0

$$HATCHES/1,6,-6435.28613,9839.15918,-4383.16455,4201.00195,-4366.23828,4207.12451,-6418.35938,9845.28027,-6401.43213,9851.40430,-4349.31104,4213.24707,-4332.38428,4219.37012,-6384.50537,9857.52637,-6367.57861,9863.64844,-4315.45752,4225.49219,-4298.53125,4231.61523,-6350.65186,9869.77148

$$LAYER/424.0

$$HATCHES/1,6,-6435.28613,9839.15918,-4383.16455,4201.00195,-4366.23828,4207.12451,-6418.35938,9845.28027,-6401.43213,9851.40430,-4349.31104,4213.24707,-4332.38428,4219.37012,-6384.50537,9857.52637,-6367.57861,9863.64844,-4315.45752,4225.49219,-4298.53125,4231.61523,-6350.65186,9869.77148

$$LAYER/432.0

$$HATCHES/1,6,-6435.28613,9839.15918,-4383.16455,4201.00195,-4366.23828,4207.12451,-6418.35938,9845.28027,-6401.43213,9851.40430,-4349.31104,4213.24707,-4332.38428,4219.37012,-6384.50537,9857.52637,-6367.57861,9863.64844,-4315.45752,4225.49219,-4298.53125,4231.61523,-6350.65186,9869.77148

$$LAYER/440.0

$$HATCHES/1,6,-6435.28613,9839.15918,-4383.16455,4201.00195,-4366.23828,4207.12451,-6418.35938,9845.28027,-6401.43213,9851.40430,-4349.31104,4213.24707,-4332.38428,4219.37012,-6384.50537,9857.52637,-6367.57861,9863.64844,-4315.45752,4225.49219,-4298.53125,4231.61523,-6350.65186,9869.77148

$$LAYER/448.0

$$HATCHES/1,6,-6435.28613,9839.15918,-4383.16455,4201.00195,-4366.23828,4207.12451,-6418.35938,9845.28027,-6401.43213,9851.40430,-4349.31104,4213.24707,-4332.38428,4219.37012,-6384.50537,9857.52637,-6367.57861,9863.64844,-4315.45752,4225.49219,-4298.53125,4231.61523,-6350.65186,9869.77148

$$LAYER/456.0

$$HATCHES/1,6,-6435.28613,9839.15918,-4383.16455,4201.00195,-4366.23828,4207.12451,-6418.35938,9845.28027,-6401.43213,9851.40430,-4349.31104,4213.24707,-4332.38428,4219.37012,-6384.50537,9857.52637,-6367.57861,9863.64844,-4315.45752,4225.49219,-4298.53125,4231.61523,-6350.65186,9869.77148

$$LAYER/464.0

$$HATCHES/1,6,-6435.28613,9839.15918,-4383.16455,4201.00195,-4366.23828,4207.12451,-6418.35938,9845.28027,-6401.43213,9851.40430,-4349.31104,4213.24707,-4332.38428,4219.37012,-

6384.50537,9857.52637,-6367.57861,9863.64844,-4315.45752,4225.49219,-4298.53125,4231.61523,-6350.65186,9869.77148

$$LAYER/472.0

$$HATCHES/1,6,-6435.28613,9839.15918,-4383.16455,4201.00195,-4366.23828,4207.12451,-6418.35938,9845.28027,-6401.43213,9851.40430,-4349.31104,4213.24707,-4332.38428,4219.37012,-6384.50537,9857.52637,-6367.57861,9863.64844,-4315.45752,4225.49219,-4298.53125,4231.61523,-6350.65186,9869.77148

$$LAYER/480.0

$$HATCHES/1,6,-6435.28613,9839.15918,-4383.16455,4201.00195,-4366.23828,4207.12451,-6418.35938,9845.28027,-6401.43213,9851.40430,-4349.31104,4213.24707,-4332.38428,4219.37012,-6384.50537,9857.52637,-6367.57861,9863.64844,-4315.45752,4225.49219,-4298.53125,4231.61523,-6350.65186,9869.77148

$$LAYER/488.0

$$HATCHES/1,6,-6435.28613,9839.15918,-4383.16455,4201.00195,-4366.23828,4207.12451,-6418.35938,9845.28027,-6401.43213,9851.40430,-4349.31104,4213.24707,-4332.38428,4219.37012,-6384.50537,9857.52637,-6367.57861,9863.64844,-4315.45752,4225.49219,-4298.53125,4231.61523,-6350.65186,9869.77148

$$LAYER/496.0

$$HATCHES/1,6,-6435.28613,9839.15918,-4383.16455,4201.00195,-4366.23828,4207.12451,-6418.35938,9845.28027,-6401.43213,9851.40430,-4349.31104,4213.24707,-4332.38428,4219.37012,-6384.50537,9857.52637,-6367.57861,9863.64844,-4315.45752,4225.49219,-4298.53125,4231.61523,-6350.65186,9869.77148

$$LAYER/504.0

$$HATCHES/1,6,-6435.28613,9839.15918,-4383.16455,4201.00195,-4366.23828,4207.12451,-6418.35938,9845.28027,-6401.43213,9851.40430,-4349.31104,4213.24707,-4332.38428,4219.37012,-6384.50537,9857.52637,-6367.57861,9863.64844,-4315.45752,4225.49219,-4298.53125,4231.61523,-6350.65186,9869.77148

$$LAYER/512.0

$$HATCHES/1,6,-6435.28613,9839.15918,-4383.16455,4201.00195,-4366.23828,4207.12451,-6418.35938,9845.28027,-6401.43213,9851.40430,-4349.31104,4213.24707,-4332.38428,4219.37012,-6384.50537,9857.52637,-6367.57861,9863.64844,-4315.45752,4225.49219,-4298.53125,4231.61523,-6350.65186,9869.77148

$$LAYER/520.0

$$HATCHES/1,6,-6435.28613,9839.15918,-4383.16455,4201.00195,-4366.23828,4207.12451,-6418.35938,9845.28027,-6401.43213,9851.40430,-4349.31104,4213.24707,-4332.38428,4219.37012,-6384.50537,9857.52637,-6367.57861,9863.64844,-4315.45752,4225.49219,-4298.53125,4231.61523,-6350.65186,9869.77148

$$LAYER/528.0

$$HATCHES/1,6,-6435.28613,9839.15918,-4383.16455,4201.00195,-4366.23828,4207.12451,-6418.35938,9845.28027,-6401.43213,9851.40430,-4349.31104,4213.24707,-4332.38428,4219.37012,-6384.50537,9857.52637,-6367.57861,9863.64844,-4315.45752,4225.49219,-4298.53125,4231.61523,-6350.65186,9869.77148

$$LAYER/536.0

$$HATCHES/1,6,-6435.28613,9839.15918,-4383.16455,4201.00195,-4366.23828,4207.12451,-6418.35938,9845.28027,-6401.43213,9851.40430,-4349.31104,4213.24707,-4332.38428,4219.37012,-6384.50537,9857.52637,-6367.57861,9863.64844,-4315.45752,4225.49219,-4298.53125,4231.61523,-6350.65186,9869.77148

$$LAYER/544.0

$$HATCHES/1,6,-6435.28613,9839.15918,-4383.16455,4201.00195,-4366.23828,4207.12451,-6418.35938,9845.28027,-6401.43213,9851.40430,-4349.31104,4213.24707,-4332.38428,4219.37012,-6384.50537,9857.52637,-6367.57861,9863.64844,-4315.45752,4225.49219,-4298.53125,4231.61523,-6350.65186,9869.77148

$$LAYER/552.0

$$HATCHES/1,6,-6435.28613,9839.15918,-4383.16455,4201.00195,-4366.23828,4207.12451,-6418.35938,9845.28027,-6401.43213,9851.40430,-4349.31104,4213.24707,-4332.38428,4219.37012,-6384.50537,9857.52637,-6367.57861,9863.64844,-4315.45752,4225.49219,-4298.53125,4231.61523,-6350.65186,9869.77148

$$LAYER/560.0

$$HATCHES/1,6,-6435.28613,9839.15918,-4383.16455,4201.00195,-4366.23828,4207.12451,-6418.35938,9845.28027,-6401.43213,9851.40430,-4349.31104,4213.24707,-4332.38428,4219.37012,-6384.50537,9857.52637,-6367.57861,9863.64844,-4315.45752,4225.49219,-4298.53125,4231.61523,-6350.65186,9869.77148

$$LAYER/568.0

$$HATCHES/1,6,-6435.28613,9839.15918,-4383.16455,4201.00195,-4366.23828,4207.12451,-6418.35938,9845.28027,-6401.43213,9851.40430,-4349.31104,4213.24707,-4332.38428,4219.37012,-6384.50537,9857.52637,-6367.57861,9863.64844,-4315.45752,4225.49219,-4298.53125,4231.61523,-6350.65186,9869.77148

$$LAYER/576.0

$$HATCHES/1,6,-6435.28613,9839.15918,-4383.16455,4201.00195,-4366.23828,4207.12451,-6418.35938,9845.28027,-6401.43213,9851.40430,-4349.31104,4213.24707,-4332.38428,4219.37012,-

6384.50537,9857.52637,-6367.57861,9863.64844,-4315.45752,4225.49219,-4298.53125,4231.61523,-6350.65186,9869.77148

$$LAYER/584.0

$$HATCHES/1,6,-6435.28613,9839.15918,-4383.16455,4201.00195,-4366.23828,4207.12451,-6418.35938,9845.28027,-6401.43213,9851.40430,-4349.31104,4213.24707,-4332.38428,4219.37012,-6384.50537,9857.52637,-6367.57861,9863.64844,-4315.45752,4225.49219,-4298.53125,4231.61523,-6350.65186,9869.77148

$$LAYER/592.0

$$HATCHES/1,6,-6435.28613,9839.15918,-4383.16455,4201.00195,-4366.23828,4207.12451,-6418.35938,9845.28027,-6401.43213,9851.40430,-4349.31104,4213.24707,-4332.38428,4219.37012,-6384.50537,9857.52637,-6367.57861,9863.64844,-4315.45752,4225.49219,-4298.53125,4231.61523,-6350.65186,9869.77148

$$LAYER/600.0

$$HATCHES/1,6,-6435.28613,9839.15918,-4383.16455,4201.00195,-4366.23828,4207.12451,-6418.35938,9845.28027,-6401.43213,9851.40430,-4349.31104,4213.24707,-4332.38428,4219.37012,-6384.50537,9857.52637,-6367.57861,9863.64844,-4315.45752,4225.49219,-4298.53125,4231.61523,-6350.65186,9869.77148

$$LAYER/608.0

$$HATCHES/1,6,-6435.28613,9839.15918,-4383.16455,4201.00195,-4366.23828,4207.12451,-6418.35938,9845.28027,-6401.43213,9851.40430,-4349.31104,4213.24707,-4332.38428,4219.37012,-6384.50537,9857.52637,-6367.57861,9863.64844,-4315.45752,4225.49219,-4298.53125,4231.61523,-6350.65186,9869.77148

$$LAYER/616.0

$$HATCHES/1,6,-6435.28613,9839.15918,-4383.16455,4201.00195,-4366.23828,4207.12451,-6418.35938,9845.28027,-6401.43213,9851.40430,-4349.31104,4213.24707,-4332.38428,4219.37012,-6384.50537,9857.52637,-6367.57861,9863.64844,-4315.45752,4225.49219,-4298.53125,4231.61523,-6350.65186,9869.77148

$$LAYER/624.0

$$HATCHES/1,6,-6435.28613,9839.15918,-4383.16455,4201.00195,-4366.23828,4207.12451,-6418.35938,9845.28027,-6401.43213,9851.40430,-4349.31104,4213.24707,-4332.38428,4219.37012,-6384.50537,9857.52637,-6367.57861,9863.64844,-4315.45752,4225.49219,-4298.53125,4231.61523,-6350.65186,9869.77148

$$LAYER/632.0

$$HATCHES/1,6,-6435.28613,9839.15918,-4383.16455,4201.00195,-4366.23828,4207.12451,-6418.35938,9845.28027,-6401.43213,9851.40430,-4349.31104,4213.24707,-4332.38428,4219.37012,-6384.50537,9857.52637,-6367.57861,9863.64844,-4315.45752,4225.49219,-4298.53125,4231.61523,-6350.65186,9869.77148

$$LAYER/640.0

$$HATCHES/1,6,-6435.28613,9839.15918,-4383.16455,4201.00195,-4366.23828,4207.12451,-6418.35938,9845.28027,-6401.43213,9851.40430,-4349.31104,4213.24707,-4332.38428,4219.37012,-6384.50537,9857.52637,-6367.57861,9863.64844,-4315.45752,4225.49219,-4298.53125,4231.61523,-6350.65186,9869.77148

$$LAYER/648.0

$$HATCHES/1,6,-6435.28613,9839.15918,-4383.16455,4201.00195,-4366.23828,4207.12451,-6418.35938,9845.28027,-6401.43213,9851.40430,-4349.31104,4213.24707,-4332.38428,4219.37012,-6384.50537,9857.52637,-6367.57861,9863.64844,-4315.45752,4225.49219,-4298.53125,4231.61523,-6350.65186,9869.77148

$$LAYER/656.0

$$HATCHES/1,6,-6435.28613,9839.15918,-4383.16455,4201.00195,-4366.23828,4207.12451,-6418.35938,9845.28027,-6401.43213,9851.40430,-4349.31104,4213.24707,-4332.38428,4219.37012,-6384.50537,9857.52637,-6367.57861,9863.64844,-4315.45752,4225.49219,-4298.53125,4231.61523,-6350.65186,9869.77148

$$LAYER/664.0

$$HATCHES/1,6,-6435.28613,9839.15918,-4383.16455,4201.00195,-4366.23828,4207.12451,-6418.35938,9845.28027,-6401.43213,9851.40430,-4349.31104,4213.24707,-4332.38428,4219.37012,-6384.50537,9857.52637,-6367.57861,9863.64844,-4315.45752,4225.49219,-4298.53125,4231.61523,-6350.65186,9869.77148

$$LAYER/672.0

$$HATCHES/1,6,-6435.28613,9839.15918,-4383.16455,4201.00195,-4366.23828,4207.12451,-6418.35938,9845.28027,-6401.43213,9851.40430,-4349.31104,4213.24707,-4332.38428,4219.37012,-6384.50537,9857.52637,-6367.57861,9863.64844,-4315.45752,4225.49219,-4298.53125,4231.61523,-6350.65186,9869.77148

$$LAYER/680.0

$$HATCHES/1,6,-6435.28613,9839.15918,-4383.16455,4201.00195,-4366.23828,4207.12451,-6418.35938,9845.28027,-6401.43213,9851.40430,-4349.31104,4213.24707,-4332.38428,4219.37012,-6384.50537,9857.52637,-6367.57861,9863.64844,-4315.45752,4225.49219,-4298.53125,4231.61523,-6350.65186,9869.77148

$$LAYER/688.0

$$HATCHES/1,6,-6435.28613,9839.15918,-4383.16455,4201.00195,-4366.23828,4207.12451,-6418.35938,9845.28027,-6401.43213,9851.40430,-4349.31104,4213.24707,-4332.38428,4219.37012,-

6384.50537,9857.52637,-6367.57861,9863.64844,-4315.45752,4225.49219,-4298.53125,4231.61523,-6350.65186,9869.77148

$$LAYER/696.0

$$HATCHES/1,6,-6435.28613,9839.15918,-4383.16455,4201.00195,-4366.23828,4207.12451,-6418.35938,9845.28027,-6401.43213,9851.40430,-4349.31104,4213.24707,-4332.38428,4219.37012,-6384.50537,9857.52637,-6367.57861,9863.64844,-4315.45752,4225.49219,-4298.53125,4231.61523,-6350.65186,9869.77148

$$LAYER/704.0

$$HATCHES/1,6,-6435.28613,9839.15918,-4383.16455,4201.00195,-4366.23828,4207.12451,-6418.35938,9845.28027,-6401.43213,9851.40430,-4349.31104,4213.24707,-4332.38428,4219.37012,-6384.50537,9857.52637,-6367.57861,9863.64844,-4315.45752,4225.49219,-4298.53125,4231.61523,-6350.65186,9869.77148

$$LAYER/712.0

$$HATCHES/1,6,-6435.28613,9839.15918,-4383.16455,4201.00195,-4366.23828,4207.12451,-6418.35938,9845.28027,-6401.43213,9851.40430,-4349.31104,4213.24707,-4332.38428,4219.37012,-6384.50537,9857.52637,-6367.57861,9863.64844,-4315.45752,4225.49219,-4298.53125,4231.61523,-6350.65186,9869.77148

$$LAYER/720.0

$$HATCHES/1,6,-6435.28613,9839.15918,-4383.16455,4201.00195,-4366.23828,4207.12451,-6418.35938,9845.28027,-6401.43213,9851.40430,-4349.31104,4213.24707,-4332.38428,4219.37012,-6384.50537,9857.52637,-6367.57861,9863.64844,-4315.45752,4225.49219,-4298.53125,4231.61523,-6350.65186,9869.77148

$$LAYER/728.0

$$HATCHES/1,6,-6435.28613,9839.15918,-4383.16455,4201.00195,-4366.23828,4207.12451,-6418.35938,9845.28027,-6401.43213,9851.40430,-4349.31104,4213.24707,-4332.38428,4219.37012,-6384.50537,9857.52637,-6367.57861,9863.64844,-4315.45752,4225.49219,-4298.53125,4231.61523,-6350.65186,9869.77148

$$LAYER/736.0

$$HATCHES/1,6,-6435.28613,9839.15918,-4383.16455,4201.00195,-4366.23828,4207.12451,-6418.35938,9845.28027,-6401.43213,9851.40430,-4349.31104,4213.24707,-4332.38428,4219.37012,-6384.50537,9857.52637,-6367.57861,9863.64844,-4315.45752,4225.49219,-4298.53125,4231.61523,-6350.65186,9869.77148

$$LAYER/744.0

$$HATCHES/1,6,-6435.28613,9839.15918,-4383.16455,4201.00195,-4366.23828,4207.12451,-6418.35938,9845.28027,-6401.43213,9851.40430,-4349.31104,4213.24707,-4332.38428,4219.37012,-6384.50537,9857.52637,-6367.57861,9863.64844,-4315.45752,4225.49219,-4298.53125,4231.61523,-6350.65186,9869.77148

$$LAYER/752.0

$$HATCHES/1,6,-6435.28613,9839.15918,-4383.16455,4201.00195,-4366.23828,4207.12451,-6418.35938,9845.28027,-6401.43213,9851.40430,-4349.31104,4213.24707,-4332.38428,4219.37012,-6384.50537,9857.52637,-6367.57861,9863.64844,-4315.45752,4225.49219,-4298.53125,4231.61523,-6350.65186,9869.77148

$$LAYER/760.0

$$HATCHES/1,6,-6435.28613,9839.15918,-4383.16455,4201.00195,-4366.23828,4207.12451,-6418.35938,9845.28027,-6401.43213,9851.40430,-4349.31104,4213.24707,-4332.38428,4219.37012,-6384.50537,9857.52637,-6367.57861,9863.64844,-4315.45752,4225.49219,-4298.53125,4231.61523,-6350.65186,9869.77148

$$LAYER/768.0

$$HATCHES/1,6,-6435.28613,9839.15918,-4383.16455,4201.00195,-4366.23828,4207.12451,-6418.35938,9845.28027,-6401.43213,9851.40430,-4349.31104,4213.24707,-4332.38428,4219.37012,-6384.50537,9857.52637,-6367.57861,9863.64844,-4315.45752,4225.49219,-4298.53125,4231.61523,-6350.65186,9869.77148

$$LAYER/776.0

$$HATCHES/1,6,-6435.28613,9839.15918,-4383.16455,4201.00195,-4366.23828,4207.12451,-6418.35938,9845.28027,-6401.43213,9851.40430,-4349.31104,4213.24707,-4332.38428,4219.37012,-6384.50537,9857.52637,-6367.57861,9863.64844,-4315.45752,4225.49219,-4298.53125,4231.61523,-6350.65186,9869.77148

$$LAYER/784.0

$$HATCHES/1,6,-6435.28613,9839.15918,-4383.16455,4201.00195,-4366.23828,4207.12451,-6418.35938,9845.28027,-6401.43213,9851.40430,-4349.31104,4213.24707,-4332.38428,4219.37012,-6384.50537,9857.52637,-6367.57861,9863.64844,-4315.45752,4225.49219,-4298.53125,4231.61523,-6350.65186,9869.77148

$$LAYER/792.0

$$HATCHES/1,6,-6435.28613,9839.15918,-4383.16455,4201.00195,-4366.23828,4207.12451,-6418.35938,9845.28027,-6401.43213,9851.40430,-4349.31104,4213.24707,-4332.38428,4219.37012,-6384.50537,9857.52637,-6367.57861,9863.64844,-4315.45752,4225.49219,-4298.53125,4231.61523,-6350.65186,9869.77148

$$LAYER/800.0

$$HATCHES/1,6,-6435.28613,9839.15918,-4383.16455,4201.00195,-4366.23828,4207.12451,-6418.35938,9845.28027,-6401.43213,9851.40430,-4349.31104,4213.24707,-4332.38428,4219.37012,-

6384.50537,9857.52637,-6367.57861,9863.64844,-4315.45752,4225.49219,-4298.53125,4231.61523,-6350.65186,9869.77148

$$LAYER/808.0

$$HATCHES/1,6,-6435.28613,9839.15918,-4383.16455,4201.00195,-4366.23828,4207.12451,-6418.35938,9845.28027,-6401.43213,9851.40430,-4349.31104,4213.24707,-4332.38428,4219.37012,-6384.50537,9857.52637,-6367.57861,9863.64844,-4315.45752,4225.49219,-4298.53125,4231.61523,-6350.65186,9869.77148

$$LAYER/816.0

$$HATCHES/1,6,-6435.28613,9839.15918,-4383.16455,4201.00195,-4366.23828,4207.12451,-6418.35938,9845.28027,-6401.43213,9851.40430,-4349.31104,4213.24707,-4332.38428,4219.37012,-6384.50537,9857.52637,-6367.57861,9863.64844,-4315.45752,4225.49219,-4298.53125,4231.61523,-6350.65186,9869.77148

$$LAYER/824.0

$$HATCHES/1,6,-6435.28613,9839.15918,-4383.16455,4201.00195,-4366.23828,4207.12451,-6418.35938,9845.28027,-6401.43213,9851.40430,-4349.31104,4213.24707,-4332.38428,4219.37012,-6384.50537,9857.52637,-6367.57861,9863.64844,-4315.45752,4225.49219,-4298.53125,4231.61523,-6350.65186,9869.77148

$$LAYER/832.0

$$HATCHES/1,6,-6435.28613,9839.15918,-4383.16455,4201.00195,-4366.23828,4207.12451,-6418.35938,9845.28027,-6401.43213,9851.40430,-4349.31104,4213.24707,-4332.38428,4219.37012,-6384.50537,9857.52637,-6367.57861,9863.64844,-4315.45752,4225.49219,-4298.53125,4231.61523,-6350.65186,9869.77148

$$LAYER/840.0

$$HATCHES/1,6,-6435.28613,9839.15918,-4383.16455,4201.00195,-4366.23828,4207.12451,-6418.35938,9845.28027,-6401.43213,9851.40430,-4349.31104,4213.24707,-4332.38428,4219.37012,-6384.50537,9857.52637,-6367.57861,9863.64844,-4315.45752,4225.49219,-4298.53125,4231.61523,-6350.65186,9869.77148

$$LAYER/848.0

$$HATCHES/1,6,-6435.28613,9839.15918,-4383.16455,4201.00195,-4366.23828,4207.12451,-6418.35938,9845.28027,-6401.43213,9851.40430,-4349.31104,4213.24707,-4332.38428,4219.37012,-6384.50537,9857.52637,-6367.57861,9863.64844,-4315.45752,4225.49219,-4298.53125,4231.61523,-6350.65186,9869.77148

$$LAYER/856.0

$$HATCHES/1,6,-6435.28613,9839.15918,-4383.16455,4201.00195,-4366.23828,4207.12451,-6418.35938,9845.28027,-6401.43213,9851.40430,-4349.31104,4213.24707,-4332.38428,4219.37012,-6384.50537,9857.52637,-6367.57861,9863.64844,-4315.45752,4225.49219,-4298.53125,4231.61523,-6350.65186,9869.77148

$$LAYER/864.0

$$HATCHES/1,6,-6435.28613,9839.15918,-4383.16455,4201.00195,-4366.23828,4207.12451,-6418.35938,9845.28027,-6401.43213,9851.40430,-4349.31104,4213.24707,-4332.38428,4219.37012,-6384.50537,9857.52637,-6367.57861,9863.64844,-4315.45752,4225.49219,-4298.53125,4231.61523,-6350.65186,9869.77148

$$LAYER/872.0

$$HATCHES/1,6,-6435.28613,9839.15918,-4383.16455,4201.00195,-4366.23828,4207.12451,-6418.35938,9845.28027,-6401.43213,9851.40430,-4349.31104,4213.24707,-4332.38428,4219.37012,-6384.50537,9857.52637,-6367.57861,9863.64844,-4315.45752,4225.49219,-4298.53125,4231.61523,-6350.65186,9869.77148

$$LAYER/880.0

$$HATCHES/1,6,-6435.28613,9839.15918,-4383.16455,4201.00195,-4366.23828,4207.12451,-6418.35938,9845.28027,-6401.43213,9851.40430,-4349.31104,4213.24707,-4332.38428,4219.37012,-6384.50537,9857.52637,-6367.57861,9863.64844,-4315.45752,4225.49219,-4298.53125,4231.61523,-6350.65186,9869.77148

$$LAYER/888.0

$$HATCHES/1,6,-6435.28613,9839.15918,-4383.16455,4201.00195,-4366.23828,4207.12451,-6418.35938,9845.28027,-6401.43213,9851.40430,-4349.31104,4213.24707,-4332.38428,4219.37012,-6384.50537,9857.52637,-6367.57861,9863.64844,-4315.45752,4225.49219,-4298.53125,4231.61523,-6350.65186,9869.77148

$$LAYER/896.0

$$HATCHES/1,6,-6435.28613,9839.15918,-4383.16455,4201.00195,-4366.23828,4207.12451,-6418.35938,9845.28027,-6401.43213,9851.40430,-4349.31104,4213.24707,-4332.38428,4219.37012,-6384.50537,9857.52637,-6367.57861,9863.64844,-4315.45752,4225.49219,-4298.53125,4231.61523,-6350.65186,9869.77148

$$LAYER/904.0

$$HATCHES/1,6,-6435.28613,9839.15918,-4383.16455,4201.00195,-4366.23828,4207.12451,-6418.35938,9845.28027,-6401.43213,9851.40430,-4349.31104,4213.24707,-4332.38428,4219.37012,-6384.50537,9857.52637,-6367.57861,9863.64844,-4315.45752,4225.49219,-4298.53125,4231.61523,-6350.65186,9869.77148

$$LAYER/912.0

$$HATCHES/1,6,-6435.28613,9839.15918,-4383.16455,4201.00195,-4366.23828,4207.12451,-6418.35938,9845.28027,-6401.43213,9851.40430,-4349.31104,4213.24707,-4332.38428,4219.37012,-

6384.50537,9857.52637,-6367.57861,9863.64844,-4315.45752,4225.49219,-4298.53125,4231.61523,-6350.65186,9869.77148

$$LAYER/920.0

$$HATCHES/1,6,-6435.28613,9839.15918,-4383.16455,4201.00195,-4366.23828,4207.12451,-6418.35938,9845.28027,-6401.43213,9851.40430,-4349.31104,4213.24707,-4332.38428,4219.37012,-6384.50537,9857.52637,-6367.57861,9863.64844,-4315.45752,4225.49219,-4298.53125,4231.61523,-6350.65186,9869.77148

$$LAYER/928.0

$$HATCHES/1,6,-6435.28613,9839.15918,-4383.16455,4201.00195,-4366.23828,4207.12451,-6418.35938,9845.28027,-6401.43213,9851.40430,-4349.31104,4213.24707,-4332.38428,4219.37012,-6384.50537,9857.52637,-6367.57861,9863.64844,-4315.45752,4225.49219,-4298.53125,4231.61523,-6350.65186,9869.77148

$$LAYER/936.0

$$HATCHES/1,6,-6435.28613,9839.15918,-4383.16455,4201.00195,-4366.23828,4207.12451,-6418.35938,9845.28027,-6401.43213,9851.40430,-4349.31104,4213.24707,-4332.38428,4219.37012,-6384.50537,9857.52637,-6367.57861,9863.64844,-4315.45752,4225.49219,-4298.53125,4231.61523,-6350.65186,9869.77148

$$LAYER/944.0

$$HATCHES/1,6,-6435.28613,9839.15918,-4383.16455,4201.00195,-4366.23828,4207.12451,-6418.35938,9845.28027,-6401.43213,9851.40430,-4349.31104,4213.24707,-4332.38428,4219.37012,-6384.50537,9857.52637,-6367.57861,9863.64844,-4315.45752,4225.49219,-4298.53125,4231.61523,-6350.65186,9869.77148

$$LAYER/952.0

$$HATCHES/1,6,-6435.28613,9839.15918,-4383.16455,4201.00195,-4366.23828,4207.12451,-6418.35938,9845.28027,-6401.43213,9851.40430,-4349.31104,4213.24707,-4332.38428,4219.37012,-6384.50537,9857.52637,-6367.57861,9863.64844,-4315.45752,4225.49219,-4298.53125,4231.61523,-6350.65186,9869.77148

$$LAYER/960.0

$$HATCHES/1,6,-6435.28613,9839.15918,-4383.16455,4201.00195,-4366.23828,4207.12451,-6418.35938,9845.28027,-6401.43213,9851.40430,-4349.31104,4213.24707,-4332.38428,4219.37012,-6384.50537,9857.52637,-6367.57861,9863.64844,-4315.45752,4225.49219,-4298.53125,4231.61523,-6350.65186,9869.77148

$$LAYER/968.0

$$HATCHES/1,6,-6435.28613,9839.15918,-4383.16455,4201.00195,-4366.23828,4207.12451,-6418.35938,9845.28027,-6401.43213,9851.40430,-4349.31104,4213.24707,-4332.38428,4219.37012,-6384.50537,9857.52637,-6367.57861,9863.64844,-4315.45752,4225.49219,-4298.53125,4231.61523,-6350.65186,9869.77148

$$LAYER/976.0

$$HATCHES/1,6,-6435.28613,9839.15918,-4383.16455,4201.00195,-4366.23828,4207.12451,-6418.35938,9845.28027,-6401.43213,9851.40430,-4349.31104,4213.24707,-4332.38428,4219.37012,-6384.50537,9857.52637,-6367.57861,9863.64844,-4315.45752,4225.49219,-4298.53125,4231.61523,-6350.65186,9869.77148

$$LAYER/984.0

$$HATCHES/1,6,-6435.28613,9839.15918,-4383.16455,4201.00195,-4366.23828,4207.12451,-6418.35938,9845.28027,-6401.43213,9851.40430,-4349.31104,4213.24707,-4332.38428,4219.37012,-6384.50537,9857.52637,-6367.57861,9863.64844,-4315.45752,4225.49219,-4298.53125,4231.61523,-6350.65186,9869.77148

$$LAYER/992.0

$$HATCHES/1,6,-6435.28613,9839.15918,-4383.16455,4201.00195,-4366.23828,4207.12451,-6418.35938,9845.28027,-6401.43213,9851.40430,-4349.31104,4213.24707,-4332.38428,4219.37012,-6384.50537,9857.52637,-6367.57861,9863.64844,-4315.45752,4225.49219,-4298.53125,4231.61523,-6350.65186,9869.77148

$$LAYER/1000.0

$$HATCHES/1,6,-6435.28613,9839.15918,-4383.16455,4201.00195,-4366.23828,4207.12451,-6418.35938,9845.28027,-6401.43213,9851.40430,-4349.31104,4213.24707,-4332.38428,4219.37012,-6384.50537,9857.52637,-6367.57861,9863.64844,-4315.45752,4225.49219,-4298.53125,4231.61523,-6350.65186,9869.77148

$$LAYER/1008.0

$$HATCHES/1,6,-6435.28613,9839.15918,-4383.16455,4201.00195,-4366.23828,4207.12451,-6418.35938,9845.28027,-6401.43213,9851.40430,-4349.31104,4213.24707,-4332.38428,4219.37012,-6384.50537,9857.52637,-6367.57861,9863.64844,-4315.45752,4225.49219,-4298.53125,4231.61523,-6350.65186,9869.77148

$$LAYER/1016.0

$$HATCHES/1,6,-6435.28613,9839.15918,-4383.16455,4201.00195,-4366.23828,4207.12451,-6418.35938,9845.28027,-6401.43213,9851.40430,-4349.31104,4213.24707,-4332.38428,4219.37012,-6384.50537,9857.52637,-6367.57861,9863.64844,-4315.45752,4225.49219,-4298.53125,4231.61523,-6350.65186,9869.77148

$$LAYER/1024.0

$$HATCHES/1,6,-6435.28613,9839.15918,-4383.16455,4201.00195,-4366.23828,4207.12451,-6418.35938,9845.28027,-6401.43213,9851.40430,-4349.31104,4213.24707,-4332.38428,4219.37012,-

6384.50537,9857.52637,-6367.57861,9863.64844,-4315.45752,4225.49219,-4298.53125,4231.61523,-6350.65186,9869.77148

$$LAYER/1032.0

$$HATCHES/1,6,-6435.28613,9839.15918,-4383.16455,4201.00195,-4366.23828,4207.12451,-6418.35938,9845.28027,-6401.43213,9851.40430,-4349.31104,4213.24707,-4332.38428,4219.37012,-6384.50537,9857.52637,-6367.57861,9863.64844,-4315.45752,4225.49219,-4298.53125,4231.61523,-6350.65186,9869.77148

$$LAYER/1040.0

$$HATCHES/1,6,-6435.28613,9839.15918,-4383.16455,4201.00195,-4366.23828,4207.12451,-6418.35938,9845.28027,-6401.43213,9851.40430,-4349.31104,4213.24707,-4332.38428,4219.37012,-6384.50537,9857.52637,-6367.57861,9863.64844,-4315.45752,4225.49219,-4298.53125,4231.61523,-6350.65186,9869.77148

$$LAYER/1048.0

$$HATCHES/1,6,-6435.28613,9839.15918,-4383.16455,4201.00195,-4366.23828,4207.12451,-6418.35938,9845.28027,-6401.43213,9851.40430,-4349.31104,4213.24707,-4332.38428,4219.37012,-6384.50537,9857.52637,-6367.57861,9863.64844,-4315.45752,4225.49219,-4298.53125,4231.61523,-6350.65186,9869.77148

$$LAYER/1056.0

$$HATCHES/1,6,-6435.28613,9839.15918,-4383.16455,4201.00195,-4366.23828,4207.12451,-6418.35938,9845.28027,-6401.43213,9851.40430,-4349.31104,4213.24707,-4332.38428,4219.37012,-6384.50537,9857.52637,-6367.57861,9863.64844,-4315.45752,4225.49219,-4298.53125,4231.61523,-6350.65186,9869.77148

$$LAYER/1064.0

$$HATCHES/1,6,-6435.28613,9839.15918,-4383.16455,4201.00195,-4366.23828,4207.12451,-6418.35938,9845.28027,-6401.43213,9851.40430,-4349.31104,4213.24707,-4332.38428,4219.37012,-6384.50537,9857.52637,-6367.57861,9863.64844,-4315.45752,4225.49219,-4298.53125,4231.61523,-6350.65186,9869.77148

$$LAYER/1072.0

$$HATCHES/1,6,-6435.28613,9839.15918,-4383.16455,4201.00195,-4366.23828,4207.12451,-6418.35938,9845.28027,-6401.43213,9851.40430,-4349.31104,4213.24707,-4332.38428,4219.37012,-6384.50537,9857.52637,-6367.57861,9863.64844,-4315.45752,4225.49219,-4298.53125,4231.61523,-6350.65186,9869.77148

$$LAYER/1080.0

$$HATCHES/1,6,-6435.28613,9839.15918,-4383.16455,4201.00195,-4366.23828,4207.12451,-6418.35938,9845.28027,-6401.43213,9851.40430,-4349.31104,4213.24707,-4332.38428,4219.37012,-6384.50537,9857.52637,-6367.57861,9863.64844,-4315.45752,4225.49219,-4298.53125,4231.61523,-6350.65186,9869.77148

$$LAYER/1088.0

$$HATCHES/1,6,-6435.28613,9839.15918,-4383.16455,4201.00195,-4366.23828,4207.12451,-6418.35938,9845.28027,-6401.43213,9851.40430,-4349.31104,4213.24707,-4332.38428,4219.37012,-6384.50537,9857.52637,-6367.57861,9863.64844,-4315.45752,4225.49219,-4298.53125,4231.61523,-6350.65186,9869.77148

$$LAYER/1096.0

$$HATCHES/1,6,-6435.28613,9839.15918,-4383.16455,4201.00195,-4366.23828,4207.12451,-6418.35938,9845.28027,-6401.43213,9851.40430,-4349.31104,4213.24707,-4332.38428,4219.37012,-6384.50537,9857.52637,-6367.57861,9863.64844,-4315.45752,4225.49219,-4298.53125,4231.61523,-6350.65186,9869.77148

$$LAYER/1104.0

$$HATCHES/1,6,-6435.28613,9839.15918,-4383.16455,4201.00195,-4366.23828,4207.12451,-6418.35938,9845.28027,-6401.43213,9851.40430,-4349.31104,4213.24707,-4332.38428,4219.37012,-6384.50537,9857.52637,-6367.57861,9863.64844,-4315.45752,4225.49219,-4298.53125,4231.61523,-6350.65186,9869.77148

$$LAYER/1112.0

$$HATCHES/1,6,-6435.28613,9839.15918,-4383.16455,4201.00195,-4366.23828,4207.12451,-6418.35938,9845.28027,-6401.43213,9851.40430,-4349.31104,4213.24707,-4332.38428,4219.37012,-6384.50537,9857.52637,-6367.57861,9863.64844,-4315.45752,4225.49219,-4298.53125,4231.61523,-6350.65186,9869.77148

$$LAYER/1120.0

$$HATCHES/1,6,-6435.28613,9839.15918,-4383.16455,4201.00195,-4366.23828,4207.12451,-6418.35938,9845.28027,-6401.43213,9851.40430,-4349.31104,4213.24707,-4332.38428,4219.37012,-6384.50537,9857.52637,-6367.57861,9863.64844,-4315.45752,4225.49219,-4298.53125,4231.61523,-6350.65186,9869.77148

$$LAYER/1128.0

$$HATCHES/1,6,-6435.28613,9839.15918,-4383.16455,4201.00195,-4366.23828,4207.12451,-6418.35938,9845.28027,-6401.43213,9851.40430,-4349.31104,4213.24707,-4332.38428,4219.37012,-6384.50537,9857.52637,-6367.57861,9863.64844,-4315.45752,4225.49219,-4298.53125,4231.61523,-6350.65186,9869.77148

$$LAYER/1136.0

$$HATCHES/1,6,-6435.28613,9839.15918,-4383.16455,4201.00195,-4366.23828,4207.12451,-6418.35938,9845.28027,-6401.43213,9851.40430,-4349.31104,4213.24707,-4332.38428,4219.37012,-

6384.50537,9857.52637,-6367.57861,9863.64844,-4315.45752,4225.49219,-4298.53125,4231.61523,-6350.65186,9869.77148

$$LAYER/1144.0

$$HATCHES/1,6,-6435.28613,9839.15918,-4383.16455,4201.00195,-4366.23828,4207.12451,-6418.35938,9845.28027,-6401.43213,9851.40430,-4349.31104,4213.24707,-4332.38428,4219.37012,-6384.50537,9857.52637,-6367.57861,9863.64844,-4315.45752,4225.49219,-4298.53125,4231.61523,-6350.65186,9869.77148

$$LAYER/1152.0

$$HATCHES/1,6,-6435.28613,9839.15918,-4383.16455,4201.00195,-4366.23828,4207.12451,-6418.35938,9845.28027,-6401.43213,9851.40430,-4349.31104,4213.24707,-4332.38428,4219.37012,-6384.50537,9857.52637,-6367.57861,9863.64844,-4315.45752,4225.49219,-4298.53125,4231.61523,-6350.65186,9869.77148

$$LAYER/1160.0

$$HATCHES/1,6,-6435.28613,9839.15918,-4383.16455,4201.00195,-4366.23828,4207.12451,-6418.35938,9845.28027,-6401.43213,9851.40430,-4349.31104,4213.24707,-4332.38428,4219.37012,-6384.50537,9857.52637,-6367.57861,9863.64844,-4315.45752,4225.49219,-4298.53125,4231.61523,-6350.65186,9869.77148

$$LAYER/1168.0

$$HATCHES/1,6,-6435.28613,9839.15918,-4383.16455,4201.00195,-4366.23828,4207.12451,-6418.35938,9845.28027,-6401.43213,9851.40430,-4349.31104,4213.24707,-4332.38428,4219.37012,-6384.50537,9857.52637,-6367.57861,9863.64844,-4315.45752,4225.49219,-4298.53125,4231.61523,-6350.65186,9869.77148

$$LAYER/1176.0

$$HATCHES/1,6,-6435.28613,9839.15918,-4383.16455,4201.00195,-4366.23828,4207.12451,-6418.35938,9845.28027,-6401.43213,9851.40430,-4349.31104,4213.24707,-4332.38428,4219.37012,-6384.50537,9857.52637,-6367.57861,9863.64844,-4315.45752,4225.49219,-4298.53125,4231.61523,-6350.65186,9869.77148

$$LAYER/1184.0

$$HATCHES/1,6,-6435.28613,9839.15918,-4383.16455,4201.00195,-4366.23828,4207.12451,-6418.35938,9845.28027,-6401.43213,9851.40430,-4349.31104,4213.24707,-4332.38428,4219.37012,-6384.50537,9857.52637,-6367.57861,9863.64844,-4315.45752,4225.49219,-4298.53125,4231.61523,-6350.65186,9869.77148

$$LAYER/1192.0

$$HATCHES/1,6,-6435.28613,9839.15918,-4383.16455,4201.00195,-4366.23828,4207.12451,-6418.35938,9845.28027,-6401.43213,9851.40430,-4349.31104,4213.24707,-4332.38428,4219.37012,-6384.50537,9857.52637,-6367.57861,9863.64844,-4315.45752,4225.49219,-4298.53125,4231.61523,-6350.65186,9869.77148

$$LAYER/1200.0

$$HATCHES/1,6,-6435.28613,9839.15918,-4383.16455,4201.00195,-4366.23828,4207.12451,-6418.35938,9845.28027,-6401.43213,9851.40430,-4349.31104,4213.24707,-4332.38428,4219.37012,-6384.50537,9857.52637,-6367.57861,9863.64844,-4315.45752,4225.49219,-4298.53125,4231.61523,-6350.65186,9869.77148

$$LAYER/1208.0

$$HATCHES/1,6,-6435.28613,9839.15918,-4383.16455,4201.00195,-4366.23828,4207.12451,-6418.35938,9845.28027,-6401.43213,9851.40430,-4349.31104,4213.24707,-4332.38428,4219.37012,-6384.50537,9857.52637,-6367.57861,9863.64844,-4315.45752,4225.49219,-4298.53125,4231.61523,-6350.65186,9869.77148

$$LAYER/1216.0

$$HATCHES/1,6,-6435.28613,9839.15918,-4383.16455,4201.00195,-4366.23828,4207.12451,-6418.35938,9845.28027,-6401.43213,9851.40430,-4349.31104,4213.24707,-4332.38428,4219.37012,-6384.50537,9857.52637,-6367.57861,9863.64844,-4315.45752,4225.49219,-4298.53125,4231.61523,-6350.65186,9869.77148

$$LAYER/1224.0

$$HATCHES/1,6,-6435.28613,9839.15918,-4383.16455,4201.00195,-4366.23828,4207.12451,-6418.35938,9845.28027,-6401.43213,9851.40430,-4349.31104,4213.24707,-4332.38428,4219.37012,-6384.50537,9857.52637,-6367.57861,9863.64844,-4315.45752,4225.49219,-4298.53125,4231.61523,-6350.65186,9869.77148

$$LAYER/1232.0

$$HATCHES/1,6,-6435.28613,9839.15918,-4383.16455,4201.00195,-4366.23828,4207.12451,-6418.35938,9845.28027,-6401.43213,9851.40430,-4349.31104,4213.24707,-4332.38428,4219.37012,-6384.50537,9857.52637,-6367.57861,9863.64844,-4315.45752,4225.49219,-4298.53125,4231.61523,-6350.65186,9869.77148

$$LAYER/1240.0

$$HATCHES/1,6,-6435.28613,9839.15918,-4383.16455,4201.00195,-4366.23828,4207.12451,-6418.35938,9845.28027,-6401.43213,9851.40430,-4349.31104,4213.24707,-4332.38428,4219.37012,-6384.50537,9857.52637,-6367.57861,9863.64844,-4315.45752,4225.49219,-4298.53125,4231.61523,-6350.65186,9869.77148

$$LAYER/1248.0

$$HATCHES/1,6,-6435.28613,9839.15918,-4383.16455,4201.00195,-4366.23828,4207.12451,-6418.35938,9845.28027,-6401.43213,9851.40430,-4349.31104,4213.24707,-4332.38428,4219.37012,-

6384.50537,9857.52637,-6367.57861,9863.64844,-4315.45752,4225.49219,-4298.53125,4231.61523,-6350.65186,9869.77148

$$LAYER/1256.0

$$HATCHES/1,6,-6435.28613,9839.15918,-4383.16455,4201.00195,-4366.23828,4207.12451,-6418.35938,9845.28027,-6401.43213,9851.40430,-4349.31104,4213.24707,-4332.38428,4219.37012,-6384.50537,9857.52637,-6367.57861,9863.64844,-4315.45752,4225.49219,-4298.53125,4231.61523,-6350.65186,9869.77148

$$LAYER/1264.0

$$HATCHES/1,6,-6435.28613,9839.15918,-4383.16455,4201.00195,-4366.23828,4207.12451,-6418.35938,9845.28027,-6401.43213,9851.40430,-4349.31104,4213.24707,-4332.38428,4219.37012,-6384.50537,9857.52637,-6367.57861,9863.64844,-4315.45752,4225.49219,-4298.53125,4231.61523,-6350.65186,9869.77148

$$LAYER/1272.0

$$HATCHES/1,6,-6435.28613,9839.15918,-4383.16455,4201.00195,-4366.23828,4207.12451,-6418.35938,9845.28027,-6401.43213,9851.40430,-4349.31104,4213.24707,-4332.38428,4219.37012,-6384.50537,9857.52637,-6367.57861,9863.64844,-4315.45752,4225.49219,-4298.53125,4231.61523,-6350.65186,9869.77148

$$LAYER/1280.0

$$HATCHES/1,6,-6435.28613,9839.15918,-4383.16455,4201.00195,-4366.23828,4207.12451,-6418.35938,9845.28027,-6401.43213,9851.40430,-4349.31104,4213.24707,-4332.38428,4219.37012,-6384.50537,9857.52637,-6367.57861,9863.64844,-4315.45752,4225.49219,-4298.53125,4231.61523,-6350.65186,9869.77148

$$LAYER/1288.0

$$HATCHES/1,6,-6435.28613,9839.15918,-4383.16455,4201.00195,-4366.23828,4207.12451,-6418.35938,9845.28027,-6401.43213,9851.40430,-4349.31104,4213.24707,-4332.38428,4219.37012,-6384.50537,9857.52637,-6367.57861,9863.64844,-4315.45752,4225.49219,-4298.53125,4231.61523,-6350.65186,9869.77148

$$LAYER/1296.0

$$HATCHES/1,6,-6435.28613,9839.15918,-4383.16455,4201.00195,-4366.23828,4207.12451,-6418.35938,9845.28027,-6401.43213,9851.40430,-4349.31104,4213.24707,-4332.38428,4219.37012,-6384.50537,9857.52637,-6367.57861,9863.64844,-4315.45752,4225.49219,-4298.53125,4231.61523,-6350.65186,9869.77148

$$LAYER/1304.0

$$HATCHES/1,6,-6435.28613,9839.15918,-4383.16455,4201.00195,-4366.23828,4207.12451,-6418.35938,9845.28027,-6401.43213,9851.40430,-4349.31104,4213.24707,-4332.38428,4219.37012,-6384.50537,9857.52637,-6367.57861,9863.64844,-4315.45752,4225.49219,-4298.53125,4231.61523,-6350.65186,9869.77148

$$LAYER/1312.0

$$HATCHES/1,6,-6435.28613,9839.15918,-4383.16455,4201.00195,-4366.23828,4207.12451,-6418.35938,9845.28027,-6401.43213,9851.40430,-4349.31104,4213.24707,-4332.38428,4219.37012,-6384.50537,9857.52637,-6367.57861,9863.64844,-4315.45752,4225.49219,-4298.53125,4231.61523,-6350.65186,9869.77148

$$LAYER/1320.0

$$HATCHES/1,6,-6435.28613,9839.15918,-4383.16455,4201.00195,-4366.23828,4207.12451,-6418.35938,9845.28027,-6401.43213,9851.40430,-4349.31104,4213.24707,-4332.38428,4219.37012,-6384.50537,9857.52637,-6367.57861,9863.64844,-4315.45752,4225.49219,-4298.53125,4231.61523,-6350.65186,9869.77148

$$LAYER/1328.0

$$HATCHES/1,6,-6435.28613,9839.15918,-4383.16455,4201.00195,-4366.23828,4207.12451,-6418.35938,9845.28027,-6401.43213,9851.40430,-4349.31104,4213.24707,-4332.38428,4219.37012,-6384.50537,9857.52637,-6367.57861,9863.64844,-4315.45752,4225.49219,-4298.53125,4231.61523,-6350.65186,9869.77148

$$LAYER/1336.0

$$HATCHES/1,6,-6435.28613,9839.15918,-4383.16455,4201.00195,-4366.23828,4207.12451,-6418.35938,9845.28027,-6401.43213,9851.40430,-4349.31104,4213.24707,-4332.38428,4219.37012,-6384.50537,9857.52637,-6367.57861,9863.64844,-4315.45752,4225.49219,-4298.53125,4231.61523,-6350.65186,9869.77148

$$LAYER/1344.0

$$HATCHES/1,6,-6435.28613,9839.15918,-4383.16455,4201.00195,-4366.23828,4207.12451,-6418.35938,9845.28027,-6401.43213,9851.40430,-4349.31104,4213.24707,-4332.38428,4219.37012,-6384.50537,9857.52637,-6367.57861,9863.64844,-4315.45752,4225.49219,-4298.53125,4231.61523,-6350.65186,9869.77148

$$LAYER/1352.0

$$HATCHES/1,6,-6435.28613,9839.15918,-4383.16455,4201.00195,-4366.23828,4207.12451,-6418.35938,9845.28027,-6401.43213,9851.40430,-4349.31104,4213.24707,-4332.38428,4219.37012,-6384.50537,9857.52637,-6367.57861,9863.64844,-4315.45752,4225.49219,-4298.53125,4231.61523,-6350.65186,9869.77148

$$LAYER/1360.0

$$HATCHES/1,6,-6435.28613,9839.15918,-4383.16455,4201.00195,-4366.23828,4207.12451,-6418.35938,9845.28027,-6401.43213,9851.40430,-4349.31104,4213.24707,-4332.38428,4219.37012,-

6384.50537,9857.52637,-6367.57861,9863.64844,-4315.45752,4225.49219,-4298.53125,4231.61523,-6350.65186,9869.77148

$$LAYER/1368.0

$$HATCHES/1,6,-6435.28613,9839.15918,-4383.16455,4201.00195,-4366.23828,4207.12451,-6418.35938,9845.28027,-6401.43213,9851.40430,-4349.31104,4213.24707,-4332.38428,4219.37012,-6384.50537,9857.52637,-6367.57861,9863.64844,-4315.45752,4225.49219,-4298.53125,4231.61523,-6350.65186,9869.77148

$$LAYER/1376.0

$$HATCHES/1,6,-6435.28613,9839.15918,-4383.16455,4201.00195,-4366.23828,4207.12451,-6418.35938,9845.28027,-6401.43213,9851.40430,-4349.31104,4213.24707,-4332.38428,4219.37012,-6384.50537,9857.52637,-6367.57861,9863.64844,-4315.45752,4225.49219,-4298.53125,4231.61523,-6350.65186,9869.77148

$$LAYER/1384.0

$$HATCHES/1,6,-6435.28613,9839.15918,-4383.16455,4201.00195,-4366.23828,4207.12451,-6418.35938,9845.28027,-6401.43213,9851.40430,-4349.31104,4213.24707,-4332.38428,4219.37012,-6384.50537,9857.52637,-6367.57861,9863.64844,-4315.45752,4225.49219,-4298.53125,4231.61523,-6350.65186,9869.77148

$$LAYER/1392.0

$$HATCHES/1,6,-6435.28613,9839.15918,-4383.16455,4201.00195,-4366.23828,4207.12451,-6418.35938,9845.28027,-6401.43213,9851.40430,-4349.31104,4213.24707,-4332.38428,4219.37012,-6384.50537,9857.52637,-6367.57861,9863.64844,-4315.45752,4225.49219,-4298.53125,4231.61523,-6350.65186,9869.77148

$$LAYER/1400.0

$$HATCHES/1,6,-6435.28613,9839.15918,-4383.16455,4201.00195,-4366.23828,4207.12451,-6418.35938,9845.28027,-6401.43213,9851.40430,-4349.31104,4213.24707,-4332.38428,4219.37012,-6384.50537,9857.52637,-6367.57861,9863.64844,-4315.45752,4225.49219,-4298.53125,4231.61523,-6350.65186,9869.77148

$$LAYER/1408.0

$$HATCHES/1,6,-6435.28613,9839.15918,-4383.16455,4201.00195,-4366.23828,4207.12451,-6418.35938,9845.28027,-6401.43213,9851.40430,-4349.31104,4213.24707,-4332.38428,4219.37012,-6384.50537,9857.52637,-6367.57861,9863.64844,-4315.45752,4225.49219,-4298.53125,4231.61523,-6350.65186,9869.77148

$$LAYER/1416.0

$$HATCHES/1,6,-6435.28613,9839.15918,-4383.16455,4201.00195,-4366.23828,4207.12451,-6418.35938,9845.28027,-6401.43213,9851.40430,-4349.31104,4213.24707,-4332.38428,4219.37012,-6384.50537,9857.52637,-6367.57861,9863.64844,-4315.45752,4225.49219,-4298.53125,4231.61523,-6350.65186,9869.77148

$$LAYER/1424.0

$$HATCHES/1,6,-6435.28613,9839.15918,-4383.16455,4201.00195,-4366.23828,4207.12451,-6418.35938,9845.28027,-6401.43213,9851.40430,-4349.31104,4213.24707,-4332.38428,4219.37012,-6384.50537,9857.52637,-6367.57861,9863.64844,-4315.45752,4225.49219,-4298.53125,4231.61523,-6350.65186,9869.77148

$$LAYER/1432.0

$$HATCHES/1,6,-6435.28613,9839.15918,-4383.16455,4201.00195,-4366.23828,4207.12451,-6418.35938,9845.28027,-6401.43213,9851.40430,-4349.31104,4213.24707,-4332.38428,4219.37012,-6384.50537,9857.52637,-6367.57861,9863.64844,-4315.45752,4225.49219,-4298.53125,4231.61523,-6350.65186,9869.77148

$$LAYER/1440.0

$$HATCHES/1,6,-6435.28613,9839.15918,-4383.16455,4201.00195,-4366.23828,4207.12451,-6418.35938,9845.28027,-6401.43213,9851.40430,-4349.31104,4213.24707,-4332.38428,4219.37012,-6384.50537,9857.52637,-6367.57861,9863.64844,-4315.45752,4225.49219,-4298.53125,4231.61523,-6350.65186,9869.77148

$$LAYER/1448.0

$$HATCHES/1,6,-6435.28613,9839.15918,-4383.16455,4201.00195,-4366.23828,4207.12451,-6418.35938,9845.28027,-6401.43213,9851.40430,-4349.31104,4213.24707,-4332.38428,4219.37012,-6384.50537,9857.52637,-6367.57861,9863.64844,-4315.45752,4225.49219,-4298.53125,4231.61523,-6350.65186,9869.77148

$$LAYER/1456.0

$$HATCHES/1,6,-6435.28613,9839.15918,-4383.16455,4201.00195,-4366.23828,4207.12451,-6418.35938,9845.28027,-6401.43213,9851.40430,-4349.31104,4213.24707,-4332.38428,4219.37012,-6384.50537,9857.52637,-6367.57861,9863.64844,-4315.45752,4225.49219,-4298.53125,4231.61523,-6350.65186,9869.77148

$$LAYER/1464.0

$$HATCHES/1,6,-6435.28613,9839.15918,-4383.16455,4201.00195,-4366.23828,4207.12451,-6418.35938,9845.28027,-6401.43213,9851.40430,-4349.31104,4213.24707,-4332.38428,4219.37012,-6384.50537,9857.52637,-6367.57861,9863.64844,-4315.45752,4225.49219,-4298.53125,4231.61523,-6350.65186,9869.77148

$$LAYER/1472.0

$$HATCHES/1,6,-6435.28613,9839.15918,-4383.16455,4201.00195,-4366.23828,4207.12451,-6418.35938,9845.28027,-6401.43213,9851.40430,-4349.31104,4213.24707,-4332.38428,4219.37012,-

6384.50537,9857.52637,-6367.57861,9863.64844,-4315.45752,4225.49219,-4298.53125,4231.61523,-6350.65186,9869.77148

$$LAYER/1480.0

$$HATCHES/1,6,-6435.28613,9839.15918,-4383.16455,4201.00195,-4366.23828,4207.12451,-6418.35938,9845.28027,-6401.43213,9851.40430,-4349.31104,4213.24707,-4332.38428,4219.37012,-6384.50537,9857.52637,-6367.57861,9863.64844,-4315.45752,4225.49219,-4298.53125,4231.61523,-6350.65186,9869.77148

$$LAYER/1488.0

$$HATCHES/1,6,-6435.28613,9839.15918,-4383.16455,4201.00195,-4366.23828,4207.12451,-6418.35938,9845.28027,-6401.43213,9851.40430,-4349.31104,4213.24707,-4332.38428,4219.37012,-6384.50537,9857.52637,-6367.57861,9863.64844,-4315.45752,4225.49219,-4298.53125,4231.61523,-6350.65186,9869.77148

$$LAYER/1496.0

$$HATCHES/1,6,-6435.28613,9839.15918,-4383.16455,4201.00195,-4366.23828,4207.12451,-6418.35938,9845.28027,-6401.43213,9851.40430,-4349.31104,4213.24707,-4332.38428,4219.37012,-6384.50537,9857.52637,-6367.57861,9863.64844,-4315.45752,4225.49219,-4298.53125,4231.61523,-6350.65186,9869.77148

$$LAYER/1504.0

$$HATCHES/1,6,-6435.28613,9839.15918,-4383.16455,4201.00195,-4366.23828,4207.12451,-6418.35938,9845.28027,-6401.43213,9851.40430,-4349.31104,4213.24707,-4332.38428,4219.37012,-6384.50537,9857.52637,-6367.57861,9863.64844,-4315.45752,4225.49219,-4298.53125,4231.61523,-6350.65186,9869.77148

$$LAYER/1512.0

$$HATCHES/1,6,-6435.28613,9839.15918,-4383.16455,4201.00195,-4366.23828,4207.12451,-6418.35938,9845.28027,-6401.43213,9851.40430,-4349.31104,4213.24707,-4332.38428,4219.37012,-6384.50537,9857.52637,-6367.57861,9863.64844,-4315.45752,4225.49219,-4298.53125,4231.61523,-6350.65186,9869.77148

$$LAYER/1520.0

$$HATCHES/1,6,-6435.28613,9839.15918,-4383.16455,4201.00195,-4366.23828,4207.12451,-6418.35938,9845.28027,-6401.43213,9851.40430,-4349.31104,4213.24707,-4332.38428,4219.37012,-6384.50537,9857.52637,-6367.57861,9863.64844,-4315.45752,4225.49219,-4298.53125,4231.61523,-6350.65186,9869.77148

$$LAYER/1528.0

$$HATCHES/1,6,-6435.28613,9839.15918,-4383.16455,4201.00195,-4366.23828,4207.12451,-6418.35938,9845.28027,-6401.43213,9851.40430,-4349.31104,4213.24707,-4332.38428,4219.37012,-6384.50537,9857.52637,-6367.57861,9863.64844,-4315.45752,4225.49219,-4298.53125,4231.61523,-6350.65186,9869.77148

$$LAYER/1536.0

$$HATCHES/1,6,-6435.28613,9839.15918,-4383.16455,4201.00195,-4366.23828,4207.12451,-6418.35938,9845.28027,-6401.43213,9851.40430,-4349.31104,4213.24707,-4332.38428,4219.37012,-6384.50537,9857.52637,-6367.57861,9863.64844,-4315.45752,4225.49219,-4298.53125,4231.61523,-6350.65186,9869.77148

$$LAYER/1544.0

$$HATCHES/1,6,-6435.28613,9839.15918,-4383.16455,4201.00195,-4366.23828,4207.12451,-6418.35938,9845.28027,-6401.43213,9851.40430,-4349.31104,4213.24707,-4332.38428,4219.37012,-6384.50537,9857.52637,-6367.57861,9863.64844,-4315.45752,4225.49219,-4298.53125,4231.61523,-6350.65186,9869.77148

$$LAYER/1552.0

$$HATCHES/1,6,-6435.28613,9839.15918,-4383.16455,4201.00195,-4366.23828,4207.12451,-6418.35938,9845.28027,-6401.43213,9851.40430,-4349.31104,4213.24707,-4332.38428,4219.37012,-6384.50537,9857.52637,-6367.57861,9863.64844,-4315.45752,4225.49219,-4298.53125,4231.61523,-6350.65186,9869.77148

$$LAYER/1560.0

$$HATCHES/1,6,-6435.28613,9839.15918,-4383.16455,4201.00195,-4366.23828,4207.12451,-6418.35938,9845.28027,-6401.43213,9851.40430,-4349.31104,4213.24707,-4332.38428,4219.37012,-6384.50537,9857.52637,-6367.57861,9863.64844,-4315.45752,4225.49219,-4298.53125,4231.61523,-6350.65186,9869.77148

$$LAYER/1568.0

$$HATCHES/1,6,-6435.28613,9839.15918,-4383.16455,4201.00195,-4366.23828,4207.12451,-6418.35938,9845.28027,-6401.43213,9851.40430,-4349.31104,4213.24707,-4332.38428,4219.37012,-6384.50537,9857.52637,-6367.57861,9863.64844,-4315.45752,4225.49219,-4298.53125,4231.61523,-6350.65186,9869.77148

$$LAYER/1576.0

$$HATCHES/1,6,-6435.28613,9839.15918,-4383.16455,4201.00195,-4366.23828,4207.12451,-6418.35938,9845.28027,-6401.43213,9851.40430,-4349.31104,4213.24707,-4332.38428,4219.37012,-6384.50537,9857.52637,-6367.57861,9863.64844,-4315.45752,4225.49219,-4298.53125,4231.61523,-6350.65186,9869.77148

$$LAYER/1584.0

$$HATCHES/1,6,-6435.28613,9839.15918,-4383.16455,4201.00195,-4366.23828,4207.12451,-6418.35938,9845.28027,-6401.43213,9851.40430,-4349.31104,4213.24707,-4332.38428,4219.37012,-

6384.50537,9857.52637,-6367.57861,9863.64844,-4315.45752,4225.49219,-4298.53125,4231.61523,-6350.65186,9869.77148

$$LAYER/1592.0

$$HATCHES/1,6,-6435.28613,9839.15918,-4383.16455,4201.00195,-4366.23828,4207.12451,-6418.35938,9845.28027,-6401.43213,9851.40430,-4349.31104,4213.24707,-4332.38428,4219.37012,-6384.50537,9857.52637,-6367.57861,9863.64844,-4315.45752,4225.49219,-4298.53125,4231.61523,-6350.65186,9869.77148

$$LAYER/1600.0

$$HATCHES/1,6,-6435.28613,9839.15918,-4383.16455,4201.00195,-4366.23828,4207.12451,-6418.35938,9845.28027,-6401.43213,9851.40430,-4349.31104,4213.24707,-4332.38428,4219.37012,-6384.50537,9857.52637,-6367.57861,9863.64844,-4315.45752,4225.49219,-4298.53125,4231.61523,-6350.65186,9869.77148

$$LAYER/1608.0

$$HATCHES/1,6,-6435.28613,9839.15918,-4383.16455,4201.00195,-4366.23828,4207.12451,-6418.35938,9845.28027,-6401.43213,9851.40430,-4349.31104,4213.24707,-4332.38428,4219.37012,-6384.50537,9857.52637,-6367.57861,9863.64844,-4315.45752,4225.49219,-4298.53125,4231.61523,-6350.65186,9869.77148

$$LAYER/1616.0

$$HATCHES/1,6,-6435.28613,9839.15918,-4383.16455,4201.00195,-4366.23828,4207.12451,-6418.35938,9845.28027,-6401.43213,9851.40430,-4349.31104,4213.24707,-4332.38428,4219.37012,-6384.50537,9857.52637,-6367.57861,9863.64844,-4315.45752,4225.49219,-4298.53125,4231.61523,-6350.65186,9869.77148

$$LAYER/1624.0

$$HATCHES/1,6,-6435.28613,9839.15918,-4383.16455,4201.00195,-4366.23828,4207.12451,-6418.35938,9845.28027,-6401.43213,9851.40430,-4349.31104,4213.24707,-4332.38428,4219.37012,-6384.50537,9857.52637,-6367.57861,9863.64844,-4315.45752,4225.49219,-4298.53125,4231.61523,-6350.65186,9869.77148

$$LAYER/1632.0

$$HATCHES/1,6,-6435.28613,9839.15918,-4383.16455,4201.00195,-4366.23828,4207.12451,-6418.35938,9845.28027,-6401.43213,9851.40430,-4349.31104,4213.24707,-4332.38428,4219.37012,-6384.50537,9857.52637,-6367.57861,9863.64844,-4315.45752,4225.49219,-4298.53125,4231.61523,-6350.65186,9869.77148

$$LAYER/1640.0

$$HATCHES/1,6,-6435.28613,9839.15918,-4383.16455,4201.00195,-4366.23828,4207.12451,-6418.35938,9845.28027,-6401.43213,9851.40430,-4349.31104,4213.24707,-4332.38428,4219.37012,-6384.50537,9857.52637,-6367.57861,9863.64844,-4315.45752,4225.49219,-4298.53125,4231.61523,-6350.65186,9869.77148

$$LAYER/1648.0

$$HATCHES/1,6,-6435.28613,9839.15918,-4383.16455,4201.00195,-4366.23828,4207.12451,-6418.35938,9845.28027,-6401.43213,9851.40430,-4349.31104,4213.24707,-4332.38428,4219.37012,-6384.50537,9857.52637,-6367.57861,9863.64844,-4315.45752,4225.49219,-4298.53125,4231.61523,-6350.65186,9869.77148

$$LAYER/1656.0

$$HATCHES/1,6,-6435.28613,9839.15918,-4383.16455,4201.00195,-4366.23828,4207.12451,-6418.35938,9845.28027,-6401.43213,9851.40430,-4349.31104,4213.24707,-4332.38428,4219.37012,-6384.50537,9857.52637,-6367.57861,9863.64844,-4315.45752,4225.49219,-4298.53125,4231.61523,-6350.65186,9869.77148

$$LAYER/1664.0

$$HATCHES/1,6,-6435.28613,9839.15918,-4383.16455,4201.00195,-4366.23828,4207.12451,-6418.35938,9845.28027,-6401.43213,9851.40430,-4349.31104,4213.24707,-4332.38428,4219.37012,-6384.50537,9857.52637,-6367.57861,9863.64844,-4315.45752,4225.49219,-4298.53125,4231.61523,-6350.65186,9869.77148

$$LAYER/1672.0

$$HATCHES/1,6,-6435.28613,9839.15918,-4383.16455,4201.00195,-4366.23828,4207.12451,-6418.35938,9845.28027,-6401.43213,9851.40430,-4349.31104,4213.24707,-4332.38428,4219.37012,-6384.50537,9857.52637,-6367.57861,9863.64844,-4315.45752,4225.49219,-4298.53125,4231.61523,-6350.65186,9869.77148

$$LAYER/1680.0

$$HATCHES/1,6,-6435.28613,9839.15918,-4383.16455,4201.00195,-4366.23828,4207.12451,-6418.35938,9845.28027,-6401.43213,9851.40430,-4349.31104,4213.24707,-4332.38428,4219.37012,-6384.50537,9857.52637,-6367.57861,9863.64844,-4315.45752,4225.49219,-4298.53125,4231.61523,-6350.65186,9869.77148

$$LAYER/1688.0

$$HATCHES/1,6,-6435.28613,9839.15918,-4383.16455,4201.00195,-4366.23828,4207.12451,-6418.35938,9845.28027,-6401.43213,9851.40430,-4349.31104,4213.24707,-4332.38428,4219.37012,-6384.50537,9857.52637,-6367.57861,9863.64844,-4315.45752,4225.49219,-4298.53125,4231.61523,-6350.65186,9869.77148

$$LAYER/1696.0

$$HATCHES/1,6,-6435.28613,9839.15918,-4383.16455,4201.00195,-4366.23828,4207.12451,-6418.35938,9845.28027,-6401.43213,9851.40430,-4349.31104,4213.24707,-4332.38428,4219.37012,-

6384.50537,9857.52637,-6367.57861,9863.64844,-4315.45752,4225.49219,-4298.53125,4231.61523,-6350.65186,9869.77148

$$LAYER/1704.0

$$HATCHES/1,6,-6435.28613,9839.15918,-4383.16455,4201.00195,-4366.23828,4207.12451,-6418.35938,9845.28027,-6401.43213,9851.40430,-4349.31104,4213.24707,-4332.38428,4219.37012,-6384.50537,9857.52637,-6367.57861,9863.64844,-4315.45752,4225.49219,-4298.53125,4231.61523,-6350.65186,9869.77148

$$LAYER/1712.0

$$HATCHES/1,6,-6435.28613,9839.15918,-4383.16455,4201.00195,-4366.23828,4207.12451,-6418.35938,9845.28027,-6401.43213,9851.40430,-4349.31104,4213.24707,-4332.38428,4219.37012,-6384.50537,9857.52637,-6367.57861,9863.64844,-4315.45752,4225.49219,-4298.53125,4231.61523,-6350.65186,9869.77148

$$LAYER/1720.0

$$HATCHES/1,6,-6435.28613,9839.15918,-4383.16455,4201.00195,-4366.23828,4207.12451,-6418.35938,9845.28027,-6401.43213,9851.40430,-4349.31104,4213.24707,-4332.38428,4219.37012,-6384.50537,9857.52637,-6367.57861,9863.64844,-4315.45752,4225.49219,-4298.53125,4231.61523,-6350.65186,9869.77148

$$LAYER/1728.0

$$HATCHES/1,6,-6435.28613,9839.15918,-4383.16455,4201.00195,-4366.23828,4207.12451,-6418.35938,9845.28027,-6401.43213,9851.40430,-4349.31104,4213.24707,-4332.38428,4219.37012,-6384.50537,9857.52637,-6367.57861,9863.64844,-4315.45752,4225.49219,-4298.53125,4231.61523,-6350.65186,9869.77148

$$LAYER/1736.0

$$HATCHES/1,6,-6435.28613,9839.15918,-4383.16455,4201.00195,-4366.23828,4207.12451,-6418.35938,9845.28027,-6401.43213,9851.40430,-4349.31104,4213.24707,-4332.38428,4219.37012,-6384.50537,9857.52637,-6367.57861,9863.64844,-4315.45752,4225.49219,-4298.53125,4231.61523,-6350.65186,9869.77148

$$LAYER/1744.0

$$HATCHES/1,6,-6435.28613,9839.15918,-4383.16455,4201.00195,-4366.23828,4207.12451,-6418.35938,9845.28027,-6401.43213,9851.40430,-4349.31104,4213.24707,-4332.38428,4219.37012,-6384.50537,9857.52637,-6367.57861,9863.64844,-4315.45752,4225.49219,-4298.53125,4231.61523,-6350.65186,9869.77148

$$LAYER/1752.0

$$HATCHES/1,6,-6435.28613,9839.15918,-4383.16455,4201.00195,-4366.23828,4207.12451,-6418.35938,9845.28027,-6401.43213,9851.40430,-4349.31104,4213.24707,-4332.38428,4219.37012,-6384.50537,9857.52637,-6367.57861,9863.64844,-4315.45752,4225.49219,-4298.53125,4231.61523,-6350.65186,9869.77148

$$LAYER/1760.0

$$HATCHES/1,6,-6435.28613,9839.15918,-4383.16455,4201.00195,-4366.23828,4207.12451,-6418.35938,9845.28027,-6401.43213,9851.40430,-4349.31104,4213.24707,-4332.38428,4219.37012,-6384.50537,9857.52637,-6367.57861,9863.64844,-4315.45752,4225.49219,-4298.53125,4231.61523,-6350.65186,9869.77148

$$LAYER/1768.0

$$HATCHES/1,6,-6435.28613,9839.15918,-4383.16455,4201.00195,-4366.23828,4207.12451,-6418.35938,9845.28027,-6401.43213,9851.40430,-4349.31104,4213.24707,-4332.38428,4219.37012,-6384.50537,9857.52637,-6367.57861,9863.64844,-4315.45752,4225.49219,-4298.53125,4231.61523,-6350.65186,9869.77148

$$LAYER/1776.0

$$HATCHES/1,6,-6435.28613,9839.15918,-4383.16455,4201.00195,-4366.23828,4207.12451,-6418.35938,9845.28027,-6401.43213,9851.40430,-4349.31104,4213.24707,-4332.38428,4219.37012,-6384.50537,9857.52637,-6367.57861,9863.64844,-4315.45752,4225.49219,-4298.53125,4231.61523,-6350.65186,9869.77148

$$LAYER/1784.0

$$HATCHES/1,6,-6435.28613,9839.15918,-4383.16455,4201.00195,-4366.23828,4207.12451,-6418.35938,9845.28027,-6401.43213,9851.40430,-4349.31104,4213.24707,-4332.38428,4219.37012,-6384.50537,9857.52637,-6367.57861,9863.64844,-4315.45752,4225.49219,-4298.53125,4231.61523,-6350.65186,9869.77148

$$LAYER/1792.0

$$HATCHES/1,6,-6435.28613,9839.15918,-4383.16455,4201.00195,-4366.23828,4207.12451,-6418.35938,9845.28027,-6401.43213,9851.40430,-4349.31104,4213.24707,-4332.38428,4219.37012,-6384.50537,9857.52637,-6367.57861,9863.64844,-4315.45752,4225.49219,-4298.53125,4231.61523,-6350.65186,9869.77148

$$LAYER/1800.0

$$HATCHES/1,6,-6435.28613,9839.15918,-4383.16455,4201.00195,-4366.23828,4207.12451,-6418.35938,9845.28027,-6401.43213,9851.40430,-4349.31104,4213.24707,-4332.38428,4219.37012,-6384.50537,9857.52637,-6367.57861,9863.64844,-4315.45752,4225.49219,-4298.53125,4231.61523,-6350.65186,9869.77148

$$LAYER/1808.0

$$HATCHES/1,6,-6435.28613,9839.15918,-4383.16455,4201.00195,-4366.23828,4207.12451,-6418.35938,9845.28027,-6401.43213,9851.40430,-4349.31104,4213.24707,-4332.38428,4219.37012,-

6384.50537,9857.52637,-6367.57861,9863.64844,-4315.45752,4225.49219,-4298.53125,4231.61523,-6350.65186,9869.77148

$$LAYER/1816.0

$$HATCHES/1,6,-6435.28613,9839.15918,-4383.16455,4201.00195,-4366.23828,4207.12451,-6418.35938,9845.28027,-6401.43213,9851.40430,-4349.31104,4213.24707,-4332.38428,4219.37012,-6384.50537,9857.52637,-6367.57861,9863.64844,-4315.45752,4225.49219,-4298.53125,4231.61523,-6350.65186,9869.77148

$$LAYER/1824.0

$$HATCHES/1,6,-6435.28613,9839.15918,-4383.16455,4201.00195,-4366.23828,4207.12451,-6418.35938,9845.28027,-6401.43213,9851.40430,-4349.31104,4213.24707,-4332.38428,4219.37012,-6384.50537,9857.52637,-6367.57861,9863.64844,-4315.45752,4225.49219,-4298.53125,4231.61523,-6350.65186,9869.77148

$$LAYER/1832.0

$$HATCHES/1,6,-6435.28613,9839.15918,-4383.16455,4201.00195,-4366.23828,4207.12451,-6418.35938,9845.28027,-6401.43213,9851.40430,-4349.31104,4213.24707,-4332.38428,4219.37012,-6384.50537,9857.52637,-6367.57861,9863.64844,-4315.45752,4225.49219,-4298.53125,4231.61523,-6350.65186,9869.77148

$$LAYER/1840.0

$$HATCHES/1,6,-6435.28613,9839.15918,-4383.16455,4201.00195,-4366.23828,4207.12451,-6418.35938,9845.28027,-6401.43213,9851.40430,-4349.31104,4213.24707,-4332.38428,4219.37012,-6384.50537,9857.52637,-6367.57861,9863.64844,-4315.45752,4225.49219,-4298.53125,4231.61523,-6350.65186,9869.77148

$$LAYER/1848.0

$$HATCHES/1,6,-6435.28613,9839.15918,-4383.16455,4201.00195,-4366.23828,4207.12451,-6418.35938,9845.28027,-6401.43213,9851.40430,-4349.31104,4213.24707,-4332.38428,4219.37012,-6384.50537,9857.52637,-6367.57861,9863.64844,-4315.45752,4225.49219,-4298.53125,4231.61523,-6350.65186,9869.77148

$$LAYER/1856.0

$$HATCHES/1,6,-6435.28613,9839.15918,-4383.16455,4201.00195,-4366.23828,4207.12451,-6418.35938,9845.28027,-6401.43213,9851.40430,-4349.31104,4213.24707,-4332.38428,4219.37012,-6384.50537,9857.52637,-6367.57861,9863.64844,-4315.45752,4225.49219,-4298.53125,4231.61523,-6350.65186,9869.77148

$$LAYER/1864.0

$$HATCHES/1,6,-6435.28613,9839.15918,-4383.16455,4201.00195,-4366.23828,4207.12451,-6418.35938,9845.28027,-6401.43213,9851.40430,-4349.31104,4213.24707,-4332.38428,4219.37012,-6384.50537,9857.52637,-6367.57861,9863.64844,-4315.45752,4225.49219,-4298.53125,4231.61523,-6350.65186,9869.77148

$$LAYER/1872.0

$$HATCHES/1,6,-6435.28613,9839.15918,-4383.16455,4201.00195,-4366.23828,4207.12451,-6418.35938,9845.28027,-6401.43213,9851.40430,-4349.31104,4213.24707,-4332.38428,4219.37012,-6384.50537,9857.52637,-6367.57861,9863.64844,-4315.45752,4225.49219,-4298.53125,4231.61523,-6350.65186,9869.77148

$$LAYER/1880.0

$$HATCHES/1,6,-6435.28613,9839.15918,-4383.16455,4201.00195,-4366.23828,4207.12451,-6418.35938,9845.28027,-6401.43213,9851.40430,-4349.31104,4213.24707,-4332.38428,4219.37012,-6384.50537,9857.52637,-6367.57861,9863.64844,-4315.45752,4225.49219,-4298.53125,4231.61523,-6350.65186,9869.77148

$$LAYER/1888.0

$$HATCHES/1,6,-6435.28613,9839.15918,-4383.16455,4201.00195,-4366.23828,4207.12451,-6418.35938,9845.28027,-6401.43213,9851.40430,-4349.31104,4213.24707,-4332.38428,4219.37012,-6384.50537,9857.52637,-6367.57861,9863.64844,-4315.45752,4225.49219,-4298.53125,4231.61523,-6350.65186,9869.77148

$$LAYER/1896.0

$$HATCHES/1,6,-6435.28613,9839.15918,-4383.16455,4201.00195,-4366.23828,4207.12451,-6418.35938,9845.28027,-6401.43213,9851.40430,-4349.31104,4213.24707,-4332.38428,4219.37012,-6384.50537,9857.52637,-6367.57861,9863.64844,-4315.45752,4225.49219,-4298.53125,4231.61523,-6350.65186,9869.77148

$$LAYER/1904.0

$$HATCHES/1,6,-6435.28613,9839.15918,-4383.16455,4201.00195,-4366.23828,4207.12451,-6418.35938,9845.28027,-6401.43213,9851.40430,-4349.31104,4213.24707,-4332.38428,4219.37012,-6384.50537,9857.52637,-6367.57861,9863.64844,-4315.45752,4225.49219,-4298.53125,4231.61523,-6350.65186,9869.77148

$$LAYER/1912.0

$$HATCHES/1,6,-6435.28613,9839.15918,-4383.16455,4201.00195,-4366.23828,4207.12451,-6418.35938,9845.28027,-6401.43213,9851.40430,-4349.31104,4213.24707,-4332.38428,4219.37012,-6384.50537,9857.52637,-6367.57861,9863.64844,-4315.45752,4225.49219,-4298.53125,4231.61523,-6350.65186,9869.77148

$$LAYER/1920.0

$$HATCHES/1,6,-6435.28613,9839.15918,-4383.16455,4201.00195,-4366.23828,4207.12451,-6418.35938,9845.28027,-6401.43213,9851.40430,-4349.31104,4213.24707,-4332.38428,4219.37012,-

6384.50537,9857.52637,-6367.57861,9863.64844,-4315.45752,4225.49219,-4298.53125,4231.61523,-6350.65186,9869.77148

$$LAYER/1928.0

$$HATCHES/1,6,-6435.28613,9839.15918,-4383.16455,4201.00195,-4366.23828,4207.12451,-6418.35938,9845.28027,-6401.43213,9851.40430,-4349.31104,4213.24707,-4332.38428,4219.37012,-6384.50537,9857.52637,-6367.57861,9863.64844,-4315.45752,4225.49219,-4298.53125,4231.61523,-6350.65186,9869.77148

$$LAYER/1936.0

$$HATCHES/1,6,-6435.28613,9839.15918,-4383.16455,4201.00195,-4366.23828,4207.12451,-6418.35938,9845.28027,-6401.43213,9851.40430,-4349.31104,4213.24707,-4332.38428,4219.37012,-6384.50537,9857.52637,-6367.57861,9863.64844,-4315.45752,4225.49219,-4298.53125,4231.61523,-6350.65186,9869.77148

$$LAYER/1944.0

$$HATCHES/1,6,-6435.28613,9839.15918,-4383.16455,4201.00195,-4366.23828,4207.12451,-6418.35938,9845.28027,-6401.43213,9851.40430,-4349.31104,4213.24707,-4332.38428,4219.37012,-6384.50537,9857.52637,-6367.57861,9863.64844,-4315.45752,4225.49219,-4298.53125,4231.61523,-6350.65186,9869.77148

$$LAYER/1952.0

$$HATCHES/1,6,-6435.28613,9839.15918,-4383.16455,4201.00195,-4366.23828,4207.12451,-6418.35938,9845.28027,-6401.43213,9851.40430,-4349.31104,4213.24707,-4332.38428,4219.37012,-6384.50537,9857.52637,-6367.57861,9863.64844,-4315.45752,4225.49219,-4298.53125,4231.61523,-6350.65186,9869.77148

$$LAYER/1960.0

$$HATCHES/1,6,-6435.28613,9839.15918,-4383.16455,4201.00195,-4366.23828,4207.12451,-6418.35938,9845.28027,-6401.43213,9851.40430,-4349.31104,4213.24707,-4332.38428,4219.37012,-6384.50537,9857.52637,-6367.57861,9863.64844,-4315.45752,4225.49219,-4298.53125,4231.61523,-6350.65186,9869.77148

$$LAYER/1968.0

$$HATCHES/1,6,-6435.28613,9839.15918,-4383.16455,4201.00195,-4366.23828,4207.12451,-6418.35938,9845.28027,-6401.43213,9851.40430,-4349.31104,4213.24707,-4332.38428,4219.37012,-6384.50537,9857.52637,-6367.57861,9863.64844,-4315.45752,4225.49219,-4298.53125,4231.61523,-6350.65186,9869.77148

$$LAYER/1976.0

$$HATCHES/1,6,-6435.28613,9839.15918,-4383.16455,4201.00195,-4366.23828,4207.12451,-6418.35938,9845.28027,-6401.43213,9851.40430,-4349.31104,4213.24707,-4332.38428,4219.37012,-6384.50537,9857.52637,-6367.57861,9863.64844,-4315.45752,4225.49219,-4298.53125,4231.61523,-6350.65186,9869.77148

$$LAYER/1984.0

$$HATCHES/1,6,-6435.28613,9839.15918,-4383.16455,4201.00195,-4366.23828,4207.12451,-6418.35938,9845.28027,-6401.43213,9851.40430,-4349.31104,4213.24707,-4332.38428,4219.37012,-6384.50537,9857.52637,-6367.57861,9863.64844,-4315.45752,4225.49219,-4298.53125,4231.61523,-6350.65186,9869.77148

$$LAYER/1992.0

$$HATCHES/1,6,-6435.28613,9839.15918,-4383.16455,4201.00195,-4366.23828,4207.12451,-6418.35938,9845.28027,-6401.43213,9851.40430,-4349.31104,4213.24707,-4332.38428,4219.37012,-6384.50537,9857.52637,-6367.57861,9863.64844,-4315.45752,4225.49219,-4298.53125,4231.61523,-6350.65186,9869.77148

$$LAYER/2000.0

$$HATCHES/1,6,-6435.28613,9839.15918,-4383.16455,4201.00195,-4366.23828,4207.12451,-6418.35938,9845.28027,-6401.43213,9851.40430,-4349.31104,4213.24707,-4332.38428,4219.37012,-6384.50537,9857.52637,-6367.57861,9863.64844,-4315.45752,4225.49219,-4298.53125,4231.61523,-6350.65186,9869.77148

$$LAYER/2008.0

$$HATCHES/1,6,-6435.28613,9839.15918,-4383.16455,4201.00195,-4366.23828,4207.12451,-6418.35938,9845.28125,-6401.43311,9851.40527,-4349.31104,4213.24707,-4332.38428,4219.37012,-6384.50586,9857.52734,-6367.57910,9863.64941,-4315.45752,4225.49219,-4298.53125,4231.61523,-6350.65234,9869.77148

$$LAYER/2016.0

$$HATCHES/1,6,-6435.28613,9839.15918,-4383.16455,4201.00195,-4366.23828,4207.12451,-6418.35938,9845.28027,-6401.43213,9851.40430,-4349.31104,4213.24707,-4332.38428,4219.37012,-6384.50537,9857.52637,-6367.57861,9863.64844,-4315.45752,4225.49219,-4298.53125,4231.61523,-6350.65186,9869.77148

$$LAYER/2024.0

$$HATCHES/1,6,-6435.28613,9839.15918,-4383.16455,4201.00195,-4366.23828,4207.12451,-6418.35938,9845.28027,-6401.43213,9851.40430,-4349.31104,4213.24707,-4332.38428,4219.37012,-6384.50537,9857.52637,-6367.57861,9863.64844,-4315.45752,4225.49219,-4298.53125,4231.61523,-6350.65186,9869.77148

$$LAYER/2032.0

$$HATCHES/1,6,-6435.28613,9839.15918,-4383.16455,4201.00195,-4366.23828,4207.12451,-6418.35938,9845.28027,-6401.43213,9851.40430,-4349.31104,4213.24707,-4332.38428,4219.37012,-

6384.50537,9857.52637,-6367.57861,9863.64844,-4315.45752,4225.49219,-4298.53125,4231.61523,-6350.65186,9869.77148

$$LAYER/2040.0

$$HATCHES/1,6,-6435.28613,9839.15918,-4383.16455,4201.00195,-4366.23828,4207.12451,-6418.35938,9845.28027,-6401.43213,9851.40430,-4349.31104,4213.24707,-4332.38428,4219.37012,-6384.50537,9857.52637,-6367.57861,9863.64844,-4315.45752,4225.49219,-4298.53125,4231.61523,-6350.65186,9869.77148

$$LAYER/2048.0

$$HATCHES/1,6,-6435.28613,9839.15918,-4383.16455,4201.00195,-4366.23828,4207.12451,-6418.35938,9845.28027,-6401.43213,9851.40430,-4349.31104,4213.24707,-4332.38428,4219.37012,-6384.50537,9857.52637,-6367.57861,9863.64844,-4315.45752,4225.49219,-4298.53125,4231.61523,-6350.65186,9869.77148

$$LAYER/2056.0

$$HATCHES/1,6,-6435.28760,9839.16309,-4383.16455,4201.00195,-4366.23828,4207.12451,-6418.36084,9845.28516,-6401.43359,9851.40820,-4349.31104,4213.24707,-4332.38428,4219.37012,-6384.50684,9857.52930,-6367.57959,9863.65039,-4315.45752,4225.49219,-4298.53125,4231.61523,-6350.65234,9869.77246

$$LAYER/2064.0

$$HATCHES/1,6,-6435.28613,9839.15918,-4383.16455,4201.00195,-4366.23828,4207.12451,-6418.35938,9845.28027,-6401.43213,9851.40430,-4349.31104,4213.24707,-4332.38428,4219.37012,-6384.50537,9857.52637,-6367.57861,9863.64844,-4315.45752,4225.49219,-4298.53125,4231.61523,-6350.65186,9869.77148

$$LAYER/2072.0

$$HATCHES/1,6,-6435.28613,9839.15918,-4383.16455,4201.00195,-4366.23828,4207.12451,-6418.35938,9845.28027,-6401.43213,9851.40430,-4349.31104,4213.24707,-4332.38428,4219.37012,-6384.50537,9857.52637,-6367.57861,9863.64844,-4315.45752,4225.49219,-4298.53125,4231.61523,-6350.65186,9869.77148

$$LAYER/2080.0

$$HATCHES/1,6,-6435.28613,9839.15918,-4383.16455,4201.00195,-4366.23828,4207.12451,-6418.35938,9845.28027,-6401.43213,9851.40430,-4349.31104,4213.24707,-4332.38428,4219.37012,-6384.50537,9857.52637,-6367.57861,9863.64844,-4315.45752,4225.49219,-4298.53125,4231.61523,-6350.65186,9869.77148

$$LAYER/2088.0

$$HATCHES/1,6,-6435.28613,9839.15918,-4383.16455,4201.00195,-4366.23828,4207.12451,-6418.35938,9845.28027,-6401.43213,9851.40430,-4349.31104,4213.24707,-4332.38428,4219.37012,-6384.50537,9857.52637,-6367.57861,9863.64844,-4315.45752,4225.49219,-4298.53125,4231.61523,-6350.65186,9869.77148

$$LAYER/2096.0

$$HATCHES/1,6,-6435.28613,9839.15918,-4383.16455,4201.00195,-4366.23828,4207.12451,-6418.35938,9845.28027,-6401.43213,9851.40430,-4349.31104,4213.24707,-4332.38428,4219.37012,-6384.50537,9857.52637,-6367.57861,9863.64844,-4315.45752,4225.49219,-4298.53125,4231.61523,-6350.65186,9869.77148

$$LAYER/2104.0

$$HATCHES/1,6,-6435.28613,9839.15918,-4383.16455,4201.00195,-4366.23828,4207.12451,-6418.35938,9845.28027,-6401.43213,9851.40430,-4349.31104,4213.24707,-4332.38428,4219.37012,-6384.50537,9857.52637,-6367.57861,9863.64844,-4315.45752,4225.49219,-4298.53125,4231.61523,-6350.65186,9869.77148

$$LAYER/2112.0

$$HATCHES/1,6,-6435.28906,9839.16895,-4383.16455,4201.00195,-4366.23828,4207.12451,-6418.36279,9845.28906,-6401.43457,9851.41016,-4349.31104,4213.24707,-4332.38428,4219.37012,-6384.50732,9857.53027,-6367.57959,9863.65039,-4315.45752,4225.49219,-4298.53125,4231.61523,-6350.65186,9869.77051

$$LAYER/2120.0

$$HATCHES/1,6,-6435.28613,9839.15918,-4383.16455,4201.00195,-4366.23828,4207.12451,-6418.35938,9845.28027,-6401.43213,9851.40430,-4349.31104,4213.24707,-4332.38428,4219.37012,-6384.50537,9857.52637,-6367.57861,9863.64844,-4315.45752,4225.49219,-4298.53125,4231.61523,-6350.65186,9869.77148

$$LAYER/2128.0

$$HATCHES/1,6,-6435.28613,9839.15918,-4383.16455,4201.00195,-4366.23828,4207.12451,-6418.35938,9845.28027,-6401.43213,9851.40430,-4349.31104,4213.24707,-4332.38428,4219.37012,-6384.50537,9857.52637,-6367.57861,9863.64844,-4315.45752,4225.49219,-4298.53125,4231.61523,-6350.65186,9869.77148

$$LAYER/2136.0

$$HATCHES/1,6,-6435.28613,9839.15918,-4383.16455,4201.00195,-4366.23828,4207.12451,-6418.35938,9845.28027,-6401.43213,9851.40430,-4349.31104,4213.24707,-4332.38428,4219.37012,-6384.50537,9857.52637,-6367.57861,9863.64844,-4315.45752,4225.49219,-4298.53125,4231.61523,-6350.65186,9869.77148

$$LAYER/2144.0

$$HATCHES/1,6,-6435.28613,9839.15918,-4383.16455,4201.00195,-4366.23828,4207.12451,-6418.35938,9845.28027,-6401.43213,9851.40430,-4349.31104,4213.24707,-4332.38428,4219.37012,-

6384.50537,9857.52637,-6367.57861,9863.64844,-4315.45752,4225.49219,-4298.53125,4231.61523,-6350.65186,9869.77148

$$LAYER/2152.0

$$HATCHES/1,6,-6435.28613,9839.15918,-4383.16455,4201.00195,-4366.23828,4207.12451,-6418.35938,9845.28027,-6401.43213,9851.40430,-4349.31104,4213.24707,-4332.38428,4219.37012,-6384.50537,9857.52637,-6367.57861,9863.64844,-4315.45752,4225.49219,-4298.53125,4231.61523,-6350.65186,9869.77148

$$LAYER/2160.0

$$HATCHES/1,6,-6435.28613,9839.15918,-4383.16455,4201.00195,-4366.23828,4207.12451,-6418.35938,9845.28027,-6401.43213,9851.40430,-4349.31104,4213.24707,-4332.38428,4219.37012,-6384.50537,9857.52637,-6367.57861,9863.64844,-4315.45752,4225.49219,-4298.53125,4231.61523,-6350.65186,9869.77148

$$LAYER/2168.0

$$HATCHES/1,6,-6435.28613,9839.15918,-4383.16455,4201.00195,-4366.23828,4207.12451,-6418.35938,9845.28027,-6401.43213,9851.40430,-4349.31104,4213.24707,-4332.38428,4219.37012,-6384.50537,9857.52637,-6367.57861,9863.64844,-4315.45752,4225.49219,-4298.53125,4231.61523,-6350.65186,9869.77148

$$LAYER/2176.0

$$HATCHES/1,6,-6435.28613,9839.15918,-4383.16455,4201.00195,-4366.23828,4207.12451,-6418.35938,9845.28027,-6401.43213,9851.40430,-4349.31104,4213.24707,-4332.38428,4219.37012,-6384.50537,9857.52637,-6367.57861,9863.64844,-4315.45752,4225.49219,-4298.53125,4231.61523,-6350.65186,9869.77148

$$LAYER/2184.0

$$HATCHES/1,6,-6435.28613,9839.15918,-4383.16455,4201.00195,-4366.23828,4207.12451,-6418.35938,9845.28027,-6401.43213,9851.40430,-4349.31104,4213.24707,-4332.38428,4219.37012,-6384.50537,9857.52637,-6367.57861,9863.64844,-4315.45752,4225.49219,-4298.53125,4231.61523,-6350.65186,9869.77148

$$LAYER/2192.0

$$HATCHES/1,6,-6435.28613,9839.15918,-4383.16455,4201.00195,-4366.23828,4207.12451,-6418.35938,9845.28027,-6401.43213,9851.40430,-4349.31104,4213.24707,-4332.38428,4219.37012,-6384.50537,9857.52637,-6367.57861,9863.64844,-4315.45752,4225.49219,-4298.53125,4231.61523,-6350.65186,9869.77148

$$LAYER/2200.0

$$HATCHES/1,6,-6435.28613,9839.15918,-4383.16455,4201.00195,-4366.23828,4207.12451,-6418.35938,9845.28027,-6401.43213,9851.40430,-4349.31104,4213.24707,-4332.38428,4219.37012,-6384.50537,9857.52637,-6367.57861,9863.64844,-4315.45752,4225.49219,-4298.53125,4231.61523,-6350.65186,9869.77148

$$LAYER/2208.0

$$HATCHES/1,6,-6435.28613,9839.15918,-4383.16455,4201.00195,-4366.23828,4207.12451,-6418.35938,9845.28027,-6401.43213,9851.40430,-4349.31104,4213.24707,-4332.38428,4219.37012,-6384.50537,9857.52637,-6367.57861,9863.64844,-4315.45752,4225.49219,-4298.53125,4231.61523,-6350.65186,9869.77148

$$LAYER/2216.0

$$HATCHES/1,6,-6435.28613,9839.15918,-4383.16455,4201.00195,-4366.23828,4207.12451,-6418.35938,9845.28027,-6401.43213,9851.40430,-4349.31104,4213.24707,-4332.38428,4219.37012,-6384.50537,9857.52637,-6367.57861,9863.64844,-4315.45752,4225.49219,-4298.53125,4231.61523,-6350.65186,9869.77148

$$LAYER/2224.0

$$HATCHES/1,6,-6435.28613,9839.15918,-4383.16455,4201.00195,-4366.23828,4207.12451,-6418.35938,9845.28027,-6401.43213,9851.40430,-4349.31104,4213.24707,-4332.38428,4219.37012,-6384.50537,9857.52637,-6367.57861,9863.64844,-4315.45752,4225.49219,-4298.53125,4231.61523,-6350.65186,9869.77148

$$LAYER/2232.0

$$HATCHES/1,6,-6435.28613,9839.15918,-4383.16455,4201.00195,-4366.23828,4207.12451,-6418.35938,9845.28027,-6401.43213,9851.40430,-4349.31104,4213.24707,-4332.38428,4219.37012,-6384.50537,9857.52637,-6367.57861,9863.64844,-4315.45752,4225.49219,-4298.53125,4231.61523,-6350.65186,9869.77148

$$LAYER/2240.0

$$HATCHES/1,6,-6435.28613,9839.15918,-4383.16455,4201.00195,-4366.23828,4207.12451,-6418.35938,9845.28027,-6401.43213,9851.40430,-4349.31104,4213.24707,-4332.38428,4219.37012,-6384.50537,9857.52637,-6367.57861,9863.64844,-4315.45752,4225.49219,-4298.53125,4231.61523,-6350.65186,9869.77148

$$LAYER/2248.0

$$HATCHES/1,6,-6435.28613,9839.15918,-4383.16455,4201.00195,-4366.23828,4207.12451,-6418.35938,9845.28027,-6401.43213,9851.40430,-4349.31104,4213.24707,-4332.38428,4219.37012,-6384.50537,9857.52637,-6367.57861,9863.64844,-4315.45752,4225.49219,-4298.53125,4231.61523,-6350.65186,9869.77148

$$LAYER/2256.0

$$HATCHES/1,6,-6435.28613,9839.15918,-4383.16455,4201.00195,-4366.23828,4207.12451,-6418.35938,9845.28027,-6401.43213,9851.40430,-4349.31104,4213.24707,-4332.38428,4219.37012,-

6384.50537,9857.52637,-6367.57861,9863.64844,-4315.45752,4225.49219,-4298.53125,4231.61523,-6350.65186,9869.77148

$$LAYER/2264.0

$$HATCHES/1,6,-6435.28613,9839.15918,-4383.16455,4201.00195,-4366.23828,4207.12451,-6418.35938,9845.28027,-6401.43213,9851.40430,-4349.31104,4213.24707,-4332.38428,4219.37012,-6384.50537,9857.52637,-6367.57861,9863.64844,-4315.45752,4225.49219,-4298.53125,4231.61523,-6350.65186,9869.77148

$$LAYER/2272.0

$$HATCHES/1,6,-6435.28613,9839.15918,-4383.16455,4201.00195,-4366.23828,4207.12451,-6418.35938,9845.28027,-6401.43213,9851.40430,-4349.31104,4213.24707,-4332.38428,4219.37012,-6384.50537,9857.52637,-6367.57861,9863.64844,-4315.45752,4225.49219,-4298.53125,4231.61523,-6350.65186,9869.77148

$$LAYER/2280.0

$$HATCHES/1,6,-6435.28613,9839.15918,-4383.16455,4201.00195,-4366.23828,4207.12451,-6418.35938,9845.28027,-6401.43213,9851.40430,-4349.31104,4213.24707,-4332.38428,4219.37012,-6384.50537,9857.52637,-6367.57861,9863.64844,-4315.45752,4225.49219,-4298.53125,4231.61523,-6350.65186,9869.77148

$$LAYER/2288.0

$$HATCHES/1,6,-6435.28613,9839.15918,-4383.16455,4201.00195,-4366.23828,4207.12451,-6418.35938,9845.28027,-6401.43213,9851.40430,-4349.31104,4213.24707,-4332.38428,4219.37012,-6384.50537,9857.52637,-6367.57861,9863.64844,-4315.45752,4225.49219,-4298.53125,4231.61523,-6350.65186,9869.77148

$$LAYER/2296.0

$$HATCHES/1,6,-6435.28613,9839.15918,-4383.16455,4201.00195,-4366.23828,4207.12451,-6418.35938,9845.28027,-6401.43213,9851.40430,-4349.31104,4213.24707,-4332.38428,4219.37012,-6384.50537,9857.52637,-6367.57861,9863.64844,-4315.45752,4225.49219,-4298.53125,4231.61523,-6350.65186,9869.77148

$$LAYER/2304.0

$$HATCHES/1,6,-6435.28613,9839.15918,-4383.16455,4201.00195,-4366.23828,4207.12451,-6418.35938,9845.28027,-6401.43213,9851.40430,-4349.31104,4213.24707,-4332.38428,4219.37012,-6384.50537,9857.52637,-6367.57861,9863.64844,-4315.45752,4225.49219,-4298.53125,4231.61523,-6350.65186,9869.77148

$$LAYER/2312.0

$$HATCHES/1,6,-6435.28613,9839.15918,-4383.16455,4201.00195,-4366.23828,4207.12451,-6418.35938,9845.28027,-6401.43213,9851.40430,-4349.31104,4213.24707,-4332.38428,4219.37012,-6384.50537,9857.52637,-6367.57861,9863.64844,-4315.45752,4225.49219,-4298.53125,4231.61523,-6350.65186,9869.77148

$$LAYER/2320.0

$$HATCHES/1,6,-6435.28613,9839.15918,-4383.16455,4201.00195,-4366.23828,4207.12451,-6418.35938,9845.28027,-6401.43213,9851.40430,-4349.31104,4213.24707,-4332.38428,4219.37012,-6384.50537,9857.52637,-6367.57861,9863.64844,-4315.45752,4225.49219,-4298.53125,4231.61523,-6350.65186,9869.77148

$$LAYER/2328.0

$$HATCHES/1,6,-6435.28613,9839.15918,-4383.16455,4201.00195,-4366.23828,4207.12451,-6418.35938,9845.28027,-6401.43213,9851.40430,-4349.31104,4213.24707,-4332.38428,4219.37012,-6384.50537,9857.52637,-6367.57861,9863.64844,-4315.45752,4225.49219,-4298.53125,4231.61523,-6350.65186,9869.77148

$$LAYER/2336.0

$$HATCHES/1,6,-6435.28613,9839.15918,-4383.16455,4201.00195,-4366.23828,4207.12451,-6418.35938,9845.28027,-6401.43213,9851.40430,-4349.31104,4213.24707,-4332.38428,4219.37012,-6384.50537,9857.52637,-6367.57861,9863.64844,-4315.45752,4225.49219,-4298.53125,4231.61523,-6350.65186,9869.77148

$$LAYER/2344.0

$$HATCHES/1,6,-6435.28613,9839.15918,-4383.16455,4201.00195,-4366.23828,4207.12451,-6418.35938,9845.28027,-6401.43213,9851.40430,-4349.31104,4213.24707,-4332.38428,4219.37012,-6384.50537,9857.52637,-6367.57861,9863.64844,-4315.45752,4225.49219,-4298.53125,4231.61523,-6350.65186,9869.77148

$$LAYER/2352.0

$$HATCHES/1,6,-6435.28613,9839.15918,-4383.16455,4201.00195,-4366.23828,4207.12451,-6418.35938,9845.28027,-6401.43213,9851.40430,-4349.31104,4213.24707,-4332.38428,4219.37012,-6384.50537,9857.52637,-6367.57861,9863.64844,-4315.45752,4225.49219,-4298.53125,4231.61523,-6350.65186,9869.77148

$$LAYER/2360.0

$$HATCHES/1,6,-6435.28613,9839.15918,-4383.16455,4201.00195,-4366.23828,4207.12451,-6418.35938,9845.28027,-6401.43213,9851.40430,-4349.31104,4213.24707,-4332.38428,4219.37012,-6384.50537,9857.52637,-6367.57861,9863.64844,-4315.45752,4225.49219,-4298.53125,4231.61523,-6350.65186,9869.77148

$$LAYER/2368.0

$$HATCHES/1,6,-6435.28613,9839.15918,-4383.16455,4201.00195,-4366.23828,4207.12451,-6418.35938,9845.28027,-6401.43213,9851.40430,-4349.31104,4213.24707,-4332.38428,4219.37012,-

6384.50537,9857.52637,-6367.57861,9863.64844,-4315.45752,4225.49219,-4298.53125,4231.61523,-6350.65186,9869.77148

$$LAYER/2376.0

$$HATCHES/1,6,-6435.28613,9839.15918,-4383.16455,4201.00195,-4366.23828,4207.12451,-6418.35938,9845.28027,-6401.43213,9851.40430,-4349.31104,4213.24707,-4332.38428,4219.37012,-6384.50537,9857.52637,-6367.57861,9863.64844,-4315.45752,4225.49219,-4298.53125,4231.61523,-6350.65186,9869.77148

$$LAYER/2384.0

$$HATCHES/1,6,-6435.28613,9839.15918,-4383.16455,4201.00195,-4366.23828,4207.12451,-6418.35938,9845.28027,-6401.43213,9851.40430,-4349.31104,4213.24707,-4332.38428,4219.37012,-6384.50537,9857.52637,-6367.57861,9863.64844,-4315.45752,4225.49219,-4298.53125,4231.61523,-6350.65186,9869.77148

$$LAYER/2392.0

$$HATCHES/1,6,-6435.28613,9839.15918,-4383.16455,4201.00195,-4366.23828,4207.12451,-6418.35938,9845.28027,-6401.43213,9851.40430,-4349.31104,4213.24707,-4332.38428,4219.37012,-6384.50537,9857.52637,-6367.57861,9863.64844,-4315.45752,4225.49219,-4298.53125,4231.61523,-6350.65186,9869.77148

$$LAYER/2400.0

$$HATCHES/1,6,-6435.28613,9839.15918,-4383.16455,4201.00195,-4366.23828,4207.12451,-6418.35938,9845.28027,-6401.43213,9851.40430,-4349.31104,4213.24707,-4332.38428,4219.37012,-6384.50537,9857.52637,-6367.57861,9863.64844,-4315.45752,4225.49219,-4298.53125,4231.61523,-6350.65186,9869.77148

$$LAYER/2408.0

$$HATCHES/1,6,-6435.28613,9839.15918,-4383.16455,4201.00195,-4366.23828,4207.12451,-6418.35938,9845.28027,-6401.43213,9851.40430,-4349.31104,4213.24707,-4332.38428,4219.37012,-6384.50537,9857.52637,-6367.57861,9863.64844,-4315.45752,4225.49219,-4298.53125,4231.61523,-6350.65186,9869.77148

$$LAYER/2416.0

$$HATCHES/1,6,-6435.28613,9839.15918,-4383.16455,4201.00195,-4366.23828,4207.12451,-6418.35938,9845.28027,-6401.43213,9851.40430,-4349.31104,4213.24707,-4332.38428,4219.37012,-6384.50537,9857.52637,-6367.57861,9863.64844,-4315.45752,4225.49219,-4298.53125,4231.61523,-6350.65186,9869.77148

$$LAYER/2424.0

$$HATCHES/1,6,-6435.28613,9839.15918,-4383.16455,4201.00195,-4366.23828,4207.12451,-6418.35938,9845.28027,-6401.43213,9851.40430,-4349.31104,4213.24707,-4332.38428,4219.37012,-6384.50537,9857.52637,-6367.57861,9863.64844,-4315.45752,4225.49219,-4298.53125,4231.61523,-6350.65186,9869.77148

$$LAYER/2432.0

$$HATCHES/1,6,-6435.28613,9839.15918,-4383.16455,4201.00195,-4366.23828,4207.12451,-6418.35938,9845.28027,-6401.43213,9851.40430,-4349.31104,4213.24707,-4332.38428,4219.37012,-6384.50537,9857.52637,-6367.57861,9863.64844,-4315.45752,4225.49219,-4298.53125,4231.61523,-6350.65186,9869.77148

$$LAYER/2440.0

$$HATCHES/1,6,-6435.28613,9839.15918,-4383.16455,4201.00195,-4366.23828,4207.12451,-6418.35938,9845.28027,-6401.43213,9851.40430,-4349.31104,4213.24707,-4332.38428,4219.37012,-6384.50537,9857.52637,-6367.57861,9863.64844,-4315.45752,4225.49219,-4298.53125,4231.61523,-6350.65186,9869.77148

$$LAYER/2448.0

$$HATCHES/1,6,-6435.28613,9839.15918,-4383.16455,4201.00195,-4366.23828,4207.12451,-6418.35938,9845.28027,-6401.43213,9851.40430,-4349.31104,4213.24707,-4332.38428,4219.37012,-6384.50537,9857.52637,-6367.57861,9863.64844,-4315.45752,4225.49219,-4298.53125,4231.61523,-6350.65186,9869.77148

$$LAYER/2456.0

$$HATCHES/1,6,-6435.28613,9839.15918,-4383.16455,4201.00195,-4366.23828,4207.12451,-6418.35938,9845.28027,-6401.43213,9851.40430,-4349.31104,4213.24707,-4332.38428,4219.37012,-6384.50537,9857.52637,-6367.57861,9863.64844,-4315.45752,4225.49219,-4298.53125,4231.61523,-6350.65186,9869.77148

$$LAYER/2464.0

$$HATCHES/1,6,-6435.28613,9839.15918,-4383.16455,4201.00195,-4366.23828,4207.12451,-6418.35938,9845.28027,-6401.43213,9851.40430,-4349.31104,4213.24707,-4332.38428,4219.37012,-6384.50537,9857.52637,-6367.57861,9863.64844,-4315.45752,4225.49219,-4298.53125,4231.61523,-6350.65186,9869.77148

$$LAYER/2472.0

$$HATCHES/1,6,-6435.28613,9839.15918,-4383.16455,4201.00195,-4366.23828,4207.12451,-6418.35938,9845.28027,-6401.43213,9851.40430,-4349.31104,4213.24707,-4332.38428,4219.37012,-6384.50537,9857.52637,-6367.57861,9863.64844,-4315.45752,4225.49219,-4298.53125,4231.61523,-6350.65186,9869.77148

$$LAYER/2480.0

$$HATCHES/1,6,-6435.28613,9839.15918,-4383.16455,4201.00195,-4366.23828,4207.12451,-6418.35938,9845.28027,-6401.43213,9851.40430,-4349.31104,4213.24707,-4332.38428,4219.37012,-

6384.50537,9857.52637,-6367.57861,9863.64844,-4315.45752,4225.49219,-4298.53125,4231.61523,-6350.65186,9869.77148

$$LAYER/2488.0

$$HATCHES/1,6,-6435.28613,9839.15918,-4383.16455,4201.00195,-4366.23828,4207.12451,-6418.35938,9845.28027,-6401.43213,9851.40430,-4349.31104,4213.24707,-4332.38428,4219.37012,-6384.50537,9857.52637,-6367.57861,9863.64844,-4315.45752,4225.49219,-4298.53125,4231.61523,-6350.65186,9869.77148

$$LAYER/2496.0

$$HATCHES/1,6,-6435.28613,9839.15918,-4383.16455,4201.00195,-4366.23828,4207.12451,-6418.35938,9845.28027,-6401.43213,9851.40430,-4349.31104,4213.24707,-4332.38428,4219.37012,-6384.50537,9857.52637,-6367.57861,9863.64844,-4315.45752,4225.49219,-4298.53125,4231.61523,-6350.65186,9869.77148

$$LAYER/2504.0

$$HATCHES/1,6,-6435.28613,9839.15918,-4383.16455,4201.00195,-4366.23828,4207.12451,-6418.35938,9845.28027,-6401.43213,9851.40430,-4349.31104,4213.24707,-4332.38428,4219.37012,-6384.50537,9857.52637,-6367.57861,9863.64844,-4315.45752,4225.49219,-4298.53125,4231.61523,-6350.65186,9869.77148

$$LAYER/2512.0

$$HATCHES/1,6,-6435.28613,9839.15918,-4383.16455,4201.00195,-4366.23828,4207.12451,-6418.35938,9845.28027,-6401.43213,9851.40430,-4349.31104,4213.24707,-4332.38428,4219.37012,-6384.50537,9857.52637,-6367.57861,9863.64844,-4315.45752,4225.49219,-4298.53125,4231.61523,-6350.65186,9869.77148

$$LAYER/2520.0

$$HATCHES/1,6,-6435.28613,9839.15918,-4383.16455,4201.00195,-4366.23828,4207.12451,-6418.35938,9845.28027,-6401.43213,9851.40430,-4349.31104,4213.24707,-4332.38428,4219.37012,-6384.50537,9857.52637,-6367.57861,9863.64844,-4315.45752,4225.49219,-4298.53125,4231.61523,-6350.65186,9869.77148

$$LAYER/2528.0

$$HATCHES/1,6,-6435.28613,9839.15918,-4383.16455,4201.00195,-4366.23828,4207.12451,-6418.35938,9845.28027,-6401.43213,9851.40430,-4349.31104,4213.24707,-4332.38428,4219.37012,-6384.50537,9857.52637,-6367.57861,9863.64844,-4315.45752,4225.49219,-4298.53125,4231.61523,-6350.65186,9869.77148

$$LAYER/2536.0

$$HATCHES/1,6,-6435.28613,9839.15918,-4383.16455,4201.00195,-4366.23828,4207.12451,-6418.35938,9845.28027,-6401.43213,9851.40430,-4349.31104,4213.24707,-4332.38428,4219.37012,-6384.50537,9857.52637,-6367.57861,9863.64844,-4315.45752,4225.49219,-4298.53125,4231.61523,-6350.65186,9869.77148

$$LAYER/2544.0

$$HATCHES/1,6,-6435.28613,9839.15918,-4383.16455,4201.00195,-4366.23828,4207.12451,-6418.35938,9845.28027,-6401.43213,9851.40430,-4349.31104,4213.24707,-4332.38428,4219.37012,-6384.50537,9857.52637,-6367.57861,9863.64844,-4315.45752,4225.49219,-4298.53125,4231.61523,-6350.65186,9869.77148

$$LAYER/2552.0

$$HATCHES/1,6,-6435.28613,9839.15918,-4383.16455,4201.00195,-4366.23828,4207.12451,-6418.35938,9845.28027,-6401.43213,9851.40430,-4349.31104,4213.24707,-4332.38428,4219.37012,-6384.50537,9857.52637,-6367.57861,9863.64844,-4315.45752,4225.49219,-4298.53125,4231.61523,-6350.65186,9869.77148

$$LAYER/2560.0

$$HATCHES/1,6,-6435.28613,9839.15918,-4383.16455,4201.00195,-4366.23828,4207.12451,-6418.35938,9845.28027,-6401.43213,9851.40430,-4349.31104,4213.24707,-4332.38428,4219.37012,-6384.50537,9857.52637,-6367.57861,9863.64844,-4315.45752,4225.49219,-4298.53125,4231.61523,-6350.65186,9869.77148

$$LAYER/2568.0

$$HATCHES/1,6,-6435.28613,9839.15918,-4383.16455,4201.00195,-4366.23828,4207.12451,-6418.35938,9845.28027,-6401.43213,9851.40430,-4349.31104,4213.24707,-4332.38428,4219.37012,-6384.50537,9857.52637,-6367.57861,9863.64844,-4315.45752,4225.49219,-4298.53125,4231.61523,-6350.65186,9869.77148

$$LAYER/2576.0

$$HATCHES/1,6,-6435.28613,9839.15918,-4383.16455,4201.00195,-4366.23828,4207.12451,-6418.35938,9845.28027,-6401.43213,9851.40430,-4349.31104,4213.24707,-4332.38428,4219.37012,-6384.50537,9857.52637,-6367.57861,9863.64844,-4315.45752,4225.49219,-4298.53125,4231.61523,-6350.65186,9869.77148

$$LAYER/2584.0

$$HATCHES/1,6,-6435.28613,9839.15918,-4383.16455,4201.00195,-4366.23828,4207.12451,-6418.35938,9845.28027,-6401.43213,9851.40430,-4349.31104,4213.24707,-4332.38428,4219.37012,-6384.50537,9857.52637,-6367.57861,9863.64844,-4315.45752,4225.49219,-4298.53125,4231.61523,-6350.65186,9869.77148

$$LAYER/2592.0

$$HATCHES/1,6,-6435.28613,9839.15918,-4383.16455,4201.00195,-4366.23828,4207.12451,-6418.35938,9845.28027,-6401.43213,9851.40430,-4349.31104,4213.24707,-4332.38428,4219.37012,-

6384.50537,9857.52637,-6367.57861,9863.64844,-4315.45752,4225.49219,-4298.53125,4231.61523,-6350.65186,9869.77148

$$LAYER/2600.0

$$HATCHES/1,6,-6435.28613,9839.15918,-4383.16455,4201.00195,-4366.23828,4207.12451,-6418.35938,9845.28027,-6401.43213,9851.40430,-4349.31104,4213.24707,-4332.38428,4219.37012,-6384.50537,9857.52637,-6367.57861,9863.64844,-4315.45752,4225.49219,-4298.53125,4231.61523,-6350.65186,9869.77148

$$LAYER/2608.0

$$HATCHES/1,6,-6435.28613,9839.15918,-4383.16455,4201.00195,-4366.23828,4207.12451,-6418.35938,9845.28027,-6401.43213,9851.40430,-4349.31104,4213.24707,-4332.38428,4219.37012,-6384.50537,9857.52637,-6367.57861,9863.64844,-4315.45752,4225.49219,-4298.53125,4231.61523,-6350.65186,9869.77148

$$LAYER/2616.0

$$HATCHES/1,6,-6435.28613,9839.15918,-4383.16455,4201.00195,-4366.23828,4207.12451,-6418.35938,9845.28027,-6401.43213,9851.40430,-4349.31104,4213.24707,-4332.38428,4219.37012,-6384.50537,9857.52637,-6367.57861,9863.64844,-4315.45752,4225.49219,-4298.53125,4231.61523,-6350.65186,9869.77148

$$LAYER/2624.0

$$HATCHES/1,6,-6435.28613,9839.15918,-4383.16455,4201.00195,-4366.23828,4207.12451,-6418.35938,9845.28027,-6401.43213,9851.40430,-4349.31104,4213.24707,-4332.38428,4219.37012,-6384.50537,9857.52637,-6367.57861,9863.64844,-4315.45752,4225.49219,-4298.53125,4231.61523,-6350.65186,9869.77148

$$LAYER/2632.0

$$HATCHES/1,6,-6435.28613,9839.15918,-4383.16455,4201.00195,-4366.23828,4207.12451,-6418.35938,9845.28027,-6401.43213,9851.40430,-4349.31104,4213.24707,-4332.38428,4219.37012,-6384.50537,9857.52637,-6367.57861,9863.64844,-4315.45752,4225.49219,-4298.53125,4231.61523,-6350.65186,9869.77148

$$LAYER/2640.0

$$HATCHES/1,6,-6435.28613,9839.15918,-4383.16455,4201.00195,-4366.23828,4207.12451,-6418.35938,9845.28027,-6401.43213,9851.40430,-4349.31104,4213.24707,-4332.38428,4219.37012,-6384.50537,9857.52637,-6367.57861,9863.64844,-4315.45752,4225.49219,-4298.53125,4231.61523,-6350.65186,9869.77148

$$LAYER/2648.0

$$HATCHES/1,6,-6435.28613,9839.15918,-4383.16455,4201.00195,-4366.23828,4207.12451,-6418.35938,9845.28027,-6401.43213,9851.40430,-4349.31104,4213.24707,-4332.38428,4219.37012,-6384.50537,9857.52637,-6367.57861,9863.64844,-4315.45752,4225.49219,-4298.53125,4231.61523,-6350.65186,9869.77148

$$LAYER/2656.0

$$HATCHES/1,6,-6435.28613,9839.15918,-4383.16455,4201.00195,-4366.23828,4207.12451,-6418.35938,9845.28027,-6401.43213,9851.40430,-4349.31104,4213.24707,-4332.38428,4219.37012,-6384.50537,9857.52637,-6367.57861,9863.64844,-4315.45752,4225.49219,-4298.53125,4231.61523,-6350.65186,9869.77148

$$LAYER/2664.0

$$HATCHES/1,6,-6435.28613,9839.15918,-4383.16455,4201.00195,-4366.23828,4207.12451,-6418.35938,9845.28027,-6401.43213,9851.40430,-4349.31104,4213.24707,-4332.38428,4219.37012,-6384.50537,9857.52637,-6367.57861,9863.64844,-4315.45752,4225.49219,-4298.53125,4231.61523,-6350.65186,9869.77148

$$LAYER/2672.0

$$HATCHES/1,6,-6435.28613,9839.15918,-4383.16455,4201.00195,-4366.23828,4207.12451,-6418.35938,9845.28027,-6401.43213,9851.40430,-4349.31104,4213.24707,-4332.38428,4219.37012,-6384.50537,9857.52637,-6367.57861,9863.64844,-4315.45752,4225.49219,-4298.53125,4231.61523,-6350.65186,9869.77148

$$LAYER/2680.0

$$HATCHES/1,6,-6435.28613,9839.15918,-4383.16455,4201.00195,-4366.23828,4207.12451,-6418.35938,9845.28027,-6401.43213,9851.40430,-4349.31104,4213.24707,-4332.38428,4219.37012,-6384.50537,9857.52637,-6367.57861,9863.64844,-4315.45752,4225.49219,-4298.53125,4231.61523,-6350.65186,9869.77148

$$LAYER/2688.0

$$HATCHES/1,6,-6435.28613,9839.15918,-4383.16455,4201.00195,-4366.23828,4207.12451,-6418.35938,9845.28027,-6401.43213,9851.40430,-4349.31104,4213.24707,-4332.38428,4219.37012,-6384.50537,9857.52637,-6367.57861,9863.64844,-4315.45752,4225.49219,-4298.53125,4231.61523,-6350.65186,9869.77148

$$LAYER/2696.0

$$HATCHES/1,6,-6435.28613,9839.15918,-4383.16455,4201.00195,-4366.23828,4207.12451,-6418.35938,9845.28027,-6401.43213,9851.40430,-4349.31104,4213.24707,-4332.38428,4219.37012,-6384.50537,9857.52637,-6367.57861,9863.64844,-4315.45752,4225.49219,-4298.53125,4231.61523,-6350.65186,9869.77148

$$LAYER/2704.0

$$HATCHES/1,6,-6435.28613,9839.15918,-4383.16455,4201.00195,-4366.23828,4207.12451,-6418.35938,9845.28027,-6401.43213,9851.40430,-4349.31104,4213.24707,-4332.38428,4219.37012,-

6384.50537,9857.52637,-6367.57861,9863.64844,-4315.45752,4225.49219,-4298.53125,4231.61523,-6350.65186,9869.77148

$$LAYER/2712.0

$$HATCHES/1,6,-6435.28613,9839.15918,-4383.16455,4201.00195,-4366.23828,4207.12451,-6418.35938,9845.28027,-6401.43213,9851.40430,-4349.31104,4213.24707,-4332.38428,4219.37012,-6384.50537,9857.52637,-6367.57861,9863.64844,-4315.45752,4225.49219,-4298.53125,4231.61523,-6350.65186,9869.77148

$$LAYER/2720.0

$$HATCHES/1,6,-6435.28613,9839.15918,-4383.16455,4201.00195,-4366.23828,4207.12451,-6418.35938,9845.28027,-6401.43213,9851.40430,-4349.31104,4213.24707,-4332.38428,4219.37012,-6384.50537,9857.52637,-6367.57861,9863.64844,-4315.45752,4225.49219,-4298.53125,4231.61523,-6350.65186,9869.77148

$$LAYER/2728.0

$$HATCHES/1,6,-6435.28613,9839.15918,-4383.16455,4201.00195,-4366.23828,4207.12451,-6418.35938,9845.28027,-6401.43213,9851.40430,-4349.31104,4213.24707,-4332.38428,4219.37012,-6384.50537,9857.52637,-6367.57861,9863.64844,-4315.45752,4225.49219,-4298.53125,4231.61523,-6350.65186,9869.77148

$$LAYER/2736.0

$$HATCHES/1,6,-6435.28613,9839.15918,-4383.16455,4201.00195,-4366.23828,4207.12451,-6418.35938,9845.28027,-6401.43213,9851.40430,-4349.31104,4213.24707,-4332.38428,4219.37012,-6384.50537,9857.52637,-6367.57861,9863.64844,-4315.45752,4225.49219,-4298.53125,4231.61523,-6350.65186,9869.77148

$$LAYER/2744.0

$$HATCHES/1,6,-6435.28613,9839.15918,-4383.16455,4201.00195,-4366.23828,4207.12451,-6418.35938,9845.28027,-6401.43213,9851.40430,-4349.31104,4213.24707,-4332.38428,4219.37012,-6384.50537,9857.52637,-6367.57861,9863.64844,-4315.45752,4225.49219,-4298.53125,4231.61523,-6350.65186,9869.77148

$$LAYER/2752.0

$$HATCHES/1,6,-6435.28613,9839.15918,-4383.16455,4201.00195,-4366.23828,4207.12451,-6418.35938,9845.28027,-6401.43213,9851.40430,-4349.31104,4213.24707,-4332.38428,4219.37012,-6384.50537,9857.52637,-6367.57861,9863.64844,-4315.45752,4225.49219,-4298.53125,4231.61523,-6350.65186,9869.77148

$$LAYER/2760.0

$$HATCHES/1,6,-6435.28613,9839.15918,-4383.16455,4201.00195,-4366.23828,4207.12451,-6418.35938,9845.28027,-6401.43213,9851.40430,-4349.31104,4213.24707,-4332.38428,4219.37012,-6384.50537,9857.52637,-6367.57861,9863.64844,-4315.45752,4225.49219,-4298.53125,4231.61523,-6350.65186,9869.77148

$$LAYER/2768.0

$$HATCHES/1,6,-6435.28613,9839.15918,-4383.16455,4201.00195,-4366.23828,4207.12451,-6418.35938,9845.28027,-6401.43213,9851.40430,-4349.31104,4213.24707,-4332.38428,4219.37012,-6384.50537,9857.52637,-6367.57861,9863.64844,-4315.45752,4225.49219,-4298.53125,4231.61523,-6350.65186,9869.77148

$$LAYER/2776.0

$$HATCHES/1,6,-6435.28613,9839.15918,-4383.16455,4201.00195,-4366.23828,4207.12451,-6418.35938,9845.28027,-6401.43213,9851.40430,-4349.31104,4213.24707,-4332.38428,4219.37012,-6384.50537,9857.52637,-6367.57861,9863.64844,-4315.45752,4225.49219,-4298.53125,4231.61523,-6350.65186,9869.77148

$$LAYER/2784.0

$$HATCHES/1,6,-6435.28613,9839.15918,-4383.16455,4201.00195,-4366.23828,4207.12451,-6418.35938,9845.28027,-6401.43213,9851.40430,-4349.31104,4213.24707,-4332.38428,4219.37012,-6384.50537,9857.52637,-6367.57861,9863.64844,-4315.45752,4225.49219,-4298.53125,4231.61523,-6350.65186,9869.77148

$$LAYER/2792.0

$$HATCHES/1,6,-6435.28613,9839.15918,-4383.16455,4201.00195,-4366.23828,4207.12451,-6418.35938,9845.28027,-6401.43213,9851.40430,-4349.31104,4213.24707,-4332.38428,4219.37012,-6384.50537,9857.52637,-6367.57861,9863.64844,-4315.45752,4225.49219,-4298.53125,4231.61523,-6350.65186,9869.77148

$$LAYER/2800.0

$$HATCHES/1,6,-6435.28613,9839.15918,-4383.16455,4201.00195,-4366.23828,4207.12451,-6418.35938,9845.28027,-6401.43213,9851.40430,-4349.31104,4213.24707,-4332.38428,4219.37012,-6384.50537,9857.52637,-6367.57861,9863.64844,-4315.45752,4225.49219,-4298.53125,4231.61523,-6350.65186,9869.77148

$$LAYER/2808.0

$$HATCHES/1,6,-6435.28613,9839.15918,-4383.16455,4201.00195,-4366.23828,4207.12451,-6418.35938,9845.28027,-6401.43213,9851.40430,-4349.31104,4213.24707,-4332.38428,4219.37012,-6384.50537,9857.52637,-6367.57861,9863.64844,-4315.45752,4225.49219,-4298.53125,4231.61523,-6350.65186,9869.77148

$$LAYER/2816.0

$$HATCHES/1,6,-6435.28613,9839.15918,-4383.16455,4201.00195,-4366.23828,4207.12451,-6418.35938,9845.28027,-6401.43213,9851.40430,-4349.31104,4213.24707,-4332.38428,4219.37012,-

6384.50537,9857.52637,-6367.57861,9863.64844,-4315.45752,4225.49219,-4298.53125,4231.61523,-6350.65186,9869.77148

$$LAYER/2824.0

$$HATCHES/1,6,-6435.28613,9839.15918,-4383.16455,4201.00195,-4366.23828,4207.12451,-6418.35938,9845.28027,-6401.43213,9851.40430,-4349.31104,4213.24707,-4332.38428,4219.37012,-6384.50537,9857.52637,-6367.57861,9863.64844,-4315.45752,4225.49219,-4298.53125,4231.61523,-6350.65186,9869.77148

$$LAYER/2832.0

$$HATCHES/1,6,-6435.28613,9839.15918,-4383.16455,4201.00195,-4366.23828,4207.12451,-6418.35938,9845.28027,-6401.43213,9851.40430,-4349.31104,4213.24707,-4332.38428,4219.37012,-6384.50537,9857.52637,-6367.57861,9863.64844,-4315.45752,4225.49219,-4298.53125,4231.61523,-6350.65186,9869.77148

$$LAYER/2840.0

$$HATCHES/1,6,-6435.28613,9839.15918,-4383.16455,4201.00195,-4366.23828,4207.12451,-6418.35938,9845.28027,-6401.43213,9851.40430,-4349.31104,4213.24707,-4332.38428,4219.37012,-6384.50537,9857.52637,-6367.57861,9863.64844,-4315.45752,4225.49219,-4298.53125,4231.61523,-6350.65186,9869.77148

$$LAYER/2848.0

$$HATCHES/1,6,-6435.28613,9839.15918,-4383.16455,4201.00195,-4366.23828,4207.12451,-6418.35938,9845.28027,-6401.43213,9851.40430,-4349.31104,4213.24707,-4332.38428,4219.37012,-6384.50537,9857.52637,-6367.57861,9863.64844,-4315.45752,4225.49219,-4298.53125,4231.61523,-6350.65186,9869.77148

$$LAYER/2856.0

$$HATCHES/1,6,-6435.28613,9839.15918,-4383.16455,4201.00195,-4366.23828,4207.12451,-6418.35938,9845.28027,-6401.43213,9851.40430,-4349.31104,4213.24707,-4332.38428,4219.37012,-6384.50537,9857.52637,-6367.57861,9863.64844,-4315.45752,4225.49219,-4298.53125,4231.61523,-6350.65186,9869.77148

$$LAYER/2864.0

$$HATCHES/1,6,-6435.28613,9839.15918,-4383.16455,4201.00195,-4366.23828,4207.12451,-6418.35938,9845.28027,-6401.43213,9851.40430,-4349.31104,4213.24707,-4332.38428,4219.37012,-6384.50537,9857.52637,-6367.57861,9863.64844,-4315.45752,4225.49219,-4298.53125,4231.61523,-6350.65186,9869.77148

$$LAYER/2872.0

$$HATCHES/1,6,-6435.28613,9839.15918,-4383.16455,4201.00195,-4366.23828,4207.12451,-6418.35938,9845.28027,-6401.43213,9851.40430,-4349.31104,4213.24707,-4332.38428,4219.37012,-6384.50537,9857.52637,-6367.57861,9863.64844,-4315.45752,4225.49219,-4298.53125,4231.61523,-6350.65186,9869.77148

$$LAYER/2880.0

$$HATCHES/1,6,-6435.28613,9839.15918,-4383.16455,4201.00195,-4366.23828,4207.12451,-6418.35938,9845.28027,-6401.43213,9851.40430,-4349.31104,4213.24707,-4332.38428,4219.37012,-6384.50537,9857.52637,-6367.57861,9863.64844,-4315.45752,4225.49219,-4298.53125,4231.61523,-6350.65186,9869.77148

$$LAYER/2888.0

$$HATCHES/1,6,-6435.28613,9839.15918,-4383.16455,4201.00195,-4366.23828,4207.12451,-6418.35938,9845.28027,-6401.43213,9851.40430,-4349.31104,4213.24707,-4332.38428,4219.37012,-6384.50537,9857.52637,-6367.57861,9863.64844,-4315.45752,4225.49219,-4298.53125,4231.61523,-6350.65186,9869.77148

$$LAYER/2896.0

$$HATCHES/1,6,-6435.28613,9839.15918,-4383.16455,4201.00195,-4366.23828,4207.12451,-6418.35938,9845.28027,-6401.43213,9851.40430,-4349.31104,4213.24707,-4332.38428,4219.37012,-6384.50537,9857.52637,-6367.57861,9863.64844,-4315.45752,4225.49219,-4298.53125,4231.61523,-6350.65186,9869.77148

$$LAYER/2904.0

$$HATCHES/1,6,-6435.28613,9839.15918,-4383.16455,4201.00195,-4366.23828,4207.12451,-6418.35938,9845.28027,-6401.43213,9851.40430,-4349.31104,4213.24707,-4332.38428,4219.37012,-6384.50537,9857.52637,-6367.57861,9863.64844,-4315.45752,4225.49219,-4298.53125,4231.61523,-6350.65186,9869.77148

$$LAYER/2912.0

$$HATCHES/1,6,-6435.28613,9839.15918,-4383.16455,4201.00195,-4366.23828,4207.12451,-6418.35938,9845.28027,-6401.43213,9851.40430,-4349.31104,4213.24707,-4332.38428,4219.37012,-6384.50537,9857.52637,-6367.57861,9863.64844,-4315.45752,4225.49219,-4298.53125,4231.61523,-6350.65186,9869.77148

$$LAYER/2920.0

$$HATCHES/1,6,-6435.28613,9839.15918,-4383.16455,4201.00195,-4366.23828,4207.12451,-6418.35938,9845.28027,-6401.43213,9851.40430,-4349.31104,4213.24707,-4332.38428,4219.37012,-6384.50537,9857.52637,-6367.57861,9863.64844,-4315.45752,4225.49219,-4298.53125,4231.61523,-6350.65186,9869.77148

$$LAYER/2928.0

$$HATCHES/1,6,-6435.28613,9839.15918,-4383.16455,4201.00195,-4366.23828,4207.12451,-6418.35938,9845.28027,-6401.43213,9851.40430,-4349.31104,4213.24707,-4332.38428,4219.37012,-

6384.50537,9857.52637,-6367.57861,9863.64844,-4315.45752,4225.49219,-4298.53125,4231.61523,-6350.65186,9869.77148

$$LAYER/2936.0

$$HATCHES/1,6,-6435.28613,9839.15918,-4383.16455,4201.00195,-4366.23828,4207.12451,-6418.35938,9845.28027,-6401.43213,9851.40430,-4349.31104,4213.24707,-4332.38428,4219.37012,-6384.50537,9857.52637,-6367.57861,9863.64844,-4315.45752,4225.49219,-4298.53125,4231.61523,-6350.65186,9869.77148

$$LAYER/2944.0

$$HATCHES/1,6,-6435.28613,9839.15918,-4383.16455,4201.00195,-4366.23828,4207.12451,-6418.35938,9845.28027,-6401.43213,9851.40430,-4349.31104,4213.24707,-4332.38428,4219.37012,-6384.50537,9857.52637,-6367.57861,9863.64844,-4315.45752,4225.49219,-4298.53125,4231.61523,-6350.65186,9869.77148

$$LAYER/2952.0

$$HATCHES/1,6,-6435.28613,9839.15918,-4383.16455,4201.00195,-4366.23828,4207.12451,-6418.35938,9845.28027,-6401.43213,9851.40430,-4349.31104,4213.24707,-4332.38428,4219.37012,-6384.50537,9857.52637,-6367.57861,9863.64844,-4315.45752,4225.49219,-4298.53125,4231.61523,-6350.65186,9869.77148

$$LAYER/2960.0

$$HATCHES/1,6,-6435.28613,9839.15918,-4383.16455,4201.00195,-4366.23828,4207.12451,-6418.35938,9845.28027,-6401.43213,9851.40430,-4349.31104,4213.24707,-4332.38428,4219.37012,-6384.50537,9857.52637,-6367.57861,9863.64844,-4315.45752,4225.49219,-4298.53125,4231.61523,-6350.65186,9869.77148

$$LAYER/2968.0

$$HATCHES/1,6,-6435.28613,9839.15918,-4383.16455,4201.00195,-4366.23828,4207.12451,-6418.35938,9845.28027,-6401.43213,9851.40430,-4349.31104,4213.24707,-4332.38428,4219.37012,-6384.50537,9857.52637,-6367.57861,9863.64844,-4315.45752,4225.49219,-4298.53125,4231.61523,-6350.65186,9869.77148

$$LAYER/2976.0

$$HATCHES/1,6,-6435.28613,9839.15918,-4383.16455,4201.00195,-4366.23828,4207.12451,-6418.35938,9845.28027,-6401.43213,9851.40430,-4349.31104,4213.24707,-4332.38428,4219.37012,-6384.50537,9857.52637,-6367.57861,9863.64844,-4315.45752,4225.49219,-4298.53125,4231.61523,-6350.65186,9869.77148

$$LAYER/2984.0

$$HATCHES/1,6,-6435.28613,9839.15918,-4383.16455,4201.00195,-4366.23828,4207.12451,-6418.35938,9845.28027,-6401.43213,9851.40430,-4349.31104,4213.24707,-4332.38428,4219.37012,-6384.50537,9857.52637,-6367.57861,9863.64844,-4315.45752,4225.49219,-4298.53125,4231.61523,-6350.65186,9869.77148

$$LAYER/2992.0

$$HATCHES/1,6,-6435.28613,9839.15918,-4383.16455,4201.00195,-4366.23828,4207.12451,-6418.35938,9845.28027,-6401.43213,9851.40430,-4349.31104,4213.24707,-4332.38428,4219.37012,-6384.50537,9857.52637,-6367.57861,9863.64844,-4315.45752,4225.49219,-4298.53125,4231.61523,-6350.65186,9869.77148

$$LAYER/3000.0

$$HATCHES/1,6,-6435.28613,9839.15918,-4383.16455,4201.00195,-4366.23828,4207.12451,-6418.35938,9845.28027,-6401.43213,9851.40430,-4349.31104,4213.24707,-4332.38428,4219.37012,-6384.50537,9857.52637,-6367.57861,9863.64844,-4315.45752,4225.49219,-4298.53125,4231.61523,-6350.65186,9869.77148

$$LAYER/3008.0

$$HATCHES/1,6,-6435.28613,9839.15918,-4383.16455,4201.00195,-4366.23828,4207.12451,-6418.35938,9845.28027,-6401.43213,9851.40430,-4349.31104,4213.24707,-4332.38428,4219.37012,-6384.50537,9857.52637,-6367.57861,9863.64844,-4315.45752,4225.49219,-4298.53125,4231.61523,-6350.65186,9869.77148

$$LAYER/3016.0

$$HATCHES/1,6,-6435.28613,9839.15918,-4383.16455,4201.00195,-4366.23828,4207.12451,-6418.35938,9845.28027,-6401.43213,9851.40430,-4349.31104,4213.24707,-4332.38428,4219.37012,-6384.50537,9857.52637,-6367.57861,9863.64844,-4315.45752,4225.49219,-4298.53125,4231.61523,-6350.65186,9869.77148

$$LAYER/3024.0

$$HATCHES/1,6,-6435.28613,9839.15918,-4383.16455,4201.00195,-4366.23828,4207.12451,-6418.35938,9845.28027,-6401.43213,9851.40430,-4349.31104,4213.24707,-4332.38428,4219.37012,-6384.50537,9857.52637,-6367.57861,9863.64844,-4315.45752,4225.49219,-4298.53125,4231.61523,-6350.65186,9869.77148

$$LAYER/3032.0

$$HATCHES/1,6,-6435.28613,9839.15918,-4383.16455,4201.00195,-4366.23828,4207.12451,-6418.35938,9845.28027,-6401.43213,9851.40430,-4349.31104,4213.24707,-4332.38428,4219.37012,-6384.50537,9857.52637,-6367.57861,9863.64844,-4315.45752,4225.49219,-4298.53125,4231.61523,-6350.65186,9869.77148

$$LAYER/3040.0

$$HATCHES/1,6,-6435.28613,9839.15918,-4383.16455,4201.00195,-4366.23828,4207.12451,-6418.35938,9845.28027,-6401.43213,9851.40430,-4349.31104,4213.24707,-4332.38428,4219.37012,-

6384.50537,9857.52637,-6367.57861,9863.64844,-4315.45752,4225.49219,-4298.53125,4231.61523,-6350.65186,9869.77148

$$LAYER/3048.0

$$HATCHES/1,6,-6435.28613,9839.15918,-4383.16455,4201.00195,-4366.23828,4207.12451,-6418.35938,9845.28027,-6401.43213,9851.40430,-4349.31104,4213.24707,-4332.38428,4219.37012,-6384.50537,9857.52637,-6367.57861,9863.64844,-4315.45752,4225.49219,-4298.53125,4231.61523,-6350.65186,9869.77148

$$LAYER/3056.0

$$HATCHES/1,6,-6435.28613,9839.15918,-4383.16455,4201.00195,-4366.23828,4207.12451,-6418.35938,9845.28027,-6401.43213,9851.40430,-4349.31104,4213.24707,-4332.38428,4219.37012,-6384.50537,9857.52637,-6367.57861,9863.64844,-4315.45752,4225.49219,-4298.53125,4231.61523,-6350.65186,9869.77148

$$LAYER/3064.0

$$HATCHES/1,6,-6435.28613,9839.15918,-4383.16455,4201.00195,-4366.23828,4207.12451,-6418.35938,9845.28027,-6401.43213,9851.40430,-4349.31104,4213.24707,-4332.38428,4219.37012,-6384.50537,9857.52637,-6367.57861,9863.64844,-4315.45752,4225.49219,-4298.53125,4231.61523,-6350.65186,9869.77148

$$LAYER/3072.0

$$HATCHES/1,6,-6435.28613,9839.15918,-4383.16455,4201.00195,-4366.23828,4207.12451,-6418.35938,9845.28027,-6401.43213,9851.40430,-4349.31104,4213.24707,-4332.38428,4219.37012,-6384.50537,9857.52637,-6367.57861,9863.64844,-4315.45752,4225.49219,-4298.53125,4231.61523,-6350.65186,9869.77148

$$LAYER/3080.0

$$HATCHES/1,6,-6435.28613,9839.15918,-4383.16455,4201.00195,-4366.23828,4207.12451,-6418.35938,9845.28027,-6401.43213,9851.40430,-4349.31104,4213.24707,-4332.38428,4219.37012,-6384.50537,9857.52637,-6367.57861,9863.64844,-4315.45752,4225.49219,-4298.53125,4231.61523,-6350.65186,9869.77148

$$LAYER/3088.0

$$HATCHES/1,6,-6435.28613,9839.15918,-4383.16455,4201.00195,-4366.23828,4207.12451,-6418.35938,9845.28027,-6401.43213,9851.40430,-4349.31104,4213.24707,-4332.38428,4219.37012,-6384.50537,9857.52637,-6367.57861,9863.64844,-4315.45752,4225.49219,-4298.53125,4231.61523,-6350.65186,9869.77148

$$LAYER/3096.0

$$HATCHES/1,6,-6435.28613,9839.15918,-4383.16455,4201.00195,-4366.23828,4207.12451,-6418.35938,9845.28027,-6401.43213,9851.40430,-4349.31104,4213.24707,-4332.38428,4219.37012,-6384.50537,9857.52637,-6367.57861,9863.64844,-4315.45752,4225.49219,-4298.53125,4231.61523,-6350.65186,9869.77148

$$LAYER/3104.0

$$HATCHES/1,6,-6435.28613,9839.15918,-4383.16455,4201.00195,-4366.23828,4207.12451,-6418.35938,9845.28027,-6401.43213,9851.40430,-4349.31104,4213.24707,-4332.38428,4219.37012,-6384.50537,9857.52637,-6367.57861,9863.64844,-4315.45752,4225.49219,-4298.53125,4231.61523,-6350.65186,9869.77148

$$LAYER/3112.0

$$HATCHES/1,6,-6435.28613,9839.15918,-4383.16455,4201.00195,-4366.23828,4207.12451,-6418.35938,9845.28027,-6401.43213,9851.40430,-4349.31104,4213.24707,-4332.38428,4219.37012,-6384.50537,9857.52637,-6367.57861,9863.64844,-4315.45752,4225.49219,-4298.53125,4231.61523,-6350.65186,9869.77148

$$LAYER/3120.0

$$HATCHES/1,6,-6435.28613,9839.15918,-4383.16455,4201.00195,-4366.23828,4207.12451,-6418.35938,9845.28027,-6401.43213,9851.40430,-4349.31104,4213.24707,-4332.38428,4219.37012,-6384.50537,9857.52637,-6367.57861,9863.64844,-4315.45752,4225.49219,-4298.53125,4231.61523,-6350.65186,9869.77148

$$LAYER/3128.0

$$HATCHES/1,6,-6435.28613,9839.15918,-4383.16455,4201.00195,-4366.23828,4207.12451,-6418.35938,9845.28027,-6401.43213,9851.40430,-4349.31104,4213.24707,-4332.38428,4219.37012,-6384.50537,9857.52637,-6367.57861,9863.64844,-4315.45752,4225.49219,-4298.53125,4231.61523,-6350.65186,9869.77148

$$LAYER/3136.0

$$HATCHES/1,6,-6435.28613,9839.15918,-4383.16455,4201.00195,-4366.23828,4207.12451,-6418.35938,9845.28027,-6401.43213,9851.40430,-4349.31104,4213.24707,-4332.38428,4219.37012,-6384.50537,9857.52637,-6367.57861,9863.64844,-4315.45752,4225.49219,-4298.53125,4231.61523,-6350.65186,9869.77148

$$LAYER/3144.0

$$HATCHES/1,6,-6435.28613,9839.15918,-4383.16455,4201.00195,-4366.23828,4207.12451,-6418.35938,9845.28027,-6401.43213,9851.40430,-4349.31104,4213.24707,-4332.38428,4219.37012,-6384.50537,9857.52637,-6367.57861,9863.64844,-4315.45752,4225.49219,-4298.53125,4231.61523,-6350.65186,9869.77148

$$LAYER/3152.0

$$HATCHES/1,6,-6435.28613,9839.15918,-4383.16455,4201.00195,-4366.23828,4207.12451,-6418.35938,9845.28027,-6401.43213,9851.40430,-4349.31104,4213.24707,-4332.38428,4219.37012,-

6384.50537,9857.52637,-6367.57861,9863.64844,-4315.45752,4225.49219,-4298.53125,4231.61523,-6350.65186,9869.77148

$$LAYER/3160.0

$$HATCHES/1,6,-6435.28613,9839.15918,-4383.16455,4201.00195,-4366.23828,4207.12451,-6418.35938,9845.28027,-6401.43213,9851.40430,-4349.31104,4213.24707,-4332.38428,4219.37012,-6384.50537,9857.52637,-6367.57861,9863.64844,-4315.45752,4225.49219,-4298.53125,4231.61523,-6350.65186,9869.77148

$$LAYER/3168.0

$$HATCHES/1,6,-6435.28613,9839.15918,-4383.16455,4201.00195,-4366.23828,4207.12451,-6418.35938,9845.28027,-6401.43213,9851.40430,-4349.31104,4213.24707,-4332.38428,4219.37012,-6384.50537,9857.52637,-6367.57861,9863.64844,-4315.45752,4225.49219,-4298.53125,4231.61523,-6350.65186,9869.77148

$$LAYER/3176.0

$$HATCHES/1,6,-6435.28613,9839.15918,-4383.16455,4201.00195,-4366.23828,4207.12451,-6418.35938,9845.28027,-6401.43213,9851.40430,-4349.31104,4213.24707,-4332.38428,4219.37012,-6384.50537,9857.52637,-6367.57861,9863.64844,-4315.45752,4225.49219,-4298.53125,4231.61523,-6350.65186,9869.77148

$$LAYER/3184.0

$$HATCHES/1,6,-6435.28613,9839.15918,-4383.16455,4201.00195,-4366.23828,4207.12451,-6418.35938,9845.28027,-6401.43213,9851.40430,-4349.31104,4213.24707,-4332.38428,4219.37012,-6384.50537,9857.52637,-6367.57861,9863.64844,-4315.45752,4225.49219,-4298.53125,4231.61523,-6350.65186,9869.77148

$$LAYER/3192.0

$$HATCHES/1,6,-6435.28613,9839.15918,-4383.16455,4201.00195,-4366.23828,4207.12451,-6418.35938,9845.28027,-6401.43213,9851.40430,-4349.31104,4213.24707,-4332.38428,4219.37012,-6384.50537,9857.52637,-6367.57861,9863.64844,-4315.45752,4225.49219,-4298.53125,4231.61523,-6350.65186,9869.77148

$$LAYER/3200.0

$$HATCHES/1,6,-6435.28613,9839.15918,-4383.16455,4201.00195,-4366.23828,4207.12451,-6418.35938,9845.28027,-6401.43213,9851.40430,-4349.31104,4213.24707,-4332.38428,4219.37012,-6384.50537,9857.52637,-6367.57861,9863.64844,-4315.45752,4225.49219,-4298.53125,4231.61523,-6350.65186,9869.77148

$$LAYER/3208.0

$$HATCHES/1,6,-6435.28613,9839.15918,-4383.16455,4201.00195,-4366.23828,4207.12451,-6418.35938,9845.28027,-6401.43213,9851.40430,-4349.31104,4213.24707,-4332.38428,4219.37012,-6384.50537,9857.52637,-6367.57861,9863.64844,-4315.45752,4225.49219,-4298.53125,4231.61523,-6350.65186,9869.77148

$$LAYER/3216.0

$$HATCHES/1,6,-6435.28613,9839.15918,-4383.16455,4201.00195,-4366.23828,4207.12451,-6418.35938,9845.28027,-6401.43213,9851.40430,-4349.31104,4213.24707,-4332.38428,4219.37012,-6384.50537,9857.52637,-6367.57861,9863.64844,-4315.45752,4225.49219,-4298.53125,4231.61523,-6350.65186,9869.77148

$$LAYER/3224.0

$$HATCHES/1,6,-6435.28613,9839.15918,-4383.16455,4201.00195,-4366.23828,4207.12451,-6418.35938,9845.28027,-6401.43213,9851.40430,-4349.31104,4213.24707,-4332.38428,4219.37012,-6384.50537,9857.52637,-6367.57861,9863.64844,-4315.45752,4225.49219,-4298.53125,4231.61523,-6350.65186,9869.77148

$$LAYER/3232.0

$$HATCHES/1,6,-6435.28613,9839.15918,-4383.16455,4201.00195,-4366.23828,4207.12451,-6418.35938,9845.28027,-6401.43213,9851.40430,-4349.31104,4213.24707,-4332.38428,4219.37012,-6384.50537,9857.52637,-6367.57861,9863.64844,-4315.45752,4225.49219,-4298.53125,4231.61523,-6350.65186,9869.77148

$$LAYER/3240.0

$$HATCHES/1,6,-6435.28613,9839.15918,-4383.16455,4201.00195,-4366.23828,4207.12451,-6418.35938,9845.28027,-6401.43213,9851.40430,-4349.31104,4213.24707,-4332.38428,4219.37012,-6384.50537,9857.52637,-6367.57861,9863.64844,-4315.45752,4225.49219,-4298.53125,4231.61523,-6350.65186,9869.77148

$$LAYER/3248.0

$$HATCHES/1,6,-6435.28613,9839.15918,-4383.16455,4201.00195,-4366.23828,4207.12451,-6418.35938,9845.28027,-6401.43213,9851.40430,-4349.31104,4213.24707,-4332.38428,4219.37012,-6384.50537,9857.52637,-6367.57861,9863.64844,-4315.45752,4225.49219,-4298.53125,4231.61523,-6350.65186,9869.77148

$$LAYER/3256.0

$$HATCHES/1,6,-6435.28613,9839.15918,-4383.16455,4201.00195,-4366.23828,4207.12451,-6418.35938,9845.28027,-6401.43213,9851.40430,-4349.31104,4213.24707,-4332.38428,4219.37012,-6384.50537,9857.52637,-6367.57861,9863.64844,-4315.45752,4225.49219,-4298.53125,4231.61523,-6350.65186,9869.77148

$$LAYER/3264.0

$$HATCHES/1,6,-6435.28613,9839.15918,-4383.16455,4201.00195,-4366.23828,4207.12451,-6418.35938,9845.28027,-6401.43213,9851.40430,-4349.31104,4213.24707,-4332.38428,4219.37012,-

6384.50537,9857.52637,-6367.57861,9863.64844,-4315.45752,4225.49219,-4298.53125,4231.61523,-6350.65186,9869.77148

$$LAYER/3272.0

$$HATCHES/1,6,-6435.28613,9839.15918,-4383.16455,4201.00195,-4366.23828,4207.12451,-6418.35938,9845.28027,-6401.43213,9851.40430,-4349.31104,4213.24707,-4332.38428,4219.37012,-6384.50537,9857.52637,-6367.57861,9863.64844,-4315.45752,4225.49219,-4298.53125,4231.61523,-6350.65186,9869.77148

$$LAYER/3280.0

$$HATCHES/1,6,-6435.28613,9839.15918,-4383.16455,4201.00195,-4366.23828,4207.12451,-6418.35938,9845.28027,-6401.43213,9851.40430,-4349.31104,4213.24707,-4332.38428,4219.37012,-6384.50537,9857.52637,-6367.57861,9863.64844,-4315.45752,4225.49219,-4298.53125,4231.61523,-6350.65186,9869.77148

$$LAYER/3288.0

$$HATCHES/1,6,-6435.28613,9839.15918,-4383.16455,4201.00195,-4366.23828,4207.12451,-6418.35938,9845.28027,-6401.43213,9851.40430,-4349.31104,4213.24707,-4332.38428,4219.37012,-6384.50537,9857.52637,-6367.57861,9863.64844,-4315.45752,4225.49219,-4298.53125,4231.61523,-6350.65186,9869.77148

$$LAYER/3296.0

$$HATCHES/1,6,-6435.28613,9839.15918,-4383.16455,4201.00195,-4366.23828,4207.12451,-6418.35938,9845.28027,-6401.43213,9851.40430,-4349.31104,4213.24707,-4332.38428,4219.37012,-6384.50537,9857.52637,-6367.57861,9863.64844,-4315.45752,4225.49219,-4298.53125,4231.61523,-6350.65186,9869.77148

$$LAYER/3304.0

$$HATCHES/1,6,-6435.28613,9839.15918,-4383.16455,4201.00195,-4366.23828,4207.12451,-6418.35938,9845.28027,-6401.43213,9851.40430,-4349.31104,4213.24707,-4332.38428,4219.37012,-6384.50537,9857.52637,-6367.57861,9863.64844,-4315.45752,4225.49219,-4298.53125,4231.61523,-6350.65186,9869.77148

$$LAYER/3312.0

$$HATCHES/1,6,-6435.28613,9839.15918,-4383.16455,4201.00195,-4366.23828,4207.12451,-6418.35938,9845.28027,-6401.43213,9851.40430,-4349.31104,4213.24707,-4332.38428,4219.37012,-6384.50537,9857.52637,-6367.57861,9863.64844,-4315.45752,4225.49219,-4298.53125,4231.61523,-6350.65186,9869.77148

$$LAYER/3320.0

$$HATCHES/1,6,-6435.28613,9839.15918,-4383.16455,4201.00195,-4366.23828,4207.12451,-6418.35938,9845.28027,-6401.43213,9851.40430,-4349.31104,4213.24707,-4332.38428,4219.37012,-6384.50537,9857.52637,-6367.57861,9863.64844,-4315.45752,4225.49219,-4298.53125,4231.61523,-6350.65186,9869.77148

$$LAYER/3328.0

$$HATCHES/1,6,-6435.28613,9839.15918,-4383.16455,4201.00195,-4366.23828,4207.12451,-6418.35938,9845.28027,-6401.43213,9851.40430,-4349.31104,4213.24707,-4332.38428,4219.37012,-6384.50537,9857.52637,-6367.57861,9863.64844,-4315.45752,4225.49219,-4298.53125,4231.61523,-6350.65186,9869.77148

$$LAYER/3336.0

$$HATCHES/1,6,-6435.28613,9839.15918,-4383.16455,4201.00195,-4366.23828,4207.12451,-6418.35938,9845.28027,-6401.43213,9851.40430,-4349.31104,4213.24707,-4332.38428,4219.37012,-6384.50537,9857.52637,-6367.57861,9863.64844,-4315.45752,4225.49219,-4298.53125,4231.61523,-6350.65186,9869.77148

$$LAYER/3344.0

$$HATCHES/1,6,-6435.28613,9839.15918,-4383.16455,4201.00195,-4366.23828,4207.12451,-6418.35938,9845.28027,-6401.43213,9851.40430,-4349.31104,4213.24707,-4332.38428,4219.37012,-6384.50537,9857.52637,-6367.57861,9863.64844,-4315.45752,4225.49219,-4298.53125,4231.61523,-6350.65186,9869.77148

$$LAYER/3352.0

$$HATCHES/1,6,-6435.28613,9839.15918,-4383.16455,4201.00195,-4366.23828,4207.12451,-6418.35938,9845.28027,-6401.43213,9851.40430,-4349.31104,4213.24707,-4332.38428,4219.37012,-6384.50537,9857.52637,-6367.57861,9863.64844,-4315.45752,4225.49219,-4298.53125,4231.61523,-6350.65186,9869.77148

$$LAYER/3360.0

$$HATCHES/1,6,-6435.28613,9839.15918,-4383.16455,4201.00195,-4366.23828,4207.12451,-6418.35938,9845.28027,-6401.43213,9851.40430,-4349.31104,4213.24707,-4332.38428,4219.37012,-6384.50537,9857.52637,-6367.57861,9863.64844,-4315.45752,4225.49219,-4298.53125,4231.61523,-6350.65186,9869.77148

$$LAYER/3368.0

$$HATCHES/1,6,-6435.28613,9839.15918,-4383.16455,4201.00195,-4366.23828,4207.12451,-6418.35938,9845.28027,-6401.43213,9851.40430,-4349.31104,4213.24707,-4332.38428,4219.37012,-6384.50537,9857.52637,-6367.57861,9863.64844,-4315.45752,4225.49219,-4298.53125,4231.61523,-6350.65186,9869.77148

$$LAYER/3376.0

$$HATCHES/1,6,-6435.28613,9839.15918,-4383.16455,4201.00195,-4366.23828,4207.12451,-6418.35938,9845.28027,-6401.43213,9851.40430,-4349.31104,4213.24707,-4332.38428,4219.37012,-

6384.50537,9857.52637,-6367.57861,9863.64844,-4315.45752,4225.49219,-4298.53125,4231.61523,-6350.65186,9869.77148

$$LAYER/3384.0

$$HATCHES/1,6,-6435.28613,9839.15918,-4383.16455,4201.00195,-4366.23828,4207.12451,-6418.35938,9845.28027,-6401.43213,9851.40430,-4349.31104,4213.24707,-4332.38428,4219.37012,-6384.50537,9857.52637,-6367.57861,9863.64844,-4315.45752,4225.49219,-4298.53125,4231.61523,-6350.65186,9869.77148

$$LAYER/3392.0

$$HATCHES/1,6,-6435.28613,9839.15918,-4383.16455,4201.00195,-4366.23828,4207.12451,-6418.35938,9845.28027,-6401.43213,9851.40430,-4349.31104,4213.24707,-4332.38428,4219.37012,-6384.50537,9857.52637,-6367.57861,9863.64844,-4315.45752,4225.49219,-4298.53125,4231.61523,-6350.65186,9869.77148

$$LAYER/3400.0

$$HATCHES/1,6,-6435.28613,9839.15918,-4383.16455,4201.00195,-4366.23828,4207.12451,-6418.35938,9845.28027,-6401.43213,9851.40430,-4349.31104,4213.24707,-4332.38428,4219.37012,-6384.50537,9857.52637,-6367.57861,9863.64844,-4315.45752,4225.49219,-4298.53125,4231.61523,-6350.65186,9869.77148

$$LAYER/3408.0

$$HATCHES/1,6,-6435.28613,9839.15918,-4383.16455,4201.00195,-4366.23828,4207.12451,-6418.35938,9845.28027,-6401.43213,9851.40430,-4349.31104,4213.24707,-4332.38428,4219.37012,-6384.50537,9857.52637,-6367.57861,9863.64844,-4315.45752,4225.49219,-4298.53125,4231.61523,-6350.65186,9869.77148

$$LAYER/3416.0

$$HATCHES/1,6,-6435.28613,9839.15918,-4383.16455,4201.00195,-4366.23828,4207.12451,-6418.35938,9845.28027,-6401.43213,9851.40430,-4349.31104,4213.24707,-4332.38428,4219.37012,-6384.50537,9857.52637,-6367.57861,9863.64844,-4315.45752,4225.49219,-4298.53125,4231.61523,-6350.65186,9869.77148

$$LAYER/3424.0

$$HATCHES/1,6,-6435.28613,9839.15918,-4383.16455,4201.00195,-4366.23828,4207.12451,-6418.35938,9845.28027,-6401.43213,9851.40430,-4349.31104,4213.24707,-4332.38428,4219.37012,-6384.50537,9857.52637,-6367.57861,9863.64844,-4315.45752,4225.49219,-4298.53125,4231.61523,-6350.65186,9869.77148

$$LAYER/3432.0

$$HATCHES/1,6,-6435.28613,9839.15918,-4383.16455,4201.00195,-4366.23828,4207.12451,-6418.35938,9845.28027,-6401.43213,9851.40430,-4349.31104,4213.24707,-4332.38428,4219.37012,-6384.50537,9857.52637,-6367.57861,9863.64844,-4315.45752,4225.49219,-4298.53125,4231.61523,-6350.65186,9869.77148

$$LAYER/3440.0

$$HATCHES/1,6,-6435.28613,9839.15918,-4383.16455,4201.00195,-4366.23828,4207.12451,-6418.35938,9845.28027,-6401.43213,9851.40430,-4349.31104,4213.24707,-4332.38428,4219.37012,-6384.50537,9857.52637,-6367.57861,9863.64844,-4315.45752,4225.49219,-4298.53125,4231.61523,-6350.65186,9869.77148

$$LAYER/3448.0

$$HATCHES/1,6,-6435.28613,9839.15918,-4383.16455,4201.00195,-4366.23828,4207.12451,-6418.35938,9845.28027,-6401.43213,9851.40430,-4349.31104,4213.24707,-4332.38428,4219.37012,-6384.50537,9857.52637,-6367.57861,9863.64844,-4315.45752,4225.49219,-4298.53125,4231.61523,-6350.65186,9869.77148

$$LAYER/3456.0

$$HATCHES/1,6,-6435.28613,9839.15918,-4383.16455,4201.00195,-4366.23828,4207.12451,-6418.35938,9845.28027,-6401.43213,9851.40430,-4349.31104,4213.24707,-4332.38428,4219.37012,-6384.50537,9857.52637,-6367.57861,9863.64844,-4315.45752,4225.49219,-4298.53125,4231.61523,-6350.65186,9869.77148

$$LAYER/3464.0

$$HATCHES/1,6,-6435.28613,9839.15918,-4383.16455,4201.00195,-4366.23828,4207.12451,-6418.35938,9845.28027,-6401.43213,9851.40430,-4349.31104,4213.24707,-4332.38428,4219.37012,-6384.50537,9857.52637,-6367.57861,9863.64844,-4315.45752,4225.49219,-4298.53125,4231.61523,-6350.65186,9869.77148

$$LAYER/3472.0

$$HATCHES/1,6,-6435.28613,9839.15918,-4383.16455,4201.00195,-4366.23828,4207.12451,-6418.35938,9845.28027,-6401.43213,9851.40430,-4349.31104,4213.24707,-4332.38428,4219.37012,-6384.50537,9857.52637,-6367.57861,9863.64844,-4315.45752,4225.49219,-4298.53125,4231.61523,-6350.65186,9869.77148

$$LAYER/3480.0

$$HATCHES/1,6,-6435.28613,9839.15918,-4383.16455,4201.00195,-4366.23828,4207.12451,-6418.35938,9845.28027,-6401.43213,9851.40430,-4349.31104,4213.24707,-4332.38428,4219.37012,-6384.50537,9857.52637,-6367.57861,9863.64844,-4315.45752,4225.49219,-4298.53125,4231.61523,-6350.65186,9869.77148

$$LAYER/3488.0

$$HATCHES/1,6,-6435.28613,9839.15918,-4383.16455,4201.00195,-4366.23828,4207.12451,-6418.35938,9845.28027,-6401.43213,9851.40430,-4349.31104,4213.24707,-4332.38428,4219.37012,-

6384.50537,9857.52637,-6367.57861,9863.64844,-4315.45752,4225.49219,-4298.53125,4231.61523,-6350.65186,9869.77148

$$LAYER/3496.0

$$HATCHES/1,6,-6435.28613,9839.15918,-4383.16455,4201.00195,-4366.23828,4207.12451,-6418.35938,9845.28027,-6401.43213,9851.40430,-4349.31104,4213.24707,-4332.38428,4219.37012,-6384.50537,9857.52637,-6367.57861,9863.64844,-4315.45752,4225.49219,-4298.53125,4231.61523,-6350.65186,9869.77148

$$LAYER/3504.0

$$HATCHES/1,6,-6435.28613,9839.15918,-4383.16455,4201.00195,-4366.23828,4207.12451,-6418.35938,9845.28027,-6401.43213,9851.40430,-4349.31104,4213.24707,-4332.38428,4219.37012,-6384.50537,9857.52637,-6367.57861,9863.64844,-4315.45752,4225.49219,-4298.53125,4231.61523,-6350.65186,9869.77148

$$LAYER/3512.0

$$HATCHES/1,6,-6435.28613,9839.15918,-4383.16455,4201.00195,-4366.23828,4207.12451,-6418.35938,9845.28027,-6401.43213,9851.40430,-4349.31104,4213.24707,-4332.38428,4219.37012,-6384.50537,9857.52637,-6367.57861,9863.64844,-4315.45752,4225.49219,-4298.53125,4231.61523,-6350.65186,9869.77148

$$LAYER/3520.0

$$HATCHES/1,6,-6435.28613,9839.15918,-4383.16455,4201.00195,-4366.23828,4207.12451,-6418.35938,9845.28027,-6401.43213,9851.40430,-4349.31104,4213.24707,-4332.38428,4219.37012,-6384.50537,9857.52637,-6367.57861,9863.64844,-4315.45752,4225.49219,-4298.53125,4231.61523,-6350.65186,9869.77148

$$LAYER/3528.0

$$HATCHES/1,6,-6435.28613,9839.15918,-4383.16455,4201.00195,-4366.23828,4207.12451,-6418.35938,9845.28027,-6401.43213,9851.40430,-4349.31104,4213.24707,-4332.38428,4219.37012,-6384.50537,9857.52637,-6367.57861,9863.64844,-4315.45752,4225.49219,-4298.53125,4231.61523,-6350.65186,9869.77148

$$LAYER/3536.0

$$HATCHES/1,6,-6435.28613,9839.15918,-4383.16455,4201.00195,-4366.23828,4207.12451,-6418.35938,9845.28027,-6401.43213,9851.40430,-4349.31104,4213.24707,-4332.38428,4219.37012,-6384.50537,9857.52637,-6367.57861,9863.64844,-4315.45752,4225.49219,-4298.53125,4231.61523,-6350.65186,9869.77148

$$LAYER/3544.0

$$HATCHES/1,6,-6435.28613,9839.15918,-4383.16455,4201.00195,-4366.23828,4207.12451,-6418.35938,9845.28027,-6401.43213,9851.40430,-4349.31104,4213.24707,-4332.38428,4219.37012,-6384.50537,9857.52637,-6367.57861,9863.64844,-4315.45752,4225.49219,-4298.53125,4231.61523,-6350.65186,9869.77148

$$LAYER/3552.0

$$HATCHES/1,6,-6435.28613,9839.15918,-4383.16455,4201.00195,-4366.23828,4207.12451,-6418.35938,9845.28027,-6401.43213,9851.40430,-4349.31104,4213.24707,-4332.38428,4219.37012,-6384.50537,9857.52637,-6367.57861,9863.64844,-4315.45752,4225.49219,-4298.53125,4231.61523,-6350.65186,9869.77148

$$LAYER/3560.0

$$HATCHES/1,6,-6435.28613,9839.15918,-4383.16455,4201.00195,-4366.23828,4207.12451,-6418.35938,9845.28027,-6401.43213,9851.40430,-4349.31104,4213.24707,-4332.38428,4219.37012,-6384.50537,9857.52637,-6367.57861,9863.64844,-4315.45752,4225.49219,-4298.53125,4231.61523,-6350.65186,9869.77148

$$LAYER/3568.0

$$HATCHES/1,6,-6435.28613,9839.15918,-4383.16455,4201.00195,-4366.23828,4207.12451,-6418.35938,9845.28027,-6401.43213,9851.40430,-4349.31104,4213.24707,-4332.38428,4219.37012,-6384.50537,9857.52637,-6367.57861,9863.64844,-4315.45752,4225.49219,-4298.53125,4231.61523,-6350.65186,9869.77148

$$LAYER/3576.0

$$HATCHES/1,6,-6435.28613,9839.15918,-4383.16455,4201.00195,-4366.23828,4207.12451,-6418.35938,9845.28027,-6401.43213,9851.40430,-4349.31104,4213.24707,-4332.38428,4219.37012,-6384.50537,9857.52637,-6367.57861,9863.64844,-4315.45752,4225.49219,-4298.53125,4231.61523,-6350.65186,9869.77148

$$LAYER/3584.0

$$HATCHES/1,6,-6435.28613,9839.15918,-4383.16455,4201.00195,-4366.23828,4207.12451,-6418.35938,9845.28027,-6401.43213,9851.40430,-4349.31104,4213.24707,-4332.38428,4219.37012,-6384.50537,9857.52637,-6367.57861,9863.64844,-4315.45752,4225.49219,-4298.53125,4231.61523,-6350.65186,9869.77148

$$LAYER/3592.0

$$HATCHES/1,6,-6435.28613,9839.15918,-4383.16455,4201.00195,-4366.23828,4207.12451,-6418.35938,9845.28027,-6401.43213,9851.40430,-4349.31104,4213.24707,-4332.38428,4219.37012,-6384.50537,9857.52637,-6367.57861,9863.64844,-4315.45752,4225.49219,-4298.53125,4231.61523,-6350.65186,9869.77148

$$LAYER/3600.0

$$HATCHES/1,6,-6435.28613,9839.15918,-4383.16455,4201.00195,-4366.23828,4207.12451,-6418.35938,9845.28027,-6401.43213,9851.40430,-4349.31104,4213.24707,-4332.38428,4219.37012,-

6384.50537,9857.52637,-6367.57861,9863.64844,-4315.45752,4225.49219,-4298.53125,4231.61523,-6350.65186,9869.77148

$$LAYER/3608.0

$$HATCHES/1,6,-6435.28613,9839.15918,-4383.16455,4201.00195,-4366.23828,4207.12451,-6418.35938,9845.28027,-6401.43213,9851.40430,-4349.31104,4213.24707,-4332.38428,4219.37012,-6384.50537,9857.52637,-6367.57861,9863.64844,-4315.45752,4225.49219,-4298.53125,4231.61523,-6350.65186,9869.77148

$$LAYER/3616.0

$$HATCHES/1,6,-6435.28613,9839.15918,-4383.16455,4201.00195,-4366.23828,4207.12451,-6418.35938,9845.28027,-6401.43213,9851.40430,-4349.31104,4213.24707,-4332.38428,4219.37012,-6384.50537,9857.52637,-6367.57861,9863.64844,-4315.45752,4225.49219,-4298.53125,4231.61523,-6350.65186,9869.77148

$$LAYER/3624.0

$$HATCHES/1,6,-6435.28613,9839.15918,-4383.16455,4201.00195,-4366.23828,4207.12451,-6418.35938,9845.28027,-6401.43213,9851.40430,-4349.31104,4213.24707,-4332.38428,4219.37012,-6384.50537,9857.52637,-6367.57861,9863.64844,-4315.45752,4225.49219,-4298.53125,4231.61523,-6350.65186,9869.77148

$$LAYER/3632.0

$$HATCHES/1,6,-6435.28613,9839.15918,-4383.16455,4201.00195,-4366.23828,4207.12451,-6418.35938,9845.28027,-6401.43213,9851.40430,-4349.31104,4213.24707,-4332.38428,4219.37012,-6384.50537,9857.52637,-6367.57861,9863.64844,-4315.45752,4225.49219,-4298.53125,4231.61523,-6350.65186,9869.77148

$$LAYER/3640.0

$$HATCHES/1,6,-6435.28613,9839.15918,-4383.16455,4201.00195,-4366.23828,4207.12451,-6418.35938,9845.28027,-6401.43213,9851.40430,-4349.31104,4213.24707,-4332.38428,4219.37012,-6384.50537,9857.52637,-6367.57861,9863.64844,-4315.45752,4225.49219,-4298.53125,4231.61523,-6350.65186,9869.77148

$$LAYER/3648.0

$$HATCHES/1,6,-6435.28613,9839.15918,-4383.16455,4201.00195,-4366.23828,4207.12451,-6418.35938,9845.28027,-6401.43213,9851.40430,-4349.31104,4213.24707,-4332.38428,4219.37012,-6384.50537,9857.52637,-6367.57861,9863.64844,-4315.45752,4225.49219,-4298.53125,4231.61523,-6350.65186,9869.77148

$$LAYER/3656.0

$$HATCHES/1,6,-6435.28613,9839.15918,-4383.16455,4201.00195,-4366.23828,4207.12451,-6418.35938,9845.28027,-6401.43213,9851.40430,-4349.31104,4213.24707,-4332.38428,4219.37012,-6384.50537,9857.52637,-6367.57861,9863.64844,-4315.45752,4225.49219,-4298.53125,4231.61523,-6350.65186,9869.77148

$$LAYER/3664.0

$$HATCHES/1,6,-6435.28613,9839.15918,-4383.16455,4201.00195,-4366.23828,4207.12451,-6418.35938,9845.28027,-6401.43213,9851.40430,-4349.31104,4213.24707,-4332.38428,4219.37012,-6384.50537,9857.52637,-6367.57861,9863.64844,-4315.45752,4225.49219,-4298.53125,4231.61523,-6350.65186,9869.77148

$$LAYER/3672.0

$$HATCHES/1,6,-6435.28613,9839.15918,-4383.16455,4201.00195,-4366.23828,4207.12451,-6418.35938,9845.28027,-6401.43213,9851.40430,-4349.31104,4213.24707,-4332.38428,4219.37012,-6384.50537,9857.52637,-6367.57861,9863.64844,-4315.45752,4225.49219,-4298.53125,4231.61523,-6350.65186,9869.77148

$$LAYER/3680.0

$$HATCHES/1,6,-6435.28613,9839.15918,-4383.16455,4201.00195,-4366.23828,4207.12451,-6418.35938,9845.28027,-6401.43213,9851.40430,-4349.31104,4213.24707,-4332.38428,4219.37012,-6384.50537,9857.52637,-6367.57861,9863.64844,-4315.45752,4225.49219,-4298.53125,4231.61523,-6350.65186,9869.77148

$$LAYER/3688.0

$$HATCHES/1,6,-6435.28613,9839.15918,-4383.16455,4201.00195,-4366.23828,4207.12451,-6418.35938,9845.28027,-6401.43213,9851.40430,-4349.31104,4213.24707,-4332.38428,4219.37012,-6384.50537,9857.52637,-6367.57861,9863.64844,-4315.45752,4225.49219,-4298.53125,4231.61523,-6350.65186,9869.77148

$$LAYER/3696.0

$$HATCHES/1,6,-6435.28613,9839.15918,-4383.16455,4201.00195,-4366.23828,4207.12451,-6418.35938,9845.28027,-6401.43213,9851.40430,-4349.31104,4213.24707,-4332.38428,4219.37012,-6384.50537,9857.52637,-6367.57861,9863.64844,-4315.45752,4225.49219,-4298.53125,4231.61523,-6350.65186,9869.77148

$$LAYER/3704.0

$$HATCHES/1,6,-6435.28613,9839.15918,-4383.16455,4201.00195,-4366.23828,4207.12451,-6418.35938,9845.28027,-6401.43213,9851.40430,-4349.31104,4213.24707,-4332.38428,4219.37012,-6384.50537,9857.52637,-6367.57861,9863.64844,-4315.45752,4225.49219,-4298.53125,4231.61523,-6350.65186,9869.77148

$$LAYER/3712.0

$$HATCHES/1,6,-6435.28613,9839.15918,-4383.16455,4201.00195,-4366.23828,4207.12451,-6418.35938,9845.28027,-6401.43213,9851.40430,-4349.31104,4213.24707,-4332.38428,4219.37012,-

6384.50537,9857.52637,-6367.57861,9863.64844,-4315.45752,4225.49219,-4298.53125,4231.61523,-6350.65186,9869.77148

$$LAYER/3720.0

$$HATCHES/1,6,-6435.28613,9839.15918,-4383.16455,4201.00195,-4366.23828,4207.12451,-6418.35938,9845.28027,-6401.43213,9851.40430,-4349.31104,4213.24707,-4332.38428,4219.37012,-6384.50537,9857.52637,-6367.57861,9863.64844,-4315.45752,4225.49219,-4298.53125,4231.61523,-6350.65186,9869.77148

$$LAYER/3728.0

$$HATCHES/1,6,-6435.28613,9839.15918,-4383.16455,4201.00195,-4366.23828,4207.12451,-6418.35938,9845.28027,-6401.43213,9851.40430,-4349.31104,4213.24707,-4332.38428,4219.37012,-6384.50537,9857.52637,-6367.57861,9863.64844,-4315.45752,4225.49219,-4298.53125,4231.61523,-6350.65186,9869.77148

$$LAYER/3736.0

$$HATCHES/1,6,-6435.28613,9839.15918,-4383.16455,4201.00195,-4366.23828,4207.12451,-6418.35938,9845.28027,-6401.43213,9851.40430,-4349.31104,4213.24707,-4332.38428,4219.37012,-6384.50537,9857.52637,-6367.57861,9863.64844,-4315.45752,4225.49219,-4298.53125,4231.61523,-6350.65186,9869.77148

$$LAYER/3744.0

$$HATCHES/1,6,-6435.28613,9839.15918,-4383.16455,4201.00195,-4366.23828,4207.12451,-6418.35938,9845.28027,-6401.43213,9851.40430,-4349.31104,4213.24707,-4332.38428,4219.37012,-6384.50537,9857.52637,-6367.57861,9863.64844,-4315.45752,4225.49219,-4298.53125,4231.61523,-6350.65186,9869.77148

$$LAYER/3752.0

$$HATCHES/1,6,-6435.28613,9839.15918,-4383.16455,4201.00195,-4366.23828,4207.12451,-6418.35938,9845.28027,-6401.43213,9851.40430,-4349.31104,4213.24707,-4332.38428,4219.37012,-6384.50537,9857.52637,-6367.57861,9863.64844,-4315.45752,4225.49219,-4298.53125,4231.61523,-6350.65186,9869.77148

$$LAYER/3760.0

$$HATCHES/1,6,-6435.28613,9839.15918,-4383.16455,4201.00195,-4366.23828,4207.12451,-6418.35938,9845.28027,-6401.43213,9851.40430,-4349.31104,4213.24707,-4332.38428,4219.37012,-6384.50537,9857.52637,-6367.57861,9863.64844,-4315.45752,4225.49219,-4298.53125,4231.61523,-6350.65186,9869.77148

$$LAYER/3768.0

$$HATCHES/1,6,-6435.28613,9839.15918,-4383.16455,4201.00195,-4366.23828,4207.12451,-6418.35938,9845.28027,-6401.43213,9851.40430,-4349.31104,4213.24707,-4332.38428,4219.37012,-6384.50537,9857.52637,-6367.57861,9863.64844,-4315.45752,4225.49219,-4298.53125,4231.61523,-6350.65186,9869.77148

$$LAYER/3776.0

$$HATCHES/1,6,-6435.28613,9839.15918,-4383.16455,4201.00195,-4366.23828,4207.12451,-6418.35938,9845.28027,-6401.43213,9851.40430,-4349.31104,4213.24707,-4332.38428,4219.37012,-6384.50537,9857.52637,-6367.57861,9863.64844,-4315.45752,4225.49219,-4298.53125,4231.61523,-6350.65186,9869.77148

$$LAYER/3784.0

$$HATCHES/1,6,-6435.28613,9839.15918,-4383.16455,4201.00195,-4366.23828,4207.12451,-6418.35938,9845.28027,-6401.43213,9851.40430,-4349.31104,4213.24707,-4332.38428,4219.37012,-6384.50537,9857.52637,-6367.57861,9863.64844,-4315.45752,4225.49219,-4298.53125,4231.61523,-6350.65186,9869.77148

$$LAYER/3792.0

$$HATCHES/1,6,-6435.28613,9839.15918,-4383.16455,4201.00195,-4366.23828,4207.12451,-6418.35938,9845.28027,-6401.43213,9851.40430,-4349.31104,4213.24707,-4332.38428,4219.37012,-6384.50537,9857.52637,-6367.57861,9863.64844,-4315.45752,4225.49219,-4298.53125,4231.61523,-6350.65186,9869.77148

$$LAYER/3800.0

$$HATCHES/1,6,-6435.28613,9839.15918,-4383.16455,4201.00195,-4366.23828,4207.12451,-6418.35938,9845.28027,-6401.43213,9851.40430,-4349.31104,4213.24707,-4332.38428,4219.37012,-6384.50537,9857.52637,-6367.57861,9863.64844,-4315.45752,4225.49219,-4298.53125,4231.61523,-6350.65186,9869.77148

$$LAYER/3808.0

$$HATCHES/1,6,-6435.28613,9839.15918,-4383.16455,4201.00195,-4366.23828,4207.12451,-6418.35938,9845.28027,-6401.43213,9851.40430,-4349.31104,4213.24707,-4332.38428,4219.37012,-6384.50537,9857.52637,-6367.57861,9863.64844,-4315.45752,4225.49219,-4298.53125,4231.61523,-6350.65186,9869.77148

$$LAYER/3816.0

$$HATCHES/1,6,-6435.28613,9839.15918,-4383.16455,4201.00195,-4366.23828,4207.12451,-6418.35938,9845.28027,-6401.43213,9851.40430,-4349.31104,4213.24707,-4332.38428,4219.37012,-6384.50537,9857.52637,-6367.57861,9863.64844,-4315.45752,4225.49219,-4298.53125,4231.61523,-6350.65186,9869.77148

$$LAYER/3824.0

$$HATCHES/1,6,-6435.28613,9839.15918,-4383.16455,4201.00195,-4366.23828,4207.12451,-6418.35938,9845.28027,-6401.43213,9851.40430,-4349.31104,4213.24707,-4332.38428,4219.37012,-

6384.50537,9857.52637,-6367.57861,9863.64844,-4315.45752,4225.49219,-4298.53125,4231.61523,-6350.65186,9869.77148

$$LAYER/3832.0

$$HATCHES/1,6,-6435.28613,9839.15918,-4383.16455,4201.00195,-4366.23828,4207.12451,-6418.35938,9845.28027,-6401.43213,9851.40430,-4349.31104,4213.24707,-4332.38428,4219.37012,-6384.50537,9857.52637,-6367.57861,9863.64844,-4315.45752,4225.49219,-4298.53125,4231.61523,-6350.65186,9869.77148

$$LAYER/3840.0

$$HATCHES/1,6,-6435.28613,9839.15918,-4383.16455,4201.00195,-4366.23828,4207.12451,-6418.35938,9845.28027,-6401.43213,9851.40430,-4349.31104,4213.24707,-4332.38428,4219.37012,-6384.50537,9857.52637,-6367.57861,9863.64844,-4315.45752,4225.49219,-4298.53125,4231.61523,-6350.65186,9869.77148

$$LAYER/3848.0

$$HATCHES/1,6,-6435.28613,9839.15918,-4383.16455,4201.00195,-4366.23828,4207.12451,-6418.35938,9845.28027,-6401.43213,9851.40430,-4349.31104,4213.24707,-4332.38428,4219.37012,-6384.50537,9857.52637,-6367.57861,9863.64844,-4315.45752,4225.49219,-4298.53125,4231.61523,-6350.65186,9869.77148

$$LAYER/3856.0

$$HATCHES/1,6,-6435.28613,9839.15918,-4383.16455,4201.00195,-4366.23828,4207.12451,-6418.35938,9845.28027,-6401.43213,9851.40430,-4349.31104,4213.24707,-4332.38428,4219.37012,-6384.50537,9857.52637,-6367.57861,9863.64844,-4315.45752,4225.49219,-4298.53125,4231.61523,-6350.65186,9869.77148

$$LAYER/3864.0

$$HATCHES/1,6,-6435.28613,9839.15918,-4383.16455,4201.00195,-4366.23828,4207.12451,-6418.35938,9845.28027,-6401.43213,9851.40430,-4349.31104,4213.24707,-4332.38428,4219.37012,-6384.50537,9857.52637,-6367.57861,9863.64844,-4315.45752,4225.49219,-4298.53125,4231.61523,-6350.65186,9869.77148

$$LAYER/3872.0

$$HATCHES/1,6,-6435.28613,9839.15918,-4383.16455,4201.00195,-4366.23828,4207.12451,-6418.35938,9845.28027,-6401.43213,9851.40430,-4349.31104,4213.24707,-4332.38428,4219.37012,-6384.50537,9857.52637,-6367.57861,9863.64844,-4315.45752,4225.49219,-4298.53125,4231.61523,-6350.65186,9869.77148

$$LAYER/3880.0

$$HATCHES/1,6,-6435.28613,9839.15918,-4383.16455,4201.00195,-4366.23828,4207.12451,-6418.35938,9845.28027,-6401.43213,9851.40430,-4349.31104,4213.24707,-4332.38428,4219.37012,-6384.50537,9857.52637,-6367.57861,9863.64844,-4315.45752,4225.49219,-4298.53125,4231.61523,-6350.65186,9869.77148

$$LAYER/3888.0

$$HATCHES/1,6,-6435.28613,9839.15918,-4383.16455,4201.00195,-4366.23828,4207.12451,-6418.35938,9845.28027,-6401.43213,9851.40430,-4349.31104,4213.24707,-4332.38428,4219.37012,-6384.50537,9857.52637,-6367.57861,9863.64844,-4315.45752,4225.49219,-4298.53125,4231.61523,-6350.65186,9869.77148

$$LAYER/3896.0

$$HATCHES/1,6,-6435.28613,9839.15918,-4383.16455,4201.00195,-4366.23828,4207.12451,-6418.35938,9845.28027,-6401.43213,9851.40430,-4349.31104,4213.24707,-4332.38428,4219.37012,-6384.50537,9857.52637,-6367.57861,9863.64844,-4315.45752,4225.49219,-4298.53125,4231.61523,-6350.65186,9869.77148

$$LAYER/3904.0

$$HATCHES/1,6,-6435.28613,9839.15918,-4383.16455,4201.00195,-4366.23828,4207.12451,-6418.35938,9845.28027,-6401.43213,9851.40430,-4349.31104,4213.24707,-4332.38428,4219.37012,-6384.50537,9857.52637,-6367.57861,9863.64844,-4315.45752,4225.49219,-4298.53125,4231.61523,-6350.65186,9869.77148

$$LAYER/3912.0

$$HATCHES/1,6,-6435.28613,9839.15918,-4383.16455,4201.00195,-4366.23828,4207.12451,-6418.35938,9845.28027,-6401.43213,9851.40430,-4349.31104,4213.24707,-4332.38428,4219.37012,-6384.50537,9857.52637,-6367.57861,9863.64844,-4315.45752,4225.49219,-4298.53125,4231.61523,-6350.65186,9869.77148

$$LAYER/3920.0

$$HATCHES/1,6,-6435.28613,9839.15918,-4383.16455,4201.00195,-4366.23828,4207.12451,-6418.35938,9845.28027,-6401.43213,9851.40430,-4349.31104,4213.24707,-4332.38428,4219.37012,-6384.50537,9857.52637,-6367.57861,9863.64844,-4315.45752,4225.49219,-4298.53125,4231.61523,-6350.65186,9869.77148

$$LAYER/3928.0

$$HATCHES/1,6,-6435.28613,9839.15918,-4383.16455,4201.00195,-4366.23828,4207.12451,-6418.35938,9845.28027,-6401.43213,9851.40430,-4349.31104,4213.24707,-4332.38428,4219.37012,-6384.50537,9857.52637,-6367.57861,9863.64844,-4315.45752,4225.49219,-4298.53125,4231.61523,-6350.65186,9869.77148

$$LAYER/3936.0

$$HATCHES/1,6,-6435.28613,9839.15918,-4383.16455,4201.00195,-4366.23828,4207.12451,-6418.35938,9845.28027,-6401.43213,9851.40430,-4349.31104,4213.24707,-4332.38428,4219.37012,-

6384.50537,9857.52637,-6367.57861,9863.64844,-4315.45752,4225.49219,-4298.53125,4231.61523,-6350.65186,9869.77148

$$LAYER/3944.0

$$HATCHES/1,6,-6435.28613,9839.15918,-4383.16455,4201.00195,-4366.23828,4207.12451,-6418.35938,9845.28027,-6401.43213,9851.40430,-4349.31104,4213.24707,-4332.38428,4219.37012,-6384.50537,9857.52637,-6367.57861,9863.64844,-4315.45752,4225.49219,-4298.53125,4231.61523,-6350.65186,9869.77148

$$LAYER/3952.0

$$HATCHES/1,6,-6435.28613,9839.15918,-4383.16455,4201.00195,-4366.23828,4207.12451,-6418.35938,9845.28027,-6401.43213,9851.40430,-4349.31104,4213.24707,-4332.38428,4219.37012,-6384.50537,9857.52637,-6367.57861,9863.64844,-4315.45752,4225.49219,-4298.53125,4231.61523,-6350.65186,9869.77148

$$LAYER/3960.0

$$HATCHES/1,6,-6435.28613,9839.15918,-4383.16455,4201.00195,-4366.23828,4207.12451,-6418.35938,9845.28027,-6401.43213,9851.40430,-4349.31104,4213.24707,-4332.38428,4219.37012,-6384.50537,9857.52637,-6367.57861,9863.64844,-4315.45752,4225.49219,-4298.53125,4231.61523,-6350.65186,9869.77148

$$LAYER/3968.0

$$HATCHES/1,6,-6435.28613,9839.15918,-4383.16455,4201.00195,-4366.23828,4207.12451,-6418.35938,9845.28027,-6401.43213,9851.40430,-4349.31104,4213.24707,-4332.38428,4219.37012,-6384.50537,9857.52637,-6367.57861,9863.64844,-4315.45752,4225.49219,-4298.53125,4231.61523,-6350.65186,9869.77148

$$LAYER/3976.0

$$HATCHES/1,6,-6435.28613,9839.15918,-4383.16455,4201.00195,-4366.23828,4207.12451,-6418.35938,9845.28027,-6401.43213,9851.40430,-4349.31104,4213.24707,-4332.38428,4219.37012,-6384.50537,9857.52637,-6367.57861,9863.64844,-4315.45752,4225.49219,-4298.53125,4231.61523,-6350.65186,9869.77148

$$LAYER/3984.0

$$HATCHES/1,6,-6435.28613,9839.15918,-4383.16455,4201.00195,-4366.23828,4207.12451,-6418.35938,9845.28027,-6401.43213,9851.40430,-4349.31104,4213.24707,-4332.38428,4219.37012,-6384.50537,9857.52637,-6367.57861,9863.64844,-4315.45752,4225.49219,-4298.53125,4231.61523,-6350.65186,9869.77148

$$LAYER/3992.0

$$HATCHES/1,6,-6435.28613,9839.15918,-4383.16455,4201.00195,-4366.23828,4207.12451,-6418.35938,9845.28027,-6401.43213,9851.40430,-4349.31104,4213.24707,-4332.38428,4219.37012,-6384.50537,9857.52637,-6367.57861,9863.64844,-4315.45752,4225.49219,-4298.53125,4231.61523,-6350.65186,9869.77148

$$LAYER/4000.0

$$HATCHES/1,6,-6435.28613,9839.15918,-4383.16455,4201.00195,-4366.23828,4207.12451,-6418.35938,9845.28027,-6401.43213,9851.40430,-4349.31104,4213.24707,-4332.38428,4219.37012,-6384.50537,9857.52637,-6367.57861,9863.64844,-4315.45752,4225.49219,-4298.53125,4231.61523,-6350.65186,9869.77148

$$LAYER/4008.0

$$HATCHES/1,6,-6435.28613,9839.15918,-4383.16455,4201.00195,-4366.23828,4207.12451,-6418.35938,9845.28125,-6401.43311,9851.40527,-4349.31104,4213.24707,-4332.38428,4219.37012,-6384.50586,9857.52734,-6367.57910,9863.64941,-4315.45752,4225.49219,-4298.53125,4231.61523,-6350.65234,9869.77148

$$LAYER/4016.0

$$HATCHES/1,6,-6435.28613,9839.15918,-4383.16455,4201.00195,-4366.23828,4207.12451,-6418.35938,9845.28027,-6401.43213,9851.40430,-4349.31104,4213.24707,-4332.38428,4219.37012,-6384.50537,9857.52637,-6367.57861,9863.64844,-4315.45752,4225.49219,-4298.53125,4231.61523,-6350.65186,9869.77148

$$LAYER/4024.0

$$HATCHES/1,6,-6435.28613,9839.15918,-4383.16455,4201.00195,-4366.23828,4207.12451,-6418.35938,9845.28027,-6401.43213,9851.40430,-4349.31104,4213.24707,-4332.38428,4219.37012,-6384.50537,9857.52637,-6367.57861,9863.64844,-4315.45752,4225.49219,-4298.53125,4231.61523,-6350.65186,9869.77148

$$LAYER/4032.0

$$HATCHES/1,6,-6435.28613,9839.15918,-4383.16455,4201.00195,-4366.23828,4207.12451,-6418.35938,9845.28027,-6401.43213,9851.40430,-4349.31104,4213.24707,-4332.38428,4219.37012,-6384.50537,9857.52637,-6367.57861,9863.64844,-4315.45752,4225.49219,-4298.53125,4231.61523,-6350.65186,9869.77148

$$LAYER/4040.0

$$HATCHES/1,6,-6435.28613,9839.15918,-4383.16455,4201.00195,-4366.23828,4207.12451,-6418.35938,9845.28027,-6401.43213,9851.40430,-4349.31104,4213.24707,-4332.38428,4219.37012,-6384.50537,9857.52637,-6367.57861,9863.64844,-4315.45752,4225.49219,-4298.53125,4231.61523,-6350.65186,9869.77148

$$LAYER/4048.0

$$HATCHES/1,6,-6435.28613,9839.15918,-4383.16455,4201.00195,-4366.23828,4207.12451,-6418.35938,9845.28027,-6401.43213,9851.40430,-4349.31104,4213.24707,-4332.38428,4219.37012,-

6384.50537,9857.52637,-6367.57861,9863.64844,-4315.45752,4225.49219,-4298.53125,4231.61523,-6350.65186,9869.77148

$$LAYER/4056.0

$$HATCHES/1,6,-6435.28760,9839.16309,-4383.16455,4201.00195,-4366.23828,4207.12451,-6418.36084,9845.28516,-6401.43359,9851.40820,-4349.31104,4213.24707,-4332.38428,4219.37012,-6384.50684,9857.52930,-6367.57959,9863.65039,-4315.45752,4225.49219,-4298.53125,4231.61523,-6350.65234,9869.77246

$$LAYER/4064.0

$$HATCHES/1,6,-6435.28613,9839.15918,-4383.16455,4201.00195,-4366.23828,4207.12451,-6418.35938,9845.28027,-6401.43213,9851.40430,-4349.31104,4213.24707,-4332.38428,4219.37012,-6384.50537,9857.52637,-6367.57861,9863.64844,-4315.45752,4225.49219,-4298.53125,4231.61523,-6350.65186,9869.77148

$$LAYER/4072.0

$$HATCHES/1,6,-6435.28613,9839.15918,-4383.16455,4201.00195,-4366.23828,4207.12451,-6418.35938,9845.28027,-6401.43213,9851.40430,-4349.31104,4213.24707,-4332.38428,4219.37012,-6384.50537,9857.52637,-6367.57861,9863.64844,-4315.45752,4225.49219,-4298.53125,4231.61523,-6350.65186,9869.77148

$$LAYER/4080.0

$$HATCHES/1,6,-6435.28613,9839.15918,-4383.16455,4201.00195,-4366.23828,4207.12451,-6418.35938,9845.28027,-6401.43213,9851.40430,-4349.31104,4213.24707,-4332.38428,4219.37012,-6384.50537,9857.52637,-6367.57861,9863.64844,-4315.45752,4225.49219,-4298.53125,4231.61523,-6350.65186,9869.77148

$$LAYER/4088.0

$$HATCHES/1,6,-6435.28613,9839.15918,-4383.16455,4201.00195,-4366.23828,4207.12451,-6418.35938,9845.28027,-6401.43213,9851.40430,-4349.31104,4213.24707,-4332.38428,4219.37012,-6384.50537,9857.52637,-6367.57861,9863.64844,-4315.45752,4225.49219,-4298.53125,4231.61523,-6350.65186,9869.77148

$$LAYER/4096.0

$$HATCHES/1,6,-6435.28613,9839.15918,-4383.16455,4201.00195,-4366.23828,4207.12451,-6418.35938,9845.28027,-6401.43213,9851.40430,-4349.31104,4213.24707,-4332.38428,4219.37012,-6384.50537,9857.52637,-6367.57861,9863.64844,-4315.45752,4225.49219,-4298.53125,4231.61523,-6350.65186,9869.77148

$$LAYER/4104.0

$$HATCHES/1,6,-6435.28613,9839.15918,-4383.16455,4201.00195,-4366.23828,4207.12451,-6418.35938,9845.28027,-6401.43213,9851.40430,-4349.31104,4213.24707,-4332.38428,4219.37012,-6384.50537,9857.52637,-6367.57861,9863.64844,-4315.45752,4225.49219,-4298.53125,4231.61523,-6350.65186,9869.77148

$$LAYER/4112.0

$$HATCHES/1,6,-6435.28906,9839.16895,-4383.16455,4201.00195,-4366.23828,4207.12451,-6418.36279,9845.28906,-6401.43457,9851.41016,-4349.31104,4213.24707,-4332.38428,4219.37012,-6384.50732,9857.53027,-6367.57959,9863.65039,-4315.45752,4225.49219,-4298.53125,4231.61523,-6350.65186,9869.77051

$$LAYER/4120.0

$$HATCHES/1,6,-6435.28613,9839.15918,-4383.16455,4201.00195,-4366.23828,4207.12451,-6418.35938,9845.28027,-6401.43213,9851.40430,-4349.31104,4213.24707,-4332.38428,4219.37012,-6384.50537,9857.52637,-6367.57861,9863.64844,-4315.45752,4225.49219,-4298.53125,4231.61523,-6350.65186,9869.77148

$$LAYER/4128.0

$$HATCHES/1,6,-6435.28613,9839.15918,-4383.16455,4201.00195,-4366.23828,4207.12451,-6418.35938,9845.28027,-6401.43213,9851.40430,-4349.31104,4213.24707,-4332.38428,4219.37012,-6384.50537,9857.52637,-6367.57861,9863.64844,-4315.45752,4225.49219,-4298.53125,4231.61523,-6350.65186,9869.77148

$$LAYER/4136.0

$$HATCHES/1,6,-6435.28613,9839.15918,-4383.16455,4201.00195,-4366.23828,4207.12451,-6418.35938,9845.28027,-6401.43213,9851.40430,-4349.31104,4213.24707,-4332.38428,4219.37012,-6384.50537,9857.52637,-6367.57861,9863.64844,-4315.45752,4225.49219,-4298.53125,4231.61523,-6350.65186,9869.77148

$$LAYER/4144.0

$$HATCHES/1,6,-6435.28613,9839.15918,-4383.16455,4201.00195,-4366.23828,4207.12451,-6418.35938,9845.28027,-6401.43213,9851.40430,-4349.31104,4213.24707,-4332.38428,4219.37012,-6384.50537,9857.52637,-6367.57861,9863.64844,-4315.45752,4225.49219,-4298.53125,4231.61523,-6350.65186,9869.77148

$$LAYER/4152.0

$$HATCHES/1,6,-6435.28613,9839.15918,-4383.16455,4201.00195,-4366.23828,4207.12451,-6418.35938,9845.28027,-6401.43213,9851.40430,-4349.31104,4213.24707,-4332.38428,4219.37012,-6384.50537,9857.52637,-6367.57861,9863.64844,-4315.45752,4225.49219,-4298.53125,4231.61523,-6350.65186,9869.77148

$$LAYER/4160.0

$$HATCHES/1,6,-6435.28613,9839.15918,-4383.16455,4201.00195,-4366.23828,4207.12451,-6418.35938,9845.28027,-6401.43213,9851.40430,-4349.31104,4213.24707,-4332.38428,4219.37012,-

6384.50537,9857.52637,-6367.57861,9863.64844,-4315.45752,4225.49219,-4298.53125,4231.61523,-6350.65186,9869.77148

$$LAYER/4168.0

$$HATCHES/1,6,-6435.28613,9839.15918,-4383.16455,4201.00195,-4366.23828,4207.12451,-6418.35938,9845.28027,-6401.43213,9851.40430,-4349.31104,4213.24707,-4332.38428,4219.37012,-6384.50537,9857.52637,-6367.57861,9863.64844,-4315.45752,4225.49219,-4298.53125,4231.61523,-6350.65186,9869.77148

$$LAYER/4176.0

$$HATCHES/1,6,-6435.28613,9839.15918,-4383.16455,4201.00195,-4366.23828,4207.12451,-6418.35938,9845.28027,-6401.43213,9851.40430,-4349.31104,4213.24707,-4332.38428,4219.37012,-6384.50537,9857.52637,-6367.57861,9863.64844,-4315.45752,4225.49219,-4298.53125,4231.61523,-6350.65186,9869.77148

$$LAYER/4184.0

$$HATCHES/1,6,-6435.28613,9839.15918,-4383.16455,4201.00195,-4366.23828,4207.12451,-6418.35938,9845.28027,-6401.43213,9851.40430,-4349.31104,4213.24707,-4332.38428,4219.37012,-6384.50537,9857.52637,-6367.57861,9863.64844,-4315.45752,4225.49219,-4298.53125,4231.61523,-6350.65186,9869.77148

$$LAYER/4192.0

$$HATCHES/1,6,-6435.28613,9839.15918,-4383.16455,4201.00195,-4366.23828,4207.12451,-6418.35938,9845.28027,-6401.43213,9851.40430,-4349.31104,4213.24707,-4332.38428,4219.37012,-6384.50537,9857.52637,-6367.57861,9863.64844,-4315.45752,4225.49219,-4298.53125,4231.61523,-6350.65186,9869.77148

$$LAYER/4200.0

$$HATCHES/1,6,-6435.28613,9839.15918,-4383.16455,4201.00195,-4366.23828,4207.12451,-6418.35938,9845.28027,-6401.43213,9851.40430,-4349.31104,4213.24707,-4332.38428,4219.37012,-6384.50537,9857.52637,-6367.57861,9863.64844,-4315.45752,4225.49219,-4298.53125,4231.61523,-6350.65186,9869.77148

$$LAYER/4208.0

$$HATCHES/1,6,-6435.28613,9839.15918,-4383.16455,4201.00195,-4366.23828,4207.12451,-6418.35938,9845.28027,-6401.43213,9851.40430,-4349.31104,4213.24707,-4332.38428,4219.37012,-6384.50537,9857.52637,-6367.57861,9863.64844,-4315.45752,4225.49219,-4298.53125,4231.61523,-6350.65186,9869.77148

$$LAYER/4216.0

$$HATCHES/1,6,-6435.28613,9839.15918,-4383.16455,4201.00195,-4366.23828,4207.12451,-6418.35938,9845.28027,-6401.43213,9851.40430,-4349.31104,4213.24707,-4332.38428,4219.37012,-6384.50537,9857.52637,-6367.57861,9863.64844,-4315.45752,4225.49219,-4298.53125,4231.61523,-6350.65186,9869.77148

$$LAYER/4224.0

$$HATCHES/1,6,-6435.28613,9839.15918,-4383.16455,4201.00195,-4366.23828,4207.12451,-6418.35938,9845.28027,-6401.43213,9851.40430,-4349.31104,4213.24707,-4332.38428,4219.37012,-6384.50537,9857.52637,-6367.57861,9863.64844,-4315.45752,4225.49219,-4298.53125,4231.61523,-6350.65186,9869.77148

$$LAYER/4232.0

$$HATCHES/1,6,-6435.28613,9839.15918,-4383.16455,4201.00195,-4366.23828,4207.12451,-6418.35938,9845.28027,-6401.43213,9851.40430,-4349.31104,4213.24707,-4332.38428,4219.37012,-6384.50537,9857.52637,-6367.57861,9863.64844,-4315.45752,4225.49219,-4298.53125,4231.61523,-6350.65186,9869.77148

$$LAYER/4240.0

$$HATCHES/1,6,-6435.28613,9839.15918,-4383.16455,4201.00195,-4366.23828,4207.12451,-6418.35938,9845.28027,-6401.43213,9851.40430,-4349.31104,4213.24707,-4332.38428,4219.37012,-6384.50537,9857.52637,-6367.57861,9863.64844,-4315.45752,4225.49219,-4298.53125,4231.61523,-6350.65186,9869.77148

$$LAYER/4248.0

$$HATCHES/1,6,-6435.28613,9839.15918,-4383.16455,4201.00195,-4366.23828,4207.12451,-6418.35938,9845.28027,-6401.43213,9851.40430,-4349.31104,4213.24707,-4332.38428,4219.37012,-6384.50537,9857.52637,-6367.57861,9863.64844,-4315.45752,4225.49219,-4298.53125,4231.61523,-6350.65186,9869.77148

$$LAYER/4256.0

$$HATCHES/1,6,-6435.28613,9839.15918,-4383.16455,4201.00195,-4366.23828,4207.12451,-6418.35938,9845.28027,-6401.43213,9851.40430,-4349.31104,4213.24707,-4332.38428,4219.37012,-6384.50537,9857.52637,-6367.57861,9863.64844,-4315.45752,4225.49219,-4298.53125,4231.61523,-6350.65186,9869.77148

$$LAYER/4264.0

$$HATCHES/1,6,-6435.28613,9839.15918,-4383.16455,4201.00195,-4366.23828,4207.12451,-6418.35938,9845.28027,-6401.43213,9851.40430,-4349.31104,4213.24707,-4332.38428,4219.37012,-6384.50537,9857.52637,-6367.57861,9863.64844,-4315.45752,4225.49219,-4298.53125,4231.61523,-6350.65186,9869.77148

$$LAYER/4272.0

$$HATCHES/1,6,-6435.28613,9839.15918,-4383.16455,4201.00195,-4366.23828,4207.12451,-6418.35938,9845.28027,-6401.43213,9851.40430,-4349.31104,4213.24707,-4332.38428,4219.37012,-

6384.50537,9857.52637,-6367.57861,9863.64844,-4315.45752,4225.49219,-4298.53125,4231.61523,-6350.65186,9869.77148

$$LAYER/4280.0

$$HATCHES/1,6,-6435.28613,9839.15918,-4383.16455,4201.00195,-4366.23828,4207.12451,-6418.35938,9845.28027,-6401.43213,9851.40430,-4349.31104,4213.24707,-4332.38428,4219.37012,-6384.50537,9857.52637,-6367.57861,9863.64844,-4315.45752,4225.49219,-4298.53125,4231.61523,-6350.65186,9869.77148

$$LAYER/4288.0

$$HATCHES/1,6,-6435.28613,9839.15918,-4383.16455,4201.00195,-4366.23828,4207.12451,-6418.35938,9845.28027,-6401.43213,9851.40430,-4349.31104,4213.24707,-4332.38428,4219.37012,-6384.50537,9857.52637,-6367.57861,9863.64844,-4315.45752,4225.49219,-4298.53125,4231.61523,-6350.65186,9869.77148

$$LAYER/4296.0

$$HATCHES/1,6,-6435.28613,9839.15918,-4383.16455,4201.00195,-4366.23828,4207.12451,-6418.35938,9845.28027,-6401.43213,9851.40430,-4349.31104,4213.24707,-4332.38428,4219.37012,-6384.50537,9857.52637,-6367.57861,9863.64844,-4315.45752,4225.49219,-4298.53125,4231.61523,-6350.65186,9869.77148

$$LAYER/4304.0

$$HATCHES/1,6,-6435.28613,9839.15918,-4383.16455,4201.00195,-4366.23828,4207.12451,-6418.35938,9845.28027,-6401.43213,9851.40430,-4349.31104,4213.24707,-4332.38428,4219.37012,-6384.50537,9857.52637,-6367.57861,9863.64844,-4315.45752,4225.49219,-4298.53125,4231.61523,-6350.65186,9869.77148

$$LAYER/4312.0

$$HATCHES/1,6,-6435.28613,9839.15918,-4383.16455,4201.00195,-4366.23828,4207.12451,-6418.35938,9845.28027,-6401.43213,9851.40430,-4349.31104,4213.24707,-4332.38428,4219.37012,-6384.50537,9857.52637,-6367.57861,9863.64844,-4315.45752,4225.49219,-4298.53125,4231.61523,-6350.65186,9869.77148

$$LAYER/4320.0

$$HATCHES/1,6,-6435.28613,9839.15918,-4383.16455,4201.00195,-4366.23828,4207.12451,-6418.35938,9845.28027,-6401.43213,9851.40430,-4349.31104,4213.24707,-4332.38428,4219.37012,-6384.50537,9857.52637,-6367.57861,9863.64844,-4315.45752,4225.49219,-4298.53125,4231.61523,-6350.65186,9869.77148

$$LAYER/4328.0

$$HATCHES/1,6,-6435.28613,9839.15918,-4383.16455,4201.00195,-4366.23828,4207.12451,-6418.35938,9845.28027,-6401.43213,9851.40430,-4349.31104,4213.24707,-4332.38428,4219.37012,-6384.50537,9857.52637,-6367.57861,9863.64844,-4315.45752,4225.49219,-4298.53125,4231.61523,-6350.65186,9869.77148

$$LAYER/4336.0

$$HATCHES/1,6,-6435.28613,9839.15918,-4383.16455,4201.00195,-4366.23828,4207.12451,-6418.35938,9845.28027,-6401.43213,9851.40430,-4349.31104,4213.24707,-4332.38428,4219.37012,-6384.50537,9857.52637,-6367.57861,9863.64844,-4315.45752,4225.49219,-4298.53125,4231.61523,-6350.65186,9869.77148

$$LAYER/4344.0

$$HATCHES/1,6,-6435.28613,9839.15918,-4383.16455,4201.00195,-4366.23828,4207.12451,-6418.35938,9845.28027,-6401.43213,9851.40430,-4349.31104,4213.24707,-4332.38428,4219.37012,-6384.50537,9857.52637,-6367.57861,9863.64844,-4315.45752,4225.49219,-4298.53125,4231.61523,-6350.65186,9869.77148

$$LAYER/4352.0

$$HATCHES/1,6,-6435.28613,9839.15918,-4383.16455,4201.00195,-4366.23828,4207.12451,-6418.35938,9845.28027,-6401.43213,9851.40430,-4349.31104,4213.24707,-4332.38428,4219.37012,-6384.50537,9857.52637,-6367.57861,9863.64844,-4315.45752,4225.49219,-4298.53125,4231.61523,-6350.65186,9869.77148

$$LAYER/4360.0

$$HATCHES/1,6,-6435.28613,9839.15918,-4383.16455,4201.00195,-4366.23828,4207.12451,-6418.35938,9845.28027,-6401.43213,9851.40430,-4349.31104,4213.24707,-4332.38428,4219.37012,-6384.50537,9857.52637,-6367.57861,9863.64844,-4315.45752,4225.49219,-4298.53125,4231.61523,-6350.65186,9869.77148

$$LAYER/4368.0

$$HATCHES/1,6,-6435.28613,9839.15918,-4383.16455,4201.00195,-4366.23828,4207.12451,-6418.35938,9845.28027,-6401.43213,9851.40430,-4349.31104,4213.24707,-4332.38428,4219.37012,-6384.50537,9857.52637,-6367.57861,9863.64844,-4315.45752,4225.49219,-4298.53125,4231.61523,-6350.65186,9869.77148

$$LAYER/4376.0

$$HATCHES/1,6,-6435.28613,9839.15918,-4383.16455,4201.00195,-4366.23828,4207.12451,-6418.35938,9845.28027,-6401.43213,9851.40430,-4349.31104,4213.24707,-4332.38428,4219.37012,-6384.50537,9857.52637,-6367.57861,9863.64844,-4315.45752,4225.49219,-4298.53125,4231.61523,-6350.65186,9869.77148

$$LAYER/4384.0

$$HATCHES/1,6,-6435.28613,9839.15918,-4383.16455,4201.00195,-4366.23828,4207.12451,-6418.35938,9845.28027,-6401.43213,9851.40430,-4349.31104,4213.24707,-4332.38428,4219.37012,-

6384.50537,9857.52637,-6367.57861,9863.64844,-4315.45752,4225.49219,-4298.53125,4231.61523,-6350.65186,9869.77148

$$LAYER/4392.0

$$HATCHES/1,6,-6435.28613,9839.15918,-4383.16455,4201.00195,-4366.23828,4207.12451,-6418.35938,9845.28027,-6401.43213,9851.40430,-4349.31104,4213.24707,-4332.38428,4219.37012,-6384.50537,9857.52637,-6367.57861,9863.64844,-4315.45752,4225.49219,-4298.53125,4231.61523,-6350.65186,9869.77148

$$LAYER/4400.0

$$HATCHES/1,6,-6435.28613,9839.15918,-4383.16455,4201.00195,-4366.23828,4207.12451,-6418.35938,9845.28027,-6401.43213,9851.40430,-4349.31104,4213.24707,-4332.38428,4219.37012,-6384.50537,9857.52637,-6367.57861,9863.64844,-4315.45752,4225.49219,-4298.53125,4231.61523,-6350.65186,9869.77148

$$LAYER/4408.0

$$HATCHES/1,6,-6435.28613,9839.15918,-4383.16455,4201.00195,-4366.23828,4207.12451,-6418.35938,9845.28027,-6401.43213,9851.40430,-4349.31104,4213.24707,-4332.38428,4219.37012,-6384.50537,9857.52637,-6367.57861,9863.64844,-4315.45752,4225.49219,-4298.53125,4231.61523,-6350.65186,9869.77148

$$LAYER/4416.0

$$HATCHES/1,6,-6435.28613,9839.15918,-4383.16455,4201.00195,-4366.23828,4207.12451,-6418.35938,9845.28027,-6401.43213,9851.40430,-4349.31104,4213.24707,-4332.38428,4219.37012,-6384.50537,9857.52637,-6367.57861,9863.64844,-4315.45752,4225.49219,-4298.53125,4231.61523,-6350.65186,9869.77148

$$LAYER/4424.0

$$HATCHES/1,6,-6435.28613,9839.15918,-4383.16455,4201.00195,-4366.23828,4207.12451,-6418.35938,9845.28027,-6401.43213,9851.40430,-4349.31104,4213.24707,-4332.38428,4219.37012,-6384.50537,9857.52637,-6367.57861,9863.64844,-4315.45752,4225.49219,-4298.53125,4231.61523,-6350.65186,9869.77148

$$LAYER/4432.0

$$HATCHES/1,6,-6435.28613,9839.15918,-4383.16455,4201.00195,-4366.23828,4207.12451,-6418.35938,9845.28027,-6401.43213,9851.40430,-4349.31104,4213.24707,-4332.38428,4219.37012,-6384.50537,9857.52637,-6367.57861,9863.64844,-4315.45752,4225.49219,-4298.53125,4231.61523,-6350.65186,9869.77148

$$LAYER/4440.0

$$HATCHES/1,6,-6435.28613,9839.15918,-4383.16455,4201.00195,-4366.23828,4207.12451,-6418.35938,9845.28027,-6401.43213,9851.40430,-4349.31104,4213.24707,-4332.38428,4219.37012,-6384.50537,9857.52637,-6367.57861,9863.64844,-4315.45752,4225.49219,-4298.53125,4231.61523,-6350.65186,9869.77148

$$LAYER/4448.0

$$HATCHES/1,6,-6435.28613,9839.15918,-4383.16455,4201.00195,-4366.23828,4207.12451,-6418.35938,9845.28027,-6401.43213,9851.40430,-4349.31104,4213.24707,-4332.38428,4219.37012,-6384.50537,9857.52637,-6367.57861,9863.64844,-4315.45752,4225.49219,-4298.53125,4231.61523,-6350.65186,9869.77148

$$LAYER/4456.0

$$HATCHES/1,6,-6435.28613,9839.15918,-4383.16455,4201.00195,-4366.23828,4207.12451,-6418.35938,9845.28027,-6401.43213,9851.40430,-4349.31104,4213.24707,-4332.38428,4219.37012,-6384.50537,9857.52637,-6367.57861,9863.64844,-4315.45752,4225.49219,-4298.53125,4231.61523,-6350.65186,9869.77148

$$LAYER/4464.0

$$HATCHES/1,6,-6435.28613,9839.15918,-4383.16455,4201.00195,-4366.23828,4207.12451,-6418.35938,9845.28027,-6401.43213,9851.40430,-4349.31104,4213.24707,-4332.38428,4219.37012,-6384.50537,9857.52637,-6367.57861,9863.64844,-4315.45752,4225.49219,-4298.53125,4231.61523,-6350.65186,9869.77148

$$LAYER/4472.0

$$HATCHES/1,6,-6435.28613,9839.15918,-4383.16455,4201.00195,-4366.23828,4207.12451,-6418.35938,9845.28027,-6401.43213,9851.40430,-4349.31104,4213.24707,-4332.38428,4219.37012,-6384.50537,9857.52637,-6367.57861,9863.64844,-4315.45752,4225.49219,-4298.53125,4231.61523,-6350.65186,9869.77148

$$LAYER/4480.0

$$HATCHES/1,6,-6435.28613,9839.15918,-4383.16455,4201.00195,-4366.23828,4207.12451,-6418.35938,9845.28027,-6401.43213,9851.40430,-4349.31104,4213.24707,-4332.38428,4219.37012,-6384.50537,9857.52637,-6367.57861,9863.64844,-4315.45752,4225.49219,-4298.53125,4231.61523,-6350.65186,9869.77148

$$LAYER/4488.0

$$HATCHES/1,6,-6435.28613,9839.15918,-4383.16455,4201.00195,-4366.23828,4207.12451,-6418.35938,9845.28027,-6401.43213,9851.40430,-4349.31104,4213.24707,-4332.38428,4219.37012,-6384.50537,9857.52637,-6367.57861,9863.64844,-4315.45752,4225.49219,-4298.53125,4231.61523,-6350.65186,9869.77148

$$LAYER/4496.0

$$HATCHES/1,6,-6435.28613,9839.15918,-4383.16455,4201.00195,-4366.23828,4207.12451,-6418.35938,9845.28027,-6401.43213,9851.40430,-4349.31104,4213.24707,-4332.38428,4219.37012,-

6384.50537,9857.52637,-6367.57861,9863.64844,-4315.45752,4225.49219,-4298.53125,4231.61523,-6350.65186,9869.77148

$$LAYER/4504.0

$$HATCHES/1,6,-6435.28613,9839.15918,-4383.16455,4201.00195,-4366.23828,4207.12451,-6418.35938,9845.28027,-6401.43213,9851.40430,-4349.31104,4213.24707,-4332.38428,4219.37012,-6384.50537,9857.52637,-6367.57861,9863.64844,-4315.45752,4225.49219,-4298.53125,4231.61523,-6350.65186,9869.77148

$$LAYER/4512.0

$$HATCHES/1,6,-6435.28613,9839.15918,-4383.16455,4201.00195,-4366.23828,4207.12451,-6418.35938,9845.28027,-6401.43213,9851.40430,-4349.31104,4213.24707,-4332.38428,4219.37012,-6384.50537,9857.52637,-6367.57861,9863.64844,-4315.45752,4225.49219,-4298.53125,4231.61523,-6350.65186,9869.77148

$$LAYER/4520.0

$$HATCHES/1,6,-6435.28613,9839.15918,-4383.16455,4201.00195,-4366.23828,4207.12451,-6418.35938,9845.28027,-6401.43213,9851.40430,-4349.31104,4213.24707,-4332.38428,4219.37012,-6384.50537,9857.52637,-6367.57861,9863.64844,-4315.45752,4225.49219,-4298.53125,4231.61523,-6350.65186,9869.77148

$$LAYER/4528.0

$$HATCHES/1,6,-6435.28613,9839.15918,-4383.16455,4201.00195,-4366.23828,4207.12451,-6418.35938,9845.28027,-6401.43213,9851.40430,-4349.31104,4213.24707,-4332.38428,4219.37012,-6384.50537,9857.52637,-6367.57861,9863.64844,-4315.45752,4225.49219,-4298.53125,4231.61523,-6350.65186,9869.77148

$$LAYER/4536.0

$$HATCHES/1,6,-6435.28613,9839.15918,-4383.16455,4201.00195,-4366.23828,4207.12451,-6418.35938,9845.28027,-6401.43213,9851.40430,-4349.31104,4213.24707,-4332.38428,4219.37012,-6384.50537,9857.52637,-6367.57861,9863.64844,-4315.45752,4225.49219,-4298.53125,4231.61523,-6350.65186,9869.77148

$$LAYER/4544.0

$$HATCHES/1,6,-6435.28613,9839.15918,-4383.16455,4201.00195,-4366.23828,4207.12451,-6418.35938,9845.28027,-6401.43213,9851.40430,-4349.31104,4213.24707,-4332.38428,4219.37012,-6384.50537,9857.52637,-6367.57861,9863.64844,-4315.45752,4225.49219,-4298.53125,4231.61523,-6350.65186,9869.77148

$$LAYER/4552.0

$$HATCHES/1,6,-6435.28613,9839.15918,-4383.16455,4201.00195,-4366.23828,4207.12451,-6418.35938,9845.28027,-6401.43213,9851.40430,-4349.31104,4213.24707,-4332.38428,4219.37012,-6384.50537,9857.52637,-6367.57861,9863.64844,-4315.45752,4225.49219,-4298.53125,4231.61523,-6350.65186,9869.77148

$$LAYER/4560.0

$$HATCHES/1,6,-6435.28613,9839.15918,-4383.16455,4201.00195,-4366.23828,4207.12451,-6418.35938,9845.28027,-6401.43213,9851.40430,-4349.31104,4213.24707,-4332.38428,4219.37012,-6384.50537,9857.52637,-6367.57861,9863.64844,-4315.45752,4225.49219,-4298.53125,4231.61523,-6350.65186,9869.77148

$$LAYER/4568.0

$$HATCHES/1,6,-6435.28613,9839.15918,-4383.16455,4201.00195,-4366.23828,4207.12451,-6418.35938,9845.28027,-6401.43213,9851.40430,-4349.31104,4213.24707,-4332.38428,4219.37012,-6384.50537,9857.52637,-6367.57861,9863.64844,-4315.45752,4225.49219,-4298.53125,4231.61523,-6350.65186,9869.77148

$$LAYER/4576.0

$$HATCHES/1,6,-6435.28613,9839.15918,-4383.16455,4201.00195,-4366.23828,4207.12451,-6418.35938,9845.28027,-6401.43213,9851.40430,-4349.31104,4213.24707,-4332.38428,4219.37012,-6384.50537,9857.52637,-6367.57861,9863.64844,-4315.45752,4225.49219,-4298.53125,4231.61523,-6350.65186,9869.77148

$$LAYER/4584.0

$$HATCHES/1,6,-6435.28613,9839.15918,-4383.16455,4201.00195,-4366.23828,4207.12451,-6418.35938,9845.28027,-6401.43213,9851.40430,-4349.31104,4213.24707,-4332.38428,4219.37012,-6384.50537,9857.52637,-6367.57861,9863.64844,-4315.45752,4225.49219,-4298.53125,4231.61523,-6350.65186,9869.77148

$$LAYER/4592.0

$$HATCHES/1,6,-6435.28613,9839.15918,-4383.16455,4201.00195,-4366.23828,4207.12451,-6418.35938,9845.28027,-6401.43213,9851.40430,-4349.31104,4213.24707,-4332.38428,4219.37012,-6384.50537,9857.52637,-6367.57861,9863.64844,-4315.45752,4225.49219,-4298.53125,4231.61523,-6350.65186,9869.77148

$$LAYER/4600.0

$$HATCHES/1,6,-6435.28613,9839.15918,-4383.16455,4201.00195,-4366.23828,4207.12451,-6418.35938,9845.28027,-6401.43213,9851.40430,-4349.31104,4213.24707,-4332.38428,4219.37012,-6384.50537,9857.52637,-6367.57861,9863.64844,-4315.45752,4225.49219,-4298.53125,4231.61523,-6350.65186,9869.77148

$$LAYER/4608.0

$$HATCHES/1,6,-6435.28613,9839.15918,-4383.16455,4201.00195,-4366.23828,4207.12451,-6418.35938,9845.28027,-6401.43213,9851.40430,-4349.31104,4213.24707,-4332.38428,4219.37012,-

6384.50537,9857.52637,-6367.57861,9863.64844,-4315.45752,4225.49219,-4298.53125,4231.61523,-6350.65186,9869.77148

$$LAYER/4616.0

$$HATCHES/1,6,-6435.28613,9839.15918,-4383.16455,4201.00195,-4366.23828,4207.12451,-6418.35938,9845.28027,-6401.43213,9851.40430,-4349.31104,4213.24707,-4332.38428,4219.37012,-6384.50537,9857.52637,-6367.57861,9863.64844,-4315.45752,4225.49219,-4298.53125,4231.61523,-6350.65186,9869.77148

$$LAYER/4624.0

$$HATCHES/1,6,-6435.28613,9839.15918,-4383.16455,4201.00195,-4366.23828,4207.12451,-6418.35938,9845.28027,-6401.43213,9851.40430,-4349.31104,4213.24707,-4332.38428,4219.37012,-6384.50537,9857.52637,-6367.57861,9863.64844,-4315.45752,4225.49219,-4298.53125,4231.61523,-6350.65186,9869.77148

$$LAYER/4632.0

$$HATCHES/1,6,-6435.28613,9839.15918,-4383.16455,4201.00195,-4366.23828,4207.12451,-6418.35938,9845.28027,-6401.43213,9851.40430,-4349.31104,4213.24707,-4332.38428,4219.37012,-6384.50537,9857.52637,-6367.57861,9863.64844,-4315.45752,4225.49219,-4298.53125,4231.61523,-6350.65186,9869.77148

$$LAYER/4640.0

$$HATCHES/1,6,-6435.28613,9839.15918,-4383.16455,4201.00195,-4366.23828,4207.12451,-6418.35938,9845.28027,-6401.43213,9851.40430,-4349.31104,4213.24707,-4332.38428,4219.37012,-6384.50537,9857.52637,-6367.57861,9863.64844,-4315.45752,4225.49219,-4298.53125,4231.61523,-6350.65186,9869.77148

$$LAYER/4648.0

$$HATCHES/1,6,-6435.28613,9839.15918,-4383.16455,4201.00195,-4366.23828,4207.12451,-6418.35938,9845.28027,-6401.43213,9851.40430,-4349.31104,4213.24707,-4332.38428,4219.37012,-6384.50537,9857.52637,-6367.57861,9863.64844,-4315.45752,4225.49219,-4298.53125,4231.61523,-6350.65186,9869.77148

$$LAYER/4656.0

$$HATCHES/1,6,-6435.28613,9839.15918,-4383.16455,4201.00195,-4366.23828,4207.12451,-6418.35938,9845.28027,-6401.43213,9851.40430,-4349.31104,4213.24707,-4332.38428,4219.37012,-6384.50537,9857.52637,-6367.57861,9863.64844,-4315.45752,4225.49219,-4298.53125,4231.61523,-6350.65186,9869.77148

$$LAYER/4664.0

$$HATCHES/1,6,-6435.28613,9839.15918,-4383.16455,4201.00195,-4366.23828,4207.12451,-6418.35938,9845.28027,-6401.43213,9851.40430,-4349.31104,4213.24707,-4332.38428,4219.37012,-6384.50537,9857.52637,-6367.57861,9863.64844,-4315.45752,4225.49219,-4298.53125,4231.61523,-6350.65186,9869.77148

$$LAYER/4672.0

$$HATCHES/1,6,-6435.28613,9839.15918,-4383.16455,4201.00195,-4366.23828,4207.12451,-6418.35938,9845.28027,-6401.43213,9851.40430,-4349.31104,4213.24707,-4332.38428,4219.37012,-6384.50537,9857.52637,-6367.57861,9863.64844,-4315.45752,4225.49219,-4298.53125,4231.61523,-6350.65186,9869.77148

$$LAYER/4680.0

$$HATCHES/1,6,-6435.28613,9839.15918,-4383.16455,4201.00195,-4366.23828,4207.12451,-6418.35938,9845.28027,-6401.43213,9851.40430,-4349.31104,4213.24707,-4332.38428,4219.37012,-6384.50537,9857.52637,-6367.57861,9863.64844,-4315.45752,4225.49219,-4298.53125,4231.61523,-6350.65186,9869.77148

$$LAYER/4688.0

$$HATCHES/1,6,-6435.28613,9839.15918,-4383.16455,4201.00195,-4366.23828,4207.12451,-6418.35938,9845.28027,-6401.43213,9851.40430,-4349.31104,4213.24707,-4332.38428,4219.37012,-6384.50537,9857.52637,-6367.57861,9863.64844,-4315.45752,4225.49219,-4298.53125,4231.61523,-6350.65186,9869.77148

$$LAYER/4696.0

$$HATCHES/1,6,-6435.28613,9839.15918,-4383.16455,4201.00195,-4366.23828,4207.12451,-6418.35938,9845.28027,-6401.43213,9851.40430,-4349.31104,4213.24707,-4332.38428,4219.37012,-6384.50537,9857.52637,-6367.57861,9863.64844,-4315.45752,4225.49219,-4298.53125,4231.61523,-6350.65186,9869.77148

$$LAYER/4704.0

$$HATCHES/1,6,-6435.28613,9839.15918,-4383.16455,4201.00195,-4366.23828,4207.12451,-6418.35938,9845.28027,-6401.43213,9851.40430,-4349.31104,4213.24707,-4332.38428,4219.37012,-6384.50537,9857.52637,-6367.57861,9863.64844,-4315.45752,4225.49219,-4298.53125,4231.61523,-6350.65186,9869.77148

$$LAYER/4712.0

$$HATCHES/1,6,-6435.28613,9839.15918,-4383.16455,4201.00195,-4366.23828,4207.12451,-6418.35938,9845.28027,-6401.43213,9851.40430,-4349.31104,4213.24707,-4332.38428,4219.37012,-6384.50537,9857.52637,-6367.57861,9863.64844,-4315.45752,4225.49219,-4298.53125,4231.61523,-6350.65186,9869.77148

$$LAYER/4720.0

$$HATCHES/1,6,-6435.28613,9839.15918,-4383.16455,4201.00195,-4366.23828,4207.12451,-6418.35938,9845.28027,-6401.43213,9851.40430,-4349.31104,4213.24707,-4332.38428,4219.37012,-

6384.50537,9857.52637,-6367.57861,9863.64844,-4315.45752,4225.49219,-4298.53125,4231.61523,-6350.65186,9869.77148

$$LAYER/4728.0

$$HATCHES/1,6,-6435.28613,9839.15918,-4383.16455,4201.00195,-4366.23828,4207.12451,-6418.35938,9845.28027,-6401.43213,9851.40430,-4349.31104,4213.24707,-4332.38428,4219.37012,-6384.50537,9857.52637,-6367.57861,9863.64844,-4315.45752,4225.49219,-4298.53125,4231.61523,-6350.65186,9869.77148

$$LAYER/4736.0

$$HATCHES/1,6,-6435.28613,9839.15918,-4383.16455,4201.00195,-4366.23828,4207.12451,-6418.35938,9845.28027,-6401.43213,9851.40430,-4349.31104,4213.24707,-4332.38428,4219.37012,-6384.50537,9857.52637,-6367.57861,9863.64844,-4315.45752,4225.49219,-4298.53125,4231.61523,-6350.65186,9869.77148

$$LAYER/4744.0

$$HATCHES/1,6,-6435.28613,9839.15918,-4383.16455,4201.00195,-4366.23828,4207.12451,-6418.35938,9845.28027,-6401.43213,9851.40430,-4349.31104,4213.24707,-4332.38428,4219.37012,-6384.50537,9857.52637,-6367.57861,9863.64844,-4315.45752,4225.49219,-4298.53125,4231.61523,-6350.65186,9869.77148

$$LAYER/4752.0

$$HATCHES/1,6,-6435.28613,9839.15918,-4383.16455,4201.00195,-4366.23828,4207.12451,-6418.35938,9845.28027,-6401.43213,9851.40430,-4349.31104,4213.24707,-4332.38428,4219.37012,-6384.50537,9857.52637,-6367.57861,9863.64844,-4315.45752,4225.49219,-4298.53125,4231.61523,-6350.65186,9869.77148

$$LAYER/4760.0

$$HATCHES/1,6,-6435.28613,9839.15918,-4383.16455,4201.00195,-4366.23828,4207.12451,-6418.35938,9845.28027,-6401.43213,9851.40430,-4349.31104,4213.24707,-4332.38428,4219.37012,-6384.50537,9857.52637,-6367.57861,9863.64844,-4315.45752,4225.49219,-4298.53125,4231.61523,-6350.65186,9869.77148

$$LAYER/4768.0

$$HATCHES/1,6,-6435.28613,9839.15918,-4383.16455,4201.00195,-4366.23828,4207.12451,-6418.35938,9845.28027,-6401.43213,9851.40430,-4349.31104,4213.24707,-4332.38428,4219.37012,-6384.50537,9857.52637,-6367.57861,9863.64844,-4315.45752,4225.49219,-4298.53125,4231.61523,-6350.65186,9869.77148

$$LAYER/4776.0

$$HATCHES/1,6,-6435.28613,9839.15918,-4383.16455,4201.00195,-4366.23828,4207.12451,-6418.35938,9845.28027,-6401.43213,9851.40430,-4349.31104,4213.24707,-4332.38428,4219.37012,-6384.50537,9857.52637,-6367.57861,9863.64844,-4315.45752,4225.49219,-4298.53125,4231.61523,-6350.65186,9869.77148

$$LAYER/4784.0

$$HATCHES/1,6,-6435.28613,9839.15918,-4383.16455,4201.00195,-4366.23828,4207.12451,-6418.35938,9845.28027,-6401.43213,9851.40430,-4349.31104,4213.24707,-4332.38428,4219.37012,-6384.50537,9857.52637,-6367.57861,9863.64844,-4315.45752,4225.49219,-4298.53125,4231.61523,-6350.65186,9869.77148

$$LAYER/4792.0

$$HATCHES/1,6,-6435.28613,9839.15918,-4383.16455,4201.00195,-4366.23828,4207.12451,-6418.35938,9845.28027,-6401.43213,9851.40430,-4349.31104,4213.24707,-4332.38428,4219.37012,-6384.50537,9857.52637,-6367.57861,9863.64844,-4315.45752,4225.49219,-4298.53125,4231.61523,-6350.65186,9869.77148

$$LAYER/4800.0

$$HATCHES/1,6,-6435.28613,9839.15918,-4383.16455,4201.00195,-4366.23828,4207.12451,-6418.35938,9845.28027,-6401.43213,9851.40430,-4349.31104,4213.24707,-4332.38428,4219.37012,-6384.50537,9857.52637,-6367.57861,9863.64844,-4315.45752,4225.49219,-4298.53125,4231.61523,-6350.65186,9869.77148

$$LAYER/4808.0

$$HATCHES/1,6,-6435.28613,9839.15918,-4383.16455,4201.00195,-4366.23828,4207.12451,-6418.35938,9845.28027,-6401.43213,9851.40430,-4349.31104,4213.24707,-4332.38428,4219.37012,-6384.50537,9857.52637,-6367.57861,9863.64844,-4315.45752,4225.49219,-4298.53125,4231.61523,-6350.65186,9869.77148

$$LAYER/4816.0

$$HATCHES/1,6,-6435.28613,9839.15918,-4383.16455,4201.00195,-4366.23828,4207.12451,-6418.35938,9845.28027,-6401.43213,9851.40430,-4349.31104,4213.24707,-4332.38428,4219.37012,-6384.50537,9857.52637,-6367.57861,9863.64844,-4315.45752,4225.49219,-4298.53125,4231.61523,-6350.65186,9869.77148

$$LAYER/4824.0

$$HATCHES/1,6,-6435.28613,9839.15918,-4383.16455,4201.00195,-4366.23828,4207.12451,-6418.35938,9845.28027,-6401.43213,9851.40430,-4349.31104,4213.24707,-4332.38428,4219.37012,-6384.50537,9857.52637,-6367.57861,9863.64844,-4315.45752,4225.49219,-4298.53125,4231.61523,-6350.65186,9869.77148

$$LAYER/4832.0

$$HATCHES/1,6,-6435.28613,9839.15918,-4383.16455,4201.00195,-4366.23828,4207.12451,-6418.35938,9845.28027,-6401.43213,9851.40430,-4349.31104,4213.24707,-4332.38428,4219.37012,-

6384.50537,9857.52637,-6367.57861,9863.64844,-4315.45752,4225.49219,-4298.53125,4231.61523,-6350.65186,9869.77148

$$LAYER/4840.0

$$HATCHES/1,6,-6435.28613,9839.15918,-4383.16455,4201.00195,-4366.23828,4207.12451,-6418.35938,9845.28027,-6401.43213,9851.40430,-4349.31104,4213.24707,-4332.38428,4219.37012,-6384.50537,9857.52637,-6367.57861,9863.64844,-4315.45752,4225.49219,-4298.53125,4231.61523,-6350.65186,9869.77148

$$LAYER/4848.0

$$HATCHES/1,6,-6435.28613,9839.15918,-4383.16455,4201.00195,-4366.23828,4207.12451,-6418.35938,9845.28027,-6401.43213,9851.40430,-4349.31104,4213.24707,-4332.38428,4219.37012,-6384.50537,9857.52637,-6367.57861,9863.64844,-4315.45752,4225.49219,-4298.53125,4231.61523,-6350.65186,9869.77148

$$LAYER/4856.0

$$HATCHES/1,6,-6435.28613,9839.15918,-4383.16455,4201.00195,-4366.23828,4207.12451,-6418.35938,9845.28027,-6401.43213,9851.40430,-4349.31104,4213.24707,-4332.38428,4219.37012,-6384.50537,9857.52637,-6367.57861,9863.64844,-4315.45752,4225.49219,-4298.53125,4231.61523,-6350.65186,9869.77148

$$LAYER/4864.0

$$HATCHES/1,6,-6435.28613,9839.15918,-4383.16455,4201.00195,-4366.23828,4207.12451,-6418.35938,9845.28027,-6401.43213,9851.40430,-4349.31104,4213.24707,-4332.38428,4219.37012,-6384.50537,9857.52637,-6367.57861,9863.64844,-4315.45752,4225.49219,-4298.53125,4231.61523,-6350.65186,9869.77148

$$LAYER/4872.0

$$HATCHES/1,6,-6435.28613,9839.15918,-4383.16455,4201.00195,-4366.23828,4207.12451,-6418.35938,9845.28027,-6401.43213,9851.40430,-4349.31104,4213.24707,-4332.38428,4219.37012,-6384.50537,9857.52637,-6367.57861,9863.64844,-4315.45752,4225.49219,-4298.53125,4231.61523,-6350.65186,9869.77148

$$LAYER/4880.0

$$HATCHES/1,6,-6435.28613,9839.15918,-4383.16455,4201.00195,-4366.23828,4207.12451,-6418.35938,9845.28027,-6401.43213,9851.40430,-4349.31104,4213.24707,-4332.38428,4219.37012,-6384.50537,9857.52637,-6367.57861,9863.64844,-4315.45752,4225.49219,-4298.53125,4231.61523,-6350.65186,9869.77148

$$LAYER/4888.0

$$HATCHES/1,6,-6435.28613,9839.15918,-4383.16455,4201.00195,-4366.23828,4207.12451,-6418.35938,9845.28027,-6401.43213,9851.40430,-4349.31104,4213.24707,-4332.38428,4219.37012,-6384.50537,9857.52637,-6367.57861,9863.64844,-4315.45752,4225.49219,-4298.53125,4231.61523,-6350.65186,9869.77148

$$LAYER/4896.0

$$HATCHES/1,6,-6435.28613,9839.15918,-4383.16455,4201.00195,-4366.23828,4207.12451,-6418.35938,9845.28027,-6401.43213,9851.40430,-4349.31104,4213.24707,-4332.38428,4219.37012,-6384.50537,9857.52637,-6367.57861,9863.64844,-4315.45752,4225.49219,-4298.53125,4231.61523,-6350.65186,9869.77148

$$LAYER/4904.0

$$HATCHES/1,6,-6435.28613,9839.15918,-4383.16455,4201.00195,-4366.23828,4207.12451,-6418.35938,9845.28027,-6401.43213,9851.40430,-4349.31104,4213.24707,-4332.38428,4219.37012,-6384.50537,9857.52637,-6367.57861,9863.64844,-4315.45752,4225.49219,-4298.53125,4231.61523,-6350.65186,9869.77148

$$LAYER/4912.0

$$HATCHES/1,6,-6435.28613,9839.15918,-4383.16455,4201.00195,-4366.23828,4207.12451,-6418.35938,9845.28027,-6401.43213,9851.40430,-4349.31104,4213.24707,-4332.38428,4219.37012,-6384.50537,9857.52637,-6367.57861,9863.64844,-4315.45752,4225.49219,-4298.53125,4231.61523,-6350.65186,9869.77148

$$LAYER/4920.0

$$HATCHES/1,6,-6435.28613,9839.15918,-4383.16455,4201.00195,-4366.23828,4207.12451,-6418.35938,9845.28027,-6401.43213,9851.40430,-4349.31104,4213.24707,-4332.38428,4219.37012,-6384.50537,9857.52637,-6367.57861,9863.64844,-4315.45752,4225.49219,-4298.53125,4231.61523,-6350.65186,9869.77148

$$LAYER/4928.0

$$HATCHES/1,6,-6435.28613,9839.15918,-4383.16455,4201.00195,-4366.23828,4207.12451,-6418.35938,9845.28027,-6401.43213,9851.40430,-4349.31104,4213.24707,-4332.38428,4219.37012,-6384.50537,9857.52637,-6367.57861,9863.64844,-4315.45752,4225.49219,-4298.53125,4231.61523,-6350.65186,9869.77148

$$LAYER/4936.0

$$HATCHES/1,6,-6435.28613,9839.15918,-4383.16455,4201.00195,-4366.23828,4207.12451,-6418.35938,9845.28027,-6401.43213,9851.40430,-4349.31104,4213.24707,-4332.38428,4219.37012,-6384.50537,9857.52637,-6367.57861,9863.64844,-4315.45752,4225.49219,-4298.53125,4231.61523,-6350.65186,9869.77148

$$LAYER/4944.0

$$HATCHES/1,6,-6435.28613,9839.15918,-4383.16455,4201.00195,-4366.23828,4207.12451,-6418.35938,9845.28027,-6401.43213,9851.40430,-4349.31104,4213.24707,-4332.38428,4219.37012,-

6384.50537,9857.52637,-6367.57861,9863.64844,-4315.45752,4225.49219,-4298.53125,4231.61523,-6350.65186,9869.77148

$$LAYER/4952.0

$$HATCHES/1,6,-6435.28613,9839.15918,-4383.16455,4201.00195,-4366.23828,4207.12451,-6418.35938,9845.28027,-6401.43213,9851.40430,-4349.31104,4213.24707,-4332.38428,4219.37012,-6384.50537,9857.52637,-6367.57861,9863.64844,-4315.45752,4225.49219,-4298.53125,4231.61523,-6350.65186,9869.77148

$$LAYER/4960.0

$$HATCHES/1,6,-6435.28613,9839.15918,-4383.16455,4201.00195,-4366.23828,4207.12451,-6418.35938,9845.28027,-6401.43213,9851.40430,-4349.31104,4213.24707,-4332.38428,4219.37012,-6384.50537,9857.52637,-6367.57861,9863.64844,-4315.45752,4225.49219,-4298.53125,4231.61523,-6350.65186,9869.77148

$$LAYER/4968.0

$$HATCHES/1,6,-6435.28613,9839.15918,-4383.16455,4201.00195,-4366.23828,4207.12451,-6418.35938,9845.28027,-6401.43213,9851.40430,-4349.31104,4213.24707,-4332.38428,4219.37012,-6384.50537,9857.52637,-6367.57861,9863.64844,-4315.45752,4225.49219,-4298.53125,4231.61523,-6350.65186,9869.77148

$$LAYER/4976.0

$$HATCHES/1,6,-6435.28613,9839.15918,-4383.16455,4201.00195,-4366.23828,4207.12451,-6418.35938,9845.28027,-6401.43213,9851.40430,-4349.31104,4213.24707,-4332.38428,4219.37012,-6384.50537,9857.52637,-6367.57861,9863.64844,-4315.45752,4225.49219,-4298.53125,4231.61523,-6350.65186,9869.77148

$$LAYER/4984.0

$$HATCHES/1,6,-6435.28613,9839.15918,-4383.16455,4201.00195,-4366.23828,4207.12451,-6418.35938,9845.28027,-6401.43213,9851.40430,-4349.31104,4213.24707,-4332.38428,4219.37012,-6384.50537,9857.52637,-6367.57861,9863.64844,-4315.45752,4225.49219,-4298.53125,4231.61523,-6350.65186,9869.77148

$$LAYER/4992.0

$$HATCHES/1,6,-6435.28613,9839.15918,-4383.16455,4201.00195,-4366.23828,4207.12451,-6418.35938,9845.28027,-6401.43213,9851.40430,-4349.31104,4213.24707,-4332.38428,4219.37012,-6384.50537,9857.52637,-6367.57861,9863.64844,-4315.45752,4225.49219,-4298.53125,4231.61523,-6350.65186,9869.77148

$$LAYER/5000.0

$$HATCHES/1,6,-6435.28613,9839.15918,-4383.16455,4201.00195,-4366.23828,4207.12451,-6418.35938,9845.28027,-6401.43213,9851.40430,-4349.31104,4213.24707,-4332.38428,4219.37012,-6384.50537,9857.52637,-6367.57861,9863.64844,-4315.45752,4225.49219,-4298.53125,4231.61523,-6350.65186,9869.77148

$$LAYER/5008.0

$$HATCHES/1,6,-6435.28613,9839.15918,-4383.16455,4201.00195,-4366.23828,4207.12451,-6418.35938,9845.28027,-6401.43213,9851.40430,-4349.31104,4213.24707,-4332.38428,4219.37012,-6384.50537,9857.52637,-6367.57861,9863.64844,-4315.45752,4225.49219,-4298.53125,4231.61523,-6350.65186,9869.77148

$$LAYER/5016.0

$$HATCHES/1,6,-6435.28613,9839.15918,-4383.16455,4201.00195,-4366.23828,4207.12451,-6418.35938,9845.28027,-6401.43213,9851.40430,-4349.31104,4213.24707,-4332.38428,4219.37012,-6384.50537,9857.52637,-6367.57861,9863.64844,-4315.45752,4225.49219,-4298.53125,4231.61523,-6350.65186,9869.77148

$$LAYER/5024.0

$$HATCHES/1,6,-6435.28613,9839.15918,-4383.16455,4201.00195,-4366.23828,4207.12451,-6418.35938,9845.28027,-6401.43213,9851.40430,-4349.31104,4213.24707,-4332.38428,4219.37012,-6384.50537,9857.52637,-6367.57861,9863.64844,-4315.45752,4225.49219,-4298.53125,4231.61523,-6350.65186,9869.77148

$$LAYER/5032.0

$$HATCHES/1,6,-6435.28613,9839.15918,-4383.16455,4201.00195,-4366.23828,4207.12451,-6418.35938,9845.28027,-6401.43213,9851.40430,-4349.31104,4213.24707,-4332.38428,4219.37012,-6384.50537,9857.52637,-6367.57861,9863.64844,-4315.45752,4225.49219,-4298.53125,4231.61523,-6350.65186,9869.77148

$$LAYER/5040.0

$$HATCHES/1,6,-6435.28613,9839.15918,-4383.16455,4201.00195,-4366.23828,4207.12451,-6418.35938,9845.28027,-6401.43213,9851.40430,-4349.31104,4213.24707,-4332.38428,4219.37012,-6384.50537,9857.52637,-6367.57861,9863.64844,-4315.45752,4225.49219,-4298.53125,4231.61523,-6350.65186,9869.77148

$$LAYER/5048.0

$$HATCHES/1,6,-6435.28613,9839.15918,-4383.16455,4201.00195,-4366.23828,4207.12451,-6418.35938,9845.28027,-6401.43213,9851.40430,-4349.31104,4213.24707,-4332.38428,4219.37012,-6384.50537,9857.52637,-6367.57861,9863.64844,-4315.45752,4225.49219,-4298.53125,4231.61523,-6350.65186,9869.77148

$$LAYER/5056.0

$$HATCHES/1,6,-6435.28613,9839.15918,-4383.16455,4201.00195,-4366.23828,4207.12451,-6418.35938,9845.28027,-6401.43213,9851.40430,-4349.31104,4213.24707,-4332.38428,4219.37012,-

6384.50537,9857.52637,-6367.57861,9863.64844,-4315.45752,4225.49219,-4298.53125,4231.61523,-6350.65186,9869.77148

$$LAYER/5064.0

$$HATCHES/1,6,-6435.28613,9839.15918,-4383.16455,4201.00195,-4366.23828,4207.12451,-6418.35938,9845.28027,-6401.43213,9851.40430,-4349.31104,4213.24707,-4332.38428,4219.37012,-6384.50537,9857.52637,-6367.57861,9863.64844,-4315.45752,4225.49219,-4298.53125,4231.61523,-6350.65186,9869.77148

$$LAYER/5072.0

$$HATCHES/1,6,-6435.28613,9839.15918,-4383.16455,4201.00195,-4366.23828,4207.12451,-6418.35938,9845.28027,-6401.43213,9851.40430,-4349.31104,4213.24707,-4332.38428,4219.37012,-6384.50537,9857.52637,-6367.57861,9863.64844,-4315.45752,4225.49219,-4298.53125,4231.61523,-6350.65186,9869.77148

$$LAYER/5080.0

$$HATCHES/1,6,-6435.28613,9839.15918,-4383.16455,4201.00195,-4366.23828,4207.12451,-6418.35938,9845.28027,-6401.43213,9851.40430,-4349.31104,4213.24707,-4332.38428,4219.37012,-6384.50537,9857.52637,-6367.57861,9863.64844,-4315.45752,4225.49219,-4298.53125,4231.61523,-6350.65186,9869.77148

$$LAYER/5088.0

$$HATCHES/1,6,-6435.28613,9839.15918,-4383.16455,4201.00195,-4366.23828,4207.12451,-6418.35938,9845.28027,-6401.43213,9851.40430,-4349.31104,4213.24707,-4332.38428,4219.37012,-6384.50537,9857.52637,-6367.57861,9863.64844,-4315.45752,4225.49219,-4298.53125,4231.61523,-6350.65186,9869.77148

$$LAYER/5096.0

$$HATCHES/1,6,-6435.28613,9839.15918,-4383.16455,4201.00195,-4366.23828,4207.12451,-6418.35938,9845.28027,-6401.43213,9851.40430,-4349.31104,4213.24707,-4332.38428,4219.37012,-6384.50537,9857.52637,-6367.57861,9863.64844,-4315.45752,4225.49219,-4298.53125,4231.61523,-6350.65186,9869.77148

$$LAYER/5104.0

$$HATCHES/1,6,-6435.28613,9839.15918,-4383.16455,4201.00195,-4366.23828,4207.12451,-6418.35938,9845.28027,-6401.43213,9851.40430,-4349.31104,4213.24707,-4332.38428,4219.37012,-6384.50537,9857.52637,-6367.57861,9863.64844,-4315.45752,4225.49219,-4298.53125,4231.61523,-6350.65186,9869.77148

$$LAYER/5112.0

$$HATCHES/1,6,-6435.28613,9839.15918,-4383.16455,4201.00195,-4366.23828,4207.12451,-6418.35938,9845.28027,-6401.43213,9851.40430,-4349.31104,4213.24707,-4332.38428,4219.37012,-6384.50537,9857.52637,-6367.57861,9863.64844,-4315.45752,4225.49219,-4298.53125,4231.61523,-6350.65186,9869.77148

$$LAYER/5120.0

$$HATCHES/1,6,-6435.28613,9839.15918,-4383.16455,4201.00195,-4366.23828,4207.12451,-6418.35938,9845.28027,-6401.43213,9851.40430,-4349.31104,4213.24707,-4332.38428,4219.37012,-6384.50537,9857.52637,-6367.57861,9863.64844,-4315.45752,4225.49219,-4298.53125,4231.61523,-6350.65186,9869.77148

$$LAYER/5128.0

$$HATCHES/1,6,-6435.28613,9839.15918,-4383.16455,4201.00195,-4366.23828,4207.12451,-6418.35938,9845.28027,-6401.43213,9851.40430,-4349.31104,4213.24707,-4332.38428,4219.37012,-6384.50537,9857.52637,-6367.57861,9863.64844,-4315.45752,4225.49219,-4298.53125,4231.61523,-6350.65186,9869.77148

$$LAYER/5136.0

$$HATCHES/1,6,-6435.28613,9839.15918,-4383.16455,4201.00195,-4366.23828,4207.12451,-6418.35938,9845.28027,-6401.43213,9851.40430,-4349.31104,4213.24707,-4332.38428,4219.37012,-6384.50537,9857.52637,-6367.57861,9863.64844,-4315.45752,4225.49219,-4298.53125,4231.61523,-6350.65186,9869.77148

$$LAYER/5144.0

$$HATCHES/1,6,-6435.28613,9839.15918,-4383.16455,4201.00195,-4366.23828,4207.12451,-6418.35938,9845.28027,-6401.43213,9851.40430,-4349.31104,4213.24707,-4332.38428,4219.37012,-6384.50537,9857.52637,-6367.57861,9863.64844,-4315.45752,4225.49219,-4298.53125,4231.61523,-6350.65186,9869.77148

$$LAYER/5152.0

$$HATCHES/1,6,-6435.28613,9839.15918,-4383.16455,4201.00195,-4366.23828,4207.12451,-6418.35938,9845.28027,-6401.43213,9851.40430,-4349.31104,4213.24707,-4332.38428,4219.37012,-6384.50537,9857.52637,-6367.57861,9863.64844,-4315.45752,4225.49219,-4298.53125,4231.61523,-6350.65186,9869.77148

$$LAYER/5160.0

$$HATCHES/1,6,-6435.28613,9839.15918,-4383.16455,4201.00195,-4366.23828,4207.12451,-6418.35938,9845.28027,-6401.43213,9851.40430,-4349.31104,4213.24707,-4332.38428,4219.37012,-6384.50537,9857.52637,-6367.57861,9863.64844,-4315.45752,4225.49219,-4298.53125,4231.61523,-6350.65186,9869.77148

$$LAYER/5168.0

$$HATCHES/1,6,-6435.28613,9839.15918,-4383.16455,4201.00195,-4366.23828,4207.12451,-6418.35938,9845.28027,-6401.43213,9851.40430,-4349.31104,4213.24707,-4332.38428,4219.37012,-

6384.50537,9857.52637,-6367.57861,9863.64844,-4315.45752,4225.49219,-4298.53125,4231.61523,-6350.65186,9869.77148

$$LAYER/5176.0

$$HATCHES/1,6,-6435.28613,9839.15918,-4383.16455,4201.00195,-4366.23828,4207.12451,-6418.35938,9845.28027,-6401.43213,9851.40430,-4349.31104,4213.24707,-4332.38428,4219.37012,-6384.50537,9857.52637,-6367.57861,9863.64844,-4315.45752,4225.49219,-4298.53125,4231.61523,-6350.65186,9869.77148

$$LAYER/5184.0

$$HATCHES/1,6,-6435.28613,9839.15918,-4383.16455,4201.00195,-4366.23828,4207.12451,-6418.35938,9845.28027,-6401.43213,9851.40430,-4349.31104,4213.24707,-4332.38428,4219.37012,-6384.50537,9857.52637,-6367.57861,9863.64844,-4315.45752,4225.49219,-4298.53125,4231.61523,-6350.65186,9869.77148

$$LAYER/5192.0

$$HATCHES/1,6,-6435.28613,9839.15918,-4383.16455,4201.00195,-4366.23828,4207.12451,-6418.35938,9845.28027,-6401.43213,9851.40430,-4349.31104,4213.24707,-4332.38428,4219.37012,-6384.50537,9857.52637,-6367.57861,9863.64844,-4315.45752,4225.49219,-4298.53125,4231.61523,-6350.65186,9869.77148

$$LAYER/5200.0

$$HATCHES/1,6,-6435.28613,9839.15918,-4383.16455,4201.00195,-4366.23828,4207.12451,-6418.35938,9845.28027,-6401.43213,9851.40430,-4349.31104,4213.24707,-4332.38428,4219.37012,-6384.50537,9857.52637,-6367.57861,9863.64844,-4315.45752,4225.49219,-4298.53125,4231.61523,-6350.65186,9869.77148

$$LAYER/5208.0

$$HATCHES/1,6,-6435.28613,9839.15918,-4383.16455,4201.00195,-4366.23828,4207.12451,-6418.35938,9845.28027,-6401.43213,9851.40430,-4349.31104,4213.24707,-4332.38428,4219.37012,-6384.50537,9857.52637,-6367.57861,9863.64844,-4315.45752,4225.49219,-4298.53125,4231.61523,-6350.65186,9869.77148

$$LAYER/5216.0

$$HATCHES/1,6,-6435.28613,9839.15918,-4383.16455,4201.00195,-4366.23828,4207.12451,-6418.35938,9845.28027,-6401.43213,9851.40430,-4349.31104,4213.24707,-4332.38428,4219.37012,-6384.50537,9857.52637,-6367.57861,9863.64844,-4315.45752,4225.49219,-4298.53125,4231.61523,-6350.65186,9869.77148

$$LAYER/5224.0

$$HATCHES/1,6,-6435.28613,9839.15918,-4383.16455,4201.00195,-4366.23828,4207.12451,-6418.35938,9845.28027,-6401.43213,9851.40430,-4349.31104,4213.24707,-4332.38428,4219.37012,-6384.50537,9857.52637,-6367.57861,9863.64844,-4315.45752,4225.49219,-4298.53125,4231.61523,-6350.65186,9869.77148

$$LAYER/5232.0

$$HATCHES/1,6,-6435.28613,9839.15918,-4383.16455,4201.00195,-4366.23828,4207.12451,-6418.35938,9845.28027,-6401.43213,9851.40430,-4349.31104,4213.24707,-4332.38428,4219.37012,-6384.50537,9857.52637,-6367.57861,9863.64844,-4315.45752,4225.49219,-4298.53125,4231.61523,-6350.65186,9869.77148

$$LAYER/5240.0

$$HATCHES/1,6,-6435.28613,9839.15918,-4383.16455,4201.00195,-4366.23828,4207.12451,-6418.35938,9845.28027,-6401.43213,9851.40430,-4349.31104,4213.24707,-4332.38428,4219.37012,-6384.50537,9857.52637,-6367.57861,9863.64844,-4315.45752,4225.49219,-4298.53125,4231.61523,-6350.65186,9869.77148

$$LAYER/5248.0

$$HATCHES/1,6,-6435.28613,9839.15918,-4383.16455,4201.00195,-4366.23828,4207.12451,-6418.35938,9845.28027,-6401.43213,9851.40430,-4349.31104,4213.24707,-4332.38428,4219.37012,-6384.50537,9857.52637,-6367.57861,9863.64844,-4315.45752,4225.49219,-4298.53125,4231.61523,-6350.65186,9869.77148

$$LAYER/5256.0

$$HATCHES/1,6,-6435.28613,9839.15918,-4383.16455,4201.00195,-4366.23828,4207.12451,-6418.35938,9845.28027,-6401.43213,9851.40430,-4349.31104,4213.24707,-4332.38428,4219.37012,-6384.50537,9857.52637,-6367.57861,9863.64844,-4315.45752,4225.49219,-4298.53125,4231.61523,-6350.65186,9869.77148

$$LAYER/5264.0

$$HATCHES/1,6,-6435.28613,9839.15918,-4383.16455,4201.00195,-4366.23828,4207.12451,-6418.35938,9845.28027,-6401.43213,9851.40430,-4349.31104,4213.24707,-4332.38428,4219.37012,-6384.50537,9857.52637,-6367.57861,9863.64844,-4315.45752,4225.49219,-4298.53125,4231.61523,-6350.65186,9869.77148

$$LAYER/5272.0

$$HATCHES/1,6,-6435.28613,9839.15918,-4383.16455,4201.00195,-4366.23828,4207.12451,-6418.35938,9845.28027,-6401.43213,9851.40430,-4349.31104,4213.24707,-4332.38428,4219.37012,-6384.50537,9857.52637,-6367.57861,9863.64844,-4315.45752,4225.49219,-4298.53125,4231.61523,-6350.65186,9869.77148

$$LAYER/5280.0

$$HATCHES/1,6,-6435.28613,9839.15918,-4383.16455,4201.00195,-4366.23828,4207.12451,-6418.35938,9845.28027,-6401.43213,9851.40430,-4349.31104,4213.24707,-4332.38428,4219.37012,-

6384.50537,9857.52637,-6367.57861,9863.64844,-4315.45752,4225.49219,-4298.53125,4231.61523,-6350.65186,9869.77148

$$LAYER/5288.0

$$HATCHES/1,6,-6435.28613,9839.15918,-4383.16455,4201.00195,-4366.23828,4207.12451,-6418.35938,9845.28027,-6401.43213,9851.40430,-4349.31104,4213.24707,-4332.38428,4219.37012,-6384.50537,9857.52637,-6367.57861,9863.64844,-4315.45752,4225.49219,-4298.53125,4231.61523,-6350.65186,9869.77148

$$LAYER/5296.0

$$HATCHES/1,6,-6435.28613,9839.15918,-4383.16455,4201.00195,-4366.23828,4207.12451,-6418.35938,9845.28027,-6401.43213,9851.40430,-4349.31104,4213.24707,-4332.38428,4219.37012,-6384.50537,9857.52637,-6367.57861,9863.64844,-4315.45752,4225.49219,-4298.53125,4231.61523,-6350.65186,9869.77148

$$LAYER/5304.0

$$HATCHES/1,6,-6435.28613,9839.15918,-4383.16455,4201.00195,-4366.23828,4207.12451,-6418.35938,9845.28027,-6401.43213,9851.40430,-4349.31104,4213.24707,-4332.38428,4219.37012,-6384.50537,9857.52637,-6367.57861,9863.64844,-4315.45752,4225.49219,-4298.53125,4231.61523,-6350.65186,9869.77148

$$LAYER/5312.0

$$HATCHES/1,6,-6435.28613,9839.15918,-4383.16455,4201.00195,-4366.23828,4207.12451,-6418.35938,9845.28027,-6401.43213,9851.40430,-4349.31104,4213.24707,-4332.38428,4219.37012,-6384.50537,9857.52637,-6367.57861,9863.64844,-4315.45752,4225.49219,-4298.53125,4231.61523,-6350.65186,9869.77148

$$LAYER/5320.0

$$HATCHES/1,6,-6435.28613,9839.15918,-4383.16455,4201.00195,-4366.23828,4207.12451,-6418.35938,9845.28027,-6401.43213,9851.40430,-4349.31104,4213.24707,-4332.38428,4219.37012,-6384.50537,9857.52637,-6367.57861,9863.64844,-4315.45752,4225.49219,-4298.53125,4231.61523,-6350.65186,9869.77148

$$LAYER/5328.0

$$HATCHES/1,6,-6435.28613,9839.15918,-4383.16455,4201.00195,-4366.23828,4207.12451,-6418.35938,9845.28027,-6401.43213,9851.40430,-4349.31104,4213.24707,-4332.38428,4219.37012,-6384.50537,9857.52637,-6367.57861,9863.64844,-4315.45752,4225.49219,-4298.53125,4231.61523,-6350.65186,9869.77148

$$LAYER/5336.0

$$HATCHES/1,6,-6435.28613,9839.15918,-4383.16455,4201.00195,-4366.23828,4207.12451,-6418.35938,9845.28027,-6401.43213,9851.40430,-4349.31104,4213.24707,-4332.38428,4219.37012,-6384.50537,9857.52637,-6367.57861,9863.64844,-4315.45752,4225.49219,-4298.53125,4231.61523,-6350.65186,9869.77148

$$LAYER/5344.0

$$HATCHES/1,6,-6435.28613,9839.15918,-4383.16455,4201.00195,-4366.23828,4207.12451,-6418.35938,9845.28027,-6401.43213,9851.40430,-4349.31104,4213.24707,-4332.38428,4219.37012,-6384.50537,9857.52637,-6367.57861,9863.64844,-4315.45752,4225.49219,-4298.53125,4231.61523,-6350.65186,9869.77148

$$LAYER/5352.0

$$HATCHES/1,6,-6435.28613,9839.15918,-4383.16455,4201.00195,-4366.23828,4207.12451,-6418.35938,9845.28027,-6401.43213,9851.40430,-4349.31104,4213.24707,-4332.38428,4219.37012,-6384.50537,9857.52637,-6367.57861,9863.64844,-4315.45752,4225.49219,-4298.53125,4231.61523,-6350.65186,9869.77148

$$LAYER/5360.0

$$HATCHES/1,6,-6435.28613,9839.15918,-4383.16455,4201.00195,-4366.23828,4207.12451,-6418.35938,9845.28027,-6401.43213,9851.40430,-4349.31104,4213.24707,-4332.38428,4219.37012,-6384.50537,9857.52637,-6367.57861,9863.64844,-4315.45752,4225.49219,-4298.53125,4231.61523,-6350.65186,9869.77148

$$LAYER/5368.0

$$HATCHES/1,6,-6435.28613,9839.15918,-4383.16455,4201.00195,-4366.23828,4207.12451,-6418.35938,9845.28027,-6401.43213,9851.40430,-4349.31104,4213.24707,-4332.38428,4219.37012,-6384.50537,9857.52637,-6367.57861,9863.64844,-4315.45752,4225.49219,-4298.53125,4231.61523,-6350.65186,9869.77148

$$LAYER/5376.0

$$HATCHES/1,6,-6435.28613,9839.15918,-4383.16455,4201.00195,-4366.23828,4207.12451,-6418.35938,9845.28027,-6401.43213,9851.40430,-4349.31104,4213.24707,-4332.38428,4219.37012,-6384.50537,9857.52637,-6367.57861,9863.64844,-4315.45752,4225.49219,-4298.53125,4231.61523,-6350.65186,9869.77148

$$LAYER/5384.0

$$HATCHES/1,6,-6435.28613,9839.15918,-4383.16455,4201.00195,-4366.23828,4207.12451,-6418.35938,9845.28027,-6401.43213,9851.40430,-4349.31104,4213.24707,-4332.38428,4219.37012,-6384.50537,9857.52637,-6367.57861,9863.64844,-4315.45752,4225.49219,-4298.53125,4231.61523,-6350.65186,9869.77148

$$LAYER/5392.0

$$HATCHES/1,6,-6435.28613,9839.15918,-4383.16455,4201.00195,-4366.23828,4207.12451,-6418.35938,9845.28027,-6401.43213,9851.40430,-4349.31104,4213.24707,-4332.38428,4219.37012,-

6384.50537,9857.52637,-6367.57861,9863.64844,-4315.45752,4225.49219,-4298.53125,4231.61523,-6350.65186,9869.77148

$$LAYER/5400.0

$$HATCHES/1,6,-6435.28613,9839.15918,-4383.16455,4201.00195,-4366.23828,4207.12451,-6418.35938,9845.28027,-6401.43213,9851.40430,-4349.31104,4213.24707,-4332.38428,4219.37012,-6384.50537,9857.52637,-6367.57861,9863.64844,-4315.45752,4225.49219,-4298.53125,4231.61523,-6350.65186,9869.77148

$$LAYER/5408.0

$$HATCHES/1,6,-6435.28613,9839.15918,-4383.16455,4201.00195,-4366.23828,4207.12451,-6418.35938,9845.28027,-6401.43213,9851.40430,-4349.31104,4213.24707,-4332.38428,4219.37012,-6384.50537,9857.52637,-6367.57861,9863.64844,-4315.45752,4225.49219,-4298.53125,4231.61523,-6350.65186,9869.77148

$$LAYER/5416.0

$$HATCHES/1,6,-6435.28613,9839.15918,-4383.16455,4201.00195,-4366.23828,4207.12451,-6418.35938,9845.28027,-6401.43213,9851.40430,-4349.31104,4213.24707,-4332.38428,4219.37012,-6384.50537,9857.52637,-6367.57861,9863.64844,-4315.45752,4225.49219,-4298.53125,4231.61523,-6350.65186,9869.77148

$$LAYER/5424.0

$$HATCHES/1,6,-6435.28613,9839.15918,-4383.16455,4201.00195,-4366.23828,4207.12451,-6418.35938,9845.28027,-6401.43213,9851.40430,-4349.31104,4213.24707,-4332.38428,4219.37012,-6384.50537,9857.52637,-6367.57861,9863.64844,-4315.45752,4225.49219,-4298.53125,4231.61523,-6350.65186,9869.77148

$$LAYER/5432.0

$$HATCHES/1,6,-6435.28613,9839.15918,-4383.16455,4201.00195,-4366.23828,4207.12451,-6418.35938,9845.28027,-6401.43213,9851.40430,-4349.31104,4213.24707,-4332.38428,4219.37012,-6384.50537,9857.52637,-6367.57861,9863.64844,-4315.45752,4225.49219,-4298.53125,4231.61523,-6350.65186,9869.77148

$$LAYER/5440.0

$$HATCHES/1,6,-6435.28613,9839.15918,-4383.16455,4201.00195,-4366.23828,4207.12451,-6418.35938,9845.28027,-6401.43213,9851.40430,-4349.31104,4213.24707,-4332.38428,4219.37012,-6384.50537,9857.52637,-6367.57861,9863.64844,-4315.45752,4225.49219,-4298.53125,4231.61523,-6350.65186,9869.77148

$$LAYER/5448.0

$$HATCHES/1,6,-6435.28613,9839.15918,-4383.16455,4201.00195,-4366.23828,4207.12451,-6418.35938,9845.28027,-6401.43213,9851.40430,-4349.31104,4213.24707,-4332.38428,4219.37012,-6384.50537,9857.52637,-6367.57861,9863.64844,-4315.45752,4225.49219,-4298.53125,4231.61523,-6350.65186,9869.77148

$$LAYER/5456.0

$$HATCHES/1,6,-6435.28613,9839.15918,-4383.16455,4201.00195,-4366.23828,4207.12451,-6418.35938,9845.28027,-6401.43213,9851.40430,-4349.31104,4213.24707,-4332.38428,4219.37012,-6384.50537,9857.52637,-6367.57861,9863.64844,-4315.45752,4225.49219,-4298.53125,4231.61523,-6350.65186,9869.77148

$$LAYER/5464.0

$$HATCHES/1,6,-6435.28613,9839.15918,-4383.16455,4201.00195,-4366.23828,4207.12451,-6418.35938,9845.28027,-6401.43213,9851.40430,-4349.31104,4213.24707,-4332.38428,4219.37012,-6384.50537,9857.52637,-6367.57861,9863.64844,-4315.45752,4225.49219,-4298.53125,4231.61523,-6350.65186,9869.77148

$$LAYER/5472.0

$$HATCHES/1,6,-6435.28613,9839.15918,-4383.16455,4201.00195,-4366.23828,4207.12451,-6418.35938,9845.28027,-6401.43213,9851.40430,-4349.31104,4213.24707,-4332.38428,4219.37012,-6384.50537,9857.52637,-6367.57861,9863.64844,-4315.45752,4225.49219,-4298.53125,4231.61523,-6350.65186,9869.77148

$$LAYER/5480.0

$$HATCHES/1,6,-6435.28613,9839.15918,-4383.16455,4201.00195,-4366.23828,4207.12451,-6418.35938,9845.28027,-6401.43213,9851.40430,-4349.31104,4213.24707,-4332.38428,4219.37012,-6384.50537,9857.52637,-6367.57861,9863.64844,-4315.45752,4225.49219,-4298.53125,4231.61523,-6350.65186,9869.77148

$$LAYER/5488.0

$$HATCHES/1,6,-6435.28613,9839.15918,-4383.16455,4201.00195,-4366.23828,4207.12451,-6418.35938,9845.28027,-6401.43213,9851.40430,-4349.31104,4213.24707,-4332.38428,4219.37012,-6384.50537,9857.52637,-6367.57861,9863.64844,-4315.45752,4225.49219,-4298.53125,4231.61523,-6350.65186,9869.77148

$$LAYER/5496.0

$$HATCHES/1,6,-6435.28613,9839.15918,-4383.16455,4201.00195,-4366.23828,4207.12451,-6418.35938,9845.28027,-6401.43213,9851.40430,-4349.31104,4213.24707,-4332.38428,4219.37012,-6384.50537,9857.52637,-6367.57861,9863.64844,-4315.45752,4225.49219,-4298.53125,4231.61523,-6350.65186,9869.77148

$$LAYER/5504.0

$$HATCHES/1,6,-6435.28613,9839.15918,-4383.16455,4201.00195,-4366.23828,4207.12451,-6418.35938,9845.28027,-6401.43213,9851.40430,-4349.31104,4213.24707,-4332.38428,4219.37012,-

6384.50537,9857.52637,-6367.57861,9863.64844,-4315.45752,4225.49219,-4298.53125,4231.61523,-6350.65186,9869.77148

$$LAYER/5512.0

$$HATCHES/1,6,-6435.28613,9839.15918,-4383.16455,4201.00195,-4366.23828,4207.12451,-6418.35938,9845.28027,-6401.43213,9851.40430,-4349.31104,4213.24707,-4332.38428,4219.37012,-6384.50537,9857.52637,-6367.57861,9863.64844,-4315.45752,4225.49219,-4298.53125,4231.61523,-6350.65186,9869.77148

$$LAYER/5520.0

$$HATCHES/1,6,-6435.28613,9839.15918,-4383.16455,4201.00195,-4366.23828,4207.12451,-6418.35938,9845.28027,-6401.43213,9851.40430,-4349.31104,4213.24707,-4332.38428,4219.37012,-6384.50537,9857.52637,-6367.57861,9863.64844,-4315.45752,4225.49219,-4298.53125,4231.61523,-6350.65186,9869.77148

$$LAYER/5528.0

$$HATCHES/1,6,-6435.28613,9839.15918,-4383.16455,4201.00195,-4366.23828,4207.12451,-6418.35938,9845.28027,-6401.43213,9851.40430,-4349.31104,4213.24707,-4332.38428,4219.37012,-6384.50537,9857.52637,-6367.57861,9863.64844,-4315.45752,4225.49219,-4298.53125,4231.61523,-6350.65186,9869.77148

$$LAYER/5536.0

$$HATCHES/1,6,-6435.28613,9839.15918,-4383.16455,4201.00195,-4366.23828,4207.12451,-6418.35938,9845.28027,-6401.43213,9851.40430,-4349.31104,4213.24707,-4332.38428,4219.37012,-6384.50537,9857.52637,-6367.57861,9863.64844,-4315.45752,4225.49219,-4298.53125,4231.61523,-6350.65186,9869.77148

$$LAYER/5544.0

$$HATCHES/1,6,-6435.28613,9839.15918,-4383.16455,4201.00195,-4366.23828,4207.12451,-6418.35938,9845.28027,-6401.43213,9851.40430,-4349.31104,4213.24707,-4332.38428,4219.37012,-6384.50537,9857.52637,-6367.57861,9863.64844,-4315.45752,4225.49219,-4298.53125,4231.61523,-6350.65186,9869.77148

$$LAYER/5552.0

$$HATCHES/1,6,-6435.28613,9839.15918,-4383.16455,4201.00195,-4366.23828,4207.12451,-6418.35938,9845.28027,-6401.43213,9851.40430,-4349.31104,4213.24707,-4332.38428,4219.37012,-6384.50537,9857.52637,-6367.57861,9863.64844,-4315.45752,4225.49219,-4298.53125,4231.61523,-6350.65186,9869.77148

$$LAYER/5560.0

$$HATCHES/1,6,-6435.28613,9839.15918,-4383.16455,4201.00195,-4366.23828,4207.12451,-6418.35938,9845.28027,-6401.43213,9851.40430,-4349.31104,4213.24707,-4332.38428,4219.37012,-6384.50537,9857.52637,-6367.57861,9863.64844,-4315.45752,4225.49219,-4298.53125,4231.61523,-6350.65186,9869.77148

$$LAYER/5568.0

$$HATCHES/1,6,-6435.28613,9839.15918,-4383.16455,4201.00195,-4366.23828,4207.12451,-6418.35938,9845.28027,-6401.43213,9851.40430,-4349.31104,4213.24707,-4332.38428,4219.37012,-6384.50537,9857.52637,-6367.57861,9863.64844,-4315.45752,4225.49219,-4298.53125,4231.61523,-6350.65186,9869.77148

$$LAYER/5576.0

$$HATCHES/1,6,-6435.28613,9839.15918,-4383.16455,4201.00195,-4366.23828,4207.12451,-6418.35938,9845.28027,-6401.43213,9851.40430,-4349.31104,4213.24707,-4332.38428,4219.37012,-6384.50537,9857.52637,-6367.57861,9863.64844,-4315.45752,4225.49219,-4298.53125,4231.61523,-6350.65186,9869.77148

$$LAYER/5584.0

$$HATCHES/1,6,-6435.28613,9839.15918,-4383.16455,4201.00195,-4366.23828,4207.12451,-6418.35938,9845.28027,-6401.43213,9851.40430,-4349.31104,4213.24707,-4332.38428,4219.37012,-6384.50537,9857.52637,-6367.57861,9863.64844,-4315.45752,4225.49219,-4298.53125,4231.61523,-6350.65186,9869.77148

$$LAYER/5592.0

$$HATCHES/1,6,-6435.28613,9839.15918,-4383.16455,4201.00195,-4366.23828,4207.12451,-6418.35938,9845.28027,-6401.43213,9851.40430,-4349.31104,4213.24707,-4332.38428,4219.37012,-6384.50537,9857.52637,-6367.57861,9863.64844,-4315.45752,4225.49219,-4298.53125,4231.61523,-6350.65186,9869.77148

$$LAYER/5600.0

$$HATCHES/1,6,-6435.28613,9839.15918,-4383.16455,4201.00195,-4366.23828,4207.12451,-6418.35938,9845.28027,-6401.43213,9851.40430,-4349.31104,4213.24707,-4332.38428,4219.37012,-6384.50537,9857.52637,-6367.57861,9863.64844,-4315.45752,4225.49219,-4298.53125,4231.61523,-6350.65186,9869.77148

$$LAYER/5608.0

$$HATCHES/1,6,-6435.28613,9839.15918,-4383.16455,4201.00195,-4366.23828,4207.12451,-6418.35938,9845.28027,-6401.43213,9851.40430,-4349.31104,4213.24707,-4332.38428,4219.37012,-6384.50537,9857.52637,-6367.57861,9863.64844,-4315.45752,4225.49219,-4298.53125,4231.61523,-6350.65186,9869.77148

$$LAYER/5616.0

$$HATCHES/1,6,-6435.28613,9839.15918,-4383.16455,4201.00195,-4366.23828,4207.12451,-6418.35938,9845.28027,-6401.43213,9851.40430,-4349.31104,4213.24707,-4332.38428,4219.37012,-

6384.50537,9857.52637,-6367.57861,9863.64844,-4315.45752,4225.49219,-4298.53125,4231.61523,-6350.65186,9869.77148

$$LAYER/5624.0

$$HATCHES/1,6,-6435.28613,9839.15918,-4383.16455,4201.00195,-4366.23828,4207.12451,-6418.35938,9845.28027,-6401.43213,9851.40430,-4349.31104,4213.24707,-4332.38428,4219.37012,-6384.50537,9857.52637,-6367.57861,9863.64844,-4315.45752,4225.49219,-4298.53125,4231.61523,-6350.65186,9869.77148

$$LAYER/5632.0

$$HATCHES/1,6,-6435.28613,9839.15918,-4383.16455,4201.00195,-4366.23828,4207.12451,-6418.35938,9845.28027,-6401.43213,9851.40430,-4349.31104,4213.24707,-4332.38428,4219.37012,-6384.50537,9857.52637,-6367.57861,9863.64844,-4315.45752,4225.49219,-4298.53125,4231.61523,-6350.65186,9869.77148

$$LAYER/5640.0

$$HATCHES/1,6,-6435.28613,9839.15918,-4383.16455,4201.00195,-4366.23828,4207.12451,-6418.35938,9845.28027,-6401.43213,9851.40430,-4349.31104,4213.24707,-4332.38428,4219.37012,-6384.50537,9857.52637,-6367.57861,9863.64844,-4315.45752,4225.49219,-4298.53125,4231.61523,-6350.65186,9869.77148

$$LAYER/5648.0

$$HATCHES/1,6,-6435.28613,9839.15918,-4383.16455,4201.00195,-4366.23828,4207.12451,-6418.35938,9845.28027,-6401.43213,9851.40430,-4349.31104,4213.24707,-4332.38428,4219.37012,-6384.50537,9857.52637,-6367.57861,9863.64844,-4315.45752,4225.49219,-4298.53125,4231.61523,-6350.65186,9869.77148

$$LAYER/5656.0

$$HATCHES/1,6,-6435.28613,9839.15918,-4383.16455,4201.00195,-4366.23828,4207.12451,-6418.35938,9845.28027,-6401.43213,9851.40430,-4349.31104,4213.24707,-4332.38428,4219.37012,-6384.50537,9857.52637,-6367.57861,9863.64844,-4315.45752,4225.49219,-4298.53125,4231.61523,-6350.65186,9869.77148

$$LAYER/5664.0

$$HATCHES/1,6,-6435.28613,9839.15918,-4383.16455,4201.00195,-4366.23828,4207.12451,-6418.35938,9845.28027,-6401.43213,9851.40430,-4349.31104,4213.24707,-4332.38428,4219.37012,-6384.50537,9857.52637,-6367.57861,9863.64844,-4315.45752,4225.49219,-4298.53125,4231.61523,-6350.65186,9869.77148

$$LAYER/5672.0

$$HATCHES/1,6,-6435.28613,9839.15918,-4383.16455,4201.00195,-4366.23828,4207.12451,-6418.35938,9845.28027,-6401.43213,9851.40430,-4349.31104,4213.24707,-4332.38428,4219.37012,-6384.50537,9857.52637,-6367.57861,9863.64844,-4315.45752,4225.49219,-4298.53125,4231.61523,-6350.65186,9869.77148

$$LAYER/5680.0

$$HATCHES/1,6,-6435.28613,9839.15918,-4383.16455,4201.00195,-4366.23828,4207.12451,-6418.35938,9845.28027,-6401.43213,9851.40430,-4349.31104,4213.24707,-4332.38428,4219.37012,-6384.50537,9857.52637,-6367.57861,9863.64844,-4315.45752,4225.49219,-4298.53125,4231.61523,-6350.65186,9869.77148

$$LAYER/5688.0

$$HATCHES/1,6,-6435.28613,9839.15918,-4383.16455,4201.00195,-4366.23828,4207.12451,-6418.35938,9845.28027,-6401.43213,9851.40430,-4349.31104,4213.24707,-4332.38428,4219.37012,-6384.50537,9857.52637,-6367.57861,9863.64844,-4315.45752,4225.49219,-4298.53125,4231.61523,-6350.65186,9869.77148

$$LAYER/5696.0

$$HATCHES/1,6,-6435.28613,9839.15918,-4383.16455,4201.00195,-4366.23828,4207.12451,-6418.35938,9845.28027,-6401.43213,9851.40430,-4349.31104,4213.24707,-4332.38428,4219.37012,-6384.50537,9857.52637,-6367.57861,9863.64844,-4315.45752,4225.49219,-4298.53125,4231.61523,-6350.65186,9869.77148

$$LAYER/5704.0

$$HATCHES/1,6,-6435.28613,9839.15918,-4383.16455,4201.00195,-4366.23828,4207.12451,-6418.35938,9845.28027,-6401.43213,9851.40430,-4349.31104,4213.24707,-4332.38428,4219.37012,-6384.50537,9857.52637,-6367.57861,9863.64844,-4315.45752,4225.49219,-4298.53125,4231.61523,-6350.65186,9869.77148

$$LAYER/5712.0

$$HATCHES/1,6,-6435.28613,9839.15918,-4383.16455,4201.00195,-4366.23828,4207.12451,-6418.35938,9845.28027,-6401.43213,9851.40430,-4349.31104,4213.24707,-4332.38428,4219.37012,-6384.50537,9857.52637,-6367.57861,9863.64844,-4315.45752,4225.49219,-4298.53125,4231.61523,-6350.65186,9869.77148

$$LAYER/5720.0

$$HATCHES/1,6,-6435.28613,9839.15918,-4383.16455,4201.00195,-4366.23828,4207.12451,-6418.35938,9845.28027,-6401.43213,9851.40430,-4349.31104,4213.24707,-4332.38428,4219.37012,-6384.50537,9857.52637,-6367.57861,9863.64844,-4315.45752,4225.49219,-4298.53125,4231.61523,-6350.65186,9869.77148

$$LAYER/5728.0

$$HATCHES/1,6,-6435.28613,9839.15918,-4383.16455,4201.00195,-4366.23828,4207.12451,-6418.35938,9845.28027,-6401.43213,9851.40430,-4349.31104,4213.24707,-4332.38428,4219.37012,-

6384.50537,9857.52637,-6367.57861,9863.64844,-4315.45752,4225.49219,-4298.53125,4231.61523,-6350.65186,9869.77148

$$LAYER/5736.0

$$HATCHES/1,6,-6435.28613,9839.15918,-4383.16455,4201.00195,-4366.23828,4207.12451,-6418.35938,9845.28027,-6401.43213,9851.40430,-4349.31104,4213.24707,-4332.38428,4219.37012,-6384.50537,9857.52637,-6367.57861,9863.64844,-4315.45752,4225.49219,-4298.53125,4231.61523,-6350.65186,9869.77148

$$LAYER/5744.0

$$HATCHES/1,6,-6435.28613,9839.15918,-4383.16455,4201.00195,-4366.23828,4207.12451,-6418.35938,9845.28027,-6401.43213,9851.40430,-4349.31104,4213.24707,-4332.38428,4219.37012,-6384.50537,9857.52637,-6367.57861,9863.64844,-4315.45752,4225.49219,-4298.53125,4231.61523,-6350.65186,9869.77148

$$LAYER/5752.0

$$HATCHES/1,6,-6435.28613,9839.15918,-4383.16455,4201.00195,-4366.23828,4207.12451,-6418.35938,9845.28027,-6401.43213,9851.40430,-4349.31104,4213.24707,-4332.38428,4219.37012,-6384.50537,9857.52637,-6367.57861,9863.64844,-4315.45752,4225.49219,-4298.53125,4231.61523,-6350.65186,9869.77148

$$LAYER/5760.0

$$HATCHES/1,6,-6435.28613,9839.15918,-4383.16455,4201.00195,-4366.23828,4207.12451,-6418.35938,9845.28027,-6401.43213,9851.40430,-4349.31104,4213.24707,-4332.38428,4219.37012,-6384.50537,9857.52637,-6367.57861,9863.64844,-4315.45752,4225.49219,-4298.53125,4231.61523,-6350.65186,9869.77148

$$LAYER/5768.0

$$HATCHES/1,6,-6435.28613,9839.15918,-4383.16455,4201.00195,-4366.23828,4207.12451,-6418.35938,9845.28027,-6401.43213,9851.40430,-4349.31104,4213.24707,-4332.38428,4219.37012,-6384.50537,9857.52637,-6367.57861,9863.64844,-4315.45752,4225.49219,-4298.53125,4231.61523,-6350.65186,9869.77148

$$LAYER/5776.0

$$HATCHES/1,6,-6435.28613,9839.15918,-4383.16455,4201.00195,-4366.23828,4207.12451,-6418.35938,9845.28027,-6401.43213,9851.40430,-4349.31104,4213.24707,-4332.38428,4219.37012,-6384.50537,9857.52637,-6367.57861,9863.64844,-4315.45752,4225.49219,-4298.53125,4231.61523,-6350.65186,9869.77148

$$LAYER/5784.0

$$HATCHES/1,6,-6435.28613,9839.15918,-4383.16455,4201.00195,-4366.23828,4207.12451,-6418.35938,9845.28027,-6401.43213,9851.40430,-4349.31104,4213.24707,-4332.38428,4219.37012,-6384.50537,9857.52637,-6367.57861,9863.64844,-4315.45752,4225.49219,-4298.53125,4231.61523,-6350.65186,9869.77148

$$LAYER/5792.0

$$HATCHES/1,6,-6435.28613,9839.15918,-4383.16455,4201.00195,-4366.23828,4207.12451,-6418.35938,9845.28027,-6401.43213,9851.40430,-4349.31104,4213.24707,-4332.38428,4219.37012,-6384.50537,9857.52637,-6367.57861,9863.64844,-4315.45752,4225.49219,-4298.53125,4231.61523,-6350.65186,9869.77148

$$LAYER/5800.0

$$HATCHES/1,6,-6435.28613,9839.15918,-4383.16455,4201.00195,-4366.23828,4207.12451,-6418.35938,9845.28027,-6401.43213,9851.40430,-4349.31104,4213.24707,-4332.38428,4219.37012,-6384.50537,9857.52637,-6367.57861,9863.64844,-4315.45752,4225.49219,-4298.53125,4231.61523,-6350.65186,9869.77148

$$LAYER/5808.0

$$HATCHES/1,6,-6435.28613,9839.15918,-4383.16455,4201.00195,-4366.23828,4207.12451,-6418.35938,9845.28027,-6401.43213,9851.40430,-4349.31104,4213.24707,-4332.38428,4219.37012,-6384.50537,9857.52637,-6367.57861,9863.64844,-4315.45752,4225.49219,-4298.53125,4231.61523,-6350.65186,9869.77148

$$LAYER/5816.0

$$HATCHES/1,6,-6435.28613,9839.15918,-4383.16455,4201.00195,-4366.23828,4207.12451,-6418.35938,9845.28027,-6401.43213,9851.40430,-4349.31104,4213.24707,-4332.38428,4219.37012,-6384.50537,9857.52637,-6367.57861,9863.64844,-4315.45752,4225.49219,-4298.53125,4231.61523,-6350.65186,9869.77148

$$LAYER/5824.0

$$HATCHES/1,6,-6435.28613,9839.15918,-4383.16455,4201.00195,-4366.23828,4207.12451,-6418.35938,9845.28027,-6401.43213,9851.40430,-4349.31104,4213.24707,-4332.38428,4219.37012,-6384.50537,9857.52637,-6367.57861,9863.64844,-4315.45752,4225.49219,-4298.53125,4231.61523,-6350.65186,9869.77148

$$LAYER/5832.0

$$HATCHES/1,6,-6435.28613,9839.15918,-4383.16455,4201.00195,-4366.23828,4207.12451,-6418.35938,9845.28027,-6401.43213,9851.40430,-4349.31104,4213.24707,-4332.38428,4219.37012,-6384.50537,9857.52637,-6367.57861,9863.64844,-4315.45752,4225.49219,-4298.53125,4231.61523,-6350.65186,9869.77148

$$LAYER/5840.0

$$HATCHES/1,6,-6435.28613,9839.15918,-4383.16455,4201.00195,-4366.23828,4207.12451,-6418.35938,9845.28027,-6401.43213,9851.40430,-4349.31104,4213.24707,-4332.38428,4219.37012,-

6384.50537,9857.52637,-6367.57861,9863.64844,-4315.45752,4225.49219,-4298.53125,4231.61523,-6350.65186,9869.77148

$$LAYER/5848.0

$$HATCHES/1,6,-6435.28613,9839.15918,-4383.16455,4201.00195,-4366.23828,4207.12451,-6418.35938,9845.28027,-6401.43213,9851.40430,-4349.31104,4213.24707,-4332.38428,4219.37012,-6384.50537,9857.52637,-6367.57861,9863.64844,-4315.45752,4225.49219,-4298.53125,4231.61523,-6350.65186,9869.77148

$$LAYER/5856.0

$$HATCHES/1,6,-6435.28613,9839.15918,-4383.16455,4201.00195,-4366.23828,4207.12451,-6418.35938,9845.28027,-6401.43213,9851.40430,-4349.31104,4213.24707,-4332.38428,4219.37012,-6384.50537,9857.52637,-6367.57861,9863.64844,-4315.45752,4225.49219,-4298.53125,4231.61523,-6350.65186,9869.77148

$$LAYER/5864.0

$$HATCHES/1,6,-6435.28613,9839.15918,-4383.16455,4201.00195,-4366.23828,4207.12451,-6418.35938,9845.28027,-6401.43213,9851.40430,-4349.31104,4213.24707,-4332.38428,4219.37012,-6384.50537,9857.52637,-6367.57861,9863.64844,-4315.45752,4225.49219,-4298.53125,4231.61523,-6350.65186,9869.77148

$$LAYER/5872.0

$$HATCHES/1,6,-6435.28613,9839.15918,-4383.16455,4201.00195,-4366.23828,4207.12451,-6418.35938,9845.28027,-6401.43213,9851.40430,-4349.31104,4213.24707,-4332.38428,4219.37012,-6384.50537,9857.52637,-6367.57861,9863.64844,-4315.45752,4225.49219,-4298.53125,4231.61523,-6350.65186,9869.77148

$$LAYER/5880.0

$$HATCHES/1,6,-6435.28613,9839.15918,-4383.16455,4201.00195,-4366.23828,4207.12451,-6418.35938,9845.28027,-6401.43213,9851.40430,-4349.31104,4213.24707,-4332.38428,4219.37012,-6384.50537,9857.52637,-6367.57861,9863.64844,-4315.45752,4225.49219,-4298.53125,4231.61523,-6350.65186,9869.77148

$$LAYER/5888.0

$$HATCHES/1,6,-6435.28613,9839.15918,-4383.16455,4201.00195,-4366.23828,4207.12451,-6418.35938,9845.28027,-6401.43213,9851.40430,-4349.31104,4213.24707,-4332.38428,4219.37012,-6384.50537,9857.52637,-6367.57861,9863.64844,-4315.45752,4225.49219,-4298.53125,4231.61523,-6350.65186,9869.77148

$$LAYER/5896.0

$$HATCHES/1,6,-6435.28613,9839.15918,-4383.16455,4201.00195,-4366.23828,4207.12451,-6418.35938,9845.28027,-6401.43213,9851.40430,-4349.31104,4213.24707,-4332.38428,4219.37012,-6384.50537,9857.52637,-6367.57861,9863.64844,-4315.45752,4225.49219,-4298.53125,4231.61523,-6350.65186,9869.77148

$$LAYER/5904.0

$$HATCHES/1,6,-6435.28613,9839.15918,-4383.16455,4201.00195,-4366.23828,4207.12451,-6418.35938,9845.28027,-6401.43213,9851.40430,-4349.31104,4213.24707,-4332.38428,4219.37012,-6384.50537,9857.52637,-6367.57861,9863.64844,-4315.45752,4225.49219,-4298.53125,4231.61523,-6350.65186,9869.77148

$$LAYER/5912.0

$$HATCHES/1,6,-6435.28613,9839.15918,-4383.16455,4201.00195,-4366.23828,4207.12451,-6418.35938,9845.28027,-6401.43213,9851.40430,-4349.31104,4213.24707,-4332.38428,4219.37012,-6384.50537,9857.52637,-6367.57861,9863.64844,-4315.45752,4225.49219,-4298.53125,4231.61523,-6350.65186,9869.77148

$$LAYER/5920.0

$$HATCHES/1,6,-6435.28613,9839.15918,-4383.16455,4201.00195,-4366.23828,4207.12451,-6418.35938,9845.28027,-6401.43213,9851.40430,-4349.31104,4213.24707,-4332.38428,4219.37012,-6384.50537,9857.52637,-6367.57861,9863.64844,-4315.45752,4225.49219,-4298.53125,4231.61523,-6350.65186,9869.77148

$$LAYER/5928.0

$$HATCHES/1,6,-6435.28613,9839.15918,-4383.16455,4201.00195,-4366.23828,4207.12451,-6418.35938,9845.28027,-6401.43213,9851.40430,-4349.31104,4213.24707,-4332.38428,4219.37012,-6384.50537,9857.52637,-6367.57861,9863.64844,-4315.45752,4225.49219,-4298.53125,4231.61523,-6350.65186,9869.77148

$$LAYER/5936.0

$$HATCHES/1,6,-6435.28613,9839.15918,-4383.16455,4201.00195,-4366.23828,4207.12451,-6418.35938,9845.28027,-6401.43213,9851.40430,-4349.31104,4213.24707,-4332.38428,4219.37012,-6384.50537,9857.52637,-6367.57861,9863.64844,-4315.45752,4225.49219,-4298.53125,4231.61523,-6350.65186,9869.77148

$$LAYER/5944.0

$$HATCHES/1,6,-6435.28613,9839.15918,-4383.16455,4201.00195,-4366.23828,4207.12451,-6418.35938,9845.28027,-6401.43213,9851.40430,-4349.31104,4213.24707,-4332.38428,4219.37012,-6384.50537,9857.52637,-6367.57861,9863.64844,-4315.45752,4225.49219,-4298.53125,4231.61523,-6350.65186,9869.77148

$$LAYER/5952.0

$$HATCHES/1,6,-6435.28613,9839.15918,-4383.16455,4201.00195,-4366.23828,4207.12451,-6418.35938,9845.28027,-6401.43213,9851.40430,-4349.31104,4213.24707,-4332.38428,4219.37012,-

6384.50537,9857.52637,-6367.57861,9863.64844,-4315.45752,4225.49219,-4298.53125,4231.61523,-6350.65186,9869.77148

$$LAYER/5960.0

$$HATCHES/1,6,-6435.28613,9839.15918,-4383.16455,4201.00195,-4366.23828,4207.12451,-6418.35938,9845.28027,-6401.43213,9851.40430,-4349.31104,4213.24707,-4332.38428,4219.37012,-6384.50537,9857.52637,-6367.57861,9863.64844,-4315.45752,4225.49219,-4298.53125,4231.61523,-6350.65186,9869.77148

$$LAYER/5968.0

$$HATCHES/1,6,-6435.28613,9839.15918,-4383.16455,4201.00195,-4366.23828,4207.12451,-6418.35938,9845.28027,-6401.43213,9851.40430,-4349.31104,4213.24707,-4332.38428,4219.37012,-6384.50537,9857.52637,-6367.57861,9863.64844,-4315.45752,4225.49219,-4298.53125,4231.61523,-6350.65186,9869.77148

$$LAYER/5976.0

$$HATCHES/1,6,-6435.28613,9839.15918,-4383.16455,4201.00195,-4366.23828,4207.12451,-6418.35938,9845.28027,-6401.43213,9851.40430,-4349.31104,4213.24707,-4332.38428,4219.37012,-6384.50537,9857.52637,-6367.57861,9863.64844,-4315.45752,4225.49219,-4298.53125,4231.61523,-6350.65186,9869.77148

$$LAYER/5984.0

$$HATCHES/1,6,-6435.28613,9839.15918,-4383.16455,4201.00195,-4366.23828,4207.12451,-6418.35938,9845.28027,-6401.43213,9851.40430,-4349.31104,4213.24707,-4332.38428,4219.37012,-6384.50537,9857.52637,-6367.57861,9863.64844,-4315.45752,4225.49219,-4298.53125,4231.61523,-6350.65186,9869.77148

$$LAYER/5992.0

$$HATCHES/1,6,-6435.28613,9839.15918,-4383.16455,4201.00195,-4366.23828,4207.12451,-6418.35938,9845.28027,-6401.43213,9851.40430,-4349.31104,4213.24707,-4332.38428,4219.37012,-6384.50537,9857.52637,-6367.57861,9863.64844,-4315.45752,4225.49219,-4298.53125,4231.61523,-6350.65186,9869.77148

$$LAYER/6000.0

$$HATCHES/1,6,-6435.28613,9839.15918,-4383.16455,4201.00195,-4366.23828,4207.12451,-6418.35938,9845.28027,-6401.43213,9851.40430,-4349.31104,4213.24707,-4332.38428,4219.37012,-6384.50537,9857.52637,-6367.57861,9863.64844,-4315.45752,4225.49219,-4298.53125,4231.61523,-6350.65186,9869.77148

$$LAYER/6008.0

$$GEOMETRYEND